



HAL
open science

The development of simulation and atmospheric shower reconstruction tools for the study of future Cherenkov Imaging telescopes

Saeeda Sajjad

► **To cite this version:**

Saeeda Sajjad. The development of simulation and atmospheric shower reconstruction tools for the study of future Cherenkov Imaging telescopes. *Cosmology and Extra-Galactic Astrophysics [astro-ph.CO]*. Université Montpellier II - Sciences et Techniques du Languedoc, 2007. English. NNT : . tel-00408835

HAL Id: tel-00408835

<https://theses.hal.science/tel-00408835>

Submitted on 3 Aug 2009

HAL is a multi-disciplinary open access archive for the deposit and dissemination of scientific research documents, whether they are published or not. The documents may come from teaching and research institutions in France or abroad, or from public or private research centers.

L'archive ouverte pluridisciplinaire **HAL**, est destinée au dépôt et à la diffusion de documents scientifiques de niveau recherche, publiés ou non, émanant des établissements d'enseignement et de recherche français ou étrangers, des laboratoires publics ou privés.

UNIVERSITÉ MONTPELLIER II
SCIENCES ET TECHNIQUE DU LANGUEDOC

THESIS

submitted to obtain the degree of

DOCTEUR DE L'UNIVERSITÉ MONTPELLIER II

Discipline : Astroparticle physics
Formation doctorale : Physique de la matière condensée
École doctorale : Sciences chimiques et physiques

presented and publicly defended by

Saeeda SAJJAD

on the 17th of September 2007

The development of simulation
and atmospheric shower reconstruction tools
for the study of
future Cherenkov Imaging telescopes

Jury

MM.
Fabrice Feinstein , President
Jacques Dumarchez , Rapporteur
Gérard Fontaine , Rapporteur
Edmond Giraud , Supervisor
Manel Martínez , Examiner
Alain Falvard , Examiner

You cannot teach a man anything; you can only help him find it within himself.
Galileo Galilei (1564-1642)

ACKNOWLEDGEMENTS

My sincere thanks go out to all the members of the jury for their input in various capacities. In particular, I am grateful to the rapporteurs for this thesis, Jacques Dumarchez and Gérard Fontaine, for the time they spent reading this document and giving valuable feedback on it. I would also like to thank Fabrice Feinstein who presided this jury and Manel Martínez for his participation as examiner. I am specially grateful to Edmond Giraud for his support as supervisor of this PhD.

My warm thanks go out to Alain Falvard under whose direction the work presented in this thesis was carried out. It has been a privilege and a pleasure to work with him, learn from him, discuss with him and have his support and guidance through all of it.

I would also like to thank everyone at the LPTA and in particular those from the astroparticle group: Yves Gallant, Agnieszka Jacholkowska, Nukri Komin, Morgan LeDelliou, Alexandre Marcowith, Emmanuel Moulin, Eric Nuss, Frederic Piron. Many thanks to Georges Vasileaidis for his help on many occasions.

Many thanks also to Françoise Amat, Dominique Caron, Josette Cellier, Nicolas Clementin, Jacqueline Dinthillac, Françoise Duceau, Aicha Halouani, Jacques Maurand, Stéphane Rivoire and Claude Zurbach for their help. Special thanks to Sylviane Colaiocco for the enjoyable time spent together.

These acknowledgements would not be complete without mentioning Michèle Bourgeat whose warm presence was a precious source of support. I would also like to thank Claudia Lavalley for the many discussions we had together and all her support when I was writing this thesis. I am also thankful to Mariusz Sapinski for his company and help early on, and for the fun times we had together as well as Javier Bussons Gordo for his sincerity and support, and for the lovely moments I had with him and his beautiful family.

This PhD would not have been the same without the constant support, encouragement and camaraderie of Julien Bolmont and Richard Britto who both started their PhD at the same time as I did. They were later joined by Sylvain Guiriec whose support and presence were equally precious and Armand Fiasson whose company I also appreciated a lot.

Many thanks also to Julien Lavalley, Christian Farnier and Veronique Pelassa as well as Sean Bailly, Dominique Chevriaux, Andrea Chiavassa, Mohamed Faquir, Radouane Gannouji, Marwan Gebran, Romain Gicquaud, Federico Manna, Nada Sahoury, Lionel Touzellier.

There were also people outside the LPTA who helped me and I would particularly like to thank David Maurin and Elisabeth Brion for the moral encouragement they provided.

My gratitude also goes out to François Delduc, Jean François Mathiot, Michèle Chadelas and the lady from the bureau des hébergements in Lyon for their help and support during my DEA.

I have also been lucky to have some wonderful teachers throughout my life as a student and this thesis owes them in more ways than one. It would be impossible for me to name them all

here but I would like to mention A. H. Nayyar, Naseem Zafar, Khurshid Hasanain, Zafar Iqbal, Pervez Hoodbhoy and Azra Nuruddin who had the deepest influence on the way I studied physics.

I would also like to thank Tom for cultivating a place where support and encouragement are so freely exchanged and all those whose company and contributions there have been a valuable source of strength for me.

Finally, I would like to thank the many friends met in France as well as those from Pakistan. I would specially like to thank Rabia, Maya and Viviann without whom this period would have been much harder to go through. Many thanks also to my family, aunts, uncles and cousins.

My last words here go out to my brother and mother who believed in me even through the hardest of times. Aqil thank you for being a great brother and Ammi thank you for all you have taught me about life and for being my strength since the day I was born.

CONTENTS

Title page	1
Acknowledgements	5
Contents	7
I Introduction	15
1 The context in gamma-ray astronomy	17
1.1 The sources	17
Current status of knowledge	18
1.2 Gamma-ray telescopes	18
1.2.1 Energy domains	18
Satellites: low energy domain	18
Ground based Cherenkov telescopes: medium to high energy domain	18
Ground based extensive air shower detectors: very high energy domain	19
1.2.2 Sky coverage and angular resolution	19
1.2.3 Sensitivity	20
1.3 Future Telescopes	21
1.3.1 Future IACT systems	21
Sensitivity	21
Field of view	22
Angular resolution	23
Energy resolution	23
Energy range and requirements	23
1.3.2 Introduction to this thesis and outline	24
II Atmospheric showers and their simulation	27
2 Electromagnetic showers in the atmosphere	29
2.1 The atmosphere and its models	29
2.1.1 Composition and layers	29
2.1.2 A complex system	30
2.1.3 Atmosphere Models	30

	Atmosphere monitoring in ground based telescopes	30
	Simplified models	31
	The Isothermal model	31
	The U. S. Standard atmosphere (Linsley's parametrisation)	31
2.2	Shower generation and development	33
2.2.1	The first interaction: pair production	33
2.2.2	Bremsstrahlung	34
2.2.3	Particle Multiplication and high energy secondaries	35
	Heitler's model	35
2.2.4	Critical energy and the low energy regime	36
2.2.5	Other/Minor processes	36
2.3	Shower morphology	37
2.3.1	Main features illustrated through examples of showers	37
2.3.2	Longitudinal development	38
	Fraction of the shower cut-off at observation level	40
2.3.3	Lateral profile	42
3	Cherenkov emission in atmospheric showers	43
3.1	Basic facts	43
3.2	Cherenkov emission profile in an electromagnetic shower	44
3.2.1	Role of the atmosphere	44
3.2.2	Longitudinal profile of the Cherenkov emission	45
	Dependence on primary angle	47
3.2.3	The number of Cherenkov photons produced	48
3.3	Extinction and transmission	49
3.3.1	Absorption	49
3.3.2	Scattering	50
	Rayleigh scattering	50
	Mie scattering	50
3.4	Cherenkov light density on the ground	50
3.4.1	Geometry	50
3.4.2	Dependence on primary energy	53
3.4.3	Low altitude materialisations	55
3.4.4	Effect of ground altitude	56
	Effect on the total number of Cherenkov photons	58
3.4.5	Primary zenith angle	58
3.4.6	Wave front and temporal distribution	60
3.5	Effect of geographical parameters	62
3.5.1	Effect of the atmosphere profile	62
3.5.2	Effect of the geomagnetic field	63
4	Atmospheric shower simulations with CORSIKA	65
4.1	Introduction	65
4.2	Simulations with CORSIKA	65
4.3	Shower generation in CORSIKA	66
4.3.1	Electromagnetic interactions	66
4.3.2	Hadronic interactions	66
	Low energy interactions	67
	High energy interactions	67
4.3.3	Particle tracking	67

Minimum particle energy	67
4.4 Cherenkov light treatment in CORSIKA	69
4.5 Atmosphere and transmission of Cherenkov light	70
4.5.1 Atmosphere models	70
4.5.2 Atmospheric extinction	71
4.6 Mirror reflectivity and photomultiplier quantum efficiency	71
4.7 CORSIKA output	72
4.8 Personal addition	72
4.9 Comparison with known results	73
III IACT, their simulation and shower images	75
5 Imaging Atmospheric Cherenkov Telescopes and their simulation	77
5.1 Introduction	77
5.2 Telescope parts	78
5.2.1 The reflector	78
Parabolic mirrors	78
The parabola	79
Reflective property	79
Implications for point sources at various distances	79
Coma aberration	80
Isochronism	82
Different reflector types	82
5.2.2 Camera and electronics	83
5.3 Telescope simulation	83
5.3.1 Simplification and choices	83
5.3.2 Flexibility	84
5.3.3 Principle	85
Intersection	85
Reflection	85
Image formation on the camera	86
5.3.4 Implementation	86
Image reading program	87
5.3.5 Example of simulation	87
6 Shower images and their properties	91
6.1 Introduction	91
What do we mean by an image?	91
A note on the terminology used	92
6.2 General ideas concerning shower images	92
6.2.1 Assumptions	93
6.2.2 Single point mapping	93
6.2.3 Shower axis mapping	94
6.2.4 Non-linearity of the mapping and camera coordinate system	95
6.3 Source position in the sky	96
6.4 Shower core and the orientation of the shower image	97
6.5 General shape of the image	98
6.5.1 The effect of the telescope distance from the core	98
The height of emission of photons	100

6.6	The number of photo-electrons contained in the image	100
6.6.1	Cherenkov photon density on the ground and its dependence on various factors	100
6.6.2	Telescope characteristics	103
6.7	Image resolution	103
IV	Shower reconstruction and ideas for γ-hadron separation	107
Preliminaries		109
	Working with real images	109
	The system used for the studies presented in this part	110
7	Source and shower core position reconstruction	111
	Multi-telescope images of the same shower	111
7.1	Source position reconstruction	114
7.1.1	Principle and likelihood function	114
7.1.2	Gaussian probability density function for the transverse profile	115
	Determining the value of σ_t for the reconstruction methods	117
7.1.3	Implementation of the source reconstruction method	119
	Preliminary scan	121
	Main features	121
	The effect of shower core position	122
	Likelihood maximisation with Minuit	124
7.1.4	Results	124
	Examples	125
	General results	126
	Dependence on energy and shower core	128
	The efficiency of reconstruction	129
7.2	Core position reconstruction	131
7.2.1	Image orientation and core position	131
7.2.2	Principle and likelihood function	131
	Correction due to the source position	132
7.2.3	Implementation of the shower core reconstruction method	132
	Preliminary scan	132
	The effect of shower core position	134
	Likelihood maximisation with Minuit	134
7.2.4	Results	134
	Dependence on energy and shower core	137
	The efficiency of reconstruction	138
7.3	Additional considerations	138
7.3.1	The impact of coma aberration	138
7.3.2	Image cleaning	139
	Image cleaning methods	140
	Effects on shower parameter reconstruction	140
	Examples	140
	Effect on parameter reconstruction precision	142
	Remarks on the optimum image cleaning threshold	144
7.3.3	Transverse profiles and σ_t revisited	144
	A discussion on the quality of the Gaussian fits	146

	The Gaussian approximation: χ^2 of the Gaussian fits	146
	The impact of isolated pixels or bunches: comparing σ_t with the root mean square	146
	The dependence of σ_t on the distance between the telescope and the shower core position	150
	The effect of image cleaning on σ_t 's dependence on the distance between the core and telescope positions	152
	The effect of σ_t value on source and shower reconstruction	153
7.3.4	A note on χ^2 minimisation of fits and its possible use	153
	The Gaussian approximation for the transverse profile is rough	154
	The dependence on the value of σ_t	154
7.3.5	Use of the longitudinal asymmetry in the images	156
8	Energy reconstruction	159
8.1	Principle: the relationship between the number of Cherenkov photons and shower energy	159
8.2	Photo-electron number tables	161
8.3	Implementation	161
8.4	Results	162
8.5	Discussion on various aspects of energy reconstruction	164
8.5.1	Giving different weights to the information from different telescopes	164
8.5.2	The asymmetry of the number of photo-electron distributions in telescope images	166
	The effect on energy reconstruction	168
8.5.3	Using most probable value tables for energy reconstruction	171
	Fits and value table	171
	Results	172
8.5.4	Link of the asymmetry with the altitude of first interaction in the shower	172
8.5.5	Possible solution for improving the reconstruction of energy	176
8.6	Conclusion and remarks on the limitations of the method	176
8.7	Reconstruction of the longitudinal profile and Cherenkov photon trajectories	179
8.7.1	The method	181
	A note on the reflection of photons by the mirror centre	181
8.7.2	Reconstructed longitudinal profiles	181
9	Ideas for gamma-hadron separation	183
9.1	Introduction	183
9.2	Hadronic showers and their images	184
9.2.1	Hadronic shower development	184
9.2.2	Cherenkov photon production and density on the ground	186
9.2.3	Hadron shower images	188
9.2.4	Hadrons as a source of background for γ -observations	193
9.3	Ideas for γ -hadron separation	193
9.3.1	Using the χ^2 of the source and core reconstruction fits	193
9.3.2	Reconstructed longitudinal profile	195
9.3.3	Using the reconstructed point of emission of Cherenkov photons	197
	The distribution of d_{min} in γ -ray and hadronic showers	198
	Two dimensional distributions between d_{min} and reconstructed height of emission	201
	The application of cuts on the reconstruction point of emission	203

9.3.4	Conclusions	204
V	Application and conclusions	207
10	Future imaging atmospheric telescopes: performance of possible array configurations for gamma photons in the GeV-TeV range	209
10.1	Introduction	209
10.2	Energy domains and choices for telescopes	210
10.2.1	High energy domain $300 \text{ GeV} < E < 10 \text{ TeV}$	210
10.2.2	Low energy domain $E < 300 \text{ GeV}$	210
10.2.3	Very high energy domain $E > 10 \text{ TeV}$	211
10.3	The altitude of observation	211
10.4	A note on some other parameters	212
10.4.1	Pixel size	212
10.4.2	The field of view	212
10.5	Optimising inter-telescope distance	212
10.5.1	Shower parameter reconstruction as a function of inter-telescope distance	213
	Source reconstruction	213
	Shower core reconstruction	214
	Energy reconstruction	217
	Effective area	217
	Conclusions	218
10.6	Array design	219
10.6.1	Low altitude configurations	219
	Low energy part	219
	High energy part	219
	Obtaining a denser system	219
10.6.2	High altitude configurations	220
10.7	Study of the γ -ray observation capability of the large arrays	220
10.7.1	Results	220
	Effective area	221
	Source reconstruction	221
	Reconstruction of the core position on the ground	222
	Energy resolution	223
10.7.2	Comparison with four-telescope array	224
10.8	Conclusions and perspective	226
11	Conclusions	229
11.1	Summary	229
11.2	Future directions	230
11.2.1	Telescope simulation program	230
11.2.2	γ -ray reconstruction methods	230
11.2.3	Gamma-hadron separation	231
11.2.4	Future IACT arrays	232
	Appendix	233
A	Figures	233

B Longitudinal profile parametrisation 239

Summary in French 243

C Résumé en français	243
C.1 Introduction	243
C.1.1 Les sources	243
C.1.2 Les télescopes gamma et leurs caractéristiques	244
Satellites	244
Télescopes Tcherenkov au sol	244
Télescopes pour les grandes gerbes atmosphériques au sol	244
C.1.3 Buts des futurs télescopes imageurs	245
C.1.4 Contenu de la thèse	246
C.2 Les gerbes atmosphériques et leur simulation	246
C.2.1 Les gerbes électromagnétiques dans l'atmosphère	246
L'atmosphère terrestre et ses modèles	246
Production d'une cascade	247
La première interaction: production de paire	247
Bremsstrahlung	247
Multiplication des particules, énergie critique et régime de basse énergie	248
Morphologie des cascades	248
C.2.2 Émission Tcherenkov dans les gerbes atmosphériques	249
Profil d'émission Cherenkov dans une gerbe électromagnétique	249
Le profil longitudinal de l'émission Tcherenkov	249
Extinction et transmission	249
Densité de lumière Cherenkov sur le sol	250
C.2.3 Simulation des gerbes atmosphériques avec CORSIKA	251
C.3 Télescopes imageurs Tcherenkov : simulations et image des gerbes	251
C.3.1 Les télescopes à imagerie par effet Tcherenkov atmosphérique et leur simulation	251
Choix de la forme du miroir	251
Camera	252
Sortie	252
Flexibilité du programme de simulation	252
C.3.2 Les images des gerbes et leurs propriétés	252
La morphologie des images et leur orientation	252
Le nombre de photo-électrons dans les images	253
C.4 La reconstruction des gerbes et propositions pour la séparation γ -hadrons	255
C.4.1 Reconstruction de la position de la source et du pied de gerbe	255
La reconstruction de la source	255
Résultats	256
La reconstruction du pied de gerbe	257
Résultats	258
Considérations additionnelles	258
Nettoyage de l'image	258
Discussion sur l'utilisation de σ_t dans la reconstruction de la source et du pied de gerbe	260
Le χ^2 des ajustements pour la maximisation de vraisemblance	260

	Remarque sur l'utilisation de la symétrie longitudinale des images	261
C.4.2	Reconstruction de l'énergie	261
	Résultats	261
	Solution possible pour améliorer la reconstruction de l'énergie	262
C.4.3	Propositions pour la séparation γ -hadrons	262
	Les gerbes hadroniques et leurs images	263
	Le développement des gerbes hadroniques	263
	L'émission de photons Tcherenkov	264
	Les images des gerbes hadroniques et les hadrons en tant que fond pour les observations de photons gamma	264
	Propositions pour la séparation hadron-gamma	265
	L'utilisation du χ^2 des ajustements pour la reconstruction de la source et du pied de gerbe	265
	Profils longitudinaux reconstruits	266
	L'utilisation du point d'émission reconstruit des photons Tcherenkov	266
C.5	Application et conclusion	269
C.5.1	Futur des imageurs atmosphériques : capacités de détection de deux réseaux de télescopes pour les photons dans la gamme GeV-TeV	269
	Les domaines d'énergie et les paramètres des réseaux de télescopes	269
	Haute énergie : 300 GeV - 10 TeV	269
	Basse énergie : < 30 GeV	269
	Distance optimale entre les télescopes	269
	Configurations possibles de réseaux d'IAC	271
	Configurations pour la basse altitude	271
	Configurations à haute altitude	271
	Les performances des réseaux possibles pour les photons gamma	271
C.5.2	Conclusion et directions futures	272
	Programme de simulation de télescope	274
	Reconstruction des paramètres de rayons gamma	274
	Séparation hadron-gamma	275
	Futurs réseaux de télescopes Tcherenkov imageurs	275
	Bibliography	277
	Abstract	281

*P*_{ART} *I*

*I*NTRODUCTION

CHAPTER 1

THE CONTEXT IN GAMMA-RAY ASTRONOMY

In astrophysics, we “observe” different phenomena and objects either directly through different kinds of emissions or indirectly i. e. by observing their impact on other objects (e. g. through gravitational effects, deduction of the presence of dark matter etc..) These different kinds of emissions from astrophysical objects include charged cosmic rays (CR), different parts of the electromagnetic spectrum, neutrinos, gravitational waves etc.. Moreover, the field is rapidly evolving: the last century has seen astronomy develop from being mainly based on visible light to its current state where it uses a wide variety of “information carriers” from astrophysical objects. In particular, observations in the electromagnetic spectrum now range from the radio wave domain (with wavelengths beyond 3 m) to the γ -ray domain (with wavelengths smaller than 0.01 nm or energies beyond a few 100 keV).

1.1 The sources

γ -ray astronomy provides us with an access to the most violent and energetic phenomena in our galaxy and beyond it: the non-thermal universe. While these violent events give emission in low energy wavelengths as well, it is the emission from the thermal universe that dominates at these energies. On the other hand γ -ray emissions allow us to solely observe high energy phenomenon in the universe. Moreover, the gamma photons are not affected by the presence of galactic and extra-galactic magnetic fields, therefore retaining the direction of their source. The production of γ -rays requires the acceleration and interaction of relativistic particles at very high energies. The main mechanisms of production of γ -rays include the collision of charged cosmic rays with the interstellar medium, particle-antiparticle annihilation and the acceleration and deviation of charged particles through electromagnetic fields. This emission through acceleration can occur through Bremsstrahlung, synchrotron emission and Compton diffusion. In addition to these, high energy electrons can transfer part of their energy to an X-ray photon, in a collision, converting it into a γ -ray photon.

The high energy phenomena leading to the production of these γ -rays include supernovae explosions and their remnants which are capable of accelerating charged particle to very high energies. The jets of pulsars also have particles moving close to the speed of light. Similarly, the accretion disks, formed in binary systems with a black hole or a neutron star, are also responsible for the emission of γ -rays. Extra-galactic phenomena which produce γ -rays include Active Galactic Nuclei (AGN) with relativistic jets formed due to massive compact objects at their centre. Gamma Ray Bursts (GRB) are the most violent events in the known universe and are also sources of γ -rays. Observations also show a diffuse galactic emission, resulting from

the interaction of cosmic rays with the interstellar medium as well as a diffuse extra-galactic emission partially associated with unresolved AGN.

Current status of knowledge

Some of these objects, like SN explosions and their remnants, have been known for a long time, yet it is only with the observations in recent times that we have begun to understand the mechanisms involved. Others, like AGNs, GRBs, micro-quasars..., have only been discovered recently. In all cases, a large number of questions remain concerning these objects. Various models have been developed to describe them. However, it is through further observations that some of these models will be accepted, rejected or constrained. For instance the mechanisms involved in the propagation of pulsar winds and their interaction with the environment, jet formation and dynamics in AGNs, the acceleration processes involved in GRBs and their progenitors need to be better understood. Moreover, as mechanisms of γ -ray production involve high energy cosmic rays, their observation gives us information about the acceleration of interaction of CRs as well. These observations also help us in our understanding in adjacent fields such as cosmology and particle physics. The cosmic infra-red background could be probed by the γ -ray observations of distant sources like AGNs. This would allow a better understanding of star and galaxy formation. Direct constraints on particle physics models such as supersymmetry could be obtained through γ -ray observations as well.

The study and understanding of these γ -emitting objects is a nascent science and most of our limited knowledge about them comes from multi-messenger observations in recent times. Future observations including γ -ray observations will be expected to allow us to probe deeper into their physics and the different mechanisms involved. These goals along with the experience gained in γ -ray observations sets out the program for the next generation of telescopes.

1.2 Gamma-ray telescopes

1.2.1 Energy domains

Currently, satellite and ground based γ -ray observations complement each other as far as energy domains are concerned.

Satellites: low energy domain

At low energies ranging from a few hundred keV to a few tens of GeV, the fluxes from the γ -sources remain sufficiently high for observations to be made, even with the restrained collecting area of satellite based telescopes. Moreover, at these energies, the γ -photon interacts with the atmosphere and is quickly absorbed by it, prohibiting any kind of observations on the ground.

Ground based Cherenkov telescopes: medium to high energy domain

At higher energies γ -rays can produce reasonably large cascades of secondaries when they enter Earth's atmosphere. These cascades (or showers) can be detected through direct or indirect means (depending mostly on the energy) by ground based telescopes and used to reconstruct information about the primary γ -photon. The production of these showers will be discussed in detail in chapter 2.

In the energy domain between a few tens of GeVs and a few hundred GeVs, observations can be made through both ground based telescopes and satellites, providing a means of intercalibration. As the fluxes tend to diminish with the energy, larger surfaces of collection are needed

to observe a significant number of photons and the capacity of satellite based telescopes for making observations diminishes.

The size of the atmospheric showers, i. e. the number of secondary particles produced and the depth it reaches in the atmosphere, increases with the energy of the primary. Below a few TeV, only a limited number of charged particles in the shower reaches the ground. This number increases if the detector is placed at higher altitudes, but this does not systematically allow for observations based on direct detection of the shower. At these energies, it is the Cherenkov photon emission from the charged particles of the shower that is used to “observe” the shower indirectly. The information obtained from the Cherenkov photons is used to reconstruct the atmospheric shower and through it the original primary γ -photon. The emission of Cherenkov photons from electromagnetic showers and its transmission through the atmosphere is described in detail in chapter 3.

Two different types of telescopes make use of the Atmospheric Cherenkov Technique (ACT): samplers and imagers. Samplers are able to sample the Cherenkov wavefront through a large number of heliostats (often from converted solar centrals), spread over a large field (at least several hundreds of square metres). Past and current detectors of this genre include CELESTE, STACEE and CACTUS.

Imaging Atmospheric Cherenkov Telescopes (IACT) use mirrors to reflect the Cherenkov light from the showers and to obtain their image on an array of pixels (camera). Various characteristics of the image, such as its shape, content etc. are used to reconstruct the characteristics of the γ -shower. The energy domain for optimum performance by current-day imagers lies between a few hundred GeV and a few TeV, but observations are also possible over a much broader range. Observations through this kind of telescopes began with the Whipple telescope in 1989, through a single telescope with a 10 m diameter mirror. Subsequent telescopes including CAT, CANGAROO and HEGRA improved the technique. The HEGRA telescope system was the first to use stereo imaging through 5 telescopes in the 1990s. The current generation of IACT includes four major telescope arrays: HESS(Namibia), CANGAROO-II (Australia), MAGIC (Canary Islands) and VERITAS(Arizona, U. S. A.).

Ground based extensive air shower detectors: very high energy domain

At energies beyond a few TeV, the showers are sufficiently large for direct detection to become possible. In this case the charged particles (mainly e^\pm) are seen directly by placing detectors on the ground. At these energies the γ -ray flux from the sources decreases significantly so that very large detecting surfaces are needed. These telescopes are placed at high altitude (3-4 km a. s. l.) so that a larger number of charged particles from the showers can be observed by the detector(s). The current-day telescopes include TIBET, ARGO and MILAGRO, GRAPES-3, GAMMA etc..

1.2.2 Sky coverage and angular resolution

Here too, the detection techniques are complementary for different kinds of telescopes. The current-day IACT telescopes have limited fields of view of about 4-5 degrees. This means that large scale surveys of the sky are difficult to perform with these instruments. On the other hand the extensive air shower telescopes have a nearly all sky coverage. These two kinds of telescopes operate in mainly different energy domains with an overlap in the TeV domain. One of the improvements for future IACTs would therefore be for them to have larger fields of view. We will come back to this point later on. At the same time, the IACT telescopes have better angular resolution (around 0.1° for current-day telescopes) as compared to the large field of view telescopes which have a typical resolution of around half a degree. Depending on the

objectives of the telescope, the satellite based instruments can have different fields of view. The EGRET instrument on board the Compton Gamma Ray Observatory (CGRO) in the 1990s had a field of view of about 0.5 steradians. The BATSE instrument, on board the same satellite, whose goal was to monitor the sky for GRBs, had a field of view corresponding to the entire sky except the part occulted by the Earth.

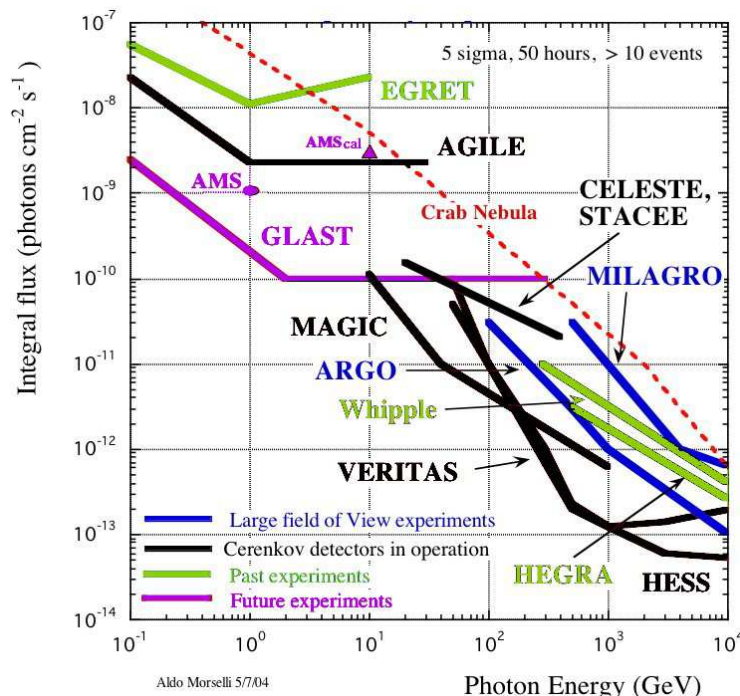


Figure 1.1: The integral flux sensitivity of several past, current and future gamma-ray telescopes as a function of the energy of observation. The figure is taken from [1] but the colours have been changed to represent the current situation. Since this figure was created several years ago, when most these telescopes had not started observations, the values given here correspond to proposed sensitivities. These curves are therefore just an indication of the performance expected from these telescopes. They are presented here, in order to give an idea of the capacities of various types of telescopes. The flux from the Crab nebula is shown through the red dotted line.

1.2.3 Sensitivity

Figure 1.1 shows the flux sensitivity of several past, present and future γ -ray telescopes as a function of the energy of observation. As we have mentioned before, the flux from the sources tend to decrease with energy. This implies that the higher the energy domain in which the telescopes are working, the higher the sensitivity they are required to have. As an example one can see the flux from the Crab nebula (used as a reference in γ -ray astronomy) through the dotted line in figure 1.1.

The figure shows that space based telescopes (EGRET, AGILE and GLAST) have sensitivities that improve with the energy, up to about 1 GeV. Beyond this, there is not much improvement, leading to poorer performance in this energy domain. On the higher energy side one distinguishes samplers (STACEE, CELESTE), which operate in a domain ranging from a few tens of GeV to a several hundreds of GeV, and have less sensitivity than the IACT (MAGIC,

VERITAS, HESS). The domain of optimum performance for HESS and VERITAS is apparent beyond around 300 GeV. The telescope threshold is much lower than this energy, but the sensitivity drops very quickly below it. The large field of view telescopes MILAGRO and ARGO are also represented. Their threshold energy tends to be higher and the optimum range for sensitivity even higher (above several TeV for MILAGRO). The future telescopes will be expected to be more sensitive in order to probe the γ -ray universe more deeply. This is true for the optimum range for each kind of telescope but for other energies as well.

1.3 Future Telescopes

Figure 1.2 shows the sensitivity of two future telescopes along with some of the existing ones (HESS, MAGIC, VERITAS, MILAGRO). The first IACT telescope Whipple is also represented. In the low energy domain, where observations are mostly carried out through satellites, the GLAST telescope will be launched in early 2008. It will cover the sky in the 20 MeV-300 GeV range through its LAT instrument and monitor GRB in the keV-30 MeV range through the GBM. Like its predecessors (such as EGRET), its sensitivity will be optimum up to a few GeV. Its sensitivity will also be at least 40 times more important than EGRET's and it is expected to detect thousands of γ -ray sources. Its energy resolution is expected to be around 10% and angular resolution around 30". The Large Area Telescope (LAT) instrument will have a relatively large field of view of about 2 sr and the GLAST Burst Monitor (GBM) will view the entire sky (except the region occulted by the Earth).

Proposals for future wide field of view, extensive air shower telescopes exist as well. As an example, the figure 1.2 shows the sensitivity of the proposed wide field telescope HAWC. The telescope will make use of the MILAGRO technique for direct observations of atmospheric showers through the detection of their charged particles through the Cherenkov light produced by them in a large pond of water. The telescope will allow all sky surveys in the energy range from about a TeV to 100 TeV with an improved sensitivity (around 15 times the sensitivity of MILAGRO). The advantage of the large field of view telescopes is the possibility of discovering new γ -ray emitting regions in the sky as well as the observation of transient sources like GRBs. Also while they are less sensitive to point sources than IACT telescopes, their extended source sensitivity is better than with imaging telescopes.

1.3.1 Future IACT systems

The current generation of IACT has shown that currently they are the best suited telescopes to make observations in the few tens of GeV-TeV range. Beyond a few TeV their energy domain overlaps with wide field of view telescopes, but these observations tend to be complementary to each other in terms of sensitivity, angular and energy resolution and sky coverage. It can therefore be safely said that IACT telescopes will play a crucial role in the next generation of ground based instruments.

Sensitivity

The future IACT systems will be expected to be more performing in a number of different respects, but one of the most pressing improvements required of them will be greater sensitivity in the energy range where they currently operate. The number of γ -ray sources in the GeV-TeV domain has grown in the recent years through the observations of the current generation of telescopes in particular the galactic centre survey performed by HESS. This implies that

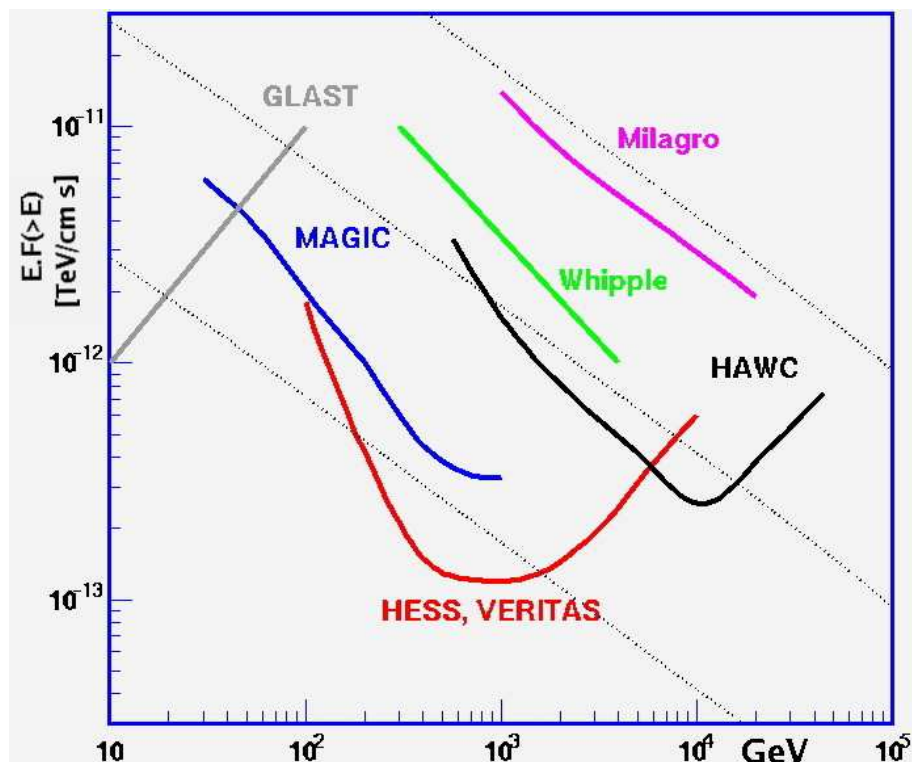


Figure 1.2: The integral flux sensitivity versus minimum energy of several current-day and future gamma-ray telescopes as a function of the energy of observation. The figure is taken from [2]

the number of sources requiring additional observation time for deeper and more probing observations to be made is growing as well. The improved sensitivity will allow high statistics observations to be made for these sources and also newer sources to be discovered in fewer hours. This aspect is even more important, since IACT have small fields of view and can only see a very limited part of the sky at a given time. The relatively good angular and energy resolutions will allow them to probe into source morphology and spectrum. High sensitivity will also allow give access to better temporal information from highly variable sources such as AGNs.

The sensitivity depends on a number of factors: the surface of collection, the γ -identification and background rejection capability and the angular resolution for point source sensitivity. Several telescope parameters can be modified to improve this sensitivity, although as we will see below this also depends on the energy domain.

Field of view

This is not necessarily the second most important requirement in terms of priorities for future IACT, but is related to some of the points discussed above. A larger field of view will allow the survey of larger sections of the sky at a given time, sometimes allowing the study of more than one source at the same time. This will also allow better studies of extended sources. Additionally, larger fields of view can also contribute towards better shower reconstruction and sensitivity in the TeV domain by enabling the observation of showers through telescopes positioned at large distances from the impact position of the shower.

The current generation of IACTs uses parabolic or Davis-Cotton type mirrors. These types of mirror have off-axis aberrations which become important for larger fields of view. The field of view of current telescopes is therefore limited to 4-5 degrees. The field of view of future

telescopes could be improved either by using different mirror designs (elliptic mirrors have good imaging properties for fields of up to 10° , but poorer on-axis performance) or telescope designs with secondary optics like Schmidt type telescopes which could have fields of view of up to 15° .

Angular resolution

One of the impacts of angular resolution is improved sensitivity for point sources, since smaller number of background events are included when the direction of the source is identified more precisely. Additionally, this leads to better identification of point sources as well as more detailed studies of the structure of extended sources. In general, the angular resolution may benefit from sharper shower images.

Energy resolution

As far as the energy resolution is concerned, studies of the power law spectra of γ -ray emission from sources can be achieved through current energy resolutions of around 10%. The study of various cut-offs, regime shifts, emission lines etc. would be improved through better energy resolution. The energy resolution is however limited by the intrinsic fluctuations of the number of Cherenkov photons produced in electromagnetic showers and the signal obtained in telescope images.

Energy range and requirements

The problems involved in improving γ -ray observations for IACT, depend on the energy range being considered. As a result, the solutions to achieving the above mentioned goals for various parameters depend on the energy domain as well. As mentioned above (and as obvious from their sensitivity curves), the domain where current IACT best operate lies between roughly 300 GeV to a few tens of TeV. This is also the energy domain where IACT telescopes are the main instruments observing the γ -ray sky. In this energy range, the most effective way to improve the sensitivity would be through an increase of the effective area of the system. This can be achieved by spreading a large number of telescopes over a large surface. The use of a larger field of view should help improve the sensitivity as well, specially in the TeV range.

As mentioned before in the energy domain beyond a few TeV, the flux from the sources diminishes requiring very large collection surfaces to obtain statistically significant observations. This is also an energy domain where observations will overlap with the large field of view telescopes mentioned above. As the γ -ray photons produce very large showers in this energy domain, the use of smaller telescope sizes (less than ten metres diameter) still yields images that can be used to reconstruct γ -showers and obtain good angular resolution.

The energy range below 300 GeV, will be covered by spatial telescope GLAST as well, although its sensitivity is less important at these energies. As far as IACT systems are concerned, the quality of observations in this energy range deteriorates, due to the combined effect of more fluctuations in the shower development process, higher background levels, as well as the impact of the Earth's magnetic field on low energy showers. The shower images obtained at these energies with medium sized telescopes (10-15 m diameters) have smaller numbers of photo-electrons and are often not clearly defined. This results in the poor reconstruction of shower parameters, which leads to poor energy and angular resolution. The identification of γ -showers and separation from hadronic background is problematic as well. The key to improving the γ -ray observations and array sensitivity in this energy domain would be to collect a maximum amount of light from showers in order to obtain more exploitable images. This can

be achieved through several parameters: the use of larger telescopes, observations at higher altitudes (with denser Cherenkov photon flux) and technological improvements such as high quantum efficiency photomultipliers.

1.3.2 Introduction to this thesis and outline

We have seen through the above discussion that the optimisation of various parameters for future telescopes depends on a large number of factors. The energy range and physics goals determine the requirements for the future systems. A large number of parameters, such as the telescope size, number, field of view, altitude of observation, photomultiplier efficiency, mirror type and pixel size, have an impact on the performance of a telescope system. The optimisation of these parameters in order to meet the physics goals requires dedicated studies and simulation tools capable of carrying out these studies. It is within this context that the work on this thesis was undertaken. Our goal was to understand different aspects of γ -ray observation through IACT systems, as well as develop simulation and shower reconstruction tools to evaluate the performance of different telescope configurations. These tools rely on methods that focus on the most important aspects of telescopes and the reconstruction of shower parameters through their images. Some details and technical precisions are ignored in order to avoid getting encumbered by too many parameters yet provide robust methods for the evaluation of telescope capabilities. Moreover, the tools provide the possibility to have further additions in the future.

Since IACT use the atmospheric showers and the Cherenkov light emitted by them to detect gamma-rays and gather information about them, the knowledge of their properties is of fundamental importance for the understanding of telescope systems and their characteristics. **Part II** of the thesis, therefore, deals with atmospheric showers and their simulations.

Chapter 2, begins by a presentation of the earth's atmosphere and its role as a calorimeter: a medium in which gamma-rays interact, producing electromagnetic showers and depositing their energy. We present some of the salient features of these atmospheric showers and give a parametrisation for their longitudinal profiles.

Chapter 3, deals with the Cherenkov emission from these atmospheric showers. Our aim was to gain an understanding of the different characteristics of this emission and the various parameters affecting it, since these will eventually determine the performance of different telescope systems. We begin by a discussion on the Cherenkov emission itself, highlighting the role played by the atmosphere in it. We then present the longitudinal profile of this emission in the atmosphere as well as a discussion on the number of Cherenkov photons produced. We also briefly discuss the transmission of these photons through the atmosphere. We then devote a large section of the chapter to a discussion on the density of the Cherenkov light reaching the ground. The understanding of this particular aspect is important since the telescope images of the electromagnetic showers are obtained through this light. We mainly discuss the geometry and intensity of the density pattern on the ground and how it is affected by various shower parameters such as the primary gamma photon's energy and angle of incidence, as well as observational parameters such as the altitude of observation.

In **chapter 4**, we move on to the more practical aspects of our study of atmospheric showers and present CORSIKA, the simulation tool used for understanding the characteristics of atmospheric showers. This tool has also been used, throughout the thesis, for generating the showers used in the various studies carried out on telescope systems.

Part III deals with IACT, their simulation and the important characteristics of the shower images obtained by them.

Chapter 5 begins with a description of the imaging atmospheric telescopes and a discussion on the use of parabolic mirrors, and ends with a description of the simulation code we have

developed in order to study the response of IACT arrays to atmospheric showers.

The understanding of the links between various features of the shower images and the parameters of the primary gamma-ray is important since these very links are exploited to reconstruct shower parameters from the telescope images. In **chapter 6**, we therefore present the main characteristics of electromagnetic shower images and their relationship with shower parameters such as source position in the sky and shower core position.

Part IV presents the methods for the reconstruction of various parameters of the primary gamma-ray as well as ideas for the separation of gamma-showers from hadronic showers.

Chapter 7 contains a detailed presentation of the methods we have developed for the reconstruction of the source position in the sky and the shower core position on the ground. For both methods, the principle and its implementation are presented. These are followed by the results obtained from the application of the method to a test telescope system and a discussion of these results. A section is also devoted to the discussion on some of the finer points concerning these methods.

Chapter 8 similarly deals with the method developed for the reconstruction of the energy of the primary γ -ray. The principle, implementation and application to a test system is presented along with a discussion on how to further improve the method.

Chapter 9 gives a brief presentation of hadronic showers and how they constitute a source of noise for γ -ray observations. Simulated images obtained from telescopes viewing hadronic showers are shown and compared with γ -ray shower images. A method for reconstructing the longitudinal profile of showers from telescope images is also given along with a proposition on how to use the parameters obtained from this reconstruction to discriminate between hadron and γ -induced showers.

Finally **part V** gives an example of the application of the tools and methods developed in order to design IACT arrays and evaluate their capacity for γ -ray observations. This part also contains the concluding chapter of this thesis.

Chapter 10 uses the tools developed on two telescope array designs and compares the results obtained at two different altitudes. The telescopes arrays are designed and different parameters such as telescope size and number chosen, keeping in mind the above discussion on the different energy domains. The inter-telescope distance is optimised through simulations. Finally, the response of the telescope arrays are studied through simulations of γ -ray showers at various energies.

Chapter 11 presents a number of conclusions drawn from this work and also gives possible directions for future research.

Appendix C of this document contains a 33 page summary in French of the work presented in this thesis.

*P*_{ART II}

*A*_{TMOSPHERIC}
SHOWERS AND THEIR SIMULATION

CHAPTER 2

ELECTROMAGNETIC SHOWERS IN THE ATMOSPHERE

As described earlier, in ground based γ -ray astronomy, the incident photon is “observed” through the shower it generates in the atmosphere. A γ -photon induces a cascade of particles through a series of essentially electromagnetic processes. Cherenkov light is emitted by the charged particles of this shower when they have velocities greater than the velocity of light in the surrounding atmosphere. The ground based Imaging Atmospheric Cherenkov Telescopes (IACT) use this Cherenkov light to determine the characteristics of the shower and extract information about the initial γ -photon.

This establishes the understanding of shower generation, development processes and Cherenkov emission properties as prerequisites to any study of ground based γ -ray telescopes. In this chapter, we discuss the production of atmospheric showers and their properties. The chapter opens with a brief description of the atmosphere i.e. not only the medium in which the incoming particle develops a shower, but also the medium responsible for the emission of the Cherenkov photons and their transmission to the ground, where they are observed.

We then go on to describe the different processes occurring in a γ -ray induced shower and how they contribute to shower development. We discuss shower morphology and its dependence on primary energy.

These shower characteristics were studied through a series of simulations using the air shower simulation package CORSIKA [3]. A more detailed description of these simulations is given in chapter 4.

2.1 The atmosphere and its models

2.1.1 Composition and layers

The earth’s atmosphere is a layer of gases surrounding the planet and retained by its gravity. Its main component is air, a mixture of Nitrogen (78.08%), Oxygen (20.97%), Argon (0.9%) and traces of rare gases¹.

The temperature of the earth’s atmosphere varies with altitude. Figure 2.1 shows the typical variation of temperature with altitude in the earth’s atmosphere. These temperature variations are due to the varying absorption of solar radiation at different altitudes and separate the atmosphere into different layers.

¹Other gases include Carbon Dioxide, Neon, Methane, Helium, Krypton, Hydrogen, Xenon

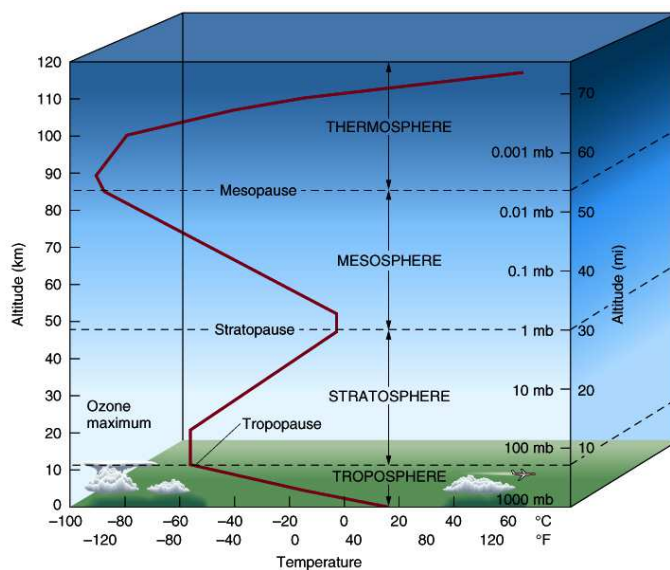


Figure 2.1: The typical temperature profile throughout the atmosphere (figure taken from [4]).

2.1.2 A complex system

The layer boundaries vary horizontally i. e. with geographical location. For instance, the troposphere can be as thin as ~ 8 km in the polar region or as thick as ~ 17 km in the tropics.

Apart from this a multitude of impurities are present in the atmosphere. The presence of some of them can have an important impact on Cherenkov light emission and propagation. This topic will be touched briefly in sections 3.2, 3.4 as well as 3.5.1. Here some of the impurities most relevant to ground based astronomy are described briefly.

H_2O exists in its three states in the atmosphere. The bulk of water vapours is present in the troposphere². The presence of ozone O_3 in the stratosphere is responsible for the temperature peak in the stratopause region.

Other common impurities include tiny liquid and solid particles suspended in the air known as aerosols. Aerosol particles exist in a large variety of sizes, shapes and compositions³. They occur mostly in the lower part of the atmosphere where diurnal variations as well as wind speed impact are greatest.

Aerosols, ozone and water vapour levels are not only site dependent, but also show time dependent variations. Most weather related phenomena occur in the troposphere. The composition of air itself varies with the altitude specially beyond 100 km above sea level. A more detailed description of the atmosphere can , for example, be obtained from [5].

2.1.3 Atmosphere Models

Atmosphere monitoring in ground based telescopes

Ground based telescopes using extensive air shower formation in the atmosphere need to take into account the local variations of the atmosphere and its impact on the performance

²The presence of this important greenhouse gas is responsible for the rise of temperature in the troposphere

³Aerosols are both naturally occurring ($\sim 90\%$) as well as man produced ($\sim 10\%$). One distinguishes larger particles ($> 1 \mu m$) mostly produced in dust storms and sea salt from sea spray and smaller particles ($< 1 \mu m$) mostly released during processes like the formation of sulphate particles during volcanic eruptions and soot and smoke during burning processes

of the telescope. For this purpose most experiments have dedicated atmosphere monitoring instruments.

Simplified models

For the general study of various phenomena in the atmosphere it is useful to work with simplified models. Such models assume the atmosphere to be purely composed of air. They can be expressed through simple mathematical expressions and enable to have an overall picture of the phenomena in ideal conditions. The impact of any deviation from this “standard” situation can then be studied as a subsequent step.

The Isothermal model

In the simplest model of the atmosphere, the net vertical force acting on a column of air is considered to be zero and the temperature is assumed to be uniform throughout the atmosphere (see, for example, [5] for a mathematical treatment of the problem). This means that the pressure and density increases in order to support the weight of the overlying atmosphere as altitude decreases. This gives an exponential dependence of the mass overburden $T(h)$ on the altitude h which can be expressed as

$$T(h) = be^{-\frac{h}{h_0}},$$

where $b \cong 1030 \text{ g/cm}^2$ [6] and $h_0 = 8.4 \text{ km}$. The mass overburden $T(h)$ is the mass of air contained above altitude h in a cylinder with a cm^2 base and is expressed in g/cm^2 . The density is then given by the derivative $\rho(h) = -dT(h)/dh$. The value of mass overburden at sea level is 1030 g/cm^2 in the isothermal model. The mass overburden and density profiles of the isothermal model are shown in figure 2.2.

The U. S. Standard atmosphere (Linsley’s parametrisation)

The U. S. standard atmosphere model gives idealised profiles for various parameters including density, temperature and pressure for a steady state atmosphere [7]. The last version of the model was established in 1976. Different parametrisations of the model have been established. Among them, J. Linsley’s parametrisation [8] divides the atmosphere into 5 layers up to 112 km, which is assumed to be the atmosphere boundary. In the lower four layers, the density has an exponential dependence similar to the isothermal model. A different parametrisation of each of these layers takes into account the temperature variations from layer to layer.

$$T(h) = a_i + b_i e^{-\frac{h}{c_i}} \quad i = 1, \dots, 4. \quad (2.1)$$

The fifth layer ($> 100 \text{ km}$) has a linear dependence on h

$$T(h) = a_5 + b_5 \frac{h}{c_5}. \quad (2.2)$$

Table 2.1 gives the parameters a , b and c for the U. S. Standard atmosphere parametrisation by J. Linsley. These parameters are selected in such a way that $T(h)$ is continuous at the layer boundaries and can be differentiated, while ρ which is obtained by differentiating $T(h)$, has slight discontinuities. Figure 2.2 shows the mass overburden and density profiles.

Another parametrisation of the U. S. standard atmosphere is due to M. Shibata [6]. Not having used this parametrisation in our studies, we do not describe it here, but we compare

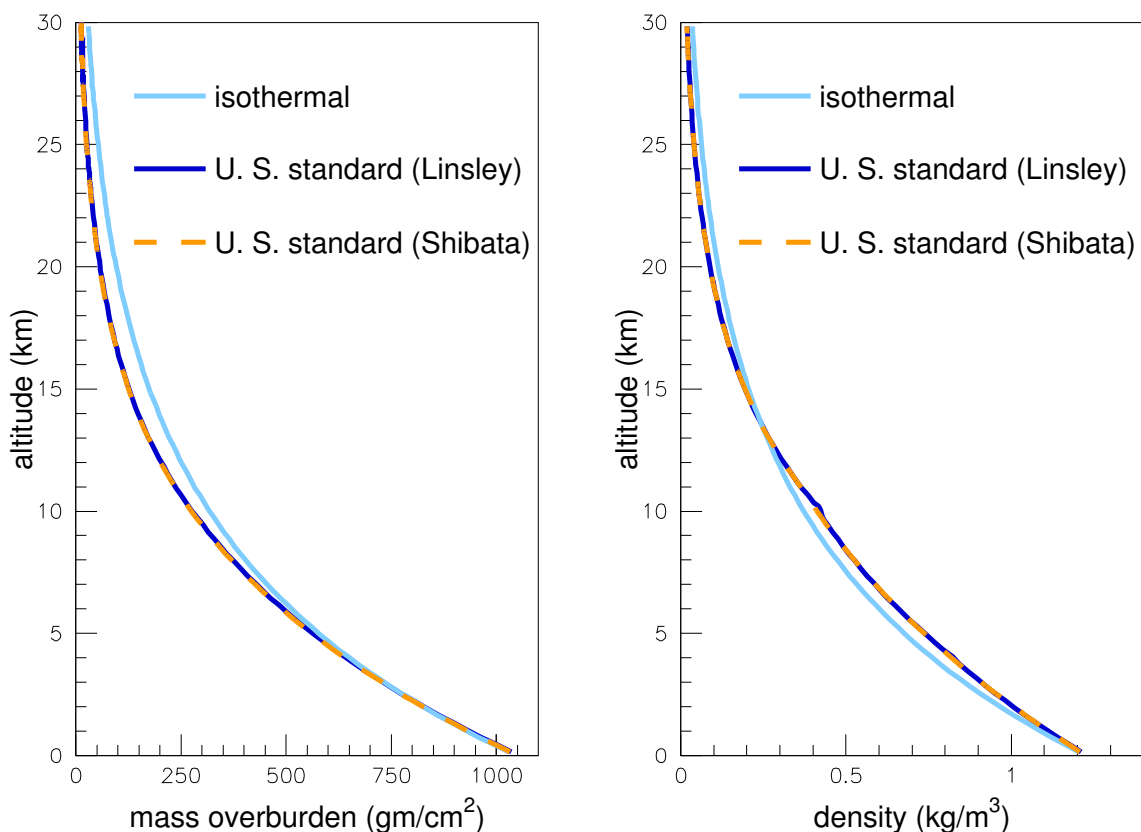


Figure 2.2: Comparison of the U. S. Standard and Isothermal atmosphere models. Both Linsley's and Shibata's parametrisations for the U. S. Standard model are shown. The left graph shows the mass overburden profile as a function of altitude, while the right graph shows the density as a function of altitude. One notices the presence of discontinuities in the density profile of the U. S. Standard model.

Layer i	Altitude h (km)	a_i (g/cm ²)	b_i (g/cm ²)	c_i (cm)
1	0... 4	-186.5562	1222.6562	994186.38
2	4... 10	-94.919	1144.9069	878153.55
3	10... 40	0.61289	1305.5948	636143.04
4	40... 100	0.0	540.1778	772170.16
5	>100	0.01128292	1	10^9

Table 2.1: Parameters of the U. S. Standard atmosphere (after J. Linsley)

	Isothermal	U. S. Standard	
		J. Linsley	M. Shibata
$T(0)$ (g/cm ²)	1030	1036	1033
$\rho(0)$ (kg/m ³)	1.226	1.23	1.226

Table 2.2: Comparison of mass overburden at sea level in different atmospheric models

it with the isothermal model and J. Linsley's parametrisation of the U. S. standard model in figure 2.2 and table 2.2. The profiles of both parametrisations of the U. S. model are similar. The discontinuities visible in the density profile of Linsley's parametrisation are not present in Shibata's parametrisation.

The U. S. standard model is one of the many models implemented in CORSIKA⁴. All the simulations realised for different studies presented in this thesis, have been done using this model with Linsley's parametrisation, in the CORSIKA program.

In general, atmospheric models can use different types of parametrisations and/or value tables for different altitudes. We do not go into the description of other models since they are not used in the studies presented in this thesis.

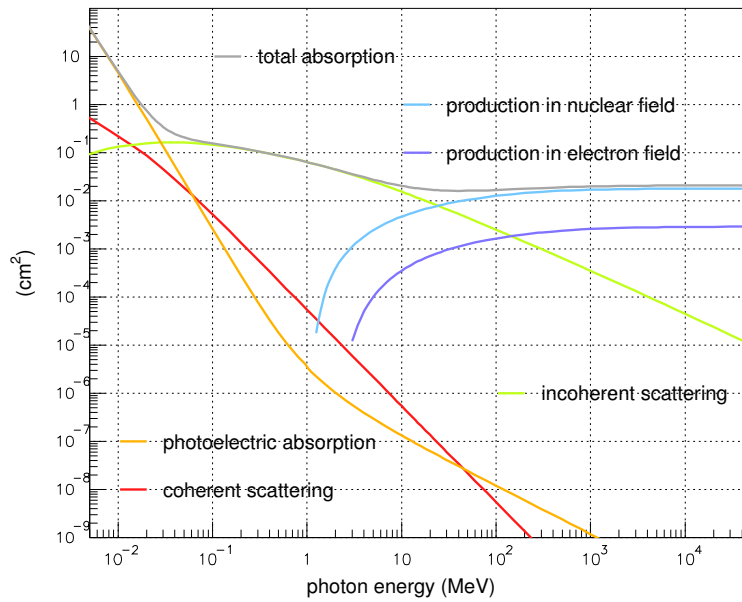


Figure 2.3: Generated curves for the contributions of different processes to photon cross section per gram of air traversed. The curves were computed by XCOM [9] for a mixture containing N₂ (78.1%), O₂ (21%) and Ar (0.9%). The cross section of interaction at high energy inferred from the curve is $(0.018+0.00289) \text{ cm}^2 = 0.02089$ and compares well with the value $7/9X_0 = 0.02122$

2.2 Shower generation and development

2.2.1 The first interaction: pair production

The predominant photon-matter interaction mode varies with the energy of the photons. Figure 2.3 gives generated contributions to the photon cross section, in air, at various energies. While at lower energies, interaction takes place mostly through the photoelectric effect along with scattering processes, most interactions in the γ -ray domain result in the production of an

⁴The predefined atmosphere models in CORSIKA all follow the five layered model given by equations 2.1 and 2.2 with different values of the parameters a , b and c (see [3]). This is further discussed in section 4.5.1

electron-positron pair⁵, making it the relevant process as far as the initial development of the electromagnetic shower is concerned. The threshold of the process corresponds to an energy of $h\nu > 2m_e c^2 = 1.022$ MeV where m_e is the mass of an electron. The mean free path for pair production in a given material is expressed as $9X_0/7$, where X_0 is the radiation length in that material. The probability $dP(z)$ of a photon materialising within a depth range dz after penetrating through a distance z in the material is, therefore, given by

$$dP(z) = \frac{7}{9X_0} e^{-\frac{7z}{9X_0}} dz.$$

In the case of air $X_0 = 36.66$ g/cm². In the U. S. standard atmosphere model (see section 2.1.3), a depth of one radiation length from the top of the atmosphere corresponds to an altitude of 22.8 km. This means that the average position of first interaction corresponds to an altitude of 21.2 km. Figure 2.4 shows the simulated distribution of the depth (expressed in units of X_0) in the atmosphere at which first interaction occurs.

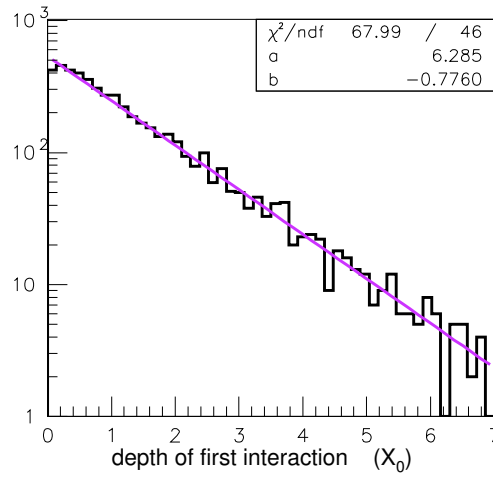


Figure 2.4: A histogram of the depth of the first interaction in the atmosphere for 5000 simulated γ -showers. The depth of interaction z is expressed in units of X_0 ($t = z/X_0$). The distribution is fitted with an exponential function $f(t) = ae^{bt}$. The fit parameter b implies a mean free path of $X_0/(0.776 \pm 0.008)$, which compares well with the mean free path of pair production i. e. $9X_0/7 \sim X_0/0.778$. The showers are simulated with CORSIKA version 6.020.

2.2.2 Bremsstrahlung

The electron and positron resulting from pair production will in turn interact with the surrounding air and lose energy. Figure 2.5 shows the energy deposited per radiation length, through different processes, as a function of energy. At high energies, the predominant mode of energy loss is through bremsstrahlung radiation i.e. the emission of high energy photons as electrons are accelerated in the Coulomb fields of the atomic nuclei. The average energy of the electron after passing through a material of thickness z is given to a good approximation by

$$E(z) = E_0 e^{-\frac{z}{X_0}}, \quad (2.3)$$

⁵This is not true for very high energies ($> 10^{20}$ eV), where photonuclear cross sections become larger than for pair production. The pair production process remains the relevant process in the energy domain concerning ground based γ -ray telescopes.

where E_0 is the initial energy of the electron. This implies that the electron loses 63% of its energy on the average after having passed through one radiation length of material.

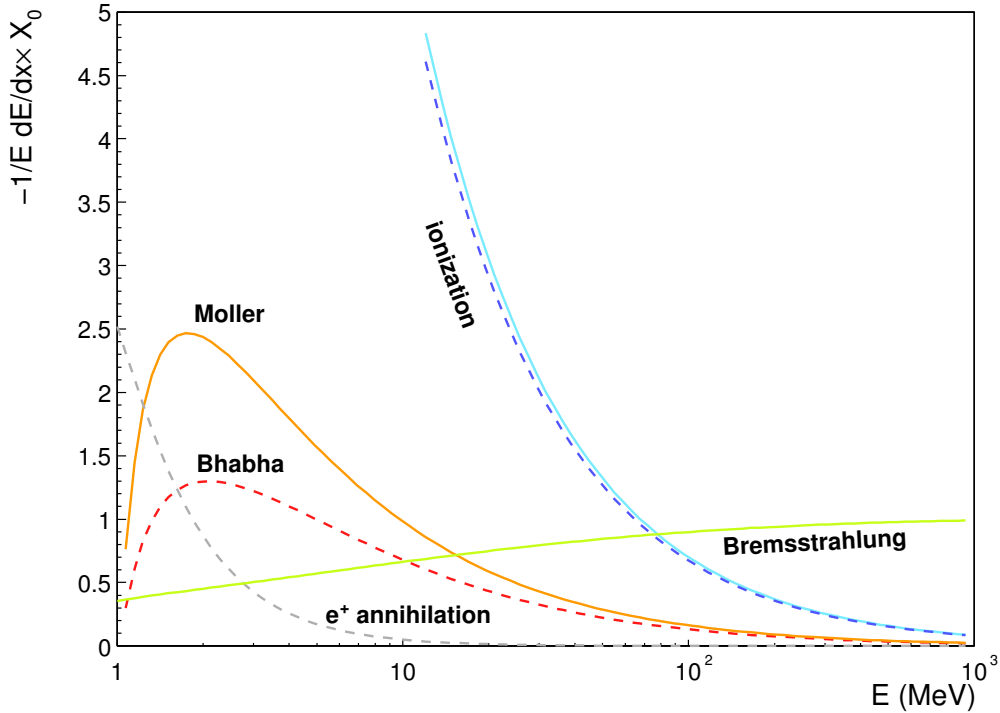


Figure 2.5: Energy loss per unit radiation length X_0 for electrons (solid line) and positrons (dashed line). The figure is taken from [10].

2.2.3 Particle Multiplication and high energy secondaries

The bremsstrahlung photons, themselves (as long as they have sufficiently high energies), will interact with the surrounding material and create more electron-positron pairs which in turn will produce still more bremsstrahlung photons and so on.

Heitler's model

An estimation of the rapidly growing number of particles and the energy they carry can be obtained through the very basic Heitler's model [11]. From equation 2.3, one can obtain the splitting length R , i.e. the average length of material passed through after which an electron loses half of its energy through radiation. This value is given by $R = X_0 \ln 2$. In Heitler's model (figure 2.6), an electron or positron radiates a single photon after travelling one splitting length R . After travelling the same distance, photons materialise into electron-positron pairs. In either instance, the energy of a particle is equally divided between the two outgoing particles. After n splitting lengths $z = nR$, the total number of particles grows to $N(z) = 2^n$ and the average energy carried by each of these particles is $E(z) = \frac{E_0}{2^n}$.

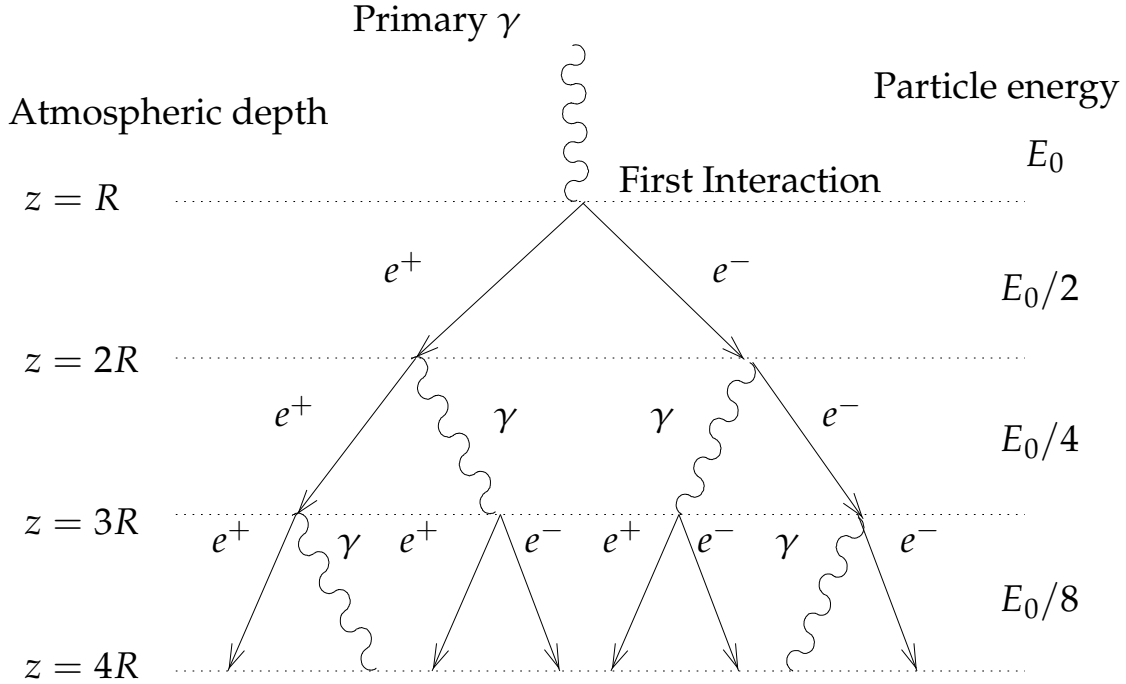


Figure 2.6: Shower development described through Heitler's model. Here $R = X_0 \ln 2$.

2.2.4 Critical energy and the low energy regime

The critical energy is defined as the energy at which the rate of energy loss through bremsstrahlung and ionisation equal each other. Below this point electrons lose their energy mostly through ionisation. In an alternate (almost equivalent) definition, Rossi [12] defines the critical energy as the energy at which the ionisation loss rate per radiation length is equal to the electron energy. The empirical evaluation of the critical energy using Rossi's definition gives

$$E_c \sim \frac{710 \text{ MeV}}{Z + 0.92}$$

in gases, giving the value of $E_c = 86 \text{ MeV}$ for air. This value is similar to the one found from figure 2.5.

As the subdivision of the initial particle's energy continues with the multiplication of the number of particles, at some point, the average particle energy becomes lower than E_c . Beyond this point, the multiplication process stops and the number of particles in the shower starts decreasing as more and more particles of the shower are absorbed by the surrounding air through ionisation.

In Heitler's model, the expression $\frac{E_0}{2^{n_c}} = E_c$ gives the number of splitting lengths n_c required for the average particle energy to be E_c . The position of this point z_{max} gives the maximum of shower development and can be calculated knowing that $z_{max} = n_c R$. This gives $z_{max} = X_0 \ln(\frac{E_0}{E_c})$. This also implies that the number of particles at this point is $N(z_{max}) = \text{int}(\frac{E_0}{E_c})$.

2.2.5 Other/Minor processes

While the main processes involved in γ -induced showers are electron-positron pair production and bremsstrahlung, other processes with smaller cross sections are responsible for the production of muons and hadrons in these showers. These include $\mu^+ \mu^-$ pair production and

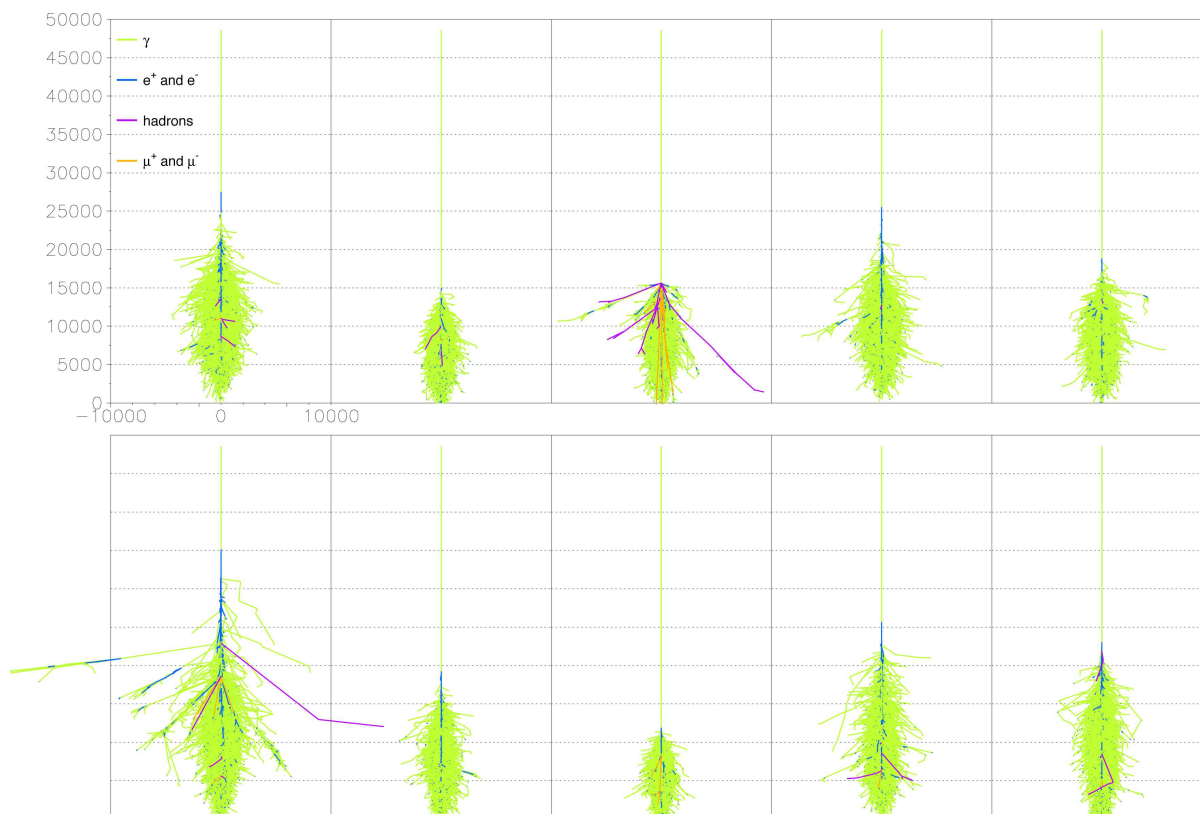


Figure 2.7: 10 different γ -initiated showers of 500 GeV. The units of the vertical and horizontal axes are metres.

photo-nuclear production of muons. The $\mu^+\mu^-$ production is similar to the electron-positron pair production process. Since the muon rest mass is much larger than the electron mass, the threshold of these events is higher $\sim 211 \text{ MeV} = 2xm_\mu c^2$ where m_μ is the mass of a muon. A detailed discussion on the occurrence of this process in electromagnetic showers and its use in astronomy can be found in [13].

The inelastic interaction of photons with nuclei is responsible for the production of hadronic components and muons in electromagnetic showers. The cross-section of these processes remains very low as compared to the pair production cross-section at the energies ground based gamma-ray astronomy is concerned with. At very high energies ($\sim 10^{20}$ eV), the cross-section for the process becomes more important and is responsible for the production of hadronic showers with gamma-ray primaries. More details concerning photoproduction in high energy γ -ray showers can be found in [14].

2.3 Shower morphology

2.3.1 Main features illustrated through examples of showers

We present a few examples of showers in order to illustrate the points discussed so far and bring out some of the salient features concerning shower morphology. A more detailed description of the longitudinal and lateral profiles will be given later on. We have generated the images shown here using the CORSIKA option which allows the plotting of the tracks of individual particles in

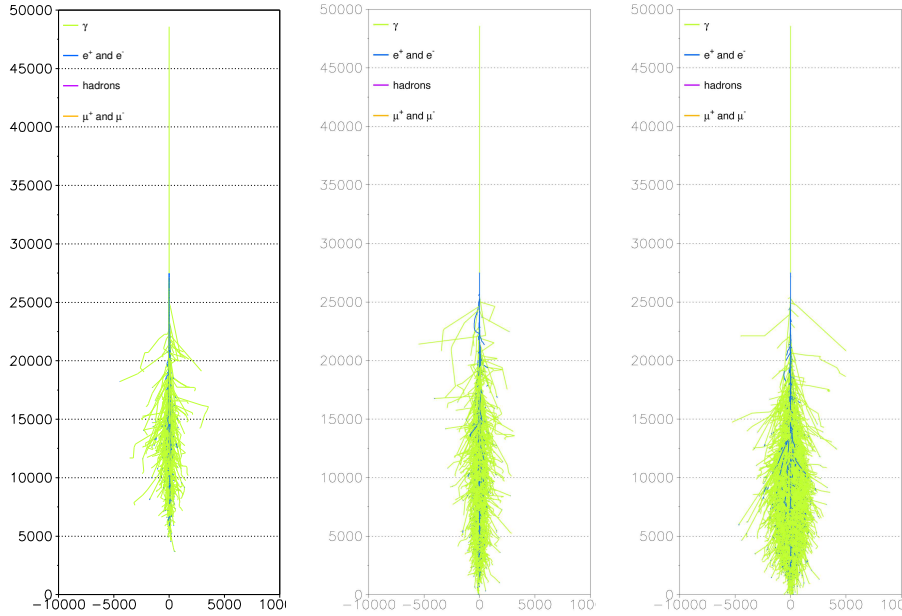


Figure 2.8: γ -initiated showers of 10, 100 and 1000 GeV (from left to right). The units of the vertical and horizontal axes are metres.

a shower. The different colours correspond to the different types of particles.

Figure 2.7 shows ten 500 GeV showers. The altitude of first interaction is different in each case. All showers have an elongated shape, with the longitudinal development spanning several thousands of metres, while the lateral development spans a few hundreds of metres at most. Several showers have small muonic and hadronic components as well.

In figure 2.8, we compare showers of three different energies: 10, 100 and 1000 GeV (from left to right). In order to compare the shower size and development we have generated showers with the same altitude of first interaction. The 10 GeV shower develops almost completely above ~ 5000 m a. s. l., while the 100 GeV shower development goes on till altitudes close to the sea level are reached. As for the 1000 GeV shower, it does not complete its development before reaching sea level. This illustrates the points discussed earlier i. e. the dependence of the longitudinal size of the shower and the position of the maximum of development as a function of the energy. One also notices the increase of the number of traces and their density as a function of the energy.

2.3.2 Longitudinal development

The average longitudinal profile of the energy deposition of an electromagnetic shower can be described by the function [15]:

$$\frac{dE}{dt} = E_0 \beta \frac{(\beta t)^{\alpha-1} e^{-\beta t}}{\Gamma(\alpha)}, \quad (2.4)$$

where $t = z/X_0$ is the number of radiation lengths contained in the depth z reached in the atmosphere. z is expressed in g/cm^2 and $\Gamma(\alpha) = \int_0^\infty e^{-z} z^{\alpha-1} dz$. It is convenient to express the depth in units of radiation length as this removes the dependence on atmosphere composition and model. Moreover, in what follows, we will also express the energy in units of critical energy i. e. $y = E/E_c$ for the same reasons. The rising part of the shower profile where particle multiplication occurs is described by $t^{\alpha-1}$ and the low energy regime by the exponential $e^{-\beta t}$.

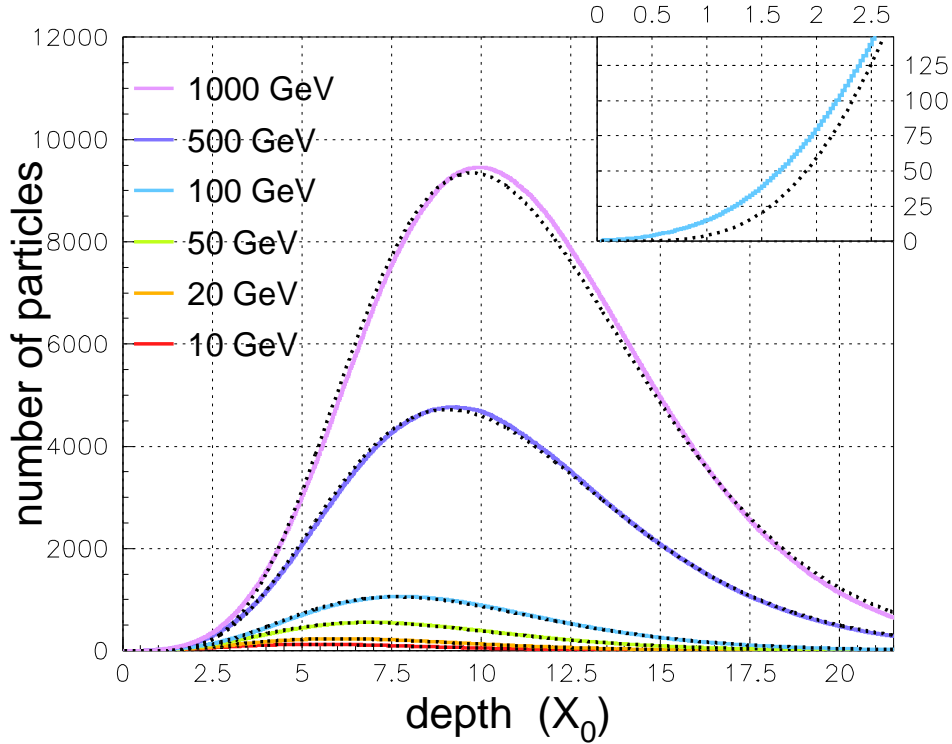


Figure 2.9: The average longitudinal profiles in terms of number of particles (electrons and gamma) are shown (coloured lines) for various energies. The curves are fitted with the function $f(t) = C(\beta t)^{\alpha-1}e^{-\beta t}$ and the result of the fits are shown through the dotted lines. A zoom of the first couple of radiation lengths for the 100 GeV curve is shown in the top right corner. The curves are drawn in linear coordinates in order to present the typical shape of shower profiles. In figure 2.11 we have presented the results of these fits in log scale where the curves from lower energies can be better visualised. Zooms of the first couple of radiation lengths for all the energies can be found in figure A.1 in the appendix on page 233.

The shower maximum depth is then given by

$$t_{max} = \frac{\alpha - 1}{\beta}.$$

As the deposition of energy in the atmosphere closely follows the development of the shower, the function in equation 2.4 can be used to describe the longitudinal profile of the shower in terms of the number of particles as well. We have done a series of simulation with CORSIKA⁶ and present the average longitudinal profiles in terms of particle number in figure 2.9. Each curve is fitted with the function $f(t) = C(\beta t)^{\alpha-1}e^{-\beta t}$. The shower profiles are well represented by the fits except for the first couple of radiation lengths. This is highlighted in the zoom of the first few radiation lengths of the 100 GeV profile presented on the top right corner of figure 2.9.

As discussed previously, the number of particles in the shower increases with the energy. We show the dependence of the number of particles at the maximum of shower development

⁶Corsika version 6.020 was used with minimum energy cut-offs of 0.05 GeV for hadrons, 0.05 GeV for muons, 0.0002 GeV for electrons and photons. For a discussion on the effects of the choice of energy cut-offs see section 4.3.3

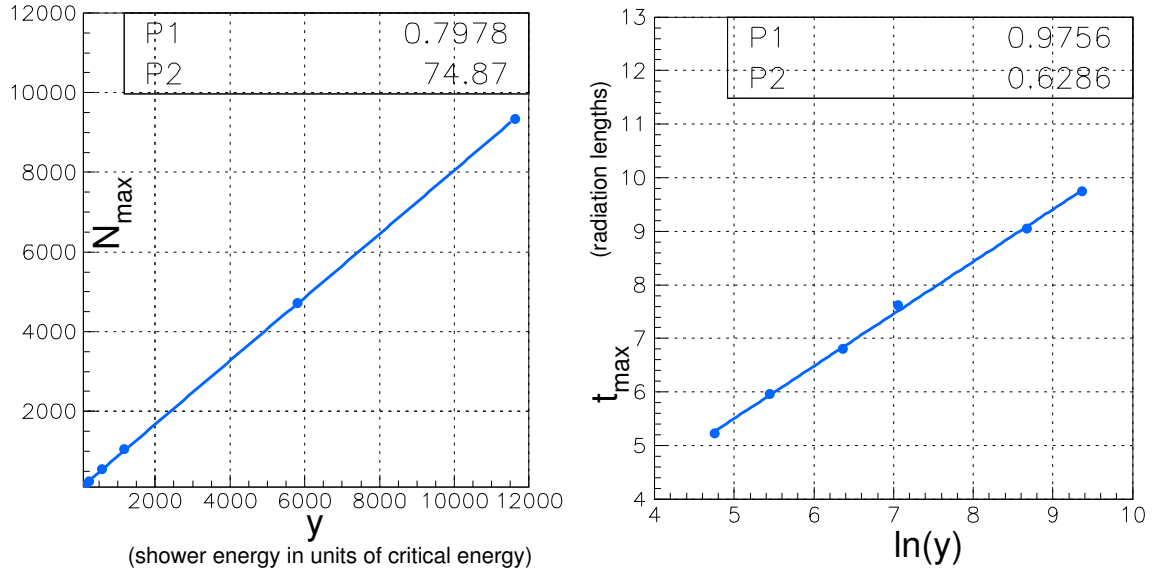


Figure 2.10: Left: The dependence of the number of particles at the maximum of shower development (N_{max}) as a function of shower energy expressed in units of critical energy ($y = E/E_c$). Right: The dependence of the depth of the maximum of shower development (in radiation lengths) in terms of $\ln(y)$. The points are fitted with the function $f(x) = P_1 x + P_2$.

(N_{max}) on the energy y in figure 2.10 (left). The following linear dependence is found:

$$N_{max} = 33.35 + 0.8y.$$

Similarly, as the shower energy increases, it takes a larger number of interactions for the average energy of the particles to reach the critical energy. As a result, the depth of the maximum of shower development increases with the energy. For instance, the maximum of 1000 GeV showers occurs at an altitude of ~ 8 km on the average, while for 10 GeV showers this occurs at around 12 km. Figure 2.10 (right) gives the position of the maximum as a function of $\ln(y)$. The following linear dependence is found by fitting these points:

$$t_{max} = 0.98 \ln(y) + 0.63.$$

Another parametrisation of the shower maximum position in air can be found in [16], while [17] and [18] give general forms of parametrisations for electromagnetic showers.

We have also found parametrisations for α/β , $1/\beta$ and the fluctuations in these longitudinal profiles. These can be found in appendix B (page 239).

We will also present a detailed parametrisation of the longitudinal profiles of electromagnetic showers in terms of their Cherenkov emission in section 3.2.2.

Fraction of the shower cut-off at observation level

Depending on the altitude of observation and the altitude of first interaction in the shower, the entire shower may not develop above the ground level. In figure 2.11 (left), we present the average longitudinal profiles obtained from the fits described in the previous section and compare them with four different altitudes of observation. The percentage of shower cut-off at various altitudes is then reported in figure 2.11 (right). While most showers at the energies shown here develop fully above the sea level and show the loss of a few percent at the most at

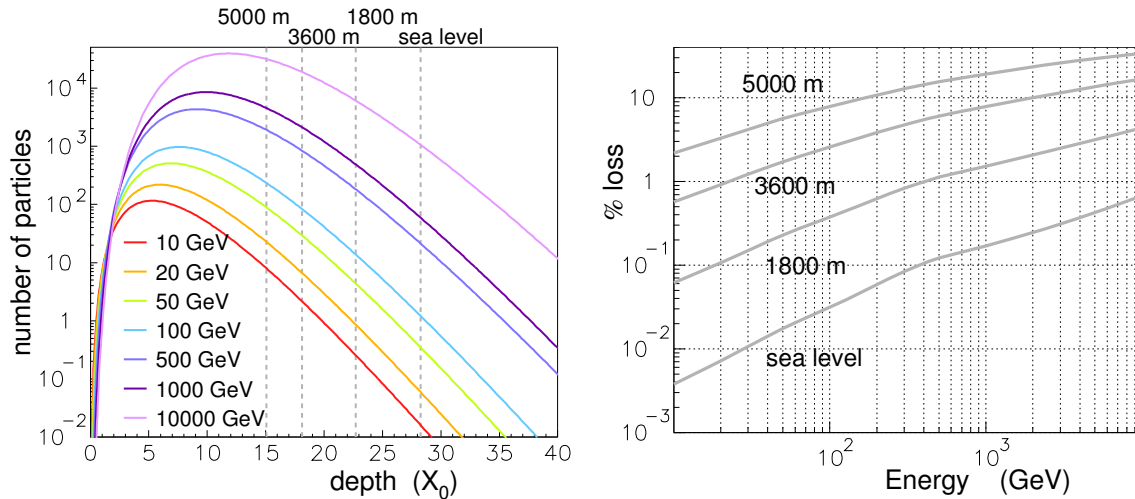


Figure 2.11: Left: The parametrised longitudinal profiles at various energies obtained by fitting the average longitudinal profiles of showers as presented on page 39. The development of the showers is compared with the four different altitudes of observation. Right: The percentage of longitudinal profile cut off for different altitudes of observation as a function of the shower energy.

1800 metres, the losses are greater at 5000 metres. For 10 TeV showers around 40% of the average shower is cut off at the ground level. Low energy showers on the other hand develop fully above the ground even at high altitudes of observation. We will come back to this point when we discuss the impact of the altitude of observation on the reconstruction of the primary γ -photon.

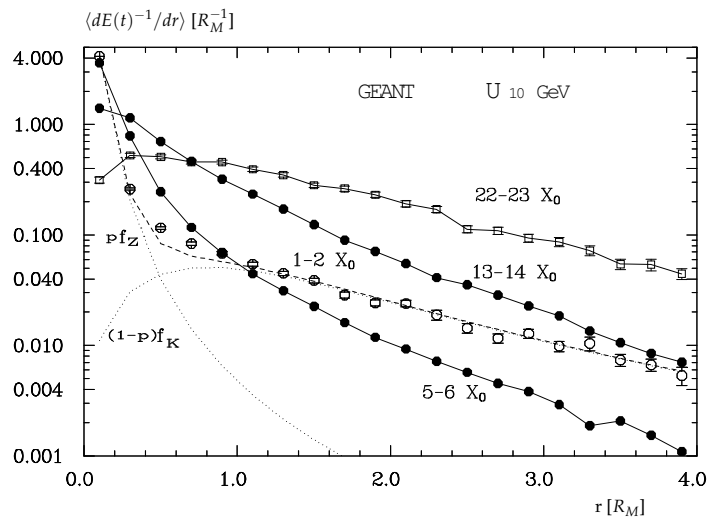


Figure 2.12: Lateral distribution of the shower energy expressed in units of Molière radius at different depths of shower development. The figure is taken from [18] and gives distributions for a 10 GeV gamma induced shower in uranium. As the distance is expressed in units of R_M , one expects similar distributions for showers in air.

2.3.3 Lateral profile

The lateral spread of the shower is mainly determined by the multiple Coulomb scattering of the charged particles (mostly electrons in electromagnetic showers) as they interact with the air atoms. Contributions from other phenomena like bremsstrahlung and pair production are relatively small, specially at high energies. The lateral distribution can be scaled fairly accurately with the Molière radius

$$R_M = X_0 \frac{E_s}{E_c},$$

where $E_s \approx 21 \text{ MeV}$ [17]. This implies that $R_M \approx \frac{8.95}{\rho} \text{ cm}$ where ρ is the density of air in g/cm^3 . In the U. S. standard model (see section 2.1.3), the Molière radius is ~ 73 metres at sea level and ~ 210 metres at 10 km altitude. On the average, 90% of the energy of a shower lies within R_M and about 99% is contained within $3.5 R_M$. The distribution is characterised by a distinct maximum in the core of the shower which vanishes as the shower develops. Grindhammer et al. [18] show that the distribution is nearly flat at the beginning and the end of the shower but is steeper around the maximum of shower development (see figure 2.12).

The lateral distributions are often represented as the sum of two Gaussian functions. Grindhammer et al. describe them with the function

$$f(r) = p \frac{2rR_C^2}{(r^2 + R_C^2)^2} + (1 - p) \frac{2rR_T^2}{(r^2 + R_T^2)^2},$$

where R_C and R_T are phenomenological functions of t and $\ln(y)$ and correspond to the core and tail component of the radial distribution respectively.

CHAPTER 3

CHERENKOV EMISSION IN ATMOSPHERIC SHOWERS

As can be seen from the longitudinal profiles of gamma-ray induced showers in chapter 2, a very small number of charged particles of the shower reach the ground ¹ for energies up to 1000 GeV. One can not deduce information about the primary γ -photon by detecting this relatively low number of particles.

At the same time, the charged particles of the showers with speeds greater than the speed of light in the atmosphere emit Cherenkov photons. Ground based imaging telescopes collect this light in order to obtain an “image” of the atmospheric shower and obtain information about the primary γ -photon through this image.

In order to study ground based imaging telescopes we therefore need to develop an understanding of the various features of Cherenkov emission. We begin this chapter with a brief description of the Cherenkov emission process and its dependence on the atmosphere, as well as the Cherenkov emission profile resulting from a shower.

The understanding of the Cherenkov light density pattern in the ground is of central importance in imaging telescopes since it is by detecting this light that the information about the primary γ -photon is obtained. We, therefore, give a simplified geometrical description of the Cherenkov photon distribution on the ground. We, then, discuss its various properties and their dependence on parameters such as primary energy and angle, and altitude of observation. we illustrate these with the help of results obtained from shower simulations by CORSIKA.

3.1 Basic facts

As a charged particle passes through matter, it produces a local polarisation in the material. If the velocity of this charged particle is greater than the velocity of light in that material, then this polarisation gives rise to a macroscopic electromagnetic field which results in the emission of Cherenkov photons (see figure 3.1). The angle of emission of these photons with respect to the charged particle’s trajectory is given by

$$\cos \theta_c = \frac{1}{\beta\eta} = \frac{c_{air}}{v} \quad , \quad (3.1)$$

where η is the refractive index of the material and $v = \beta c$ is the particle’s velocity. Since $\cos \theta_c \leq 1$, the threshold for Cherenkov emission is given by $\beta_{thr} = 1/\eta$. The threshold energy

¹This depends on the altitude of observation, but even for a 5000 metres altitude, the number of charged particles on the ground is quite low.

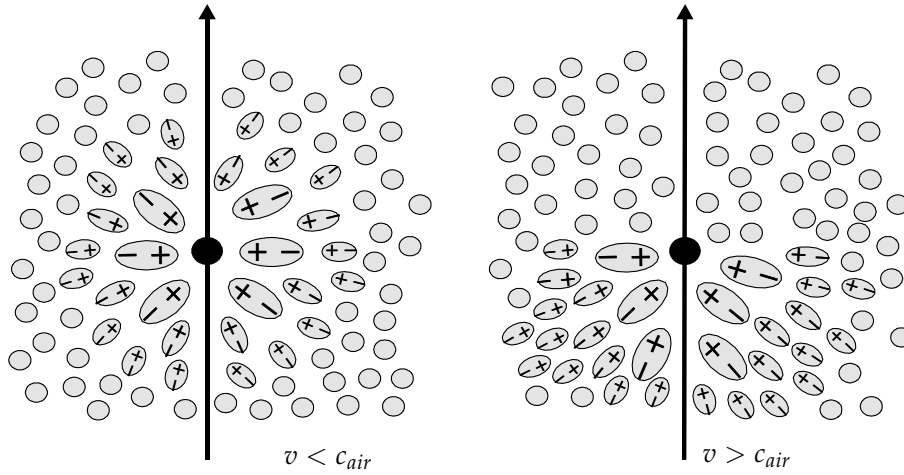


Figure 3.1: The polarisation of a dielectric material due to the passage of a charged particle. When the particle has a lower speed than the speed of light in that material, the net macroscopic field is zero (left), while in the case where the particle's speed is greater than the speed of light in the dielectric, there is a net polarisation which leads to the emission of Cherenkov photons

of the process therefore depends on the mass of the particle and the refractive index of air:

$$E_{thr} = \gamma_{thr} m_0 c^2 = \frac{m_0 c^2}{\sqrt{1 - \frac{1}{\eta^2}}}. \quad (3.2)$$

The number of Cherenkov photons produced per unit path length per unit wavelength interval by a particle of charge ze is given by

$$\frac{d^2 N}{dx d\lambda} = \frac{2\pi\alpha z^2}{\lambda^2} \left(1 - \frac{1}{\beta^2 \eta^2}\right) = \frac{2\pi\alpha z^2}{\lambda^2} \sin^2 \theta_c, \quad (3.3)$$

where α is the fine structure constant and λ the wavelength of the Cherenkov photons. The atmosphere becomes opaque to photons at smaller wavelengths (see section 3.3.1) and the detectors themselves operate only within the 300-700 nm wavelength range. One also notes that the refractive index is itself a function of wavelength, but since it changes very little within the 300-700 nm wavelength interval it is treated as being independent of λ (see figure A.2 in the appendix).

3.2 Cherenkov emission profile in an electromagnetic shower

3.2.1 Role of the atmosphere

The Cherenkov emission threshold and angle will be affected by the atmosphere profile through equations 3.2 and 3.1. The refractive index of the atmosphere depends not only on its density but also several factors like pressure variation, temperature, water vapour contents...

In a simplified model, only the dependence on the density is retained in the following form:

$$\frac{\eta(h) - 1}{\eta(0) - 1} = \frac{\rho(h)}{\rho(0)},$$

where h is the altitude in the atmosphere and $\eta(0)$ and $\rho(0)$ are the refractive index and density at sea level, respectively. The refractive index of air at sea level at STP conditions being $\eta(0) = 1.000293$, this can be expressed as²

$$\eta(h) = 1 + 0.000293 \frac{\rho(h)}{\rho(0)}. \quad (3.4)$$

Figure 3.2 (left) shows the variation of the refractive index in the U. S. Standard and Isothermal models (see section 2.1.3 for a description of the models). The figure in the centre shows the resulting increase in the energy thresholds for a muon and an electron to radiate Cherenkov photons with increasing altitude in the atmosphere. At any given altitude, the angle of emission θ_c , then, only depends on the energy of the charged particle and lies between the two limiting values $\theta_c = 0$ at the threshold and $\theta_c = \theta_{c \max}$ where $\theta_{c \max} = \arccos(1/\eta)$ for $\beta = 1$. The right plot in figure 3.2 shows the variation of this limiting angle with altitude. We see that as particles move deeper in the atmosphere, they tend to emit Cherenkov photons at wider angles.

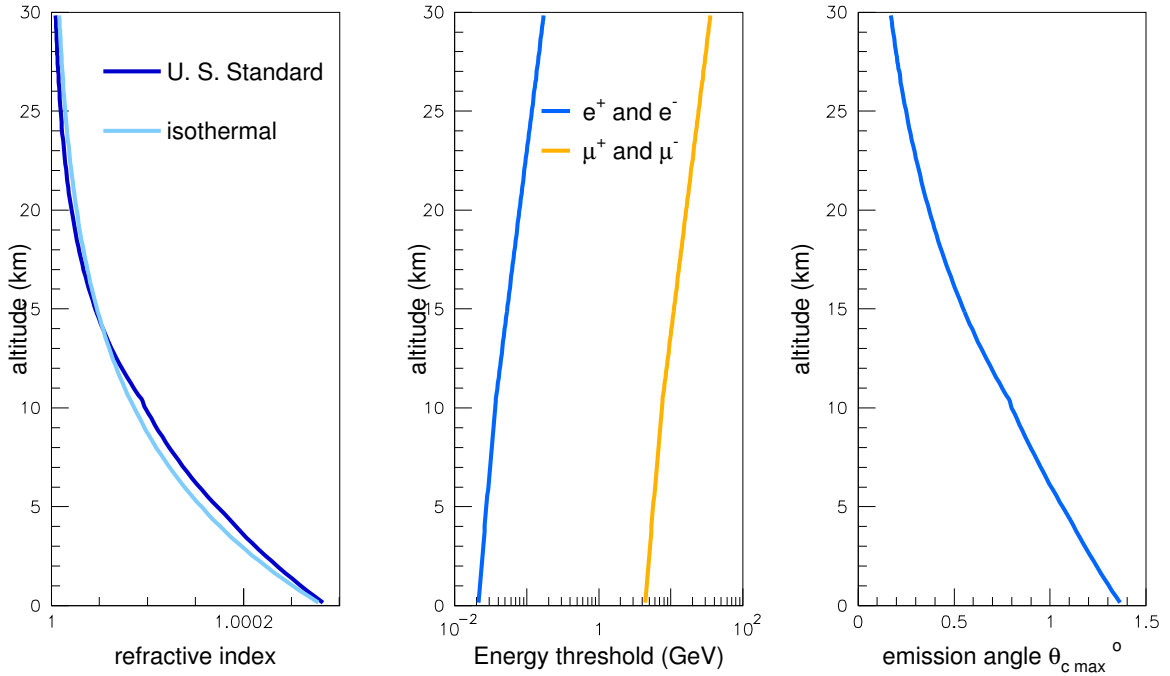


Figure 3.2: The refractive index of the atmosphere is calculated using equation 3.4 with the U. S. standard and the isothermal models and presented as a function of altitude in the left plot. The plot in the centre shows the energy threshold for Cherenkov emission for a muon and an electron at various altitudes in the U. S. standard model. In the right figure, we show the variation of the maximum angle for Cherenkov emission $\theta_{c \max} = \arccos(1/\eta)$, i. e. when the particle travels at the speed of light in the U. S. standard model.

3.2.2 Longitudinal profile of the Cherenkov emission

Atmospheric showers emit Cherenkov photons whenever the charged particles of the shower are above the Cherenkov emission threshold described above. The total number of Cherenkov

²In CORSIKA the value $\eta(0) = 1.000283$ is used.

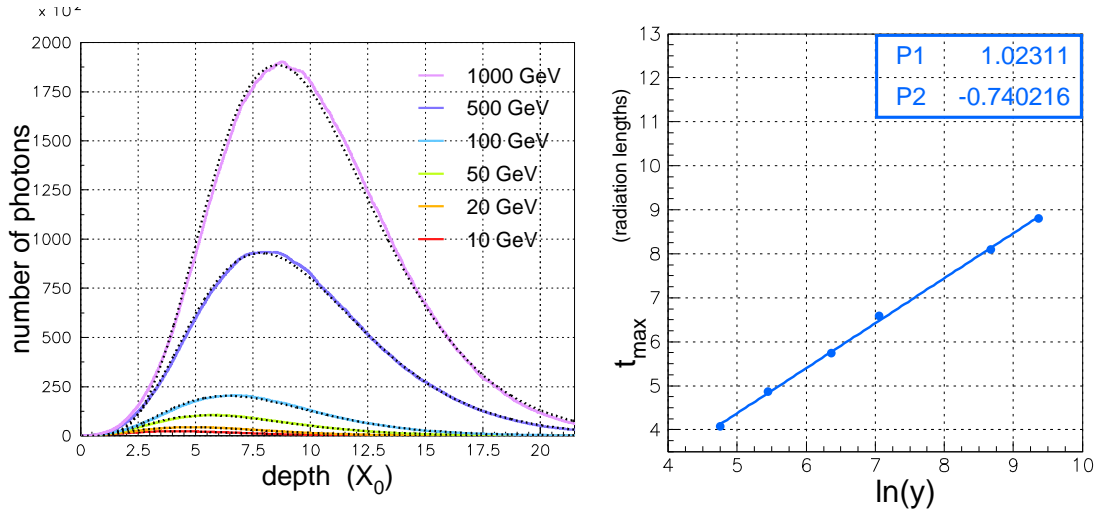


Figure 3.3: Left: The average longitudinal profile in terms of the number of Cherenkov photons emitted at each depth for various energies. These distributions are fitted with the function $f(t) = C(\beta t)^{\alpha-1}e^{-\beta t}$ (dotted lines). The same profiles are shown in log scale in figure A.3 on page 234 in the appendix. Right: The dependence of the maximum of the Cherenkov photon emission profile (points) on the energy expressed in units of critical energy ($y = E/E_c$). The points are fitted with the line $f(x)=P_1x+P_2$.

photons emitted by the shower at various depths closely follows the longitudinal profile of the shower itself. Figure 3.4 shows the simulated longitudinal profiles of showers of various energies in terms of the number of Cherenkov photons emitted at each depth. As with the profiles in terms of the number of particles discussed in section 2.3.2, these profiles can be described by the function

$$\frac{dN}{dt} = N_o\beta \frac{(\beta t)^{\alpha-1}e^{-\beta t}}{\Gamma(\alpha)}, \quad (3.5)$$

where N_o is the total number of Cherenkov photons emitted by the shower. Also, as with the discussion in section 2.3.2, the length is described in units of X_o i. e. $t = z/X_o$ (with z expressed in g/cm^2), and the energy in units of critical energy i. e. $y = E/E_c$ in this section. The use of these units minimises the dependence on the material being considered. The position of the maximum, the shower's centre of gravity and variance are then given by

$$\begin{aligned} t_{max} &= \frac{\alpha - 1}{\beta}, \\ \langle t \rangle &= \frac{\alpha}{\beta}, \\ \langle t^2 \rangle &= \frac{\alpha(\alpha - \beta)}{\beta^2}, \end{aligned}$$

respectively. It can also be shown that the higher order moments are given by

$$\langle t^n \rangle = \frac{(\alpha + n - 1) \cdots \alpha}{\beta^n}.$$

We have fitted the average Cherenkov photon emission profiles shown in figure 3.3 (left) with the function $f(t) = C(\beta t)^{\alpha-1}e^{-\beta t}$ in order to obtain a parametrisation of these profiles. The

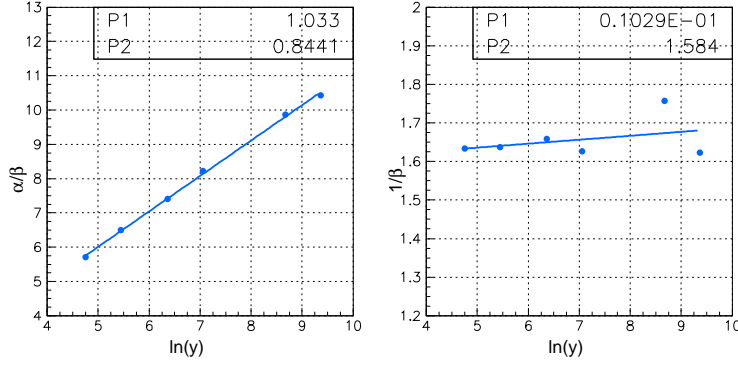


Figure 3.4: The dependence of the average value of α/β and $1/\beta$ on the shower energy expressed in units of critical energy ($y = E/E_c$). These points are obtained by fitting the profiles in figure 3.3 (left) and are here fitted with the line $f(x)=P_1x+P_2$.

position of the maximum of Cherenkov emission development t_{max} shows a linear dependence on $\ln(y)$. In figure 3.3 (right) we show the position t_{max} as a function of the energy. The points obtained from the fits of the longitudinal profiles shown in figure 3.3 (left) are fitted with a line which gives the following parametrisation:

$$t_{max} = -0.74 + 1.02 \ln(y).$$

The average values of α/β and $1/\beta$ obtained from the fits are linearly dependent on $\ln(y)$ as well. This dependence is shown in figure 3.4 and gives us the following parametrisations:

$$\begin{aligned} \frac{\alpha}{\beta} &= 0.84 + 1.03 \ln(y) \\ \frac{1}{\beta} &= 1.58 + 0.01 \ln(y). \end{aligned}$$

One notes that $1/\beta$, which is responsible for the decaying part of the profile has very little dependence on the energy.

The parameters β/α and $1/\alpha$ have Gaussian distributions which can be used to obtain a parametrisation for the fluctuations in γ -initiated showers. As an example, we show the distribution of β/α and $1/\alpha$ for 100 GeV showers in figure 3.5. The standard deviation σ is obtained by fitting each distribution with a Gaussian function. In figure 3.6, we present the ratio $\sigma_{\beta/\alpha}/(\beta/\alpha)$ (left) and $\sigma_{1/\alpha}/(1/\alpha)$ (right) as a function of the energy. The points can be fitted with a line and yield the following parametrisations:

$$\begin{aligned} \frac{\sigma_{\beta/\alpha}}{\beta/\alpha} &= 0.35 - 0.03 \ln(y) \\ \frac{\sigma_{1/\alpha}}{1/\alpha} &= 2.6 - 0.22 \ln(y). \end{aligned}$$

One also notes that there is no correlation between the two parameters β/α and $1/\alpha$ (figure 3.5(right)). The parametrisation thus obtained can be used to generate random profiles for γ -initiated showers. These parametrisations have been used in [19] to study the percentage of the Cherenkov emission cut-off at different energies for different altitudes of observation. A similar parametrisation for the longitudinal profiles in terms of the number of particles is given in appendix B.

Dependence on primary angle At a given energy, the shower maximum occurs higher in the atmosphere for primary gamma rays incident at larger zenith angles since a larger amount of matter is traversed between two different altitudes. The result is a compression (in terms of

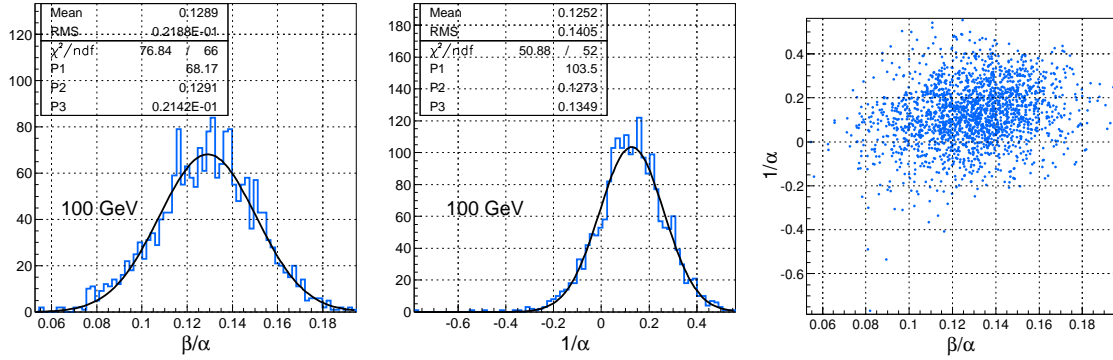


Figure 3.5: The distribution of β/α (left) and $1/\alpha$ (centre) for 100 GeV showers. Both distributions are fitted with the Gaussian function $f(x) = P1x^{-0.5(\frac{x-P2}{P3})^2}$. The right plot shows the absence of correlation between β/α and $1/\alpha$ for 100 GeV showers.

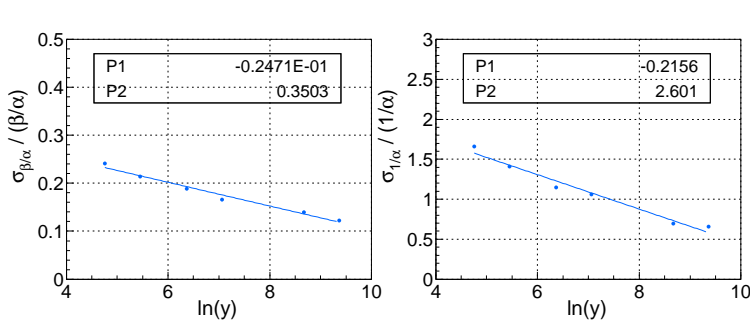


Figure 3.6: The dependence of $\sigma(v)/v$ on the energy of the showers, where $v = \beta/\alpha$ (in the left figure) and $v = 1/\alpha$ (in the right figure). The points obtained from the distributions of β/α and $1/\alpha$ are fitted with the line $f(x)=P_1x+P_2$, and the results of the fit shown on the plots.

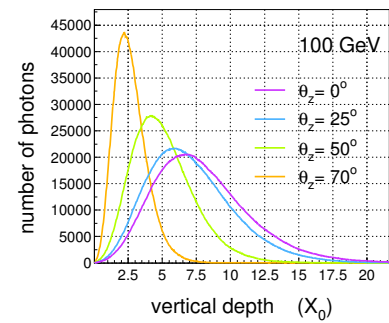


Figure 3.7: Comparison of Cherenkov photon longitudinal profiles for different primary zenith angles at a fixed energy (100 GeV).

altitude) of the shower profile away from the ground such that the shower has a smaller penetration in the atmosphere. This is shown in figure 3.7 where the average profiles for different primary zenith angles are compared for 100 GeV showers. Note that the shower profile will be compressed when measured in a direction perpendicular to the ground, but it will also be slightly elongated when measured along the axis of the shower, as it develops at greater height and therefore in a less dense atmosphere.

3.2.3 The number of Cherenkov photons produced

The total number of Cherenkov photons emitted by an electromagnetic shower depends on the energy as shown in figure 3.8 (left) and table 3.1. One also notice a weak dependence on the zenith angle which can be explained by the differences in the density of the atmosphere at which showers with different zenith angles develop (see above). Figure 3.8 (right) and the last column of table 3.1 illustrate the presence of intrinsic fluctuations in electromagnetic showers. At lower energies, the shower size and form varies more from shower to shower. This factor introduces a natural limit to our ability for linking a Cherenkov photon number to a primary energy and will play a role in the reconstruction of shower parameters from observations (see chapters 6,7 and 8).

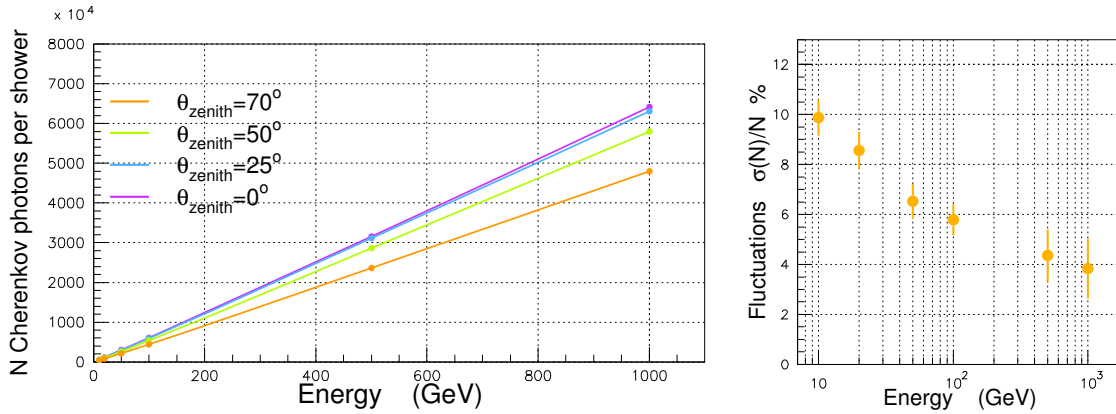


Figure 3.8: Left: The average number of Cherenkov photons emitted as a function of primary γ energy, for several zenith angles. Right: Intrinsic fluctuations of the number of Cherenkov photons emitted in a shower as a function of the energy, for zenith angle= 0°

	0°	25°	50°	70°	N_{showers}	fluctuations %
10 GeV	5.5×10^5	5.4×10^5	4.8×10^5	3.9×10^5	10000	9.88
20 GeV	1.1×10^6	1.1×10^6	1×10^6	8.1×10^5	5000	8.56
50 GeV	3×10^6	2.9×10^6	2.6×10^6	2.1×10^6	2000	6.53
100 GeV	6.1×10^6	5.9×10^6	5.4×10^6	4.4×10^6	1000	5.79
500 GeV	3.2×10^7	3.1×10^7	2.9×10^7	2.4×10^7	200	4.36
500 GeV	6.4×10^7	6.3×10^7	5.8×10^7	4.8×10^7	100	3.84

Table 3.1: The average number of Cherenkov photons produced for different primary energies and different zenith angles. The number of showers simulated at each energy is shown in the second last column. The last column shows the intrinsic fluctuation ($\sigma(N)/N$) of the Cherenkov photon number at each energy for showers generated with zenith angle= 0° .

3.3 Extinction and transmission

As Cherenkov light travels through the atmosphere before reaching the ground, it undergoes various processes leading to a loss or modification of the intensity on the ground.

3.3.1 Absorption

Part of the absorption occurs due to the presence of various molecules in the atmosphere. O_3 absorbs wavelengths below 340 nm and occurs at different altitudes [20]. O_2 absorption occurs below 240 nm and thus does not affect the atmospheric Cherenkov instruments which are sensitive only in the 300 nm - 700 nm range³. Some absorption occurs due to the presence of aerosols as well. Figure 3.9 (left) shows the impact of O_3 and O_2 absorption on transmission of light.

³This sensitivity range of the Cherenkov instruments comes mainly from the photomultipliers (PM) and to a lesser extent the mirrors used in the telescopes. Both have various degrees of efficiency at various wavelengths and are most efficient in the 300 nm - 700 nm range. In fact, the quantum efficiency of PMs approaches zero outside this range. These points are briefly discussed in chapters 4 et 5.

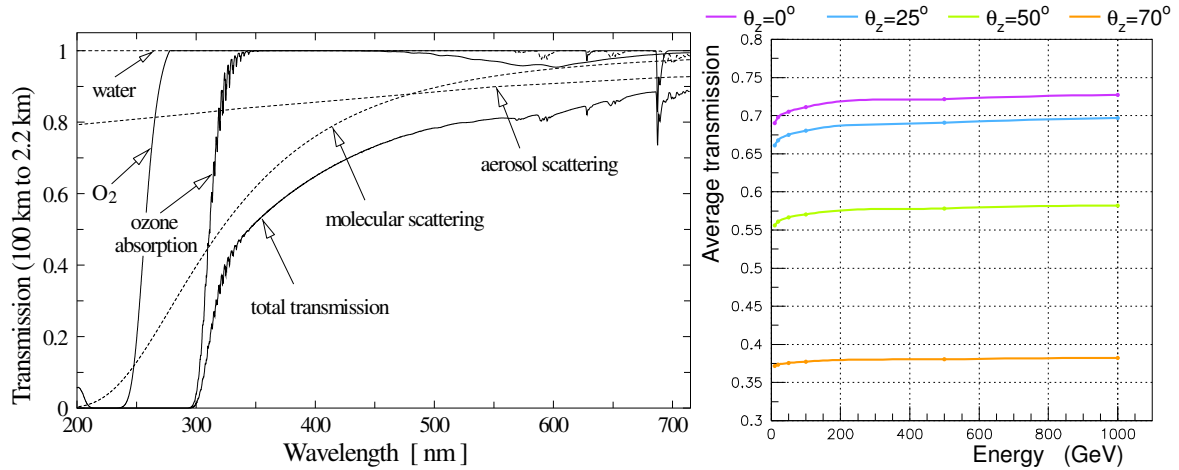


Figure 3.9: Left: The impact of different absorbers and scatterers on the transmission of light from space (~ 100 km) to an altitude of 2.2 km is shown as a function wavelength. The figure is taken from [20]. Right: The simulated average transmission of Cherenkov photons through the atmosphere at primary energies. The Cherenkov photons are simulated in the 300 nm - 700 nm range.

3.3.2 Scattering

Two types of target particles give rise to two separate scattering phenomena.

Rayleigh scattering occurs due the presence of air molecules and has a strongly wavelength dependent cross section ($\propto \lambda^{-4}$). It is responsible for most of the extinction in the Cherenkov instrument sensitive range.

Mie scattering occurs with larger particles (mostly aerosols) and has very little wavelength dependence. Instead it depends on the size, shape and composition of the particles.

Some of the scattered light may fall in the viewing angle of the instrument, but only a small amount of it is collected along with the direct light with short integration time instruments. Scattering is therefore often considered and treated as an absorption process.

Among the sources of extinction O_3 and aerosols are both site and time dependent. An accurate model of the atmosphere for a given site takes these effects into account. However, they are not considered for general studies through simulations.

In figure 3.9 (right), we plot the average total (all wavelengths) extinction as a function of energy for CORSIKA simulated showers. While there is very little energy dependence, the extinction decreases significantly with the primary γ -ray zenith angle. As shower development occurs higher in the atmosphere, Cherenkov light is emitted higher as well and has to pass through more layers of the atmosphere before reaching the ground.

3.4 Cherenkov light density on the ground

3.4.1 Geometry

The lateral distribution of the Cherenkov light on the ground depends on the altitude and angle of emission of each photon. Figure 3.10 (left) shows the arrival position of Cherenkov photons

on the ground as a function of the altitude of emission for photons with the maximum angle of emission $\theta_{c\ max}$ (see section 3.2) with respect to the vertical. The figure on the right illustrates the geometry of the Cherenkov density profile on the ground for the same angle of emission. At higher altitudes where the atmosphere is rarer, the Cherenkov photons are emitted with smaller angles. A Cherenkov photon emitted at an altitude of 21 km (\sim average height of first interaction) will reach sea level at a distance of about 120 metres from the shower axis. The furthest lateral distance (\sim 140 metres) is travelled by photons from around 12 km. Deeper in the atmosphere, the emission angle increases, but since photons are emitted closer to the ground, they reach smaller horizontal distances on the ground. The cumulation of Cherenkov light from various heights in the 100-140 metres range, results in a ring like Cherenkov light maximum on the ground. At higher altitudes of observation, the maximum lateral distance of arrival by the photons is smaller (e.g. \sim 90 metres for 5 km altitude), the ring is narrower and denser (as the cumulation occurs over a small distance) and the overall photon density on the ground is greater.

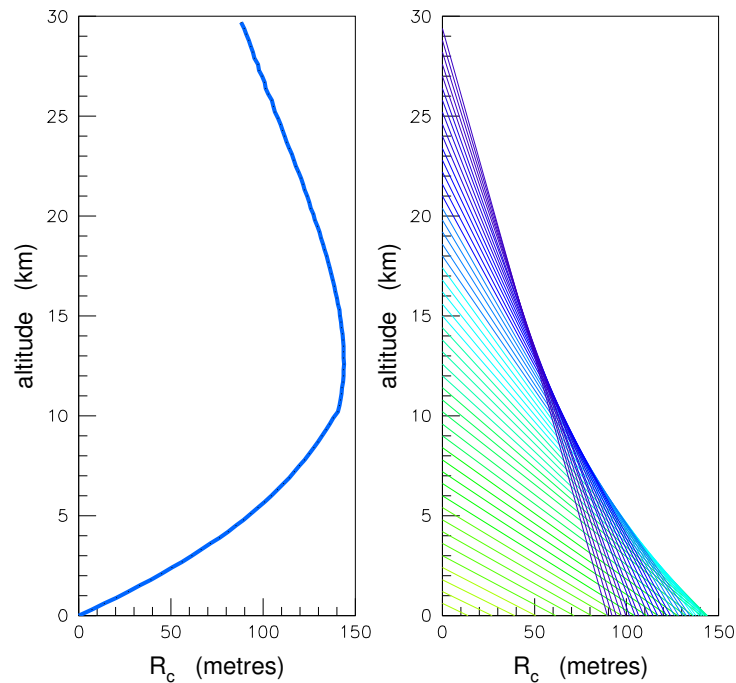


Figure 3.10: The position R_c of Cherenkov photon arrival on the ground at sea level as a function of the altitude of emission. This is calculated for the maximum angle of emission $\theta_{c\ max}$ as described in section 3.2 for an electron moving perpendicular to the ground.

In figure 3.11 and 3.12, we show the typical distribution of Cherenkov photons on the ground for simulated γ -showers. The Cherenkov ring-like structure is present in the three distributions and the bulk of the photons is contained within it. Although, Cherenkov photons can be found up to distances of several kilometres.

The difference between the simplified schematic representation in figure 3.10 and real electromagnetic showers is mainly due to the presence of a large number of charged particles undergoing multiple scattering which randomises the direction of their trajectories with respect to the original primary direction⁴.

⁴In fact a single muon produces a Cherenkov distribution similar to the one given by figure 3.11 and 3.12 as it travels a long distance in the atmosphere without interaction. This topic is briefly touched in section 9.2.2.

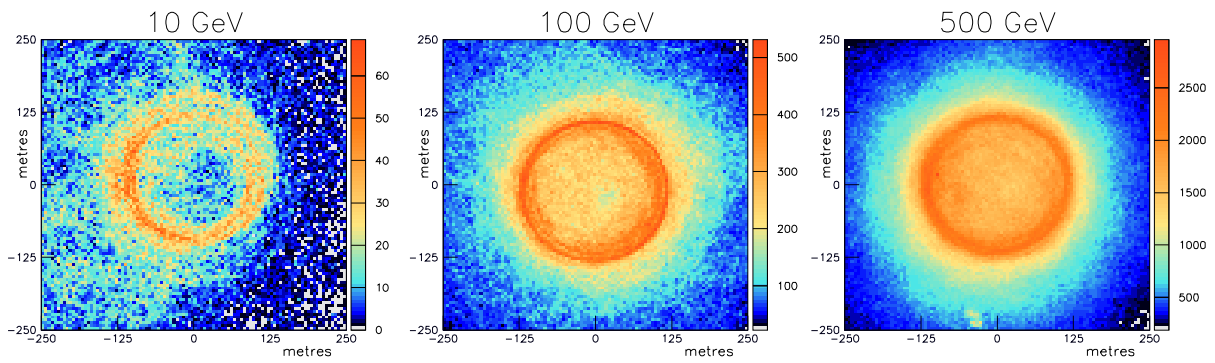


Figure 3.11: Cherenkov photon distributions on the ground (2200 metres altitude) for three simulated γ -ray induced showers of 10, 100 and 500 GeV. A surface area of $500 \times 500 \text{ m}^2$ is presented in each figure.

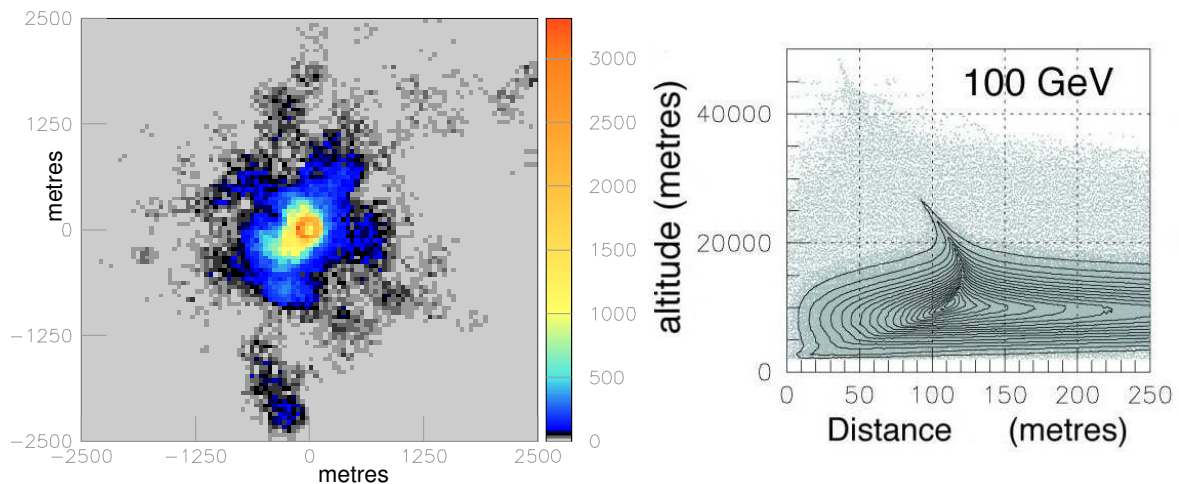


Figure 3.12: Cherenkov photon distribution on the ground (in a $5 \times 5 \text{ km}^2$ field) for a 10 GeV simulated γ -ray shower at 2200 metres altitude. The shower is the same as the one whose distribution is shown in figure 3.11

Figure 3.13: Two dimensional scatter plot of the altitude of emission of Cherenkov photons (ordinate axis) and their arrival position on the ground at 2200 m altitude (abscissae axis) for 500 simulated γ -ray showers of 100 GeV each.

We have plotted the 2-dimensional distribution of the altitude of emission (ordinate axis) and the arrival position on the ground measured from the shower axis (abscissae axis) of the Cherenkov photons produced in 500 simulated showers (figure 3.13). As we go deeper in the atmosphere, the shower contains more particles and becomes broader due to multiple scattering. As a result, the Cherenkov photons are emitted at different angles and distances with respect to the shower axis, with some of them arriving on the ground at distances well beyond 200 metres. The most important emission at each altitude (densest regions of the plot identifiable by the contours) still occurs along a curve similar to that from figure 3.10. The position of shower maximum is identifiable at around 10 km altitude with photons reaching the ground around 110-120 metres from the axis. The Cherenkov ring position occurs at around

120 metres instead of the 150 metres we saw in figure 3.10, since the altitude of observation is 2200 metres instead of sea level. The ring has mostly photons from 10-20 km altitudes.

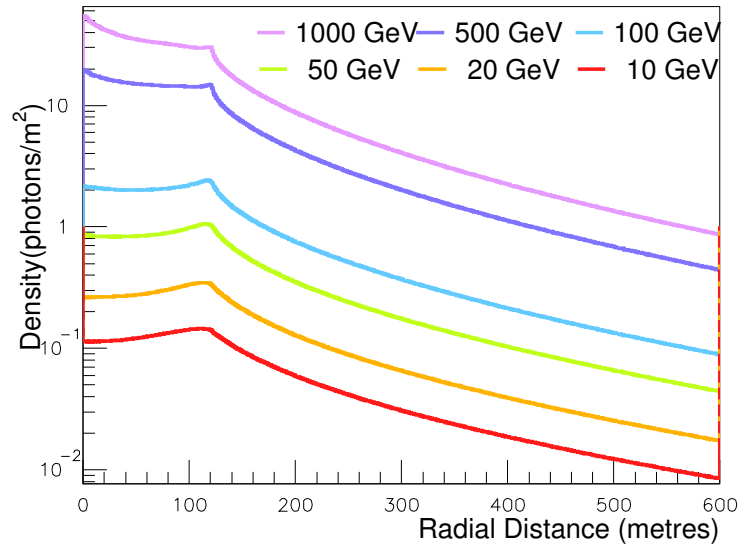


Figure 3.14: The average density of Cherenkov photons on the ground (expressed in photons per m^2) as a function of the distance from the shower core for simulated γ -ray showers of various energies at 2200 m of altitude.

3.4.2 Dependence on primary energy

The effect of primary energy is twofold. First, as presented in section 3.2.3, the total number of Cherenkov photons produced in a shower is proportional to primary energy. Consequently, the density of the Cherenkov photons on the ground has the same energy dependence. This effect is visible in the examples of Cherenkov light distributions presented in figure 3.11. As a further step, simulations were done in order to obtain the average density profiles at various energies. The results are presented in figure 3.14. We note that there is no impact on the Cherenkov ring size of 120 metres whose origin is purely geometric.

The second impact of the energy change on the Cherenkov distribution on the ground is due to the increase of shower maximum depth and shower size with energy. This is visible in figure 3.15, where Cherenkov photon emission altitude is plotted versus the arrival position on the ground for 2200 metres altitude for showers of various energies. As the shower maximum occurs deeper in the atmosphere with increasing shower energy, more Cherenkov photons are emitted closer to the ground (below 10 km) and have arrival positions at smaller distances from the axis. The cumulation of photons due to this effect results in an increase of density close to the shower axis. This peak is particularly visible for the 500 GeV and 1000 GeV curves in figure 3.14, where the density is actually greater than that of the Cherenkov ring itself.

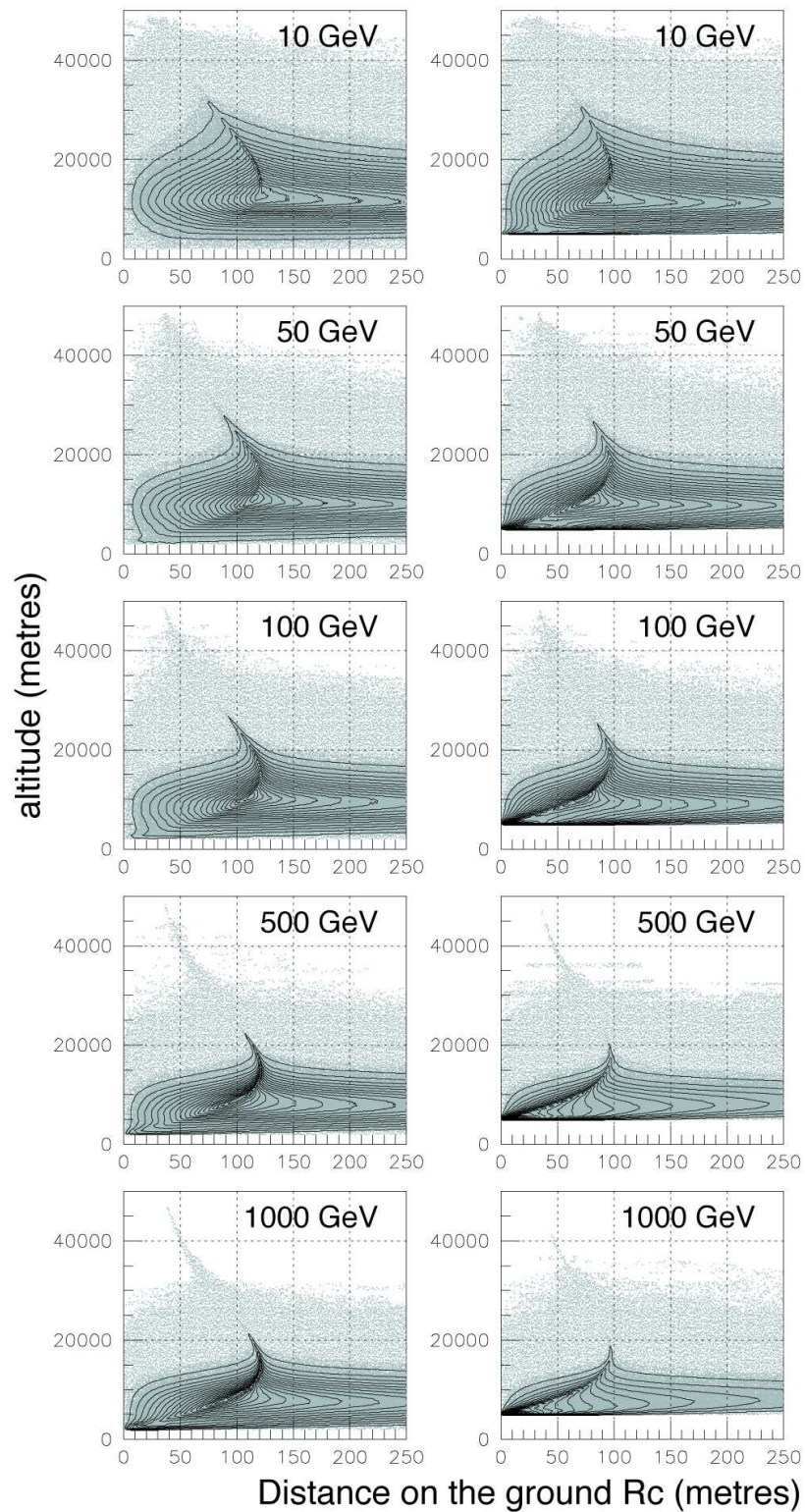


Figure 3.15: The Cherenkov photon emission altitude (ordinate axis) plotted against their arrival position on the ground (2200 m altitude on the left and 5000 m on the right) for simulated γ -ray showers. The number of showers simulated were 10000, 5000, 1000, 500, 200 and 100 for 10, 20, 50, 100, 500 and 1000 GeV respectively.

3.4.3 Low altitude materialisations

Some showers materialise very low in the atmosphere. When this occurs, the shower development is often cut off by the ground and the bulk of Cherenkov photons emitted close to it. In this case, most of the Cherenkov photons emitted by the shower can not travel very large distances and have impact positions on the ground that are very close to the shower core. In figure 3.16 we show plots for two such showers (10 GeV in the top row and 1000 GeV in the bottom one) with an altitude of first interaction about 6 km a. s. l.. The left plots show the two-dimensional plot of the altitude of emission of Cherenkov photons in the shower (ordinate axis) and their arrival position on the ground (abscissae axis). One can see that at both energies the bulk of Cherenkov photons arrive within 40-50 metres of the shower impact position. This results in a peak in the Cherenkov density profile on the ground, near the shower impact position. This is shown in the right plots (black curve), where this profile is compared with the average profile at that energy (coloured line). As expected, while the positions close to the shower impact point (at 0 m) have a greater density than the average profile, the density at larger distances is very low. One also notices that there is no identifiable Cherenkov ring.

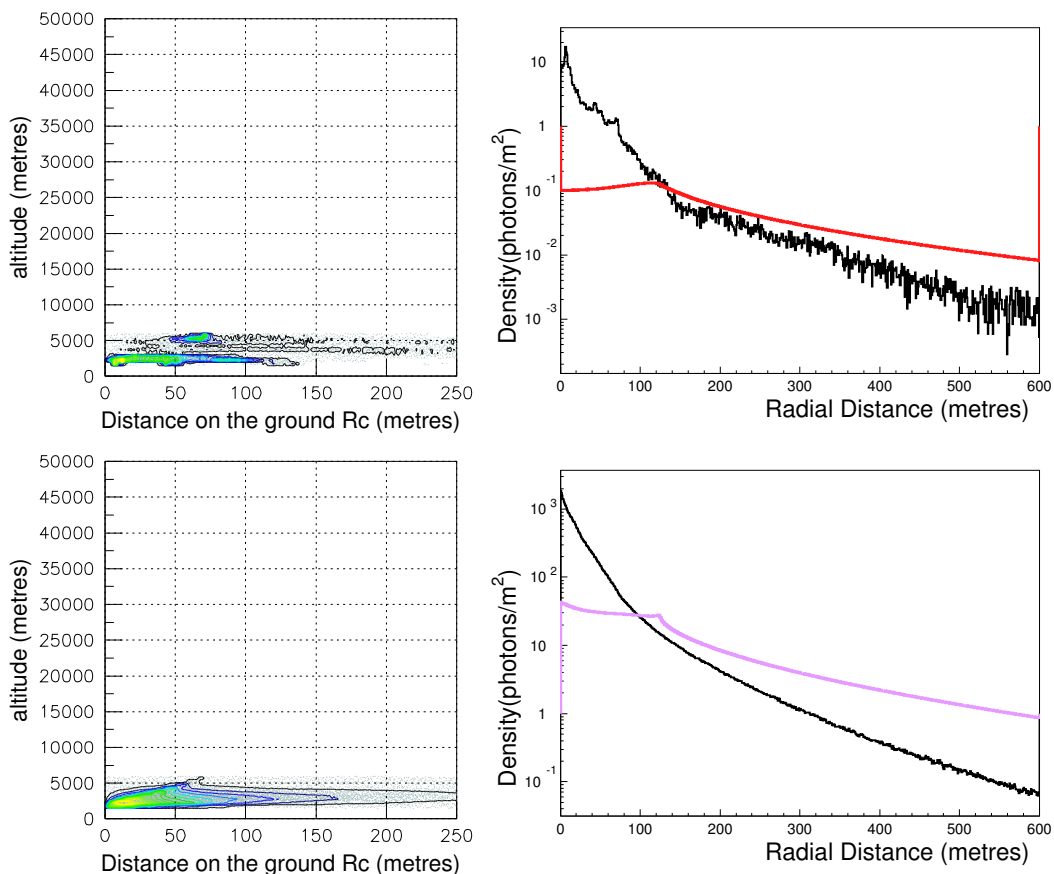


Figure 3.16: Left: The two-dimensional plot of the altitude of emission of Cherenkov photons in the shower (ordinate axis) and their arrival position on the ground (abscissae axis) for a 10 GeV shower (top) and a 1000 GeV shower (bottom) with altitudes of first interaction in the atmosphere around 6000 m a. s. l. The right plot shows the profile of the Cherenkov density on the ground obtained for the same shower (black line). This is compared with the average density of Cherenkov photons on the ground for showers of the same energy (coloured line).

These are very extreme cases and do not occur often. Yet, we have seen occasional showers like these in the random generations of showers. When they do occur, they can have an important impact on the calculations of average profiles and parameters for showers of a given energy. As an example, it takes about 10000 showers to absorb the effect of one such shower on the Cherenkov density profile on the ground at 10 GeV. The study of these extreme cases is also important since it allows to bring out the difference of behaviour for different altitudes of materialisation and thus helps us understand the development of showers with moderate altitude materialisations as well. We will see in later chapters, that the altitude of materialisation has an impact on the images obtained from the showers and also the reconstruction of the shower parameters from the images.

3.4.4 Effect of ground altitude

As we briefly mentioned in section 3.4.1, figure 3.10 shows that at higher altitudes of observation, the Cherenkov ring will be smaller, narrower and denser. Also, in figure 3.15, we presented the Cherenkov photon emission altitude and arrival position on the ground for 2200 metres (left) and 5000 m (right) altitudes. At higher altitudes, the shower is closer to the ground and all the Cherenkov photons travel smaller distances before reaching the ground and therefore form a smaller Cherenkov ring. Moreover, since essentially the same amount of photons gets distributed in a smaller area⁵, the Cherenkov photon density is more important as well⁶. In figure 3.17, we compare the average flux of simulated γ -showers at 2200 metres and 5000 metres. The Cherenkov ring radius is around 90 metres for the 5000 m curves and the density is several times more important in comparison with the 2200 m curves. At distances beyond the Cherenkov ring (several hundred metres), the density is comparable to that at lower altitudes. At even larger distances (beyond several hundred metres) the density of Cherenkov photons on the ground becomes higher for lower altitudes of observations. This effect is particularly visible in the 1000 and 500 GeV curves in figure 3.17 (left). This occurs since the Cherenkov photons get to travel larger distances (horizontally and vertically) when the ground level is lower. The progression of the same photon will be stopped earlier when the ground level is higher, resulting in an arrival position on the ground that is closer to the shower impact position. For showers of lower energy the cross over takes place at larger distances as can be seen from figure 3.17 (right) for the 10 GeV curves.

One also notices an accentuation of the central peak (discussed in the previous section) for higher energies due to the proximity of the shower maximum. The low energy curves too tend to show an increase in density at the centre as compared to the density profiles for 2200 m curves. For higher energies, shower development is still going on at these altitudes. This is illustrated through the example of the Cherenkov photon distribution, due to a 500 GeV γ -ray shower, at various altitudes in figure 3.18. In the figure for 3000 m altitude, one notices the decrease of the Cherenkov ring radius and the apparition of a few intense points towards the centre of the ring. In the 5000 m altitude image, these points are greater in number and more intense. They correspond to the impact of shower particles (mostly electrons and positrons) on the ground. This can be seen in figure 3.19 where the Cherenkov photon density from a 500 GeV shower obtained at 3600 m is shown along with the impact positions of individual

⁵This is specially true for low energies at which showers are smaller and are not cut off before reaching the ground. Even for the higher energies studied in this chapter, the bulk of the Cherenkov emission occurs above 5000 metres altitude. We recall that we evaluated the average fraction of the shower cut off before reaching the ground for various shower energies and altitudes of observation in section 2.3.2.

⁶When the altitude of observation is 5000 metres the Cherenkov photons get essentially distributed in the 90 m radius Cherenkov ring area. At lower altitudes e. g. 2200 metres, the same Cherenkov photons get distributed in a 120 m radius Cherenkov ring.

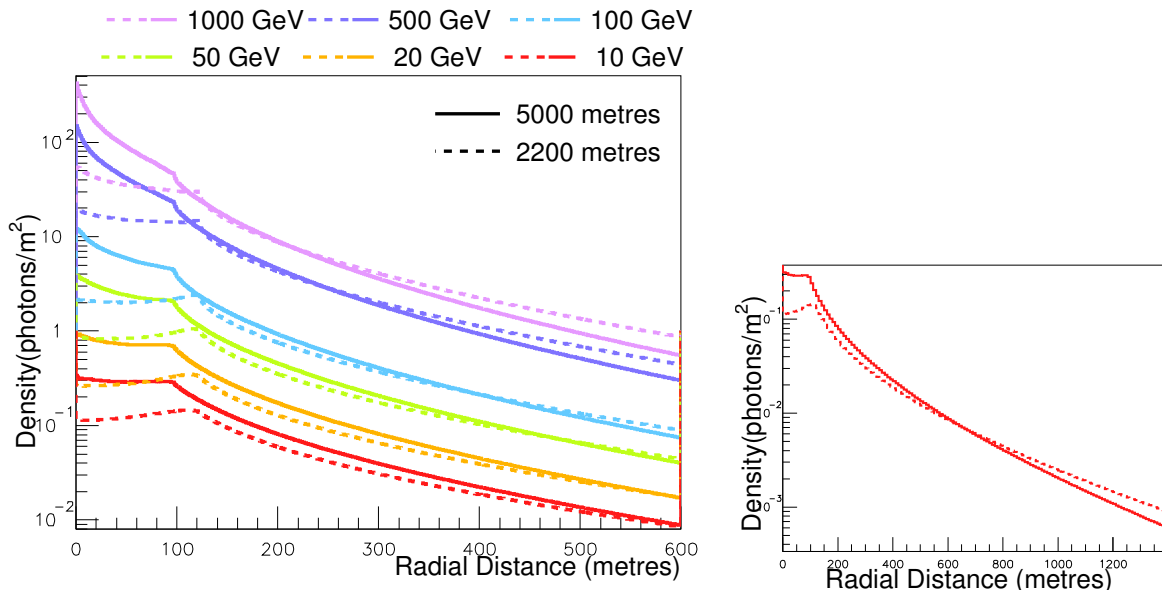


Figure 3.17: The left figure shows the comparison of the average density of Cherenkov photons on the ground (photons per m²) at 2200 and 5000 m altitudes for simulated showers of various energies. In the right figure, we show the comparison of the density curves for low energy showers (10 GeV) up to a distance of 1300 metres from the shower core.

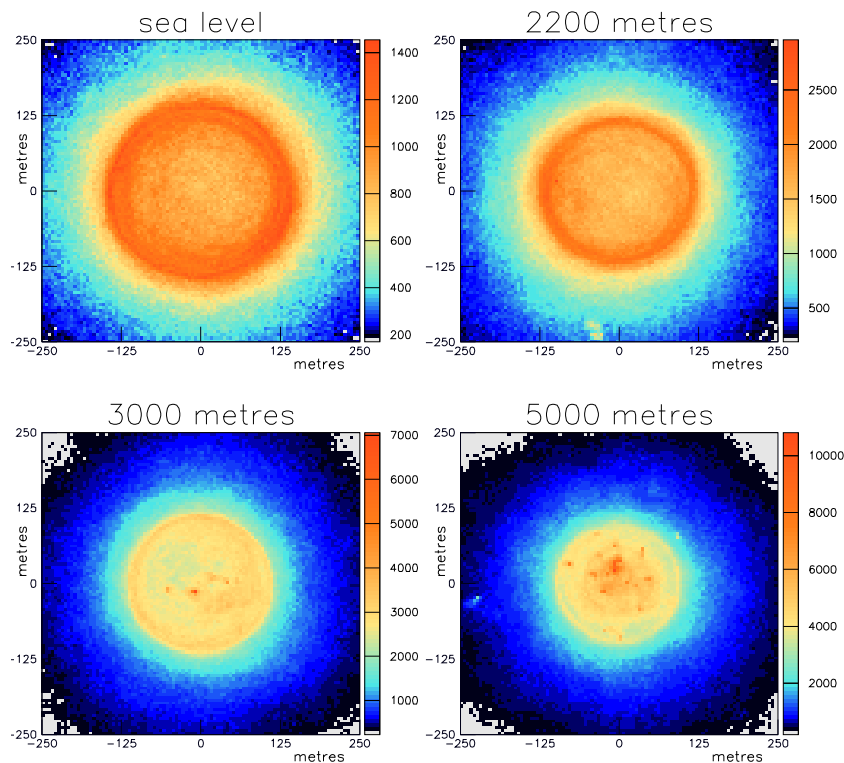


Figure 3.18: Comparison of the Cherenkov photon distribution on the ground for a 500 GeV γ -ray shower at four different altitudes.

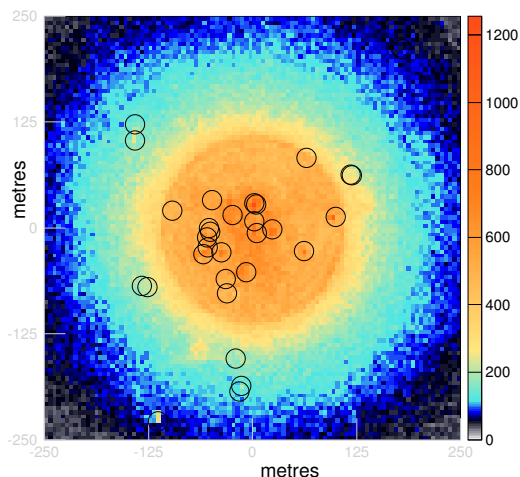


Figure 3.19: The Cherenkov photon distribution on the ground, obtained from a 500 GeV shower at 3600 m a. s. l.. The impact position of the electrons and positrons arriving on the ground are shown through black circles. No muons arrive on the ground level.

electrons and positrons (black circles). When a charged particle from the shower arrives on the ground, it is still radiating Cherenkov photons, which results in a sharp density peak around its position of impact. Figure 3.18 also shows that there is also an overall increase in density close to the shower core position at higher altitudes. One also notes that the outline of the ring itself seems to be sharper at higher altitude. This can be understood from figure 3.10, where we see that at high altitude, the region where the Cherenkov photons from various altitudes overlap is narrower than at lower altitudes.

Effect on the total number of Cherenkov photons

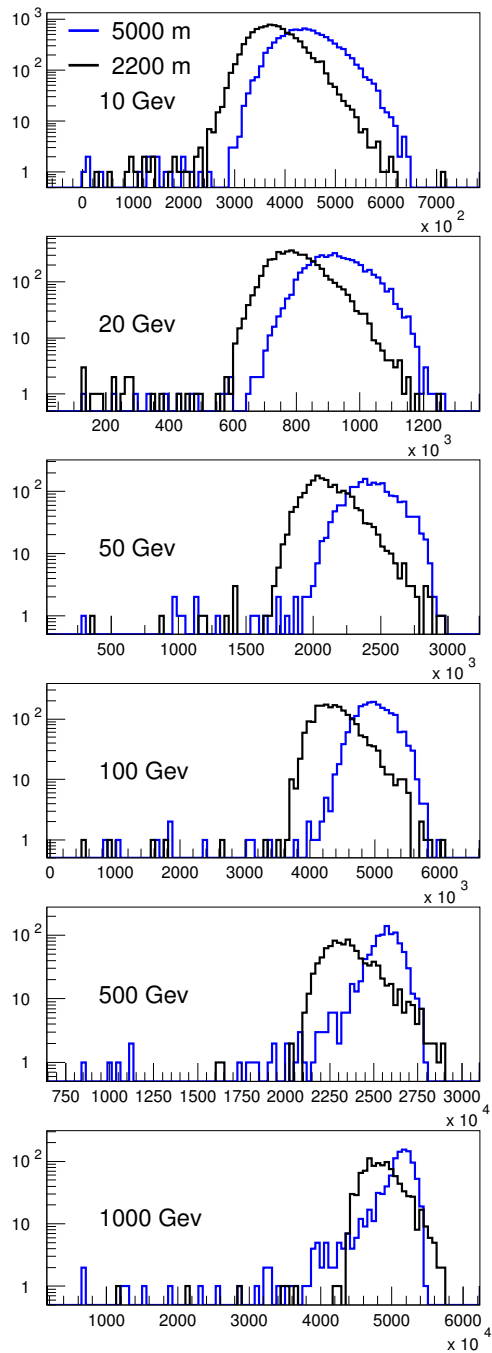
The altitude affects the total number of Cherenkov photons reaching the ground in several ways.

- Since the shower is closer to the ground at higher altitudes, the Cherenkov photons have fewer layers of atmosphere to traverse and therefore are less subject to atmospheric absorption.
- At the same time, more showers reach the ground while still in the development phase. This is specially true for showers with low altitude first interactions. In such cases, the shower would have emitted more Cherenkov photons, had it not been stopped by the ground.

As a result of these two effects, showers that fully develop above the higher level of observation, will tend to have more Cherenkov photons that reach the ground at higher altitude than at lower altitude. At the same time, showers that are not fully contained above the ground will tend to have fewer photons depending on their individual longitudinal development. This leads to the apparition of tails in the distributions of the number of Cherenkov photons obtained on the ground at higher altitudes. This is seen in figure 3.20 (specially at higher energies), where we compare the distributions at 2200 m altitude with those at 5000 m for various energies.

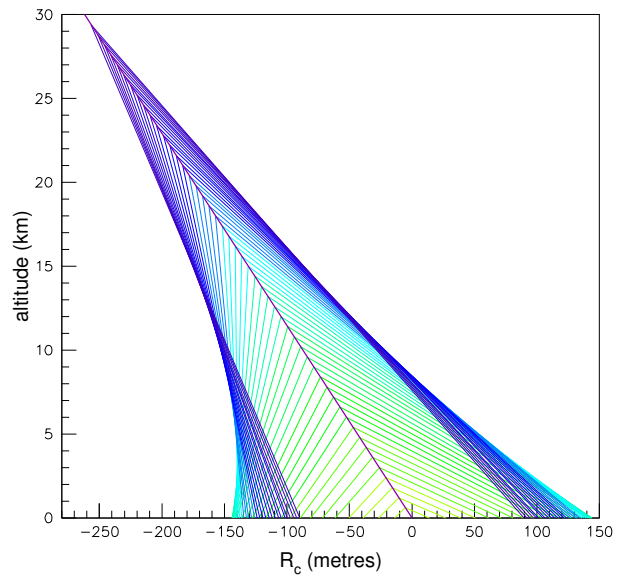
3.4.5 Primary zenith angle

Shower inclination, also, affects the Cherenkov photon distribution on the ground. As zenith angle increases, the Cherenkov ring tends to get elongated in that direction. A schematic representation of Cherenkov light emitted at various altitudes by an electron with a 0.5° inclined trajectory is given in figure 3.21(a). We have chosen different vertical and horizontal scales in order to put an emphasis on the inclined geometry. As the elongation of the Cherenkov ring

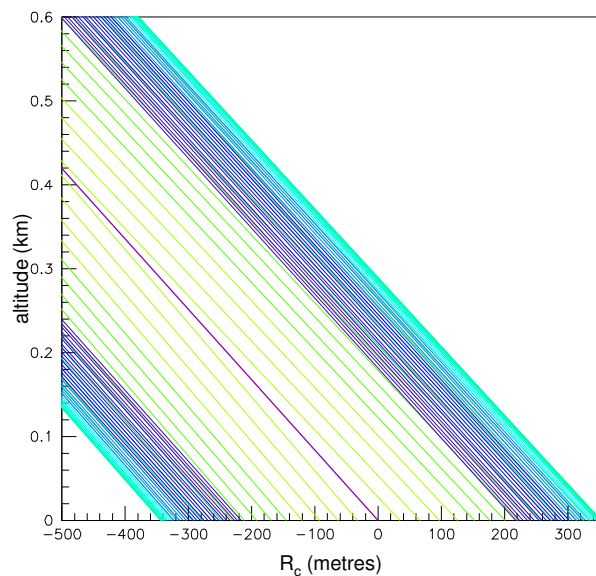


Number of Cherenkov photons on the ground

Figure 3.20: The distributions of the total number of Cherenkov photons, from a shower, obtained on the ground are compared for low altitude (2200 m in black) and high altitude (5000 m green) for different energies.

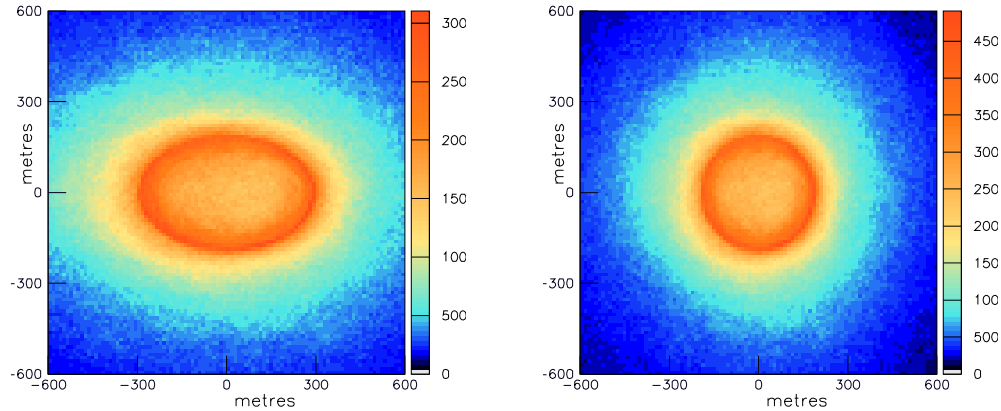


(a) The electron trajectory has a 0.5° zenith inclination, we have chosen unequal horizontal and vertical scales in order to emphasize the inclined geometry.



(b) The electron path has a 50° zenith angle. A large zenith angle is chosen, and only the last few kilometres above sea level shown, in order to reveal the elongation of the Cherenkov ring, which here goes beyond 300 metres.

Figure 3.21: The path travelled by Cherenkov photons emitted at various altitudes by an electron with inclined trajectory. The Cherenkov photons are emitted with an angle $\theta_{c \max}$ with respect to the electron trajectory as calculated in section 3.2.



(a) The Cherenkov photon distribution from the shower on the ground at an altitude of 2200 metres.

(b) The Cherenkov photon distribution from the same shower obtained in a plane perpendicular to the shower axis. The axis intersects the plane at the altitude of 2200 metres.

Figure 3.22: The Cherenkov photon distributions from a 500 GeV γ -ray shower with 50° primary zenith angle.

is hardly visible for a small angle, a similar diagram (3.21(b)) is presented for Cherenkov light trajectory from a 50° inclined axis, for the last few hundred metres above sea level. Here, the furthest distance reached by the Cherenkov photons is around 300 metres from the axis.

For comparison with a simulated shower, we present the elongated Cherenkov photon light distribution on the ground for a 500 GeV γ -shower with 50° zenith angle in figure 3.22(a). In figure 3.22(b), we present the distribution of Cherenkov photons from the same shower as they would arrive on a plane perpendicular to the shower axis. The Cherenkov light density is symmetric with respect to the shower axis and the distribution resembles that for a 0° zenith angle shower (e. g. in figure 3.18 top-right) except for the larger radius of the Cherenkov ring. The increase in Cherenkov ring size occurs since for larger zenith angles, the shower develops higher in the atmosphere (see section 3.2.2). Consequently, the Cherenkov photons emitted travel larger distances before arriving on the ground, hence increasing the spread of the Cherenkov light cone⁷. In figure 3.23, we present the Cherenkov photon density in the plane perpendicular to the shower axis as a function of radial distance for various energies and angles. The Cherenkov ring radius increases with increasing zenith angle and since roughly the same amount of light (light from the Cherenkov cone) gets distributed over a larger surface area, the density of Cherenkov photons decreases.

3.4.6 Wave front and temporal distribution

The Cherenkov photons and particles in the shower front, have ground arrival times that depend on their position of emission in the shower and their arrival position on the ground. In figure 3.24, we have plotted the arrival times of Cherenkov photons as a function of their arrival position on the ground in a 50 GeV γ -ray shower. The different colours correspond to different altitudes of emission. We see that, in general photons arriving at larger distances from the core arrive at later times since they travel larger distances.

The particles of the shower have higher velocities than the velocity of light in the air, therefore the shower reaches lower altitudes before the Cherenkov photons emitted at higher altitudes.

⁷The Cherenkov light emitted by a charged particle forms a cone whose angle is given by equation 3.1

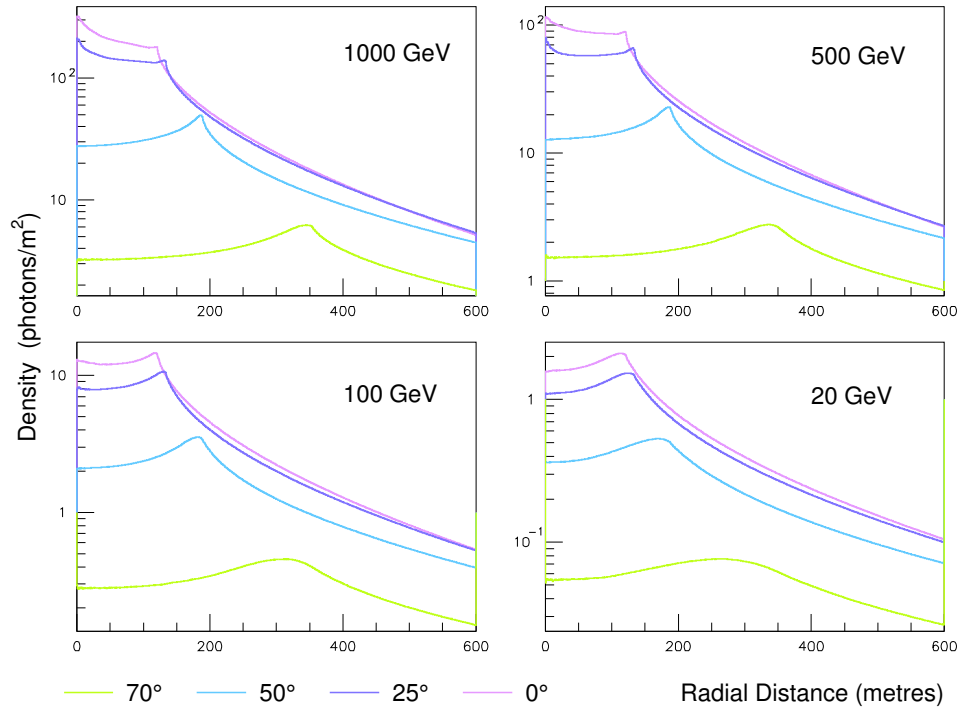


Figure 3.23: The comparison of the average density of Cherenkov photons on the ground as a function of the distance from the shower core for showers generated with different primary angles. The comparison is done for showers of 1000, 500, 100 and 20 GeV. The angle by angle comparison of density profiles for all energies can be seen in figure A.4 in the appendix.

Consequently, in the region close to the core, i. e. within the Cherenkov ring region, photons emitted at higher altitudes arrive later than those emitted lower.

For arrival positions beyond the Cherenkov ring, the Cherenkov photons emitted at lower altitudes have to travel larger distances and since they are emitted after those from higher altitudes, they reach the ground at later times.

As we have not used the temporal information in the methods and studies presented in this thesis, we will not be discussing the arrival time characteristics in the rest of this thesis. However, it needs to be mentioned that the arrival times of Cherenkov photons on the ground can provide with additional means to reconstruct and access information about the original γ -ray. We mention some of these possibilities here.

As we have seen above, the arrival times of the Cherenkov photons depend on the distance from the shower core. This implies that the arrival times of Cherenkov photons obtained on different telescopes in an IACT array could, potentially, be used in the reconstruction of the shower core position. In addition to that, figure 3.24 gives the arrival times for Cherenkov photons from a shower with 0° zenith angle. As a result, the arrival time distribution is symmetric around the shower core position. In showers that are inclined with respect to the zenith, the Cherenkov photons from one side of the shower will arrive earlier than those from the other side. This asymmetry in the arrival times of Cherenkov photons on various telescopes in the array could be used in the determination of the source position of the initial γ -ray. We have also seen above how the arrival times of Cherenkov photons at one position on the ground, depend on their altitude of emission. Depending on the energy of the initial shower, the altitude of observation and the integration time of the instruments this property could be used to gain

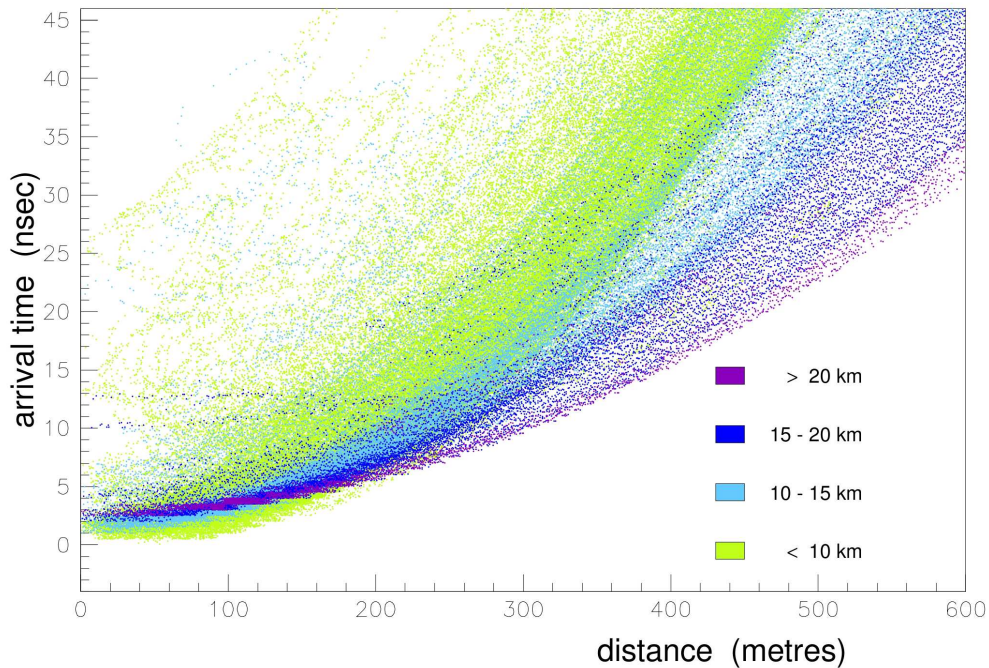


Figure 3.24: The arrival times of Cherenkov photons on the ground as a function of the arrival position at 2200 m altitude from a 50 GeV γ -ray shower. Four ranges of altitudes of emission are represented by four different colours. The zero of the ordinate axis corresponds to the arrival time of the first Cherenkov photon on the ground.

information about the longitudinal profile of the shower. Finally, while one expects the arrival time distribution from electromagnetic showers to follow the pattern described above, the same distribution for hadronic showers is expected to be less smooth and show a large number of fluctuations (see chapter 9 for a discussion on hadronic showers and their comparison with electromagnetic showers). These differences could potentially be exploited to discriminate the γ -induced showers from the hadronic background.

We finish by adding a word of caution concerning the above comments. While these potential uses can be inferred from the distribution of the arrival times of Cherenkov photons shown above, a better assessment of their feasibility can only be obtained by looking at the Cherenkov photon arrival times obtained in the telescope camera. As we will see in chapter 6, a number of Cherenkov photons falling on the telescope do not contribute to shower images. This is specially true when the telescope is situated far from the shower core position. Moreover, the integration times of the IACT telescopes may not allow the finer characteristics of the arrival time distributions to be used for accessing information about the original γ -ray.

3.5 Effect of geographical parameters

3.5.1 Effect of the atmosphere profile

As briefly discussed in section 2.1, the atmosphere profile and content depends on the geographical location of the site as well as time (diurnal, seasonal variations etc.). For instance, the troposphere has about half the thickness in the polar regions as compared with the tropics

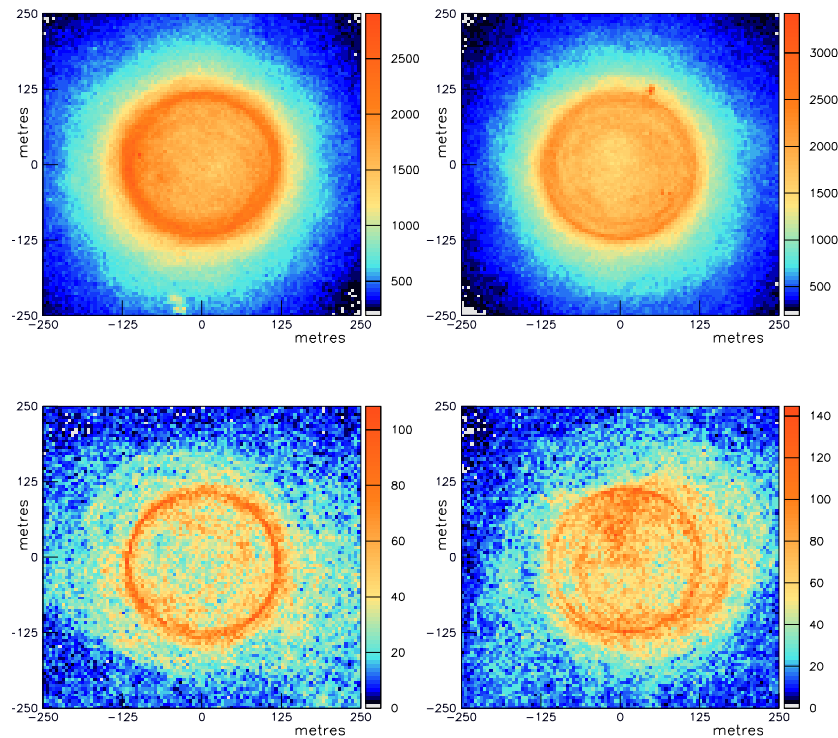


Figure 3.25: The effect of the magnetic field on the Cherenkov photon distribution on the ground for a 500 GeV shower (top) and a 200 GeV shower (bottom). The plots on the left show the distribution in the absence of any magnetic field while the distributions on the right are obtained in the presence of a magnetic field of $B_x = 20.4\mu T$ and $B_z = 43.23\mu T$. The altitude of observation is 2200 metres.

and O_3 and aerosol contents are both time and site dependent. These differences can introduce significant changes in Cherenkov light emission, transmission through the atmosphere and density profile on the ground. It has been shown in [20] that the use of different atmosphere models for the tropical and polar regions can lead to up to 60% differences in the Cherenkov photon density profile on the ground while seasonal variations at mid-latitudes can be responsible for as much as 15-20% change. The effect of occasional events like the mount Pinatubo volcanic eruption can cause a 5-10% variation in the atmospheric extinction for a period of one to two years.

3.5.2 Effect of the geomagnetic field

The trajectory of the charged particles in the atmospheric shower will be deviated due to the presence of the geomagnetic field. As a result, the Cherenkov photon distribution on the ground will also be distorted or rotated. In figure 3.25, we give the Cherenkov photon distribution for a 500 GeV and a 200 GeV shower. The distributions on the left are those obtained without the presence of magnetic field and the ones on the right with a magnetic field of $B_x = 20.4\mu T$ and $B_z = 43.23\mu T$. While there is some change in the distribution for the 500 GeV photon, the distortion is much more noticeable for the low energy shower. One can identify the presence of several ring like structures in the bottom right figure. At higher energies, the effects are less apparent due to the very large number of charged particles in the shower.

CHAPTER 4

ATMOSPHERIC SHOWER SIMULATIONS WITH CORSIKA

4.1 Introduction

An atmospheric shower is a complex object, with a large number of degrees of freedom (many particles), and where not only many processes take place and affect each other, but these processes are of stochastic nature. The evaluation of various physically interesting quantities like the energy of the particles in the shower, their trajectories, the number of Cherenkov photons emitted, their distribution on the ground etc., needs to take their random nature into account. Monte Carlo simulations treat these quantities as random variables and evaluate them from calculations based on fundamental interaction processes known from theory and/or measured or extrapolated from particle physics experiments.

These simulations are important tools for understanding the atmospheric showers themselves, their fluctuations and the impact of various parameters and conditions on their development. As mentioned before, this understanding is the first requirement for ground based γ -ray astronomy.

Moreover, the output from these simulations can be used to study the response of ground based detectors by simulating the detectors' response. The understanding of a particular detector's response to different types and energies of showers allows us to develop, test and evaluate different tools for analysing experimental data from that detector. It is also necessary when planning experiments or observations as well as designing future instruments adapted to measure physically interesting quantities.

In a complete study, these simulations may be used to generate the showers from the particles coming from a source (point or diffuse). To these are added, the showers from various sources of noise. The resulting signal in the simulated telescope/telescopes and the resulting analysis of the data is used to evaluate the detector's capabilities.

CORSIKA is one of the most widely used program for atmospheric shower simulations. It brings all the elements and codes needed to simulate various processes into a structure capable of generating atmospheric showers.

We have used CORSIKA for the work presented in this thesis and give a description of some of its salient features in this chapter.

4.2 Simulations with CORSIKA

Initially developed as a simulation tool for the KASCADE experiment [21] and first released in 1990, CORSIKA (COsmic Ray SIMulations for Kascade) has since undergone many updates

and the addition of several major packages and options. Since we have used CORSIKA version 6.020, released on the 24th of March 2003 for all the work presented in this report, the description of the CORSIKA program given below concerns this version, except where explicitly stated.

CORSIKA enables the detailed Monte Carlo simulations for particles from ≈ 1 GeV up to energies greater than 10^{20} eV. A total of 50 elementary particles including γ , e^\pm , μ^\pm , π^0 , π^\pm and protons as well as nuclei up to iron can be simulated.

Each particle in the shower is tracked through the atmosphere until it interacts with air nuclei or disintegrates.

Different kinds of fundamental interactions are treated through different packages (e. g. EGS4 for electromagnetic interactions).

A detailed description of the physics and parametrisations used in CORSIKA is given in the CORSIKA physics guide [3]. In what follows, we will only briefly describe some of the main packages and features of CORSIKA in order to understand some of the features and limitations concerning the simulations presented in this thesis. We will specially look at the treatment of Cherenkov photon emission and transmission since it plays a central role in ground based γ -ray astronomy.

4.3 Shower generation in CORSIKA

4.3.1 Electromagnetic interactions

The well known and widely used EGS4 (Electron and Gamma Shower version 4) package [22] performs detailed Monte Carlo simulations of electron and gamma electromagnetic interactions and transport for energies from a few keV up to a few TeV. In CORSIKA, EGS4 is used by extending the cross sections and branching ratios up to $\sim 10^{20}$ eV and assuming QED is still valid. The package treats annihilation, bremsstrahlung, Bhabha, Møller and multiple scattering for electrons and positrons as well as e^+e^- pair production, Compton scattering and photoelectric effect for photons.

Other electromagnetic processes not included in the EGS4 package like the $\mu^+\mu^-$ pair production, muon bremsstrahlung and e^+e^- pair production by muons have also been taken into account by CORSIKA authors. The deflection of charged particle paths in the earth's magnetic field and the LPM effect (Landau-Pomeranchuk-Migdal effect [23] [24] which reduces the pair production and bremsstrahlung cross-sections at very high energies) are also taken into account.

The EGS4 treatment provides detailed energy, position and time information for each electromagnetic particle in the shower. For a more rapid but less precise simulation, the NKG (Nishimura Kamata Greisen) [25] analytical approach parametrises the total electron densities at various depths and selected points.

4.3.2 Hadronic interactions

In air showers well in the TeV range, the energy of collisions exceeds those attained in the man-made accelerators. Since no experimental data is available, theoretical models are extrapolated to simulate hadronic interactions at high energies. To date, this remains one of the most important sources of uncertainties in the numerical simulation of high energy hadronic showers. There are many models, with different approaches, proposing solutions to the high energy hadronic interaction problem. Several energy dependent hadronic interaction packages are available in CORSIKA.

Low energy interactions

While the particles in the earlier part of an air shower are in the high energy range, the bulk of the particles has energies well below 100 GeV. CORSIKA has two packages that can be chosen to simulate low energy interactions.

The GHEISHA (Gamma Hadron Electron Interaction SHower) code is also used in the detector simulation code GEANT and has proven to be quite reliable in describing interactions in several experiments. GHEISHA takes over hadronic interaction simulations below energies around 80 GeV.

The UrQMD (Ultra-relativistic Quantum Molecular Dynamics) package specially simulates low-energy hadron-nucleus and nucleus-nucleus interactions.

Since CORSIKA version 6.142 (December 2002), the low energy part of FLUKA (FLUctuating KAScade) for simulating hadronic interactions has also been incorporated in CORSIKA.

High energy interactions

Several packages can be selected for the simulation of the high energy (above ~ 80 GeV) hadronic interactions in CORSIKA. We give their names here for completeness. These include VENUS (Very Energetic NUClear Scattering), QGSJET (Quark Gluon String Model with JETs), SIBYLL, NEXUS(NEXt generation of Unified Scattering approach) which combines the VENUS and QGSJET approach, HDPM (Hybrid Dual Parton Model) and DPMJET (Dual Parton Model with JETs). More details about these packages can be found from the CORSIKA physics guide [3] or the current version of the CORSIKA user's guide [26].

4.3.3 Particle tracking

The tracking of each particle in the shower is done by updating its position and time coordinates, and energy until its interaction with air nuclei or disintegration. Particle tracking takes into account ionisation losses for charged particles. It also includes Coulomb multiple scattering for electrons and muons. The deviation of charged particles by the earth's magnetic field can also be taken into account if required. The intensity and direction of the magnetic field is entered by the user. Default values are those for the KASCADE experience¹ location.

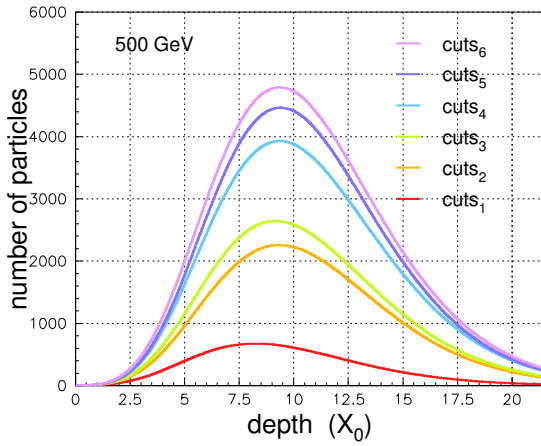
Minimum particle energy

Each particle type (hadrons, muons, electrons and photons) has a user defined minimum energy cut-off, below which tracking stops and the particle's remaining energy is considered as being deposited in the surrounding air. In figure 4.1, we present the average longitudinal profile for 500 GeV showers obtained with five different values of the minimum energy cut-off for electrons and gamma photons. These values are given in table 4.1. The set of cut-off values, cuts_6 contains the minimum values of cut-offs allowed in CORSIKA.

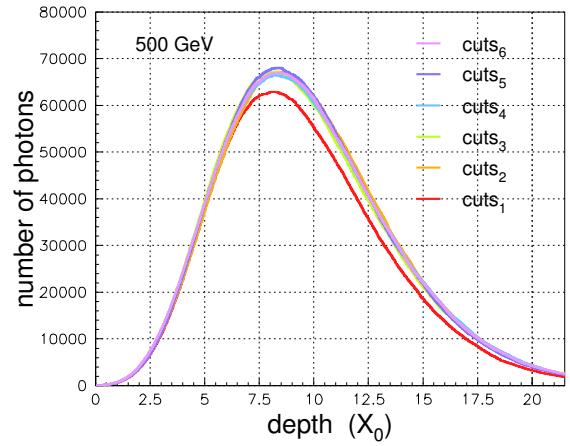
Figure 4.1 shows that the particle number in the γ , e^+ and e^- profiles increases with the decrease in cut-off energy since more particles with lower energies are kept in the simulation. Although the difference between the profiles gets smaller for lower cut-offs, values lower than the set number 6 may still yield a different profile. This point needs to be kept in view while doing any study involving the normalisation of the particle longitudinal profiles.

The Cherenkov photon emission profile is less affected by the different values of cut-offs. Since the low energy charged particles are under the Cherenkov emission threshold, the absence or presence of these low energy particles does not affect the Cherenkov light emitted

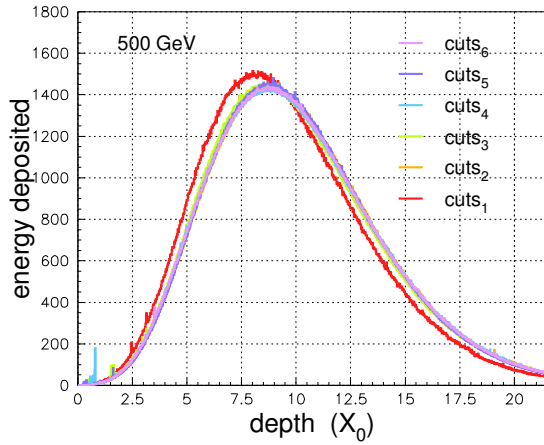
¹magnetic field strength= $47.80\mu T$, declination angle= $-9'$, inclination angle= $64^\circ 44'$



(a) Average longitudinal profiles in terms of the total number of particles in the shower i. e. e^+ , e^- and γ .



(b) Average longitudinal profiles in terms of the number of Cherenkov photons.



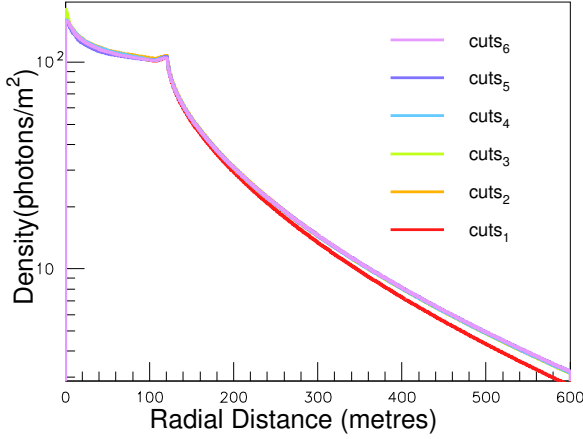
(c) Average profiles of the energy deposited (in MeV).

Figure 4.1: Comparison of the average longitudinal profiles (in terms of the number of particles, Cherenkov photon number and the energy deposited) for various cut-off energies for electrons and γ -photons in the simulation. The different profile colours correspond to different sets of cut-offs ($\text{cuts}_{1..6}$) whose values are given in table 4.1. The average is done over 600 simulated γ -ray showers at 500 GeV.

by the shower. As can be seen in figure 4.1(b), only the first set of cut-offs (cuts_1) gives a longitudinal profile with less Cherenkov emission. Moreover this difference lies mostly around the maximum and the decaying part of the profile.

The profiles for the energy deposited in the atmosphere also show little difference from one set of cut-offs to another except for the first set of cuts, where more energy is deposited in the earlier part of shower development and the maximum occurs earlier. This occurs because in the first set of cut-offs (cuts_1), the cut-off value for the charged particles is greater than the critical energy. As a result, the shower maximum occurs earlier, since the number of charged particles starts decreasing before the critical energy. As the energy of these particles is added to the energy deposited at each level, this explains the greater energy deposits in the early part of the shower.

We also compare the impact on the density of Cherenkov photons obtained on the ground in figure 4.2 and see that Cherenkov photon distribution is hardly affected by the cut-off values. The only difference is the lower Cherenkov photon density for the first set of cut-offs at large distances from the shower core. Since Cherenkov telescopes, use the Cherenkov photons arriving on the ground, any value of cut-off from cuts_2 to cuts_6 can be chosen without having an effect on the telescope studies. But for any studies involving the number of charged particles,



Energy cut-offs in GeV

	hadrons	muons	electrons	photons
cuts ₁	0.05	0.05	0.05	0.05
cuts ₂	0.05	0.05	0.005	0.005
cuts ₃	0.05	0.05	0.003	0.003
cuts ₄	0.05	0.05	0.0005	0.0005
cuts ₅	0.05	0.05	0.0002	0.0002
cuts ₆	0.05	0.05	0.00005	0.00005

Figure 4.2: Comparison of the average Cherenkov photon density on the ground with 5 sets of energy cut-offs for 600 γ -induced simulated showers of 500 GeV. The sets of cuts are those given in table 4.1 and the colour code is the one used in figure 4.1

Table 4.1: Table giving the 5 sets of minimum energy cut-offs for various particles used to study cut-off effect on shower and Cherenkov light simulation.

a careful choice of the cut-off values needs to be made. For the work presented in this thesis, we have used cuts₆ whenever showers and their properties have been studied. For the rest of the studies (those focusing on the Cherenkov emission and the images obtained from it), the cut-offs have been set to the values given by cuts₂.

4.4 Cherenkov light treatment in CORSIKA

Cherenkov light is emitted by electrons, muons and charged hadrons whenever they have speeds greater than the speed of light in the surrounding atmosphere. In this section, we give a brief and simplified description of the Cherenkov emission treatment in CORSIKA with the goal of underlining the main features and principles of Cherenkov emission in CORSIKA and how they affect the output from simulations. We, therefore, leave out the details of how the actual computation is done.

Each particle track step (between two interactions) is checked for the Cherenkov light emission condition:

$$\eta\beta > 1,$$

with $\beta = \sqrt{1 - m^2c^4/E^2}$, where c is the velocity of light in vacuum, m the mass of the particle and E its energy. The refractive index of air $\eta(h)$ is calculated from

$$\eta(h) = 1 + 0.000283 \frac{\rho(h)}{\rho(0)},$$

where $\rho(0)$ is the density of the atmosphere at sea level, $\rho(h)$ the density at altitude h in the atmosphere and 1.000283 is the refractive index of air at sea level (see also section 3.2.1). The Cherenkov photons are emitted according to the distribution function $1/\lambda^2$ within a wavelength range ($\lambda_{min} - \lambda_{max}$) defined by the user. This corresponds to a uniform distribution in terms of the energy. The total number of Cherenkov photons emitted in the step length ds is calculated from

$$\frac{dN}{ds} = 2\pi \alpha z^2 \sin^2 \theta_c \int_{\lambda_{min}}^{\lambda_{max}} \frac{1}{\lambda^2} d\lambda,$$

where α is the fine structure constant, z is the charge of the particle and θ_c is the angle of Cherenkov emission with respect to the particle trajectory. θ_c is calculated from

$$\cos \theta_c = \frac{1}{\beta \eta}.$$

The azimuthal emission direction is taken randomly. In CORSIKA, Cherenkov photons are treated in bunches. The maximum number of Cherenkov photons emitted in a bunch is defined by the user. The particle track step is further subdivided into substeps such that the number of Cherenkov photons emitted in each substep does not exceed the user-defined bunch size. This has the advantage of reducing computational effort, but must be done with care. In high energy showers ($E > 1$ Tev), the number of Cherenkov photons emitted is high enough so that the emission of Cherenkov photons in small (5-10) photon bunches does not affect the overall distribution of the Cherenkov light. However, in low energy showers (specially below 100 GeV), the fluctuations from shower to shower are very important and the Cherenkov photons cannot be grouped without significant loss of information. For all the results presented in this thesis, a bunch size of 1 photon was used. We also note that the treatment in bunches, as described above, can lead to the apparition of fractions of photons in the CORSIKA output.

4.5 Atmosphere and transmission of Cherenkov light

The atmosphere used in CORSIKA has the composition of pure air i. e. N_2 (78.1%), O_2 (21%) and Ar (0.9%).

4.5.1 Atmosphere models

In CORSIKA, the density profile of the atmosphere can be handled in several ways. We have already given the parametrisation of the U. S. Standard model in five layers used in CORSIKA (see section 2.1.3). In fact, the basic internal atmosphere model follows this five layered parametrisation for several atmospheres. We recall the expressions for the mass overburden expresses in g/cm^2 :

$$T(h) = a_i + b_i e^{-\frac{h}{c_i}} \quad i = 1, \dots, 4.$$

The fifth layer (> 100 km) has a linear dependence on h

$$T(h) = a_5 + b_5 \frac{h}{c_5}.$$

The layer boundaries are situated at 4 km, 10 km, 40 km, 100 km and 112.8 km (which is considered as the atmosphere boundary). Several atmosphere models including the U. S. Standard (details in section 2.1.3), Central European, South pole, are parametrised this way. User defined values of the parameters a_i , b_i and c_i and layer boundary positions can also be used. The additional Bernlohr package allows the use of MODTRAN [27] (program for atmospheric transmission and radiance calculations) generated tables for the density, mass overburden and refractive index. We have used the U. S. standard model for all the results presented in this thesis.

The standard CORSIKA atmospheric layers are flat. While a curved atmosphere can be simulated and is needed for large zenith angles, we have used the standard option for all the simulation work presented here.

4.5.2 Atmospheric extinction

A detailed simulation of the atmospheric transmission of Cherenkov light would need to include simulations of all phenomena like the absorption through various types of scattering and the presence of different kinds of impurities in the atmosphere. A simpler way of taking extinction into account is by tabulating its values for different wavelengths and altitudes in the atmosphere and applying those values, knowing the wavelength of the Cherenkov photons and their height of emission. For the work presented in this thesis, we have used the standard extinction table supplied with CORSIKA. In figure 4.3, we give the extinction coefficients for Cherenkov photons emitted at different altitudes and observed at sea level.

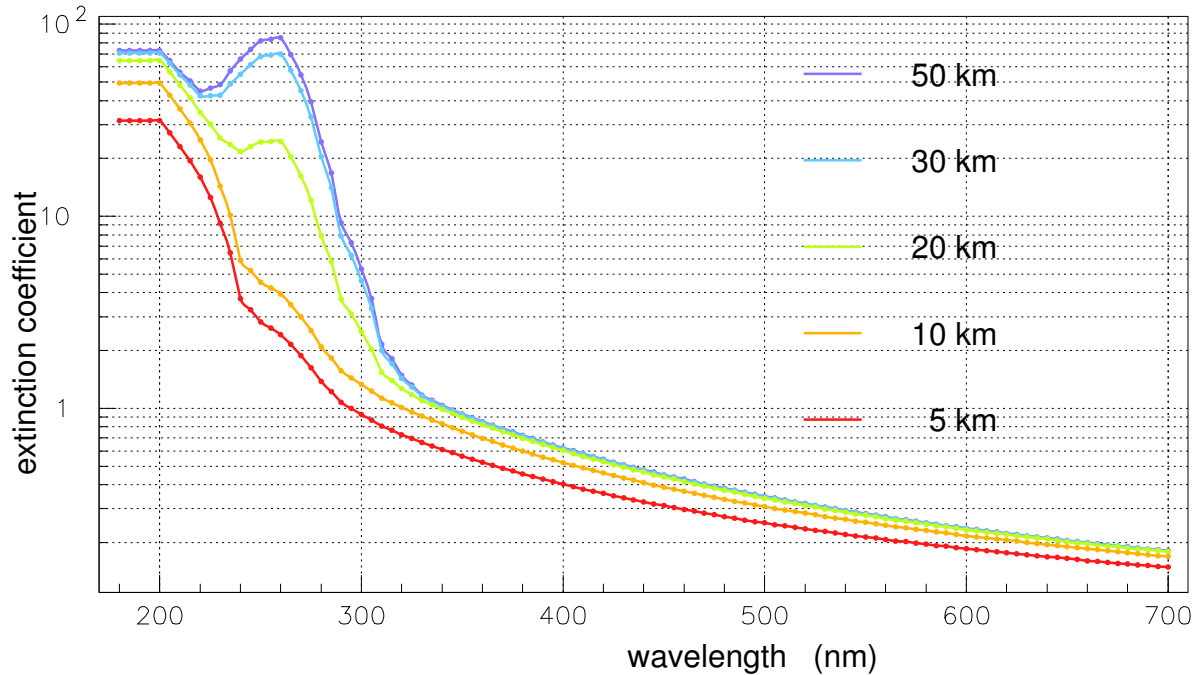


Figure 4.3: Extinction coefficients $\beta(\lambda, h)$ in the atmosphere as a function of wavelength for photons emitted at various altitudes and observed at sea level. The probability of the transmission of a photon of wavelength λ , from an altitude h to sea level is calculated through $P = e^{-\beta(\lambda, h)/w}$, where w is the direction cosine of the photon trajectory with respect to the vertical.

4.6 Mirror reflectivity and photomultiplier quantum efficiency

Although telescope parts and features are discussed in chapter 5, we do mention a couple of aspects here that can be taken into account by CORSIKA along with the shower simulation.

All the Cherenkov photons incident on the telescope and the camera do not contribute to the shower image obtained on the camera. This is because neither the mirror nor the photomultipliers are 100 % efficient. The mirror reflectivity and the quantum efficiency are taken into account as a part of the telescope simulation. They can also be included earlier in the simulation of Cherenkov light. This option can be selected by the user and requires the knowledge of photomultiplier quantum efficiency and mirror reflectivity as a function of wavelength. In all the telescope simulations presented in this thesis, we have used the mirror reflectivity (measured for the recoated mirrors of the Whipple telescope in September 1993) and quantum efficiency

values (measured for the Hamamatsu R1398HA photomultipliers) provided along with CORSIKA. The efficiency of these two effects is presented as a function of photon wavelength in figure 4.4.

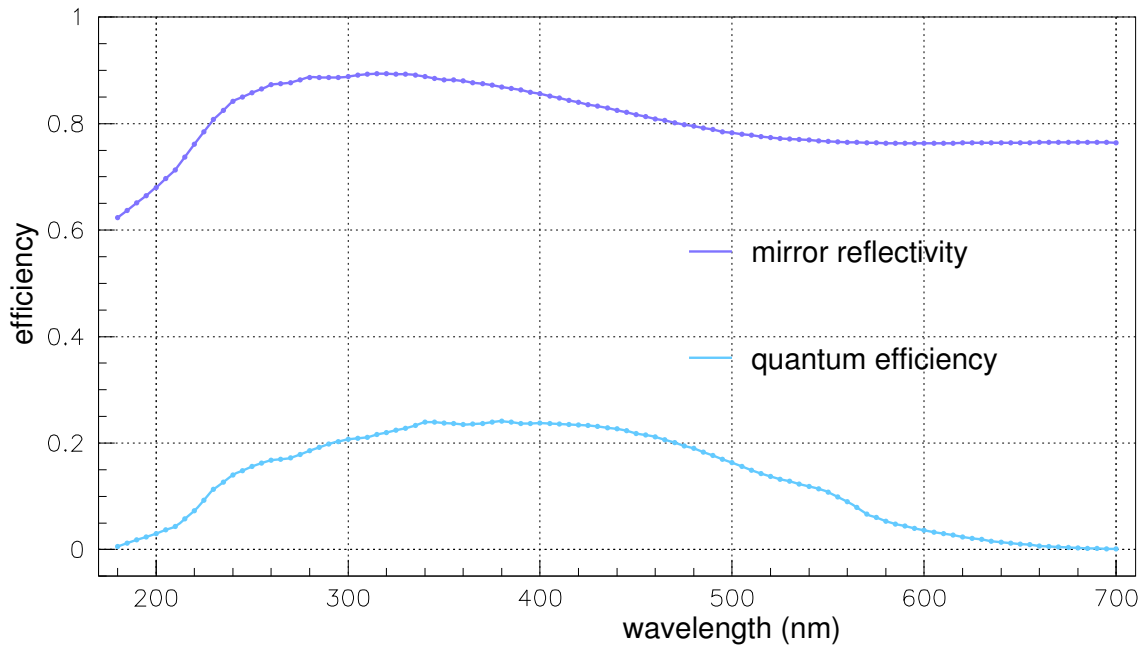


Figure 4.4: Mirror reflectivity and quantum efficiency as a function of photon wavelength as provided with CORSIKA. The reflectivity is that measured for the recoated mirrors of the Whipple telescope in September 1993 and the quantum efficiency values are those of the Hamamatsu R1398HA photomultiplier.

4.7 CORSIKA output

CORSIKA's standard output contains detailed information about each particle arriving at a user defined observation level. The particle arrival position and time, type, energy, and direction along with important parameters for the simulation and individual showers are written in a binary file. Similar information is also written out for the Cherenkov photon bunches arriving at the observation level. This includes, bunch size, arrival time and position, direction, and altitude of production for each photon bunch. The longitudinal development of showers, in terms of particle number as well as energy deposits, can also be written in an output file.

One option allows the generation of binary files containing the individual tracks and energies of electromagnetic, muonic and hadronic particles of a shower in the atmosphere. All the shower images presented in chapter 2 have been generated this way.

4.8 Personal addition

We have developed a CORSIKA extension in order to carry out the different studies in this thesis. The most important feature of this extension is an imaging telescope simulation tool. It uses the Cherenkov photon output for showers in CORSIKA to obtain the image of the shower

in the telescope camera. The purpose of this extension is to obtain a flexible tool allowing the study of different telescope configurations. We will present this tool, in detail, in chapter 5.

Other features are relatively elementary and include various ways of retrieving information from CORSIKA simulations. As mentioned above the standard CORSIKA standard output consists of binary files with particle and Cherenkov photon information. While this allows the storage of the data and its availability for various types of studies, the files produced can very easily occupy important disk space. We have therefore implemented the possibility of writing data in various files or histograms as required. Some of the information not accessible in the standard output of CORSIKA is also retrieved from the corresponding part of the code. Calculations and distribution fits are done where needed.

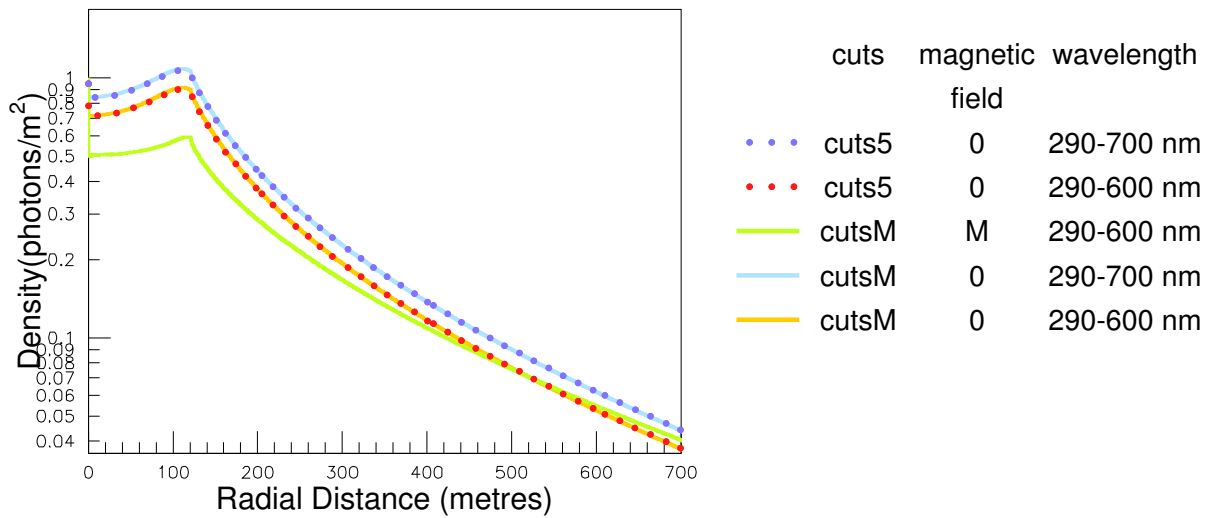


Figure 4.5: The comparison of the average Cherenkov photon density on the ground for 10 GeV showers obtained with different values of energy cut-offs, wavelength ranges and magnetic field values. Cuts5 corresponds to the energy cuts given in table 4.1, while cutsM corresponds to the values 0.3, 0.3, 0.02, 0.02 GeV for hadron, muon, electron and photon cut-offs, respectively. A magnetic field with vertical component $B_z = 23.0$ and $B_x = 29.5 \mu T$ is used for the light green curve. This value corresponds to the geomagnetic field at La Palma. No magnetic field is simulated to obtain the other curves. The wavelength range used for each curve for Cherenkov radiation production (290-600 or 290-700) is also shown.

4.9 Comparison with known results

In order to check the accuracy and correctness of our simulations and choice of parameters we compared the results of a set of simulations for 10 GeV showers with the results obtained by the MAGIC collaboration² in [31]. In figure 4.5, we show the curves obtained for the Cherenkov photon density on the ground with several combinations of simulation parameters and compare with the curves in [31]. The dotted dark blue and red curves use the cut-off energies given for the set cuts5 in table 4.1. For the former, the Cherenkov photons are emitted in a wavelength band ranging from 290 to 700 nm, while for the latter they are generated in the range 290-600 nm. This results in a slight decrease of the flux obtained on the ground. For the three other

²See for example [28], [29] and [30].

curves we use values of cut-off energies used by MAGIC collaboration members from [32] i. e. 0.3, 0.3, 0.02, 0.02 GeV for hadron, muon, electron and photon cut-offs, respectively. The simulations are then carried out in the 290 to 700 nm range (light blue curve) and 90-600 nm (orange curve). The curves obtained give the same values of flux as those obtained by the cuts5 series. This is in accordance with our remarks in section 4.3.3 where we show that the flux on the ground does not change for cut-off energies below 0.05 GeV for electrons and photons. The flux obtained by all these simulations is overestimated (specially for positions close to the shower core) in comparison with the curves given in [31]. Finally, we add the geomagnetic field for the MAGIC telescope location at La Palma (green curve) and are able to reproduce the curves shown in [31]. These results also serve to illustrate the impact of the magnetic field on the Cherenkov photon density distribution on the ground. Note that when the magnetic field is applied, this leads to lower density (as compared to the simulations where the magnetic field is not simulated) close to the shower core. However, this tendency is reversed at larger distances (beyond ~ 600 metres, where the Cherenkov photon density is higher than for the other simulations). One also notes the difference arising due to the Cherenkov photon production wavelength band which can be significant if the photomultipliers of the system respond to the low wavelength domain. In the studies presented in the rest of this thesis we have generated Cherenkov photons in the wavelength band 300-700 nm.

*P*_{ART} III

*I*ACT, THEIR SIMULATION AND
SHOWER IMAGES

CHAPTER 5

IMAGING ATMOSPHERIC CHERENKOV TELESCOPES AND THEIR SIMULATION

5.1 Introduction

In part II, we saw how a γ -photon entering the earth's atmosphere interacts with the particles in it and produces a mainly electromagnetic shower. We discussed the important properties of this shower and the emission of Cherenkov photons by the charged particles in it when their velocity is greater than the velocity of light in air. We also saw how these Cherenkov photons transmitted through the atmosphere and got distributed on the ground. Imaging Atmospheric Cherenkov Telescopes obtain an image of the shower by collecting the Cherenkov light from the shower through mirrors and projecting it onto a camera. This image can then be analysed to reconstruct information about the original γ -photon.

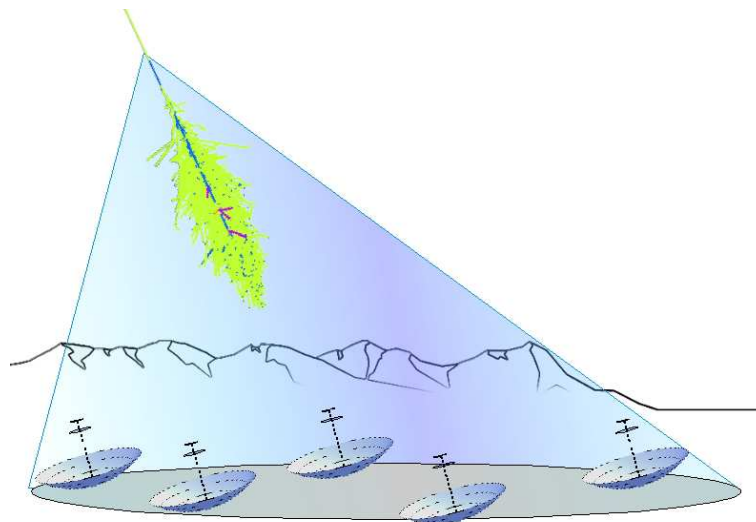


Figure 5.1: Imaging Atmospheric Cherenkov Telescopes observe γ -rays by collecting the Cherenkov light emitted by the showers they produce in the atmosphere.

IACT systems can vary greatly in terms of various parameters like mirror size and shape, telescope number and position etc.. Depending on the performance required of the system, some configurations may be more adapted than others. In order to study the characteristics and detection capacity of various types of telescope systems, we have developed an IACT simulation program. This package uses the output of the atmospheric shower simulation Monte

Carlo program CORSIKA [3] described in chapter 4 and can be adapted to use the output from other sources too.

Detailed and adapted telescope simulation programs exist within present-day IACT collaborations. These programs are made in order to accurately reproduce the performance of a particular telescope. However, our purpose is to have an easily accessible tool with which more general studies (like comparisons of various systems) can be done. We therefore laid emphasis on making the package very flexible so as to be able to simulate different kinds of IACT systems. At the same time, the properties of the simulated telescopes are kept ideal. Such ideal telescopes can be used to study the effects of various basic parameters on the performance of an IACT configuration. Once configurations with more interesting properties have been identified this way, the more realistic details of telescope properties can be added to the simulations.

Although mirror shape may eventually be changed, for now parabolic mirrors have been selected since they are the simplest to simulate apart from being adapted to the simulation of telescopes with smaller field of view and isochronous properties.

In this chapter, we begin by describing the different parts of an imaging atmospheric Cherenkov telescope. In particular, we discuss mirror design and its contribution to the various properties of the shower image, emphasising on parabolic mirrors.

In the second part of this chapter, we present the IACT simulation package we have developed, the choices made regarding its principle of working and their implementation. We finish by giving several examples of systems simulated through it.

5.2 Telescope parts

One of the ways of using the Cherenkov light from the showers is by obtaining an 'image' of the shower through it. The image of the shower thus produced is a geometrical mapping of the shower through the Cherenkov light that reaches the detector. An Imaging Atmospheric Cherenkov Telescope consists of an optical reflector which collects the Cherenkov light from the atmospheric shower and projects it onto a camera where photomultipliers convert the light signal to electric signal. The signal is then amplified and digitised in order to be stored and used to reconstruct information about the original shower-producing particle. We describe some of the important parts of the telescope in the following sections.

5.2.1 The reflector

Several types of shapes and configurations exist and are usually considered for telescope design. Each shape has advantages and drawbacks of its own and the choice of a particular shape for a telescope system depends on several factors, e. g. the performances required, cost etc.. We begin by giving the features of a parabolic mirror along with a description of the formation of images through it. Then we briefly discuss some of the other mirror designs and their properties.

Parabolic mirrors

Parabolic mirrors are paraboloids of revolution with a given diameter and focal length. Their main properties include perfectly focused image formation at the focus for infinite distance objects along the axis, isochronism... We illustrate some of the properties of the 3-dimensional paraboloid through a description of the 2-dimensional parabola.

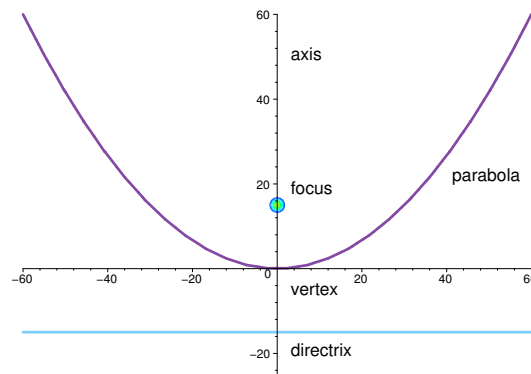


Figure 5.2: Plot of a parabola with focus (0,15) and vertex (0,0) in the y-z plane.

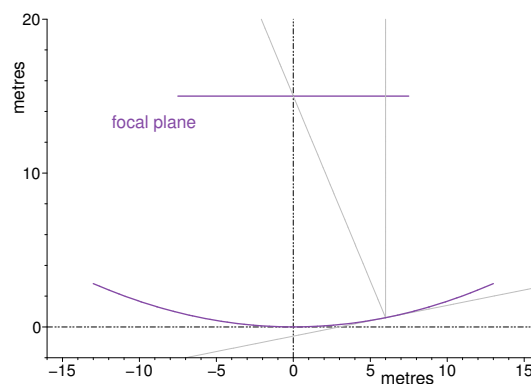


Figure 5.3: The reflection of a ray parallel to the parabola axis gives a ray passing through the focus or equivalently an incident ray passing through the focus gives a ray parallel to the axis after reflection from a parabola. The computation for the diagram is done with MAPLE 10.

The parabola A parabola is a conic section and is the locus of all points in the plane that are equidistant from a fixed line and a fixed point. The fixed point does not lie on the fixed line and is called the focus, while the fixed line is known as the directrix. For the parabola given in figure 5.2, this is expressed in the following way:

$$z^2 = 4 f y, \quad (5.1)$$

where f is the focal distance of the parabola, z and y being the vertical and horizontal axes, respectively. Its axis is the straight line that passes through the focus and is perpendicular to the directrix. The point where the axis intersects the parabola is known as the vertex.

Reflective property A parabola has the special property that an incident ray parallel to the axis of symmetry is reflected at the focus and vice versa. This property is illustrated in figure 5.3. As a consequence, if the rays from a given object are all parallel to the parabola axis then the image of the object will be a point at the focus.

Implications for point sources at various distances A point source emits rays in various directions. For a point source at a very large distance, the rays arriving on the mirror are practically parallel. This means that its image will converge perfectly at the focus of the parabola. Figure 5.4 (left) shows the reflection of parallel incident rays by the parabola.

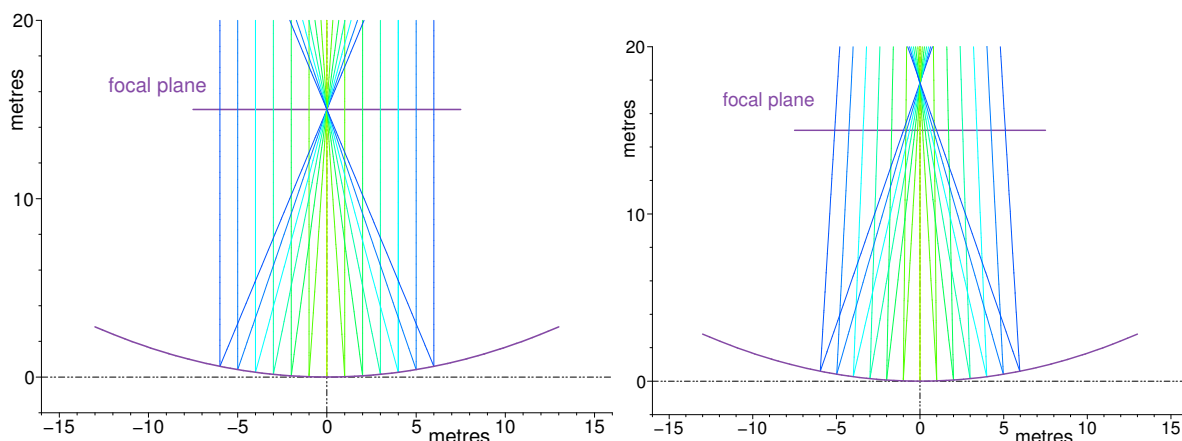


Figure 5.4: Left: Incident rays parallel to the axis of the parabola give a perfectly focused image at the focus. Right: The reflected rays from a source at 100 metres focus at a point more than a metre beyond the focal plane. The mirror shown has a focal length of 15 metres. The computation for both diagrams was done with MAPLE 10.

If the point source is closer to the mirror, then the incident rays are no longer parallel and the reflected rays converge at a point on the axis beyond f . As long as the source distance from the mirror remains greater than $2f$, the position for the convergence of the image remains between f and $2f$. In figure 5.4(right), we show the reflection of the rays from such a point source at $\sim 7f$. The resulting image is focused at a distance of about $0.2f$ from the focal plane. Typical parabolic mirrors in IACT systems have focal lengths between 10 to 30 metres, while the average altitude of the maximum of shower development is around 10 km of altitude. The typical position at which the image focuses is therefore between 1.5 cm (for $f = 10$ metres) and 9.4 cm (for $f = 30$ metres) from the focal plane.

Coma aberration While rays parallel to the axis of the parabola converge exactly at the focus, this is not the case for off-axis parallel incident rays. This results in an aberration of the off-axis image. The greater the incidence angle with respect to the axis, the greater this aberration. Figure 5.5 illustrates the reflection of off-axis parallel rays by a parabola. We do this for 10° incident rays in order to bring out the aberration; current day IACT have total fields of view of up to 5° implying maximum angles incidence of 2.5° . In the right diagram, the rays reflected from the negative side of the axis and those reflected from the positive side of the axis are shown in two different colours. This shows that since the rays reflected by the incidence side of the axis travel longer distances, the aberration they cause is greater than the one obtained from the other side.

In figure 5.6, we show the image obtained from parallel rays incident on a paraboloid at various angles. While the rays converge perfectly for 0° incident angle, the spread of the image increases with increasing angle. The coordinate system of the focal plane can be expressed in degrees since rays with different incident angles converge at different positions on the focal plane. This point will be revisited in chapter 6 (page 95). Note that the aberration is more important and asymmetric in the direction parallel to the light rays and is less important but symmetric in the perpendicular direction. This is known as the coma of the paraboloid since the point appears to have cometary coma. Moreover, we also see the presence of two distributions in each image. As explained above, the larger one corresponds to the photons reflected from the incidence side of the paraboloid axis and the smaller one from the further side.

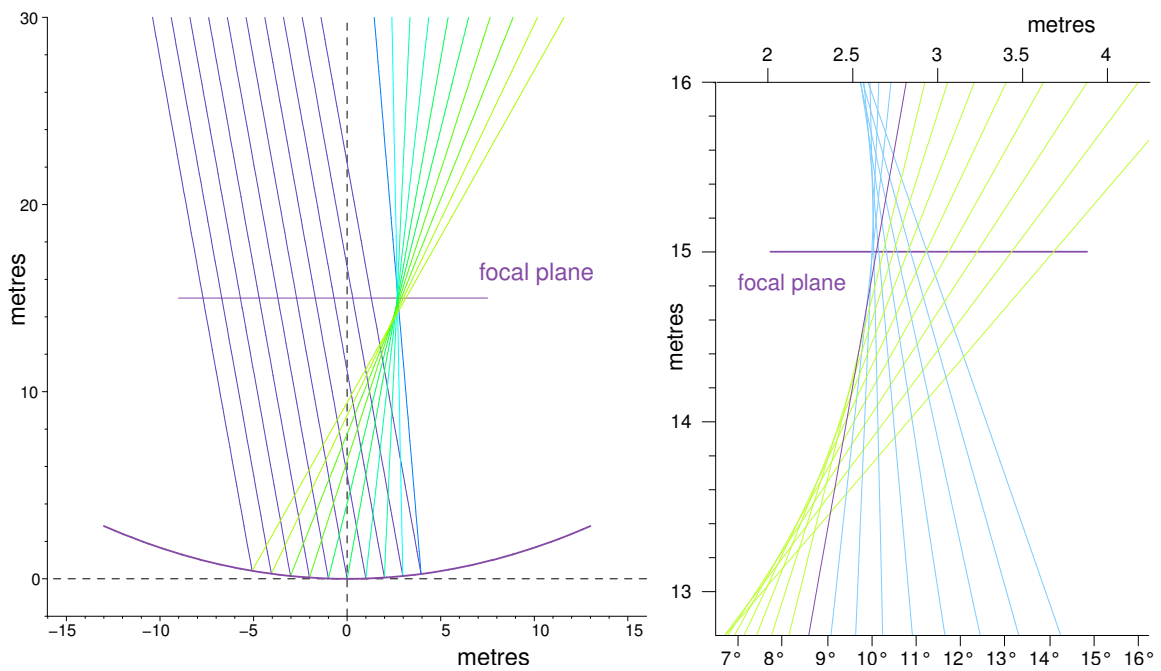


Figure 5.5: The left diagram represents the reflection of 10 parallel rays making an angle of 10° with the parabola axis. In the right diagram, we zoom on the focal plane area where the reflected rays arrive. In addition to the rays shown in the left figure, 7 more rays are added in order to highlight the dispersion in the arrival positions. The ray reflected from the vertex (0,0) of the parabola is shown in violet. In order to show the difference of dispersion for both sides, the rays reflected from the negative side of the vertex are shown in light green, while those from the positive side are shown in light blue.

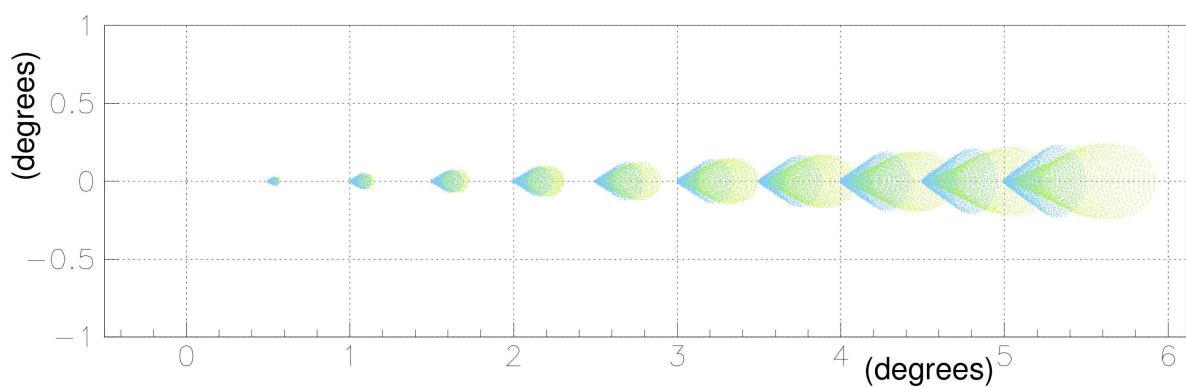


Figure 5.6: Image obtained on the focal plane from the reflection of parallel rays from a paraboloid mirror for various angles of incidence with respect to the paraboloid axis. The mirror diameter is 12.5 metres and focal length 15 metres. The angles vary from 0° to 5° with increments of 0.5° . Each ray is sent on one element of a 120×120 plane grid.

In figure 5.7, we show the variation of coma size with incident angle. The centroid of the distribution gives an idea of how the aberration shifts the position of an image. Since the aberration is symmetric in the transverse direction, the centroid of the image in that direction is the same as the generated angle. In the tangential direction, we see that the shift between the generated direction and the centroid increases with increasing incident angle. The root mean square of the distribution is a measure of the spread of the reconstructed image and has a linear dependence on the incident angle for both the tangential and transverse directions. The values of the r. m. s. are, however, much greater in the tangential direction. An estimation of the aberration in the transverse direction is important for the methods of reconstruction for the source and shower core positions that we have developed, since these methods use information from the transverse distribution of the image. We will further discuss this point in chapter 7.

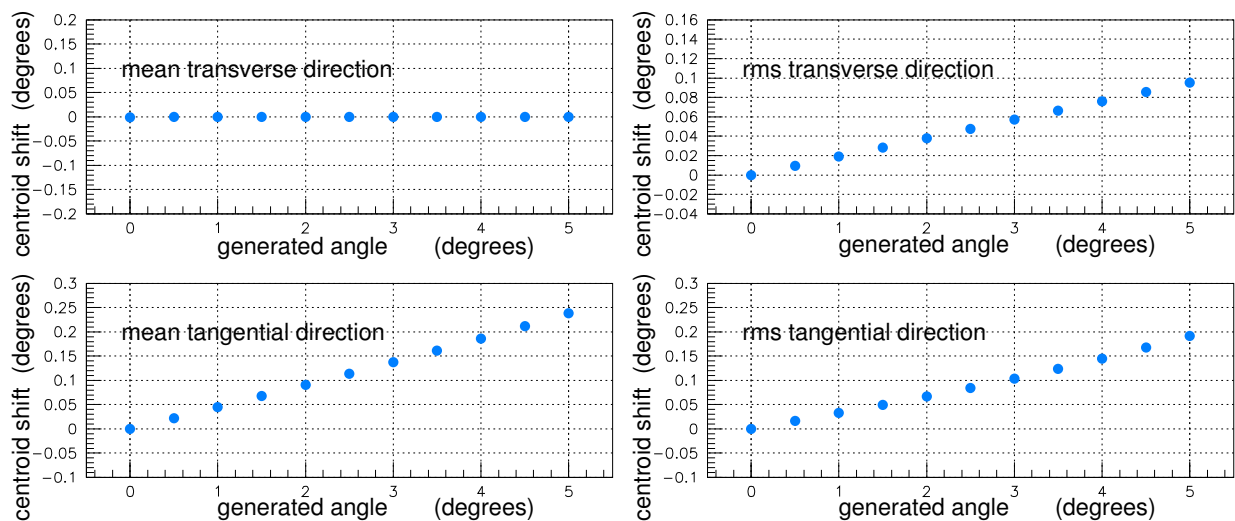


Figure 5.7: The variation of the aberration in the transverse direction (top) and tangential direction (bottom) with different incident angles.

Isochronism Rays travelling parallel to the axis and originating at the same distance from the directrix will travel equal distances as they are reflected by the parabola and arrive at the focus. This is known as the isochronous property of the parabola since rays parallel to the axis arrive at the same time at the focus. Rays travelling parallel to each other but not parallel to the axis show approximately isochronous properties too. They can be considered as isochronous in the case of IACT keeping in mind the dimensions of the mirrors and their focal lengths.

Different reflector types

In IACT systems, the most common reflector shapes are the tessellated parabolic design and the Davies-Cotton design [33]. Tessellated parabolic mirrors with small mirror segments are used since it is too costly to produce single piece mirrors with diameters of several metres. The small mirrors are usually spherical and they are arranged in such a way that their tangents (at the centre of each individual mirror) coincide with the tangents of a paraboloid shape. The radii of curvature of the small mirrors can either be constant ($2f$) or graded. The use of graded tessellated parabolic reflectors improves coma aberration for smaller angles of incidence ([34], [35]).

In the Davies-Cotton design, small spherical mirrors are arranged on a spheroid with a radius equal to the focal length of the telescope. The radius of curvature of the small mirrors is $2f$ and their normals pass through a point at a distance $2f$ along the axis of the telescope. Compared to the tessellated parabolic design, the Davies-Cotton mirror shows similar aberrations for small incident angles and has significantly better performance at larger angles (up to 5 degrees). This better imaging comes at the expense of timing accuracy.

It has also been shown in [34], that good imaging performance can be obtained for even wider fields of view (up to 10 degrees) by using a Davies-Cotton like design but using an elliptical gross shape. This system has poorer time resolution and near-axis imaging.

Also, telescope systems comprising secondary optics and allowing fields of view up to 15° are also being investigated (see for example [36] and [37]).

5.2.2 Camera and electronics

We give a very simplified description of the camera and electronics in a telescope. The camera is made up of a multitude of photomultipliers. When a photon falls on the camera, it contributes to the signal of the photomultiplier it falls upon. This leads to the pixelisation of the image of the shower. The level of pixelisation depends on the number and size of individual photomultipliers. The photons incident on the camera are converted to photo-electrons as they interact with matter. These photo-electrons are then converted to an electric signal by the photomultipliers. The process is not entirely efficient, hence the need to take the quantum efficiency of the photomultipliers into account. Moreover, there are fluctuations in the process of conversion to an electric pulse within the photomultiplier. After the photomultiplier, the signal is amplified and then converted to digital form so as to be saved and used later if needed.

5.3 Telescope simulation

A telescope simulation package takes a Cherenkov photon as input and traces its trajectory within a given telescope and its camera. When all the Cherenkov photons, from a simulated atmospheric shower, falling on the telescope are passed through the program, then the result is the simulated image of the shower. Our goal was to create such a tool in order to study the performance of different IACT systems and arrays. In order to do this, emphasis was laid on flexibility in telescope configuration. Some choices and simplifications were also made.

5.3.1 Simplification and choices

Each telescope consists of a single-piece parabolic mirror reflector. In a real telescope, the mirror is either tessellated or has a Davies-Cotton structure. The discontinuities of the mirror are responsible for some loss of signal, specially in the case of the Davies-Cotton design. Details like this and the losses from the presence of the frame are ignored as well. Such a simplified version of telescopes can be useful in comparing different telescope configurations initially. A simple paraboloid is easier to code and running the program is less time consuming. More realistic and detailed simulations can be done as a subsequent step. Moreover, the simple single-piece telescope mirror in the program can eventually be replaced by a more complex design.

The choice of a parabolic mirror is more adapted to small field of view telescopes since the coma aberrations become more important. Other mirror designs are more adapted for large fields of view. Although this approach has not been used for the studies presented in

this thesis, the isochronism (see section 5.2.1) of the paraboloid gives the possibility of using temporal information for the analysis of images.

Among other simplifications, the camera pixels have all a basic square shape. The mirror reflectivity and quantum efficiency of photomultipliers used are those supplied with CORSIKA (see section 4.6) for the Whipple telescope and the Hamamatsu R1398HA photomultiplier respectively. These values, too, can easily be replaced if required.

5.3.2 Flexibility

In order to have the possibility to simulate the widest possible choice of telescope configurations and arrays, most of the telescope parameters can be set freely and independently of each other.

An individual telescope is completely defined by its position, orientation, diameter, focal length as well as camera size and position. These parameters are described in figure 5.8.

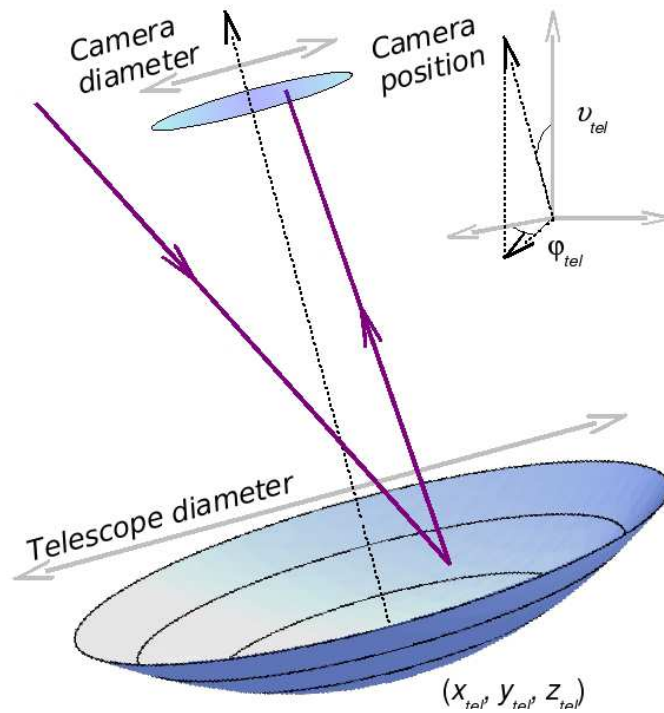


Figure 5.8: Diagram illustrating the principle of the telescope and various parameters.

The position is given through the coordinates of the vertex of paraboloid $x_{tel}, y_{tel}, z_{tel}$ in the ground frame of reference. This frame of reference corresponds to the CORSIKA frame of reference if it is the source of the telescope input. The height z_{tel} is measured with respect to the altitude of observation.

The orientation of the telescope is given by the azimuthal and zenith angle of the paraboloid axis i. e. ϕ_{tel} and θ_{tel} . The focal length f and diameter d can be set independently of each other allowing the simulation of telescopes with different f/d ratios.

The camera position is given as its distance from the vertex along the paraboloid axis. Although, the camera is usually positioned on the focal plane, we wanted this to remain flexible for any corrections or adjustments that may be needed (see reflective property on page 79). The camera has a circular shape and its diameter can be set independently of other parameters. The pixels on the camera are set to have a sky coverage of $0.1^\circ \times 0.1^\circ$ by default, but this value can be changed.

Telescope arrays are simulated by defining different telescopes at different positions. Since there are no restriction imposed on the positions of the telescopes simulated any kind of array configuration can be simulated. For each telescope, the individual parameters such as focal length, diameter etc. can be set individually giving the possibility of simulating arrays with several types of telescopes in it. The program has the capacity to simulate up to a hundred individual telescopes at the same time.

As long as the total number of telescopes remains under 100, several arrays can be simulated simultaneously, without the simulation of one affecting the other. This is true even when individual telescopes overlap. This can reduce the total run time when the telescope program is used within CORSIKA. The showers are simulated only once and the Cherenkov light from them can be used to obtain images on the different telescopes of each array.

5.3.3 Principle

The basic principle used in the telescope simulation program is quite simple. A light ray (Cherenkov photon) falling on a parabolic mirror is reflected by it onto the camera plane and contributes to the image, if it falls within the camera radius. .

In order to implement the reflection of a Cherenkov photon by the telescope mirror, information about the photon's arrival position on the ground and the direction cosines of its trajectory is necessary. A Cherenkov photon's trajectory through the atmosphere will change through refraction, scattering or simply absorption. But once we know that it reaches the ground, the only knowledge necessary for the purposes of reflection, concerns its point of impact on the mirror and the direction cosines of its trajectory at the point of impact.

A preliminary selection of the Cherenkov photons is carried out, by checking if the photon's arrival position on the ground lies within the radius of the telescope mirror or around it. Although we have not used this approach, this step can actually be carried out through the Bernlohr package for IACT simulation with CORSIKA which selects the Cherenkov photons incident on a telescope given its position and radius.

Intersection

With the arrival position on the ground (x_{op}, y_{op}, z_{op}) and direction cosines (u_p, v_p, w_p) , the Cherenkov photon or light ray incident on the mirror can be described by the equation of a straight line in 3 dimensions:

$$\frac{x - x_{op}}{u_p} = \frac{y - y_{op}}{v_p} = \frac{z - z_{op}}{w_p} . \quad (5.2)$$

The paraboloid mirror can be described through the following equation:

$$x^2 + y^2 = 4 f z \quad \text{with} \quad x^2 + y^2 \leq d/2, \quad (5.3)$$

where f is the focal length of the mirror and d its diameter. The position of the point of impact $(x_{int}, y_{int}, z_{int})$ of the Cherenkov photon on the mirror can be found from solving equations 5.2 and 5.3. If this point lies within the radius of the telescope then the photon falls on the telescope mirror and is reflected by it.

Reflection

Once the normal to the mirror at the point of intersection is known, the reflection of the Cherenkov photon can be carried out by keeping two properties in mind. First, the angle of the reflected

ray with respect to the normal is equal to the angle of incidence. Second, the incident ray, mirror normal and reflected ray, all three lie in the same plane. This enables the calculation of the direction cosines (u_{rp}, v_{rp}, w_{rp}) of the reflected photon enabling us to write the equation of the reflected ray trajectory as

$$\frac{x - x_{int}}{u_{rp}} = \frac{y - y_{int}}{v_{rp}} = \frac{z - z_{int}}{w_{rp}}. \quad (5.4)$$

The mirror is considered to be 100% efficient as far as its reflectivity goes. Any loss due to reflectivity, needs to be taken into account at some other point in the simulation. As discussed in section 4.6, this effect can be introduced in the shower simulation in CORSIKA.

Image formation on the camera

The camera is situated along a plane at a distance z_{cam} from the vertex of the paraboloid. The intersection of this plane with the reflected ray given by equation 5.4 gives the point of impact of the Cherenkov photon on the camera plane. When this point lies within the radius of the camera, the Cherenkov photon contributes to the image obtained on this telescope.

The entire surface of the camera is subdivided into pixels through a square grid. The Cherenkov photon contributes to the signal of the pixel on which it falls. If the quantum efficiency of the photomultipliers has been taken into account earlier in the simulation (see section 4.6), then the arrival of Cherenkov photon on the camera is considered as the addition of a photo-electron to the image.

5.3.4 Implementation

The program has been coded in FORTRAN 77 so that it can be easily integrated into CORSIKA. The program can be used in 3 different ways.

- It can be used as a separate program which reads the standard Cherenkov photon binary output files from CORSIKA and uses them as input for the telescope.
- The telescope calculations are added to CORSIKA itself. Thus as CORSIKA calculates the trajectory of each Cherenkov photon emitted by each charged particle track, the photon is also checked for reflection from the telescope mirror(s) and its trajectory to the camera is calculated. Figure A.5 in the appendix shows how telescope simulation is incorporated in the main CORSIKA code.
- The program can be used independently from CORSIKA with another source for Cherenkov photons. The images in figure 5.6 were generated by sending Cherenkov photons with parallel trajectories at the mirror while covering its entire surface.

Various elements of the program are managed through different subroutines. This segmentation allows easier modifications and cleaner integration when used with CORSIKA. As the telescope routines need to be added to various parts of the CORSIKA code, we have introduced a new user activated module corresponding to the telescope calculations to CORSIKA.

A maximum of 100 telescopes can be simulated at the same time. The implementation of several shower cores (for the same shower) possible in CORSIKA can also be done with the telescopes. Multiple observation altitudes are not implemented yet since the calculations becomes cumbersome, but can eventually be introduced.

Each camera image is a 2-dimensional histogram with each bin representing a pixel of the image. Each image can be fitted and various quantities like the Hillas parameters can be calculated. The results are then written to the output files.

Once an image is obtained, it can be saved as a histogram in an hbook format. A binary file output containing the images has also been implemented. The advantage of the binary format is its relatively efficient use of disk space and the possibility of using the same images for various kinds of analyses. The binary files also contain run information like the observation level, the telescope parameters and their positions as well as shower information like the primary energy and height of first interaction.

Image reading program

A FORTRAN 77 program for reading the image binary files has also been written. This program gives the possibility of using the shower images for various studies including the calculation of statistics concerning shower images and the use of reconstruction methods for various shower parameters. In its current form, the program contains, the possibility of fitting shower images and obtaining different parameters, creating and filling various histograms, a basic image cleaning routine, routines for the reconstruction of source position in the sky, shower core position on the ground, shower energy and reconstruction of the emission positions of Cherenkov photons. Different aspects of these methods will be discussed in later chapters.

5.3.5 Example of simulation

We end this chapter by presenting several examples of telescope systems observing the same γ -ray shower. In figures 5.9 and 5.10, we show the three different types of configurations simulated. The configuration shown in figure 5.9 is the HESS telescope configuration, with four telescopes positioned at the corners of a 120 m square. We have used two different telescopes diameters (12.5 m and 21 m). The two other configurations are among the designs proposed for future IACT systems. Both use 15 m diameter telescopes. For all the telescopes simulated here, $f/d = 1.2$ and the total field of view is of $\sim 5^\circ$. The images are obtained by observing a 500 GeV shower (with 0° zenith angle) with the different array configurations at an altitude of 2200 m a. s. l.. The images obtained from these telescope systems are shown in figures 5.11, 5.12, 5.13 and 5.14.

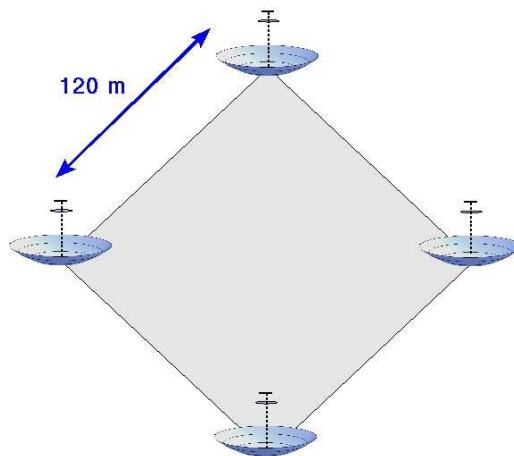


Figure 5.9: Telescope configuration used to obtain the images in figures 5.11 and 5.12.

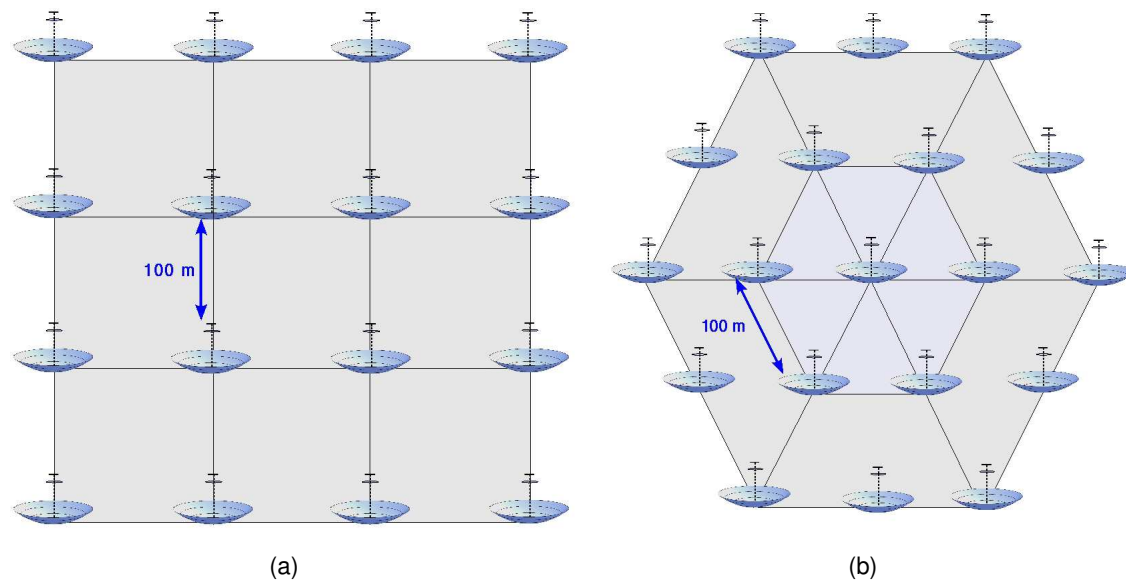


Figure 5.10: Two of the telescope configurations used to obtain the images shown in this chapter.

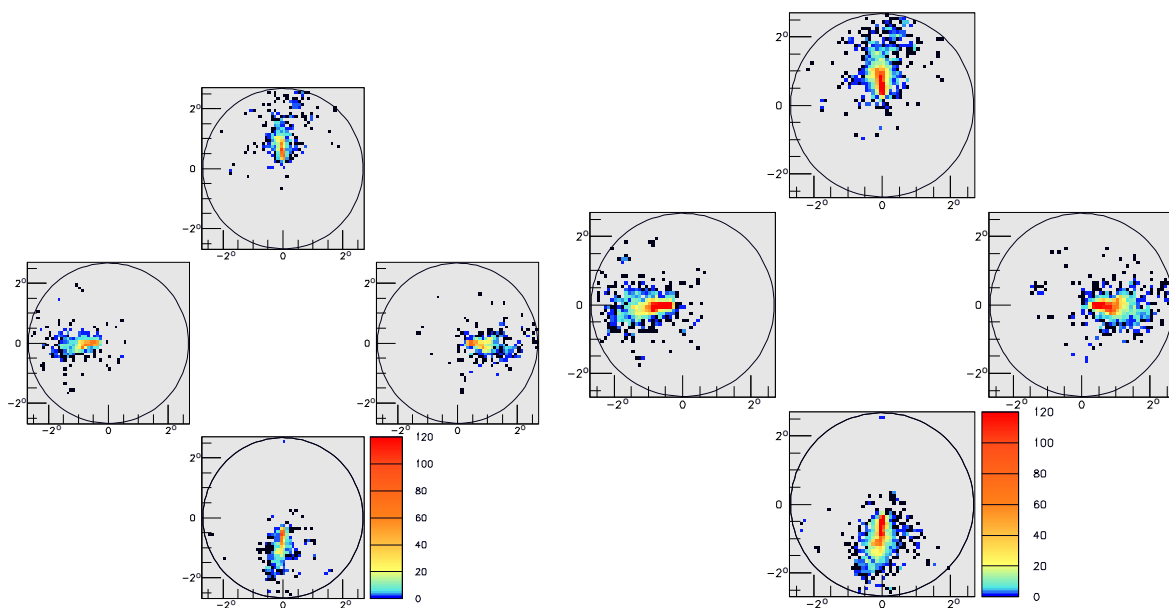


Figure 5.11: The images of a 500 GeV shower obtained on the four telescopes of a system with figure 5.9 configuration. The shower core is at (0,0) i.e. at the centre of the configuration and the telescopes are situated at 2200 metres altitude. The telescopes used to obtain the left images have 12.5 m diameters while those for the right images have 21 m diameters and $f/d = 1.2$.

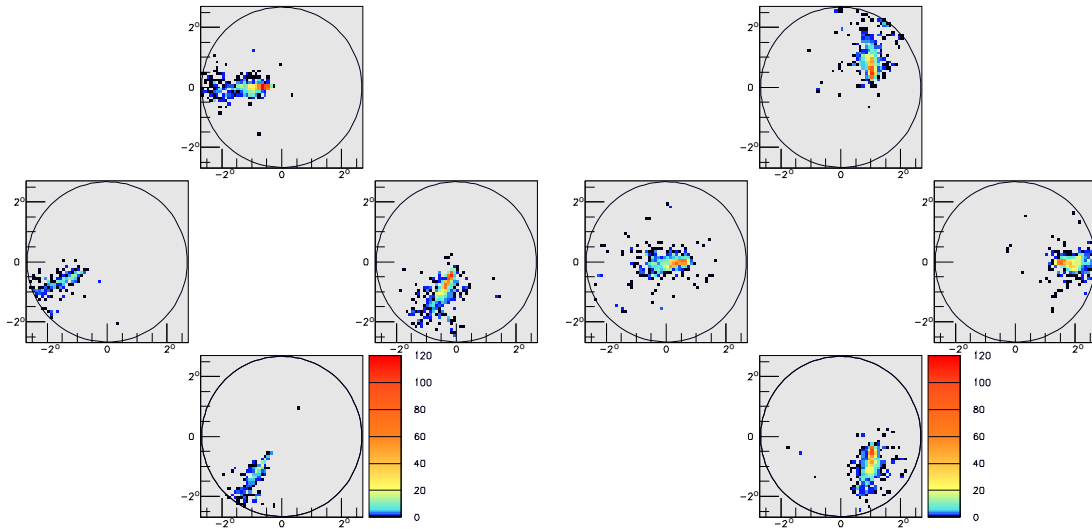


Figure 5.12: Left: The images of a 500 GeV shower with core position at (120,85) m obtained with the configuration shown in figure 5.9 with 12.5 m diameter telescopes and $f/d=1.2$. Right: The images of the same shower with core position at (0,0) m and but with each telescope with a zenith inclination of 1° . Other parameters are the same as those described in section 5.3.5.

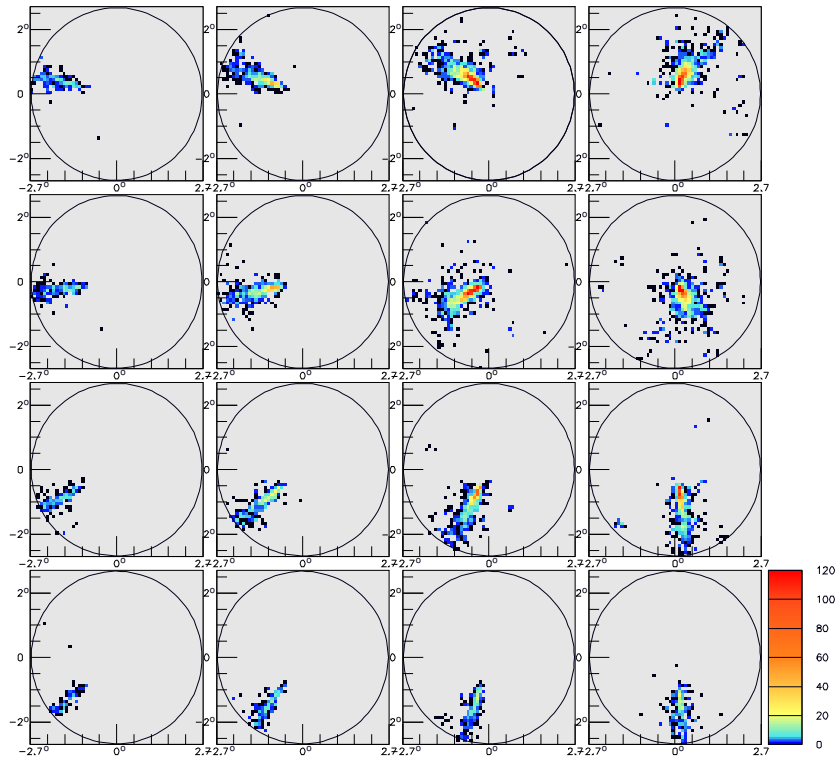


Figure 5.13: The images obtained from a 500 GeV shower with core position at (120,85) by the telescope array given in figure 5.10(a). Each telescope has a 15 m diameter with $f/d=15$ m. Other parameters are the same as those described in section 5.3.5

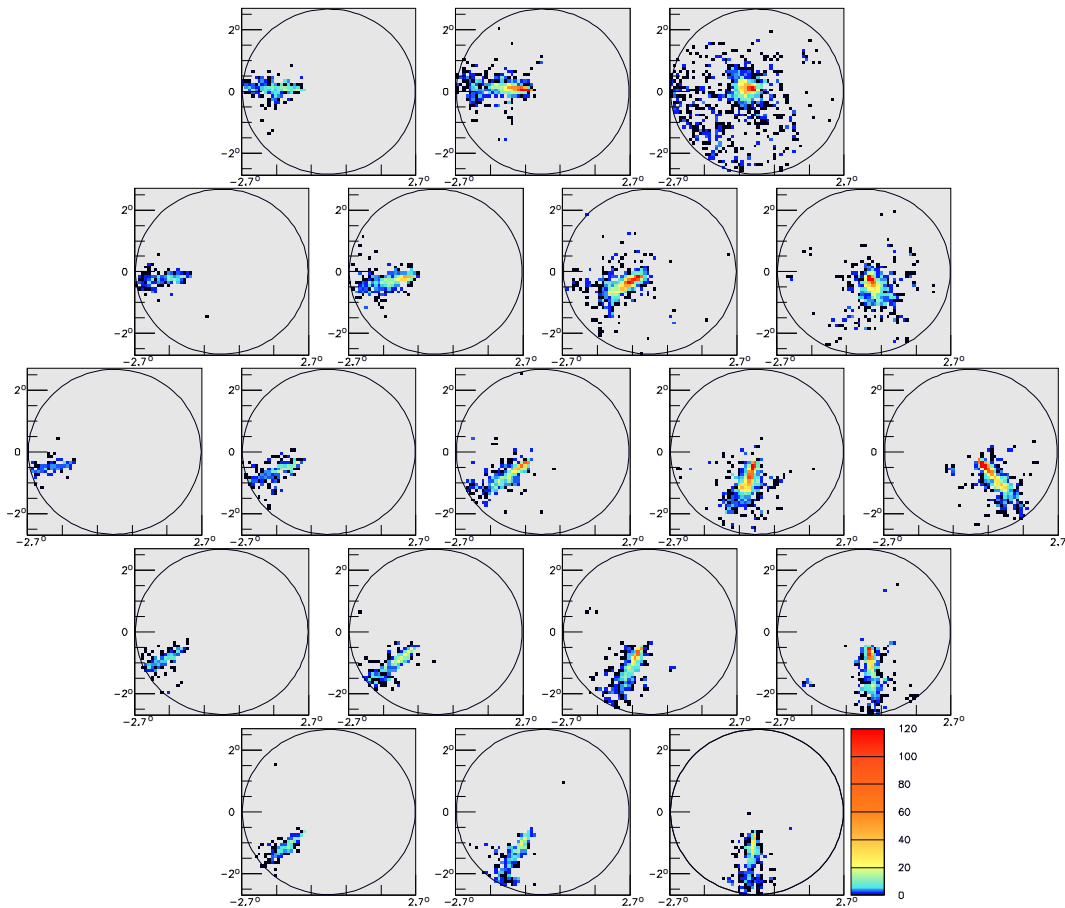


Figure 5.14: The images obtained from a 500 GeV shower with core at (120,85) by the telescope array given in figure 5.10(b). Each telescope has a 15 m diameter with $f/d=1.2$. Other parameters are the same as those described in section 5.3.5

CHAPTER 6

SHOWER IMAGES AND THEIR PROPERTIES

6.1 Introduction

In the previous chapter, we presented Imaging Atmospheric Cherenkov Telescopes and also discussed the main ideas concerning single or multiple ray reflection from parabolic mirrors. With this knowledge, we can now study the reflection of the atmospheric shower Cherenkov light by these mirrors and see how it results in the formation of shower images.

When working with real data (as opposed to simulations), these images are the only information available about the showers. Since shower parameters affect the characteristics of these images, they can be used to reconstruct¹ information about the original shower. The reconstruction methods involved require the exploitation of the relationship between image characteristics and shower parameters. In this chapter, we will, therefore, present how shower images are formed, and discuss their main characteristics and their dependence on shower parameters.

What do we mean by an image?

When the Cherenkov light from different parts of the shower falls on the mirror of a telescope, it is reflected onto the camera thus forming an image of the shower. This image is therefore a mapping of the shower through the Cherenkov light it emits. Since Cherenkov light is emitted uniformly by different parts of the shower, this image is a good representation of the shower itself. In the case of IACT, the camera surface is segmented due to the presence of photomultipliers. The resulting image is then pixelated with the content of each pixel corresponding to the signal from each photomultiplier. In general, a telescope image is a 2-dimensional array with individual elements representing each pixel.

In the simulation program (see chapter 5) implemented and used for the work presented in this thesis, the images are all treated as two dimensional histograms. Each bin of the histogram corresponds to an individual pixel. As an example, we show a histogram corresponding to the image of a 1000 GeV γ -shower in figure 6.1 (left). Each pixel corresponds to 3.5 cm \times 3.5 cm on the camera. As we will see later, the same region also corresponds to a $0.1^\circ \times 0.1^\circ$ region of the sky. The image has an elongated form reminiscent of the shower's shape. These and other topics related to the image shape and characteristics will be discussed in a detailed way in what follows.

¹This will be discussed in detail in chapters 7 and 8.

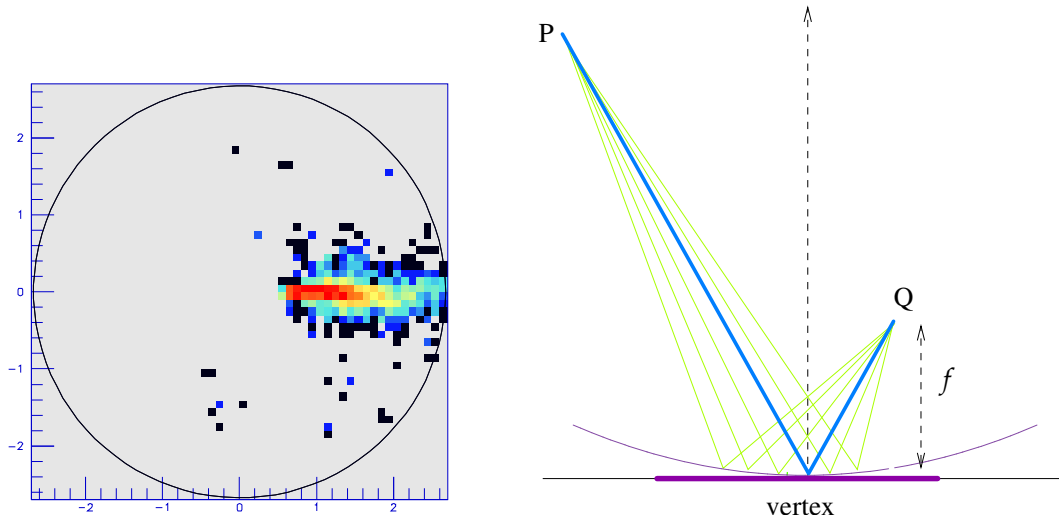


Figure 6.1: Left: The image of a 1000 GeV γ -ray shower obtained from a telescope with focal length $f=15$ m and diameter $d=12.5$ m. Each pixel corresponds to a $0.1^\circ \times 0.1^\circ$ region of the sky. Right: The schematic illustration of the reflection of rays from a single point P. The ray reflected by the vertex of the mirror is shown in blue.

A note on the terminology used

Before we go on to discuss the characteristics of shower images, we describe some of the terms used in the following discussion as well as the rest of this thesis in order to remove any ambiguity. The term **shower axis** will be used to describe the straight line corresponding to the path of the primary particle (determined from its direction and position). While the term **shower core** or **core** is often used to describe the same trajectory, we will restrict its use to refer to the point of impact of the shower axis on the ground. We also recall that the term **vertex** refers to the centre of the mirror as described in section 5.2.1.

6.2 General ideas concerning shower images: a step by step approach

Electromagnetic showers are fairly complex systems. The processes involved in shower formation are of stochastic nature. This implies the presence of statistical fluctuations in shower characteristics.

Moreover, even if the stochastic nature of showers is ignored and we study a simplified (say ellipsoid) shape to understand image formation, we have to deal with other complications. A shower has several parameters that affect the way the Cherenkov light emitted by it is reflected by the mirrors and images formed. These parameters include shower energy, orientation (or source position in the sky), altitude of first interaction, shower core position and its distance with the telescope. These parameters can simultaneously affect various characteristics of the image like its shape, size and the number of Cherenkov photons it contains. It can be difficult to separate the effect of a single parameter from others in a given image.

In what follows, we will therefore use a step by step approach to understand shower image formation by IACT. We will begin by describing how the image of a single point in 3-dimension is formed on the camera after reflection from a parabolic telescope mirror. This will be followed by a description of how the image of a line in 3-dimensions is formed after reflection and how this

line's orientation and position in space affect its image. This will then be used to understand the mapping of the source position and the impact of the core position on the orientation of the image. We will also discuss the image obtained from a 3-dimensional ellipsoid. This will be followed by a discussion on the various factors that affect the shape of a shower image and the number of photo-electrons contained in it. In the end, we will close this chapter by briefly discussing the image resolution.

6.2.1 Assumptions

In order to present the above points, we make a series of assumptions in order to remove all factors that are not key for the understanding of the dependence of image characteristics on shower parameters.

- The discussion is based on reflection by parabolic telescope mirrors. The main aspects of the description are similar for other shapes, though some adaptations may be needed depending on the mirror shape being discussed. Also, in the figures given below, we will only show the tangent to the mirror at its vertex, not the mirror itself.
- Coma aberrations (page 80) are completely ignored in the discussion given in this chapter. As far as their impact on shower parameter reconstruction is concerned, a note will be made in chapter 7. We note that the aberrations are present whenever simulated images are shown, since the program used for IACT simulations uses exact calculations for reflection.
- All images are assumed to be perfectly focused on the focal plane f . We saw in the previous chapter (page 79), that in reality only sources at infinity give focused images on the focal plane. Rays from nearer sources focus between f and $2f$. The altitude of different parts of the shower differ, but remains very large (at least several km) as compared to the telescope mirror focal length (usually 10-30 m). This implies that this assumption is reasonable since as we saw in the discussion on page 79, the position for image focalisation moves by only a few centimetres. If the need arises, this effect can eventually be taken into account by replacing the distance f by $f + \delta$, where δ depends on the altitude of the source point, in the calculations that follow.
- A single ray from each source point is used to describe the image formation of the point. Since the images are assumed to be perfectly focused and aberrations are ignored, this implies that all the rays emitted from a source point will focus at a single position after reflection. The reflection of a single ray from the source point is then sufficient to describe its image point. For simplicity's sake we choose the rays falling on the vertex of the mirror. A schematic illustration of this point is given in figure 6.1 (right), where the ray reflected by the vertex is shown in blue and all the other rays are shown in light green.
- The coordinate system used has its origin at the vertex of the parabola and z-axis along the paraboloid axis.

6.2.2 Single point mapping

We begin by presenting the formation of the image of a single point after reflection. This allows us to give a simple mathematical expression for the mapping of a point due to reflection. The same expression can then be used to describe the mapping of more complex sources like the shower axis. Figure 6.2 (left) shows the mapping of the point (x, y, z) after reflection from the

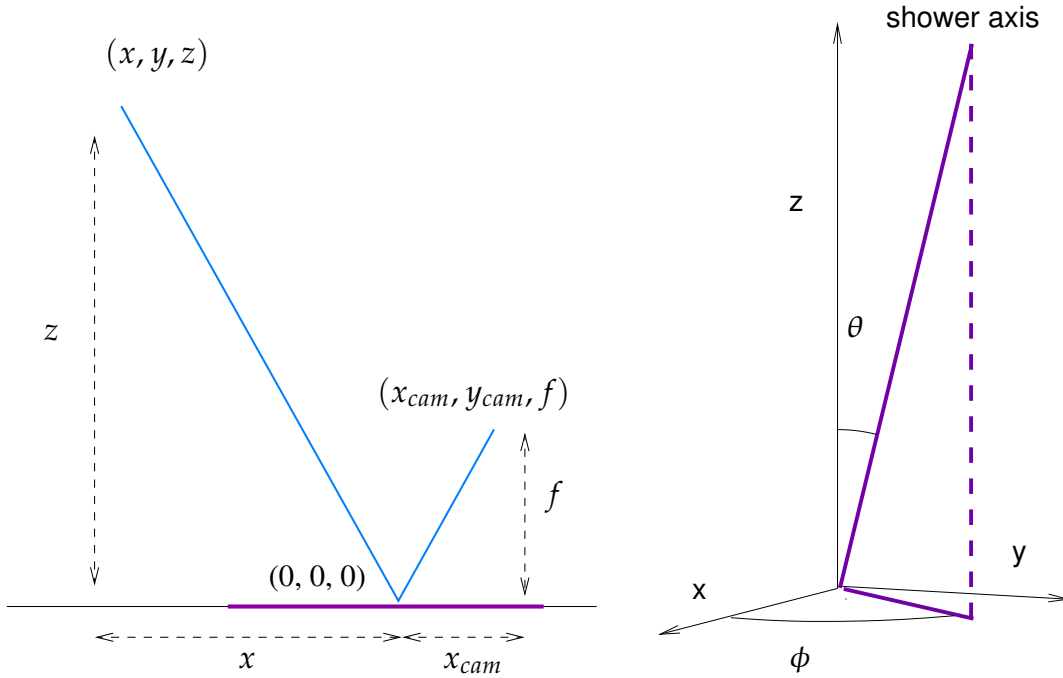


Figure 6.2: The left figure shows the mapping of a point (x, y, z) in space after reflection from the mirror. The right figure illustrates the definition of the zenith and azimuthal angles as used in this chapter. We note that this definition of the zenith angle is different from the one used in CORSIKA where the θ is measured with respect to the negative z axis.

mirror onto the focal plane. The calculations are done with a single ray emitted at (x, y, z) and incident upon the mirror vertex. The reflected ray will then arrive on the focal plane at the point

$$\begin{aligned} x_{cam} &= -\frac{f}{z} x \\ y_{cam} &= -\frac{f}{z} y, \end{aligned} \quad (6.1)$$

after reflection from the mirror. The negative sign in this set of equations implies that the image of the object obtained after reflection will be inverted. The non-linearity of the mapping, due to the presence of z in the denominator will be discussed later.

6.2.3 Shower axis mapping

The shower axis is a straight line in 3-dimensions whose orientation and position are determined by the position of the shower core and the position of the source in the sky. In the following sections, we will see that many of the aspects of shower image formation in IACT can be understood through the mapping of the shower axis alone. These aspects include, the image of the source position, the dependence of the orientation of the image on the shower core position in the telescope frame of reference...

The mapping of a straight line in 3-dimensions can be easily deduced as each point of the line will map according to the equations 6.1. Points on the shower axis follow the equation of a straight line in 3-dimensions:

$$\frac{x - x_c}{\cos\phi\sin\theta} = \frac{y - y_c}{\sin\phi\sin\theta} = \frac{z}{\cos\theta},$$

where x_c, y_c is the position of the shower core on the ground and θ and ϕ are the source zenith and azimuthal angles respectively. The zenith and azimuthal angles are defined according to figure 6.2.

Then the set of equations 6.1 becomes

$$\begin{aligned} x_{cam} &= -f \left(\frac{x_c}{z} + \cos\phi \tan\theta \right) \\ y_{cam} &= -f \left(\frac{y_c}{z} + \sin\phi \tan\theta \right) \end{aligned} \quad (6.2)$$

and describes the mapping of the points on the shower axis as a function of their altitude z .

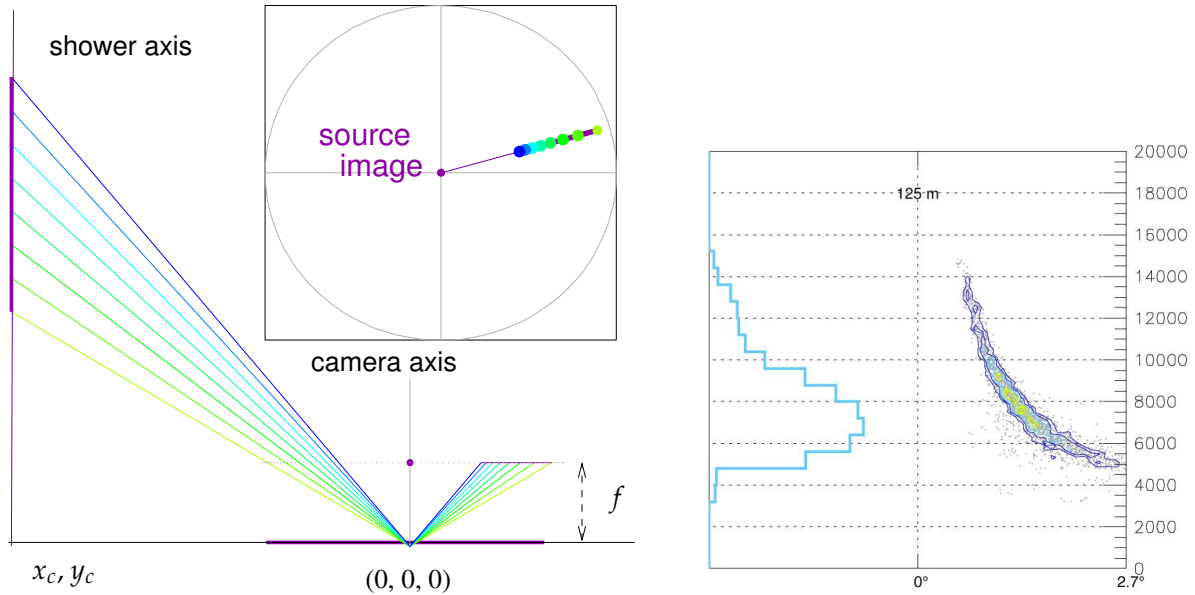


Figure 6.3: Left: Image of the axis of a vertical shower after reflection. Right: The 2-d distribution of the height of emission of Cherenkov photons in the atmosphere versus their arrival position (distance from the camera centre) on the camera, for a simulated shower of 1 TeV. The blue curve on the right is a projection of this plot on the altitude of emission axis. The ordinate axis shows altitudes ranging from sea level to 20 km a. s. l.. The telescope simulated was placed at an altitude of 2200 metres.

Figure 6.3 (left) shows how the axis image of a vertical shower ($\theta = 0$) is formed on the focal plane. The position of the source in the sky is mapped at the centre of the camera $(0, 0, f)$. The points of the axis at higher altitudes are mapped closer to the source image (i. e. close to the camera centre) and those from lower altitudes map at larger radial distances. This is also illustrated in figure 6.3 (right) where we show the arrival position on the camera (in terms of the radial distance from the centre) as a function of the altitude of emission for all Cherenkov photons of a 1 TeV γ -ray vertical shower. We can see that the Cherenkov photons emitted at the points nearest to the ground arrive the furthest from the camera centre. The maximum of emission is located around an altitude of 7 km.

6.2.4 Non-linearity of the mapping and camera coordinate system

Both left and right panels in figure 6.3 show that points that are equidistant on the shower axis are not mapped at equidistant positions on the axis image. The images of the points nearer to the ground have larger distances between them. This is because the mapping given by equation 6.1 is non-linear.

In fact, the distance between two points on the camera depends on the opening angle between the two corresponding incident rays. This is illustrated in figure 6.4 (left). For an opening angle $\delta\theta$, the distance on the camera is given by $d = f \times (\tan\theta_2 - \tan\theta_1)$, where θ_1 and θ_2 are the angles made by the two incident rays with respect to the vertical. Since IACT have usually few degrees of field of view and $\tan\theta \approx \theta$ for small θ , we obtain $d \approx f \times (\theta_2 - \theta_1) = f \times \delta\theta$. As a result the distances on the camera are often given in terms of angles. Since the camera is used to obtain an image of the sky, the distance between two points on the camera corresponds to the angular distance between two points in the sky.

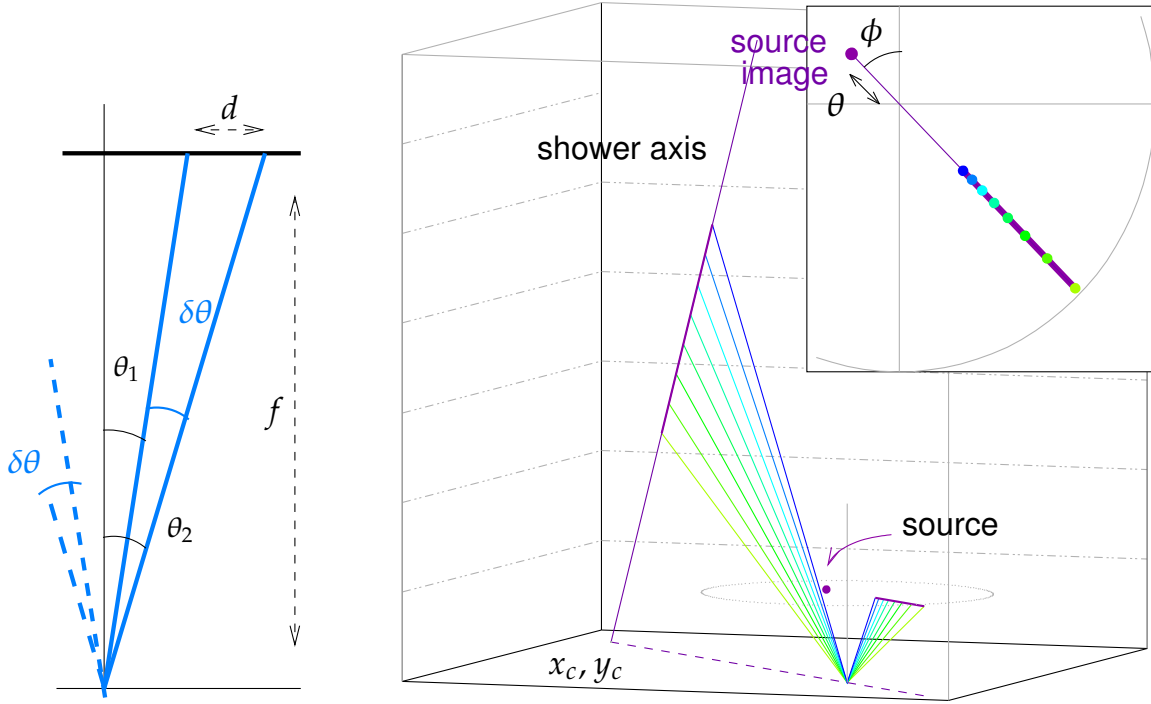


Figure 6.4: Left: Schema showing the relationship between the opening angle between two incident rays and the distance between their arrival points on the camera. Right: The mapping of the axis of an inclined shower with zenith angle θ and azimuthal angle ϕ .

6.3 Source position in the sky

The previous paragraphs discussed the mapping of the shower axis for vertical showers. We have seen that the source maps at the centre of the camera $(0, 0)$ in such instances. For more general cases (any value of θ and ϕ), the source's position can be obtained from the set of equations 6.2. The source is a point at $z \rightarrow \infty$ on the shower axis. Its image position is therefore given by

$$x_0 = -f \cos\phi \tan\theta \quad (6.3)$$

$$y_0 = -f \sin\phi \tan\theta \quad (6.4)$$

as a function of the zenith angle θ and azimuthal angle ϕ . The system described by these equations can be likened to a polar coordinate system whose pole is at the centre of the camera. Then $f \tan\theta$ is the distance of the source from the pole while $-\phi$ is the angle of the straight line joining the source position and the pole. If an angular coordinate system (as described in the

previous section) is being used then the distance between the source image and the camera centre can be approximated by θ for small θ . This is illustrated in the frame in the top-left corner of figures 6.4 and 6.5.

Figure 6.4 (right) shows how the image of the shower axis is formed for an inclined shower and how the zenith and azimuthal angles appear on the shower image. In the case discussed here, the shower axis lies within the plane formed by the shower core and the telescope axis. As a result, the axis image passes through the centre of the camera. As the shower is inclined towards the telescope, the rays from different points on the emitting part of the shower make smaller angles with the vertical. The entire axis image moves towards the centre of the camera and as a result, the position of the source image is displaced by θ from it. In such a case, ϕ also gives the orientation of the axis image since the axis image passes through the centre of the camera.

In figure 6.5, the telescope position is changed such that shower axis is no longer within the plane formed by the shower core and the telescope axis. The source position maps at exactly the same point on the camera. However, the orientation and position of the axis image changes and the shower axis image no longer passes through the centre of the camera. The angle between the axis image and the line joining the centre of the camera and the source image is a measure of the angle between the vertical plane containing the shower axis and the plane containing the shower core and the telescope axis.

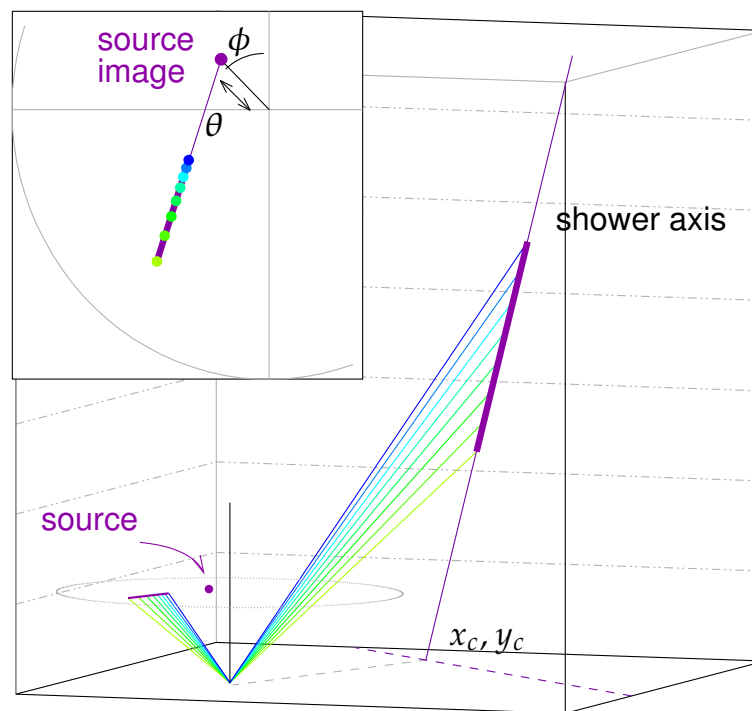


Figure 6.5: The mapping of the axis of an inclined shower when the shower axis is not contained within the plane formed by the shower core and the telescope axis.

6.4 Shower core and the orientation of the shower image

In figure 6.6, we show the mapping of the shower axis from figure 6.5 from a different perspective, in order to illustrate the orientation of the axis image. This orientation depends on

the position of the telescope T with respect to the shower core O . The image axis is parallel to the straight line joining O and T as they both make an angle α with respect to the x -axis. The distance between the two (the image axis and the straight line joining O and T) depends on the zenith and azimuthal angles of the source position (θ and ϕ respectively). In other words, if the telescope position T lies in the vertical plane containing the shower axis, then the axis image on the camera coincides with OT on the ground. This would correspond to the more simple configuration presented in figure 6.4.

6.5 General shape of the image

As we saw in chapter 2, an electromagnetic shower has a very small width to length ratio. Most of the energy of the shower is contained within $0.5X_0$ (i. e. at the most a few hundred metres) while the shower longitudinal development is spread over at least $15 - 20X_0$ (tens of kilometres) depending on the energy of the shower. The shower can therefore be viewed as very elongated elliptical region. Figure 6.7 give a schematic explanation of how different parts of the shower map on the focal plane. Four points A, B, C and D are taken on the emitting region to obtain the shape of the shower image on the camera. At a given distance R between the shower core and the telescope, the image has a roughly elliptical shape. The first image shows a view of the plane formed by the telescope axis and shower core and describes the mapping of the points A and B. They determine the length of the image which depends on R and can occupy up to several degrees on the camera. The width is determined by the points C and D whose mapping is shown in the second figure. In contrast to the length the width is practically independent of the position of the shower core and typically occupies a fraction of a degree on the image. The distortion in the elliptical shape is due to the non-linearity of the mapping. These features are visible in figure 6.8 where we show the image obtained from a simulated γ -ray shower of 1 TeV and the longitudinal and transverse profiles of the image. This image contains pixels with fractional photo-electron signal due to the way Cherenkov photons are generated in CORSIKA (see chapter 4). Once these pixels (black or dark blue) have been removed after image cleaning is performed, the core emitting region of the shower remains. This region occupies more than 2 degrees in length and about a half degree in width.

6.5.1 The effect of the telescope distance from the core

As can be seen from figure 6.7, R affects the length and position of the image. The width is not as much affected by the distance from the core since the angle subtended by the shower on the mirror, does not greatly change with distance. The image length is determined by the difference $\phi_2 - \phi_1$. This is in turn affected by the distance R . In a more general case, this will be affected by the zenith and azimuthal angles as well. R also determines how close to the centre, the points A and B will be mapped. Figure 6.9 on page 101 shows the images obtained from a single shower by changing the telescope distance from the shower core position. In the first image, the telescope is just under the shower and the image obtained is symmetric and circular, and the centroid of the image corresponds to the image of the source position (which is at the centre of the camera). As the telescope moves away from the shower core, the image becomes more elongated and moves away from the camera centre. In the last two images (beyond 120 metres distance), the image is not fully contained in the field of view due to the combination of these two effects.

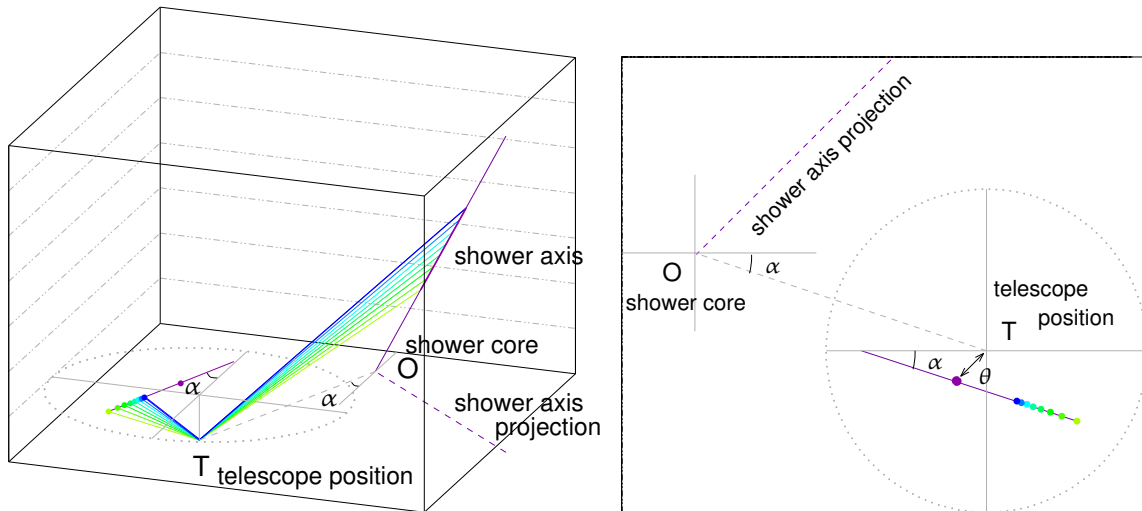


Figure 6.6: The mapping of the axis of an inclined shower when the shower axis is not contained within the plane formed by the shower core and the telescope axis. This is the same configuration as the one shown in figure 6.5 shown from two different perspectives. The left view shows how the axis image is formed while the right view shows the configuration from the top.

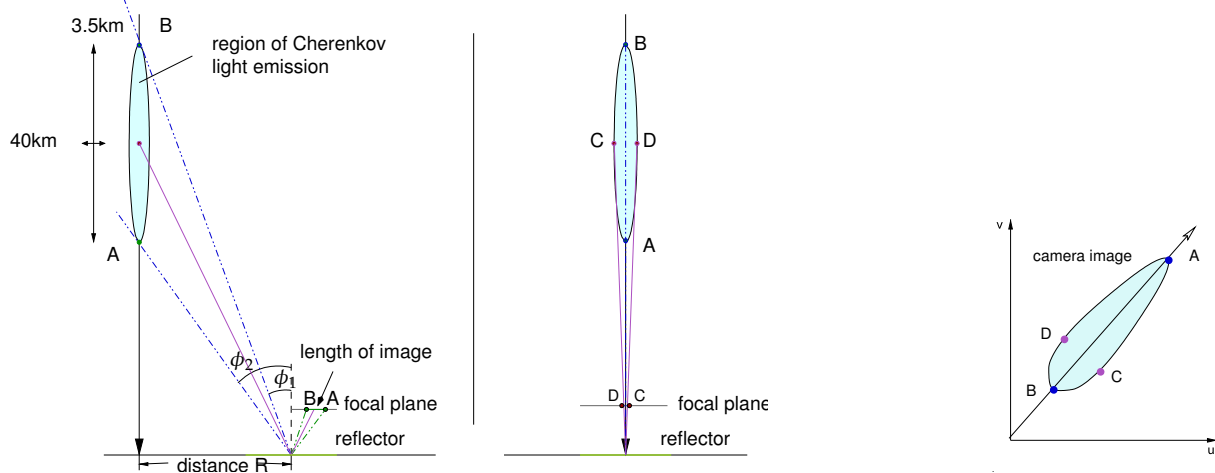


Figure 6.7: Schematic description of the mapping of the Cherenkov light from a shower onto the camera. Left: View of the plane formed by the shower axis and the telescope position. Centre: Plane perpendicular to it. Right: Image obtained on the camera. These figures are taken from [38].

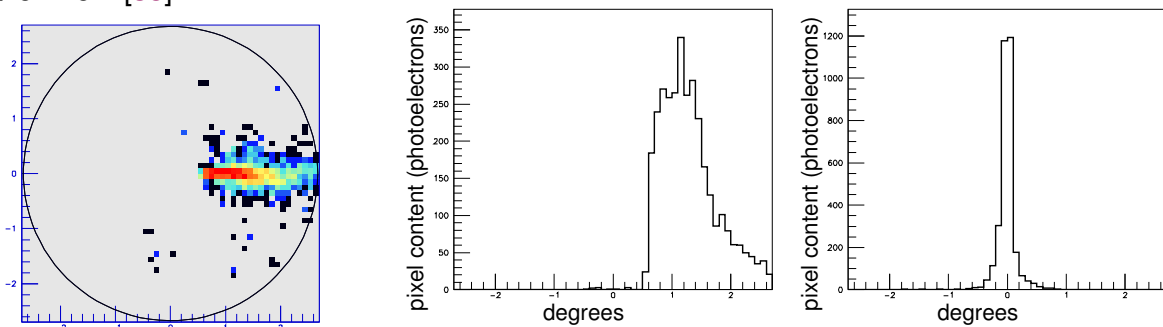


Figure 6.8: The image of 1000 GeV γ -ray shower obtained from a telescope situated at 120 metres from the shower core and its longitudinal (centre) and transverse (right) profiles.

The height of emission of photons

In the same figure, we also show the two dimensional distribution of the height of emission of the Cherenkov photons in terms of their arrival position (distance from the centre) on the camera and its projection on the height of emission axis. The following characteristics can be noticed:

- The bulk of the emission occurs between roughly 4 km and 10 km altitude.
- As the telescope position moves away from the shower core, the height of peak emission tends to increase. This can be explained by recalling figure 6.10 (left) from chapter 3 which shows the position of Cherenkov photon arrival on the ground as a function of the altitude of emission for photons with the maximum angle of emission $\theta_{c\ max}$ (see section 3.2) with respect to the vertical. The figure shows that photons emitted at higher altitudes tend to reach further distances from the core, while photons emitted at lower altitudes tend to reach the ground closer to the core position.
- According to this diagram (figure 6.10), a telescope positioned on the Cherenkov ring will have access to the Cherenkov photons emitted from the highest parts of the shower.

6.6 The number of photo-electrons contained in the image

So far, we have only discussed shower image shape and orientation and have made no comments on the number of photo-electrons making up those images. Two different types of factors determine this quantity:

- Factors that affect the Cherenkov photon density on the ground. These are mainly shower characteristics, altitude and observation conditions (atmosphere etc.).
- Telescope characteristics.

6.6.1 Cherenkov photon density on the ground and its dependence on various factors

In chapter 3 (section 3.4), we gave a detailed presentation of the various parameters affecting the Cherenkov photon density on the ground. In what follows, we will briefly recall the main characteristics of this density on the ground and then enumerate the parameters affecting it and their impact on the shower images.

In order to do this, we reproduce figure 3.10 from chapter 3 in figure 6.10 (left) here. This figure illustrates the principal aspects of the geometry of the Cherenkov photon density pattern on the ground. The photons arrive on the ground in a circular pattern around the core of the shower with a denser ring like region created by photons from various altitudes. The position and size of this ring depends on the altitude of observation. This results in density profiles such as those shown in figure 6.10 (centre). These average curves were obtained by simulating showers at various energies at 1800 m². The bulk of the emission occurs within the ring at 120 metres and the density declines quickly beyond it. The higher energy curves (500 GeV and 1000 GeV) tend to peak towards towards the core position (zero on the abscissae axis). For more details on these points, the reader should refer to section 3.4.

One can see the effect of the following factors on the Cherenkov density on the ground and consequently on the number of photo-electrons in the telescope images.

²We presented the equivalent plot for 2200 m altitude in chapter 3 (figure 3.14).

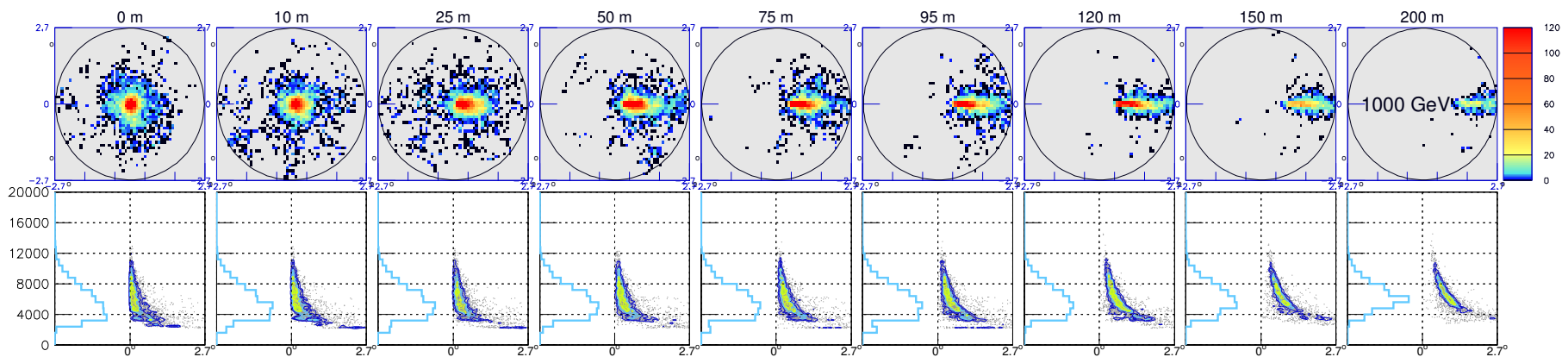


Figure 6.9: The images of a 1000 GeV shower obtained from 12.5 m diameter telescopes at various distances from the core position. The simulations are done for a ground altitude of 2200 m above sea level.

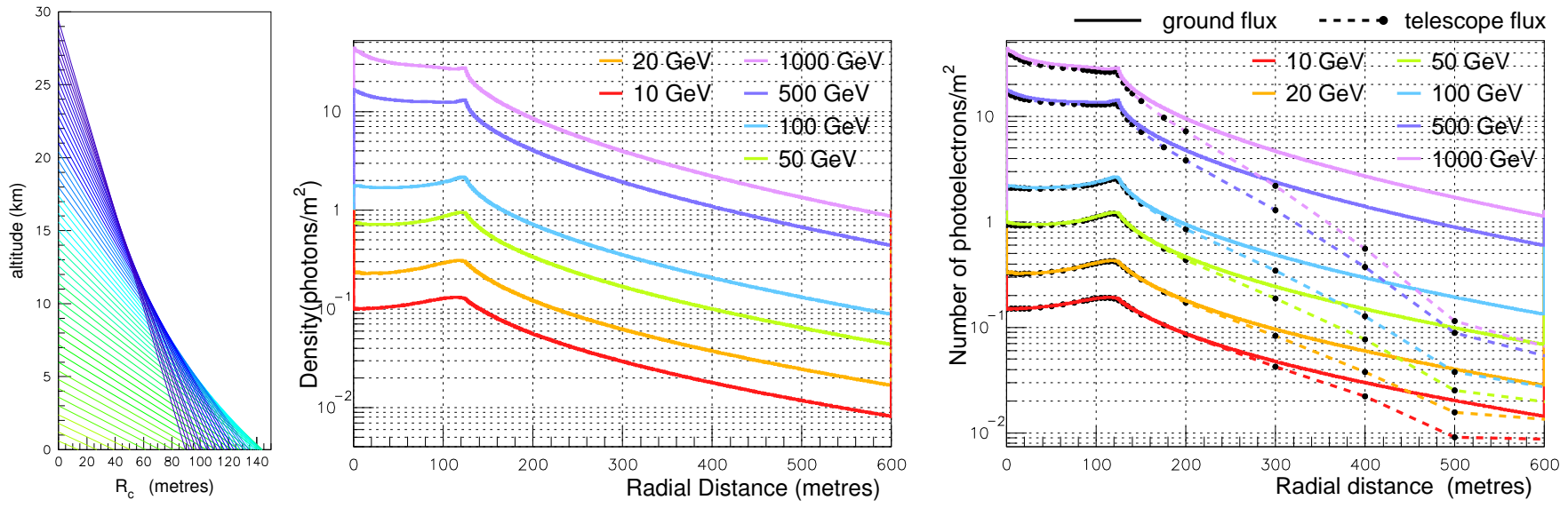


Figure 6.10: The left figure shows the position of Cherenkov photon arrival on the ground as a function of the altitude of emission for photons with the maximum angle of emission $\theta_{c\ max}$ (see section 3.2) with respect to the vertical. The figure is reproduced from section 3.4.1. The centre figure shows the average Cherenkov photon density obtained on the ground as a function of the radial distance from the shower core for showers of 6 energies simulated with ground level at 1800 m a. s. l.. The right figure compares these curves (solid line) with the photo-electron density in images from telescopes at various radial distances (dotted lines).

- **Distance from the core position** We have just seen the dependence of the Cherenkov photon density on the ground as a function of the radial distance from the core. Even if the Cherenkov photons falling on a given telescope do not all contribute to the images (this depends on their angle of incidence), the photo-electron number accepted by the telescope essentially follows the same curve. This is visible in the example in figure 6.9, where the total number of Cherenkov photons diminishes in the last two images i. e. beyond the ring position at 120 metres. In figure 6.10 (right), we compare the density profile of the Cherenkov photons on the ground (solid line) with the number of photo-electrons obtained in telescope images per square metre of the mirror surface (dashed line) at various energies. These show that within the Cherenkov ring, practically all the Cherenkov photons falling on the mirrors contribute to the shower images. As the distance increases beyond the ring, more and more photons are cut off due to their highly inclined angle of incidence on the mirrors. Among other parameters, this dependence on the distance determines the way telescopes are positioned in IACT arrays as one wants to have a sufficient number of telescopes with images that are exploitable for shower parameter reconstruction.
- **Energy** Lower energy showers are smaller and therefore tend to produce less Cherenkov light. This is seen in figure 6.10 (centre) and is also reflected in the photo-electron density curves in figure 6.10 (right). In figure 6.11, we compare the images obtained from telescopes at various distances from the core for showers of 3 different energies. While the roughly elliptical shape and the shower axis are easily identifiable for high energy showers of 500 and 1000 GeV, the 100 GeV shower images show more distortions and fluctuations due to the overall low number of photo-electrons in the image. As we go to even lower energies, these features are still harder to identify. As we will see later, this results in less efficient and sometimes problematic shower parameter reconstruction. One of the objectives for future IACT systems being the lowering of detection threshold, the methods of reconstruction and the telescope configurations need to be such that they extract maximum information out of the lower energy shower images.

One adds that the dependence on the energy combined with the dependence on the core distance are two characteristics that will be exploited in the energy reconstruction method we have used in our work. This will be discussed in detail in chapter 8.

- **The altitude of first interaction** In section 3.4.3, we saw how low materialising showers can lead to important Cherenkov photon densities close to the core position along with lower densities at larger distances. Showers that materialise higher in the atmosphere will have more moderate Cherenkov photon densities near the core position. These fluctuations in the Cherenkov photon density as a result of varying altitudes of first interaction are also reflected in the number of photo-electrons obtained in shower images. This aspect and its impact on the reconstruction of the energy will be discussed in more detail in section 8.5.4.
- **Altitude of observation** As we saw in section 3.4.4, the Cherenkov ring on the ground is smaller and denser at higher altitudes. The same dependence is found in the photo-electron number in telescope images. In figure 6.11, we presented the images of three showers of different energies obtained from telescopes at 2200 metres of altitude. Figure 6.12, shows the images of the same showers observed by telescopes at 5000 m of altitude. The total number of photo-electrons on the image is greater for telescopes within 100 metres of the shower core. Beyond that, the image content falls quickly to lesser values than those at 2200 metres.

- Other parameters like atmospheric conditions, night sky background and the geomagnetic field also affect the Cherenkov photon distribution on the ground. The sites chosen for an IACT system are chosen in such a way that they give good atmospheric conditions for the observations. A brief discussion on the transmission of Cherenkov photons through the atmosphere and the impact of the geomagnetic field can be found in chapter 3.

6.6.2 Telescope characteristics

The other type of factors affecting the number of Cherenkov photo-electrons obtained in shower images is directly related to the choice of telescope parameters.

- **Telescope size** With larger telescope mirrors, more light from the shower is collected. This can lead to better shower parameter reconstruction capacity. At the same time, larger mirrors tend to cost more and tend to collect more night sky background photons, making it harder to extract the signal in the images through image cleaning (See section 7.3.2) for a discussion on image cleaning.
- **Telescope field of view: focal length and diameter ratio**³ The field of view of the telescope is determined by the focal length and diameter ratio. A larger field of view allows the observation of a larger portion of the sky. This allows more Cherenkov photons to contribute to the shower images, specially at relatively larger distances from the shower core (Cherenkov photons with larger incident angles will also be accepted). This also has the drawback of introducing greater aberration in telescope images specially with parabolic mirrors and also getting higher levels of night sky background.
- **Other instrumental factors** Telescope characteristics such as mirror reflectivity and photomultiplier efficiency cut the number of Cherenkov photons that contribute to the shower image. These points were briefly discussed in chapter 4. Photomultipliers are responsible for around 25% losses in photo-electron number. Currently, efforts are underway to have photomultipliers with higher efficiency in order to diminish the loss of Cherenkov photons.

6.7 Image resolution

As mentioned briefly in the previous chapter, the telescope camera consists of a number of photomultipliers. The size of these photomultipliers determines the size of the pixels in the image. The smaller these pixels, the better the image resolution of the telescope. At the same time, the use of smaller photomultipliers implies that they are needed in a larger number to cover the same camera size and this tends to increase cost. Note that the use of smaller pixels (i. e. better resolved images) does not necessarily improve the reconstruction of the shower parameters and in particular the source position. We will see in the next chapter that the angular resolution of the telescope system studied is superior to the resolution of the image itself. This relationship between the pixel size and parameter reconstruction will also be briefly discussed in section 10.4.

³The discussion here concerns prime focus telescopes although the general trend (dependence of the number of photo-electrons in an image on the field of view) also applies to telescopes with secondary optics.

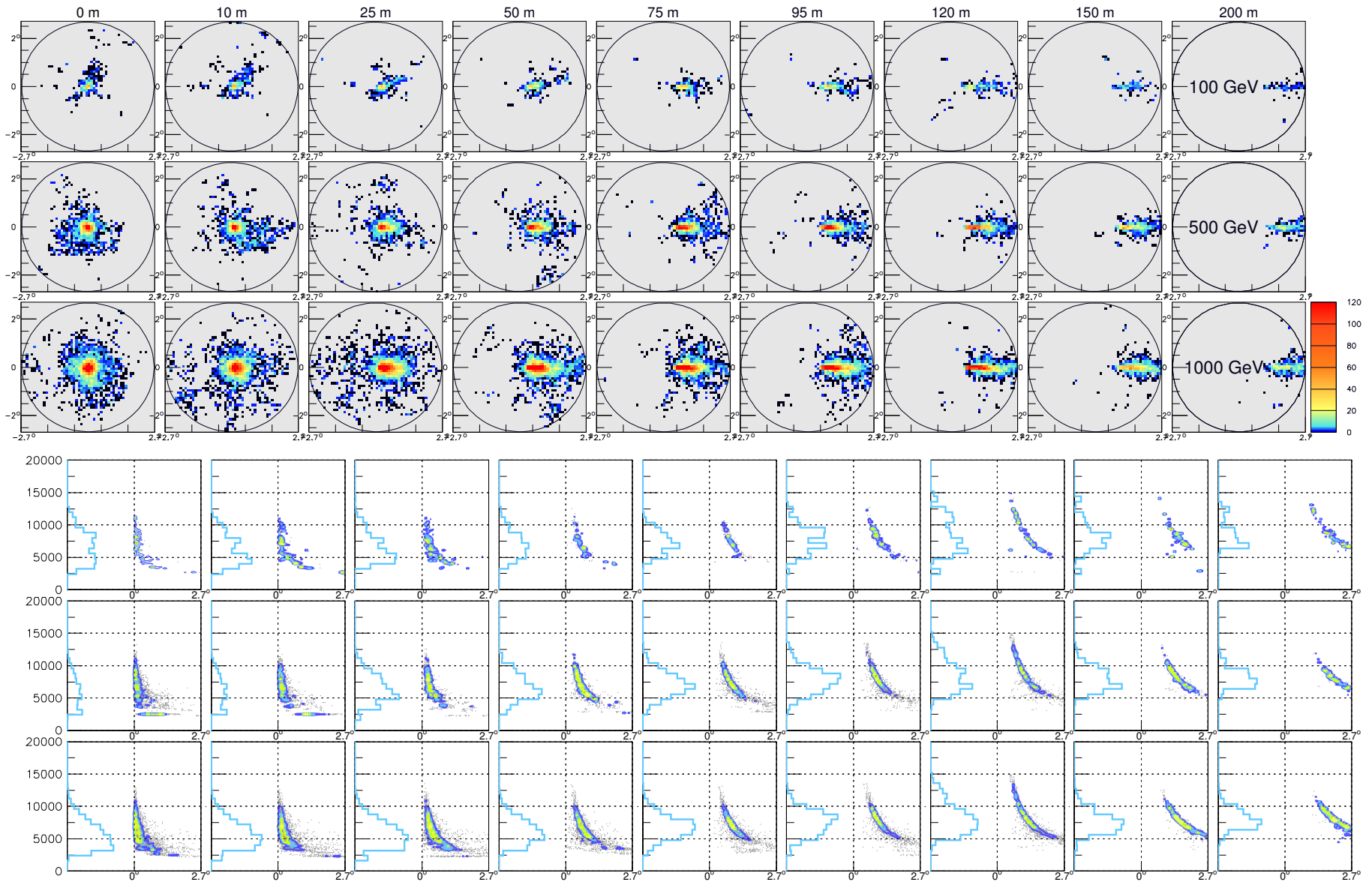


Figure 6.11: The top three rows show the images obtained for showers of 100, 500 and 1000 GeV by 12.5 m diameter telescopes at 9 distances from the shower core at 1800 m above sea level. The three bottom rows show the relationship between the altitude of emission (ordinate axis) of the Cherenkov photons and their arrival position (distance from the camera centre) on the camera (abscissae axis) for these three showers. The projection on the altitude of emission axis is also shown through the light blue curve at the left of each plot.

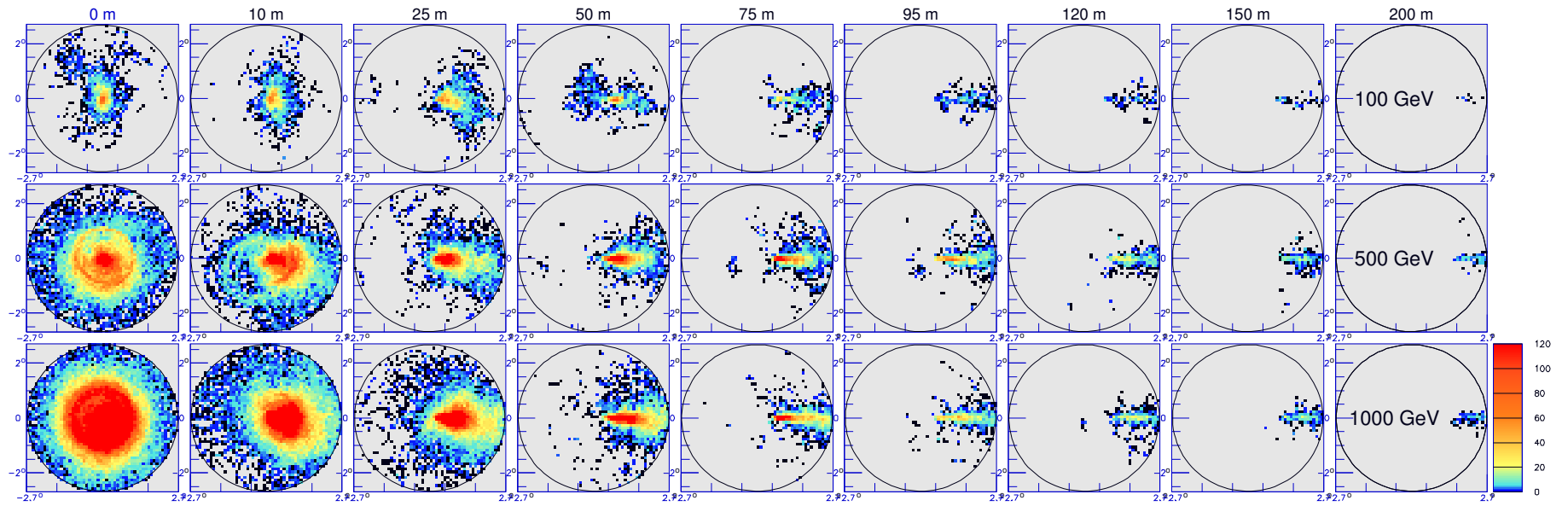


Figure 6.12: The images for 100, 500 and 1000 GeV showers obtained by 12.5 m diameter telescopes at 9 different distances from the shower core at 5000 m above sea level.

*P*_{ART IV}

S --- *HOWER RECONSTRUCTION AND IDEAS FOR γ -HADRON SEPARATION*

*P*RELIMINARIES

The goal of γ -ray astronomy is to observe γ -ray sources in the universe and gather information about their spatial structure, spectrum of emission and fluxes (intensity and time dependence of the gamma emission). In order to do the above, we need to know the trajectory (described by the source and core position) and energy of each γ -ray observed. IACT see γ -rays by obtaining Cherenkov light images of the atmospheric showers produced by them. These images are then used to estimate the parameters of the original γ -ray.

We have developed such methods to reconstruct the source position in the sky, shower core position on the ground as well as energy of the γ -shower. This was done with the intent of having methods that are easily adaptable to various IACT systems and that try to make the fullest use of the simultaneous information available from various telescopes.

In the previous chapter, we prepared the ground for the presentation of reconstruction methods by discussing the link between shower parameters and various image characteristics. In this part, we present the methods we have developed for the reconstruction of various shower parameters and discuss ideas for the discrimination between gamma and hadron-induced showers.

Chapter 7 contains a detailed presentation of the methods for the reconstruction of the source and shower core positions and the results obtained from their application to a four telescope array.

Chapter 8 describes the method for the reconstruction of the energy of the shower and results obtained by its application to a typical system.

These methods are presented in this order as the core reconstruction depends on the reconstruction of the source position. Similarly, the energy reconstruction depends on the reconstruction of the core position.

Finally, chapter 9 discusses three methods that can be used to separate gamma induced showers from hadronic showers.

Working with real images

So far, we have presented image properties through the mapping of the shower axis or the representation of the shower by an ellipsoid and given a few simulated images as illustrations. These simplified discussions bring out the relationship between various image parameters (such as image position, size and orientation) with different shower parameters (such as the core position, source position in the sky and shower energy).

Real showers involve stochastic processes. Their images are therefore less 'clean' than the description given above and the various parameters need to be determined and treated as random variables through statistical methods.

The system used for the studies presented in this part

Unless explicitly stated, the studies presented in this part have used a HESS-like configuration situated at an altitude of 1800 metres above sea level [39]. We have chosen this system so as to have the HESS public data as a reference for eventual comparisons and evaluations. The array consists of four telescopes placed at the corners of a 120 m square as shown in figure 6.13. The diagonal distance of each telescope from the centre of the square is 85 metres. The diameter of the telescopes is 12.5 metres and their focal length is 15 metres. The camera has a diameter of 1.4 metres, resulting in a field of view of $5.4^\circ \times 5.4^\circ$. The camera surface is divided into pixels of 0.1° each. All the telescope simulations have been done by using the simulation tool presented in chapter 5 with a parabolic mirror.

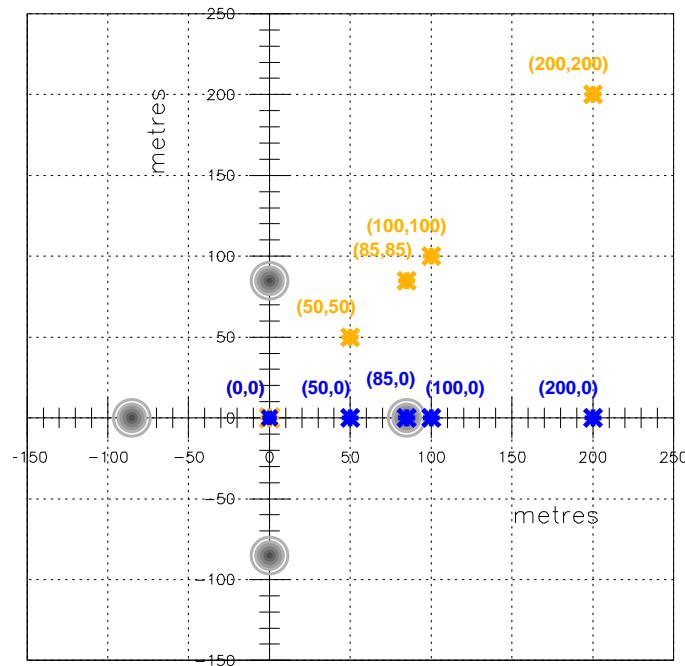


Figure 6.13: Position of the shower cores generated for simulations in the ground frame of reference. The four telescopes of the array form a square with a 120 m side and are represented by the grey dots at positions (85,0), (0,85), (-85,0) and (0,-85). The core positions are shown through blue and orange markers. See text for details.

The showers generated in all the simulations have been generated at the zenith. In order to study the effect of shower core distance from the telescope, the showers have been generated with a number of fixed core positions. These are shown in figure 6.13. There are two series of shower cores. The first one is shown through blue markers and is a series of positions at various distances towards one of the telescopes on the right. Note that the core position (85,0) is a special case where the shower is incident on top of one of the telescopes. The second series has four core positions at different distances along the diagonal of the array. One core position is also taken at the centre of the telescope system. All the telescopes point at the zenith.

CHAPTER 7

SOURCE AND SHOWER CORE POSITION RECONSTRUCTION

In this chapter, we present the methods we have developed for the reconstruction of the source position in the sky and the shower core position on the ground. We begin with a discussion on the system formed by the images of a single shower obtained through several telescopes and describe how it can be used to reconstruct the source and core positions.

In section 7.1, we present the method for the reconstruction of the source position. We give the principle of the method and its mathematical description. We then describe its implementation and present the results obtained from its application to a typical four telescope system.

Section 7.2 gives the method for the reconstruction of the shower core, its implementation and the results obtained from its application to a four telescope system.

Finally, section 7.3 deals with the effect of various parameters on source and core reconstruction. The main issues involved in these reconstruction methods are also discussed.

Multi-telescope images of the same shower

When the shower is viewed by several telescopes at different positions, then the orientation of the axis on the images (see section 6.4 for a detailed discussion) is different for each telescope¹. This is illustrated in figure 7.1 and 7.2. Figure 7.1 shows the mapping of the shower axis on the camera of four telescopes at different positions. In this figure, all four telescopes receive the light emitted from different altitudes along the shower axis. The image axis on each camera is oriented such that it points roughly towards the shower core position. This is better seen in figure 7.2 (left) where a view of the system is shown from the top. The four image axes intersect at a point that is slightly shifted from the shower core. This shift corresponds to the offset of the source image position from the centre of the camera. In figure 7.2 (right) we show the superposition of the four telescope images in the camera frame of reference. As we saw in section 6.3, each image axis points towards the source image on the camera. The source position therefore corresponds to the point of intersection of the individual image axes.

As an example, we show the simulated images of a 1000 GeV shower observed by a system of four telescopes, disposed in a square configuration in figure 7.3. The shower is simulated with zenith angle $\theta = 0$ in the frame of reference of the telescopes. The image of the source is then at the centre of the camera. The core position generated has a slight offset ($x=30$ m, $y=10$ m) from the centre of the square made by the telescopes. Since all the images are from the same shower, the source position lies at the same point on the camera for each

¹The only exception is the highly improbable case where all the telescopes are positioned along a line and the shower core lies on the same line. In order to have access to a maximum amount of information from the shower, the IACT arrays are not configured in this way.

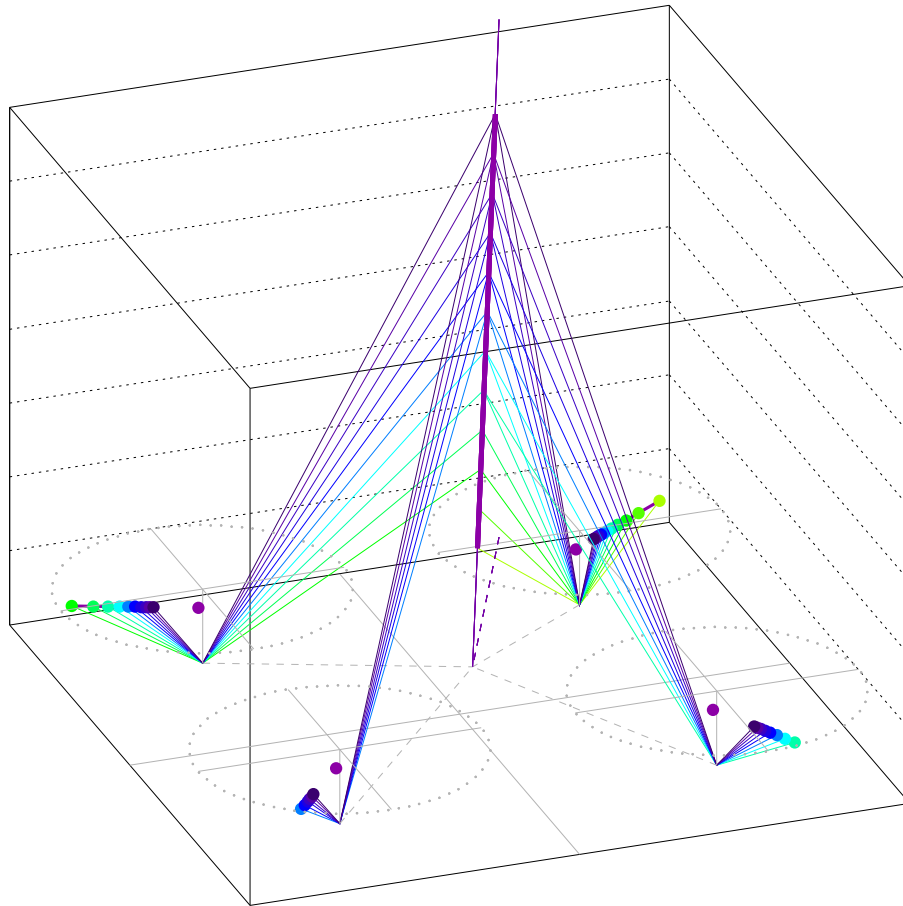


Figure 7.1: The mapping of the shower axis on the cameras of four telescopes.

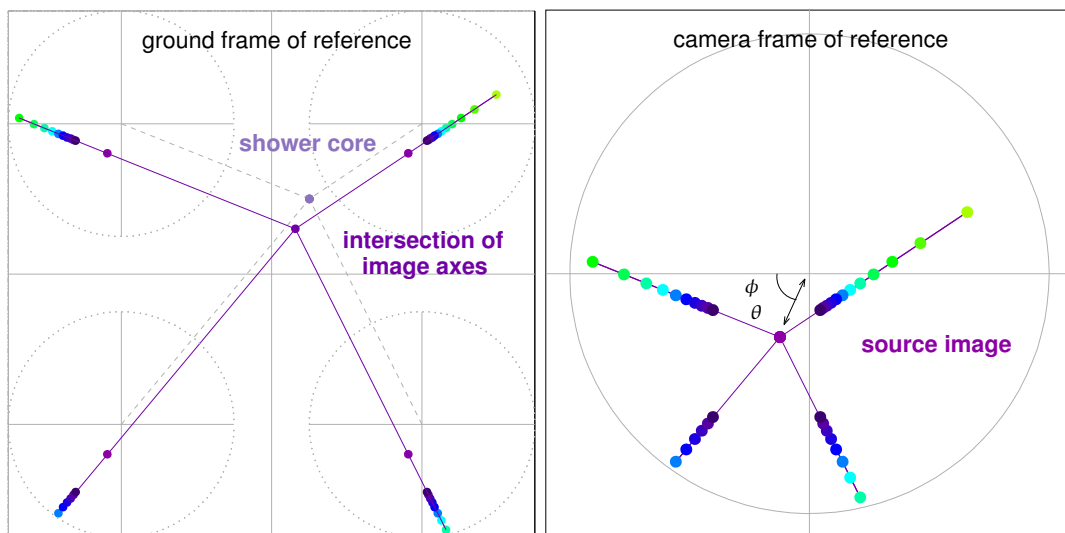


Figure 7.2: Left: The four images obtained from the mapping in figure 7.1 shown from above in the ground frame of reference. Right: The superposed images of the shower axis from the four telescopes in the camera frame of reference.

telescope and corresponds to the point of intersection of all the axes. The source and core positions can then be reconstructed by obtaining the point of intersection of the shower axes in the camera and ground frames of reference, respectively. The diagrams in figure 7.4 give a schematic description of the source (top) and core reconstruction (bottom) in the case of a four telescope system.

We note that while the same images are used to reconstruct both the source and core positions, the differences in the two methods lie in the frame of reference in which calculations are carried out and the use of the positions of the telescopes. In the case of source reconstruction, the calculations are carried out in the camera frame of reference (a two-dimensional frame of reference representing the sky), without taking the positions of the telescopes into account. For the core position calculations, the use of the position of the telescopes in addition to the information from the images allows us to locate the position of the core in the ground frame of reference. Images from other types of arrays such as those shown in section 5.3.5 also show the same properties. In what follows, we will describe these methods of reconstruction in detail.

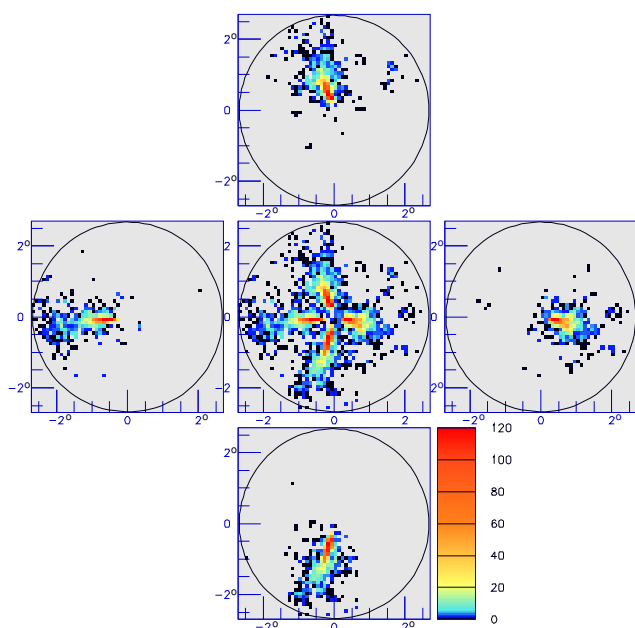


Figure 7.3: The images of a 1000 GeV shower obtained from four telescopes at 1800 m a. s. l. The plot in the centre shows the superposition of these images in the camera frame of reference.

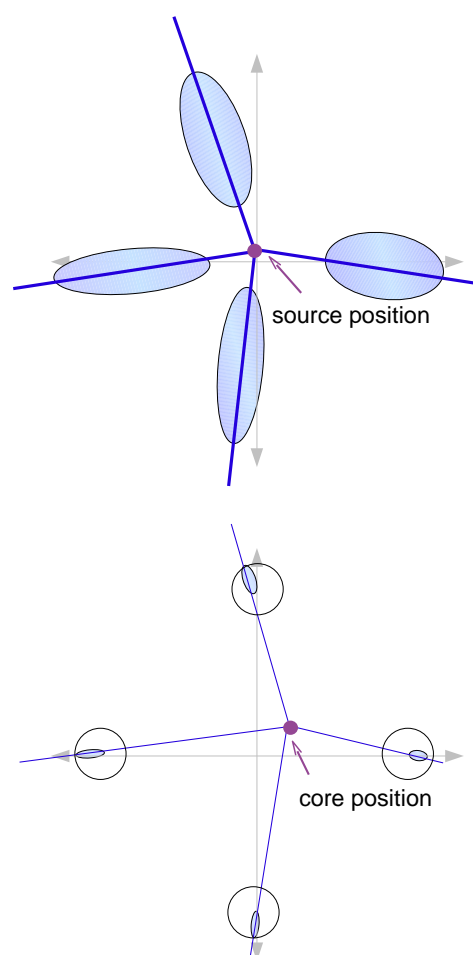


Figure 7.4: The schematic description of the source reconstruction (plot) and core reconstruction (bottom) for a four telescope system.

7.1 Source position reconstruction

In the next few sections, we describe the principle of the method and its application. We also, study an IACT array system as an example and give the results of source reconstruction for it.

7.1.1 Principle and likelihood function

Electromagnetic showers tend to have a regular shape and show symmetry around their axis. As a consequence, their images are also symmetric along the longitudinal axis. One way of determining the shower image's axis is by finding a straight line such that the photo-electrons are symmetrically distributed on both sides of the line. In a multi-telescope configuration, a straight line corresponding to the axis of each image would have to be determined such that all the axes intersect at one common point, the source position. As an additional constraint each of the axes can be made to pass through the centroid of the corresponding image.

In general, the axis of the image is a straight line in two dimensions whose equation can be written in the following form

$$y - y_o = m (x - x_o),$$

where m is the slope of the line and x_o, y_o represents the position of the source i. e. a point lying on this line. If the coordinates x_i, y_i give the position of a photo-electron on the camera, then its distance from the axis is given by

$$t_i = \frac{|m(x_i - x_o) - (y_i - y_o)|}{\sqrt{m^2 + 1}}.$$

If x_c, y_c is the position of the centroid of the image and we impose the constraint that the axis passes through it, then $m = (y_c - y_o)/(x_c - x_o)$ and the above equation can be written as

$$t_i = \frac{|(y_c - y_o)(x_i - x_o) - (y_i - y_o)(x_c - x_o)|}{\sqrt{(x_c - x_o)^2 + (y_c - y_o)^2}}.$$

A shower image consists of a number N_{pe} of photo-electrons distributed in N_{pix} pixels over the surface of the camera. The j^{th} pixel contains a signal of N_j photo-electrons. x_o, y_o remain to be determined and the centroid is given by

$$\begin{aligned} x_c &= \langle x \rangle = \frac{1}{N_{pe}} \sum_{i=1}^{N_{pe}} x_i \\ y_c &= \langle y \rangle = \frac{1}{N_{pe}} \sum_{i=1}^{N_{pe}} y_i. \end{aligned}$$

The distance of the i^{th} photo-electron from the shower axis t_i is a random variable that follows the average transverse profile distribution of electromagnetic shower images. The probability that the i^{th} photo-electron's distance from the axis lies in the interval $[t_i, t_i + dt_i]$ is given by

$$dP_i = f(t_i; x_o, y_o) dt_i,$$

where $f(t_i; x_o, y_o)$ is the probability density function p. d. f. describing the transverse profile.

For a given shower image with N_{pe} photo-electrons, the values of t_i for all the photo-electrons in this image, constitute a sample. The probability of obtaining this particular set of values of t_i is then given by

$$dP = \prod_{i=1}^{N_{pe}} f(t_i; x_o, y_o) dt_i. \quad (7.1)$$

If the hypothesised values of x_o, y_o define a straight line such that the photo-electrons of the image follow the distribution given by the p. d. f. $f(t_i; x_o, y_o)$ in the transverse direction around it, then most of the photo-electrons will fall in the high probability regions of f giving a large value of dP in equation 7.1. If on the contrary, the values of x_o, y_o do not define the axis of the image, the photo-electrons will fall in low probability regions of f and give a low value for dP . The same properties hold for the likelihood function

$$L = \prod_{i=1}^{N_{pe}} f(t_i; x_o, y_o) \quad (7.2)$$

and its logarithm. The maximisation of this function through derivation will then yield the best possible values for the source position x_o, y_o in such a way that the straight line determined by them corresponds to the shower axis image.

We have worked with a Gaussian p. d. f. describing the transverse profile of the shower images. This choice will be discussed in section 7.1.2. With

$$f(t_i; x_o, y_o) = \frac{1}{\sqrt{2\pi}\sigma_t} e^{-\frac{t_i^2}{2\sigma_t^2}},$$

the log likelihood function becomes

$$\begin{aligned} \ln(L) &= -N_{pe} \ln(\sigma_t \sqrt{2\pi}) - \sum_{i=1}^{N_{pe}} \frac{t_i^2}{2\sigma_t^2} \\ &= -N_{pe} \ln(\sigma_t \sqrt{2\pi}) - \sum_{j=1}^{N_{pix}} \frac{N_j t_j^2}{2\sigma_t^2} \end{aligned} \quad (7.3)$$

in terms of pixels and pixel content, with t_j giving the distance of the j th pixel from the straight line.

Equation 7.3 gives the likelihood function to be maximised to determine the axis of one of the images. In order to use the information from all telescope images simultaneously, we write the general likelihood to be maximised in the following way:

$$\ln(L_{all}) = -N_{tot} \ln(\sigma_t \sqrt{2\pi}) - \sum_{j=1}^{N_{tel}} \sum_{i=1}^{N_{pix}} \frac{N_{ij} t_{ij}^2}{2\sigma_t^2}. \quad (7.4)$$

Here N_{tot} is the sum of all photo-electrons in all images, N_{ij} is the photo-electron content of the i^{th} pixel in the image from the j^{th} telescope and t_{ij} is its distance given by $t_{ij} = \frac{|m(x_{ij}-x_o)-(y_{ij}-y_o)|}{\sqrt{m^2+1}}$. x_{ij} and y_{ij} are the position coordinates of this pixel. The likelihood function $\ln(L_{all})$ is also closely related to the χ^2 function of the problem:

$$\chi^2 = \sum_{j=1}^{N_{tel}} \sum_{i=1}^{N_{pix}} \frac{N_{ij} t_{ij}^2}{\sigma_t^2}. \quad (7.5)$$

This value will be used to discuss and compare the quality of fits.

7.1.2 Gaussian probability density function for the transverse profile

In the previous section, we introduced the use of a Gaussian p. d. f. representing the transverse profile of shower images. We discuss this choice in this section and determine the value for σ_t used in the likelihood function.

As the lateral distribution of electromagnetic showers in the air is symmetric and relatively compact, one expects the same characteristics in the transverse profile of the shower image. Figure 7.5 (dark blue line) shows the average transverse profile for 50 GeV shower images. The profile has a dense, compact central region spread over about half a degree. In fact the two central bins contain about 72% of the entire distribution, the four central bins contain 87% and the six central bins contain about 92 % of the total light in the average image. The rest of the light from the shower is spread over pixels on either side of this central peak. These bins are more evident in the log scale plots of the profile (7.5, right).

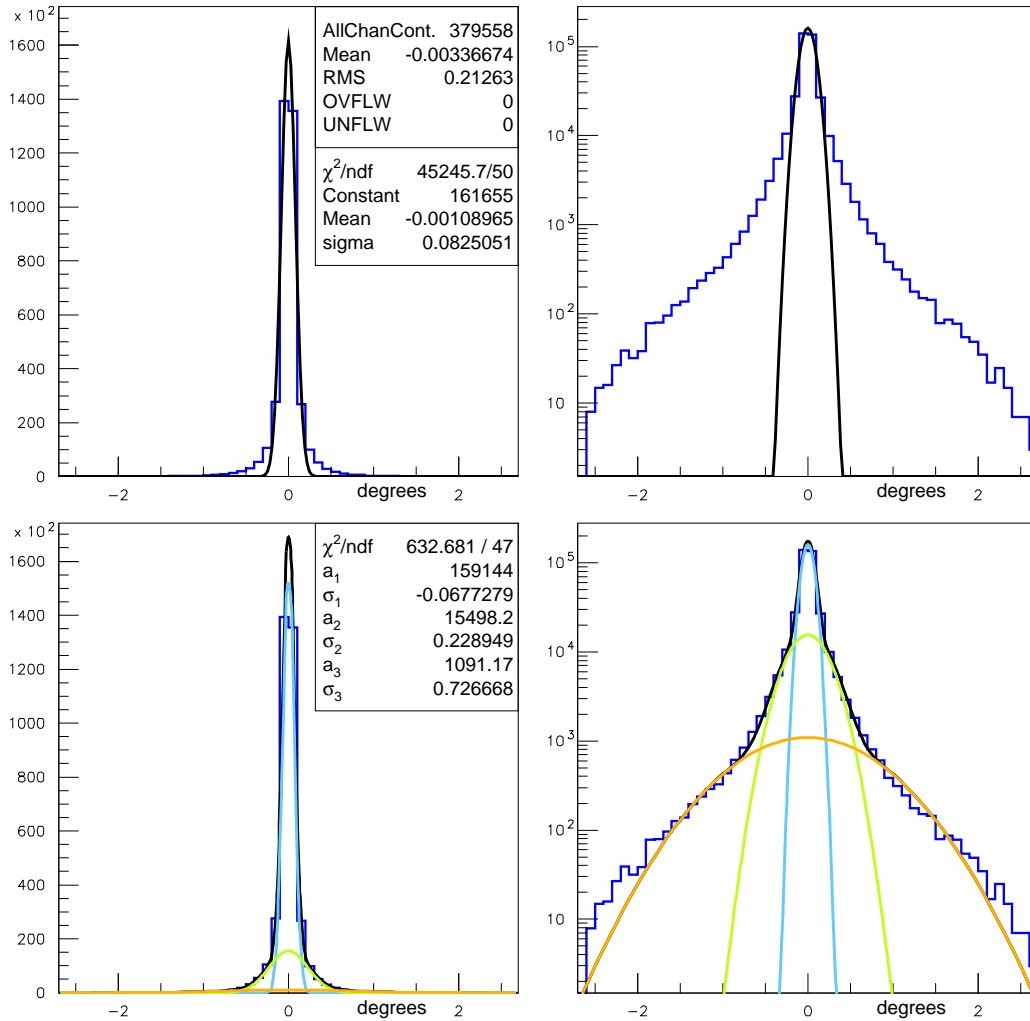


Figure 7.5: The average lateral profile for 50-GeV gamma ray showers at 1800 m altitude is shown in dark blue. In the top figures the distribution is fitted with a Gaussian function (black curve). In the bottom figures, it is fitted with the sum of three Gaussian functions (black curve). The three individual Gaussian functions are also shown (light blue, green and orange curves). The distribution and the two fits are shown in log scale in the right column. Each bin corresponds to the size of a pixel i. e. 0.1° . A total number of 1000 showers was simulated.

In order to evaluate how well the transverse profile is represented by a Gaussian p. d. f., we fit the histogram with a Gaussian function (black curve in the top two plots in figure 7.5). The curve fits well the 4 central bins, but does not take into account the side bins. A better

representation of the curve is obtained by fitting it with the sum of three Gaussian functions i. e. $f(x) = a_1 e^{-0.5 \frac{x^2}{\sigma_1^2}} + a_2 e^{-0.5 \frac{x^2}{\sigma_2^2}} + a_3 e^{-0.5 \frac{x^2}{\sigma_3^2}}$. This is shown by the black curve in the two bottom plots. The area under the curve represents the distribution's surface with an accuracy of $\sim 0.2\%$. The three individual Gaussian functions that contribute to the fit are also represented in the plots (light blue, green and orange curves). The first of these curves (light blue) resembles closely the single Gaussian fit from the top figures. It corresponds to the four central bins of the distribution and accounts for about 72% of the total fit surface. In comparison, the surface of the single Gaussian fit from the first plot amounts to 88% of the total surface obtained from the three Gaussian fit. One can conclude that the transverse profile can be reasonably well represented by a single Gaussian.

Determining the value of σ_t for the reconstruction methods

As we have used a Gaussian p. d. f. for the transverse profile for the calculations of the source position reconstruction, we need to determine the value of the parameter σ_t used in equation 7.4 and study its dependence on energy. In order to do this, we have done a series of simulations with showers at various fixed energies. All the showers were simulated at zenith angle 0° and the telescopes were placed at 85 metres from the shower core at an altitude of 1800 metres above sea level ².

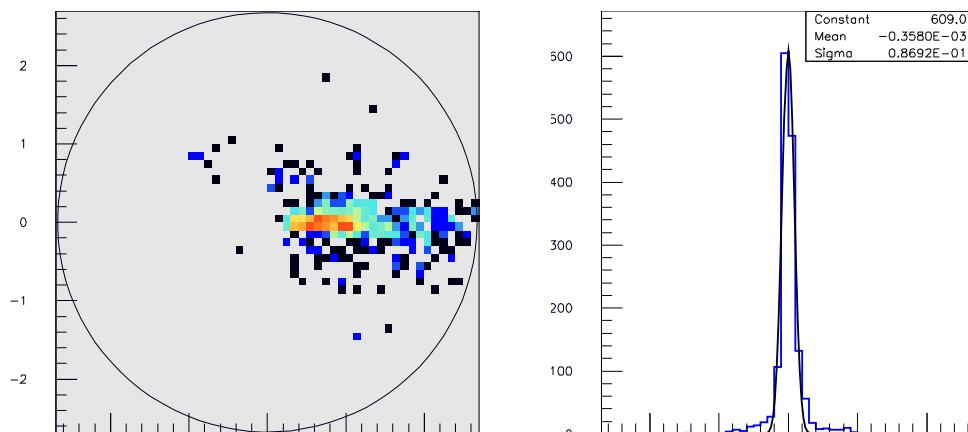


Figure 7.6: Left: The image of a 500 GeV shower obtained by a 12.5 m diameter telescope with $f=15$ m. Right: The transverse profile of the image is fitted with a Gaussian curve.

The transverse distribution of each shower image is fitted with a Gaussian function $f(x) = a e^{-\frac{1}{2} \left(\frac{x-b}{\sigma_t} \right)^2}$ and a value of the standard deviation σ_t is obtained as shown in figure 7.6. When this process is repeated for 4000 showers, a distribution of σ_t is obtained for each shower energy. In figure 7.7, we show the σ_t distributions obtained for 50 GeV and 1000 GeV showers. Both distributions have similar average values i. e. around 0.08° . At the same time, the two distributions have very different spreads: the 50 GeV distribution is less compact than the 1000 GeV one.

These two trends are displayed in figure 7.8, where we present the evolution of the standard deviation distributions as a function of the shower energy. Each point corresponds to the mean value obtained from standard deviation distributions (as shown in figure 7.7). The plot shows

²These choices correspond to the telescope array which we will be using to study the shower reconstruction methods later on. The details of the array parameters are given on page 110.

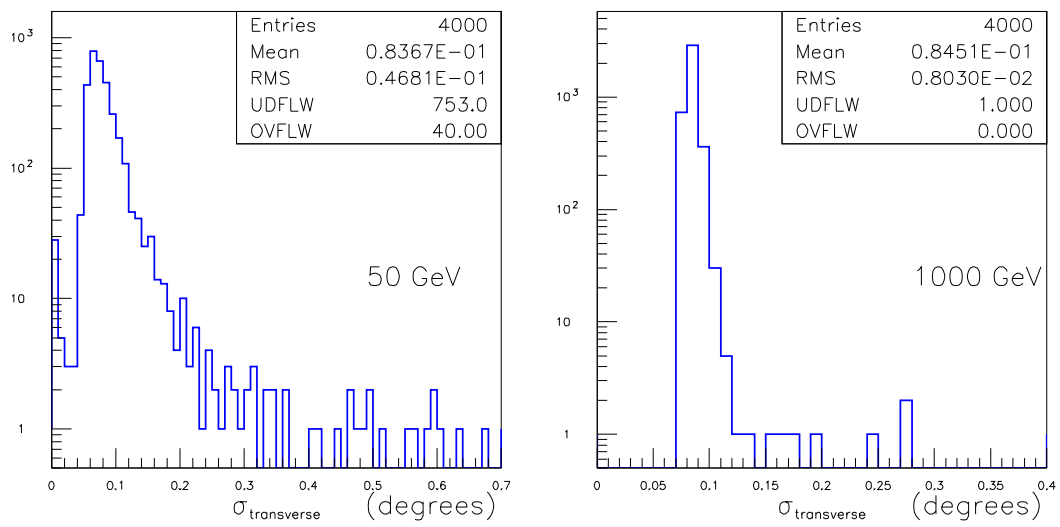


Figure 7.7: Distribution of the standard deviation for 4000 γ -showers of 50 GeV (left) and 1000 GeV (right).

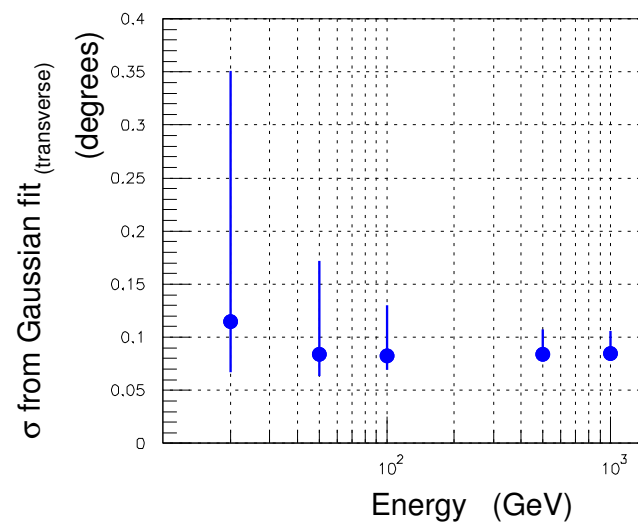


Figure 7.8: The standard deviation from Gaussian fits as a function of the energy.

that there is no significant change of the mean value with energy i. e. it remains close to 0.08° . This is to be expected since the lateral spread of the shower and therefore the width of the shower image also varies very little with energy (see discussion in chapter 2). Note that this value is similar to the $\sigma_t = 0.0825^\circ$ obtained from the fit of the 50 GeV average profile in figure 7.5(top).

The compactness of the standard deviation distributions is represented by the error bars. For each energy, the root mean square (r. m. s.) value of the σ_t distribution is calculated. This is done separately for the bins below the mean value and above it. Since the σ_t distributions are asymmetric, this leads to asymmetric error bars. One sees that the compactness of the standard deviation distributions is highly dependent on the energy. At lower energies, there is a greater dispersion of the values of σ_t obtained by the Gaussian fits of the transverse profiles. This can be understood through the examples of transverse distribution fits in figure 7.9. The images at lower energies have fewer photo-electrons and less pronounced/contrasted central regions. As a result, the influence of stray pixels away from the bulk of the image is greater on the fit. Since the showers have greater fluctuations at these energies (see chapter 3), the fit results show greater variations from one shower to the other.

The most important property concerning the use of σ_t in the method described in section 7.1.1 is that its mean value is independent of the energy. This means that this value can be used in equation 7.4 to calculate the likelihood function even though the energy of the shower is not known. As we will see in later in this chapter and the next one, this allows us to use the reconstructed source position in the sky to determine the shower core position and shower energy.

In section 7.3.3, we will describe some additional characteristics of these Gaussian fits. For instance, so far we have not discussed the presence of the small peak in the bins close to zero in the 50 GeV distribution (figure 7.7). Moreover, the number of underflows (UDFLW) shows that a lot of events have negative σ_t values. These characteristics are the result of Gaussian fits that do not converge and they will be further discussed along with the factors affecting the quality of Gaussian fits in section 7.3.3.

We also add that the discussion has so far been limited to telescopes at a fixed distance (85 m) from the shower core. We have done that in order to restrict the description of the method of source reconstruction to its essential aspects. In section 7.3.3, we will discuss the effect of the distance on the values of σ_t and the reconstruction of source and core positions.

7.1.3 Implementation of the source reconstruction method

In section 7.1.1, we described the principle for the method of source position reconstruction. The log likelihood function $\ln(L_{all})$ given in equation 7.4 uses the value of σ_t determined in the previous section and the values of x_{ij} , y_{ij} and N_{ij} for each pixel from the shower images obtained from the telescopes of the array. The reconstructed source position corresponds to those values of x_o , y_o for which $-\ln(L_{all})$ is minimum. This is done through the function minimisation tool Minuit [40].

Due to the form of the function $-\ln(L_{all})$, the use of Minuit for its minimisation requires preparatory steps. As we will see in the next section, $-\ln(L_{all})$ usually has several local minima. This means that the minimisation by Minuit needs to be done carefully. Our first attempt to find the source position for a large number of showers were made by taking the centre of the camera ($x_o = 0^\circ$, $y_o = 0^\circ$) as the starting point for Minuit. Subsequently, we took other starting points on the camera such as ($x_o = 0.5^\circ$, $y_o = 0.5^\circ$) and ($x_o = 1^\circ$, $y_o = 1^\circ$). For most showers, the reconstructed source positions were independent of the starting position used in Minuit. However, there were some showers for which the source position was reconstructed differently depending on the starting point. This problem was resolved by doing a preliminary scan of the

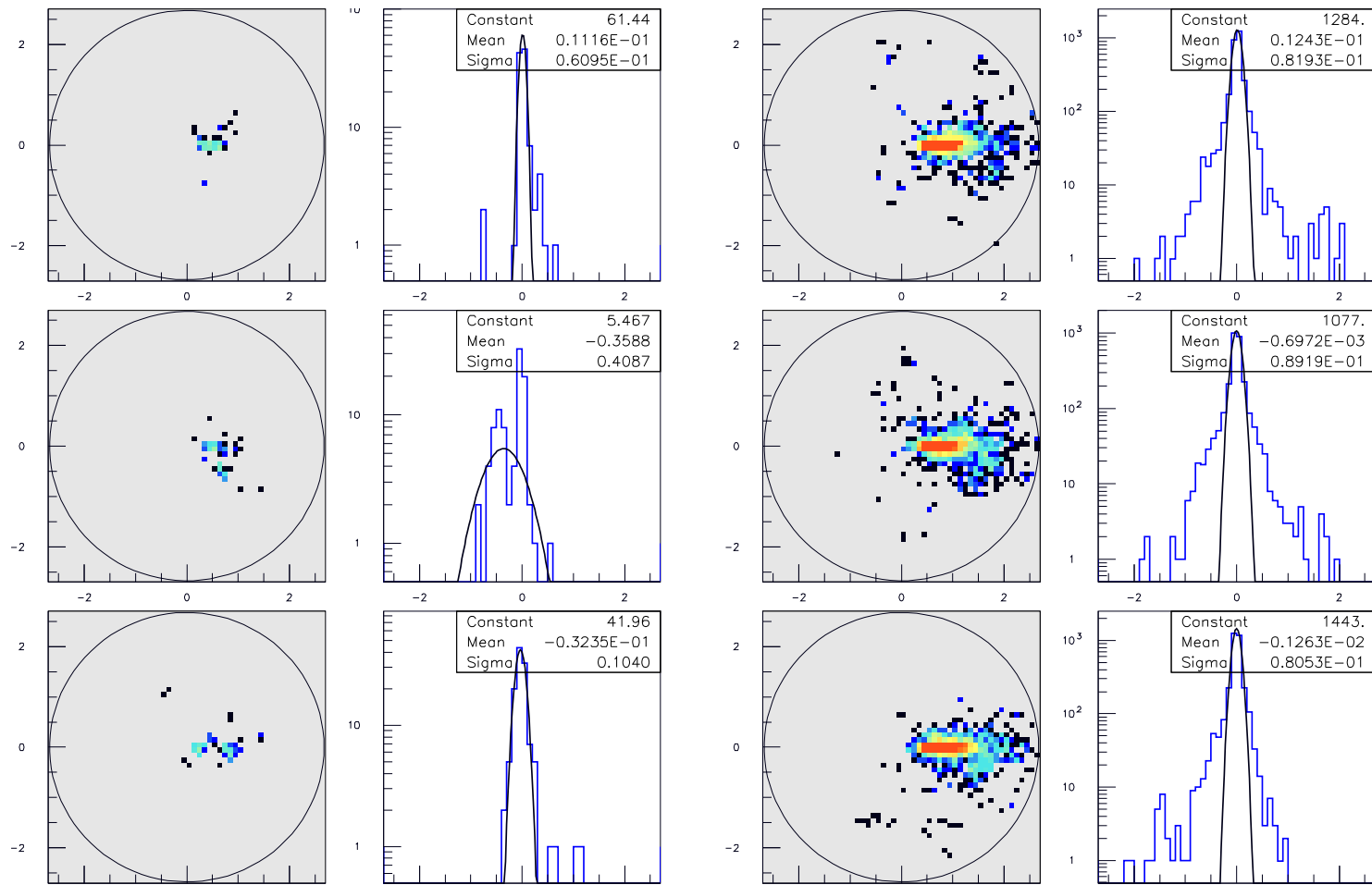


Figure 7.9: Fit of the transverse image distribution of three 50 GeV showers (left) and three 1000 GeV showers (right).

entire camera field of view in order to roughly locate the global minimum of $-\ln(L_{all})$. This rough position can then be used as a starting point for Minuit. In the next section, we will give the details of the method used for the initial scan and present some examples. We will also discuss the overall shape of the likelihood function through these examples. Note that all the examples shown in this section have been realised with the configuration presented on page 110.

Preliminary scan

The entire camera field of view is divided into a grid of equal sized squares. We then calculate the value of $-\ln(L_{all})$ at the centre of each square by using the position and content of all pixels in the telescope images. This gives us a map of the values of $-\ln(L_{all})$ for the entire field of view of the camera. The global minimum of this map gives a rough location of the source position. This is shown in figure 7.10. The left figure shows the superposition of the images obtained from the four telescopes. The centroid of each image is shown through a black circle. We recall that the generated source's image position is $(x_o = 0^\circ, y_o = 0^\circ)$ for all the examples in this chapter. The generated shower is at the centre of the telescope system (see figure 6.13). The figure on the right is obtained by dividing the entire surface into squares of 0.1° side each as represented by the dark blue grid in the plot. The value of $-\ln(L_{all})$ is calculated at the centre of each square by using the information from the telescope images. The figure presented here shows the map of this value by using the colour scale shown on the right. We have changed the normalisation of the $-\ln(L_{all})$ function so as to obtain the χ^2 value (see equation 7.5) corresponding to each segment. The centroids of the individual shower images are shown through white circles and the position of the segment with lowest χ^2 is given on the right bottom corner. The contours indicating different values of χ^2 are shown to bring out the overall morphology of the function.

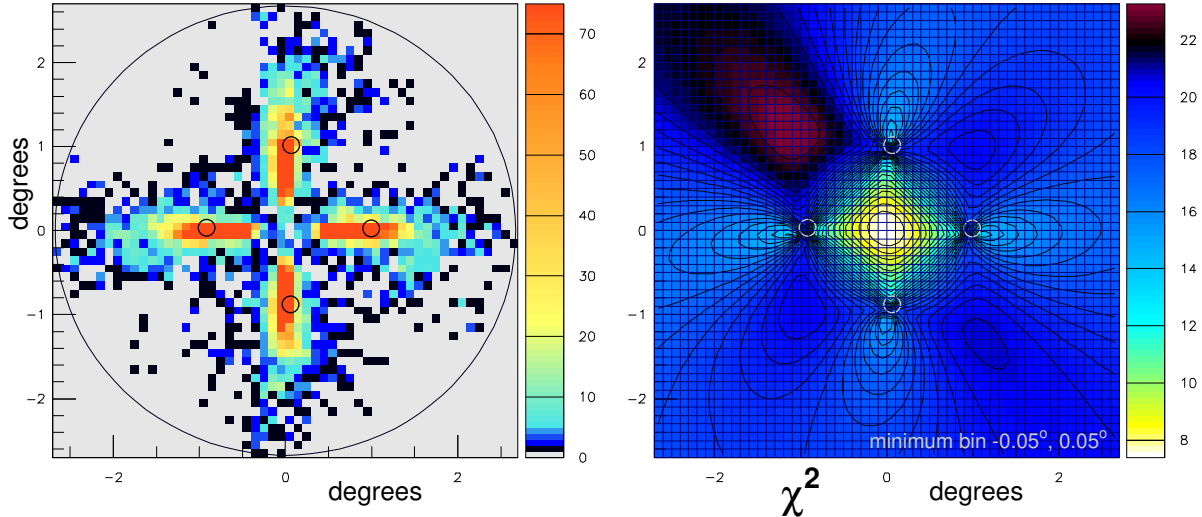


Figure 7.10: Left: The superposed images of a 1000 GeV shower obtained from four telescopes. Right: The χ^2 map obtained after performing a preliminary scan of the telescope field of view. The generated source is at $(x_o = 0^\circ, y_o = 0^\circ)$ and the centroid of the images are shown through black (left) and white (right) circles on the plots.

Main features In order to discuss the main features of the the χ^2 map we also present its horizontal and diagonal slices in figure 7.11. The left histogram shows the horizontal slice

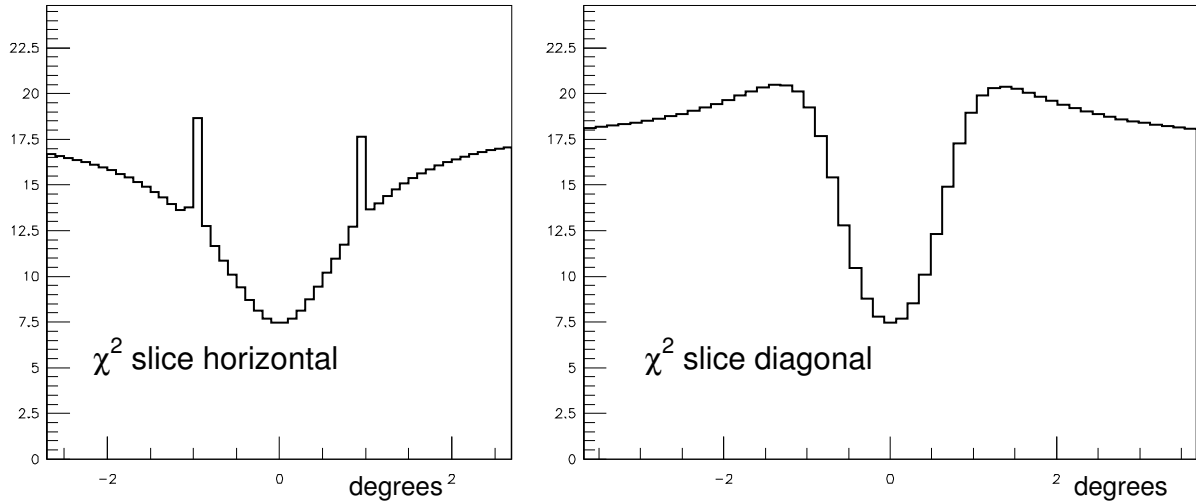


Figure 7.11: A horizontal (left) and diagonal (right) slice of the χ^2 map shown in figure 7.10. In both cases the slice passes through the bin with minimum χ^2 .

that contains the bin with minimum χ^2 value while the right plot presents the diagonal slice containing the minimum bin.

In what follows, we will discuss some of the main features of the χ^2 map.

- The function has an overall symmetry that follows closely that of the shower images.
- There is a region where the χ^2 is minimum at the centre of the scan in figure 7.10. This minimum is also visible on both plots in figure 7.11 and has a value of $\chi^2=7.4$.
- The segment with the lowest χ^2 has its centre at $(x_o = 0.05^\circ, y_o = -0.05^\circ)$.
- There are at least four local minima. They have χ^2 values between 13 and 14 and appear in light blue shades on the plot. Two of these minima appear clearly on the horizontal slice plot in figure 7.11.
- There are sharp local maxima present next to these local minima. Their position corresponds to that of the centroids of the four shower images. This is related to the constraint requiring that the individual shower image axes pass through the centroid of the corresponding image for the calculation of the likelihood function (see section 7.1.1).

The effect of shower core position We saw in chapter 6 how the shape and orientation of the shower images change as a function of the shower core's distance from the telescope. This in turn affects the shape of the likelihood and χ^2 functions.

In figures 7.12 and 7.13 we show the χ^2 maps obtained from 1000 GeV showers with cores at different positions with respect to the telescope system. The superposed shower images from the four telescopes for which the χ^2 scan is obtained are also shown above the maps.

In the first row, we show the figures corresponding to shower core positions along the diagonal of the telescope system (see orange markers in figure 6.13). The first figure corresponds to the case we have already seen i. e. with the shower core at the centre of the telescope system at $(0, 0)$ metres. The orientation of the images is symmetric and so is the χ^2 map. In the second image, the core position of the same shower is moved along the diagonal to $(50, 50)$ metres.

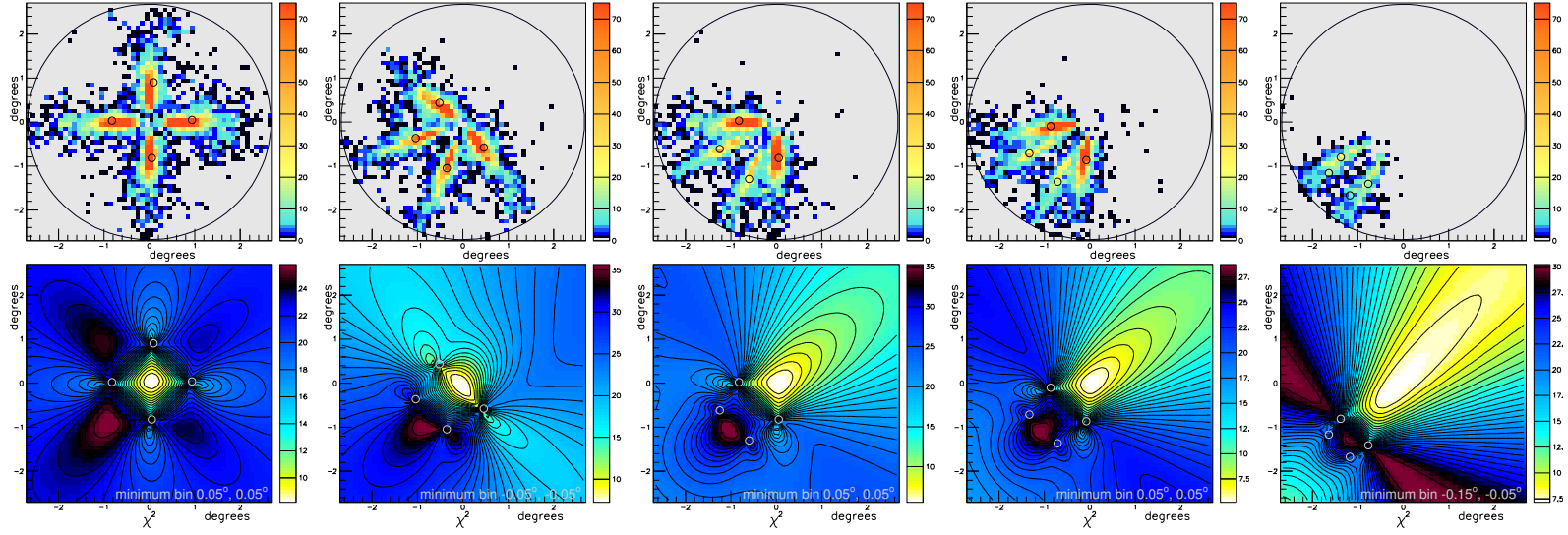


Figure 7.12: Images and corresponding preliminary scans for a 1000 GeV shower with generated core at various positions along the diagonal of the telescope array: (0,0), (50, 50), (100, 100), (200, 200) metres from left to right. These core positions are shown in figure 6.13.

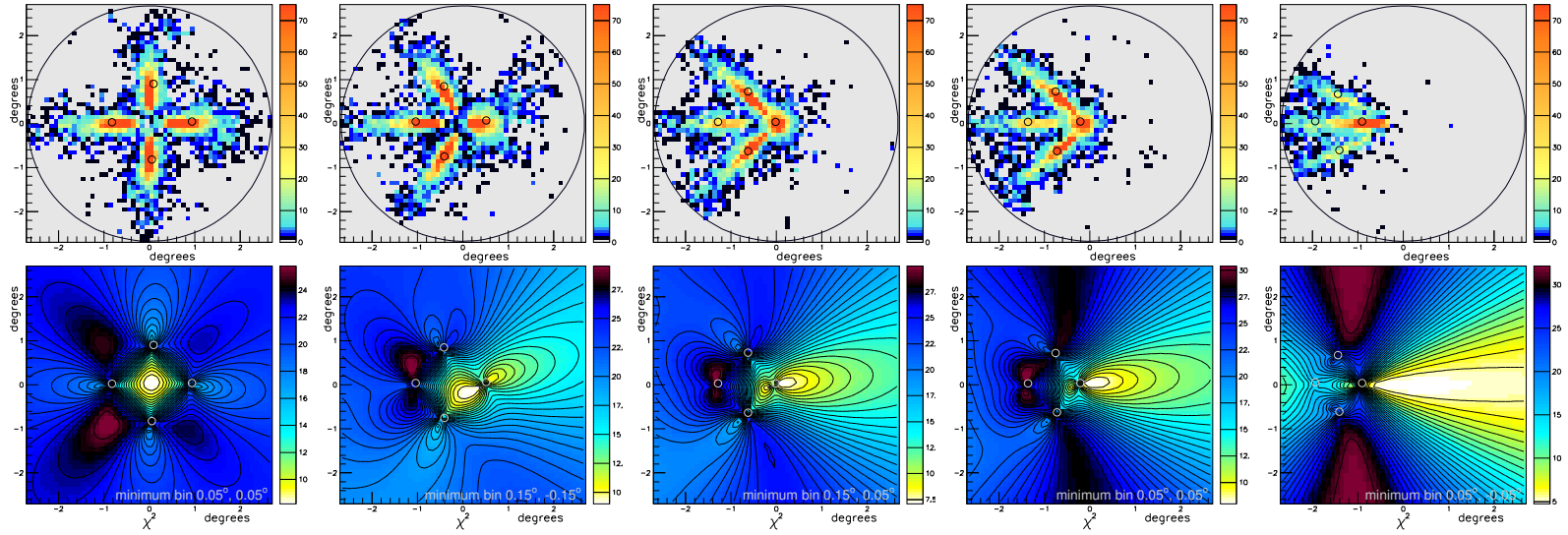


Figure 7.13: Images and corresponding preliminary scan for a 1000 GeV shower with generated core at (0, 0), (50, 0), (85, 0), (100, 0), (200, 0) metres from left to right. See figure 6.13.

The orientation of the shower images change as they point towards the new shower core position on the ground and the centroid of each image moves towards the bottom left. With this new configuration, the χ^2 map is slightly stretched in the opposite direction i. e. towards the top right. The global minimum has a slightly elongated position, though it is still situated around the centre of the camera. This is to be expected since the source was generated at (0,0) degrees. In the next three plots, the shower core is moved further away along the diagonal and the map further stretches in this direction. The shape of the global minimum is slightly more elongated when the shower core is at (85, 85) metres and (100, 100) metres. For the last plot, the shower core position is at (200, 200) metres and the region of global minimum has a large elongated shape around the (0, 0) degrees area but also stretching towards the top right corner. It should be noted that in this case, the shower core position is well outside the telescope array. In fact, all of the telescopes are situated outside the Cherenkov ring (situated at 120 metres from the core) of the shower. This tends to give poorly defined images with fewer photo-electrons on one hand and lesser angular separation between the orientations of the images on the other. These two factors lead to poor reconstruction of the shower parameters.

In the bottom row, we present the χ^2 scan obtained from the same shower with cores at different distances on the right of the telescope (see blue markers in figure 6.13). Here too, the χ^2 map gets distorted in the direction of the shower core position. One notes however, that region of global minimum is better defined in the (50,0) metres and specially in the (85,0) metres plots. This occurs because when the core is at (85,0) metres, the shower is incident right upon one of the telescopes. When the shower core is beyond this position, the minimum region is less defined. At (200, 0) metres, only one of the telescopes is close to the Cherenkov ring position. The others are well beyond it and the global minimum occupies an elongated region towards the right. As a matter of interest, we have also presented the χ^2 maps obtained with different IACT arrays in figure A.7 in the appendix.

Likelihood maximisation with Minuit

The actual minimisation of the function $-\ln(L_{all})$, given in equation 7.4, in order to find the source position is carried out with Minuit. We have used Minuit's version 96.03 in FORTRAN callable mode. The two free parameters are x_o and y_o in equation 7.4 and they are both kept unbound. The starting step size or approximate parameter error is taken to be the individual pixel size i.e. 0.1° in this telescope system. The minimising algorithm MIGRAD considered as "the best minimizer for nearly all functions" [41] is used.

The rest of the values are obtained from the shower images themselves. The position of each pixel (x_i, y_i) and its content in photo-electrons N_i is known. These values are used to calculate the centroid of each image (x_c, y_c) . A fixed value of σ_i as evaluated in section 7.1.2 is used. For the calculations presented in this chapter, we have worked with $\sigma_i=0.076^\circ$. The bin with minimum χ^2 is obtained after doing a preliminary scan of the camera field of view as described in the previous section. Its position coordinates are taken as the initial values given to the free parameters x_o, y_o in the Minuit calculations. The values of x_o and y_o obtained after the minimisation of $-\ln(L_{all})$ give the reconstructed source position in the camera coordinate system.

7.1.4 Results

The result of the above fit by the maximisation of the likelihood function is the reconstructed source position for each shower as well as the axes of the images. Before we present general results about the precision of this reconstruction, we begin by presenting a few examples and discussing some of the important features of this method.

Examples

Figure 7.14 shows the reconstruction for three 1000 GeV showers generated with 0° zenith angle and different shower cores. The orientation of the superposed images from individual telescopes reflect this change of core position. In the three cases, the images are well defined, with distinct areas of maximum emission and image orientation. This allows a good reconstruction of the individual shower image axes and source image at the centre of the camera frame of reference. The impact of the fluctuations in shower images, present mostly at the periphery of the images (blue and black pixels), is negligible since the dense, central region of the images (red and orange pixels) dominate the fit. These cases serve to illustrate the method of source position reconstruction in favourable conditions; the images are well defined since the energy of the shower is high enough and the core position sufficiently close to obtain shower images with a large number of photo-electrons. At lower energies and/or larger distances, the total number of photo-electrons in an image is lower and the orientation of the images is harder to identify. Moreover, the pixels corresponding to fluctuations in the shower have a more important impact on source reconstruction.

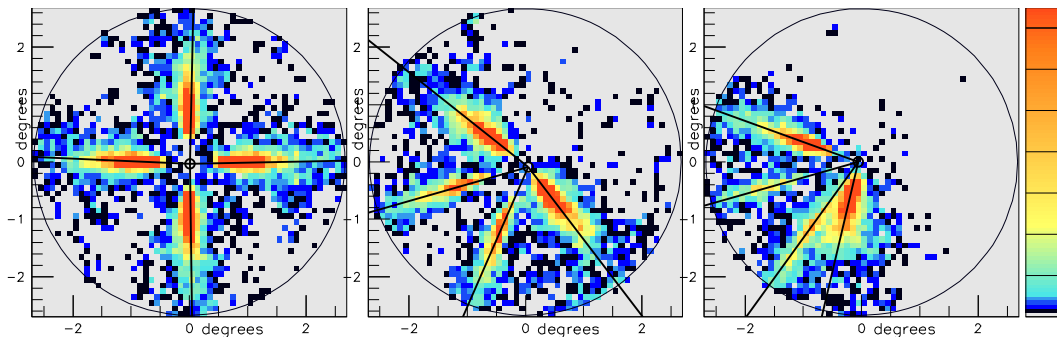


Figure 7.14: The source position reconstruction for three 1000 GeV showers. The left plot is the combined image from the four telescopes for shower whose core position on the ground is at (0, 0) metres i. e. at the centre of the four telescope array. The reconstructed shower image axes are shown through black lines and the reconstructed source position is shown through a black circle. The shower core positions for the centre and right plots are (50 m, 50 m) and (100 m, 50 m) respectively. For a description of the telescope system, see page 110.

Figure 7.15 (left), shows the images from a 100 GeV shower. The superposed images are shown in the middle along with the reconstructed axes and source position. Although, the number of photo-electrons per image is lower and the images are less defined, their orientation is still apparent. The maximisation of the likelihood function allows a good reconstruction of the source position and the image axes. On the other hand, the reconstruction of the source position does not work well for the shower images shown on the right. This 100 GeV shower is also generated with the same core position, but the images do not have a clear orientation and the pixels from the fluctuations carry an important weight in the fit through likelihood maximisation. In fact in both cases, the weight of the low signal pixels (black and blue) is more important than, in the 1000 GeV showers.

The above examples point to the importance of the following factors in source reconstruction.

- **The fluctuations in the image (scattered pixels, pixel bunches etc.) and their weight with respect to the rest of the image** As we will see later in this chapter, appropriate image cleaning can lead to better images in this respect.
- **The number of photo-electrons in an image** Images with more photo-electrons, tend

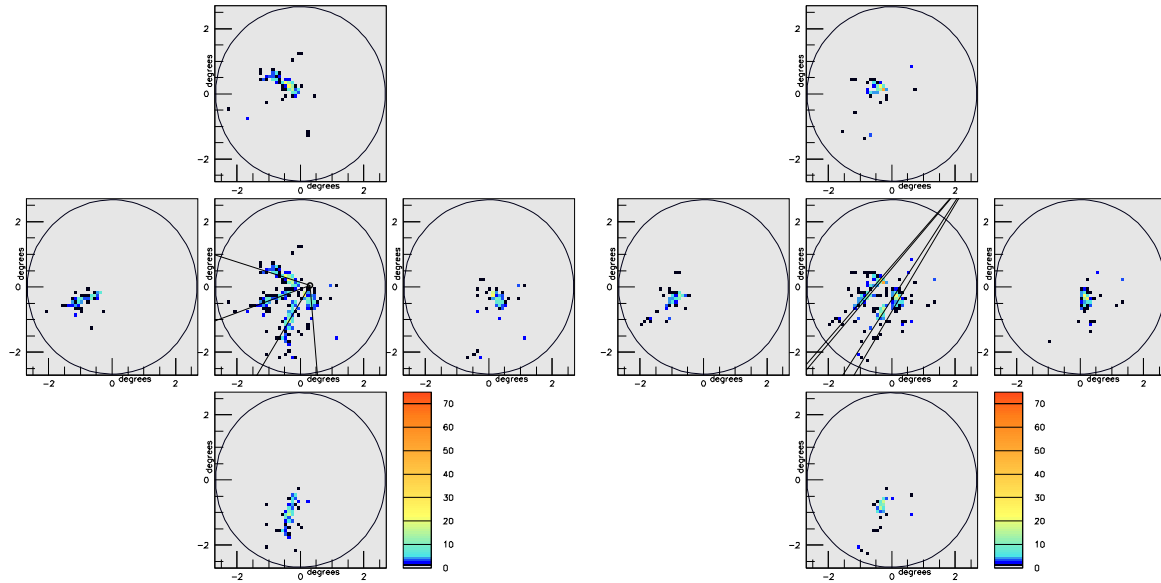


Figure 7.15: Images and source position reconstruction for two 100 GeV showers with core position (50, 50) metres. The superposed images from the four telescope as well as the reconstructed source and image axes are shown in the middle. Both showers are generated with 0° zenith angle.

to be better defined. They tend to have more important central regions and pixels from fluctuations have a lesser effect on the reconstruction.

- **The extent to which the image orientation is evident.** This point depends on the previous two to a large extent.
- **The presence of different telescopes viewing the same shower from different angles** All of the above conditions may be fulfilled, but if the telescopes are aligned in the same direction, then there is no difference of orientation between the images they obtain and the source position can not be reconstructed with this method.

Some of these points are affected by image cleaning and will be discussed again in section 7.3.2.

General results

In order to evaluate the capacity of source position reconstruction with this method, we simulated a large number of showers at various energies and shower core positions and reconstructed the source position for each shower.

In figure 7.16, we show the distribution of the reconstructed source in the camera coordinate system for 1000 GeV showers generated with cores at (0,0) metres (left), (85,85) metres (centre) and (200,200) metres (right). In the (0,0) metres core case, most of the source positions are reconstructed accurately within 0.05° of the generated source (i. e. the centre of the camera). In the next plot, the distribution of the reconstructed source is slightly broader and the source position for most showers is still reconstructed within 0.06° of the generated source. In the figure on the right, the accuracy of reconstruction is poorer. The source position is reconstructed within an elongated region along the diagonal of the camera. We note that this region corresponds to the elongated, low χ^2 region we saw in the preliminary scan figure 7.12

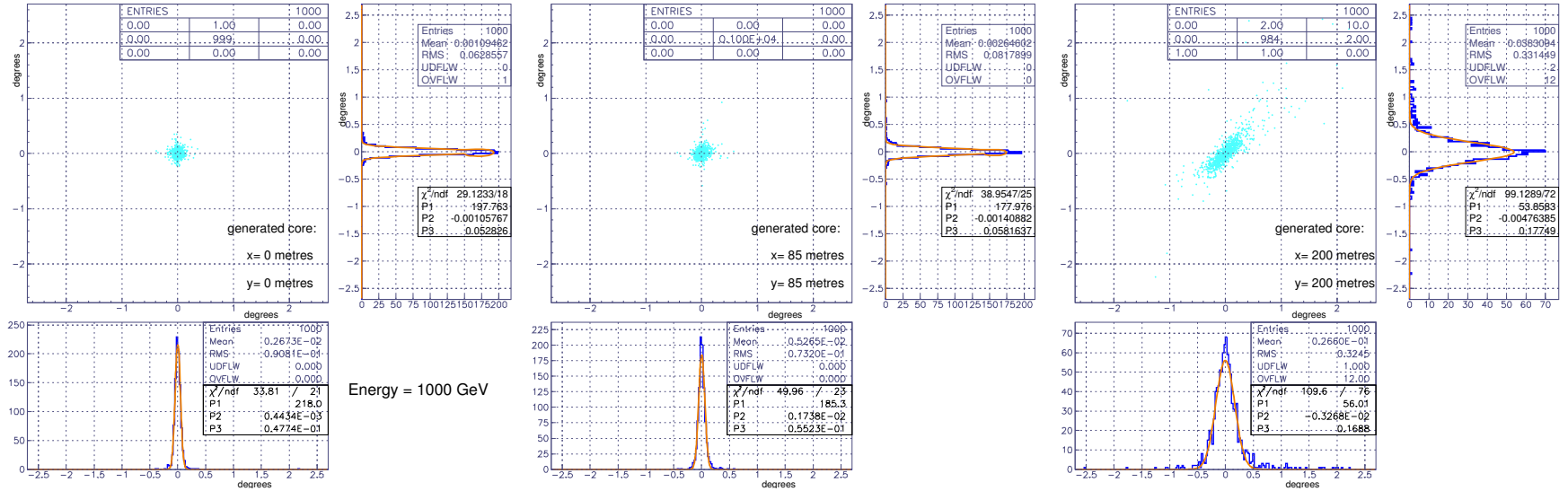


Figure 7.16: The distributions of reconstructed source position in the camera coordinate system for showers of 1000 GeV, for three shower core positions (0, 0) metres (left), (85, 85) metres (centre) and (200, 200) metres (right). 1000 showers have been generated at each core position. The projections of the distributions along the x and y axes are also shown and fitted with Gaussian curves to obtain the standard deviation.

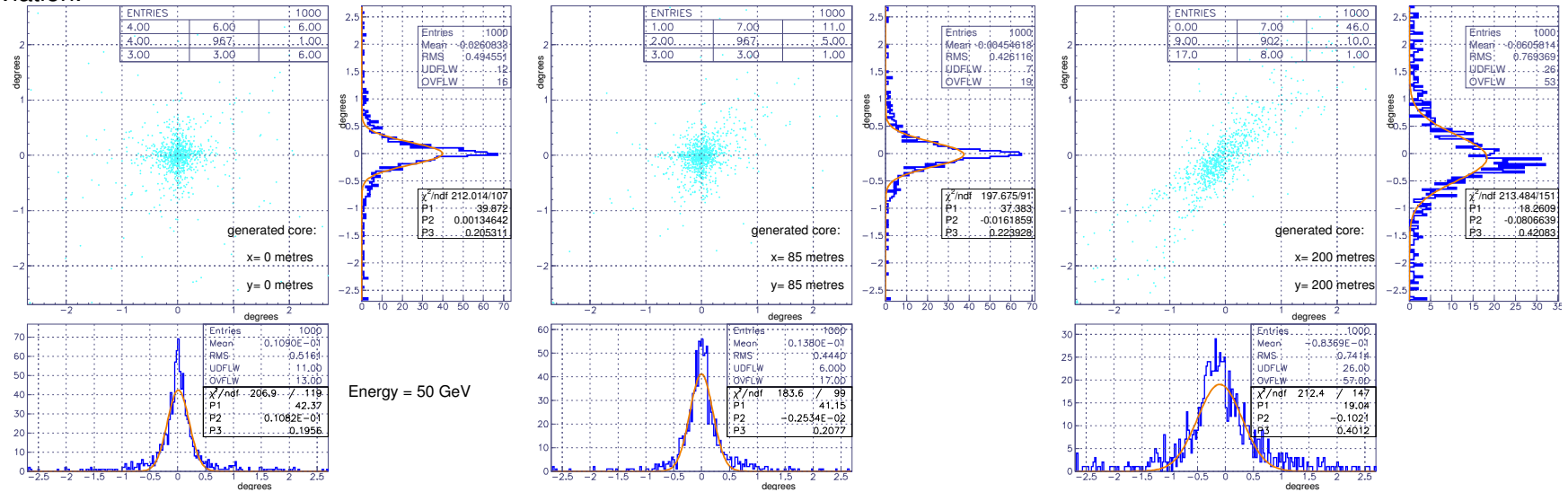


Figure 7.17: The distributions of reconstructed source position in the camera coordinate system for showers of 50 GeV, for three shower core positions (0, 0) metres (left), (85, 85) metres (centre) and (200, 200) metres (right). 1000 showers have been generated at each core position. The projections of the distributions along the x and y axes are also shown and fitted with Gaussian curves to obtain the standard deviation.

and discussed on page 122 for showers with the same core position. The telescopes are all outside the Cherenkov ring area for this core position and the reconstructed source for most of the showers is accurate within 0.2° .

In comparison, figure 7.17 shows the distributions of reconstructed source position for 50 GeV showers. All the distributions are much broader as the source is reconstructed with less accuracy at this lower energy. The precision of reconstruction is around 0.2° for the first two core positions and around 0.4° for the showers generated with (200, 200) metres core. For this core position, the distribution of the reconstructed source positions follows the same shape as that for the 1000 GeV showers and is elongated in the diagonal direction.

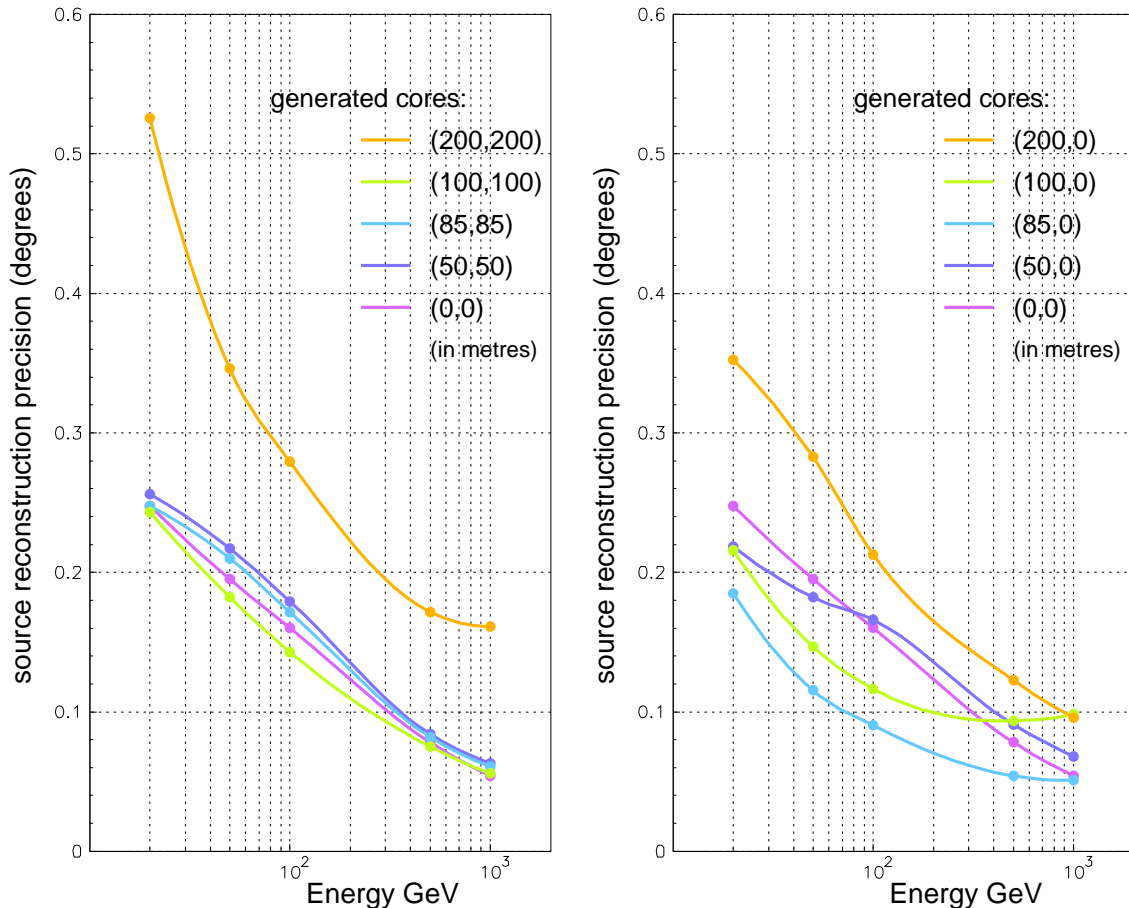


Figure 7.18: The precision of source reconstruction as a function of the energy for shower cores generated along the diagonal (left figure) and those generated towards the right (right figure) of the four telescope system. A different colour is used for each shower core position. The lines joining the plotted points are intended to guide the eye and have no physical significance. For a more detailed description of telescope system and the core positions see page 110.

Dependence on energy and shower core We present the precision of source position reconstruction as a function of generated shower energy for various core positions in figure 7.18. The energy is plotted on the abscissae axis and the precision of reconstruction in degrees is plotted on the ordinate axis. Each plotted point corresponds to the standard deviation of the distribution of the difference between the generated and reconstructed source positions. The left plot presents the precision obtained for various shower core positions along the diagonal of

the telescope system (orange markers in figure 6.13). As the images of high energy showers contain more photo-electrons and are better defined, their precision for source reconstruction is better too. One notes that for 500 GeV and 1000 GeV, the precision is better than the single pixel size i. e. 0.1° . The precision of reconstruction does not vary much with the shower core except for the (200, 200) metres core where telescopes are outside the Cherenkov ring position.

The right hand plot shows the source reconstruction precision for shower cores at various distances on the right of the telescope system (blue markers in figure 6.13). The best precision is obtained for the (85, 0) metres core position (light blue curve) where the shower impact position occurs right on top of one of the telescopes. This corresponds to what we saw in the examples of the preliminary scan in figure 7.13, where the global minimum region is better defined for this core position. The worst reconstruction is once again, for the shower core furthest from the telescope system i. e. (200, 0) metres.

In section 7.3 we will look into other factors that can affect this precision.

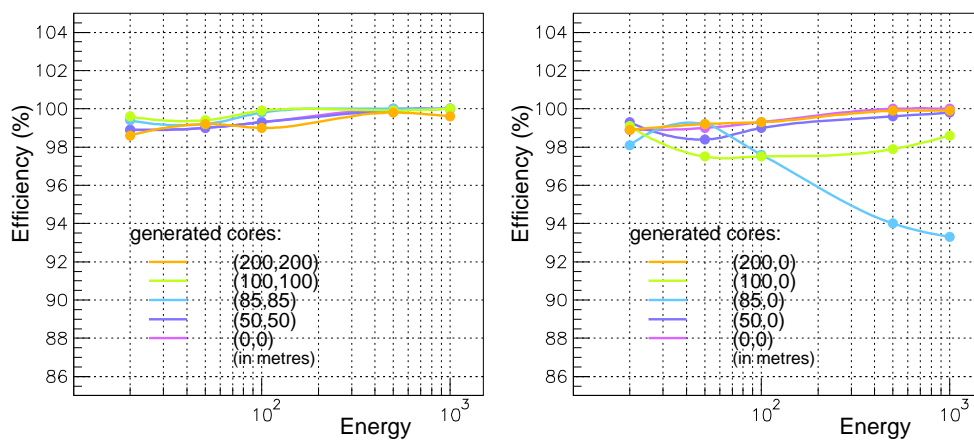


Figure 7.19: The percentage of events for which Minuit obtains a full accurate covariance matrix (indicating full convergence) for source reconstruction minimisation shown as a function of the energy. The plot on the left shows the efficiency for shower core positions generated along the diagonal of the four telescope system, while the one on the right shows the efficiency for cores generated towards the right of the four telescope system. The lines joining the plotted points are intended to guide the eye and have no physical significance.

The efficiency of reconstruction Before we discuss the efficiency of the minimisation by Minuit, we recall that before calling Minuit, we carry out a preliminary scan of the field of view of the telescope (as described on page 121) in order to obtain a rough location of the minimum of the χ^2 map. And although we have not used it in this way to obtain the results presented in this chapter, this rough location of the minimum provides with a backup solution if the minimisation through Minuit fails to converge. The rough position of the source obtained through this scan can also be further improved by carrying out a second scan with much smaller bins around the rough position of the minimum determined by the first scan.

As far as the minimisation from Minuit is concerned, we obtain an efficiency of convergence above 98% for most shower core positions. This is shown in figure 7.19 where the percentage of events for which Minuit converges normally (with full accurate covariance matrix) is shown as a function of the energy for various shower core positions. We note that the core position (85,0) (blue line in the right plot) and to a lesser extent the core position (100,0) (green line in

the same plot) have slightly lower efficiencies at higher energies. We recall that (85,0) metres is also the position of one of the telescopes. This means that the shower falls right on top of the telescope and gives a circular image on it. When this occurs, the minimisation of the likelihood function described in section 7.1.1 has difficulty converging because the image does not have an identifiable axis. The problem is apparent at higher energies where showers images have more photo-electrons and therefore a more regular circular shape when the shower core coincides with the telescope position. The shower core position (100,0) metres is only at a distance of 15 metres from one of the telescopes. The shower images from this telescope also have very little elongation, which explains the slight deterioration in efficiency for this shower core position in the mid-range energies (from 100 GeV to 500 GeV). At higher energies, the shower images have a sufficiently large number of photo-electrons for an axis to become identifiable.

While the results presented in the rest of this thesis do not make use of this possibility, this difficulty in convergence can be dealt with by modifying the likelihood function whenever a shower image tends to be circular. On those occasions, instead of assuming that the distribution is elongated and minimising the distance of the pixels with respect to a straight line, we minimise the distance of the pixels with respect to a fixed point i. e. the source position which also corresponds to the centroid of the circular image (See discussion on page 98 for the impact of telescope distance from the shower core). We have reconstructed the source position for the showers generated with core position at (85,0) metres and (100,0) metres by modifying the likelihood function in this way. This was carried out by treating the shower image as circular whenever the roughly reconstructed source position from the preliminary scan lies within one bin of the centroid of the image. The distance t_{ij} of each pixel with respect to source position, x_o, y_o , is given by $t_{ij} = \sqrt{(x_{ij} - x_o)^2 + (y_{ij} - y_o)^2}$. Here too, we work with a Gaussian p. d. f. for the distribution of t_{ij} . The value of σ_t is the same as the one used previously, i. e. 0.076° . The results obtained are shown in figure 7.20. The efficiency of convergence for both shower cores has improved, with the efficiency for the (100,0) core position showers lying close to 99% for all energies and the one for the (85,0) shower remaining above 97%. It may be possible to improve this further by optimising the condition for considering a shower image to be circular.

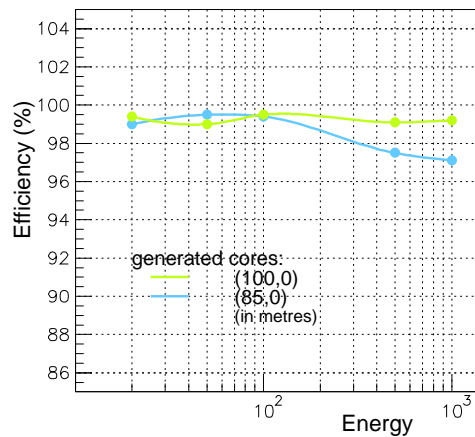


Figure 7.20: The percentage of events, as a function of the energy, for which Minuit converges for source reconstruction minimisation. Here, this is done by considering the image from a telescope to be circular whenever the source position reconstructed from the preliminary scan coincides with the centroid of the image (see text for details). We present the results for showers generated with the core positions (85,0) metres and (100, 0) metres. The lines joining the plotted points are intended to guide the eye and have no physical significance.

7.2 Core position reconstruction

7.2.1 Image orientation and core position

In the discussion on page 111, we saw that while in the frame of reference of the camera, the image axis points towards the source position, in the ground frame of reference, it points towards the position of the shower core (when the source image is at the centre of the camera). This implies that if the same shower is observed by several telescopes, the point of intersection of their axes in the ground frame of reference corresponds to the core position of the shower. In other words, if the axes of the individual images are determined and their point of intersection found, the shower core position can be reconstructed.

7.2.2 Principle and likelihood function

The principle of the shower core reconstruction method is the same as that of the source reconstruction method. The axes of all the telescope images are determined in such a way that the pixels are symmetrically distributed on both sides of the line and the axes intersect at one common point, the core position. The main difference lies in the calculations being carried out in the ground frame of reference for the core reconstruction as opposed to the camera frame of reference for the source reconstruction. In shower images, the position of pixels is available in the camera coordinate system (usually in degrees). In the ground frame of reference, the position of each pixel corresponds to

$$\begin{aligned}x_{igr} &= x_j + x_i \frac{\pi}{180} f_j \\y_{igr} &= y_j + y_i \frac{\pi}{180} f_j,\end{aligned}$$

where x_i, y_i are the coordinates of the pixel position in degrees in the camera coordinates system, f_{tel} is the focal length of the j^{th} telescope and x_j, y_j is its position in the ground coordinates system.

The other difference in comparison to the source reconstruction method concerns the constraint imposed on the reconstruction of the shower image axes. Here each of the axes is made to pass from the reconstructed source position (x_{src}, y_{src} in the ground coordinate system) instead of the centroid of the image. For this reason, the reconstruction of the source position needs to be carried out before the reconstruction of the core position. The rest of the calculations is similar to the source reconstruction calculations. The distance of each pixel from the reconstructed axis is given by

$$t_{igr} = \frac{|m(x_{igr} - x_{ogr}) - (y_{igr} - y_{ogr})|}{\sqrt{m^2 + 1}}.$$

where x_{ogr}, y_{ogr} corresponds to the core position that will be determined and $m = (y_{src} - y_{ogr}) / (x_{src} - x_{ogr})$. Through a reasoning similar to the one shown in section 7.1.1, the likelihood function to be maximised in order to reconstruct the core position is written as

$$\ln(L_{grall}) = -N_{tot} \ln(\sigma_{tgr} \sqrt{2\pi}) - \sum_{j=1}^{N_{tel}} \sum_{i=1}^{N_{pix}} \frac{N_{ij} t_{ijgr}^2}{2\sigma_{tgr}^2}. \quad (7.6)$$

where σ_{tgr} corresponds to the standard deviation of the Gaussian p. d. f. used to describe the transverse profile of the shower image. It corresponds to the value of σ_t used for source position reconstruction converted to ground coordinate system units. The corresponding χ^2 function of the problem is then given by

$$\chi_{gr}^2 = \sum_{j=1}^{N_{tel}} \sum_{i=1}^{N_{pix}} \frac{N_{ij} t_{ijgr}^2}{\sigma_{tgr}^2}. \quad (7.7)$$

Correction due to the source position

In earlier discussions (section 6.4 and page 111), we saw that in the most general case (i. e. when the source image position is not at the centre of the camera) the image axis does not point towards the core position itself but is parallel to the line joining the telescope position and the core position³. This offset corresponds to the offset of the source image from the centre of the camera. Therefore the reconstructed core position needs to be corrected for this effect for showers whose reconstructed source is not at the centre of the camera.

7.2.3 Implementation of the shower core reconstruction method

In order to determine the shower core position the log likelihood function $\ln L_{grall}$ given in equation 7.6 needs to be maximised. This is equivalent to minimising $-\ln L_{grall}$ or the χ^2 function given in equation 7.7. As with the source reconstruction implementation, this is done in two steps. After reconstructing the source position, a preliminary scan of the ground is carried out in order to locate the whereabouts of the χ^2 global minimum. This is done to avoid the local minima present in the typical χ^2 function and to obtain a more efficient minimisation through Minuit. Then as a second step, the minimisation is carried out through Minuit, by taking the global minimum determined by the preliminary scan as a starting point.

Preliminary scan

The entire surface to be scanned is divided into a grid of equal sized squares. In the examples presented in this chapter we have scanned a surface of 500 m \times 500 m, centred on the origin of the telescope system. All the generated shower cores in the simulations used in this chapter are well within this surface. The step size chosen for the scans presented in this chapter is 10 metres. The χ^2 or likelihood value is determined at the centre of each grid element and a map of the χ^2 values is obtained. In figure 7.21, we present the individual telescope images obtained for a 1000 GeV shower (left) and the ground χ^2 map obtained from them. The shower was generated with 0° zenith angle and core position at the centre of the telescope system i. e. at (0, 0) metres. The reconstructed source position is indicated on the χ^2 map through white circles (one for each telescope).

One notices that this map is similar in its form to the one obtained for source reconstruction in section 7.1.3. There is a well defined global minimum at the centre of the scanned region. One sees from figure 7.22, where we show the horizontal and diagonal slices of this χ^2 map, that the global minimum has a value of around 8. The overall shape of the function follows the symmetry of the shower images. As with the source reconstruction scan, one notices the presence of four local minima with sharp local maxima located next to them. The sharp maxima correspond to the position of the reconstructed source used in the likelihood and χ^2 function.

³Strictly speaking, this happens when the telescope does not point towards the source and the shower axis is not contained in the plane formed by the shower core and telescope axis. The second condition occurs for at least some of the telescopes in a multi-telescope system not pointing towards the source.

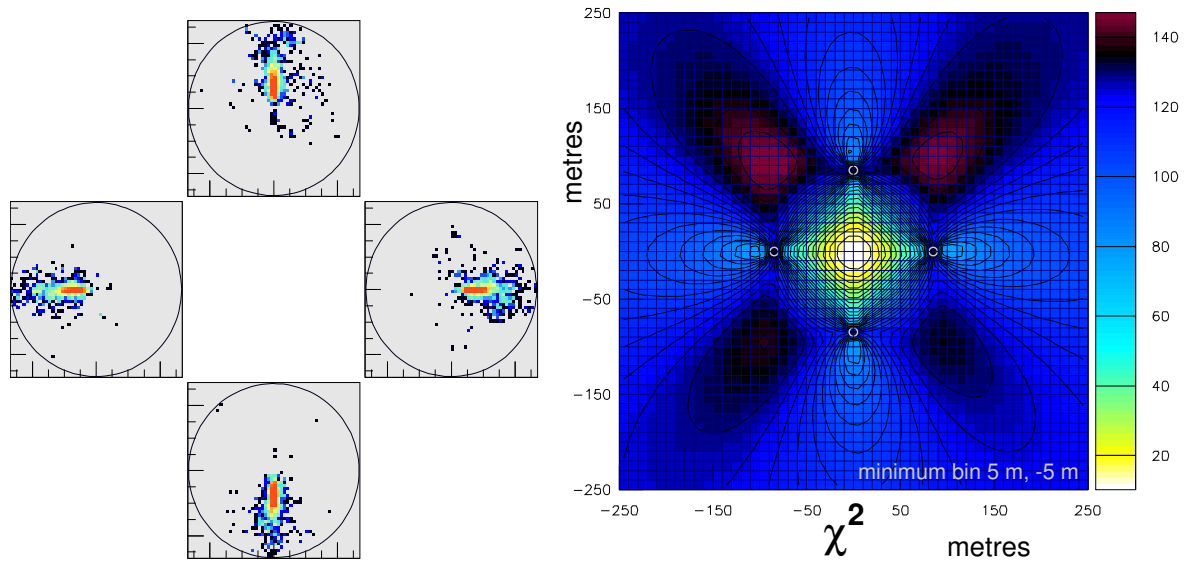


Figure 7.21: The left figure shows the images of a 1000 GeV shower obtained from the four telescope system described on page 110. The figure on the right shows the χ^2 map obtained for this shower after performing a preliminary scan of a surface of $500\text{ m} \times 500\text{ m}$ centred on the origin of the telescope system. The generated shower core position is at the centre of the telescope system. The reconstructed position of the source on each telescope is shown through white circles and the position of the bin with minimum χ^2 is given on the bottom right of the plot.

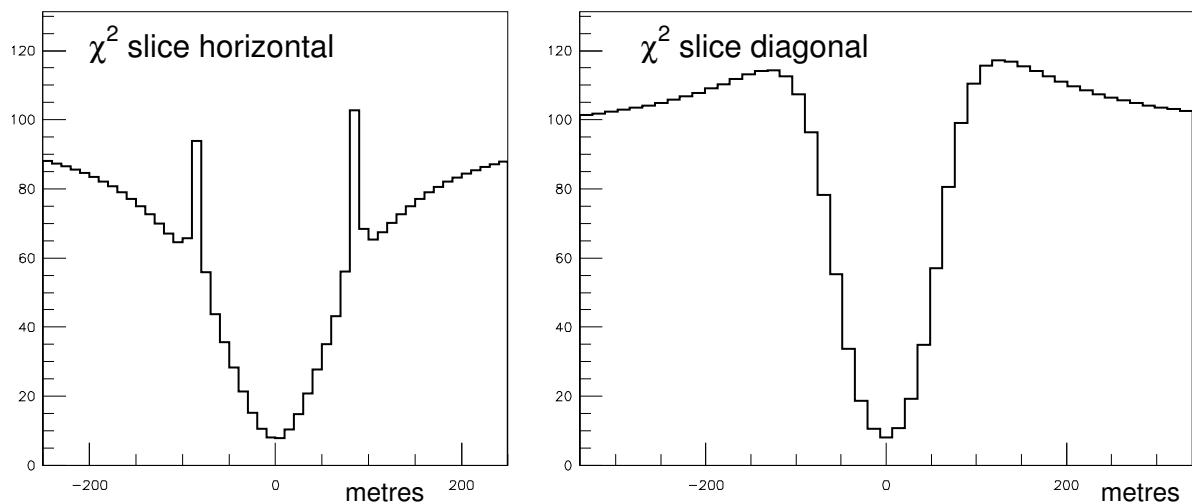


Figure 7.22: A horizontal (left) and diagonal (right) slice of the χ^2 map shown in figure 7.21. In both cases the slice passes through the bin with minimum χ^2 is shown.

The effect of shower core position Since the likelihood function was built in such a way that the global minimum of $-\ln(L_{grall})$ and χ^2_{gr} indicates the shower core position, one expects the map obtained from the preliminary scan to shift accordingly with the generated core position. In figure 7.23, we present the χ^2 maps obtained for a shower of 1000 GeV generated with different core positions along the diagonal of the telescope system (orange markers in figure 6.13). As the shower core moves away from the centre, the χ^2 map is distorted and the global minimum stretched in the same diagonal direction. Contrary to the source reconstruction preliminary scan shown in section 7.1.3, the region occupied by the global minimum is not only elongated along the diagonal direction but the minimum itself shifts in the same direction. One also notes that while centroids of the individual images shifted with change in core position in the preliminary source scan, the reconstructed source image position shown by white circles does not shift with shower core position. This is to be expected since as we saw in chapter 6, the source position maps independently of the shower core position. A local maximum corresponds to each of the reconstructed source image positions.

Figure 7.24 shows the χ^2 maps obtained for showers with cores at different distances on the right of the telescope system (blue markers in figure 6.13). The trends mentioned for the figure above, are noticeable in this case too. The position of the global minimum shifts with the core position and the overall shape of the χ^2 map is distorted towards the right side.

Likelihood maximisation with Minuit

Once the preliminary scan is carried out and the whereabouts of the global minimum determined, the function $-\ln(L_{grall})$ given in equation 7.6 is minimised through Minuit in order to determine the shower core position. The options used are the same as those for the reconstruction of the source position. The two free parameters are x_{ogr} and y_{ogr} in equation 7.6 and both are kept unbound. The starting step size is taken to be 1 metre. The positions of the pixels in the ground frame of reference as well as the individual pixel content are obtained from the telescope images. The value of σ_t is converted from degrees to metres in order to obtain σ_{tgr} and (x_{src}, y_{src}) are obtained from the reconstruction of the source position.

7.2.4 Results

In order to evaluate the capacity of source position reconstruction with this method, we simulated a large number of showers at various energies and shower cores, and reconstructed the shower core position for each shower. In figure 7.25, we show the distribution of the reconstructed core position in the ground frame of reference for 1000 GeV showers generated with cores at (0,0) metres (left), (85,85) metres (centre) and (200,200) metres (right). In the (0,0) metres core case, most of the core positions are reconstructed accurately within a few metres of the generated core position. In the next plot, most of the reconstructed core positions are still within 5 metres of the generated core at (85,85) metres. In the right most figure, the reconstructed core positions occupy a much larger elongated area around the generated core at (200,200) metres. The reconstruction precision drops to around 20 metres.

Figure 7.26 shows the distributions of the reconstructed core positions for 50 GeV showers with the same generated core positions. The accuracy of reconstruction drops considerably. The precision for the (0,0) metres and (85,85) metres core positions is around 15 metres while for the (200,200) metres core, it is more than 70 metres. This can be understood, since the shower images have low photo-electron content at this energy.

As with the source reconstruction, the shape of each distribution of the reconstructed core positions resembles the shape of the corresponding χ^2 map shown in figure 7.23.

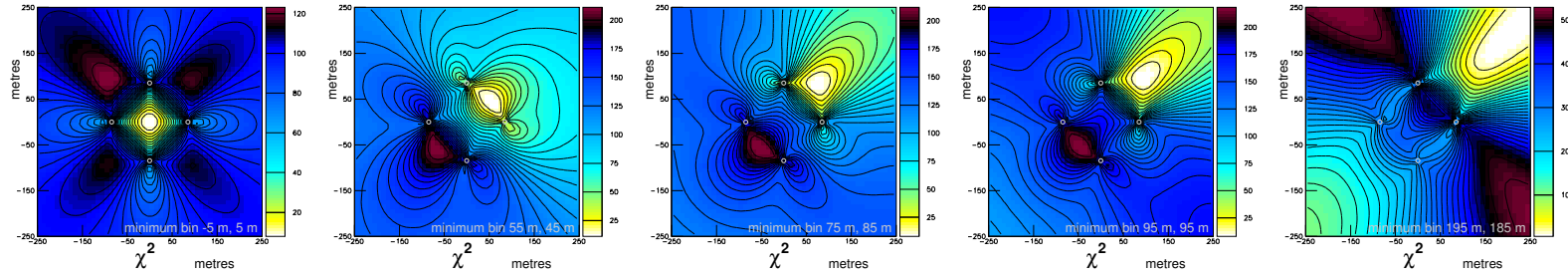


Figure 7.23: Preliminary scan of a surface of 500 m×500 m centred on the origin of the telescope system for the reconstruction of the core position of a 1000 GeV shower. The shower is generated with various core positions along the diagonal of the telescope array: (0,0), (50, 50), (100, 100), (200, 200) metres from left to right. The generated core positions are shown in figure 6.13.

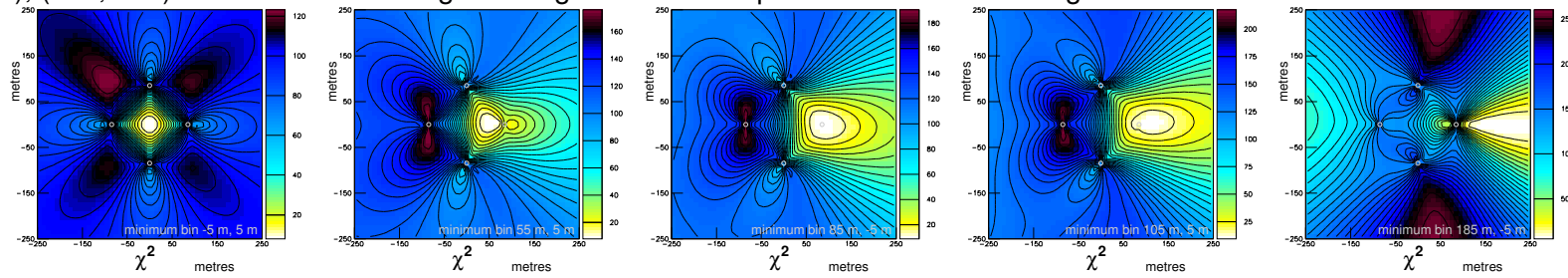


Figure 7.24: Preliminary scan for the reconstruction of the core position of a 1000 GeV shower with generated core at (0, 0), (50, 0), (85, 0), (100, 0), (200, 0) metres from left to right. See figure 6.13.

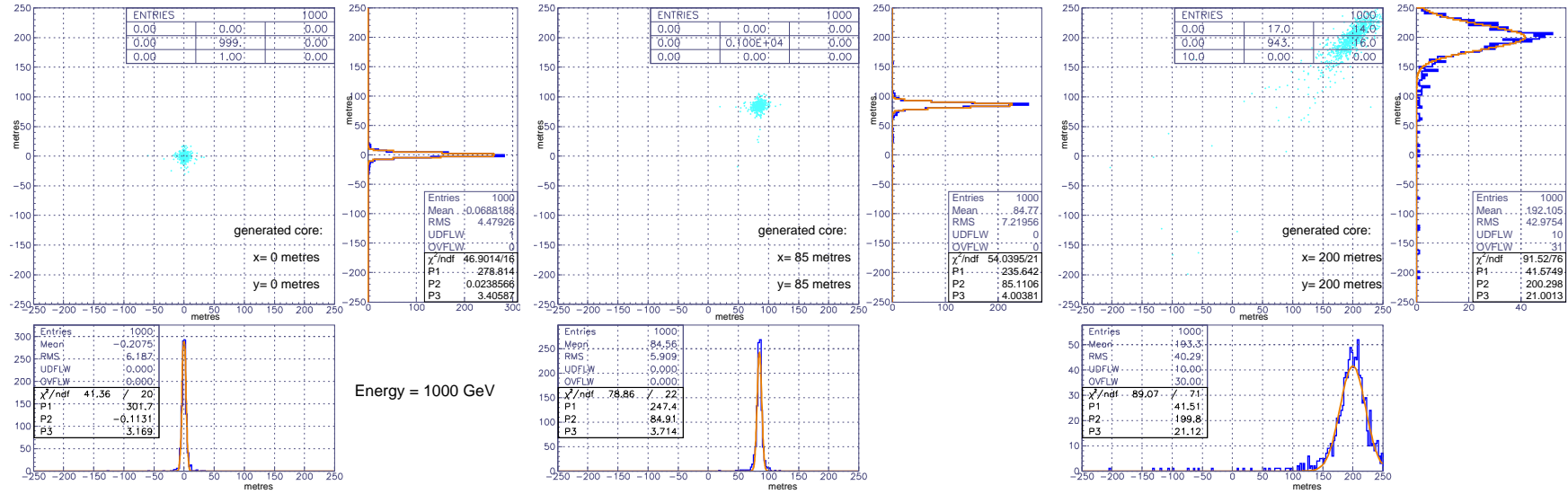


Figure 7.25: The distributions of reconstructed core positions in the ground frame of reference for showers of 1000 GeV, for three generated core positions: (0, 0) metres (left), (85, 85) metres (centre) and (200, 200) metres (right). 1000 showers have been simulated at each core position. The projections of the distributions along the x and y axes are also shown and fitted with Gaussian curves in order to obtain the standard deviation.

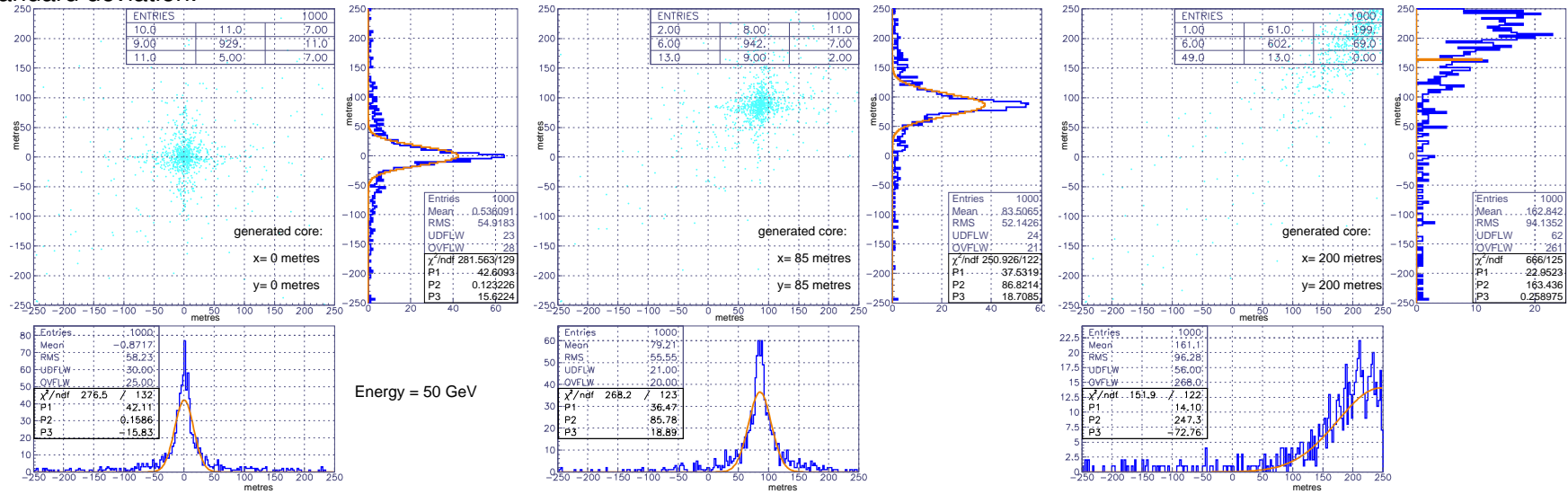


Figure 7.26: The distributions of reconstructed core position in the ground frame of reference for showers of 50 GeV, for three generated core positions: (0, 0) metres (left), (85, 85) metres (centre) and (200, 200) metres (right). 1000 showers have been simulated at each core position. The projections of the distributions along the x and y axes are also shown and fitted with Gaussian curves in order to obtain the standard deviation.

Dependence on energy and shower core In figure 7.27, we show the dependence of the precision of core reconstruction on the shower energy. The plotted points correspond to the standard deviation of the distribution of the difference between the generated and reconstructed core positions.

The left plot represents the core reconstruction precision obtained for various generated core positions along the diagonal of the telescope array (orange markers in figure 6.13). As with the source position reconstruction, the precision increases with the energy as the shower images contain more photo-electrons and image axes are better reconstructed. The core is reconstructed with a precision of less than 10 metres for the 500 and 1000 GeV showers. The precision of reconstruction does not vary much with the generated core position except for the (200, 200) metres core where telescopes are outside the Cherenkov ring position.

The right hand plot shows the reconstruction precision for shower cores at various distances on the right of the telescope array (blue markers in figure 6.13). The best precision is obtained for the (85, 0) metres core position (light blue curve) where the shower falls right on top of one of the telescopes. The poorest reconstruction takes place for the shower core furthest from the telescope array i. e. (200, 0) metres.

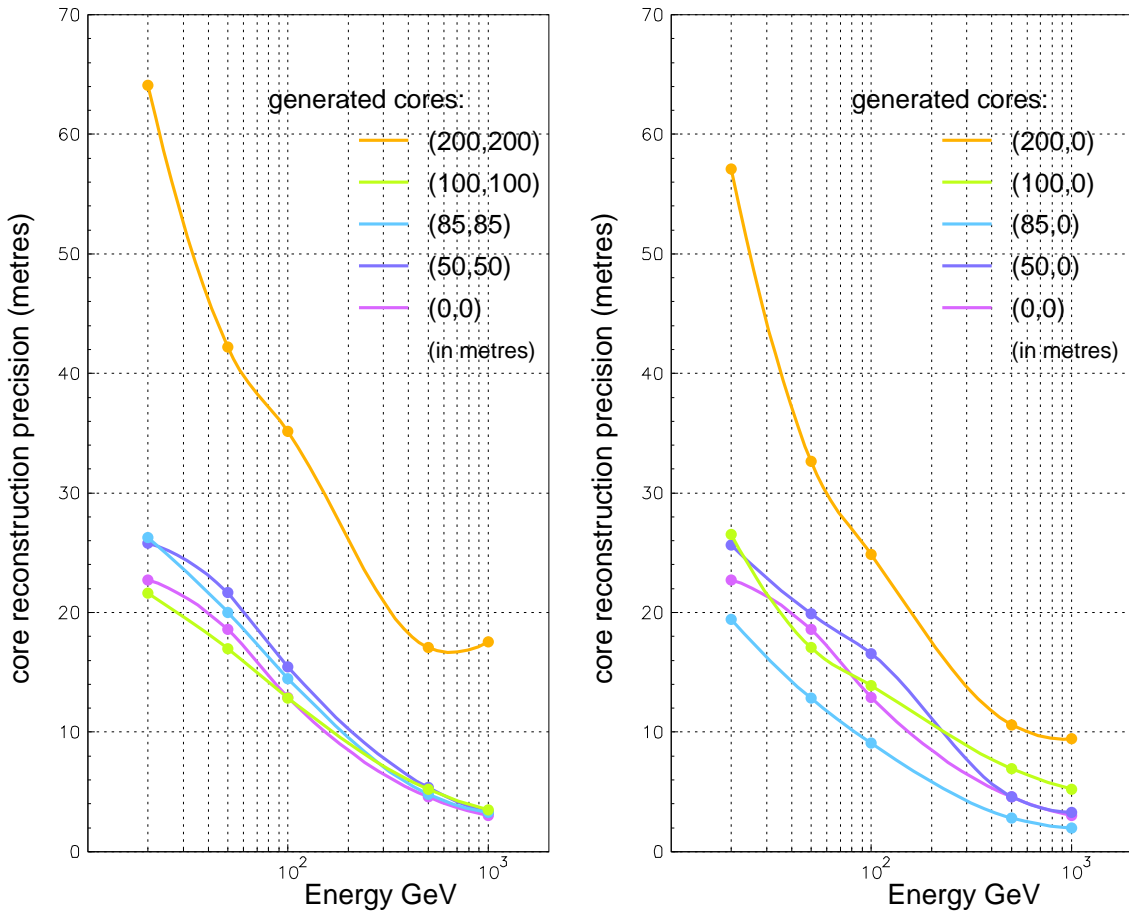


Figure 7.27: The precision of core reconstruction as a function of the energy, for cores generated along the diagonal (left) and those generated towards the right (right) of the four telescope system. The various generated shower cores are shown through different colours. The lines joining the plotted points are intended to guide the eye and have no physical significance. For more details on the telescope system and the generated core positions see page 110.

The efficiency of reconstruction We make similar comments to those we made, when discussing the efficiency of the source reconstruction method (see page 129). Here too, the preliminary scan gives a rough location of the core position and provides with a backup solution, should Minuit fail to converge. The rough position, obtained this way, could be further improved by carrying out a second scan around this position with smaller bins.

The percentage of events for which Minuit converges normally (with full accurate covariance matrix) is shown in figure 7.28 as a function of the energy, for various shower core positions. As we can see, the efficiency remains 98% for all shower core positions except (85,0) metres. In this case, the core position corresponds to the position of one of the four telescopes, resulting in a circular shower image in the camera. This means that Minuit has difficulty converging since the image does not have an identifiable axis. The problem is specially apparent at higher energies where shower images have more photo-electrons and therefore images which tend to have a more regular shape.

Just as we saw with the source reconstruction, this difficulty can be dealt with by modifying the likelihood function whenever the reconstructed source position corresponds to the centroid of a shower image (For the results presented here, we required that they lie within 1 pixel of each other). When this occurs, we minimise the distance of the pixels with respect to a fixed point corresponding to the shower core position⁴ instead of a straight line. This means that the image is considered to be circular, instead of elongated in such cases. The distance t_{igr} between the pixels and the core position x_{ogr}, y_{ogr} , is given by $t_{igr} = \sqrt{(x_{ijgr} - x_{ogr})^2 + (y_{ijgr} - y_{ogr})^2}$ where x_{ijgr}, y_{ijgr} are the coordinates of the pixel in the ground frame of reference. We work with a Gaussian p. d. f. for the distribution of t_{igr} and the value of σ_t is the same as the one used previously, i. e. 0.076° . The results obtained for the (85,0) metres and (100,0) metres core positions are shown in figure 7.29. We can see that the efficiency of reconstruction for the (85,0) metres core has improved and now lies above 97%. It may be possible to improve this further by optimising the condition for considering a shower image to be circular.

7.3 Additional considerations

7.3.1 The impact of coma aberration

In section 5.2.1, we discussed the presence of coma aberration in the images obtained by parabolic mirrors. We also quantified this aberration in the transverse and tangential direction as a function of the incidence angle. The source and shower core reconstruction methods mainly use the transverse information from images and can therefore be affected by the coma aberration in the transverse direction. From figure 5.6, we note that the value of the aberration becomes comparable to σ_t ($\sim 0.08^\circ$) at large angles of incidence (around 4°). This means that this situation does not occur unless we are working with telescopes with fields of view of 8° or larger. The field of view of the telescopes studied in this thesis is around 5° , giving us a maximum possible transverse aberration of 0.05° . This diminishes the impact of coma aberrations on the efficiency of the reconstruction methods. If telescopes with larger fields of view are being studied, it is preferable to use mirror types or telescope designs with smaller aberrations for large incidence angles.

⁴When the correction mentioned on page 132 is carried out then the position of the source corresponds to the centre of the camera (i. e.) the position of the telescope. When the shower falls on top of the telescope, this also corresponds to the shower core position.

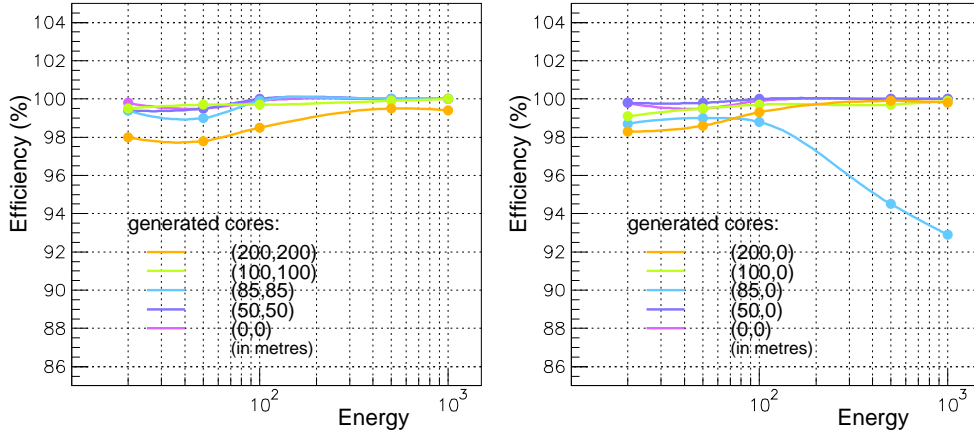


Figure 7.28: The percentage of events for which Minuit obtains a full accurate covariance matrix (indicating full convergence) for core reconstruction minimisation shown as a function of the energy. The plot on the left shows the efficiency for shower core positions generated along the diagonal of the four telescope system, while the one on the right shows the efficiency for cores generated towards the right of the four telescope system. The lines joining the plotted points are intended to guide the eye and have no physical significance.

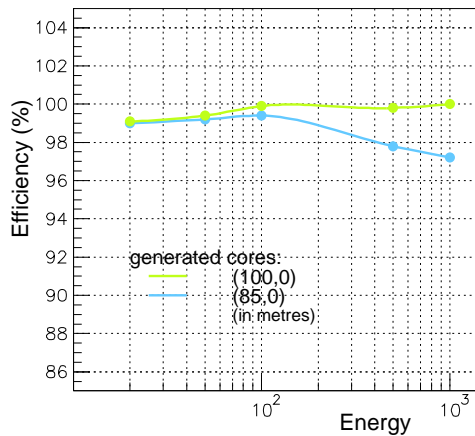


Figure 7.29: The percentage of events, as a function of the energy, for which Minuit converges for core reconstruction minimisation. Here, the core reconstruction is carried out by considering the image from a telescope to be circular whenever the source position coincides with the centroid of the image (see text for details). We present the results for showers generated with the core positions (85,0) metres and (100, 0) metres. The lines joining the plotted points are intended to guide the eye and have no physical significance.

7.3.2 Image cleaning

The examples of parameter reconstruction so far presented have been obtained with simulated showers. When observations are made with real telescopes, the camera not only receives the Cherenkov photons from the atmospheric shower, but also a certain number of photons from the unresolved stars and other sources of light pollution. These photons constitute a source of noise for the shower image. As the flux of these photons is very low as compared to the flux of Cherenkov photons from the showers, these Night Sky Background (NSB) photons give pixels with a low signal (up to a few photo-electrons) scattered randomly over the camera. In order to use the information from the shower image properly, this noise needs to be removed.

Image cleaning methods

Noise removal or image cleaning can be quite complex to carry out. One of the reasons for this is the variation in the levels of noise depending on geographical location, period of the year or month, atmospheric conditions... Measurements are usually carried out at telescopes sites to evaluate the flux from the NSB.

Apart from this, one needs to minimise the risk of removing pixels with signal from the shower. The shower image may be difficult to extricate from the noise since different showers energies have different numbers of photo-electrons. There exists a number of sophisticated algorithms adapted to the shower image problems and capable of identifying pixel clusters and their edges for this purpose.

In this chapter, our purpose is not to explore the efficiency of these methods. Rather, we want to see how the various parameter reconstruction methods work with cleaned images. For this purpose we implement a simple form of image cleaning in which we keep only the pixels with signal above a certain threshold. In figure 7.30, we show how the images of a 500 GeV and 100 GeV shower are affected as we apply different thresholds for image cleaning.

The application of the 1 photo-electron threshold gets rid of a large number of the scattered pixels with little signal (coloured in black or dark blue.) of the 500 GeV shower image. As the threshold for retaining image pixels is increased, more parts of the image that correspond to fluctuations in showers are rejected. With still higher thresholds, the remaining part of the image corresponds to the main emitting region from the shower (red-yellow pixels). Even with a threshold as high as 50 photo-electrons, the central emitting part of the image is retained as well as the information of the image's orientation. Note that the pixels with signal in the 5-15 photo-electron range are arranged slightly asymmetrically. These pixels can result in a less accurate reconstruction of the shower image axis as well as source and core positions. This asymmetry is almost removed with the higher threshold levels.

The 100 GeV shower image has fewer photo-electrons. As a result, when thresholds beyond 5 photo-electrons are applied, there is very little information left in the images. The image obtained from the 5 photo-electron threshold still has the central pixels with the most photo-electrons, but there is no information about the image orientation. As we have seen before, this information is very important for the accurate reconstruction of the source and core positions. The application of the 1 photo-electron and 2 photo-electron thresholds seem to yield better results as the stray pixels in black and dark blue are removed but the main information about shower orientation is kept. We saw in section 7.1.4 that these stray pixels can lead to poor source reconstruction at this energy.

Effects on shower parameter reconstruction

Examples As we have seen, image cleaning affects the quantity of information available in an image. This in turn affects the reconstruction of the shower parameters. Figure 7.31 shows the effect of image cleaning on the source position reconstruction for two 100 GeV showers. In the first case, the source position and the image axes are poorly reconstructed due to the multitude of scattered pixels with few photo-electrons and the irregular shape of the images. The application of the 1 photo-electron threshold actually, makes the reconstruction worse. This is due to the compact form of the shower images which makes the reconstruction of an axis difficult, but also due to the presence of a few scattered pixels with a relatively high signal (3-5 photo-electrons shown in medium blue). These pixels are more apparent in the bottom plots of the same figure where we have shown the images obtained from the individual telescopes, separately. We can see that the right image has one such pixel present away from the main shower image towards the bottom left. The top image has a similar pixel towards the bottom left

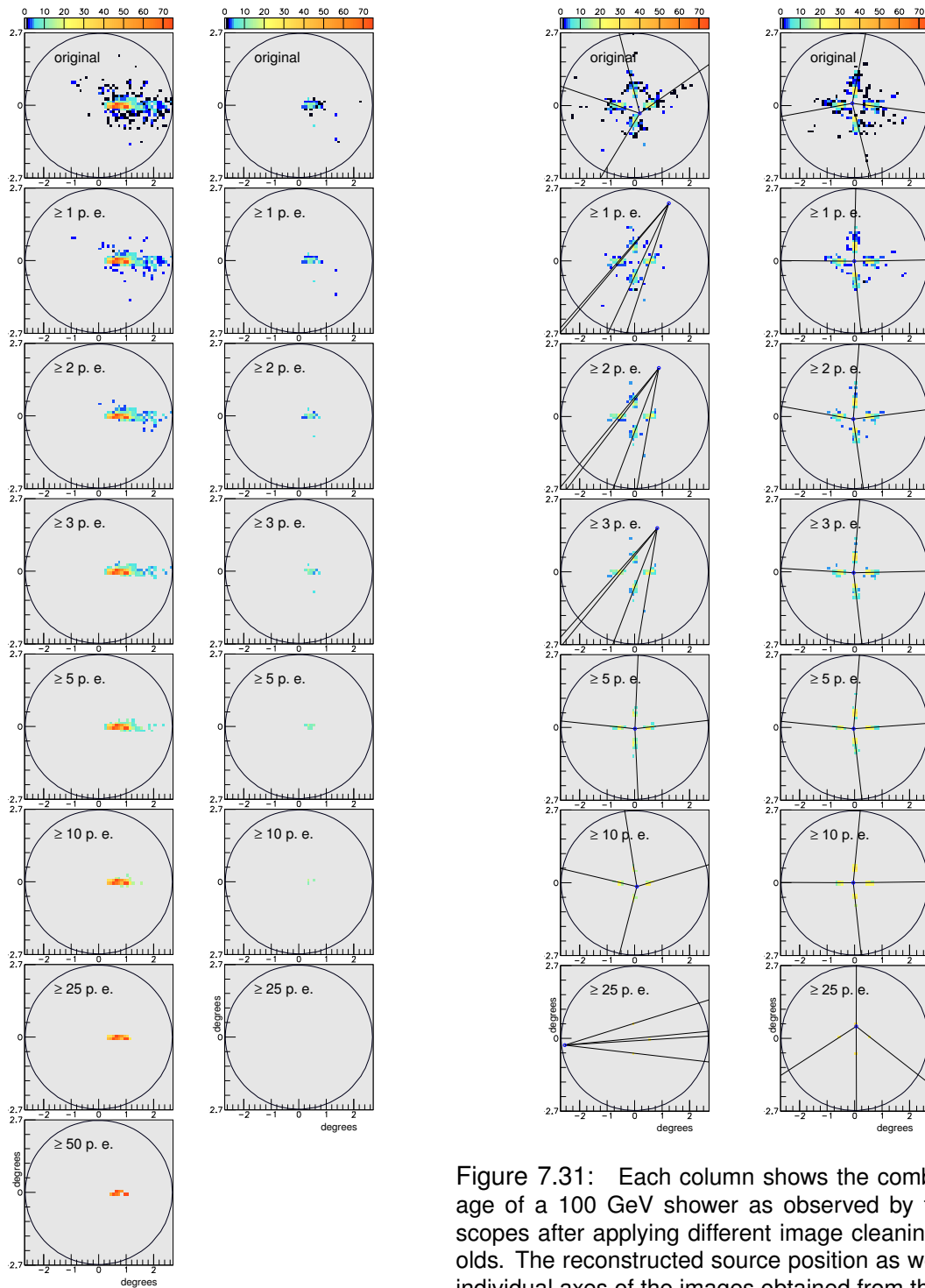
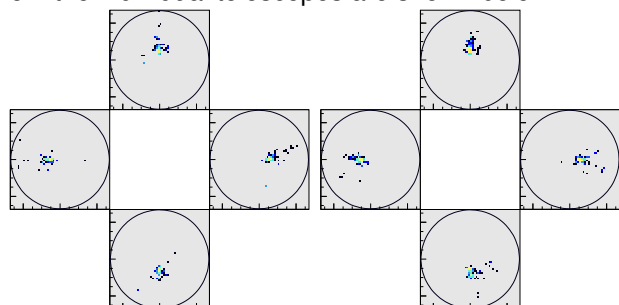


Figure 7.30: The images obtained from a 500 GeV (left), 100 GeV (centre) shower as different image cleaning thresholds are applied. We recall that the red pixels of the image should be interpreted as having at least 70 photo-electrons. Their actual content may go up well beyond 70.

Figure 7.31: Each column shows the combined image of a 100 GeV shower as observed by four telescopes after applying different image cleaning thresholds. The reconstructed source position as well as the individual axes of the images obtained from the source reconstruction method are also shown. The images from the individual telescopes are shown below.



of the main cluster. When the image cleaning threshold goes up to 2 and 3 photo-electrons, a few more scattered pixels are removed but the reconstruction only improves slightly as the two pixels mentioned above remain in the images. With a threshold of 5 photo-electrons, the stray pixels are finally removed and the reconstruction shows an important improvement. Beyond this threshold, the reconstruction quality starts deteriorating and becomes quite meaningless at 25 p. e. where only a few pixels remain. In the second case (right column), the reconstruction improves even with the application of a 1 photo-electron threshold. Here, we see that while there are a number of scattered pixels most of them do not have a high enough signal to have a negative impact on the reconstruction after the first cleaning threshold is applied. The reconstruction works well with a threshold of up to 10 photo-electrons, beyond which only a few pixels remain in the image.

We also give the example of two 500 GeV showers in figure 7.33. As we saw before in section 7.1.4, at this energy, the precision on the reconstruction of the source position is better than 0.1° even without image cleaning. The first example (left column), shows a gradual improvement as the image cleaning threshold is increased up to 3 photo-electrons. After a slight deterioration at this threshold, the reconstruction improves again, giving the best results at the 25 photo-electrons threshold. At 50 photo-electrons, the reconstruction deteriorates again. The second example (left column) has a large number of stray pixels specially in the regions at the periphery of the camera. The source reconstruction improves gradually as the image cleaning threshold is increased and the stray pixels removed. The best reconstruction is carried out at the 25 and 50 photo-electron thresholds.

In the next paragraphs, we will look at the average evolution of the source and shower core position reconstructions as a function of image cleaning thresholds. The above examples are meant to illustrate the trends we will see. But they also show that individual fluctuations can be quite important from shower to shower and that a threshold of image cleaning that works for one shower at a given energy does not necessarily yield similar results for another shower at the same energy. While we will not be looking into more adapted image cleaning methods, these remarks confirm the need for it in order to optimise parameter reconstruction.

Effect on parameter reconstruction precision The above examples also show that if image cleaning is properly done, the unnecessary information (scattered pixels, fluctuations, etc.) can be rejected while keeping the information most important for parameter reconstruction. Since the total number of photo-electrons in a shower image depends on the energy of the shower, the most adapted image cleaning threshold depends on the energy as well. In figure 7.32 (left) we show the evolution of the source position reconstruction precision as a function of image cleaning threshold. The following trends are visible for all energies.

- For each energy, the precision increases with the image cleaning threshold up to a certain optimum value. Beyond this value the precision on the reconstructed parameter drops.
- The value of the optimum threshold depends on the energy and is greater for higher energies.

These trends can be understood by looking back at the examples given above as well. When a threshold of 1 photo-electron is applied on the images, the precision improves for all energies as a large number of the scattered pixels with low signal are removed. These pixels often correspond to fluctuations in showers and their presence leads to poor reconstruction of parameters. The 20 GeV precision curve does not improve much beyond this threshold. Since the low energy shower images have fewer Cherenkov photons, crucial information for the reconstruction is lost as soon as a higher threshold for image cleaning is applied.

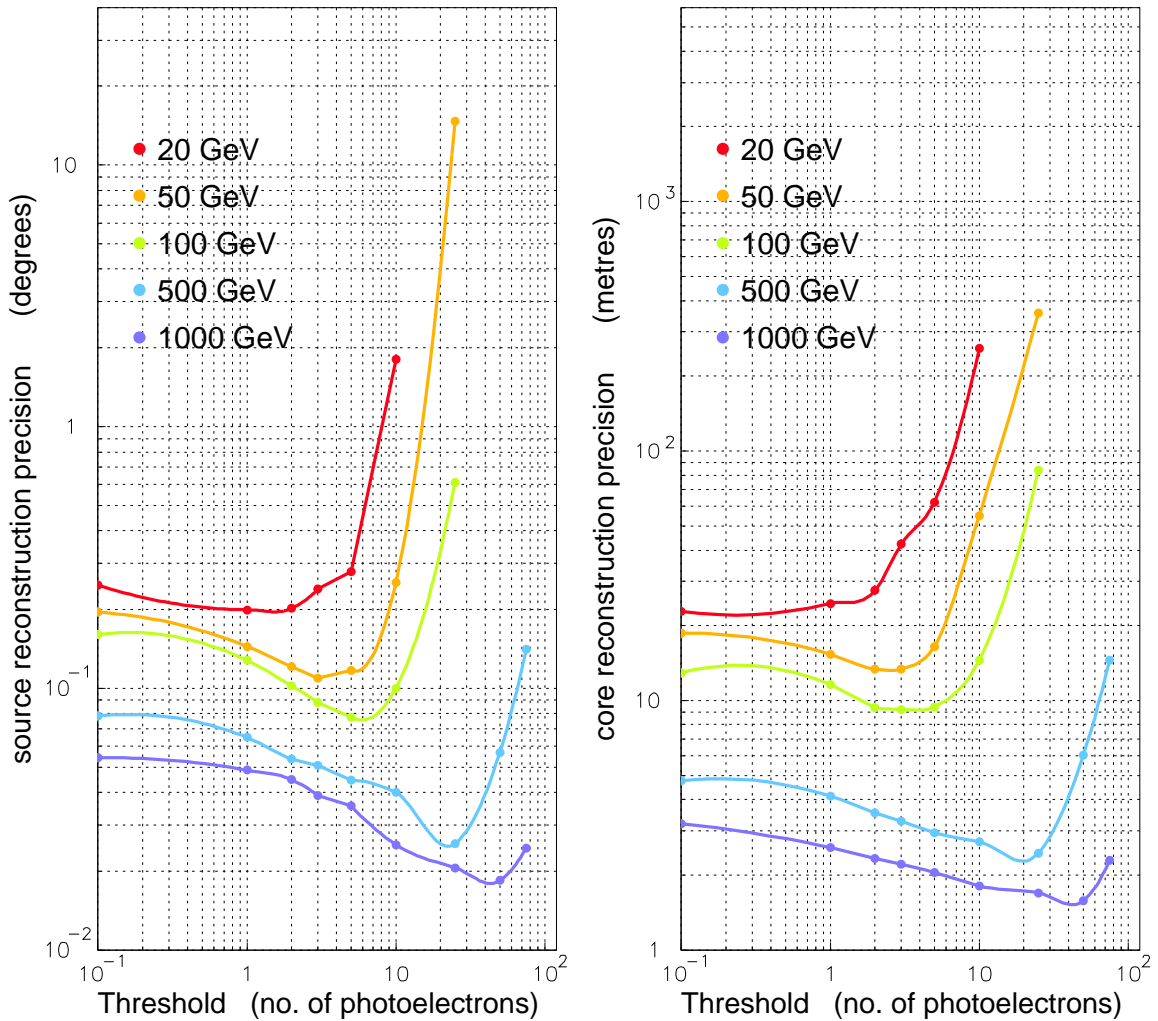


Figure 7.32: The precision of source position reconstruction (left) and shower core reconstruction (right) in terms of the threshold for image cleaning used. The energies are represented through different colours. The lines joining the plotted points are intended to guide the eye and have no physical significance.

All the other energies show further improvement in the precision up to at least the 3 photo-electron threshold which is the optimum threshold for the 50 GeV showers. For the higher energies, the precision continues to improve up to the 5 photo-electron threshold. For 100 GeV showers, the source position is reconstructed with a precision of less than one tenth of a degree, at this point. We recall that the single pixel size simulated in the telescope is of 0.1° . At this level of image cleaning, the improvement in precision occurs as most of the pixels resulting from fluctuations are removed with this threshold. These pixels are shown in shades of blue in figures 7.30, 7.31 and 7.33. In the showers shown in 7.30, they are responsible for the asymmetry of the shower images, which leads to poorer reconstruction. Some showers such as the one shown in figure 7.34 have small bunches of pixels away from the main shower images. Many of such bunches are removed with the 5 photo-electron threshold while others are removed only with higher levels of image cleaning.

Beyond the 5 photo-electron threshold, the precision for the 100 GeV showers diminishes, while that for 500 GeV and 1000 GeV showers goes on improving. While the 100 GeV show-

ers tend to lose information about image orientation at these thresholds of image cleaning, the showers images at higher energies, retain the pixels corresponding to the most important region of emission in the shower (red and yellow pixels) as well as the information about the orientation of the image (elongated form). The optimum threshold for the 500 GeV showers occurs around 25 photo-electrons where the precision of source reconstruction is around 0.03° . This is more than two times more precise than the source reconstruction with no image cleaning. The 1000 GeV source reconstruction precision improves up to at least the 50 photo-electron image cleaning threshold.

The right plot in figure 7.32 gives the evolution of the precision of shower core reconstruction in terms of the image cleaning threshold. The precision for core reconstruction at various energies shows the same trends as for the source position reconstruction, with similar values of optimum thresholds for each energy. The only exception seems to be the 20 GeV precision which deteriorates even with the 1 photo-electron threshold. While the best core reconstruction precision for 20 GeV showers remains above 20 metres, it goes down to about 10 metres for 100 GeV showers. The cores of the higher energy showers can be reconstructed with a precision of around 2 metres, when the optimum image cleaning threshold is applied to the images.

Remarks on the optimum image cleaning threshold As can be deduced from the discussion above, the optimum energy threshold is a characteristic of the shower images at a given energy. This becomes apparent when we look at the distribution of the photo-electron content of the pixels in shower images at various energies. Such distributions are shown in figure 7.35. We show the approximate optimum threshold obtained from the plots in figure 7.32 through an orange arrow. The characteristics of these distributions are specially visible in the high energy plots. There is a peak at the extreme left of the distribution, corresponding to the large number of pixels with a low number of photo-electrons. For instance, this peak corresponds to pixels with less than 20-25 photo-electrons for 500 GeV showers. As can be seen from the examples of shower images in figures 7.30 and 7.33, these pixels are mostly scattered around the main shower image and a large number of them correspond to shower fluctuations. The rest of the 500 GeV distribution in figure 7.35 corresponds to pixels with a larger number of photo-electrons. They constitute the bulk of the image, which contains most of the important information about the shower. The arrows show that the optimum image cleaning threshold seems to correspond to the limit between the two types of pixels. One also sees that while this limit is well defined for higher energies, it becomes harder to identify as we move towards lower energies. In the 20 GeV distribution, there is no clear transition from one type of pixel population to the other. This shows that the telescope system we are using is not really adapted for observations of 20 GeV showers.

In the bottom plot in figure 7.35, we also show the optimum threshold values obtained from figure 7.32 as a function of the shower energy. These are approximate values as they merely correspond to the thresholds at which the precision was best for each energy. One sees that the values tend to have a linear dependence on the energy. This property can be used to determine an adapted threshold for image cleaning for the shower images.

7.3.3 Transverse profiles and σ_t revisited

In section 7.1.2, we justified the use of a Gaussian p. d. f. for the transverse profile of shower images and determined the value of σ_t in order to use it for source and shower core reconstruction. The discussion was restricted to the most important aspects regarding transverse profiles. Here, we will do a more in-depth presentation of some of the questions concerning the

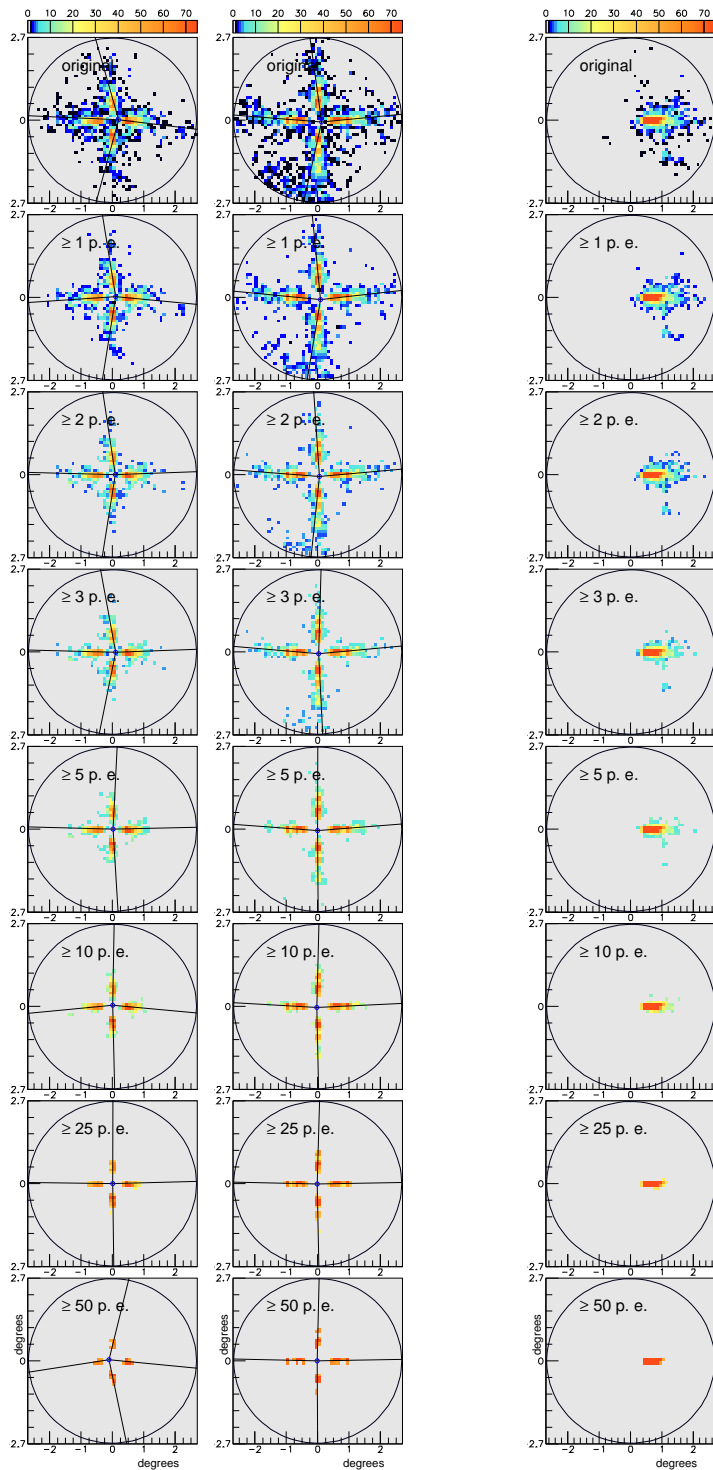


Figure 7.33: Each column shows the combined image of a 500 GeV shower as observed by four telescopes with different image cleaning thresholds. The reconstructed source position as well as the individual axes of the images obtained from the source reconstruction method are also shown.

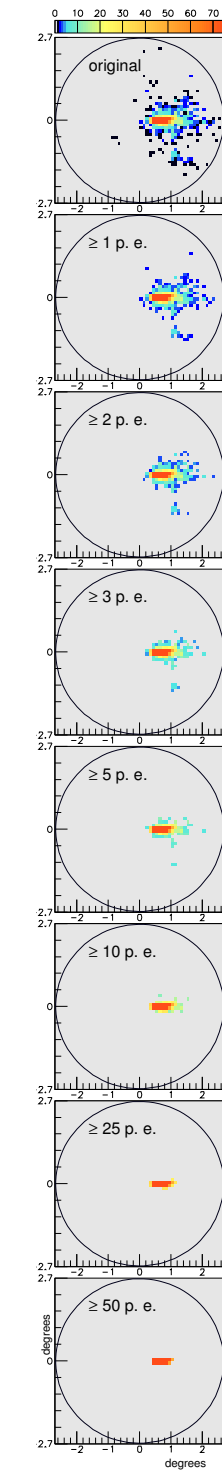


Figure 7.34: The image of a 1000 GeV shower after the application of different image cleaning thresholds.

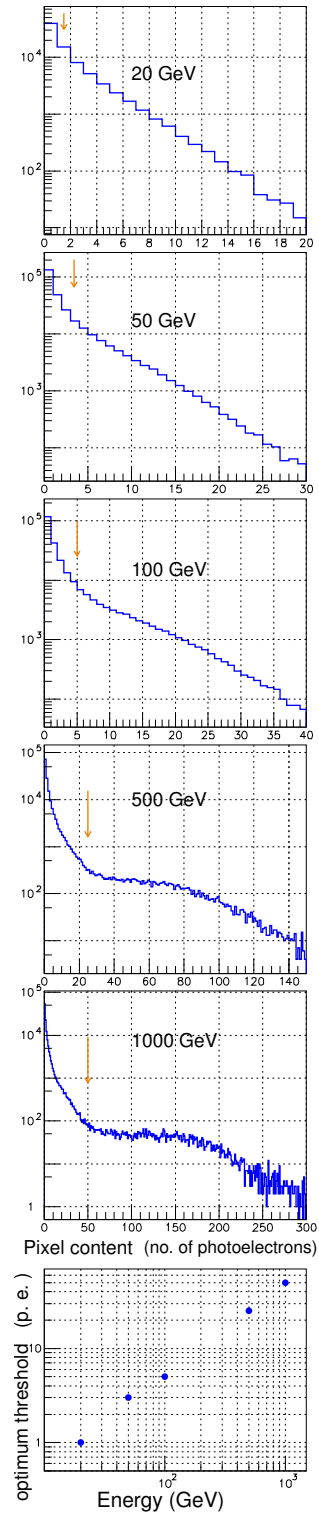


Figure 7.35: The distribution of the photo-electron content of the pixels in shower images at various energies. The arrow corresponds to the approximate optimum threshold obtained from figure 7.32. The bottom plot gives the dependence of this threshold on the energy.

use of a Gaussian function for the transverse profile of images, its impact on the source and core reconstruction and the effect of image cleaning on the choice of σ_t .

A discussion on the quality of the Gaussian fits

How well the Gaussian p. d. f. fits the transverse profiles of individual shower images determines how efficiently the source and core positions will be reconstructed using the likelihood functions given on pages 115 and 131. Here, we look at two different characteristics that allow us to judge the quality of the Gaussian fits.

In section 7.1.2, we saw that the Gaussian probability density function is an approximation of the shape of the transverse profile of shower images. Here, we further highlight this aspect of the Gaussian fits by discussing the χ^2 values obtained from them. This aspect of the Gaussian fits will have an impact on the discussion carried out later in section 7.3.4.

We also take a look at more particular cases of shower images for which the Gaussian fit does not represent the profile well. In particular, we discuss cases where the presence of isolated pixels has an impact on the value of σ_t . This discussion will also allow us to better understand the reasons for the fluctuations in the value of σ_t .

The Gaussian approximation: χ^2 of the Gaussian fits Figure 7.36 shows how the χ^2 of the Gaussian fits vary with energy. Each dot in figure 7.36 represents the mean value of the corresponding χ^2 distribution and the error bars are obtained by taking the root mean square value on either side of this mean value. The χ^2 distributions themselves are obtained by fitting the transverse profiles of the images of 4000 showers at each fixed energy with Gaussian functions. As an example, we have shown the χ^2 distributions for 50 GeV and 1000 GeV in figure 7.37.

As can be seen from these figures, the χ^2 values are closer to 1 for lower energies. In the example shown in figure 7.37, the 50 GeV distribution has a mean value of ~ 2 while for the 1000 GeV distribution it is close to 15. We have also fitted these distributions by a Landau function to obtain the Most Probable Value (MPV) at each energy. The most probable value of χ^2 for 50 GeV is close to 1, while for 1000 GeV it is around 12. This reflects the fact that the real transverse profile of shower images is not really a Gaussian function. As high energy images are better defined, the inaccuracy of the Gaussian function in describing the distribution implies that the χ^2 of the fits will be different from one. As we have already seen, the use of the Gaussian p. d. f. still allows us to reconstruct the source and core positions with good precision. However, we will see in section 7.3.4 that this has an impact on the normalisation of the χ^2 value and likelihood maps obtained for these reconstruction methods. One also notes that the 1000 GeV distribution is well fitted by the Landau function, while the low energy 50 GeV distribution has a large number of poorly reconstructed events with larger χ^2 values.

The impact of isolated pixels or bunches: comparing σ_t with the root mean square In specific cases, factors like the irregularity of the profile and in particular the presence of stray pixels and bunches away from the main shower image have an impact on the quality of the Gaussian fit of the profile.

The impact of these isolated pixels can be evaluated by comparing the root mean square (r. m. s.) value of the transverse profile with the standard deviation of the Gaussian profile (σ_t). The r. m. s. is a statistical measure of the spread of a distribution and in the case of a Gaussian distribution corresponds to the standard deviation. Given this, one expects these two values (the r. m. s. of the transverse profile distribution and σ_t obtained from fitting it with a Gaussian function) to be correlated for shower images. At the same time, the r. m. s. value is

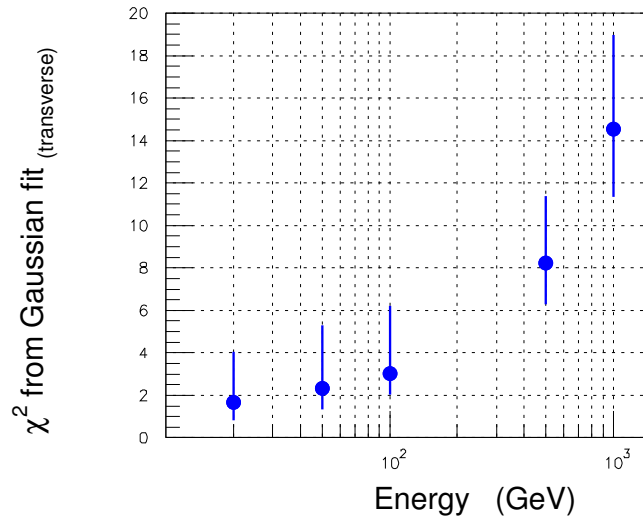


Figure 7.36: The χ^2 from Gaussian fits for the transverse profile as a function of the energy. The dots correspond to the most probable value obtained from the distribution of χ^2 for 4000 fits, while the error bars correspond to the half width maximum of the fits.

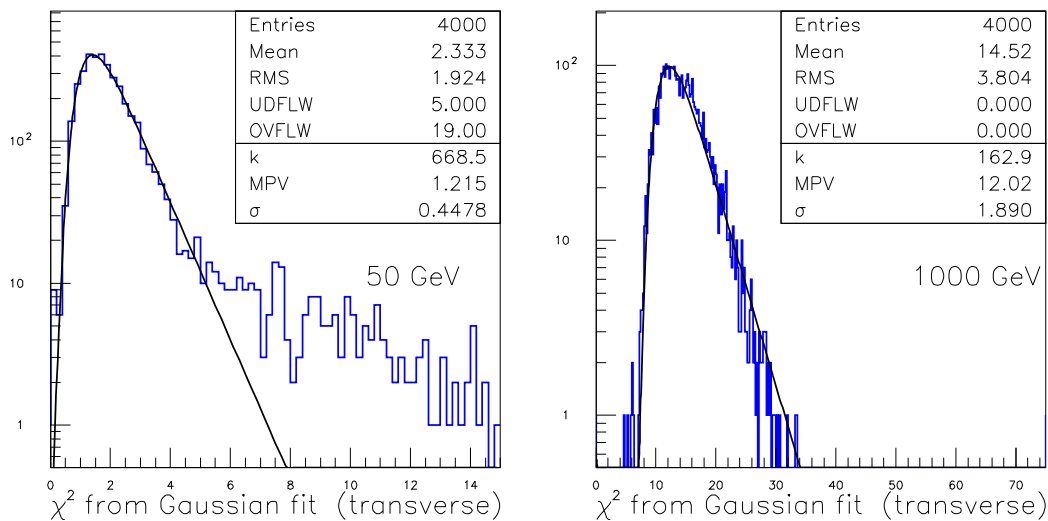


Figure 7.37: χ^2 distribution for 4000 γ -showers of 50 GeV (left) and 1000 GeV(right).The most probable value is calculated by fitting this distribution with the Landau function $f(x) = ke^{-0.5(w+e^{-w})}$ where $w = \frac{x-MPV}{\sigma}$. The result of this fit is shown in blue.

quite sensitive to the presence of the low signal isolated pixels present in many shower images. In particular, if these pixels are far away from the central part of the image they will tend to result in large r. m. s. values. On the other hand, σ_t is principally affected by the width of the central peak only, as the Gaussian fit does not take into account the pixels away from the central part of the image (see section 7.1.2). A comparison of σ_t with the r. m. s. can therefore give us an evaluation of the impact of the isolated pixels.

Figure 7.38 shows the scatter plots of these quantities for 50 GeV and 1000 GeV (blue markers). Both plots show that there is less correlation between the two parameters than

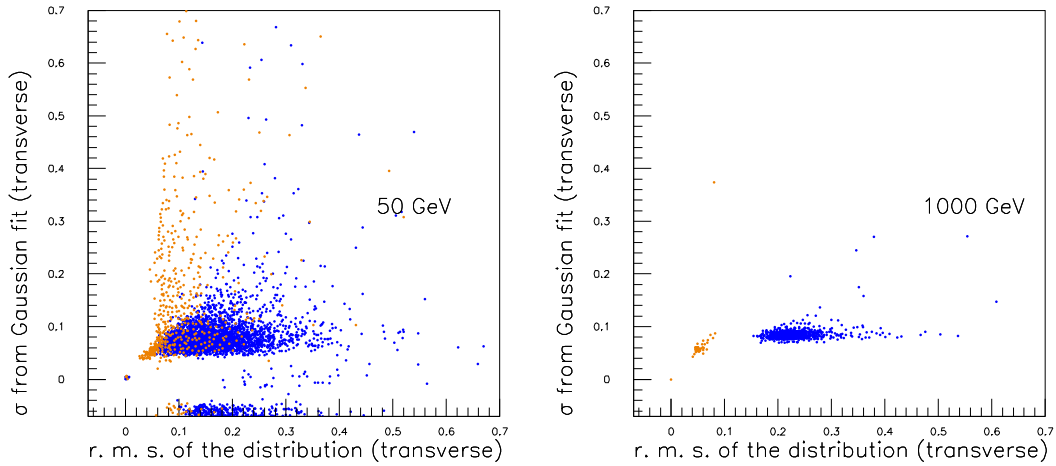


Figure 7.38: The standard deviation σ_t of the Gaussian fit versus the root mean square of the transverse distribution of 4000 γ -showers of 50 GeV (left) and 1000 GeV(right). The points in blue and orange are from the showers before and after image cleaning has been carried out, respectively. The optimum image cleaning thresholds obtained from figure 7.32 i .e. 3 photo-electrons at 50 GeV and 50 photo-electrons at 1000 GeV are applied. The units on both axes are degrees.

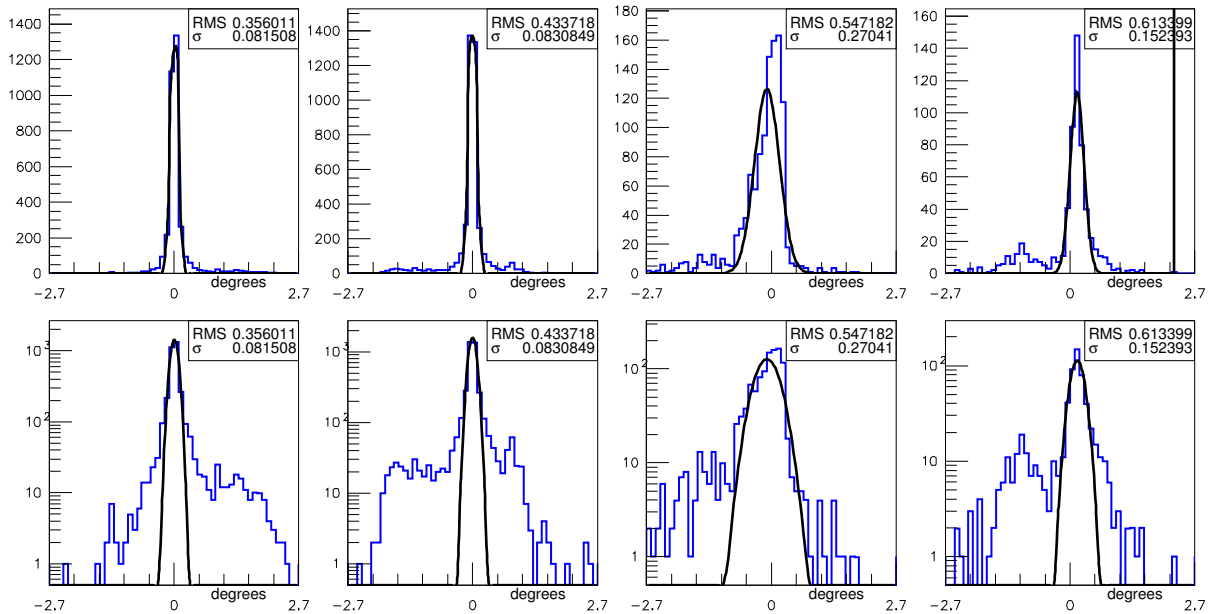


Figure 7.39: The transverse distribution of four 1000 GeV shower images. These distributions have higher than average root mean square values. The Gaussian fit of these distributions is shown in black.

expected. In fact, they seem to be completely uncorrelated at 1000 GeV. While the standard deviation obtained from the fit has a very narrow range of values mainly between 0.05 and 0.1 degrees, the values of r. m. s. vary a lot and can even go up to half a degree. One recalls that each pixel corresponds to 0.1 degree in the system used for this study.

We further explore the difference between the r. m. s. and σ_t by showing the profiles

corresponding to four 1000 GeV showers, for which the r. m. s. is greater than 0.3 degrees, in figure 7.39. For the first two showers, the central peak is well defined and there are no clear bunches on the sides. There is however a large number of photons away from the centre. As a result the fits yield $\sigma_t \sim 0.08^\circ$ i. e. values that are close to the average values shown in figure 7.8. On the other hand, the r. m. s. obtained from these distributions are 0.36° and 0.43° respectively. The third plot shows an irregular and enlarged central peak. There is also a large number of photons on the sides and some of them form a small bunch on the left of the peak. Here the deformation of the central peak affects the Gaussian fit which yields a larger value of σ_t : $\sim 0.27^\circ$. The r. m. s. is affected both by the presence of the many photons on the sides and the enlarged central peak and has a value of 0.55° . The fourth plot has a prominent bunch on the left side of the central peak as well as some deformation of the central peak. The r. m. s. value from the distribution is 0.6° and the fit yields $\sigma_t \sim 0.15^\circ$. The points corresponding to these last two showers are easily identified in the 1000 GeV plot of figure 7.38.

Fits that do not converge In some cases, the presence of isolated bunches of pixels prevents the Gaussian fit from converging. The scatter plot for 50 GeV showers in figure 7.38 (left) shows that a number of fits seem to yield negative standard deviation values. We note that such events were also visible in figure 7.7 (left) in section 7.1.2. This occurs when the Gaussian fit of the transverse profile does not converge. This usually happens in low energy showers where the total number of photo-electrons is low and the impact of the isolated pixels and bunches more important. We give the example of such a shower image in figure 7.40. This image has a small cluster of pixels outside the main shower image. This cluster is also visible in the transverse profile shown in the plot on the left and is responsible for the failure of the fit to converge. The fit yields a negative value for the standard deviation.

The impact of image cleaning One can expect these effects to diminish or disappear when image cleaning is carried out. In figure 7.41, we show the effect of different image cleaning thresholds on the transverse profile through the example of a 500 GeV shower image obtained from a telescope at 50 m from the shower core. As the image cleaning threshold increases, the Gaussian fit of the transverse profile corresponds more closely to the profile itself since most of the pixels on the sides are removed. The two plots in figure 7.38 also compares the r. m. s. and σ_t values obtained once image cleaning is carried out by using the optimum image cleaning threshold for each energy (orange markers). The 50 GeV plot shows that, in general, the value of the r. m. s. diminishes once image cleaning is carried out and that there is a clear correlation between the r. m. s. and σ_t for values below $\sim 0.09^\circ$. The few events above these values are a reflection of the irregularity of the shower images at 50 GeV and the low number of photo-electrons in the images obtained by 12.5 m diameter telescopes at this energy. One also notices an important decrease in the number of events for which the Gaussian fits do not converge. In the 1000 GeV plot, the r. m. s. values show an important decrease after image cleaning. Since the optimum threshold at 1000 GeV implies a rather severe cut on low energy pixels we are left with only the central peak of a few pixels (around 0.04°) in the transverse profiles. This gives an almost unique value for both the r. m. s. and standard deviation of the fit.

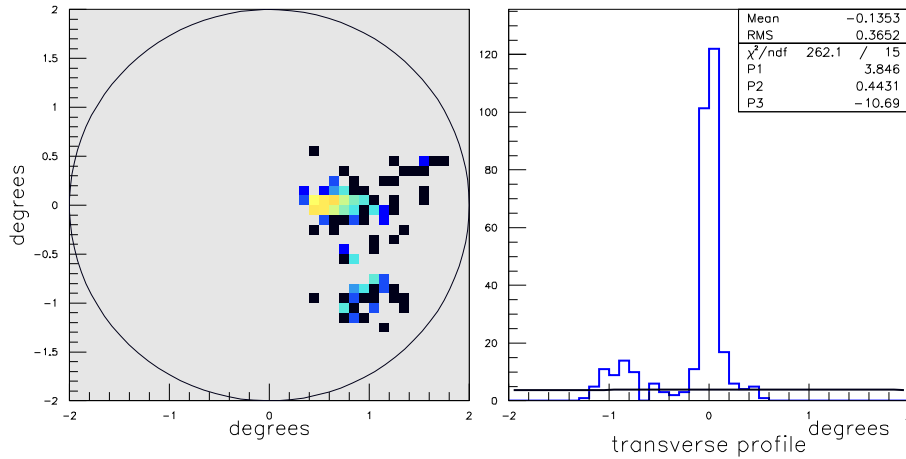


Figure 7.40: Example of a 100 GeV shower observed at an altitude of 2200 m above sea level. The shower image (left) shows a distinct separate cluster away from the main shower image. The plot on the right shows the transverse profile of this image (blue curve) and a failed attempt to fit the profile with a Gaussian curve (black line). The standard deviation (P3) of the attempted fit is negative.

The dependence of σ_t on the distance between the telescope and the shower core position

In chapter 6, we saw how the image tends to become more elongated as the telescope moves away from the shower core. We also saw that the number of photo-electrons in the image was affected by this distance. In this section, we find that some of these factors have an impact on the transverse profile and value of σ_t as well.

Figure 7.42 (top), shows the average value of σ_t as a function of telescope distance from the shower core for 500 GeV showers. This plot is obtained by generating 1000 showers at 500 GeV. Every shower is then viewed by 30 telescopes placed at various distances from the shower core. The transverse profile of each image is then fitted with a Gaussian function in order to obtain its standard deviation σ_t . The average value of σ_t from the 1000 showers is then reported on the plot. The error bars are calculated by taking the r. m. s. of the distribution below and above the mean value.

The value of σ_t is minimum (~ 0.07 degrees) around 120 metres i. e. the position of the Cherenkov ring on the ground. As we saw in chapter 3, this is the region where the bulk of the Cherenkov emission from the maximum of shower development arrives. The small error bars in the plot show that this is also the position where the fluctuations from shower to shower on the number of Cherenkov photons reaching the ground and contributing to shower images are smallest. The value of σ_t as well as the fluctuations increase as the telescope is placed closer to the shower core and less photons from the central part of the shower are incident on it. The same occurs at distances beyond the Cherenkov ring. Beyond 300 metres the number of Cherenkov photons in the shower image decreases to a point where the transverse profile of the image starts narrowing down. The error bars beyond the ring are large too since the Cherenkov photons arriving at these distances are more dependent on shower fluctuations.

In figure 7.42 (bottom), we show the variation of σ_t for several energies. Apart from the 20 GeV curve, all other energy showers show similar behaviour as a function of the distance. The value of σ_t is the same around the Cherenkov ring position. At higher energies, namely 500 and 1000 GeV, the average value of σ_t peaks near the shower core position. This is

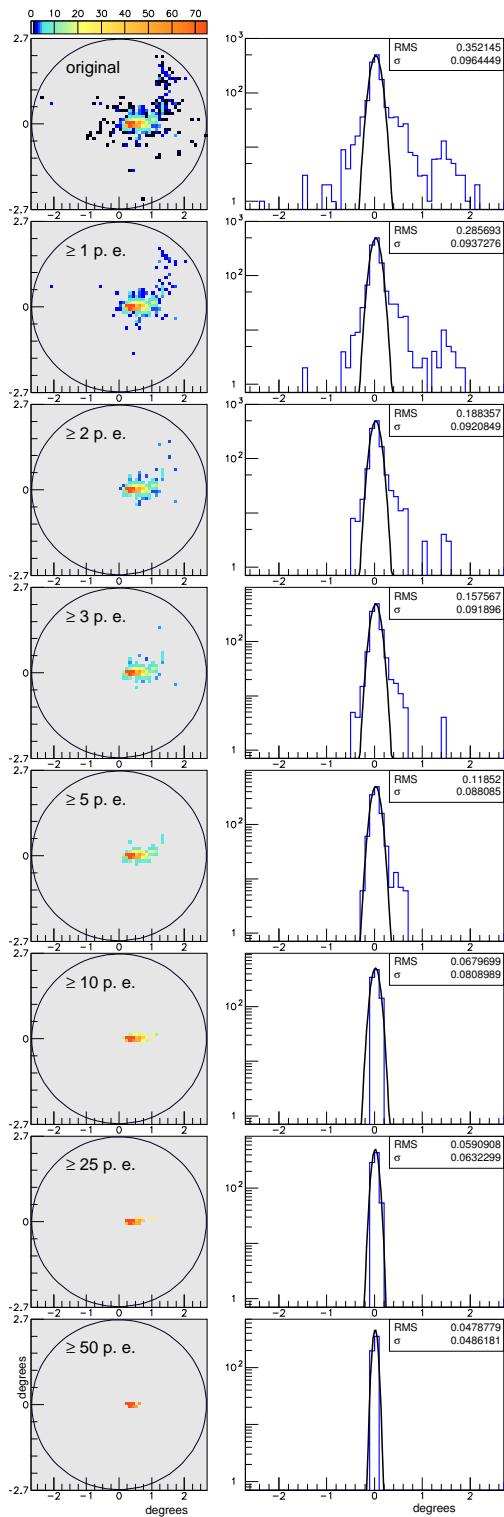


Figure 7.41: The effect of image cleaning on the transverse profile of a 500 GeV shower image and its fit by a Gaussian function. The original images are also shown in the left column.

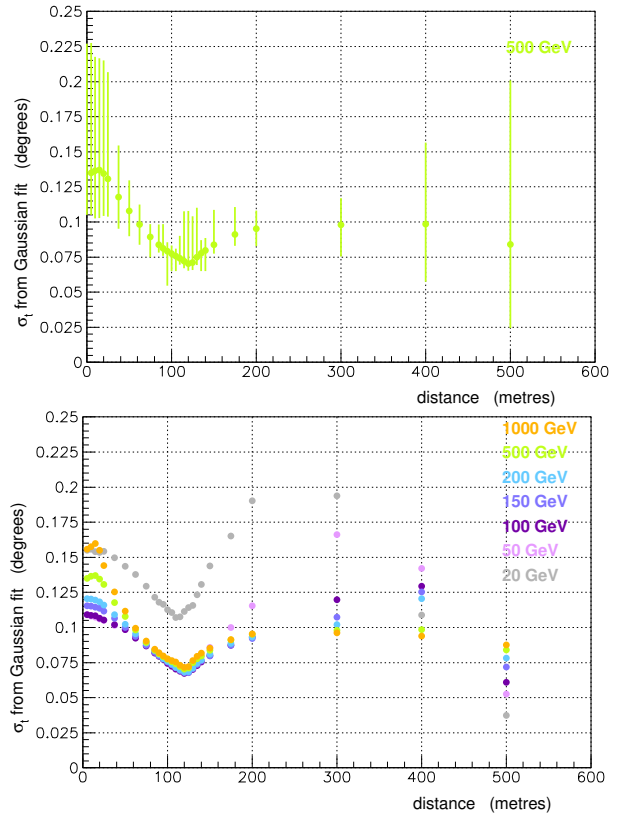


Figure 7.42: The average value of σ_t as a function of telescope distance from the shower core. The top plot shows the σ_t values for 500 GeV showers with the error bars representing the fluctuations. The bottom plot shows the σ_t dependence on the distance for various energies.

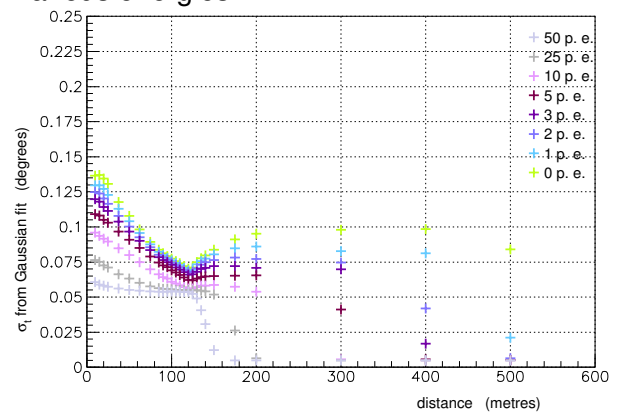


Figure 7.43: The average value of σ_t as a function of telescope distance from the shower core for 500 GeV showers, with different image cleaning thresholds (shown through different colours).

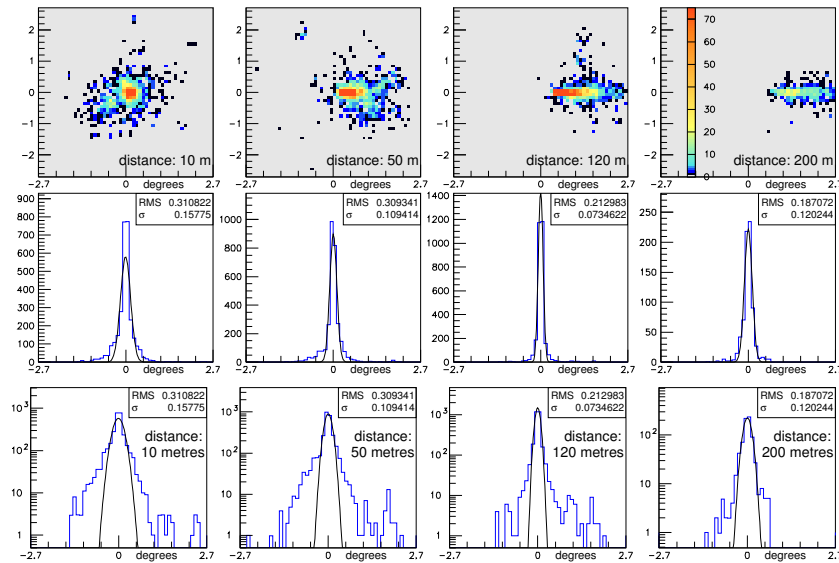


Figure 7.44: The images of a 500 GeV shower obtained by telescopes at 10, 50, 120 and 200 metres from the core positions. The transverse profile of each image, fitted by a Gaussian function, is also shown in the centre (linear scale) and bottom (log scale) plots. The r. m. s. of the distribution and σ_t from the Gaussian fit are indicated on each plot.

related to the peak in the Cherenkov photon distribution on the ground we saw in section 3.4.2. At these energies, the shower development has not terminated when the bulk of the shower reaches the ground. This results in a peak in the Cherenkov photon flux near the shower core as well as greater fluctuations in the number of photo-electrons in the shower images obtained by telescopes in this region.

We illustrate the effect of telescope distance on the shower images and their transverse profiles through the example presented in figure 7.44. The images are obtained by viewing a 500 GeV shower by a telescope at 10, 50, 120 and 200 metres distance from the core position. The transverse profiles are also shown in log scale in order to emphasize the pixels with low levels of signal. One sees that while the outer fluctuating parts of each image spread out more in the images closer to the core, the central peak of the images has relatively similar transverse size (i. e. a width of a few pixels). In the case of the first two images, there are enough photo-electrons in the pixels right next to this central peak in the image so that we end up with slightly enlarged transverse profiles. While the low-signal isolated pixels (mostly in black and dark blue) do not have an impact on the fit (see discussion in previous section), these medium-signal pixels (mostly in yellow and pale green) result in higher values of σ_t . In the third plot (at 120 metres), the image is stretched in the longitudinal direction and these medium range pixels only contribute to the central peak of the transverse profile. In the last image (at 200 m), the overall photo-electron content of the image decreases as a result the central peak is not as well defined as it is in the images within the Cherenkov ring.

The effect of image cleaning on σ_t 's dependence on the distance between the core and telescope positions We recall figure 7.41 on page 151 in which we showed the impact of applying various image cleaning thresholds on a 500 GeV shower image obtained from a telescope at 50 m from the shower core. We saw that as the image cleaning threshold increased most of the pixels corresponding to the fluctuating parts of the shower were eliminated and the profile resembled a Gaussian function more closely. One therefore expects the dependence of

the value of σ_t on the distance to diminish as various image cleaning thresholds are applied.

Figure 7.43 shows the average value of σ_t as a function of the distance for 500 GeV showers after applying various image cleaning thresholds. As the threshold of energy cleaning increases, the value of σ_t decreases for all distances. While this change is slight around the Cherenkov ring position, it becomes more important closer to the shower core or beyond the ring. With the threshold of 25 and 50 photo-electrons, σ_t has a value close to 0.05° and is almost independent of the distance, within the Cherenkov ring. We recall that in section 7.3.2, we found that 25 photo-electrons was the optimum threshold for the parameter reconstruction of 500 GeV showers. Beyond the ring position, the value of σ_t drops below 0.05° . This is to be expected as the average number of Cherenkov photons in telescope images drops at these distances. This is yet another illustration of the need for image cleaning methods that are more complex than the simple application of a threshold. More generally, if more sophisticated image cleaning methods involving cluster recognition are used one expects fewer of the medium and low signal pixels to be removed resulting in σ_t retaining some of its dependence on the distance.

The effect of σ_t value on source and shower reconstruction

The results about source and shower core presented up to this point have been obtained by using the value of σ_t obtained in section 7.1.2, for a fixed telescope distance (85 metres) and no image cleaning. We have just seen that these two factors have an effect on the value of σ_t . σ_t is used in equations 7.4 and 7.6 to calculate the likelihood function for the source and shower core position reconstruction, respectively. A change in its value will have an impact on the normalisation of the function but its form will remain the same. This implies that the use of different value of σ_t will not affect the precision on the reconstructed parameters. In figure 7.45, we present the χ^2 map for source position reconstruction for a 1000 GeV shower obtained by using three different values of σ_t . The plot on the left uses $\sigma_t = 0.075^\circ$, while the centre and right plots use $\sigma_t = 2 \times 0.075^\circ$ and $\sigma_t = 3 \times 0.075^\circ$, respectively. The shape of the maps are identical, the minimum value of χ^2 is 7.4, 1.85 and 0.82 in the three respective cases. The χ^2 maps for the core reconstruction are affected in a similar way.

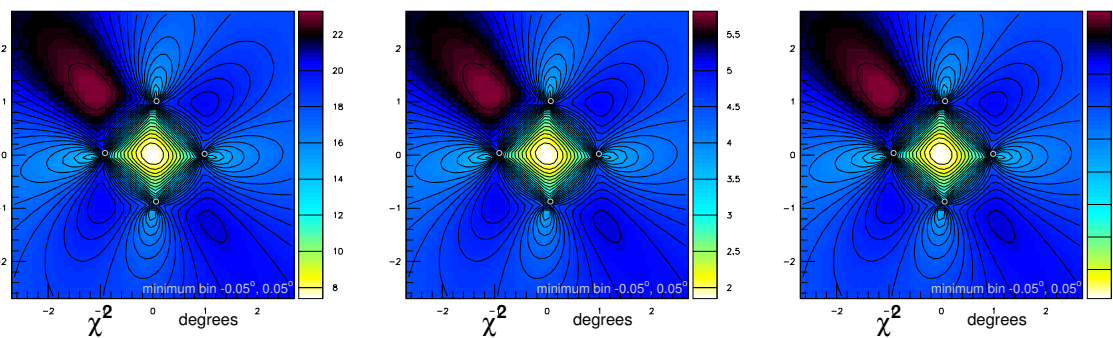


Figure 7.45: The χ^2 map obtained for the reconstruction of the source position by using three different values of σ_t : 0.075° , $2 \times 0.075^\circ$ and $3 \times 0.075^\circ$ from left to right.

7.3.4 A note on χ^2 minimisation of fits and its possible use

The χ^2 value gives an indication of the quality of a fit. With that fact in mind one can look into the possibility of using χ^2 values from the source and core position reconstruction methods to

discriminate between hadronic and electromagnetic showers. Since we have tried to optimise the source and core reconstruction fits for electromagnetic showers, one expects better χ^2 values for them. However, as we will see in what follows, there are several factors that limit the capacity of χ^2 values to be used for discrimination purposes. The use of χ^2 values for discrimination still remains possible but requires additional steps to obtain accurate χ^2 values.

The Gaussian approximation for the transverse profile is rough We saw in section 7.3.3 that the initial Gaussian fit of the transverse profile itself had large χ^2 values specially at higher energies (figure 7.36). This is reflective of the fact that the use of a Gaussian p. d. f. for the transverse profile is quite approximative; while the value of σ_t is still a good measure of the width of the transverse profile the fit is not representative of the profile's shape. We saw, at that point, that the superposition of three Gaussian functions might be a better approximation for the profile's shape. Consequently, the χ^2 values for the source and core reconstruction fits also increase with energy. In figure 7.46, we present the energy dependence of the χ^2 value for source reconstruction (left) and core reconstruction (right). Even if the parameters of showers at higher energies are easier to reconstruct and the showers themselves have fewer fluctuations leading to easier identification, this is not reflected in the χ^2 values where the effect from the Gaussian fit dominates.

The dependence on the value of σ_t As we saw in the previous section, while the value of σ_t used does not affect the results of the source and core reconstruction, it does have an impact on the χ^2 of the fit. This means that the χ^2 values will be sensitive to the choice of σ_t used in the fits. Moreover, we saw in section 7.3.3 that the choice of σ_t is not straightforward and depends on several factors; its value is affected by the distance of the telescope from the shower core and also shows a slight dependence on energy away from the Cherenkov ring (see figure 7.42). As we saw in figure 7.43, the value of σ_t also depends on image cleaning.

In figure 7.47, we see how the χ^2 values of the reconstruction fits are affected when images are cleaned but the value of σ_t is kept fixed. The left column shows the distribution of χ^2 values obtained for source reconstruction and the right column shows those for the core reconstruction for various energies. The black line represents the χ^2 values obtained from using images without image cleaning, while the blue line gives the values obtained from images cleaned with the optimum cleaning threshold (see section 7.3.2).

One notices that the distributions tend to get narrower and start closer to zero, when an image cleaning threshold is applied. This effect is specially pronounced at high energies, so much so that at 1000 GeV, most values lie below 1. The reasons for this effect are twofold.

- When image cleaning is carried out with a high threshold such a 25 or 50 photo-electrons, the resulting image is only a few pixels wide (see for example figure 7.41). This implies that the distance of each pixel's centre from the reconstructed axis is at the most around half a degree. This leads to very small values of χ^2 .
- The value of σ_t used is the one determined in section 7.1.2, i. e. for shower images without image cleaning. As we saw in section 7.3.3, the value σ_t tends to diminish with image cleaning. As we keep on using a value of σ_t that is larger than that of the image profile, this tends to lower the χ^2 values.

Different solutions can be found to address some of these concerns.

- Adapted values of σ_t could be used whenever image cleaning is carried out. This will not deal with the variation of σ_t as a function of telescope distance from the shower core, but will help to deal with the artificial lowering of the value of χ^2 discussed above.

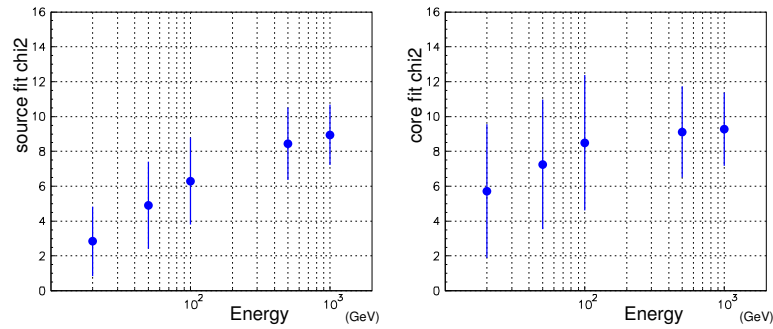


Figure 7.46: The energy dependence of the average χ^2 value for the source reconstruction fit (left) and core reconstruction fit(right). No image cleaning was carried out.

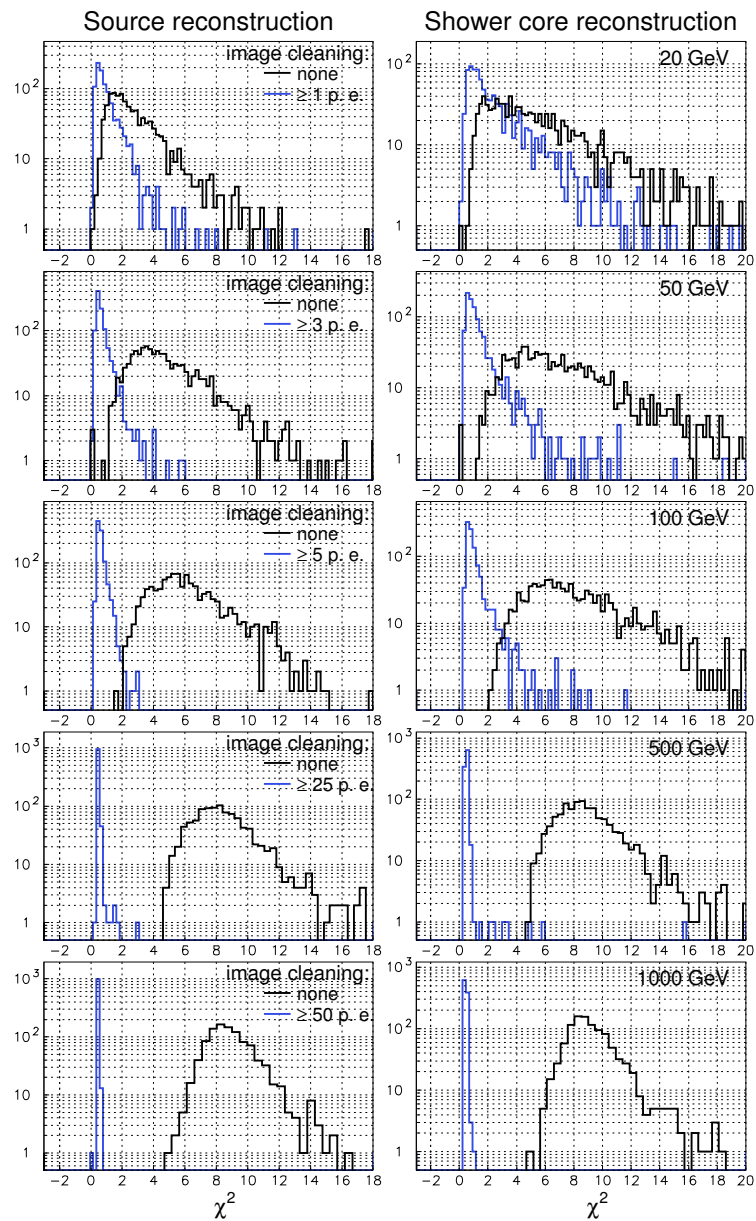


Figure 7.47: The comparison of the distributions of the χ^2 value obtained by reconstructing the source and core positions before image cleaning (black line) and after image cleaning (blue line). The left column represents the χ^2 distributions for the source reconstruction fit at 20, 50, 100, 500 and 1000 GeV and the right column shows the χ^2 distributions for the core reconstruction fit at the same energies.

- Gaussian fits of each individual shower image could be carried out in order to obtain a different value of σ_t for each telescope in the χ^2 expressions (equations 7.5 and 7.7). Since some of the transverse profile fits do not converge, or yield values that are too large, a backup solution could be to use a fixed value of σ_t whenever the fit does not work correctly.
- The reconstruction fit could be carried out in two or more steps. The first step would consist in applying the method as it currently is. The shower core position obtained from this first fit would then be used to find the appropriate value of σ_t (i. e. the value corresponding to the core distance) for each telescope. As a second iteration, the fit could then be carried out once again in order to obtain a more accurate χ^2 value.

Among the two possibilities described above, the first will have no impact on the reconstructed source and core positions as the change of σ_t value will only affect the normalisation of the χ^2 expressions. On the other hand, the second method could result in source and shower core positions that are reconstructed differently from those obtained with a single value of σ_t for all telescope images. This method could be tried in order to evaluate its efficiency. However, even if the σ_t value used is the best adapted possible, the inaccuracy of the Gaussian shape to describe the transverse profile will remain responsible for relatively poor χ^2 values. In a very sophisticated method, the Gaussian profile could be replaced with a better adapted profile but this would lead to a lot of complexity in the method. In chapter 9, we will use the fits on hadrons and see that even without taking the above mentioned steps they tend to yield greater values of χ^2 than γ -showers and could provide a means for discrimination.

7.3.5 Use of the longitudinal asymmetry in the images

So far, we have not made explicit use of the the longitudinal asymmetry in the images. This is mainly because the method we have used for the reconstruction of individual image axes depends mainly on the transverse information in the images.

However, the longitudinal profile does carry information about the source and core position of the shower. To illustrate this, we present the average longitudinal profile of 500 GeV shower images obtained from telescopes at various distances from the shower core in figure 7.48. The generated source position is (0, 0) degrees in all cases. As we had seen in chapter 6, three factors change as the telescope moves away from the shower core position:

- the shower profile gets elongated in that direction,
- the profile becomes more asymmetric

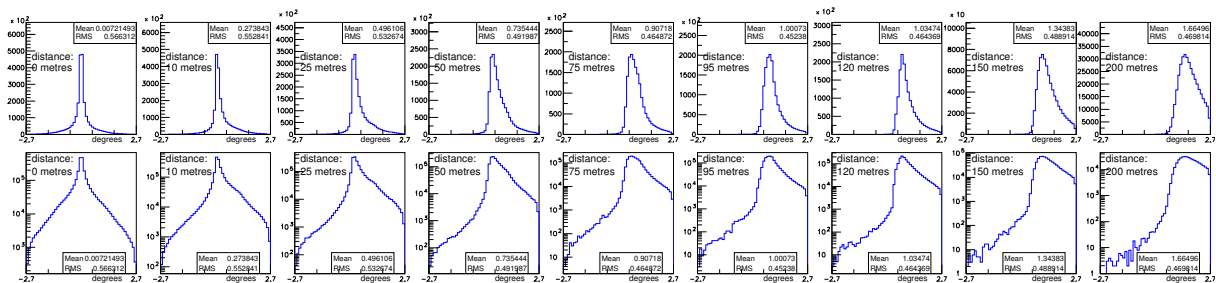


Figure 7.48: The average longitudinal profile of 500 GeV shower images obtained from telescopes at various distances from the shower core. The profiles are shown in linear scale (top row) and log scale (bottom row)

- and the position of the profile's peak moves away from the source position (at 0 in this case).

These properties show that the asymmetry of the shower images could also be used to calculate the position of the shower's source and core positions. Such calculations might further improve the precision on the reconstruction of these parameters. The use of the longitudinal information could be particularly useful for observations of high energy showers when they fall far away from the telescope array. At these energies, the number of Cherenkov photons arriving on telescopes is large enough to have exploitable images even at large distances from the shower core position. When a shower falls far from the array, the angles between the axes of the shower images from different telescopes tend to be smaller. As we have seen earlier in this chapter, the presence of different telescopes viewing the same shower from different angles is important for efficient source and core reconstruction. In such cases, the use of the longitudinal information could provide a means of better reconstructing the shower parameters.

CHAPTER 8

ENERGY RECONSTRUCTION

The method of energy reconstruction is based on a simple principle i. e. the relationship between the number of Cherenkov photons and shower energy. We first developed and applied this method in its simplest form as described in the next few sections (8.1 to 8.3). As the results (given in section 8.4) of this first application demonstrate, the over-simplification of the problem introduces some systematic errors. While the simplest approach enables us to have an evaluation of the energy, in order to have a more precise reconstruction, a number of other factors need to be taken into account.

The second part of this chapter (section 8.5) will, therefore, discuss the impact of several parameters on the energy reconstruction. In particular, we will examine the relationship between the altitude of first interaction in the atmosphere and the number of photo-electrons in a shower image and look into the impact of this relationship on the energy reconstruction. These discussions will show that in order to have a more precise determination of the energy, a more elaborate method for the energy reconstruction is required (section 8.6).

We will end this chapter by describing a method for the reconstruction of the longitudinal profile of the shower by backtracking the individual Cherenkov photons from the shower image (section 8.7). Such a method can, not only be used to improve the reconstruction of the energy, but also enable the discrimination of γ -showers from hadronic showers as we will see in chapter 9.

8.1 Principle: the relationship between the number of Cherenkov photons and shower energy

We have, on several occasions, discussed the relationship between the energy of the primary gamma-ray and the number of Cherenkov photons produced. As the primary energy increases so does the shower size and the number of charged particles with energies above the Cherenkov threshold. In section 3.2.3, we saw that the number of Cherenkov photons produced in a shower has a linear dependence on the energy. This in turn affects the density of the Cherenkov photons arriving on the ground (section 3.4.2) and the number of photo-electrons in shower images. In section 6.6, we discussed in detail the relationship between shower energy and the number of photo-electrons in an image. In fact, one can show that for a fixed telescope distance from the core, the number of photo-electrons depends linearly on the shower energy. This is presented in figure 8.1 (left) where we show the average number of photo-electrons in an image as a function of the shower energy. The values are those obtained for a 12.5 diameter telescope, positioned at a distance of 85 metres from the core, at an altitude of 1800 metres. The fluctuations are also shown through the error bars on the points. One sees that as with the total number of Cherenkov photons produced in a shower, the average photo-electron number depends linearly on the energy and the fluctuations get smaller as the energy increases. This

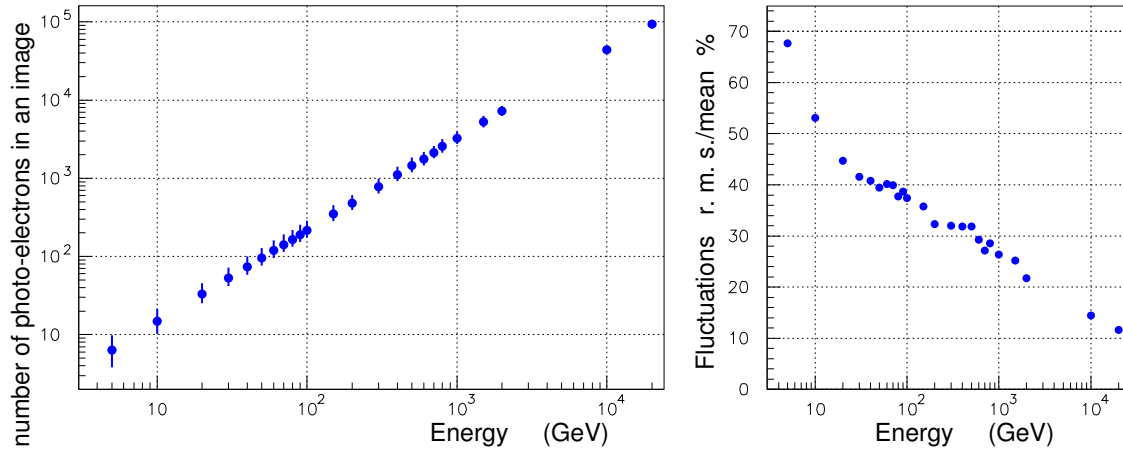


Figure 8.1: The right plot shows the average number of photo-electrons in a shower image from a 12.5 m diameter telescope, at 85 m from the shower core, as a function of the shower energy. The error bars represent the r. m. s. of the photo-electron number distribution, calculated separately above and below the mean value. The left plot shows the dependence of the intrinsic fluctuations of the number of photo-electrons (for a telescope at 85 m from the core) on the energy of the showers. The intrinsic fluctuation is calculated by dividing the r. m. s. of the photo-electron number distribution by its mean.

is also presented in figure 8.1 (right) where we show the intrinsic fluctuation of the number of photo-electrons in a shower image as a function of the energy.

Apart from the energy, the number of photo-electrons is also dependent on a number of other factors(see section 6.6). These include telescope distance from the shower core, atmospheric conditions, altitude of observation, telescope characteristics... For observations made at a given time (fixed atmospheric conditions and a given telescope (fixed altitude, telescope characteristics...)), the number of photo-electrons in images are dependent on shower related factors only, namely shower energy and distance of the telescope from the shower core and zenith angle. While we ignore this factor for the moment, we will also see later in this chapter (section 8.5.4), that in addition to the above two parameters, the altitude of first interaction also has an important impact on the number of photo-electrons in images. For simplicity's sake, we also restrict our discussion to 0° zenith angle showers only, for the time being¹. This leaves us with the shower energy and core distance from the telescope as factors determining the number of photo-electrons in a telescope image. Both quantities are unknown when shower images are obtained. These images can be used to evaluate the shower core position using the method described in section 7.2. One can then evaluate the shower energy by exploiting the linear relationship between the average number of photo-electrons in images and the energy for fixed telescope positions. In order to achieve this, one needs a table of values giving the number of photo-electrons for fixed energies and distances between the telescope and the core position. The exact energy value can then be determined by interpolating between the table values. In the next section we will briefly describe the table we have constructed for energy reconstruction.

¹The dependence of the number of photo-electron is more complex for inclined showers as the circular symmetry of the Cherenkov photon distribution on the ground is broken. We will discuss the reconstruction of energy for these showers in section 8.6.

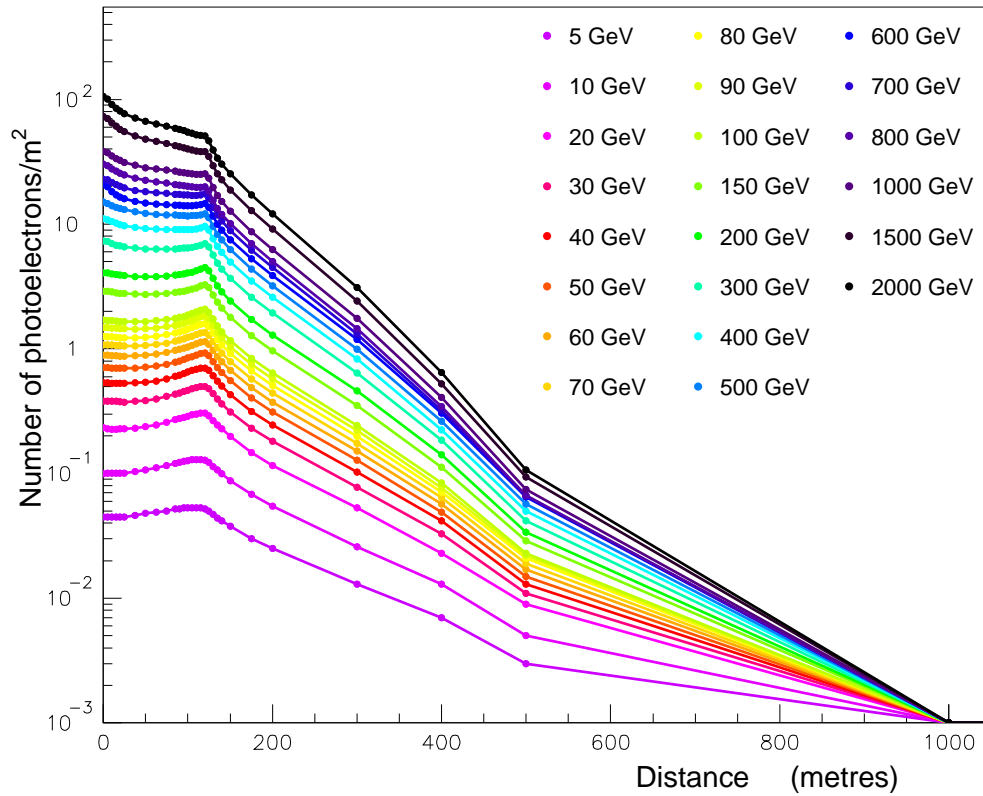


Figure 8.2: The average number of photo-electrons per metre square in shower images as a function of distance for various fixed energies between 5 GeV and 2000 GeV.

8.2 Photo-electron number tables

In order to enable the reconstruction of the shower energy, tables of the number of photo-electrons obtained at different distances from the shower core and at different energies need to be constructed. In order to do so, we did a series of shower simulations at 22 different energies between 5 and 2000 GeV. In each simulation, we placed telescopes at 30 different distances from the core position. The telescope parameters (size, focal length...) were the same as those of the test system being studied (see description on page 110). The results of these simulations are shown in figure 8.2. The distance from the shower core is represented on the abscissae axis while the number of photo-electrons per metre² is plotted on the ordinate axis. The different energies are shown through different colours. Each plotted point is obtained from the average number of photo-electrons obtained in a telescope image at that distance from the shower core. The average number of photo-electrons is divided by the total mirror surface in order to obtain the density of accepted Cherenkov photons contributing to the shower images. The mirror reflectivity and photomultiplier quantum efficiency are also taken into account when simulating the response of the telescopes.

8.3 Implementation

In a multi-telescope configuration, we find ourselves with the situation shown in figure 8.3. The number of photo-electrons on the camera of the i^{th} telescope is given by N_i and the distance of this telescope from the shower core d_i is known once the shower core position has been

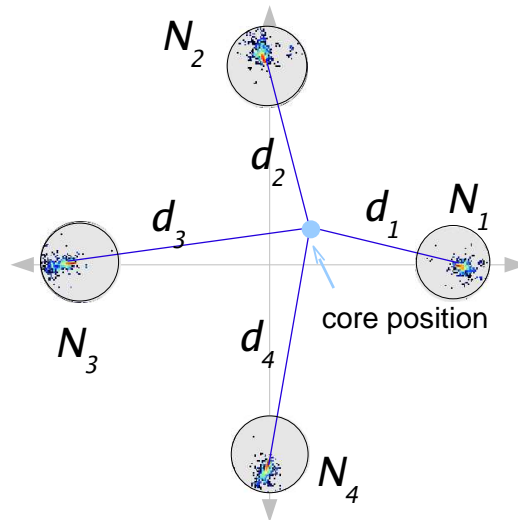


Figure 8.3: Schematic description of the different parameters used to reconstruct the shower energy.

reconstructed. These two values are then compared with the distance and number of photo-electrons in the table and the values of the table are interpolated in order to obtain the value of energy E_i corresponding to this particular image. The final reconstructed energy is then obtained by taking the average value of all E_i .

8.4 Results

We have used the method described above to reconstruct the energy of showers simulated at 20, 50, 100, 500 and 1000 GeV and observed by the telescope system described on page 110. The distributions of the reconstructed energies for all the generated energies are shown in figure 8.4. In each case, the reconstructed energies follow an asymmetric distribution with mean value slightly above the generated energy. The distributions are also fitted with Gaussian (blue curve) and Landau (purple curve) functions. One notes that while the shape of the distribution is well represented by the Landau function, it is the mean value that yields the result closest to the generated energy. Note that it is interesting to look at the mean value of this distribution since the method of reconstruction itself uses a table of mean values for the number of photo-electrons in shower images.

In order to compare the reconstructed energy with the generated energy and also evaluate the width and asymmetry of the distribution we use the Gaussian fit of the distribution. The mean value of the fitted Gaussian curve is compared with the generated energy in figure 8.5. The mean reconstructed energy obtained in this way is slightly lower than the generated energy as can be seen by comparing the plotted points with the dashed line which represents perfect energy reconstruction. The error bars represent the asymmetry of the distribution and are calculated by taking the r. m. s. of the distribution above and below the mean value obtained from the Gaussian fit.

As the shape of the distribution of the reconstructed energy is well represented by Landau functions the MPV and σ obtained from each fit is used to calculate the energy resolution $\frac{\sigma(E)}{E} = \frac{\sigma}{MPV}$ at each energy. The results are shown in figure 8.6 and show that the typical values of the energy resolution lie between 10 to 20%.

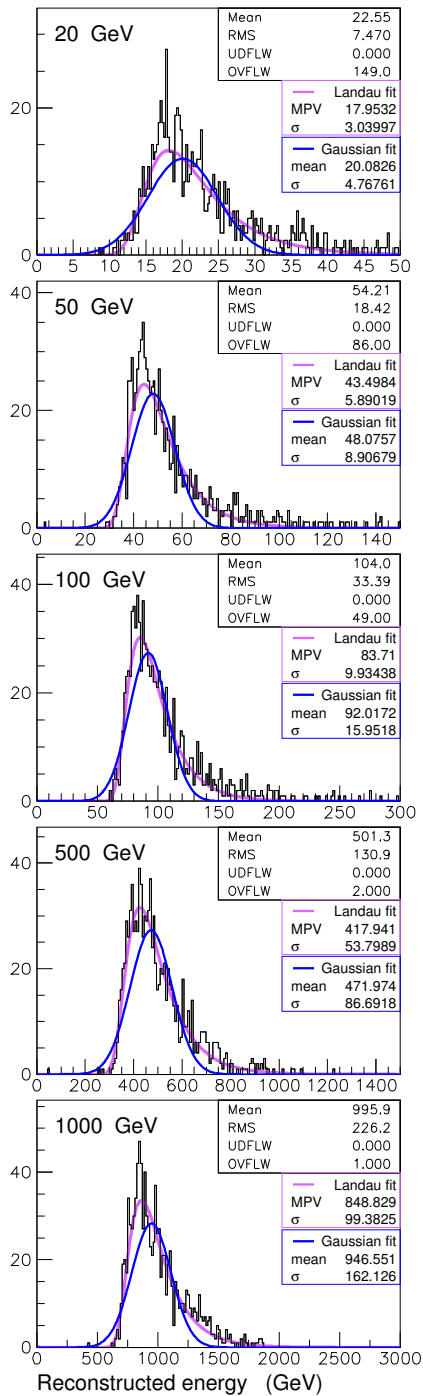


Figure 8.4: Distributions of the reconstructed energy for showers generated at 20, 50, 100, 500 and 1000 GeV showers (from top to bottom). Each distribution is fitted with a Landau function (purple curve) and a Gaussian function (blue curve). A total of 1000 showers are generated at each energy. The generated core position is (0,0) metres i. e. at the centre of the 4 telescope system.

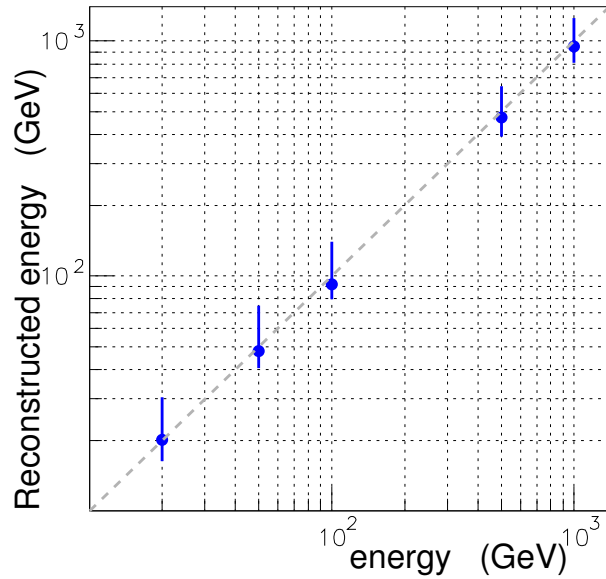


Figure 8.5: The reconstructed energy versus the generated energy of the showers. The reconstructed energy corresponds to the mean value of the Gaussian fit in figure 8.5 and the error bars correspond to the r. m. s. of the distribution above and below this mean value. The dotted line represents perfect energy reconstruction.

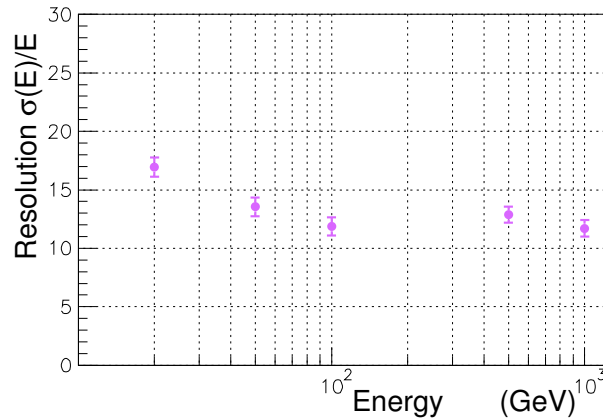


Figure 8.6: The energy resolution obtained from the Landau fit in figure 8.5 as a function of generated energy, for shower cores generated at the centre of the four telescope array.

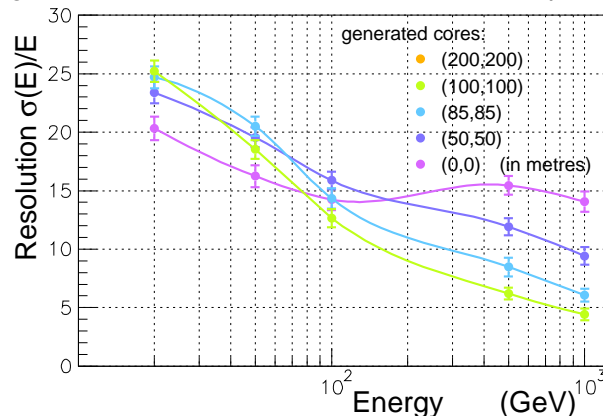


Figure 8.7: The energy resolution as a function of the generated energy for cores along the diagonal of the telescope array. The resolution is calculated from the Landau fit of reconstructed energy distributions. The lines joining the points on the plot are meant to guide the eye and do not have any physical significance.

In figure 8.7, we present the resolution obtained for other shower core positions along the diagonal of the telescope system (orange markers in figure 6.13). One sees a general trend towards improvement as the energy increases. Several factors affect the energy resolution: the fluctuations in the number of photo-electrons in shower images at that energy and distance, the precision on the reconstruction of the shower core, the precision on the reconstruction of the source position. We have already seen that there are fewer fluctuations in the number of photo-electrons at higher energies (figure 8.1 and section 8.1). Also, the energy reconstruction depends on the precision of the shower core reconstruction which in turn depends on the precision of source reconstruction. As both tend to improve with the energy, we see a general trend of improvement. One also notices that this improvement of the energy resolution with increasing energy is specially evident for shower core positions such as (50,50), (85, 85) and (100, 100) metres, i. e. away from the centre of the telescope centre. The resolution for the (0, 0) metres showers core (shown in violet) seems to vary very little with the energy. There is no obvious explanation for this result and this prompted us to further explore the dependence of the reconstruction on various parameters. We will be discussing this in the next sections.

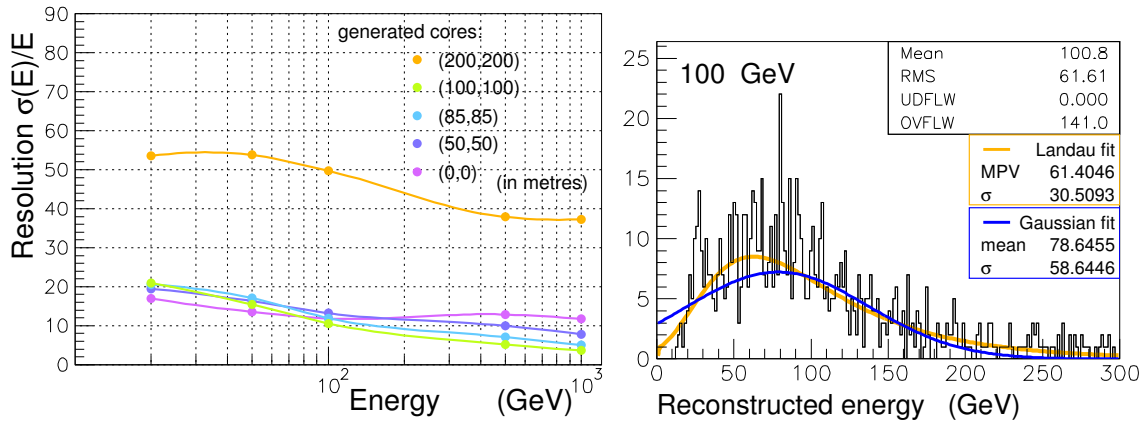


Figure 8.8: Left: the energy resolution for different core positions as a function of the generated energy. Right: The distribution of the reconstructed energy for 100 GeV showers generated with a core position of (200, 200) metres in the four telescope field.

The energy resolution for the core position (200, 200) metres does not appear on this plot as its value is above 30% for all energies. In figure 8.8 (left), we show another version of figure 8.7 with a larger vertical scale in order to show the resolution for this core position. The energy resolution degenerates sharply as the telescopes are well outside the Cherenkov ring. In order to illustrate the deterioration of the energy reconstruction at this core position, we also present the distribution of the reconstructed energies at 100 GeV so that it can be compared with the distribution in figure 8.4.

8.5 Discussion on various aspects of energy reconstruction

8.5.1 Giving different weights to the information from different telescopes

So far, we have evaluated the energy of a shower by first determining a value of energy from each telescope by using the number of photo-electrons in its image and then taking the mean of the energy values determined from all telescopes in this way. This implies giving equal weight to the energy reconstructed from each telescope. However, we know that the reliability

of the information available from a telescope depends on factors like the telescope distance from the shower core, the number of photo-electrons in the image... For instance, the number of photo-electrons in a telescope beyond the Cherenkov ring region will have a lower number of Cherenkov photons and will be less reliable for energy reconstruction. In figure 8.9 (left), we show a linear scale plot of one of the curves from the energy table (shown in figure 8.2) along with error bars corresponding to the r. m. s. of the distribution of the photo-electron number on each telescope. This gives us an indication of the fluctuations in the number of photo-electrons in shower images for various telescope distances. One notices that while the average number of photo-electrons tends to be highest when the telescope is close to the shower core, it is also in this region that the largest fluctuations in the number of photo-electrons occur. Consequently, the points closer to the Cherenkov ring are more reliable for energy reconstruction even if those closest to the shower core have larger mean values.

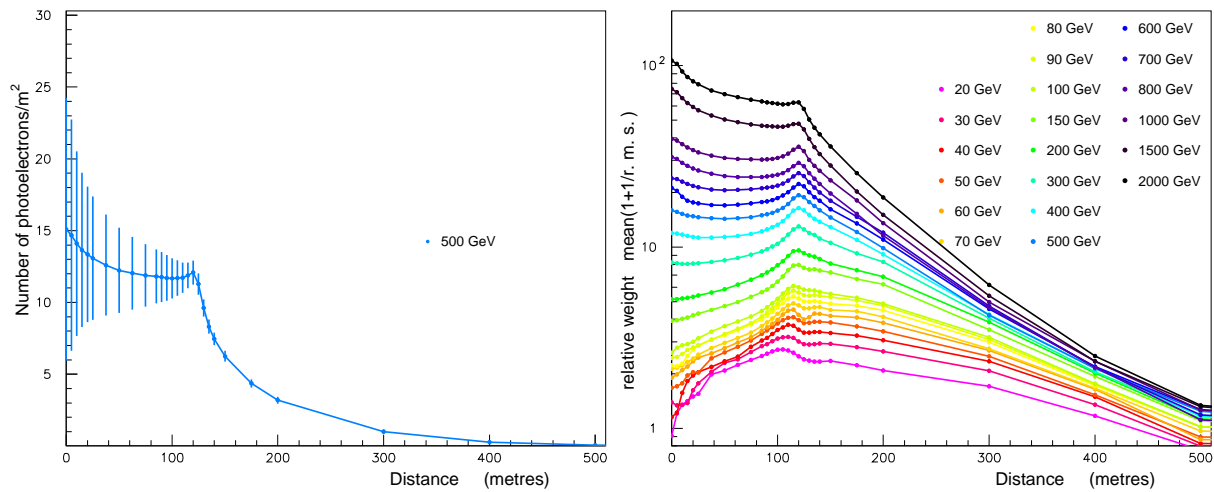


Figure 8.9: Left: The average number of photo-electrons in shower images as a function of telescope distance from the core for 500 GeV showers shown on a linear scale. The error bars correspond to the r. m. s. of the distribution of the number of photo-electrons. Right: Weights using the mean value of photo-electron numbers added to the fraction mean/r. m. s. for various energies as a function of the telescope distance from the shower core.

Keeping these points in mind we have tried two different approaches for giving weights to the information from different telescopes.

- **Approach 1:** The energy E_i calculated from the i^{th} telescope is given a weight proportional to the total number of photo-electrons N_i in the corresponding image. This implies that the information from various telescopes is weighed according to the curves given in figure 8.2.
- **Approach 2:** An additional factor N_i/f_i is added to the weight used in approach 1. f_i is the fluctuation on the number of photo-electrons in shower images of energy E_i obtained from telescopes at distance d_i from the core position. This factor diminishes the weight of the energy obtained from telescope positions that have large error bars in figure 8.9 (left). In order to compute the value of f_i at any energy and distance, a new table containing the r. m. s. values of the distributions of the number of photo-electrons at fixed energies and distances is computed and used. The weights given to the information from different telescope positions as a result of this approach are shown in figure 8.9 (right). Here we add that this approach is an attempt at taking the fluctuations at various positions into

account in a simple way. There may be other more appropriate ways to do this. This is suggested by the curves in figure 8.9 (right). One notes that these curves do not show the same trend at all energies. At higher energies, the information from the telescopes close to the core dominates in spite of the addition of the fluctuation term. On the other hand, at lower energies the information from the same telescopes has less weight than the one from the telescopes beyond the Cherenkov ring position at 120 m.

The energy resolution for various generated energies and shower cores obtained from the two methods described above are presented in figure 8.10. In both cases, the dependence of the resolution on the energy, for the core positions other than (0,0), diminishes in comparison to the resolutions presented in figure 8.7. We also see that the resolutions tend to be poorer for high energies (around 10% for 500 and 1000 GeV). These unexpected results and those presented in the previous section incited us to further investigate the parameters involved in energy reconstruction. We have, in particular, studied the photo-electron number distributions for various telescope positions. This will be presented in the next sections. In particular, we will find out that the reasons for the dependence of the fluctuations of the number of photo-electrons as a function of distance are physical. In the above, we have attempted a statistical solution for taking into account this aspect and seen that there is no simple way of dealing with this.

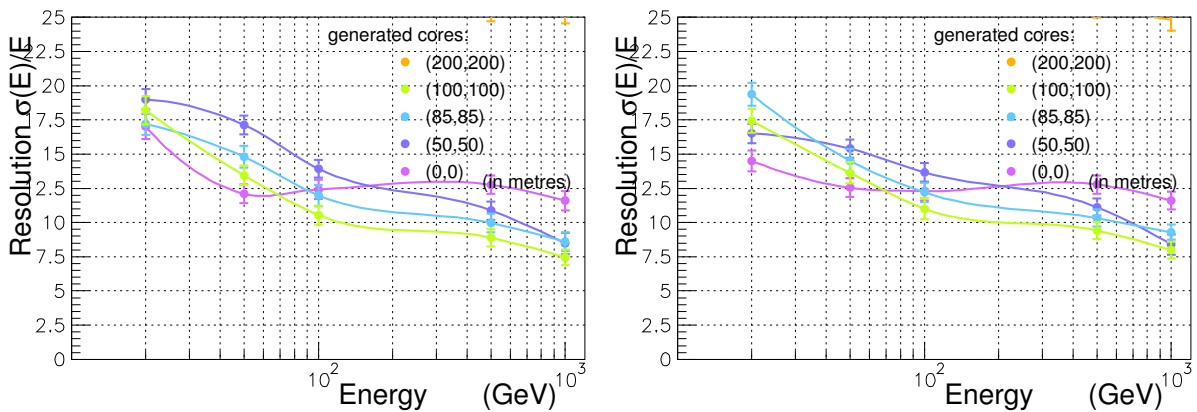


Figure 8.10: The energy resolution (obtained from Landau fits) for different shower core positions as a function of the generated shower energy. The left figure shows calculations carried out by weighing the information from different telescopes with the number of photo-electrons in the image. In the right image, an additional term corresponding to the ratio of the number of photo-electrons to the fluctuations (represented by the r. m. s. of photo-electron number for telescopes at this distance) is used for weighing the information from various telescopes.

8.5.2 The asymmetry of the number of photo-electron distributions in telescope images

We try to understand the results presented in the previous two sections by looking at the distributions of the number of photo-electrons obtained in shower images for a telescope at a fixed distance, in other words the distributions used to obtain the table of values for energy reconstruction shown in figure 8.2.

Figure 8.11 shows the distributions for 300 GeV showers at various distances from the shower core. The figure shows the following trends.

- The distributions tend to be asymmetric.
- The level of asymmetry depends on the distance of the telescope from the shower core. Distributions from telescopes near the shower core are highly asymmetric. A large number of events contribute to the main peak of values but there is also an important tail of events that tapers off towards larger values of numbers of photo-electrons per image.
- As the distance of the telescope from the core increases, this asymmetry diminishes. This occurs to the extent that the distributions for telescopes at distances of around 120 m are almost symmetric.
- At very large distances, not only does the average number of photo-electrons go down but the asymmetry tends to reverse itself; there appears a tail of events towards lower photo-electron number events.
- Similar trends are observed at all energies. The plots in figures 8.12 and 8.13 show the distributions of the number of photo-electrons in 30 and 1000 GeV shower images for various telescope distances. One notes, however, that for the 30 GeV plots, the distributions do not become symmetric even for telescopes at very large distances.
- These effects are more pronounced at high altitude. In figure 8.14, we present the same distributions for 1000 GeV showers at 3600 m. For distributions at other energies at 3600 m see appendix A.6.
- One also notes that this asymmetry of the distributions for telescopes close to the core is also responsible for the larger r. m. s. values (larger error bars in figure 8.9 (left)). While the main peak in each distribution is not much larger than for the distributions closer to

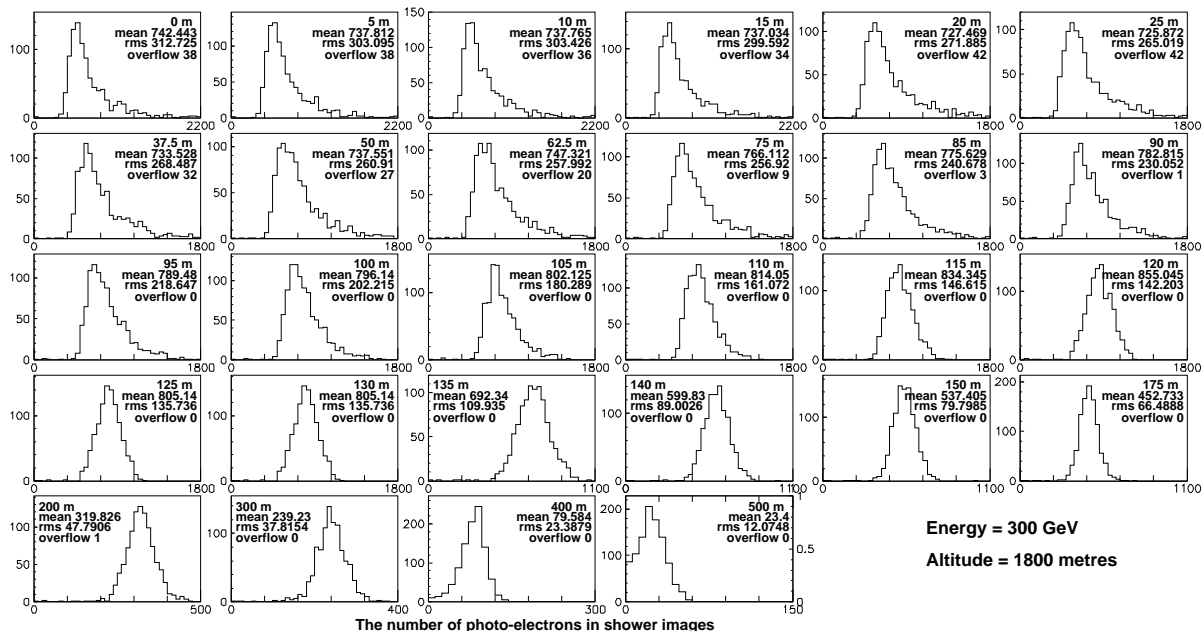


Figure 8.11: The distributions of the number of photo-electrons in 300 GeV shower images for different telescope positions. The position of the telescopes, the mean value and r. m. s. of the distribution and overflow of the histogram are shown on each plot.

the shower ring, it is the events in the tail i. e. those with a very large number of photo-electrons that increase the r. m. s. value for the curves. Note that the plots shown in figures 8.11, 8.12 and 8.13 have an increasing number of overflow events for telescopes closer to the shower core. While these events were used for the calculation of the r. m. s. presented through the error bars in figure 8.9 (left) they were not used for the calculation of the r. m. s. presented on each of these plots, leading to underestimated r. m. s. values.

The effect on energy reconstruction

This implies that the average value of the number of photo-electrons is in most cases larger than the most probable value of the distributions. The more asymmetric the distributions, the more pronounced will be this effect. In these cases, using the mean value of the distributions to compare with the number of photo-electrons obtained in a shower image will tend to yield underestimated values of the reconstructed energy. Moreover, since the level of asymmetry is different for distributions from telescopes at various distances from the shower core, the resulting offset in the reconstructed energy will be different for different telescopes. A correction for this systematic effect becomes all the more difficult. This may also explain the varying dependence of the energy resolution on the generated energy for different core positions. In fact, one can conclude from the above remarks that while the energy reconstruction method we have used yields a good estimate of the generated energy, when it comes to more precise comparisons, the results obtained from it must be used with care. This is particularly true when comparing the results at various core positions.

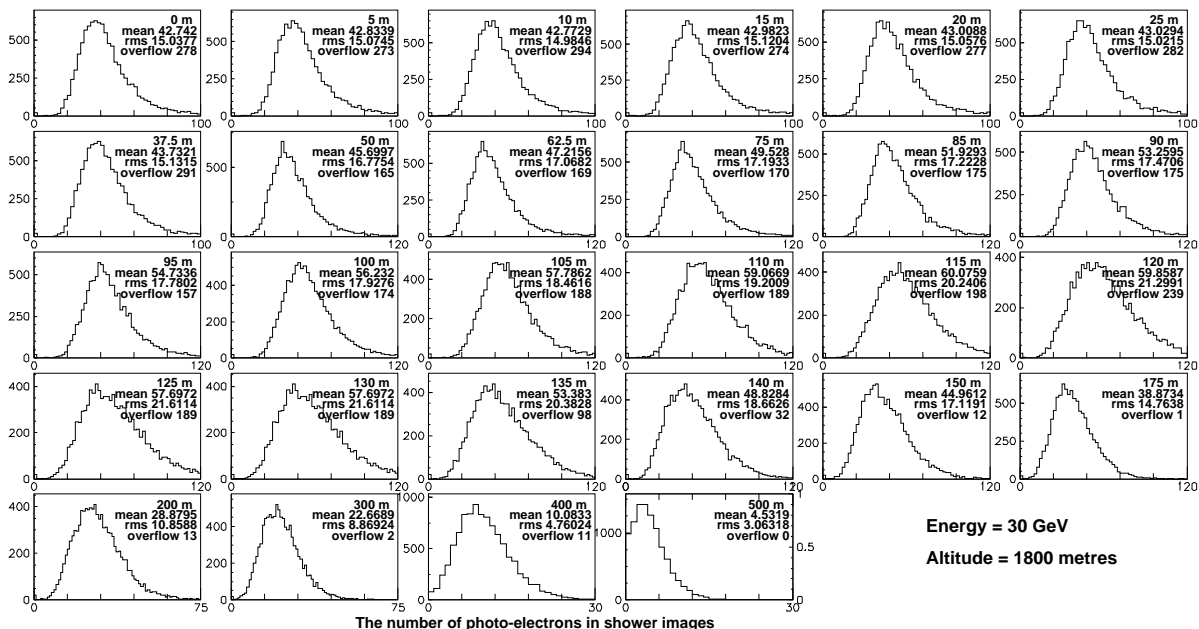


Figure 8.12: The distributions of the number of photo-electrons in 30 GeV shower images for different telescope positions. The position of the telescopes, the mean value and r. m. s. of the distribution as well as the overflow of the histogram are shown on each plot.

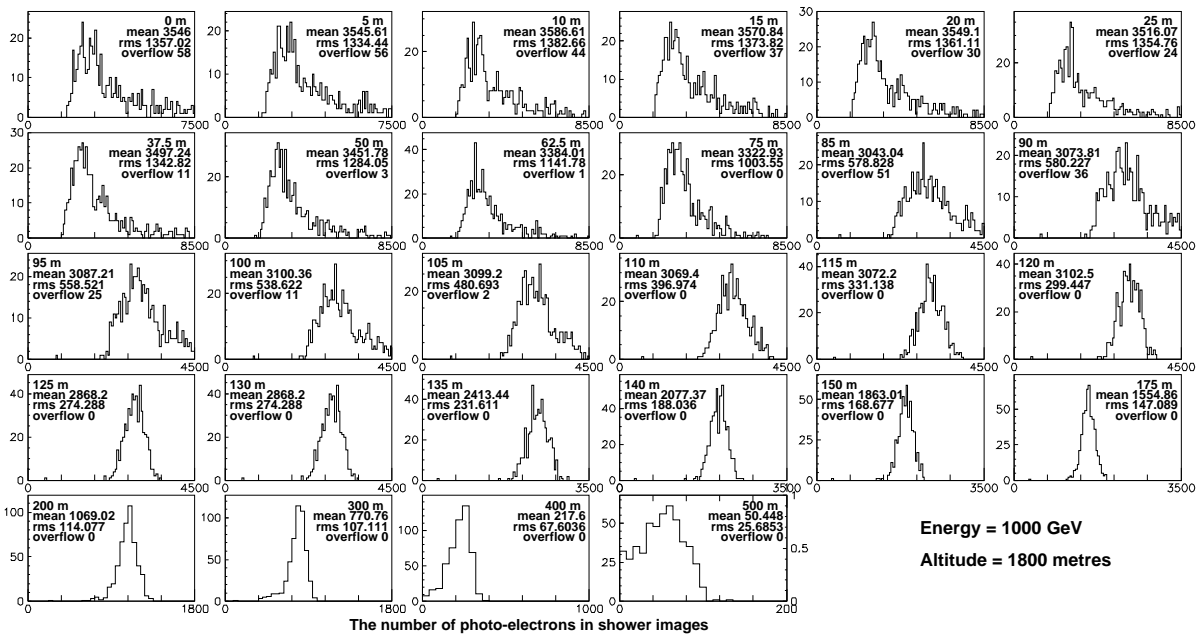


Figure 8.13: The distributions of the number of photo-electrons in 1000 GeV shower images for different telescope positions. The position of the telescopes, the mean value and r. m. s. of the distribution as well as the overflow of the histogram are shown on each plot.

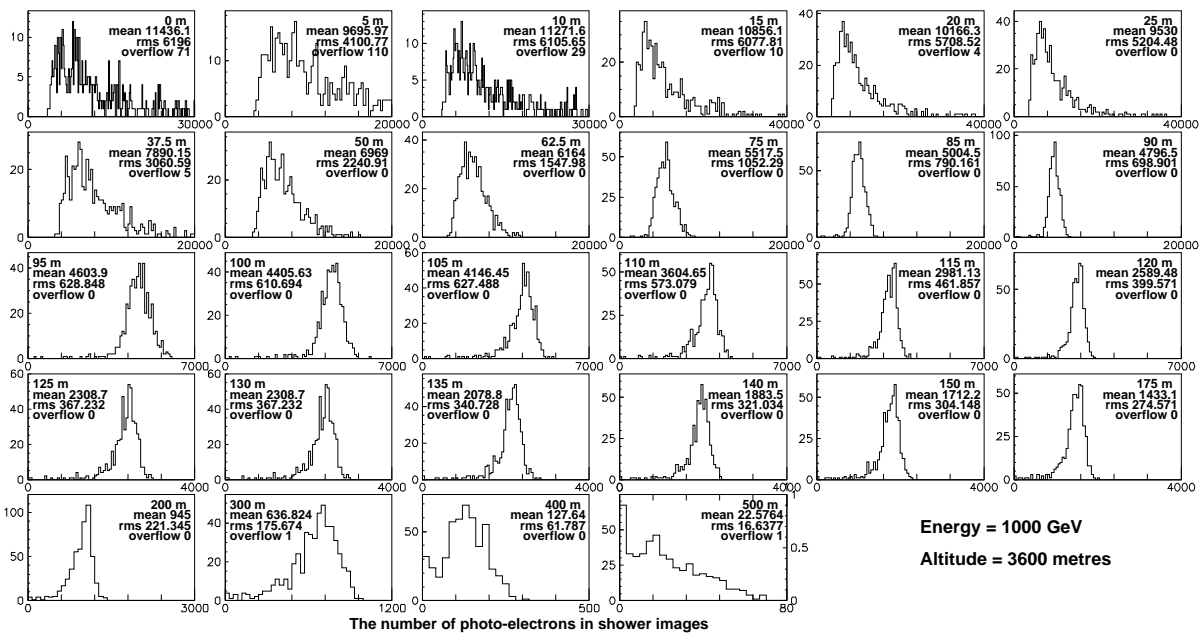


Figure 8.14: The distributions of the number of photo-electrons in 1000 GeV shower images for different telescope positions at 3600 m a. s. l.. Distributions for 30 and 300 GeV showers obtained at the same altitude of observation are given in figure A.6 of the appendix.

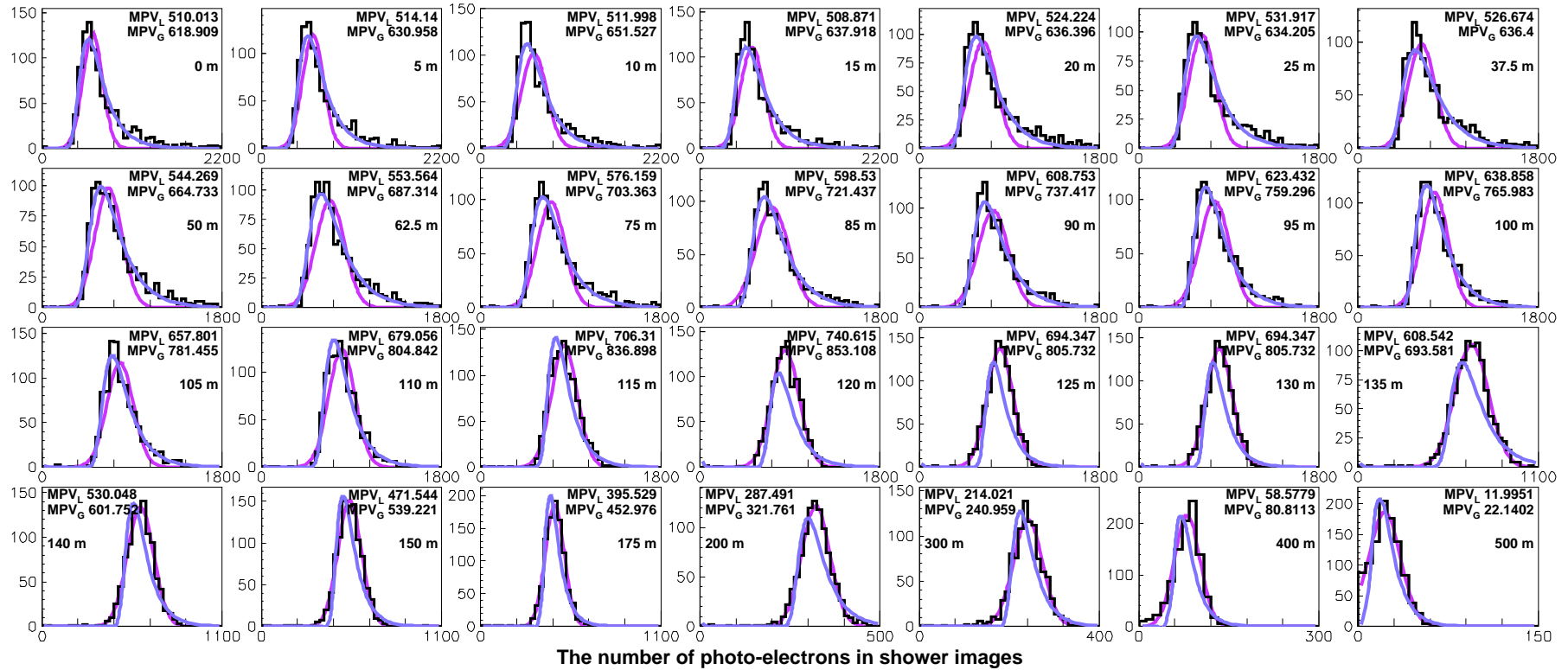


Figure 8.15: The distributions of the number of photo-electrons for 300 GeV shower images obtained from telescopes at various distances from the shower core are fitted with Landau (blue) and Gaussian (violet) functions. The values for the Most Probable Value obtained from the Landau fit and the mean of the Gaussian fit are also given on each plot.

8.5.3 Using most probable value tables for energy reconstruction

In view of the above remarks, we try to use the Most Probable value obtained from the photo-electron distributions instead of using the average number of photo-electrons.

Fits and value table

We fit the photo-electron number distributions with Landau and Gaussian functions. Figure 8.15 shows the fitted distributions for 300 GeV shower images. The blue curves correspond to the Landau fit and the violet ones to the Gaussian fit. The MPV from the Landau fit and the mean value from the Gaussian fit are also presented on the plots. These values are used to obtain new tables for the energy reconstruction. We present the table obtained from the Landau fit Most Probable Values in figure 8.16. One notes that in comparison with the mean value table presented in figure 8.2, the curves do not show a peak towards the core position even for high energy showers. In fact, the curves are almost flat within the Cherenkov ring region. Some of the distributions are harder to fit and result in irregularities in some of the curves, particularly at high energy, where fewer showers were generated to obtain these values. As with the mean value shown in figure 8.1, the dependence of the MPV obtained from the fits on the energy is linear. We show this in figure 8.17, where the MPV obtained from telescope images at 9 different distances is shown as a function of the energy. This means that the values of energy can be calculated by simple extrapolation of the values in the table for different photo-electron numbers obtained in telescope images as described in section 8.3. Also, although we have not

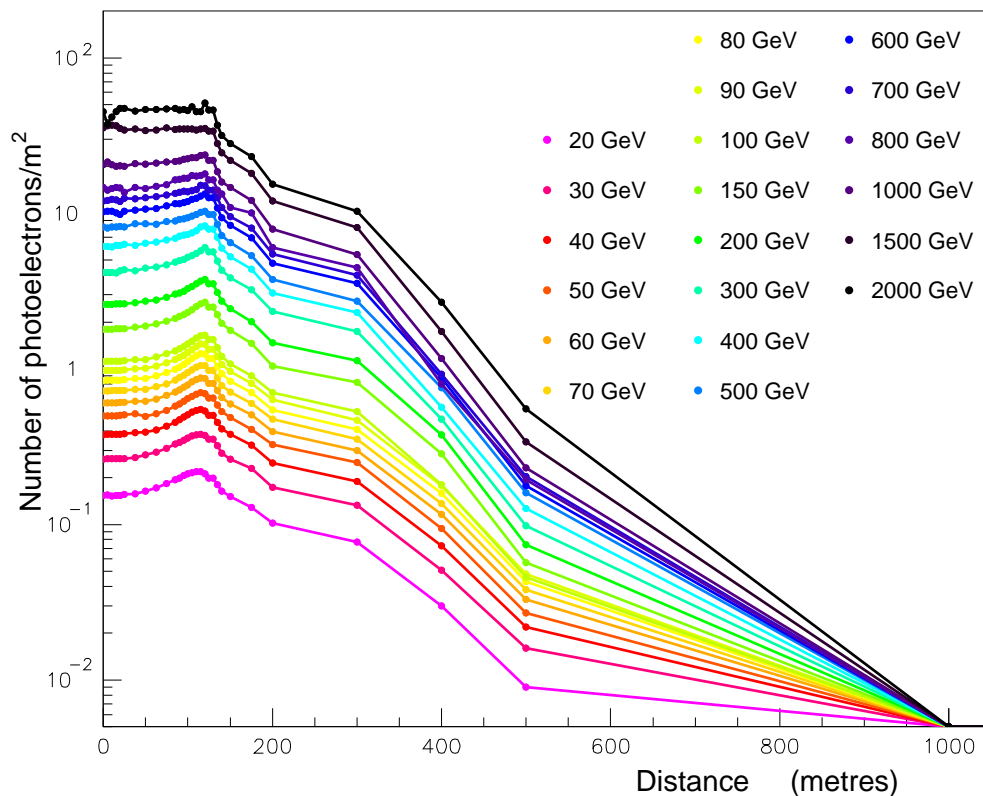


Figure 8.16: The most probable value of the number of photo-electrons in shower images as a function of the distance of the telescope from the core for various energies. The most probable value is obtained by fitting photo-electron number distributions by Landau curves.

done this for the results presented in the next section, this property can also be used to remove any irregularities in the table presented in figure 8.16.

Results

The results obtained from reconstructing the energy of 500 GeV showers through the use of the Landau fit MPV are presented in figures 8.18 and 8.19. In figure 8.18, we compare the energy resolution obtained for different shower cores by using the Landau fit MPV (centre and right plots) with the resolution obtained by using the mean value table (left plot). The use of the Landau MPV table with equal weight for the information from all telescopes (centre plot) does not have any significant impact on the resolution for the (0,0) m shower core (violet marker), while the resolution for the other core positions seem to deteriorate a little. When the information from different telescopes is weighed using the factor $N_i + N_i/f_i$ (right plot), the resolution for all core positions lie within the 10-12% range. While this means that the resolution for cores other than (0,0) m deteriorates, this also implies that the dependence of the resolution on the core position diminishes. In figure 8.19, we compare the most probable value of the reconstructed energy with the generated energy. This is done by fitting the distribution of reconstructed energies with a Landau curve (See the violet curves in figure 8.4 for an example) and plotting the ratio $(MPV - E_{gen})/E_{gen}$ in figure 8.19. When the mean value table is used for reconstruction (left), the MPV of the reconstructed energy tends to be lower than the generated energy. This is explained in the discussion concerning the effect of the asymmetry of the photo-electron number distributions presented on page 168. When the Landau MPV table is used to reconstruct the energy (centre and right) plots, then the reconstructed energy tends to be larger than the generated energy. This too can be explained on the basis of the asymmetric photo-electron distributions. Since the MPV value tends to be smaller than the average value of the photo-electron number, this implies that most of the reconstructed energies based on the number of photo-electrons in an image will be higher than the generated energy. When the information from all telescopes is given equal weight then the most probable values for the reconstructed energies for various cores lie within 20% of each other. The reconstructed energy is highest for the (0,0) m core ($\sim 15\%$ higher than the generated energy) and lowest for the (100,100) m core ($\sim 5\%$ lower than the generated energy). When the information from different telescopes is weighed through the factor $N_i + N_i/f_i$, then the MPV values of reconstructed energy from all shower cores tend to be higher than the generated energy and lie within 10% of each other. Once again, the reconstructed energy is highest for the (0,0) m core and lowest for (100,100) m core.

As with giving different weights to the information from various telescopes and using the mean value table (section 8.5.1), this method does not seem to show a major improvement. There is less difference in the energy resolution obtained for various shower cores (specially when the information for various telescopes is weighed) but at the same time the reconstructed energy tends to be overestimated with factors of up to 15 percent with respect to the generated energy. Underlying the issues with energy reconstruction, seems to be the asymmetric nature of the photo-electron distributions and the dependence of this asymmetry on the telescope position. In the next section, we will look into the physical causes of this asymmetry and suggest solutions for improving the energy reconstruction based on this understanding.

8.5.4 Link of the asymmetry with the altitude of first interaction in the shower

We begin by looking at the distribution of the number of Cherenkov photons emitted by a γ -ray shower and those arriving on the ground. Figure 8.20 shows the distribution of the number

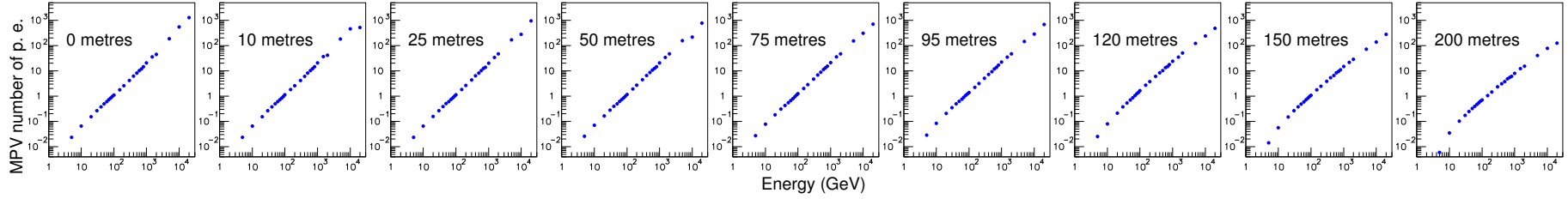


Figure 8.17: The most probable value of the number of photo-electrons as a function of the energy for telescopes at 9 different distances.

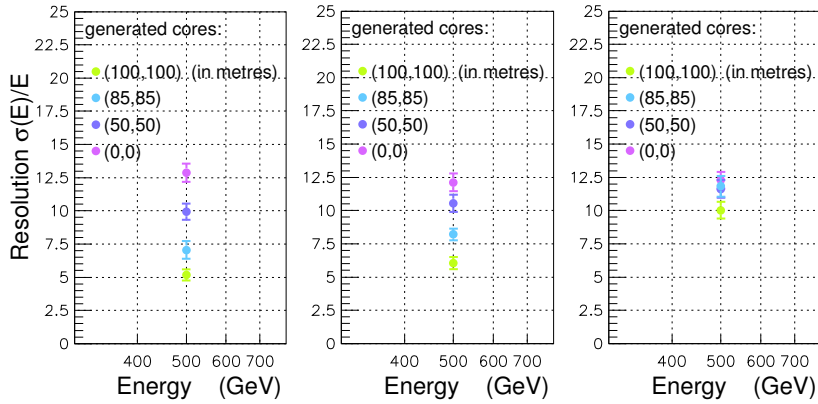


Figure 8.18: Comparison of the energy resolution for 500 GeV showers for three different methods. The left figure shows the resolution calculated by using the mean value table and giving equal weight to the information from all telescopes. The centre figure uses the MPV (Landau fit) table presented in figure 8.16 to reconstruct the energy and equal weight is given to the information from all telescopes. The figure on the right uses the same MPV curves for energy reconstruction but the information from various telescopes is weighed using the factor $N_i + N_i/f_i$ as described on page 165.

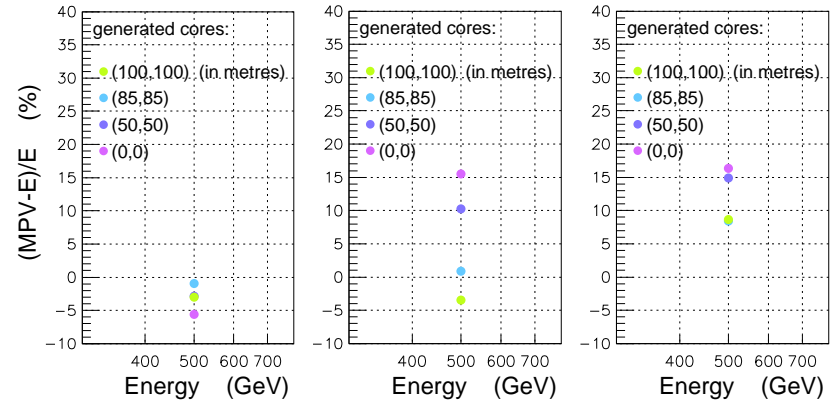


Figure 8.19: The distribution of reconstructed energies for one generated energy is fitted with a Landau curve to obtain the Most Probable Value (MPV). This value is then compared with the generated energy. The plots presented here represent the ratio $(MPV - E_{gen})/E_{gen}$ in percentage for 500 GeV showers for various core positions. For the left plot, the energy reconstruction is carried out by using the mean value table and equal weights for the information from all telescopes. The middle figure presents results for energy reconstruction carried out by using the MPV table from Landau fits with equal weight given to the information from all telescopes. The right plot uses the same MPV table but the information from each telescope is weighed by the factor $N_i + N_i/f_i$ as described on page 165.

of Cherenkov photons produced in 50, 300 and 1000 GeV γ -ray showers. Although the effect here is not as pronounced as for the photo-electron number distributions, these distributions too show a slight asymmetry. The principle reason for this asymmetry is the variation of the height of first interaction in different showers. This is shown in figure 8.21 where we plot the relationship between the altitude of first interaction (ordinate axis) and the number of Cherenkov photons emitted (abscissae axis) for 50 GeV showers. When the first interaction takes place low in the atmosphere, the number of Cherenkov photons produced tends to be larger. This occurs mainly because the number of Cherenkov photons produced per unit path length depends on the index of refraction of the air. We recall equation 3.3 from page 44:

$$\frac{d^2N}{dx d\lambda} = \frac{2\pi\alpha z^2}{\lambda^2} \left(1 - \frac{1}{\beta^2 \eta^2}\right) = \frac{2\pi\alpha z^2}{\lambda^2} \sin^2 \theta_c,$$

which gives the number of Cherenkov photons produced per unit path length per unit wavelength interval by a particle of charge ze . η is the refractive index of the material and $v = \beta c$ is the particle's velocity. The refractive index of the atmosphere at lower altitudes in the atmosphere is greater than at high altitudes where the atmosphere is rarer (see section 3.1). This implies that a similar track length for a charged particle at low altitude will emit more Cherenkov photons than it does at high altitude giving us an overall larger number of Cherenkov photons for showers that materialise lower in the atmosphere.

Moreover, the Cherenkov photons emitted lower in the atmosphere undergo less attenuation as they pass through fewer layers of the atmosphere. This implies that the effect of this asymmetry will be accentuated once the Cherenkov photons reach the ground. This is what

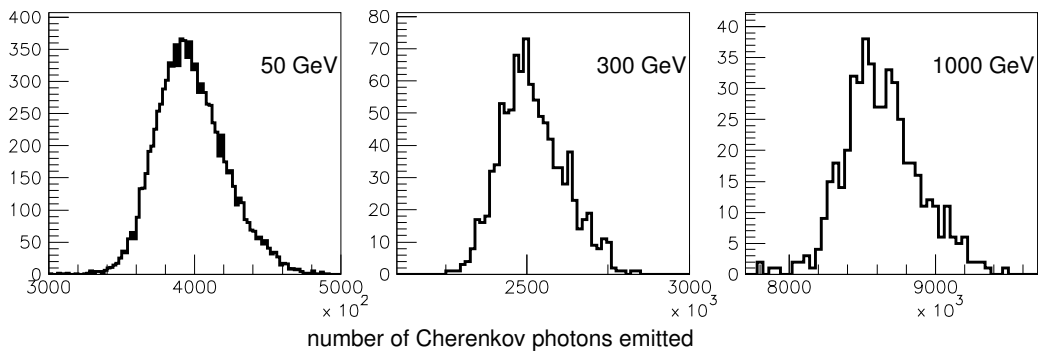


Figure 8.20: The distribution of the total number of Cherenkov photons emitted by showers of 50, 300 and 1000 GeV. Note that the simulated showers are the same as those whose photo-electron distributions are later shown in figure 8.25.

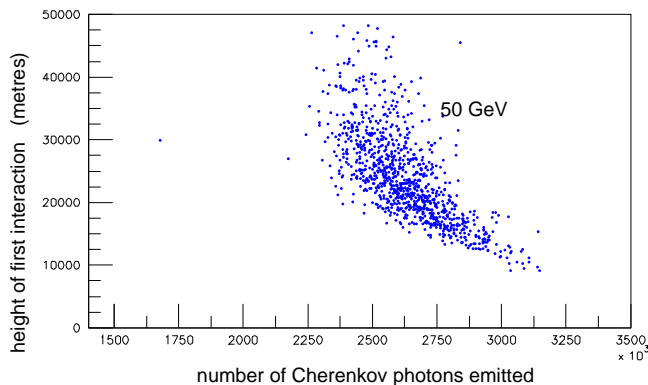


Figure 8.21: The relationship between the number of Cherenkov photons produced (abscissae axis) and the height of first interaction for 50 GeV showers.

we see in figure 8.22 where we present the distribution of the number of Cherenkov photons reaching the ground for the showers whose distributions were shown in figure 8.20. One not only sees that the overall number of Cherenkov photons diminishes in each distribution but also that their asymmetry is more pronounced. We also show the relationship between the number of Cherenkov photons obtained on the ground and the height of first interaction in figure 8.23. This confirms that lower altitudes of materialisation imply larger number of Cherenkov photons on the ground.

This provides us with an explanation for most of the characteristics concerning the asymmetry of the photo-electron number distributions on the telescopes. Showers that materialise low in the atmosphere will tend to have a larger fraction of their Cherenkov photons contribute to the image in telescopes near the shower core than those with higher altitudes of first interaction. This occurs because the Cherenkov photons emitted low in the atmosphere will travel shorter distances before they reach ground and will therefore have impact positions on the ground close to the shower core. On the other hand, the showers that develop higher in the atmosphere will have fewer Cherenkov photons that contribute to the images closer to the shower core and will be more likely to contribute in the images from telescopes away from the core. This implies that the asymmetry seen in figure 8.22 will be even further emphasized in telescopes closer to the core position. At the same time, the asymmetry will lessen as one moves away from the shower core, as fewer Cherenkov photons from low materialising showers will contribute to the images.

One sees an illustration of this in figure 8.24, where we show the relationship between

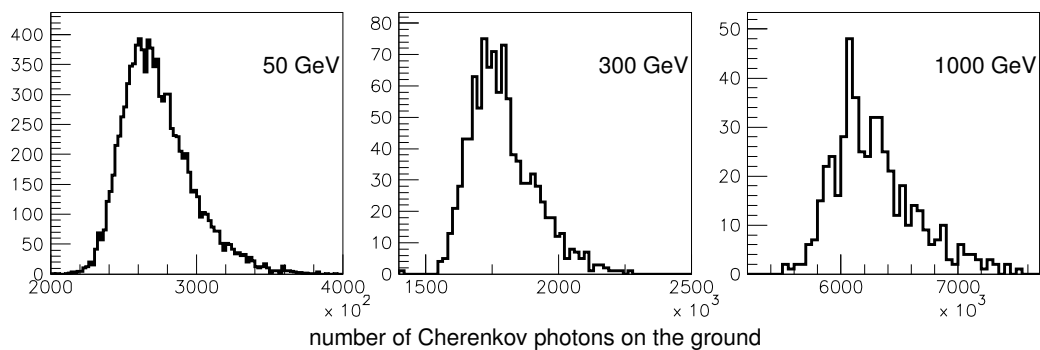


Figure 8.22: The distribution of the total number of Cherenkov photons arriving on the ground for showers of three different energies. The showers are the same as those whose distributions are shown in figure 8.20 and later in figure 8.25. The altitude of observation is 1800 metres above sea level

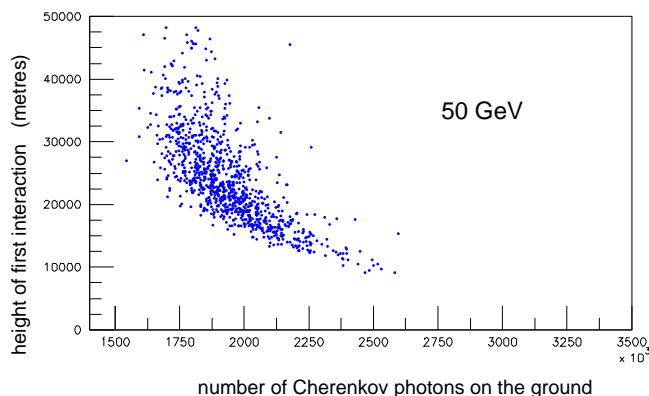


Figure 8.23: The dependence of the number of Cherenkov photons arriving on the ground on the height of first interaction for the same 50 GeV showers.

the number of photo-electrons in telescope images (abscissae axis) and the total number of Cherenkov photons on the ground (ordinate axis). As the number of Cherenkov photons on the ground is related to the height of first interaction in a shower, this also gives us the relationship between the number of photo-electrons in shower images and the height of first interaction. We also show the distributions of the number of photo-electrons for the corresponding telescopes and energies in figure 8.25. The plots show that the showers with a larger number of Cherenkov photons on the ground, and hence lower altitude of first interaction, contribute to the tail of larger values in the photo-electron number distributions. As the distance of the telescopes from the core increases, the correlation between the two quantities diminishes. This is specially true for higher energies. This corresponds to distributions that are less asymmetric. We also recall that at higher energies, the showers are larger and tend to develop closer to the ground. In some cases (specially when the first interaction occurs low in the atmosphere), this implies that part of the shower gets cut off by the ground. In this case, the telescopes close to the core position still receive a larger amount of Cherenkov light, but at larger distances they receive lesser light than with showers with higher altitudes of first interaction. One can see a hint of this trend, in the last few plots of the 300 GeV and 1000 GeV showers in figure 8.24. This behaviour is specially apparent in the last plot for 1000 GeV showers where it leads to an inversion of the asymmetry of the photo-electron number distribution.

These properties are accentuated at higher altitude where more showers get cut off before full development. Figures 8.26 and 8.27 show similar distributions for showers at 3600 m. The inversion of the asymmetry is visible for the 300 GeV and 1000 GeV distributions.

One also notes that the asymmetry of the photo-electron number distributions and through it the altitude of first interaction is also related to the r. m. s. of the distributions. As we saw earlier in the discussion, while the most probable value of the distributions for the telescopes close to the core position remains low, the mean value and the r. m. s. are larger than for the points closer to the Cherenkov ring. Here we can link the large mean and r. m. s. values to the presence of low materialising showers.

8.5.5 Possible solution for improving the reconstruction of energy

We have seen, through the discussion in the previous sections, that the uncertainty in the reconstruction of the energy specially when comparing different shower cores, mainly arises due to the varying asymmetry of photo-electron number distributions. We have also seen that this asymmetry is mainly linked to one physical parameter i. e. the altitude of first interaction of the primary γ -photon in the atmosphere and that attempts to deal with this aspect through statistical means do not give satisfactory results.

One way of dealing with this problem while reconstructing the energy would be by adding another parameter (related to the height of first interaction or the longitudinal development of showers in the atmosphere) to the tables used for the reconstruction of the energy. In section 8.7, we will see how one can reconstruct the longitudinal profile of showers from the individual pixels in a shower image. One can then use the reconstructed longitudinal profiles to obtain an estimation of the position of the maximum of shower development. The energy of the shower can then be estimated by using a table of values depending on the energy, distance of the telescope from the shower core and shower maximum in the atmosphere.

8.6 Conclusion and remarks on the limitations of the method

The method for the reconstruction of energy (as it is currently implemented) exploits the link between shower energy and the number of photo-electrons obtained in a telescope image at a

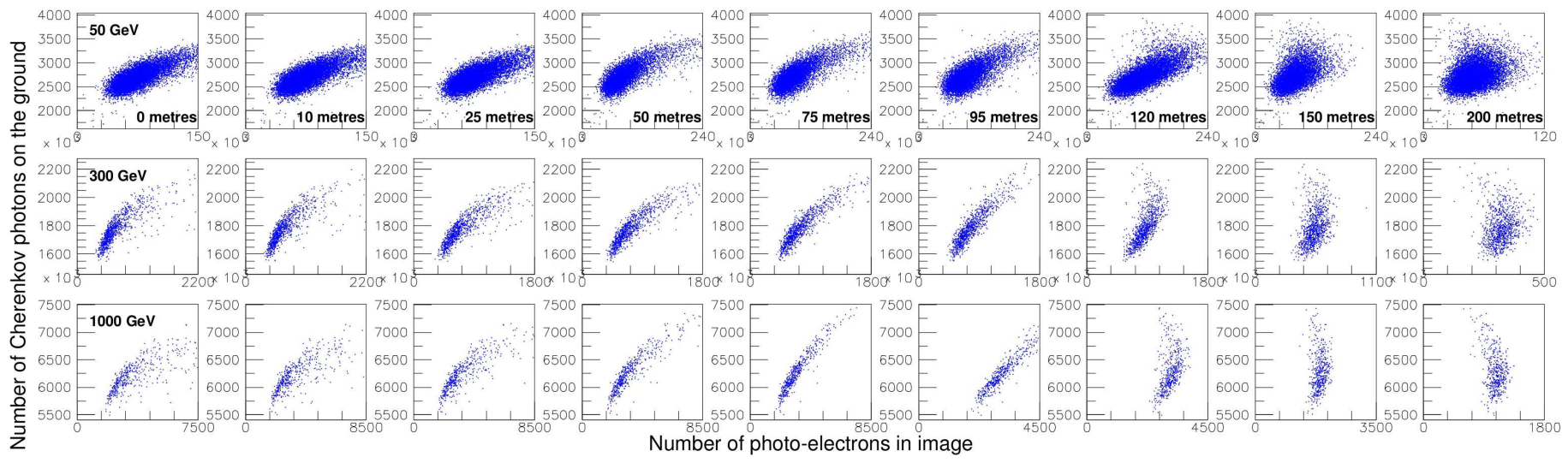


Figure 8.24: The relationship between the total number of Cherenkov photons arriving on the ground at 1800 m (ordinate axis) and the number of photo-electrons in shower images obtained from telescopes at 9 different distances from the shower core. The three rows correspond to 3 different shower energies i. e. 50, 300 and 1000 GeV.

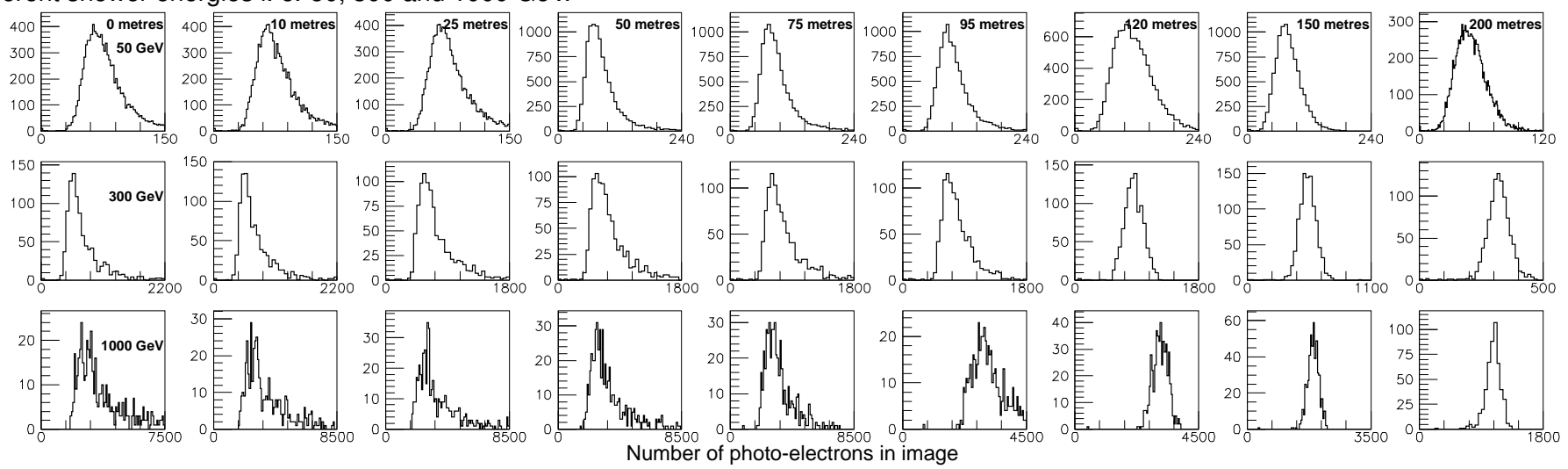


Figure 8.25: The distribution of the number of photo-electrons in the image obtained by a telescope situated at 9 different distances from the core position. The three rows correspond to 3 different shower energies namely 50, 300 and 1000 GeV.

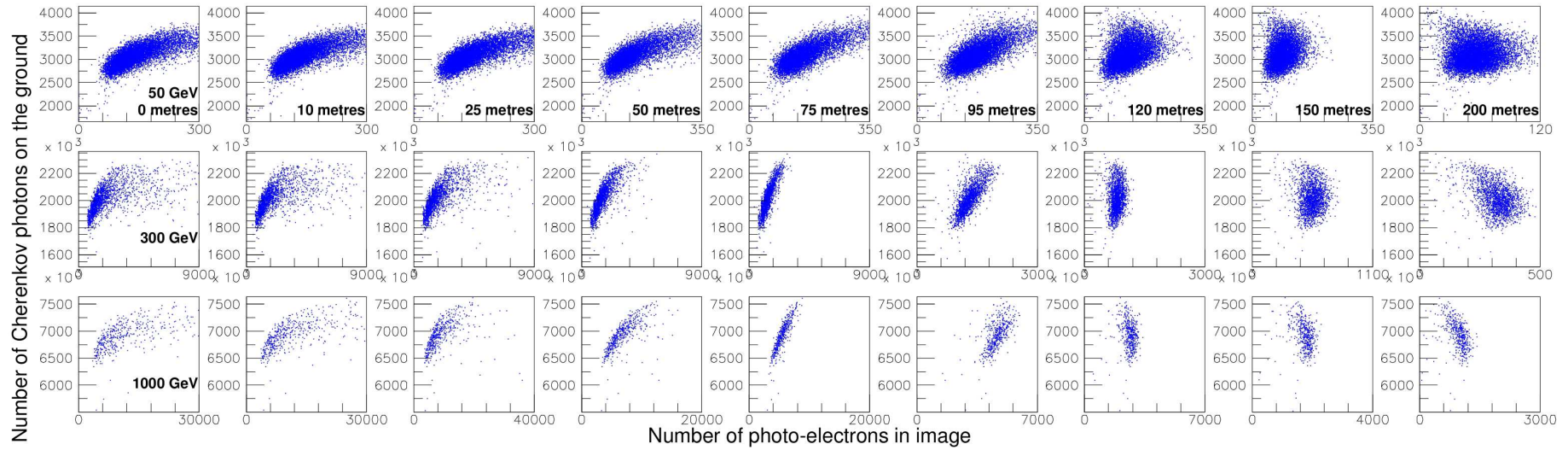


Figure 8.26: The relationship between the total number of Cherenkov photons arriving on the ground at 3600 m (ordinate axis) and the number of photo-electrons in shower images obtained from telescopes at 9 different distances from the shower core. The three rows correspond to 3 different shower energies namely 50, 300 and 1000 GeV.

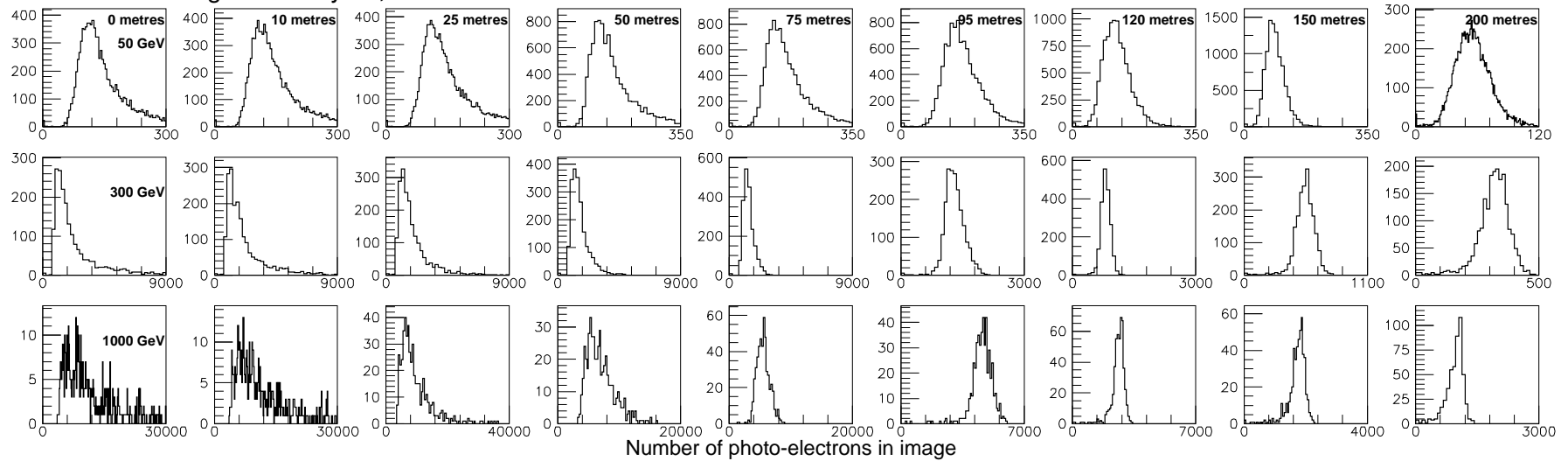


Figure 8.27: The distribution of the number of photo-electrons in the image obtained by a telescope situated at 3600 m a. s. l. for 9 different distances from the core position. The three rows correspond to 3 different shower energies namely 50, 300 and 1000 GeV.

given distance in a simple way and has several limitations.

- The method needs to be modified in order to be applied to showers with zenith angle other than 0° . As we saw in chapter 3, for inclined showers, the distribution of the Cherenkov photons on the ground is elongated in the direction tangential to the shower. In that case, the number of photo-electrons obtained at a given distance for a given energy is different depending on whether the telescope is in the tangential direction to the shower inclination or the transverse direction. One way of applying this method to inclined showers would be to evaluate the degree to which the usual circular pattern of the Cherenkov photon flux on the ground is elongated as a function of shower zenith angle. Once the source position in the sky and the shower core position on the ground is determined they can be used to evaluate the number of Cherenkov photons expected for each telescope position from the curves shown in figure 8.2.

As all the studies presented in this thesis has been done with showers with 0° zenith angle, we have not implemented or tested this method.

- The method necessitates extensive simulations in order to obtain the curves in figure 8.2. Ideally, this work needs to be done for each type of telescope used (focal length, diameter, field of view etc.) and each altitude of observation. In practice, one can use the curves generated with telescopes of one diameter for working with telescopes of different diameters as long as the telescope field of view remains the same and the difference between the diameters is not very large (e.g. several times larger telescopes). The amount of photo-electrons per metre² obtained with two different diameter telescopes with same field of view at the same position can be quite different for a single shower due to the fluctuations. However, one expects this difference to even out when averaged over a large number of showers. The use of the same curves for all telescope sizes may introduce a small error, but one expects this error to be compatible with the overall level of precision achieved with this method.
- If the method is to be implemented using the maximum of shower development as a parameter for the table of reconstruction then extensive simulations need to be carried out in order to obtain the required value table and this has not been implemented for the present work. In its current form, the method can be used to obtain a good estimation of the energy of a γ -ray shower and evaluate the performance of a detector. It has, however, shown that it is not reliable when comparing the results for various telescope positions. The results obtained from it should therefore be used only as an indication of the performance of the telescope, with the potential for corrections due to other effects.

8.7 Reconstruction of the longitudinal profile and Cherenkov photon trajectories

The images obtained from the telescopes contain information about the longitudinal and lateral development of the shower. We have seen in earlier chapters that the arrival position of a Cherenkov photon on the camera depends (among other parameters) on its point of emission in the atmosphere. This implies that by using the position of the pixels on the camera to back track the trajectory of Cherenkov photons in the atmosphere, one can reconstruct the longitudinal profile of the shower as well as other information about its spatial development. Here we describe such a method and present its application to simulated showers.

Figure 8.28: Schematic description of the reconstruction of the Cherenkov photon trajectory.

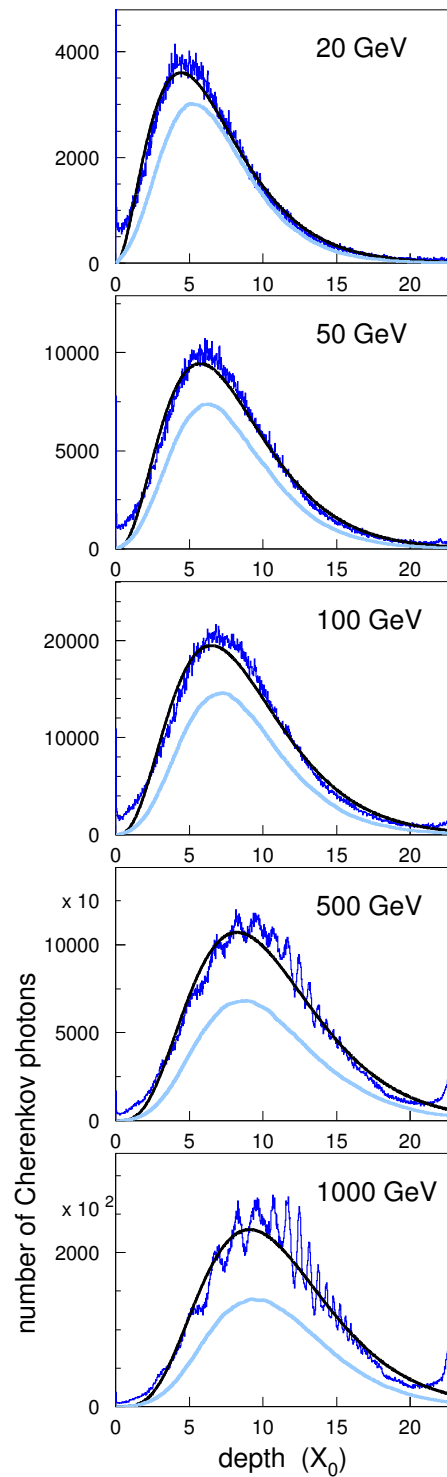
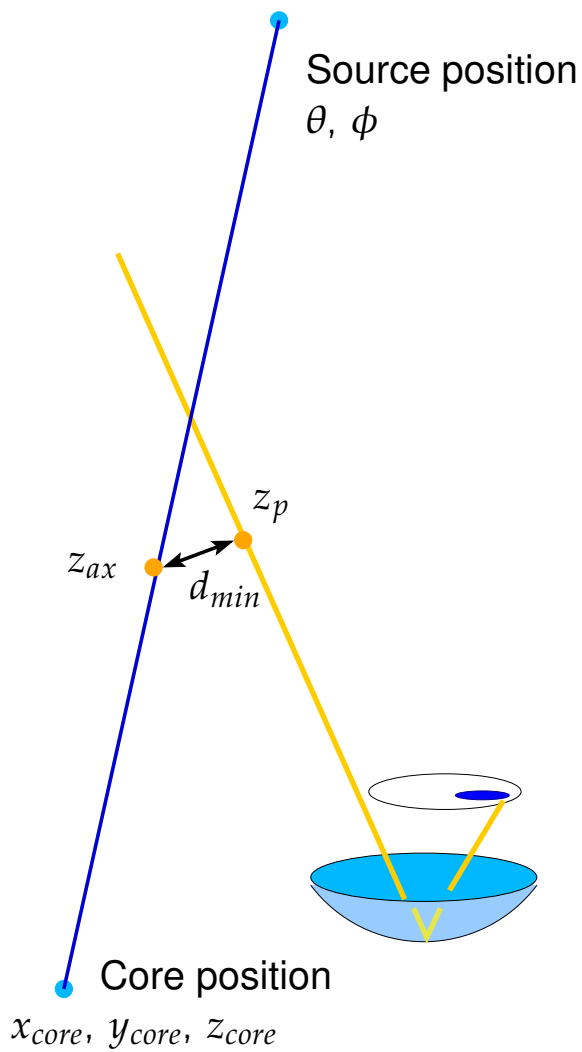


Figure 8.29: The average reconstructed longitudinal profiles obtained for γ -ray showers of different energies (dark blue). The profiles are fitted with the function $f(t) = C(\beta t)^{\alpha-1} e^{-\beta t}$ (black line). The generated longitudinal profiles are also shown through the light blue curves.

8.7.1 The method

An illustration of the method is given in figure 8.28. The trajectory of the Cherenkov photon is reconstructed by assuming reflection from the centre of the mirror and ignoring coma aberration. Knowing the impact position of the Cherenkov photon on the camera (from the position of the photomultiplier) and assuming that it was reflected by the mirror centre (or parabola vertex), one can evaluate the direction cosines of the incident Cherenkov photon. These direction cosines along with the position of the centre of the camera give a fully defined line in 3-dimensions corresponding to the reconstructed trajectory of the photon. In order to evaluate the point of emission of the Cherenkov photon, the smallest distance d_{min} of the reconstructed photon trajectory with respect to the reconstructed shower axis is calculated. This is possible since the shower axis is fully known after the reconstruction of the core position on the ground and the source. This gives two points as possible point of emission: the two extremities of the line segment joining the shower axis and the photon trajectory when they are closest to each other. The results we have obtained show that the use of either point gives similar longitudinal information. When this process is repeated for every Cherenkov photon contributing to a shower image, the coordinates of all the reconstructed points of emission can be used to obtain information about shower morphology and in particular the longitudinal profile.

A note on the reflection of photons by the mirror centre As we discussed in chapter 6, the rays from a point source at infinity are parallel when they arrive on the telescope and get focused (ignoring coma aberrations) on the focal plane to form an image of the source. If the source is nearer to the observer then the plane in which images are focused is displaced beyond the focal plane and away from the mirror. As the maximum of shower development occurs around 10 km a. s. l. for the average electromagnetic shower, the camera position of IACT telescopes are displaced so as to be on the focal plane for sources located at 10 km. Since Cherenkov emission occurs for several kilometres in the atmosphere and that the position of shower maximum may vary from shower to shower, this implies that in general Cherenkov photons from different altitudes are incident on the telescope camera. The Cherenkov photons contributing to the signal in one pixel are, therefore, not necessarily emitted from the same point. The method described above, however, implies that they will be reconstructed as having been emitted from the same point. This difference between the reconstructed points are often negligible for most cases but they can be quite important if the telescope position is close to the shower core where a small difference in the orientation of the Cherenkov photon trajectory can imply a significant difference in the reconstructed altitude of emission.

8.7.2 Reconstructed longitudinal profiles

As mentioned above, the reconstruction of the point of emission of individual photo-electrons can be used to evaluate the longitudinal profile of the showers. We have reconstructed the longitudinal profiles of simulated showers of different energies based on the images obtained from the four telescope system described on page 110. Here, we present the average profile reconstructed for these showers in figure 8.29. The generated average longitudinal profiles are also presented in the plots for comparison's sake. As can be seen, the profiles are, on the average, well reconstructed. This method is given here in order to indicate a method for the reconstruction of longitudinal profiles. Further work needs to be done in order to apply this method to energy reconstruction or γ -hadron discrimination (see chapter 9). We also note the importance of having as large a number of photo-electrons as possible in order to obtain

exploitable profiles for individual showers. This once again underlines the importance of determining telescope configurations to increase the number of photo-electrons per shower for low energy showers. The impact of pixel size, visible in the high energy profiles (500 GeV and 1000 GeV), on the accuracy of the reconstructed longitudinal profile in general, and the precision of the reconstruction of the shower maximum in particular, needs to be further explored.

CHAPTER 9

IDEAS FOR GAMMA-HADRON SEPARATION

9.1 Introduction

Like γ -photons, when hadrons enter the Earth's atmosphere, they interact with its molecules and produce a cascade of secondary particles. The main processes involved are different from those intervening in electromagnetic showers. As a result hadronic showers have different average properties than γ -induced showers. They also constitute a source of noise for γ -ray observations. γ -ray astronomy therefore relies greatly on the identification of γ -ray induced showers and the rejection of hadronic showers. This ability to extract a γ -ray signal from the background determines the detector's sensitivity to sources of various intensities.

In this chapter, we will begin by giving a brief description of hadron induced atmospheric showers and their morphology. We will also give examples of shower images obtained for hadrons and compare them with γ -ray shower images.

In the second part of this chapter, we will recall the method for the reconstruction of the longitudinal profile of showers (presented in chapter 8) and the methods for the source and core reconstruction (presented in chapter 7). We will show how the parameters obtained from these methods can provide means of discrimination between hadrons and γ -rays.

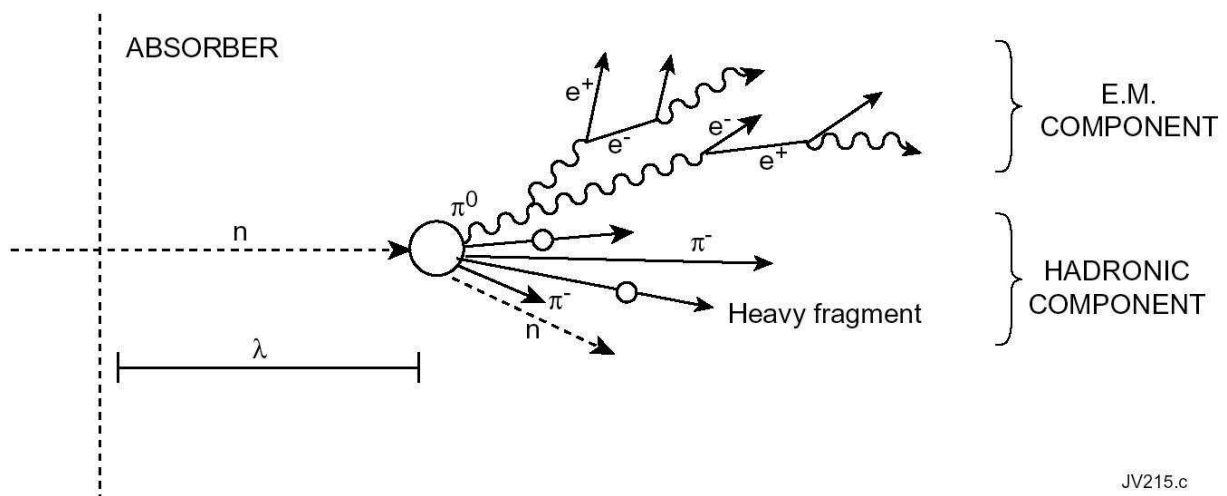


Figure 9.1: Schematic description of a hadronic shower. The figure is taken from [42].

9.2 Hadronic showers and their images

9.2.1 Hadronic shower development

When a high energy hadron undergoes inelastic interactions after entering the earth's atmosphere, it initiates a shower of particles. Secondary particles include hadrons such as neutrons, protons, kaons, pions, nuclei as well as muons and neutrinos from pion decay. The secondaries themselves interact hadronically and the result is a cascade of particles. The main characteristics of hadronic showers include the following.

- The process is characterised by the mean free path of inelastic nuclear interactions also known as the nuclear interaction length λ_I . For air (STP conditions), $\lambda_I=90 \text{ gm/cm}^2$. This length is about 2.5 times greater than the radiation length ($X_0=36.66 \text{ gm/cm}^2$) characterising electromagnetic interactions in air. This implies that, on the average, hadronic showers reach deeper in the atmosphere than electromagnetic showers. For a hadron entering the Earth's atmosphere vertically, this gives an average altitude of materialisation around 17 km a. s. l. in the U. S. standard model. One notes that this effect is not as pronounced as in other denser materials used for calorimeters in high energy physics experiments. For example, in lead, the nuclear interaction length is about 30 times larger than the radiation length while in iron this ratio is closer to 10.
- While the nuclear interaction length gives the average altitude of materialisation for hadronic showers, this position can have very large fluctuations for hadronic showers.
- An important part of the initial energy is used to break up the nuclei itself. This effect combined with other losses such as those due to excitation, backscattering... implies that the observable energy in hadronic showers is lower than for same energy electromagnetic showers.
- The processes involved in hadronic showers are more complex than those in electromagnetic showers and result in larger fluctuations.
- A large number of the secondaries are often neutral pions which disintegrate rapidly into two γ -photons. These γ -photons are responsible for the production of electromagnetic sub-showers. This is illustrated schematically in figure 9.1. The weight of this electromagnetic component can fluctuate a lot from shower to shower. The presence of these electromagnetic sub-showers is an important reason for the hadronic showers' constituting a source of background for γ -ray showers.
- While the lateral spread of an electromagnetic shower mainly occurs due to multiple scattering through small angles, in hadronic showers the nuclear interactions have an important impact on the lateral profile and result in a wider spread of the shower.

These properties are illustrated in figure 9.2 where ten proton induced showers of 500 GeV are shown. The showers are obtained through the track plotting option of CORSIKA. These can be compared with the 500 GeV γ -ray showers shown in section 2.3. Figure 9.3 also compares the general behaviour of 500 GeV proton (left) and γ -ray (right) showers by superposing 10 showers of each type. One sees more important fluctuations and the presence of sub-showers in the hadronic showers. The overall shape tends to be less streamlined than for electromagnetic showers. One can also notice the similarities (elongated shape) of the central dense region in both cases. This similarity also results in hadron induced showers being a source of background for γ -ray observations.

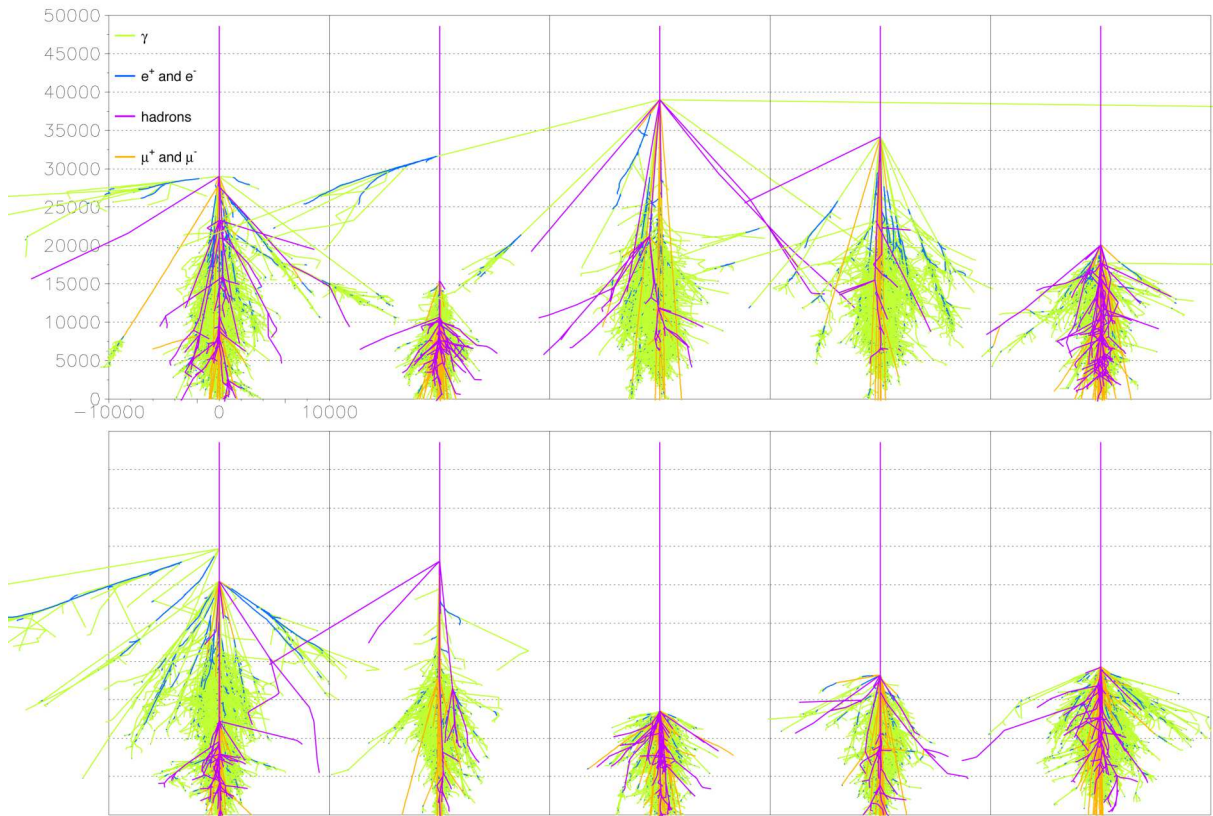


Figure 9.2: 10 different proton-initiated showers of 500 GeV. The units of the vertical and horizontal axes are metres.

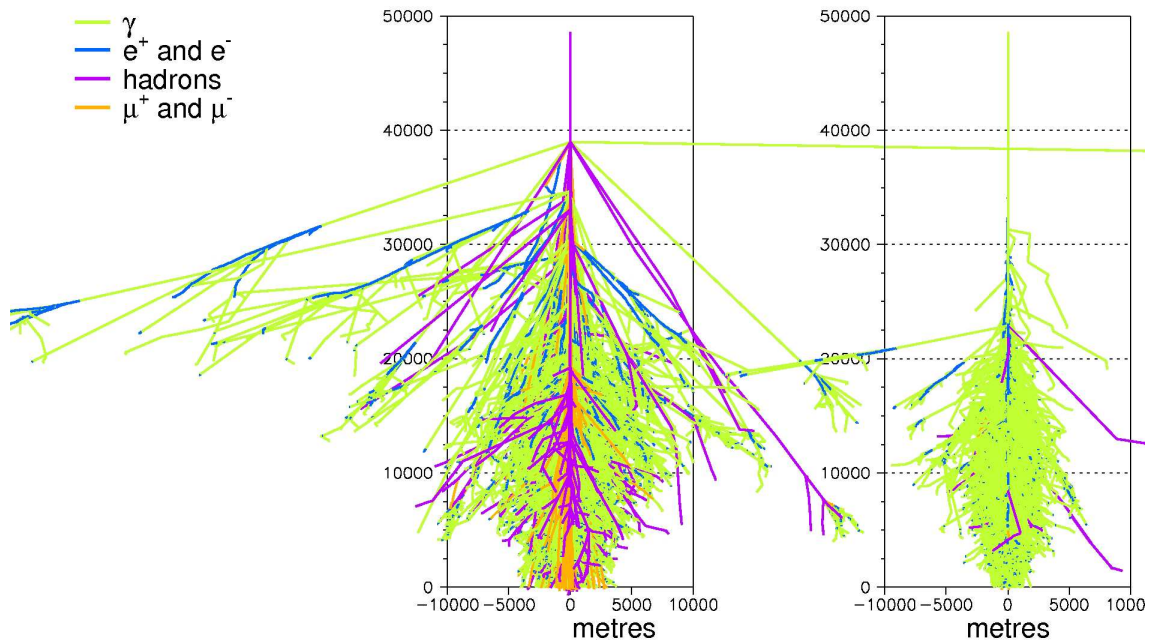


Figure 9.3: The comparison of 500 GeV hadronic (left) and γ -ray (right) showers. Each image is obtained by superposing 10 different showers in order to obtain the averaged morphology of showers.

9.2.2 Cherenkov photon production and density on the ground

As in electromagnetic showers, when the charged particles in hadronic showers have velocities that are higher than the velocity of light in the atmosphere, they emit Cherenkov photons. As we mentioned before, a part of the initial hadron energy is lost to processes that produce no visible signal. This implies that less Cherenkov light is emitted by hadronic showers than by electromagnetic showers of the same energy. We show this in figure 9.4 which compares the number of Cherenkov photons in γ -ray and proton showers. One can see that in order to obtain a similar number of Cherenkov photons, the proton energy needs to be ~ 2.5 times greater than the photon energy.

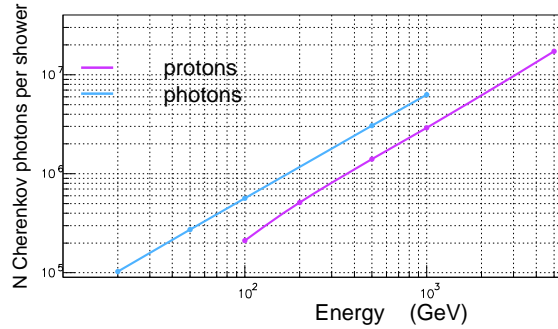


Figure 9.4: Comparison of the average number of Cherenkov photons arriving on the ground in proton (violet) and γ -ray (blue) showers. The quantum efficiency of the photomultipliers and the mirror reflectivity are also taken into account in both cases, in order to compare the number of photons capable of contributing to shower images.

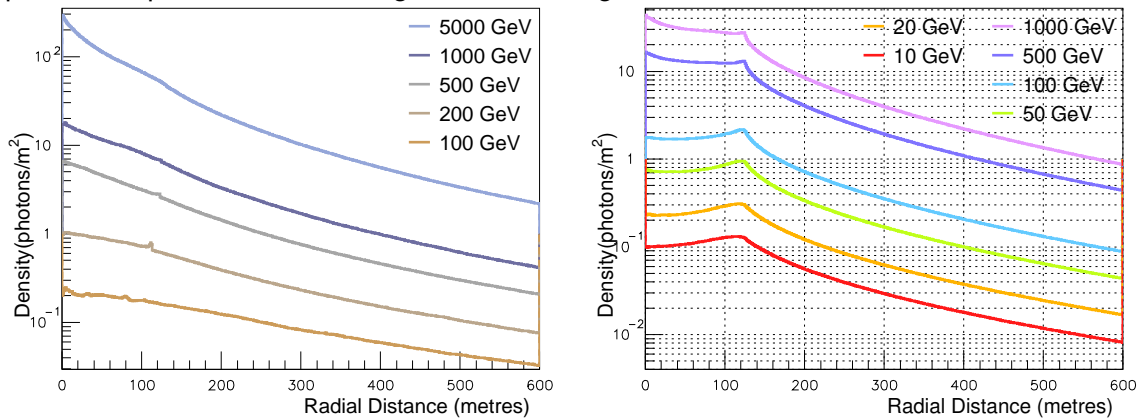


Figure 9.5: The average density of Cherenkov photons on the ground (expressed in photons per m^2) at 1800 m altitude as a function of the distance from the shower core for protons (left) and photons (right) of various energies. The fluxes are convoluted with the quantum efficiency of photomultipliers and reflectivity of mirrors.

This effect is also visible on the density of Cherenkov photons obtained on the ground. Figure 9.5 compares the density of the Cherenkov photons as a function of the distance from the shower core for various energies of protons and γ -rays. The density of photons obtained from hadronic showers is lower than from γ -ray showers of the same energy. There is also an important difference between the shape of the profiles on the ground. While γ -ray showers give a clear ring shaped pattern, the large amount of fluctuations and larger width of hadronic showers imply that no single ring like pattern emerges from the distribution.

As examples of the Cherenkov density patterns observed in proton induced showers, we show the Cherenkov photon density from 500, 1000 and 5000 GeV showers in figure 9.6. Unlike the density pattern obtained for γ -ray showers (see for example figure 3.11), the Cherenkov photons are distributed in several ring like structures on the ground as well as localised density spikes and other irregularities. These features are the result of the irregularity of the shower itself, the presence of muons in the shower, subshowers and Cherenkov photon radiating charged particles arriving on the ground. The charged particles arriving on the ground are responsible for sharp localised peaks while the ring like structure usually occur due to the presence of electromagnetic subshowers and secondary muons.

A muon interacts very little in the atmosphere and usually follows its path till it reaches the ground. As a charged particle, it radiates Cherenkov photons all along its path and produces a circular pattern with a sharp peak at the centre similar to the idealised pattern presented in figure 3.10. The Cherenkov photon density distribution on the ground for a 100 GeV muon is shown in figure 9.7.

When the irregular patterns observed in figure 9.6 are averaged over a large number of showers this tends to give the smooth profiles with a higher density towards the core position obtained in figure 9.5.

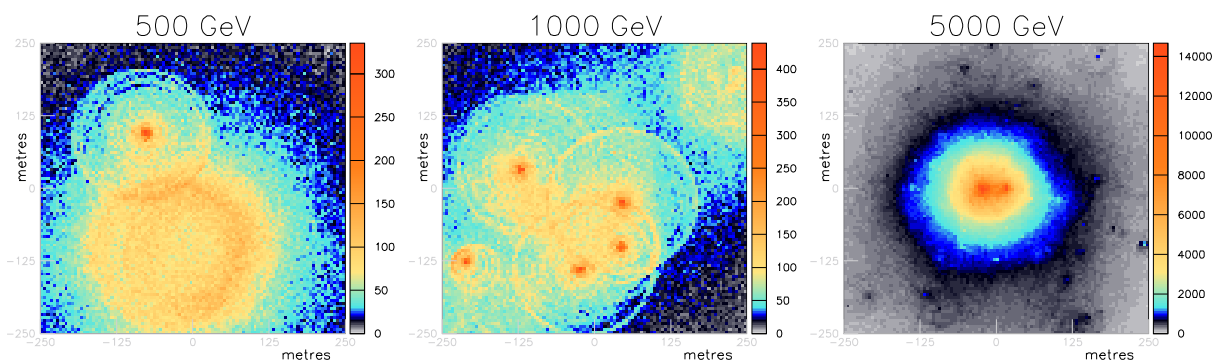


Figure 9.6: The figures show the Cherenkov photon distributions on the ground (1800 metres altitude above sea level) for three simulated proton induced showers of 500, 1000 and 5000 GeV. A surface area of $500 \times 500 \text{ m}^2$ is shown in each plot.

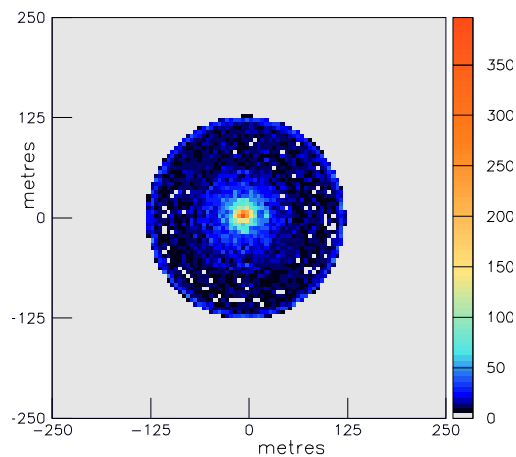


Figure 9.7: The figure shows the Cherenkov photon distribution on the ground obtained from a 100 GeV muon at an altitude of 1800 metres above sea level. A total surface area of $500 \times 500 \text{ m}^2$ is shown in the plot.

9.2.3 Hadron shower images

The fluctuations in hadronic showers and the Cherenkov light emitted by them are also reflected in their images. In figure 9.9, we present the images obtained from three different proton induced showers by telescopes at nine different distances from the core position at an altitude of 1800 m. The first row shows the images from a 500 GeV shower. The images do not have a well defined shape and contain at least two different bunches of pixels. The overall photo-electron number is low due to the relatively low energy of the shower.

The second and third rows in figure 9.9 show the images obtained from 5000 GeV proton showers. The plots in the second row have irregular images with several bunches in the first few telescopes. Beyond 75 m, the main bunch seen in the first few images becomes elongated due to the distance of the telescope from the core. It also has a more regular and well defined shape, and starts resembling a γ -shower image. This illustrates the importance of stereoscopy in γ -ray observations; while the shower images obtained from one region can resemble γ -shower images, a large number of these events can be rejected upon cross-checking with the images obtained from other telescopes. We also notice a ring-like structure (blue-green pixels) due to a secondary muon in the first few images. Muon rings will be discussed through the example in the third row.

The third row shows the images from another 5000 GeV shower. The dominant features in these images are an elongated main emission region on the right and a ring like structure towards the centre. The ring is the result of a secondary muon produced in the shower. The features of single muon images are illustrated through figure 9.8. As mentioned earlier, a muon interacts very little in the atmosphere and radiates Cherenkov photons all along its trajectory following the schematic description given in figure 3.10. This gives a circular distribution of Cherenkov photons on the ground. As the Cherenkov photons arriving on a telescope at the impact position of the muon have similar zenith angles, this results in their getting distributed in thin ring-like structure on the camera. As the telescope position is shifted from the impact position, the camera only views Cherenkov photons arriving on one side of the impact position which results in the ring's getting cut off. At large distances, beyond 100 m, only a very small portion of the ring is viewed (a few pixels large). At the same times, the image is larger in the longitudinal direction. This occurs because Cherenkov photons from various altitudes (hence with various zenith angles) overlap by arriving at this distance (see figure 3.10). For observations at 1800 m a. s. l. this overlap is greatest around 120 m from the core position.

The images obtained at such positions tend to resemble those from γ -showers. In the images shown in figure 9.9, the images can not be mistaken for those from a electromagnetic shower due to the presence of other features. However, when secondary muons from hadronic showers are relatively isolated, they can represent a source of noise for γ -observations. This problem too reflects the importance of stereo-imaging. While one may obtain γ -like images on one telescope, the event can be rejected by looking at the images from telescopes at other positions.

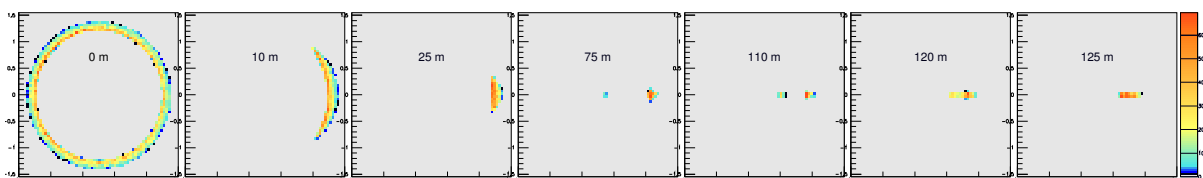


Figure 9.8: The images of a muon obtained from telescopes at various distances from the muon impact position on the ground. A smaller than usual pixel size of 0.05° has been chosen in order to emphasize the image morphology.

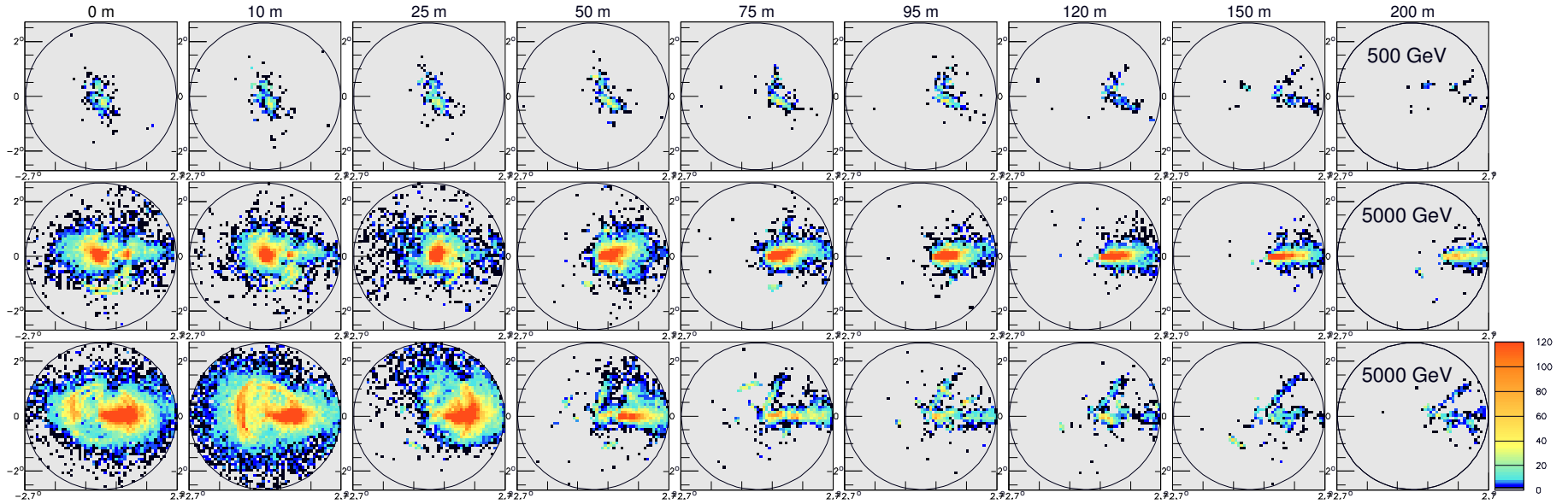


Figure 9.9: The images of three proton showers obtained from telescopes placed at 9 different distances from the core positions. The first row corresponds to a shower of 500 GeV and the other rows to two different showers of 5000 GeV.

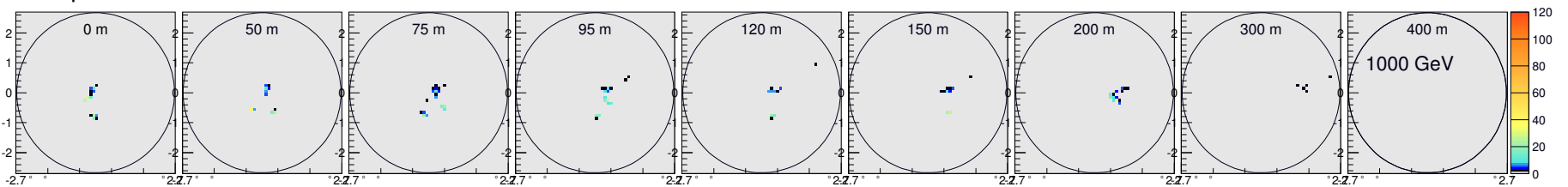


Figure 9.10: The images of a 1000 GeV proton shower obtained by telescopes at nine different distances from the shower core at 1800 a. s. l. . The shower is shown in figure 9.12.

In order to illustrate the diversity of hadron based showers we also present the images from three 1000 GeV showers. The images of the first shower, obtained from nine telescopes at different positions are presented in figure 9.10. All the images given here have very few photo-electrons. When one looks at the distribution of the Cherenkov photons on the ground (figure 9.11), one sees that instead of having a central region where most of the light from the shower is deposited, the densest regions of Cherenkov light distribution are several circular structures scattered far apart. The left plot shows three ring like structures due to the presence of muons. The densest region is circular and is partially cut off in the left plot while being clearly apparent in the centre plot. It is located around (130,-260) metres and may indicate the presence of a sub-shower. The right most plot also indicates the presence of other denser regions scattered at distances of hundreds of metres. We also look at the morphology of the shower through the particle trace plot in figure 9.12. The particularity of this shower is reinforced by the high altitude of first interaction in the atmosphere ~ 34 km a. s. l.. As a result the various particles from different parts of the shower get to travel larger distances before being absorbed or reaching the ground. The features on the ground are therefore spread out over a larger area. As an illustration of how telescopes in different positions can give different images we also show the images from four telescopes positioned close to the densest region of Cherenkov photons on the ground in figure 9.13. The images have a roughly elongated shape that resembles those for low energy γ -ray showers. The longitudinal axes of the images points towards the centre of the dense region in the ground frame of reference. This is the illustration of another way in which hadronic showers are a source of background for γ -ray observations.

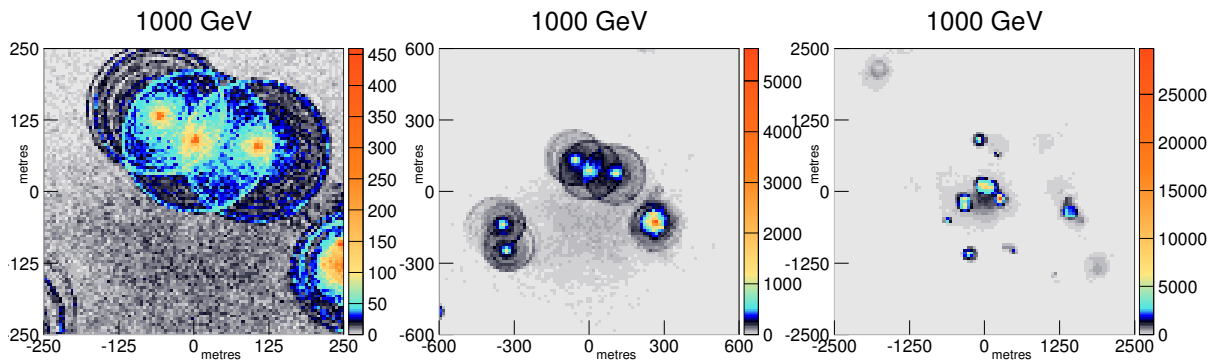


Figure 9.11: The distribution of the Cherenkov photons on the ground from the shower shown in figure 9.12. The three plots correspond to different levels of zoom. The surfaces shown are $500 \times 500 \text{ m}^2$ (left plot), $1200 \times 1200 \text{ m}^2$ (centre plot) and $5000 \times 5000 \text{ m}^2$ (right plot) with the shower core at the centre of each plot.

In contrast, we show the images from two showers with relatively low altitudes of materialisation in figure 9.14. The traces of the particles in the first shower and its Cherenkov photon distribution on the ground is shown in figure 9.15. The first interaction in the atmosphere takes place around 15 km a. s. l. and part of the shower is cut-off by the ground. We have mentioned before that hadronic showers tend to have wider lateral profiles, but also that like with other parameters, there can be very large fluctuations in the lateral spread as well. The shower shown in figure 9.15 has a relatively narrow width. The result of this factor combined with the low altitude of materialisation is an almost circular Cherenkov photon density pattern on the ground, where most of the Cherenkov photons are deposited within a couple of hundred metres from the core position. The images resulting from this shower have a large number of photo-electrons with several denser regions.

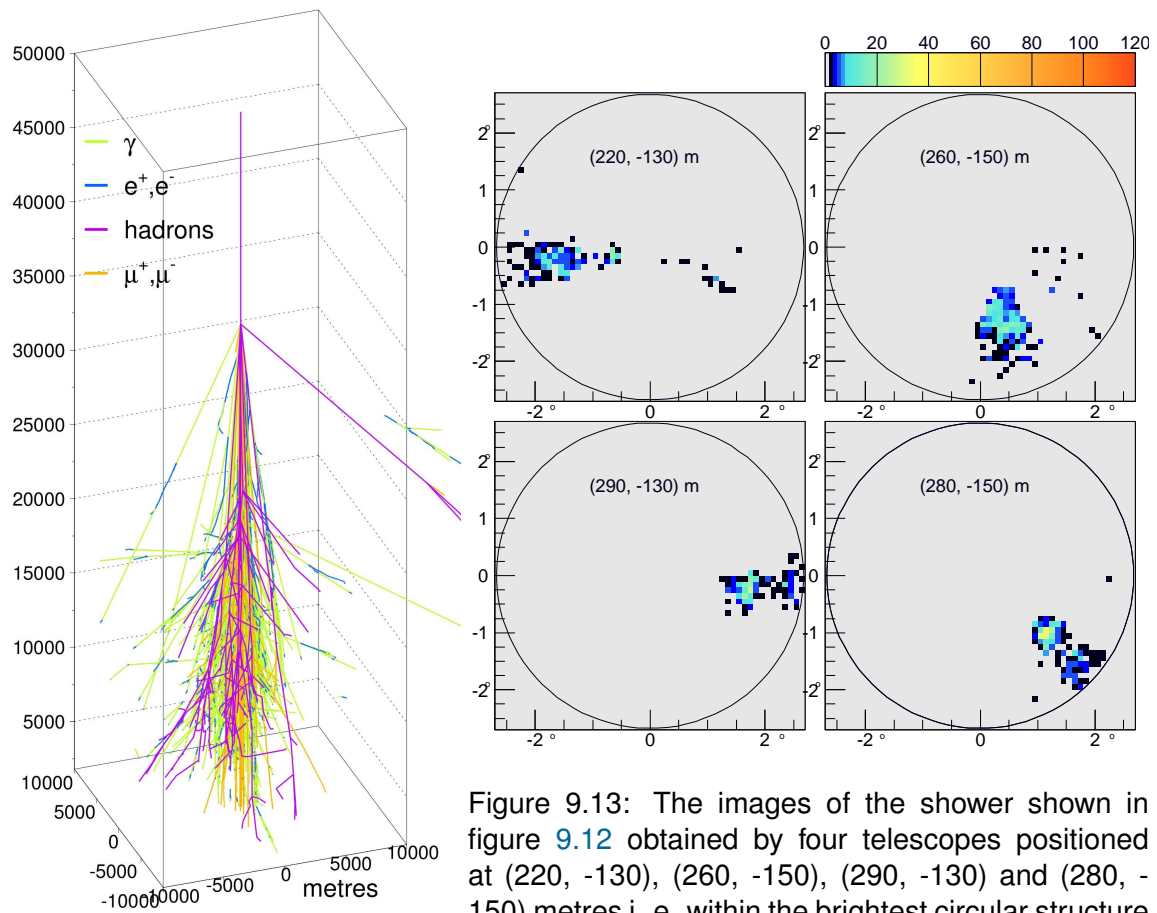


Figure 9.13: The images of the shower shown in figure 9.12 obtained by four telescopes positioned at (220, -130), (260, -150), (290, -130) and (280, -150) metres i. e. within the brightest circular structure in figure 9.11.

Figure 9.12: The particle tracks of a 1000 GeV shower with first interaction at ~ 34 km a. s. l..

The second shower (bottom row in figure 9.14) has fewer photo-electrons in its images. In addition to the irregular shape of several bunches in the image, there is also a muon ring present in the first two images. The particles traces and the Cherenkov density on the ground obtained by this shower are presented in figure 9.16. The altitude of materialisation is around 20 km, but the lateral spread of this shower is more important in comparison with the previous one. The resulting Cherenkov photon distribution on the ground has a central region contained within a couple of hundred metres where most of the light arrives. However, in comparison with the previous shower, this region shows a large number of irregular features arising from different elements of the hadronic shower.

The purpose of this discussion, through six different examples of showers, has been to bring out the cases where the hadronic showers have γ -like features and also to illustrate the large diversity of hadronic showers. While γ -ray showers at one energy all have similar features, one hadronic shower can be very different from another one at the same energy. We have also seen that this difference is not only due to different shower parameters like the height of first interaction in the atmosphere, but that it is specially due to the intrinsic nature of the inelastic nuclear interactions giving rise to these showers.

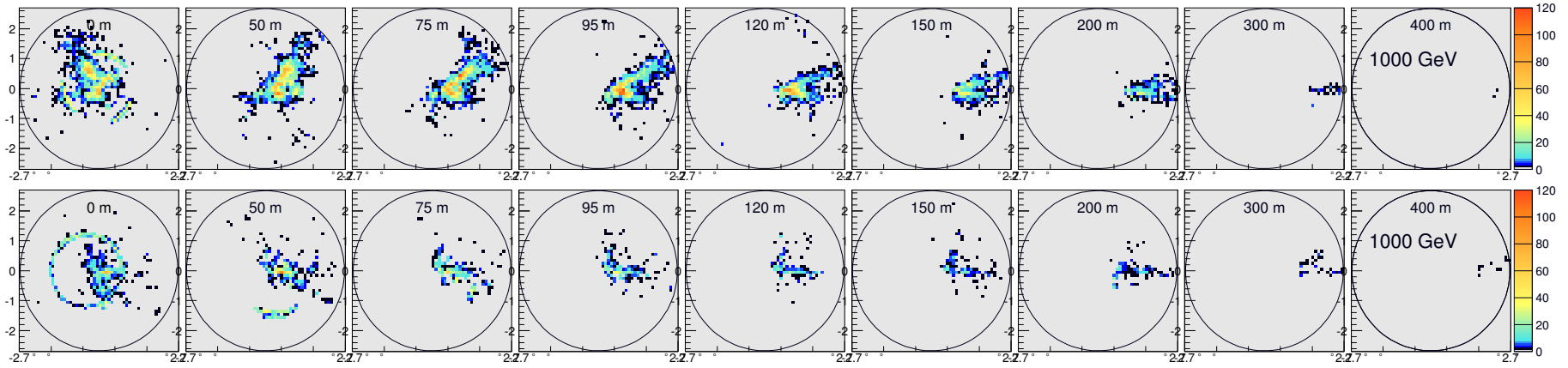


Figure 9.14: The images of two 1000 GeV proton-initiated showers obtained from telescopes at various distances from the core at 1800 m a. s. l.. The showers are shown in figures 9.15 and 9.16, respectively.

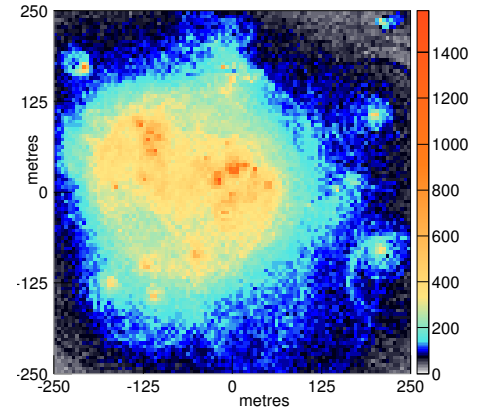
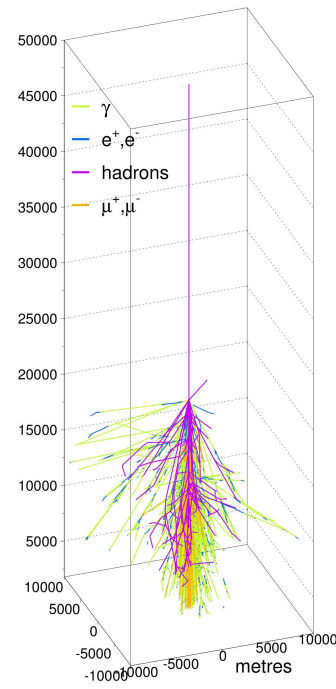
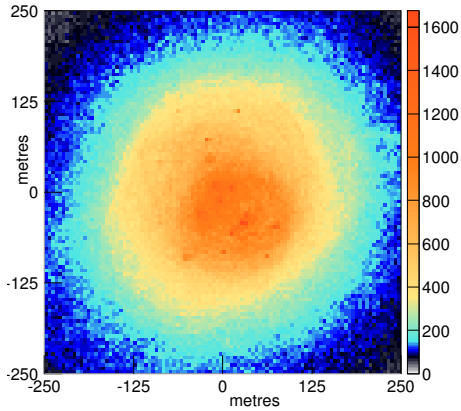
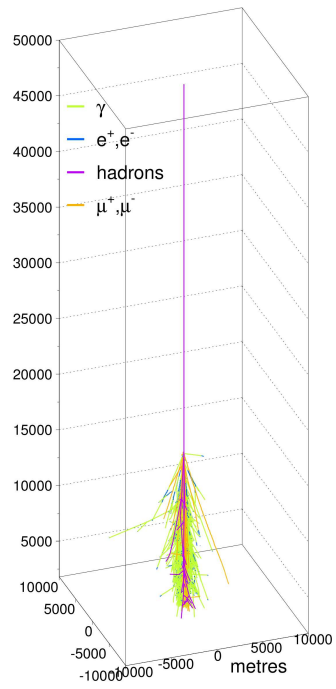


Figure 9.15: A 1000 GeV shower (left) and the distribution of Cherenkov photons it gives on the ground (right) at 1800 m a. s. l.. The shower has an altitude of materialisation at 15 km a. s. l..

Figure 9.16: A 1000 GeV shower (left) and the distribution of Cherenkov photons it gives on the ground (right) at 1800 m a. s. l.. The shower has an altitude of materialisation at 20 km a. s. l..

9.2.4 Hadrons as a source of background for γ -observations

For point sources, a first rejection of the hadrons occurs due to the angular resolution of the telescopes. Otherwise, methods for identifying hadrons based on their image characteristics are used to obtain the γ -ray signal from a source. As we have seen through the previous examples this identification may be more or less difficult depending on the shower. Some hadrons also give γ -shower like images. Here we list these cases and the ways for dealing with them.

- The presence of secondary muons in the shower can, on some telescopes, give images similar to those of γ -ray showers. These events can be rejected through stereoscopic observations.
- The presence of electromagnetic sub-showers in the hadronic showers can also lead to γ -like images. Many of these events too can be rejected through stereoscopy. One notes that the rejection of these kind of events and of showers with secondary muons can be an additional consideration for designing future telescope arrays. The inter-telescope distance and telescope size choices can be made so that they are adapted to rejecting these events.
- The rest of the hadrons are dealt with on the basis of their image properties. Some hadronic showers images have shapes and characteristics that resemble those of hadrons. For this purpose the methods for identifying γ -ray showers need to be as discriminatory as possible. The use of several methods or variables to reject hadrons based on different properties can also improve background rejection.

9.3 Ideas for γ -hadron separation

In this section we briefly present several ideas for γ -hadron separation. Although, all these ideas need further development in order to be used to evaluate the performance of IACT arrays, they are presented and applied here briefly as possible methods for γ -hadron separation. The methods will be applied to γ -ray and proton showers generated with 0° zenith angle and observed with the telescope system described on page 110 at 1800 m a. s. l.. The showers are generated with core position at the centre of the telescope system i. e. at (0, 0) m. It should be noted that by working with proton showers generated with exactly the same zenith angle as the γ -rays, we are dealing with the worst case scenario i. e. hadronic showers incident from the same direction as the γ -ray source. In reality, the hadronic background is incident with a wide range of angles.

9.3.1 Using the χ^2 of the source and core reconstruction fits

As mentioned before, the source and core reconstruction fits have been constructed in such a way that they are adapted to electromagnetic showers. One therefore expects poorer χ^2 values when the method is applied to hadronic showers. This could provide a means to separate hadrons from γ -showers. In section 7.3.4, we discussed some of the problems associated with obtaining an accurate value of χ^2 from these fits and some of the solutions to improve this aspect. Although these solutions have not been applied here, we still observe a tendency towards obtaining better χ^2 values for γ -showers than hadronic showers.

Figures 9.17 and 9.18 show the cut efficiency when showers below a fixed value of χ^2 are retained. The plots in figure 9.17 represent the efficiency for photons (left) and hadrons (right)

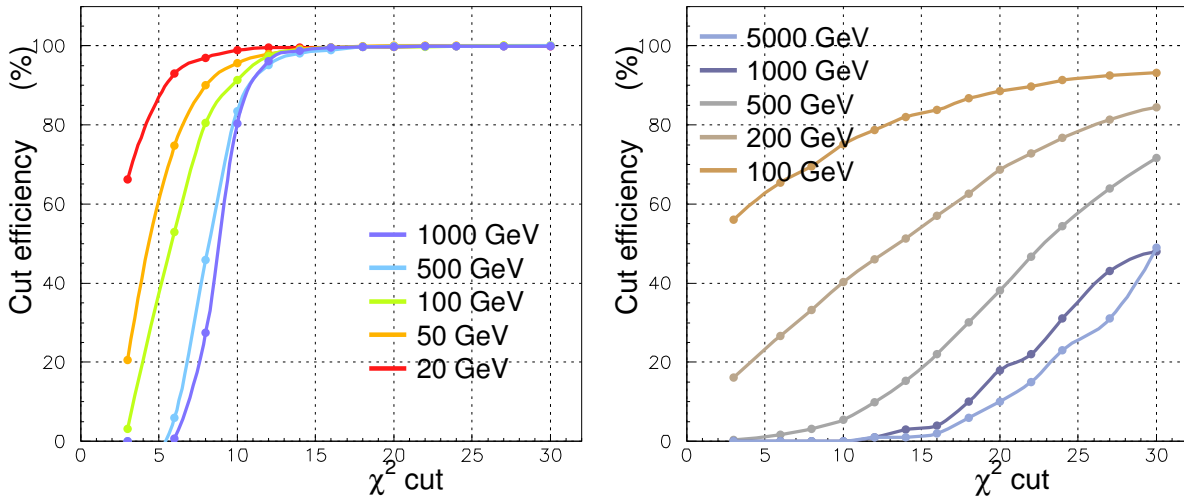


Figure 9.17: The percentage of showers retained for cuts at various values of χ^2 obtained from the source reconstruction fit. The left plot shows the results for photons while the right one corresponds to protons of various energies.

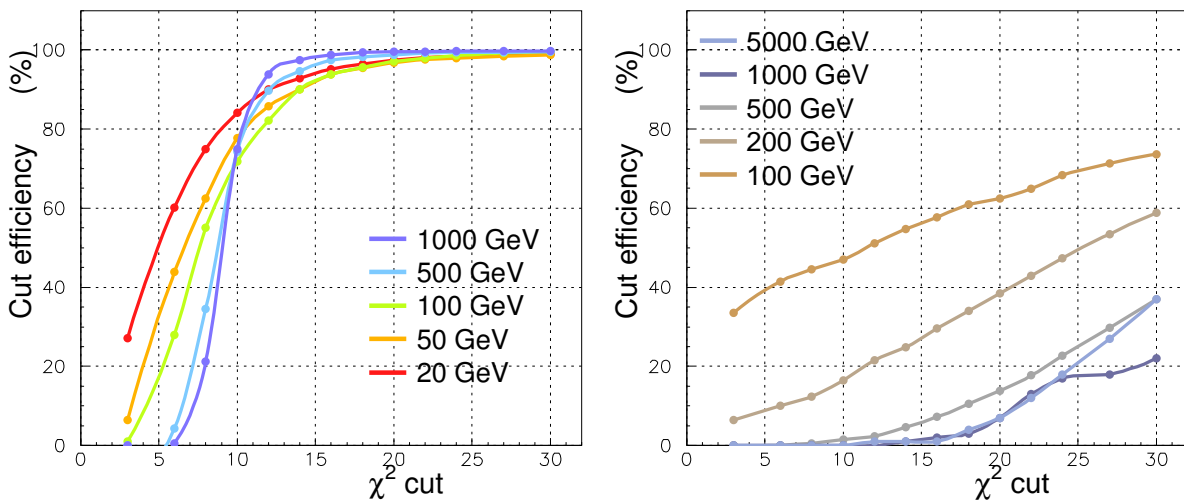


Figure 9.18: The percentage of showers retained for cuts at various values of χ^2 obtained from the core reconstruction fit. The left plot shows the results for photons while the right one corresponds to protons of various energies.

when the cut is applied on the source reconstruction fit χ^2 while the plots in figure 9.18 show the efficiency for the shower core fits. One can make the following remarks:

- At lower values of the χ^2 cut (below ~ 10), more showers of low energy are retained than those at high energy. This is true for both photons and hadrons and is related to a point that has been discussed in section 7.3.3 i. e. the χ^2 values tend to be closer to 1 for low energy showers whenever the lateral profile of the image is fitted with a Gaussian function to obtain σ_t . This occurs because the Gaussian fit is only approximative and leads to better χ^2 values at low energies where the shower images have fewer photo-electrons.

- There seems to be a threshold value of χ^2 for photon-shower fits, beyond which nearly 100% showers are retained.
- This value does not seem to depend a lot on the energy as far as the source reconstruction fits are concerned, but shows some dependence for the shower core reconstruction fits.
- One notes that the telescope system used for these simulations is the same as the one described on page 110. We have already seen that a telescope size of 12.5 m diameter is not adapted to making observations at energies lower than around 300 GeV. In view of this, we focus on the high energy showers and can say that close to 100% of the γ -showers are kept when a cut-off around 13 is applied on the χ^2 values for source reconstruction. For the core reconstruction, this value may lie between 15 and 20 depending on the energy.
- Hadrons tend to have larger values of χ^2 . A significant number of them get rejected even with cuts at very large values of the χ^2 value. This effect is more pronounced for hadrons of higher energies. The 1000 and 5000 GeV curves show that less than 10% of the hadrons are retained for χ^2 values below 15. On the other hand around 80% of the 100 GeV protons are retained for a similar χ^2 cut on the source reconstruction fit.
- The cuts on the shower core reconstruction seem to be more effective in rejecting protons while keeping photons than the cuts on the source reconstruction position.
- When we tried to apply the cut on the source reconstruction and core reconstruction χ^2 values simultaneously (cutting at the same value), the same results as those with the core reconstruction cut only were obtained, showing that the events excluded by the source reconstruction cut were also excluded by the core reconstruction cut.
- It should be noted that the results presented here are obtained without applying image cleaning methods. Although this needs to be checked, it can be expected that hadron rejection may suffer once image cleaning is carried out and a large number of stray pixels and bunches removed.
- On the other hand, one also expects a better evaluation of the χ^2 value by using some of the solutions described in section 7.3.4 as well as a possible improvement of the discrimination carried out through this method. This too needs to be checked through a detailed study and simulations.

9.3.2 Reconstructed longitudinal profile

In section 8.7, we described a method for the reconstruction of the individual Cherenkov photon trajectories and the evaluation of the shower's longitudinal profile from them. We have already discussed how γ -ray and hadron-induced showers tend to have different longitudinal profiles in the atmosphere. The comparison of the reconstructed profiles from events could be another way of separating hadrons from γ -rays. We saw in chapter 3 that the profiles of electromagnetic showers can be fitted by the function $f(t) = C(\beta t)^{\alpha-1}e^{-\beta t}$ and that the values of α , β and the fluctuations on them depended on the energy of the shower. Fitting the reconstructed longitudinal profiles by this kind of function and comparing the parameters could also provide a way to discriminate between hadrons and γ -photons. Although we have not applied this method to individual profiles from simulated showers, we present the average reconstructed longitudinal profiles for γ -photons (left) and protons (right) in figure 9.19. The reconstructed profiles are also

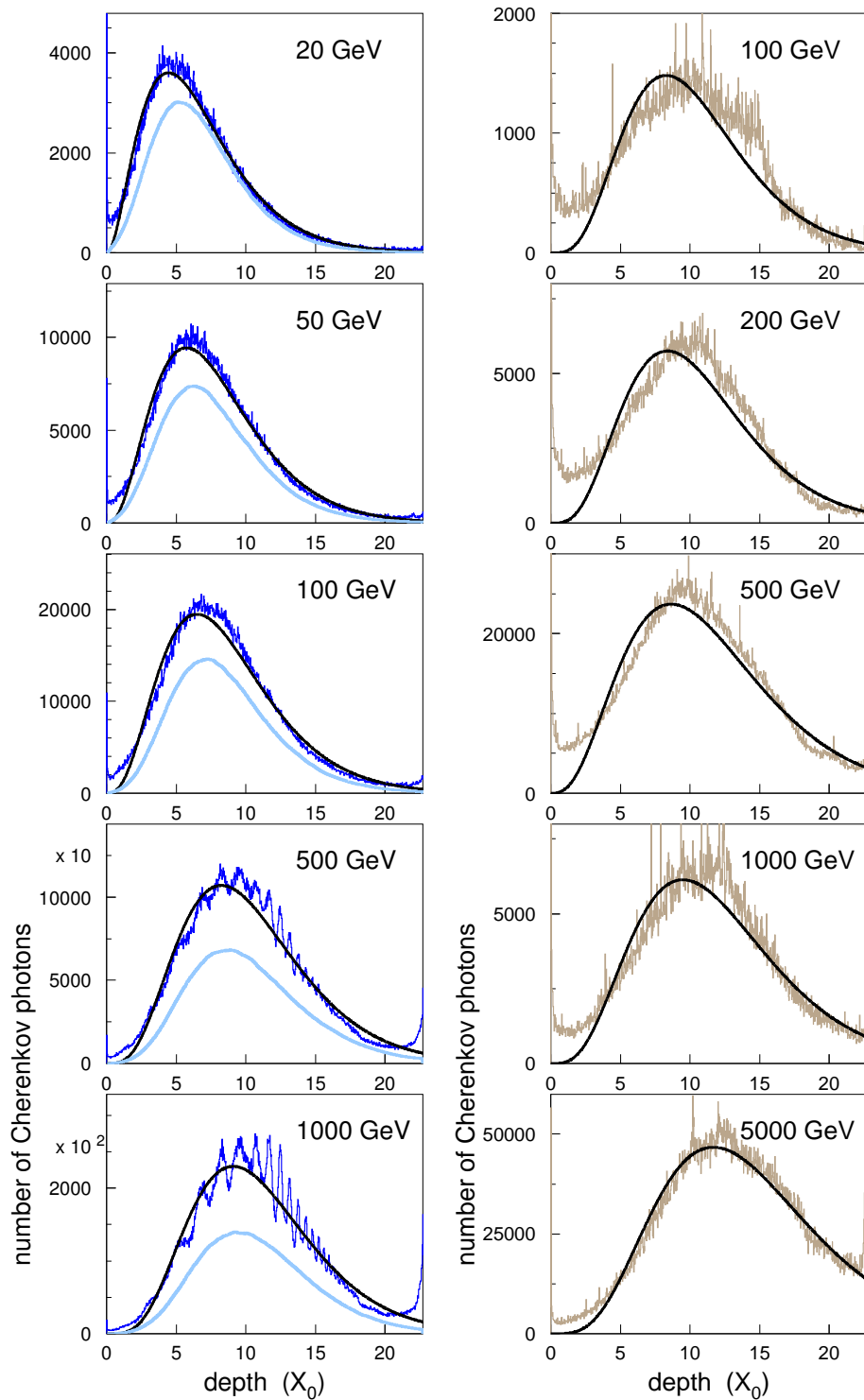


Figure 9.19: The average reconstructed longitudinal profiles obtained for γ -ray (left) and proton (right) showers of different energies (dark blue for γ -showers and beige for protons). The profiles are fitted with the function $f(t) = C(\beta t)^{\alpha-1} e^{-\beta t}$ (black line). The average generated longitudinal profiles for the γ -showers are also shown through the light blue curves.

fitted with the function $f(t) = C(\beta t)^{\alpha-1}e^{-\beta t}$ (discussed earlier in section 2.3.2). One observes the following :

- The profiles for hadronic showers tend to be more irregular than those from electromagnetic showers
- The profiles from hadrons tend to peak lower in the atmosphere.
- While the fits carried out on the average γ -shower reconstructed profiles give a good description of the distribution, the same fits on the hadron shower reconstructed profiles have a poorer correspondence with the profile.

9.3.3 Using the reconstructed point of emission of Cherenkov photons

The method provided in section 8.7 provides a way to reconstruct the point of emission of the individual Cherenkov photons contributing to shower images. We briefly recall the method and its schematic description (figure 9.20). The Cherenkov photon trajectory is reconstructed by assuming reflection from the centre of the mirror. As a result, a line in 3-dimensional space corresponding to the trajectory of the Cherenkov photon is obtained. The minimum distance of this trajectory with the shower axis is called d_{min} in the figure and also gives the reconstructed point of emission of the Cherenkov photons. In this section we chose to work with the point

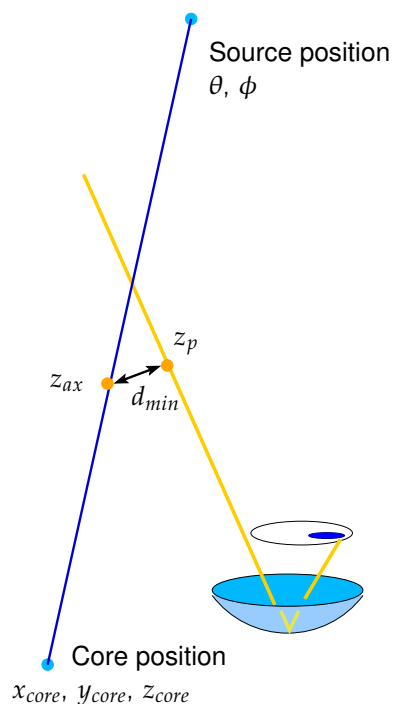


Figure 9.20: Schematic description of the reconstruction of the Cherenkov photon trajectories the longitudinal profile of the shower.

reconstructed on the shower axis z_{ax} , although the same study could have been carried out with z_p , yielding similar results.

The distribution of d_{min} in γ -ray and hadronic showers

We first begin by presenting the distributions of d_{min} obtained for various individual showers. These examples serve to illustrate the general trends for γ -ray and hadronic showers at different energies. The array of 12.5 m diameter telescopes simulated is the one described on page 110 and all the showers are generated with the core position (0,0) metres at the centre of the telescope system. Figures 9.21 and 9.22 present the distributions of d_{min} for different γ -ray showers of 1000 GeV and 100 GeV respectively. The first four plots correspond to the distribution obtained from each of the four telescopes in the array while the fifth plot gives the sum of the distributions from all telescopes.

As the electromagnetic showers tend to be more compact than hadronic showers, one expects to obtain narrow distributions of d_{min} for γ -ray showers. This property is evident for the 1000 GeV γ -ray shower distributions obtained in figure 9.21. The bulk of the light from the shower images is reconstructed within 10-15 metres of the shower axis and there are almost no Cherenkov photons reconstructed beyond 50 metres. The distributions from the first shower are slightly broader with a second hump present in some of the telescopes. This is true for the distributions obtained from individual telescopes as well as their sum. One also notes that it is expected that once image cleaning is carried out, the distributions for d_{min} will become narrower still, since most of the points of emission reconstructed away from the shower axis come from isolated pixels with low photo-electron content.

In figure 9.22, we present the same distributions for three 100 GeV showers. At this energy, the number of photo-electrons contained in images is lower and the impact of the fluctuations greater. Moreover, we saw earlier that telescope sizes larger than 12.5 metres are necessary to obtain exploitable images at 100 GeV. The impact of the fluctuations and low photo-electron number is visible on the d_{min} distributions. For the first shower, the most important fraction of the Cherenkov emission is reconstructed close to the shower axis i. e. within the first 20 metres. This is true for each of the four telescopes. In the second shower, the distributions from different telescopes yield different results. The first and third telescopes have the greatest part of the Cherenkov light reconstructed at distances beyond 60 metres. The second telescope has photons spread at various distances between 0 and 100 metres, while the fourth telescope has clean peak close to the shower axis. The resulting sum from the four telescopes has two important regions of emission, with a sharp peak close to the shower axis and a wider region between 50 and 100 metres. The third shower has similar distributions, with the third telescope giving a sharp peak close to the axis and the second and fourth telescopes giving emission regions between 50 and 100 metres.

We also look at the distributions obtained for several different proton showers. Figure 9.23 shows d_{min} distributions for 5000 GeV proton showers. As is often the case with hadronic showers, a large number of different results can be obtained since these showers can have very large variations in their development. For the first shower, three of the four telescopes have the bulk of their photons reconstructed beyond 50 metres. The third telescope is the only one giving a peak closer to the shower axis. However this peak is much broader than the sharp peaks obtained for the 1000 GeV γ -showers where most of the light was emitted in the first 10-15 metres. The sum of the distributions from all telescopes shows photon emission points are spread at various distances between 0 and 100 metres with a slightly denser region beyond 50 metres and a modest peak closer to the axis.

The second shower, has at least two telescopes with a more γ -like behaviour. The first and third telescopes have sharp peaks within the first few metres of the axis and a secondary

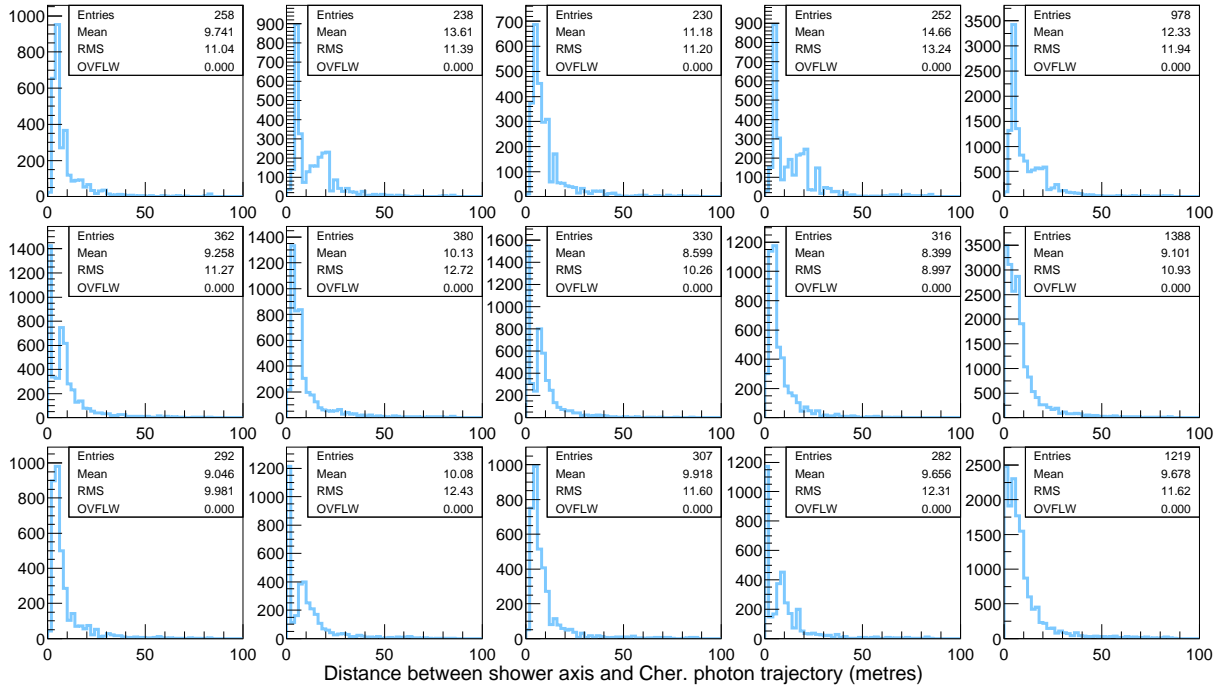


Figure 9.21: The distribution of d_{min} obtained for three different γ -ray showers of 1000 GeV. Each row corresponds to the distributions for one shower. The first four plots show the distribution obtained from each of the four telescopes of the system described on page 110, the fifth plot gives the sum of the distributions from all telescopes.

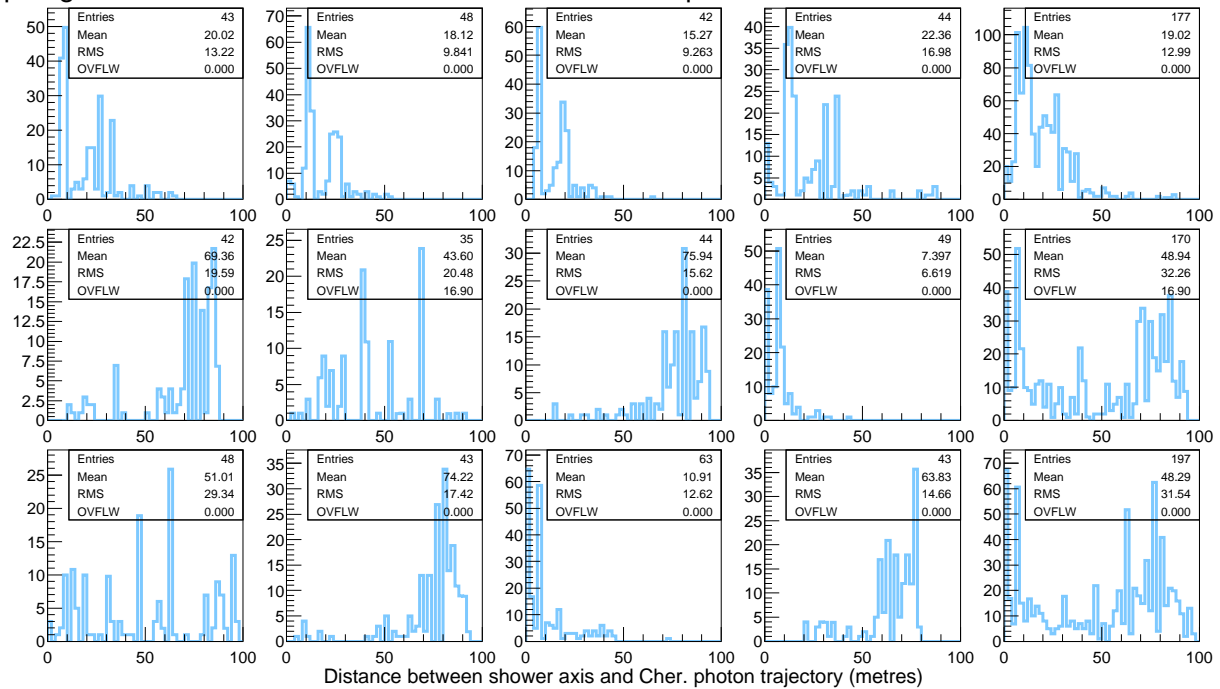


Figure 9.22: The distribution of d_{min} obtained for three different γ -ray showers of 100 GeV. Each row corresponds to the distributions for one shower. The first four plots show the distribution obtained from each of the four telescopes of the system described on page 110, the fifth plot gives the sum of the distributions from all telescopes.

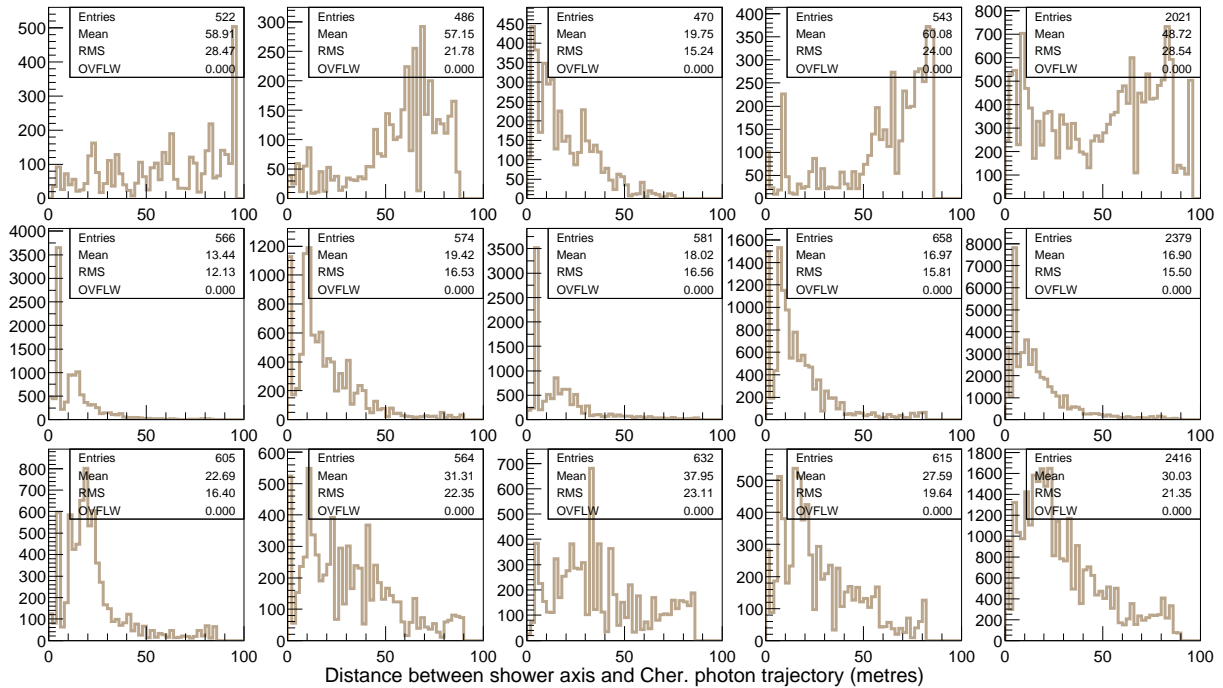


Figure 9.23: The distribution of d_{min} obtained for three different proton showers of 5000 GeV. Each row corresponds to the distributions for one shower. The first four plots show the distributions obtained from each of the four telescopes of the system described on page 110, and the fifth plot gives the sum of the distributions from all telescopes.

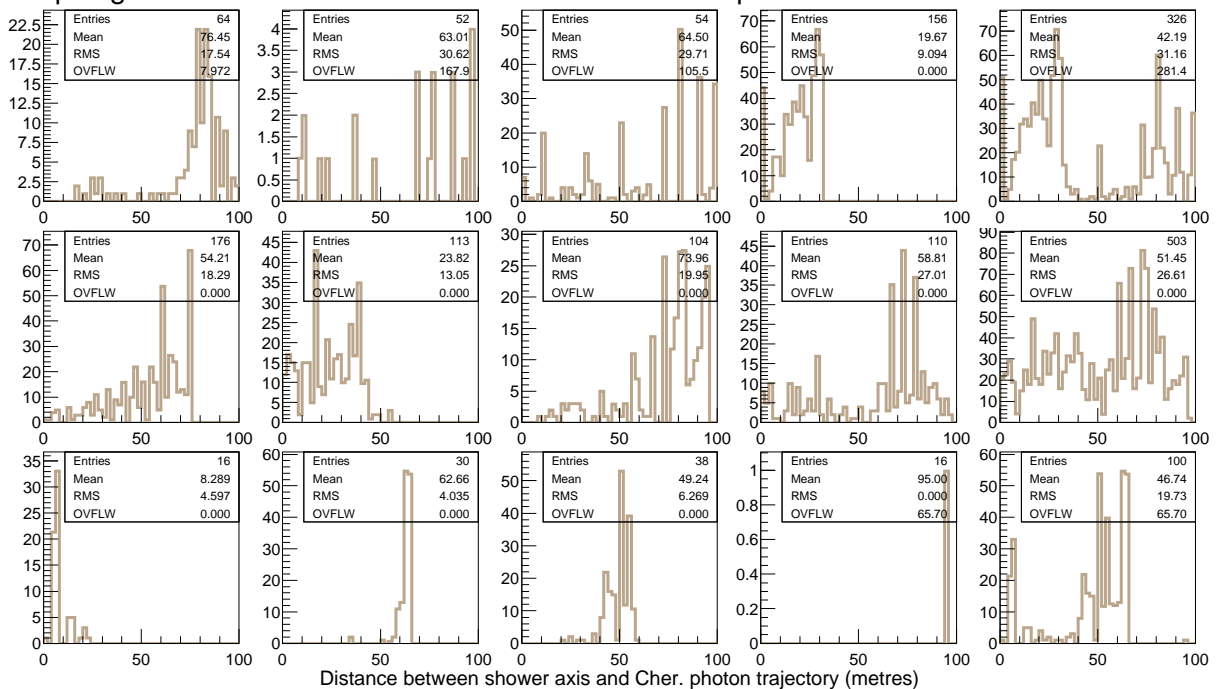


Figure 9.24: The distribution of d_{min} obtained for three different proton showers of 500 GeV. Each row corresponds to the distributions for one shower. The first four plots show the distributions obtained from each of the four telescopes of the system described on page 110, the fifth plot gives the sum of the distributions from all telescopes.

broader bunch between 10 and 50 metres. These distributions resemble those from the first of the 1000 GeV showers in figure 9.21. Though the distributions from the other two telescopes also tend to peak towards the shower axis, they are much broader and taper off to distances up to 100 metres. The third shower also shows broad distributions, with a tendency to have a slight peak towards the shower axis for at least three of the telescopes.

The 500 GeV proton showers presented in figure 9.24 show similar fluctuations with a smaller number of photo-electrons. The first shower has most of its emission reconstructed beyond 50 metres for the first three telescopes. The first telescope shows a relatively well defined peak between 70 and 100 metres, while the second and third telescopes have distributions with events scattered at different distances. The fourth telescope has a peak between 10 and 30 metres. The sum of the distributions has two broad peaks. The second shower has relatively large distributions as well, with most of them peaking away from the shower axis. The third shower has sharp peaks in all telescopes. The position of this peak changes from telescope to telescope with the first telescope giving a peak near the shower axis, the second and third telescope near 50 metres and the last telescope near 100 metres.

Based on these examples one can draw the following conclusions:

- d_{min} can be a possible means of discrimination between hadronic and γ -ray showers.
- The large number of fluctuations in γ -ray showers at low energy will make it harder to use this method for those energies. In order to improve the efficiency of the method a better adapted size of telescope could be used in order to have exploitable images.
- Some hadrons give γ -like distributions for d_{min} and may not be rejected by using this method.

Two dimensional distributions between d_{min} and reconstructed height of emission

We have just seen that d_{min} , may provide a tool for discrimination between hadrons and γ -showers. Here, we explore the possibility of using the reconstructed altitude of emission z_{ax} as a discriminating factor as well. In figure 9.25, we present the average two dimensional distributions between z_{ax} (ordinate axis) and d_{min} (abscissae axis) for γ -showers (left) and proton showers (right) at various energies. One can make the following observations:

- In all cases, the main region of emission seems to lie above the level of observation (1800 m a. s. l.) and ~ 15 km. This is true for γ -showers as well as protons.
- The altitude of the peak region of emission (darkest region) seems to occur lower in the atmosphere for hadrons than for γ -rays.
- In the case of γ -showers, the compactness of the region of denser emission depends on the energy. While for the 500 and 1000 GeV showers the region is well defined and lies within $d_{min} \leq 20$ metres, the region is broader for the lower energies. This is true for the z_{ax} distribution as well, where the reconstructed altitude of emission for lower energies occupies a much larger range at lower energies.
- The d_{min} distributions for protons are much larger than for the γ -showers and show little dependence on the energy.

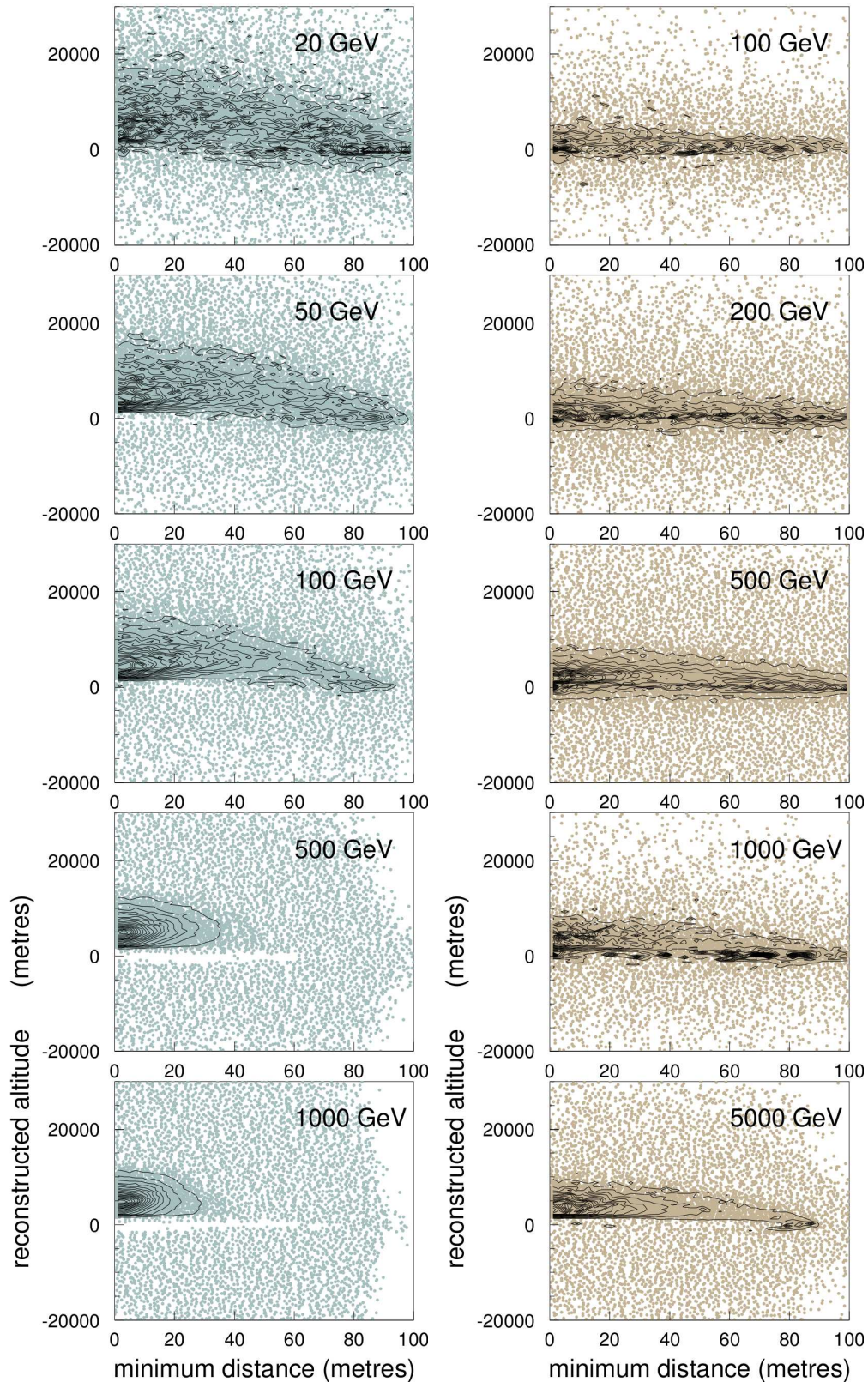


Figure 9.25: The average two dimensional distributions of z_{ax} (ordinate axis) and d_{min} (abscissae axis) for γ -showers (left) and proton showers (right) at various energies. Contours have been superposed on the 2-d scatter plots in order to emphasize the areas of greater density.

The application of cuts on the reconstruction point of emission

Based on the discussions above, we apply a series of cuts on the reconstructed d_{min} and z_{ax} values for γ -ray and hadron showers. In figure 9.26 (left plots), the cuts applied require that at least 80% of the Cherenkov light in a shower image is emitted between the altitude of observation (1800 m a. s. l) and 13.5 km and within a distance $d_{min}max$ of the reconstructed shower axis. The value of $d_{min}max$ is varied between 5 and 150 metres in order to obtain the curves presented below. The top left plot represents the percentage of γ -showers retained after the application of the cuts and the bottom left plot represents the efficiency for proton showers. In the discussion on the d_{min} distributions based on individual examples, we saw that individual telescopes have often very different distributions and that it can also be interesting to look at the sum of the distributions from all telescopes. In the right plots in figure 9.26, we therefore present the efficiencies obtained when the cuts are applied on the summed distribution from all telescopes.

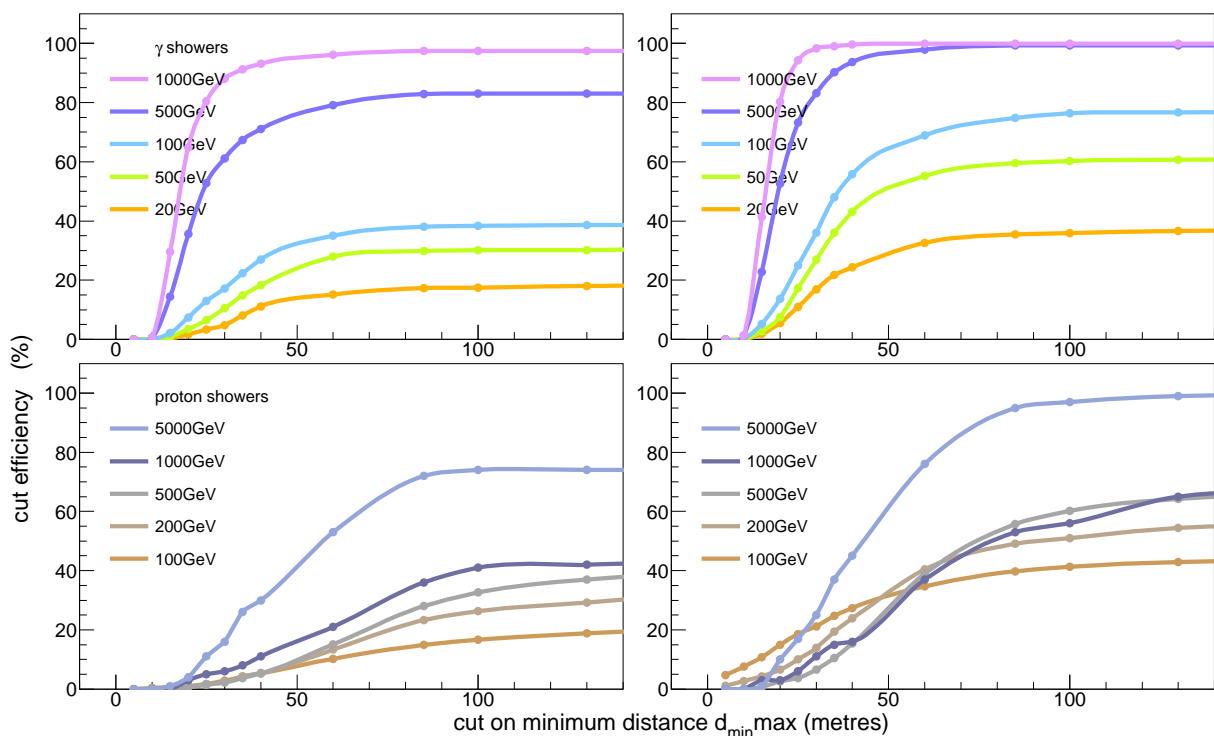


Figure 9.26: The percentage of showers retained after requiring that 80% of the Cherenkov light has reconstructed values of d_{min} below a fixed distance (abscissae axis). The efficiency curves obtained in the left plot are the result of applying these cuts on each telescope image, while the right image is obtained by applying the cuts on the summed distribution from all telescopes. Only the showers with z_{ax} between the ground level (i. e. 1800 m a. s. l.) and 13.5 km are kept. The top plots show the efficiencies for γ -ray showers while the bottom plots show the efficiencies for proton showers of various energies.

The following remarks can be made:

- For γ -ray distributions, the efficiency seems to rise with the distance up to a certain value of $d_{min}max$ beyond which a plateau like regime begins.
- The plateau like regime is reached earlier for higher energies as their distributions are more compact. This was illustrated in figure 9.25.

- While a value of $\sim 100\%$ is reached for the 1000 GeV curve, for other energies this plateau is situated at lower efficiency values. For 500 GeV it is around 80% and for the lower energies it is below 50%. This effect is due to the cut on the altitude z_{ax} and shows that at relatively lower energies, the cut on the altitude is too strict and a certain percentage of showers never pass it. In other words, requiring 80% of the light to be present between the altitude of observation and 13.5 km is too strict a condition for photons at these energies. This condition could be relaxed a little for 500 GeV showers. As for the lower energies, this shows once again that the telescope size used for their observations is not adapted and that better results may be obtained with larger telescope sizes as well as changing the percentage of Cherenkov light required to pass the cuts in each telescope.
- For protons, the rise towards the plateau regime is much slower and seems to occur beyond 100 metres for most energies.
- This implies that the application of this kind of cut to individual telescopes could provide a means to separate hadrons from γ -rays but that better adapted cuts need to be determined as a function of the reconstructed energies of various showers.
- When the cuts are applied to the summed distributions from all telescopes (right plots), the efficiency of the cuts tends to increase up to similar values of d_{minmax} . We also see, that the plateau level increases for the lower energies. The 500 GeV curve reaches $\sim 100\%$ efficiency after 50 metres, while the 100 GeV plateau reaches 70%.
- The efficiencies for the protons tend to increase as well when the cuts are applied to the sum of the distributions from all telescopes (bottom right). At the same time the rise to the plateau like regime is less steep than for the γ -rays implying that this type of cut too could be used to discriminate between hadrons and γ -rays.

We also look at the impact of the cut on reconstructed altitude (z_{ax}) of emission in figure 9.27. The above efficiencies were obtained by requiring the 80% of the light is reconstructed as having been emitted between the observation level and 13.5 km. Here, we remove any constraints on z_{ax} and look at the efficiencies obtained by applying cuts on d_{min} . The resulting efficiencies (dotted line) are compared with the efficiencies from the above plots in figure 9.27.

- We see that in both the left and right plots (i. e. when cuts are applied to individual telescopes and when they are applied to the sum of the telescope distributions), the plateau efficiency reaches 100% for all γ -ray energies.
- The plateau like regime is reached for slightly lower values of d_{minmax} for the telescope sum distributions (right) than for the individual telescope distribution (left).
- There is a similar increase in the efficiencies for the protons as well. The rise towards higher efficiency regions is much slower than for γ -rays.

9.3.4 Conclusions

We have presented at least two methods with the potential to do effective hadron-gamma discrimination. The preliminary tests carried out here, with a four telescope system and fixed energies of proton showers, seem to indicate that these methods could be further developed to provide discrimination tools. The impact of other factors such as pixel size and image cleaning also needs to be taken into account for these methods. We have also seen that the cuts that have been applied here will need to be adapted as a function of the reconstructed energy of showers as well as telescope characteristics such as telescope size, pixel size...

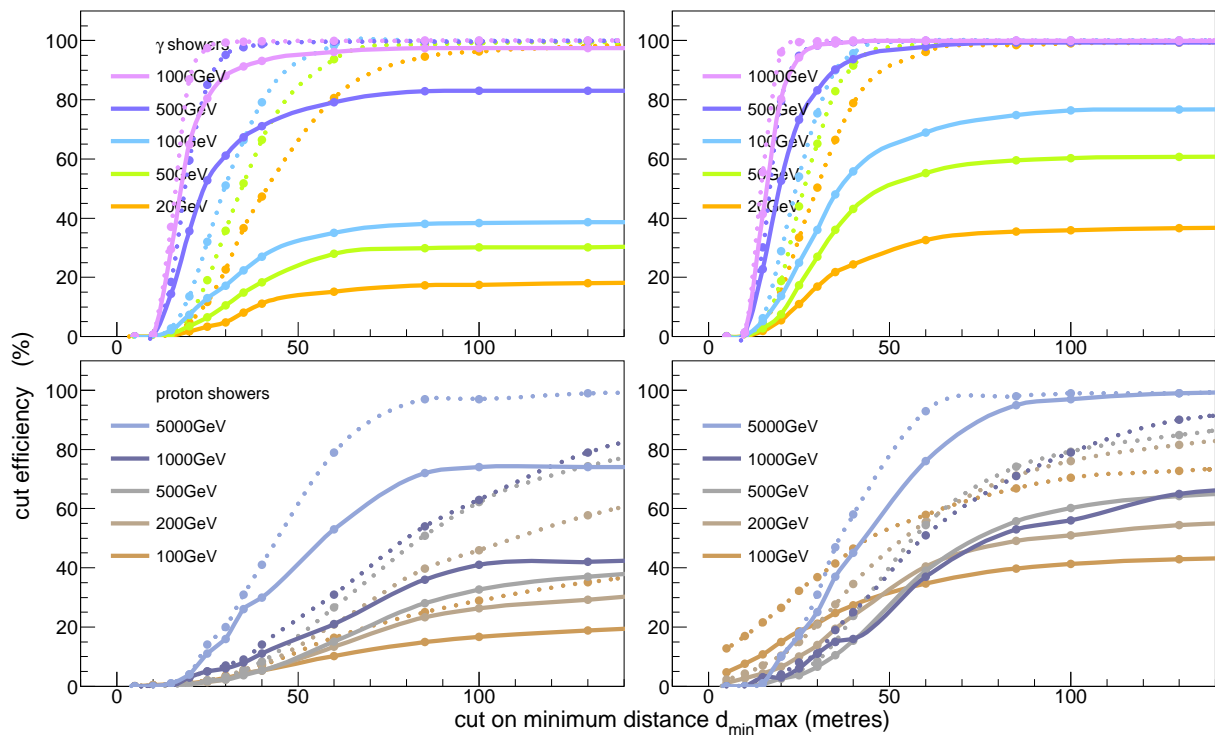


Figure 9.27: The efficiencies from figure 9.26 (solid lines) are compared with those obtained by applying similar cuts without any restriction on z_{ax} (dotted lines). The top plots show the efficiencies for γ -ray showers while the bottom plots show the efficiencies for proton showers of various energies.

*P*_{ART} *V*

A *PPLICATION AND CONCLUSIONS*

FUTURE IMAGING ATMOSPHERIC TELESCOPES: PERFORMANCE OF POSSIBLE ARRAY CONFIGURATIONS FOR GAMMA PHOTONS IN THE GEV-TEV RANGE

10.1 Introduction

As said in the introduction to this thesis, a large number of parameters and characteristics determine the final performance of a given array. The understanding of various characteristics of atmospheric showers and simulations are necessary in order to study the impact of various parameters on telescope performance and for the optimisation of these parameters in view of various physics goals. So far, we have looked at some of the important features of electromagnetic showers and the Cherenkov light they emit and developed tools that allow the simulation and the reconstruction of gamma showers. The application of these reconstruction tools to a simple four telescope system in the earlier chapters has also enabled us to understand some of the major issues involved in gamma-shower reconstruction. We can now use this information and these tools to study the response of possible future array configurations to gamma-rays. In this chapter, we present the optimisation and choices for two different IACT systems and then study their gamma-ray reconstruction capabilities through simulations.

As the optimisation of telescope parameters depends on the target energy range, we open this chapter with a description of the various energy domains in which IACT telescopes are capable of observing γ -rays. This discussion is also used to make choices about the number and size of telescopes as a function of these energy domains.

We also briefly discuss the impact of altitude on the observations by IACT and describe our choice of two altitudes of observation (1800 m and 3600 m a. s. l.) for the study presented in this chapter.

In section 10.5, we evaluate the optimum inter-telescope distance for the energy range and altitude being considered. In order to do so, we simulate a square four telescope system with varying inter-telescope distance and study its response to gamma-ray showers. The optimum inter-telescope distance is taken to be that for which the effective area, and angular and energy resolutions of the unit four telescope system are maximum.

This optimum distance is then used to design two IACT arrays with 37 and 53 telescopes

respectively. The response of these systems to gamma-ray shower is then studied through simulations and their angular and energy resolution as well as effective area and shower core reconstruction capability are evaluated.

10.2 Energy domains and choices for telescopes

The physics goals and the issues concerning gamma-ray observation both depend on the energy domain being considered¹. This implies that optimisation of various telescope parameters will depend on the energy range being considered. We, therefore, begin by taking a look at the various energy domains in which IACT arrays are capable of observing γ -rays. Looking at the performance of current day telescopes, one can divide the entire energy range accessible to IACT systems into the following three different domains:

- Low energy domain: $E < 300 \text{ GeV}$
- High energy domain: $300 \text{ GeV} < E < 10 \text{ TeV}$
- Very high energy domain: $E > 10 \text{ TeV}$

10.2.1 High energy domain $300 \text{ GeV} < E < 10 \text{ TeV}$

We begin by looking at the high energy domain since this is where the IACT systems best operate. At these energies, the showers are large enough for good angular and energy resolutions to be achieved through the use of moderate sized telescopes (10-15 m diameter). As an example, we saw in chapter 7 that one obtains less than 0.1° of angular resolution and around 10% of energy resolution with 12.5 m diameter telescopes in this energy range.

At the same time, the regular shapes of shower images and the large number of photo-electrons present in them also make it easier to separate the γ -ray showers from the hadronic background. Moreover, the gamma-ray fluxes from sources remain sufficiently high so that even with a four telescope system the current arrays have achieved sufficient sensitivity to improve observations on numerous gamma-ray sources as well as discover new ones.

The next generation of instruments will require that we further probe the γ -ray emitting universe in this domain. A higher flux sensitivity would allow the observation of more sources in shorter periods of time as well as allow the discovery of new weaker sources.

Therefore, the main goal in this energy range is to have telescope arrays with greater sensitivity. This can be achieved through the use of a large number of medium sized (10-15 m diameter) telescopes spread over a large area. For the study presented in this chapter we have chosen to use 12.5 m diameter telescopes.

10.2.2 Low energy domain $E < 300 \text{ GeV}$

As the shower size decreases with energy, the fluctuations in the showers start taking more importance. This implies that not only the shower images have fewer photo-electrons, but it becomes harder to identify the orientation of shower images (i. e. determine their axis). This makes it harder to reconstruct the various shower parameters such as the source and core positions and the energy. With fewer photo-electrons in images and more important fluctuations, gamma shower identification and the rejection of hadronic background becomes more difficult as well. The increase in the background flux makes this aspect even worse. The results presented in chapters 7 and 8 show that the use of 12.5 m diameter telescopes is not sufficient

¹A discussion on the different energy domains and the scientific objectives can, for instance, be found in [43].

to enable good shower parameter reconstruction. As discussed in the previous chapter, this mainly arises due to the low number of photo-electrons in shower images. This implies that the most important requirement in this domain is to gather the maximum amount of Cherenkov light possible for a given shower. This can be achieved through the use of large size telescope mirrors (25-30 m diameters). We have chosen to work with 30 m diameter telescopes for the studies presented in this chapter. Moreover, as the gamma-ray flux from the sources tends to increase as the energy decreases, this implies that sufficient statistics can be achieved even by using a low number of telescopes (e. g. 4-5). Note that the use of a smaller number of large telescopes also allows to keep the cost of the IACT system relatively lower.

It should also be noted that many arguments point towards the idea that we may be reaching a physical limit where observations through IACT will no longer be possible at very low energies. Below 10-20 GeV, the showers are so small, and the impact of fluctuations and the earth's magnetic field so important on them that one does not expect to be able to reconstruct shower parameters accurately at these energies. Even for higher energies (20-50 GeV), the combined effect of these factors and the increase of hadronic background cast a doubt on the possibility of gamma-ray observations. The above points are conclusions one draws by looking at shower images from these energies, the current telescopes' performance and studies like those shown in part IV. Studies dedicated to these very low energies will enable a more concrete understanding of the limitations in this domain.

10.2.3 Very high energy domain $E > 10$ TeV

One faces a different set of problems when working on very high energy gamma-rays. The showers are quite large and therefore shower parameter reconstruction is not a problem even with small sized (~ 5 -10 m diameter) telescopes. Moreover, observations can also be carried out at lower altitudes (near sea level) allowing for a larger choice of sites. However, the very low gamma-ray fluxes from multi-TeV sources require highly sensitive instruments and very large collecting surfaces. As the issues concerning this domain and the solutions to them are different from the previous two, we have chosen to focus this study on the low and high energy domain only. Note that projects like the TenTen IACT system [44] aim at creating telescopes optimised for the observations in this domain.

10.3 The altitude of observation

In earlier chapters, we took a look at the impact of altitude of observation on the Cherenkov photon density obtained on the ground (chapter 3) and the shower images obtained from them (chapter 6). These discussions show that while a number of properties are affected by the change of altitude, there are two main competing effects:

- The loss of Cherenkov light through atmospheric absorption at low altitudes of observation. This is particularly true for low energy showers which emit most of their Cherenkov light high in the atmosphere.
- The loss of information on shower longitudinal profile for high energy showers when the shower's development is stopped by the presence of the ground at high altitude. See section 2.3.2 for a discussion on the fraction of shower cut-off at various altitudes of observation for various energies.

We have therefore chosen to find a balance between these two effects for the target energy ranges by working at two intermediate altitudes of observation: 1800 m and 3600 m. Note that

while very high altitudes (~ 5000 m) have also been considered for IACT telescopes, concerns about logistics favour the selection of more moderate altitudes.

10.4 A note on some other parameters

10.4.1 Pixel size

Generally speaking, increase in image resolution (smaller pixel size) to a certain extent results in better shower parameter reconstruction as the images are better defined and their axes more easily identifiable. However, beyond a certain point the use of a smaller pixels implies that the fluctuations in images become more apparent and can actually result in poorer reconstruction of parameters. This is specially true at low energies where the intrinsic fluctuation in shower images are more important.

The choice of an ideal pixel size can therefore depend on several factors and would require dedicated studies for the optimisation. In order to limit the number of parameters whose impact is being studied, we have chosen a standard value for the pixel size: 0.1° sides for square pixels.

10.4.2 The field of view

All the studies carried out in this chapter use a field of view of 5.4° . One of the desired characteristics of future telescopes is a larger field of view. This would allow the observation of larger portions of the sky at a given time. At the same time, we have seen (in chapter 5) that as the field of view of the telescope becomes larger so do the aberrations caused by the mirror. A good telescope design tries to achieve a balance between the two tendencies. Efforts are also underway so that the effect of aberrations may be diminished through the use of different telescope and mirror designs. For instance the Davies-Cotton design [33] already used for some current generation telescopes gives less aberrations than a parabolic mirror. An elliptical mirror shape studied in [34] further improves off-axis imaging while diminishing close to the axis performance. Other studies ([36],[37]) show that telescopes with secondary mirrors allow good correction of the aberrations therefore allowing wider fields of view.

A study involving telescopes with large fields of view would ideally have to be based on simulations that use adapted mirror designs. The current version of the simulation tool described in this thesis uses parabolic mirrors. This tool could still be used to study the performance of telescopes with large fields of view but the precision on the reconstruction of various parameters would be underestimated as compared to what one would obtain with more adapted telescope designs. For this reason and also in order to avoid studying the effect of too many parameters simultaneously we have chosen to use a fixed and moderate field of view for the telescopes used in this study.

10.5 Optimising inter-telescope distance

Once the choice concerning telescope size and number has been made for the different energy ranges being studied, one can try to optimise the inter-telescope distance. There can be several ways of carrying out this optimisation. We have chosen to study the response of a telescope system to γ -rays as a function of the inter-telescope distance. In order to do so, we use a square unit of four telescopes in which inter-telescope distance is varied between 25 and 600 metres. The response of this system to γ -rays is studied for each inter-telescope distance by uniformly

generating γ -rays over a surface of $2400\text{ m} \times 2400\text{ m}$. The showers generated all have 0° zenith angle.

The gamma-ray simulations are carried out at two energies: one from each energy domain being studied (see earlier discussion in section 10.2). We have taken the lower limit of each domain since it places us in the most conservative of cases for that energy range. As the energy of γ -rays increases and showers become larger, one expects good parameter reconstruction even at larger inter-telescope distances

We therefore make the following choices for the two energy domains:

- The high energy domain simulations are carried out at 300 GeV with medium sized telescopes of 12.5 metres.
- Though the low energy domain has no clear threshold, we carry out simulations for optimisation at 50 GeV. As mentioned before, the complications in gamma-ray observations tend to become more important at lower energies. The optimisation is therefore carried out at a 'safer' energy where relatively good reconstruction is expected. The telescopes have 30 metre diameters.

10.5.1 Shower parameter reconstruction as a function of inter-telescope distance

Once the shower generation and simulation of the telescope response have been carried out, a simple trigger requiring that at least two telescopes have images with at least 50 photo-electrons is applied. The source position, core position on the ground and energy are reconstructed for all the showers passing the trigger and falling within a surface of $400\text{ m} \times 400\text{ m}$ around the array centre. The latter selection is made so that we optimise the inter-telescope distance based on showers from the region where the optimum conditions for shower parameter reconstruction exist. The effective area is calculated for all the showers passing the trigger condition. Below, we present and discuss the dependence of the source and core reconstruction precisions, energy resolution, and effective area as a function of inter-telescope distance.

Source reconstruction

The dependence of the precision of source position reconstruction on the inter-telescope distance at 1800 and 3600 m a. s. l. is shown in figure 10.1.

Initially, the precision shows an improvement as the telescopes move apart. This occurs because, when the telescopes are close together, the shower view obtained from one telescope is only slightly different from the one obtained by another telescope. This does not provide with enough cross-information to reconstruct the source position well. As the telescopes move apart, the shower images from various telescopes start providing more complementary information and this allows for an improvement in source reconstruction.

After about 100 metres of distance, the plots show a relatively flat region where the precision does not vary much with the inter-telescope distance. This corresponds to the ring position and the region around it where the Cherenkov photon flux on the ground is largest. This allows images where axis reconstruction is easier to carry out. The fluctuations in images are also smaller in this region.

Beyond this region, the source reconstruction deteriorates again. At these inter-telescope distances, if one of the telescope is in the Cherenkov ring region the others will be outside it. As the flux from Cherenkov photons decreases and the fluctuations become more important at larger distances outside of the Cherenkov ring, this makes the source reconstruction more difficult.

As can be seen from the above comments, one can determine a range of optimum inter-telescope distance by looking at figure 10.1. We make the following remarks:

- At 1800 m, there is a broad range of inter-telescope distances ranging from ~ 100 -250 m, where the precision on the source is optimum and does not vary much. Within this range, the best reconstruction seems to occur within 120 and 200 metres.
- The best reconstruction range is the same for 300 GeV showers, with medium sized telescopes and 50 GeV with large sized telescopes.
- Even with the use of 30 m telescopes for the 50 GeV showers, the precision for source reconstruction at 300 GeV remains better; it is around 0.1° for 300 GeV in the optimum range and 0.2° for 50 GeV in the same range.
- The range for best source position reconstruction is narrower at high altitude (bottom plot). A broad region where the precision does not vary a lot seems to lie between ~ 100 and 215 metres, with a narrow range for optimum performance between 120 and 175 metres. This narrow range for best reconstruction can be explained through the denser and narrower Cherenkov ring at higher altitudes (see sections 3.4.1 and 3.4.4).
- The precision of reconstruction is slightly better (by a few hundredth of a degree) at 1800 m than at 3600 m. This is visible in figure 10.2, where we superpose the results from both altitudes on the same plot.

Shower core reconstruction

The results for shower core reconstruction are shown in figure 10.3. We see trends that are similar to those seen for source reconstruction. The core reconstruction is poor when the telescopes are close together but improves rapidly as inter-telescope distance increases to 100 metres. This is followed by a flatter region where precision does not vary much. Beyond this region, the reconstruction deteriorates again. Here too, we describe the main features of the plot to determine a range for optimum inter-telescope distance:

- At 1800 m a. s. l., the optimum inter-telescope distance for core reconstruction lies between 100 and 250 metres for 300 GeV.
- This range seems to be slightly narrower for 50 GeV and lie between 100 and 200 metres.
- The precision of core reconstruction is better at 300 GeV (around 10 metres) than at 50 GeV (around 22 metres).
- At high altitude (bottom plot), the optimum range is narrower than for the same energy at low altitude. The optimum range at high altitude lies between 100 and 200 m for 300 GeV and 100 and ~ 175 m for 50 GeV.
- Contrary to what was observed for the source reconstruction, the core reconstruction precision is the same in the optimum range at both altitudes. This is visible in figure 10.4 where we compare the results from both altitudes. It even appears to improve by a few metres for the 50 GeV showers at high altitude. At very large distances (beyond 300 m), the results at low altitude are better, while at distances closer to the core (below 100 m), the reconstruction is more precise at high altitude. Once again this is explained by the smaller but denser Cherenkov ring at high altitude (see sections 3.4.1 and 3.4.4).

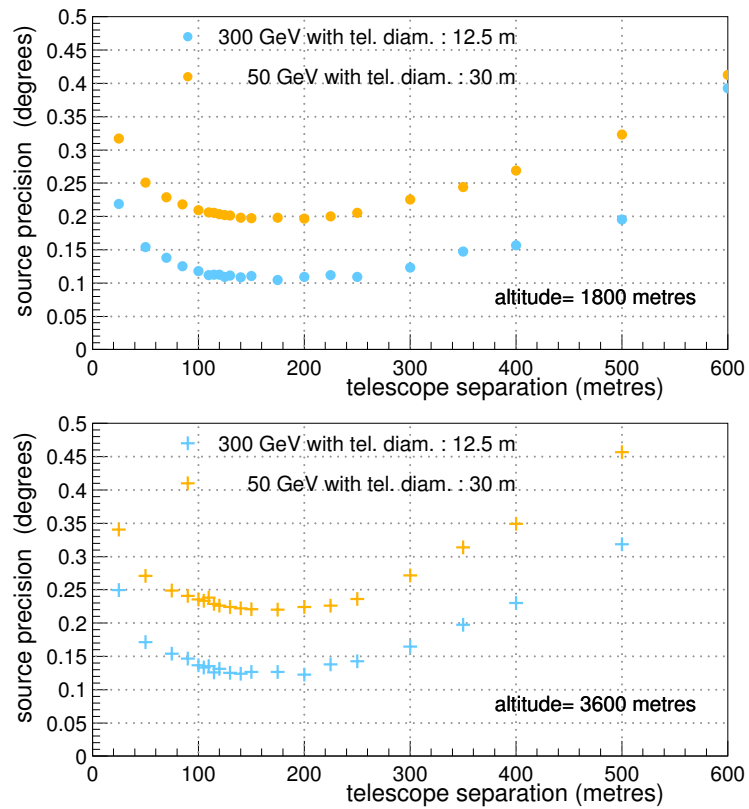


Figure 10.1: The precision on the source obtained by a four telescope system as a function of inter-telescope distance. The top and bottom plots correspond to the resolution obtained at the altitudes of 1800 m a. s. l. and 3600 m a. s. l. respectively.

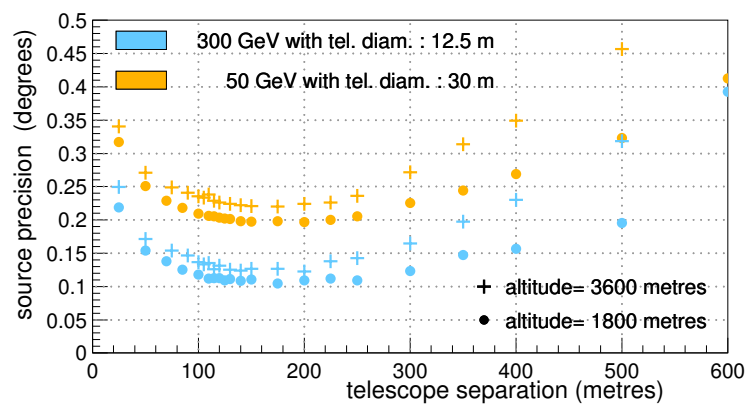


Figure 10.2: The precision on the source position obtained by a four telescope system as a function of inter-telescope distance. The values obtained for the altitudes of 1800 and 3600 m a. s. l. in figure 10.1 are compared with each other.

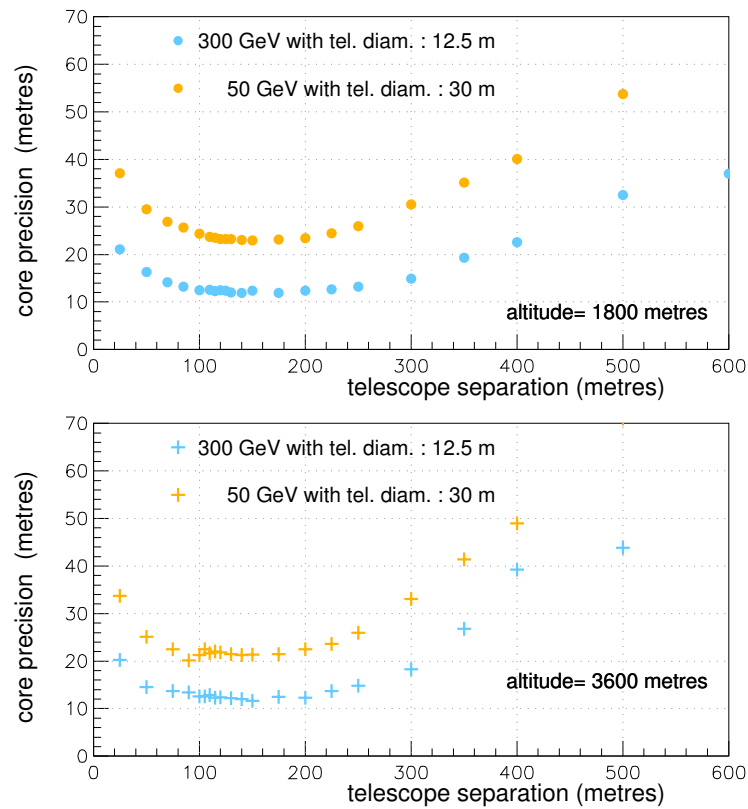


Figure 10.3: The precision of reconstruction of the shower core obtained by a four telescope system as a function of inter-telescope distance. The top and bottom plots correspond to the resolution obtained at the altitudes of 1800 m a. s. l. and 3600 m a. s. l. respectively.

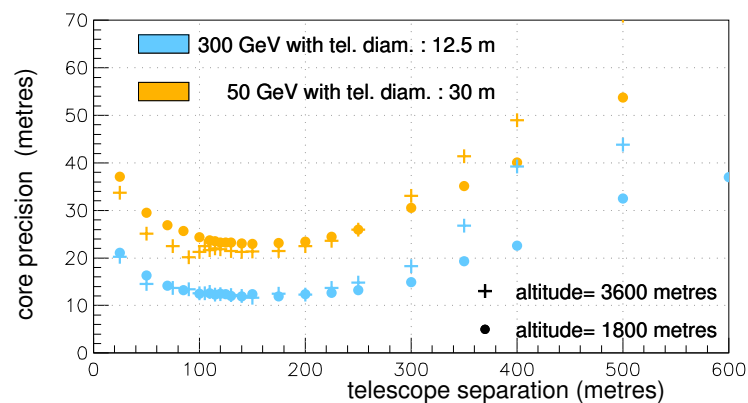


Figure 10.4: The precision on the shower core position obtained by a four telescope system as a function of inter-telescope distance. The results for the altitudes of 1800 and 3600 m a. s. l. shown in figure 10.3 are compared with each other on the same plot.

Energy reconstruction

Before we discuss the results obtained for the energy reconstruction, we recall that in chapter 8 we discussed a few problems with the energy reconstruction method we are using. We also established that while these problems do not get in the way of obtaining a good indication of the energy resolution of a telescope system at a given distance from the shower core, the method poses problems when the results from different distances are compared. The results presented in this section therefore give a good indication of the energy resolution but will not be used to evaluate an optimum range of inter-telescope distance.

The results of the energy reconstruction are presented in figure 10.5. One notes that the overall trends are similar to those observed for source and core reconstruction: a flatter region in the middle with poorer energy resolution before and after it. At the same time, the position and range of this region is somewhat different from the source and core reconstruction optimum range. One makes the following observations:

- The range where the energy is best resolves seems to lie between 200 and 350 metres.
- The energy resolution is poorer for 50 GeV showers than for 300 GeV showers.
- The resolution also deteriorates slightly at higher altitude.

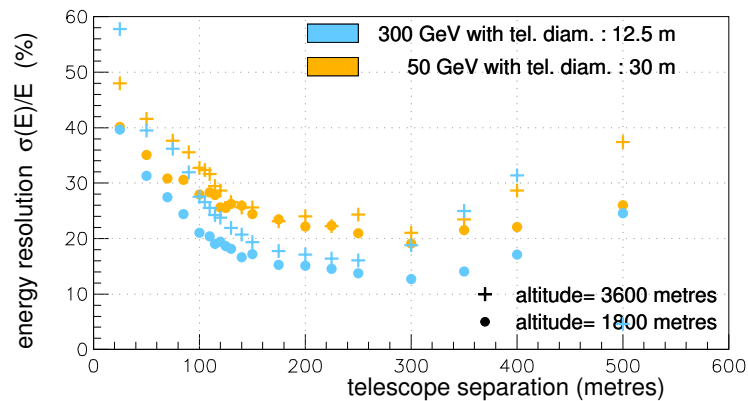


Figure 10.5: The energy resolution of a four telescope system as a function of inter-telescope distance. The values obtained for the altitudes of 1800 and 3600 m a. s. l. are compared with each other.

Effective area

The effective area of a telescope has a direct impact on the sensitivity of the instrument. It therefore provides with an additional means of determining the optimum inter-telescope distance. We have calculated the effective area of the 4-telescope unit by using the showers passing the trigger condition. The results are shown in figure 10.6 as a function of the inter-telescope distance.

One observes that the effective area shows a slight increase initially when telescope distance is increased. This occurs since the physical area covered by the telescopes increases as the telescopes are moved apart. One then arrives at a plateau like region where the effective area does not vary much. Once again this corresponds, to a large extent, to the Cherenkov ring region where the number of telescopes passing the trigger condition will be larger. Our trigger

requires that at least two telescopes fulfill the 50 photo-electron image condition. The plot shows that the number of such telescopes remains relatively stable up to a distance a little over double the ring size (around 300 metres). This occurs because when inter-telescope distance goes beyond a certain point after the Cherenkov ring, two effects enter into competition. On one hand, the physical area covered by the telescopes increases. But on the other hand, the Cherenkov photon flux decreases giving fewer showers for which the trigger condition is satisfied. As we move to even larger inter-telescope distances, the effective area shows an important decrease. At these distances the Cherenkov photon flux decreases to a point where very few showers pass the trigger condition.

We determine an optimum range of inter-telescope distances based on this plot by making the following observations:

- There is a broad region between around 50 metres and 300 metres, where the effective area does not change much.
- Within this broad range, the optimum lies in the 175-225 metre range.
- As can be expected, due to the smaller size of the Cherenkov ring at high altitudes, the effective area at 1800 m a. s. l. is larger than at 3600 m.
- Even if the Cherenkov photon density on the ground is lesser at 50 GeV than at 300 GeV, the use of 30 m telescopes allows to obtain a slightly larger area for 50 GeV than for 300 GeV with 12.5 m diameter mirrors.

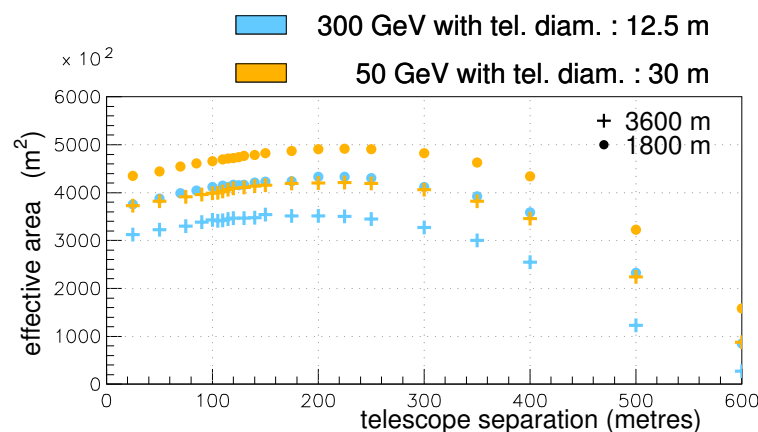


Figure 10.6: The effective area of a four telescope system at 1800 and 3600 m a. s. l. as a function of inter-telescope distance.

Conclusions

The dependence of the effective area and the source, core and energy reconstruction on the inter-telescope distance has shown us that there is an optimum range of inter-telescope distances where the IACT system studied performs best. In the case of source and core reconstruction this range lies between 100 and 200 metres at low altitude. At high altitude one gets the range 120-175 metres from the source reconstruction and 100-200 metres from the core reconstruction. The effective area is stable for a broad range: 50 - 300 metres. We will now use these results to design two large arrays of IACT and adapt them to both altitudes.

10.6 Array design

Using the results and discussion of the previous sections, one can design an IACT array aimed at making observations in the 50-10000 GeV range. We begin by presenting the choices made for the array at 1800 m a. s. l. and then rescale it to obtain an array at 3600 m a. s. l..

10.6.1 Low altitude configurations

Low energy part In section 10.2, we made and justified the choice of using a few (4 or 5) large sized telescopes to make observations in this domain. In order to have the largest possible effective area with such a limited number of telescopes, it is important that they are placed as far apart as possible without compromising on the parameter reconstruction capabilities. We therefore choose a telescope spacing at the upper edge of the optimum source and core reconstruction range i. e. 200 m. For the first configuration, we choose to work with 4 telescopes of 30 m of diameter placed on the corners of a 200 m square (see the four central markers in figure 10.7-left).

High energy part For this energy domain, we decided to use a large number of medium sized telescopes to cover a large surface area in order to get improved sensitivity. It is therefore less important to use the largest possible inter-telescope distance here. We therefore, choose an inter-telescope distance from the middle of the optimum range for source and core reconstruction shown in figures 10.1 and 10.3. As a result, thirty-three telescopes of 12.5 m diameter are added to the four large telescopes in such a way that the resulting system has an inter-telescope distance of 140 m. The resulting system is shown in figure 10.7 (left) and covers a surface with a radius of around 400 m.

Obtaining a denser system In order to study the effect of using a more densely packed IACT system, we also study a second configuration where we add 16 more medium sized telescopes

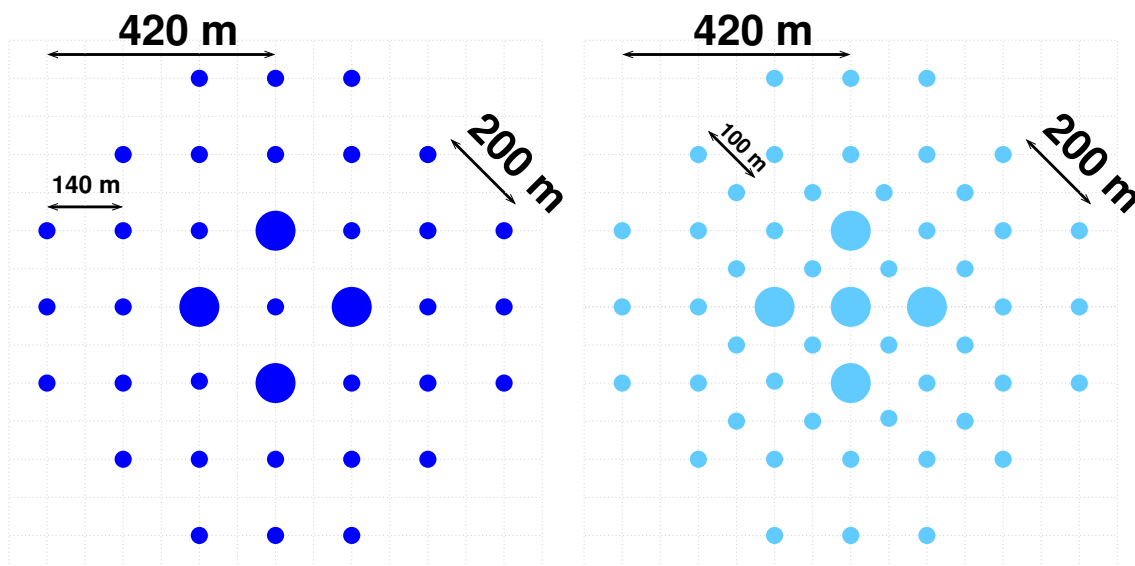


Figure 10.7: The two array configurations at 1800 m with configuration 1 on the left and configuration 2 on the right.

as shown in figure 10.7 (right). The central medium sized telescope is also replaced by a large 30 m diameter telescope. The resulting array configuration has 100 m inter-telescope distance, which corresponds to the lower edge of the optimum range for shower reconstruction.

10.6.2 High altitude configurations

At 3600 m a. s. l., the system is rescaled so that the distance between the four large telescopes is 175 m. This rescaling is done by using the ratio between the Cherenkov ring sizes on the ground at 3600 m (around 105 m radius) and at 1800 m (around 120 m radius). Additionally, one notes that 175 m also corresponds to the upper limit of the optimum shower core reconstruction range in figures 10.1 and 10.3 (bottom). Applying the same rescaling to the rest of the configuration, the separation between the medium-sized telescopes is 120 m. For the denser configuration, this distance between medium sized telescopes is 87 metres. The surface area covered by this configuration has a radius of around 350 metres. One notes that while this configuration was obtained from a simple rescaling of the low altitude configuration, one could also adopt an approach similar to the one used for the low altitude arrays to design the array at 3600 m.

In the end, we find ourselves with two different array configurations with 37 telescopes in one case and 53 in the other one. The characteristics of these arrays are summarised in table 10.1.

	Telescope size	1800 m		3600 m	
		configuration 1	configuration 2	configuration 1	configuration 2
Number	large	4	5	4	5
	medium	33	48	33	48
Distance (m)	large	200	140	175	120
	medium	140	100	120	87

Table 10.1: The number of telescopes and the distance between them in the different array configurations.

10.7 Study of the γ -ray observation capability of the large arrays

With the array designs finalised, we can study their response to γ -ray showers at various energies. In order to do so, we uniformly generate γ -rays over a surface of 2400 m \times 2400 m at fixed energies: 30, 50, 100, 300, 1000 and 10000 GeV. The trigger described earlier i. e. requiring that at least two telescopes have images with at least 50 photo-electrons is applied to the shower images. The showers passing the trigger are used to calculate the effective area. The reconstruction of the source position², shower core position on the ground and energy is carried out for only those showers that fall in a square region of 800 m \times 800 m around the array centre.

10.7.1 Results

The effective area, precision on the source and core positions, and energy resolution are presented and discussed below.

²As a matter of interest, we show examples of the χ^2 maps obtained as a result of the preliminary scan (explained in section 7.1.3) in figure A.7 in the appendix.

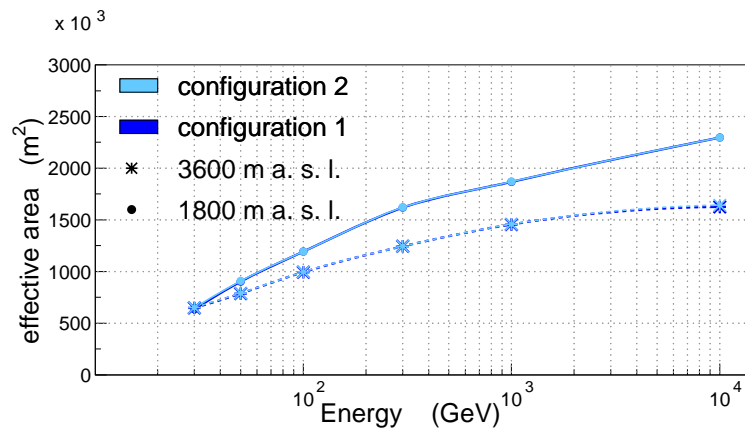


Figure 10.8: The effective area of the arrays as a function of energy. The two colours correspond to the two configurations, whereas, the different line and marker types correspond to the two different altitudes of observation. The lines joining the plotted points are intended to guide the eye and have no physical significance.

Effective area

Figure 10.8 shows the effective area of the two arrays at both altitudes of observation. As expected the effective area increases with the energy. This happens because high energy showers produce denser Cherenkov photon distributions over larger surfaces on the ground, implying that larger showers can be detected from afar.

We also see, that for higher energies, the effective area at 3600 m is smaller than at 1800 m. This is due to the combined effect of two factors. On the one hand, the array configurations at 3600 m are rescaled versions of those at 1800 m. This implies that they cover smaller surface areas on the ground. The second reason is apparent in figure 3.17 where the Cherenkov density profiles on the ground for both altitudes are shown. The figure shows that, at high altitude, the Cherenkov photon distribution on the ground is denser within the Cherenkov ring region, but beyond that, it falls off more quickly than at lower altitudes. This leads to telescope images with fewer photo-electrons at large distances from the core position. Moreover, this effect is more pronounced at higher energies. See discussion in section 3.4.4 for more details. One also notes that there is no difference between the effective area of the configurations with different telescope densities; both configurations occupy the same surface area.

Source reconstruction

The precision for the reconstruction of the source position is presented in figure 10.9 as a function of the shower energy. The results presented here have been calculated for all the showers passing the trigger conditions and falling within a surface of 800 m \times 800 m around the array centre. This implies that the precision shown in figure 10.9 is what we obtain by fitting the distribution of the distance between the generated and reconstructed source positions of all the showers generated uniformly over this surface. The precision corresponding to individual positions or areas within this surface may be different from this value³.

³In section 7.1.4, where we presented the results for the source reconstruction obtained for a four telescope system, we calculated the precision obtained for individual core positions. This was done by generating a large number of showers at each core position and fitting the corresponding distributions of the distance between the generated and reconstructed source positions.

As is usual, the precision for the reconstructed source improves with the energy since showers become larger and give better defined images on more telescopes. One also notices that the source reconstruction seems to be slightly better at lower altitude. This could be because the source reconstruction is slightly more difficult to carry out at higher altitude. But this could also simply be a consequence of using the same surface area ($800\text{ m} \times 800\text{ m}$) on both altitudes to calculate the precision on the source. The arrays simulated at 3600 m have smaller diameters (around 350 m) than those at 1800 m. This implies that the region where the best reconstruction is possible may be smaller as well. More studies would be needed to confirm the reasons for this trend.

One also notices that in the low energy domain, the use of a denser telescope system (five large telescopes instead of four) seems to result in a slight improvement of the source reconstruction. However, the difference is so slight that it would require further investigation in order to confirm or refute this trend.

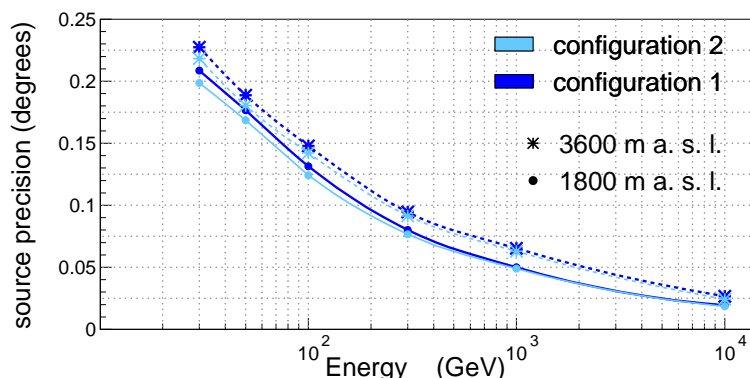


Figure 10.9: The source precision of reconstruction as a function of the energy. The results presented here have been calculated for all the showers falling within a surface of $800\text{ m} \times 800\text{ m}$ around the array centre. The lines joining the plotted points are intended to guide the eye and have no physical significance.

Reconstruction of the core position on the ground

The precision for the reconstruction of the core position on the ground is presented as a function of the generated energy in figure 10.10. As with the source reconstruction results, the values in this plot have been calculated by taking into account all the showers falling within a surface of $800\text{ m} \times 800\text{ m}$ around the array centre. Once again, this implies that the precision at different points in this region may differ from the values given here.

Many of the features of the core position reconstruction precision are the same as those for the source reconstruction. The precision for the reconstructed core position improves with energy as higher energies tend to give better defined shower images. In the high energy domain, unlike with the source reconstruction, there does not seem to be any difference between the precision obtained at higher and lower altitudes. The density of the arrays does not have an impact on the quality of core reconstruction, either, in this energy range.

However, at lower energies, specially below 100 GeV, there seems to be a slight improvement in the quality of core reconstruction at higher altitudes. The use of a denser array (five large telescopes instead of four) also seems to slightly improve the precision. However, like with the source reconstruction, these differences are so slight that further investigation is required in order to confirm or refute this trend.

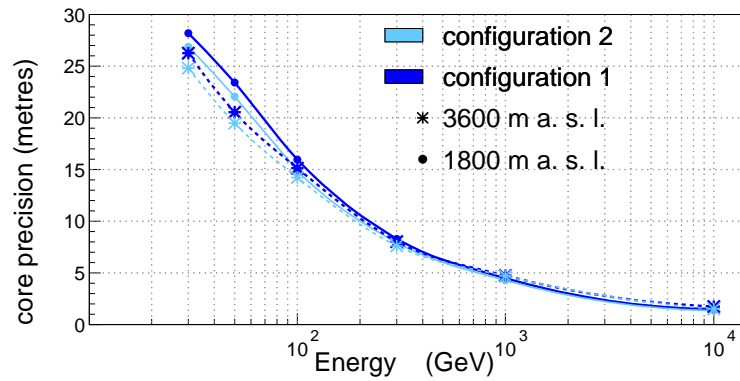


Figure 10.10: The precision of reconstruction of the shower core as a function of the energy. The results presented here have been calculated by taking into account all the showers falling within a surface of 800 m×800 m around the array centre. The lines joining the plotted points are intended to guide the eye and have no physical significance.

Energy resolution

Figure 10.11 presents the variation of the energy resolution as a function of the generated energy. As with the other reconstructed parameters, the energy resolution shows an improvement with increasing energy. This happens because the intrinsic fluctuations on the number of photo-electrons in shower images become smaller. Moreover, the energy reconstruction also depends on the source and core reconstruction which also improve with increasing energy.

The energy reconstruction at 1800 m a. s. l. is slightly better than at 3600 m a. s. l. As with the source reconstruction, this may be due to the improvement of energy reconstruction at lower altitudes, but it could also be due to the use of the same surface area (800 m×800 m) on both altitudes, to calculate the precision on the source.

Apart from this, one also notices that the use of a denser telescope system does not seem to improve the quality of energy reconstruction.

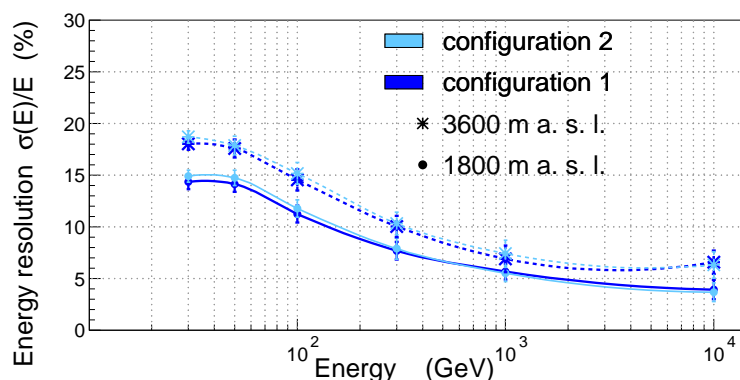


Figure 10.11: The energy resolution as a function of generated energy. The lines joining the plotted points are intended to guide the eye and have no physical significance.

10.7.2 Comparison with four-telescope array

The performance of these arrays can be compared with those of a current generation array. In chapters 7 and 8, we studied the shower reconstruction capabilities of an array with 4 telescopes of 12.5 m diameter situated at 1800 m a. s. l.. A detailed description of this array is given on page 110. Here, we begin by introducing the effective area of this telescope array as a function of the energy (see figure 10.12) and comparing it with the effective area of the large arrays studied in this chapter (figure 10.8).

In the high energy range, the effective area is at least several times larger than for an array with four medium sized telescopes. This can be seen by comparing the performance of the large arrays with the results given in figure 10.12, but also by looking at figure 10.6 where we showed the effective area obtained by a four telescope system with various inter-telescope distances. As an example, at three hundred GeV, the effective area of the four telescope system is around $500 \times 10^3 \text{ m}^2$ at 1800 m of altitude. At the same altitude and energy, the large arrays yield an effective area of $1500 \times 10^3 \text{ m}^2$. A similar improvement is obtained for lower energies when compared with an array with four medium sized telescopes. As an example, the effective area for the array with four 12.5 metre diameter telescopes at 50 GeV is around $125 \times 10^3 \text{ m}^2$ at 1800 m a. s. l. (see figure 10.12) and it is close to $800 \times 10^3 \text{ m}^2$ at 1800 m for the large array. Note that this improvement is in large part due to the use of larger telescopes for the low energy domain. This can be seen verified by looking at figure 10.6, where the effective area of an array with four 30 m telescopes is around $500 \times 10^3 \text{ m}^2$ at 1800 m.

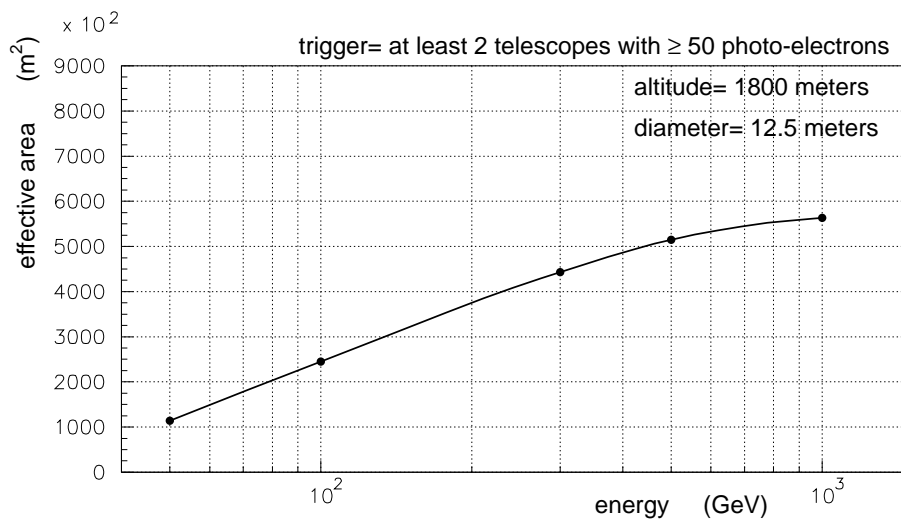


Figure 10.12: The effective area of a four telescope system (see page 110 for a detailed description of the system used) as a function of the energy. The lines joining the plotted points are intended to guide the eye and have no physical significance.

The comparison of the shower parameter reconstruction capabilities of the large arrays with those of the four telescope system presented in chapters 7 and 8 is slightly more complicated. The source and core reconstruction precisions and energy resolution of the large arrays have been calculated for all the showers passing the trigger conditions and falling within a $800 \text{ m} \times 800 \text{ m}$ around the array centre. At the same time, we recall that the reconstruction of the shower parameters for the four telescope array in chapters 7 and 8 was carried out with fixed shower core positions and without the application of a trigger condition. While this difference of methods does not allow us to compare the values obtained for both systems directly

with each other, we can still obtain information by looking at the results from each of them.

We therefore begin by recalling the results obtained for the source and core reconstruction for the four telescope array (see figures 10.13 and 10.14). At 50 GeV, the precision for source reconstruction lies close to 0.2° . It improves for the shower core positions (85,0) m and (100,0) m where we get 0.12° and 0.15° respectively. Note that (85,0) m is a particular core position as the shower falls right on top of one of the four telescopes. For the shower core positions beyond the Cherenkov ring (200,0) m and (200,200) m, the precision deteriorates significantly, giving 0.28° and 0.35° respectively. In comparison, the large arrays at 1800 m a. s. l. yield a source reconstruction precision of 0.17° over distances of up to around 400 m from the array centre (surface of $800 \times 800 \text{ m}^2$). As noted before, this is the precision obtained by fitting the distribution of the distance between the generated and reconstructed source positions of all the showers generated uniformly over this surface. Therefore, the precision obtained for specific positions within this area can fluctuate above or below this value. For instance, it is expected that the precision will increase for shower cores close to the large telescope positions. Conversely, it is also expected that the source reconstruction will deteriorate at larger distances from the array centre. At 1000 GeV, the four telescope system yields a source reconstruction precision between 0.05° and 0.1° . The precision deteriorates to 0.16° for the (200,200) m core position, when all the telescopes are well outside of the Cherenkov ring region. With the large arrays, a precision of 0.05° is achieved at 1800 m a. s. l. Once again, this precision is obtained for a uniform generation of showers over a surface of $800 \times 800 \text{ m}^2$ and may vary at individual positions on this surface. While the comparisons made above are not direct, they do show that the passage from a four telescope system to a large array (such as those studied in this chapter) can yield an improvement in source reconstruction capabilities.

Similar remarks can be made for the core reconstruction. At 50 GeV, the core reconstruction precision obtained for the four telescope array lies close to 20 metres for most shower core positions. It improves to about 13 m for the (85,0) m core position and deteriorates to 33 m and 42 m for the (200,0) m and (200,200) m respectively. With the large arrays, the precision obtained is around 22 m and 19 m with the denser arrays at 1800 m and 3500 m a. s. l. respectively for the showers passing the trigger condition and falling within a surface of $800 \times 800 \text{ m}^2$ around the ar-

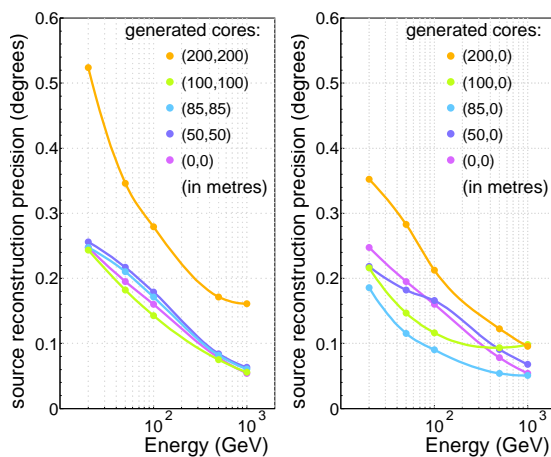


Figure 10.13: The precision of source reconstruction as a function of the energy for shower cores generated along the diagonal (left figure) and those generated towards the right (right figure) of the four telescope system. See page 110 for more details.

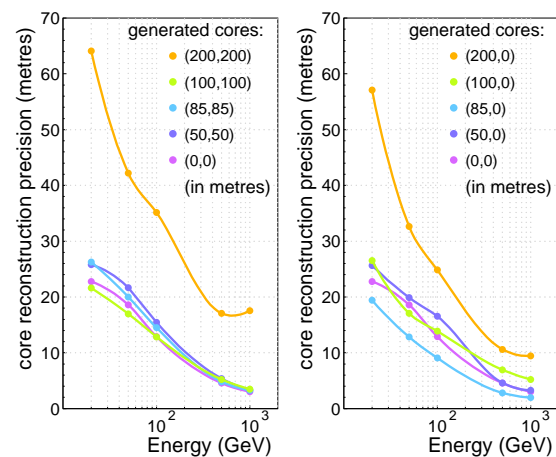


Figure 10.14: The precision of core reconstruction as a function of the energy for shower cores generated along the diagonal (left figure) and those generated towards the right (right figure) of the four telescope system. See page 110 for more details.

ray centre. At 1000 GeV, the four telescope array gives core reconstruction precisions between 3 m and 10 m for most shower core positions (figure 10.14). The precision deteriorates significantly for the (200,200) m core position (around 18 m) when the telescopes are well outside the Cherenkov ring region. With the large arrays, a precision of about 5 m is obtained for the showers passing the trigger conditions and falling within a surface of $800 \times 800 \text{ m}^2$. Once again these indirect comparisons point towards a possible improvement in the core reconstruction capabilities with large telescope arrays.

In figure 10.15, we recall the energy resolution obtained as a function of the generated energy, for various shower core positions, for the four telescope system. These results were originally presented and discussed in section 8.4. Here, we use them to compare the energy resolution of the four telescope system and the large arrays studied in the current chapter. At 50 GeV, the energy resolution for most shower core positions lies within 15 and 20%. Like with the source and core reconstruction precisions, the energy resolution deteriorates for shower core positions for which the telescopes are well outside the Cherenkov ring region of the shower. We obtain an energy resolution of more than 30 % when the core position is (200,200) m. With the large arrays, the energy resolution obtained at 50 GeV is close to 15% for the showers passing the trigger condition and falling within 400 m (surface of $800 \times 800 \text{ m}^2$) of the array centre at 1800 m a. s. l.. At 1000 GeV, the energy resolution obtained from the four-telescope array lies between 5 and 15% for most shower cores and deteriorates to values greater than 30% for the (200,200) m core position. In comparison, the large arrays give a resolution of about 6% for the showers falling within a distance of 400 m from the array centre. This shows that the use of large arrays such as the ones described in this chapter can yield an improvement for the energy reconstruction capabilities in comparison with the four medium sized telescope systems studied earlier.

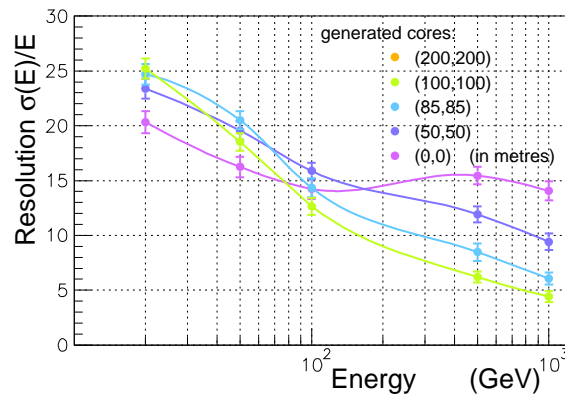


Figure 10.15: The energy resolution as a function of the generated energy for shower cores along the diagonal of the four telescope system. The resolution is calculated from the Landau fit of reconstructed energy distributions. The resolution of the (200,200) core position is well above 30% and hence does not appear on this plot. It can, however, be seen in figure 8.8 of section 8.4. Note that the lines joining various points on this plot are only meant to guide the eye and do not have any physical significance.

10.8 Conclusions and perspective

The work presented in this chapter shows the potential of the telescope simulation and γ -ray reconstruction tools to be used for the purpose of designing arrays and optimising their

parameters. The study carried out to optimise the inter-telescope distance, and the use of its results to design two large arrays, is an example of this. Moreover, the work presented here (as well as in the previous chapters) shows how the simulation and reconstruction tools can be used to test and evaluate the performance of an IACT system. Here, we were able to test two large arrays at two different altitudes. These preliminary results give an indication of the improvements possible with such large arrays in comparison with today's telescopes.

We also had different strategies for the choice and optimisation of IACT array parameters. The choice of the number of telescopes and their size was based on the target energy range and the knowledge about the capacities of current-day telescopes in these domains. The optimisation of the inter-telescope distance was carried out by evaluating the telescope performance as a function of the distance through simulations. The final choices for the large arrays were made based on the results from these methods and the physics goals for the arrays.

This chapter has also yielded a number of directions for future work. To begin with, we gave a preliminary evaluation of the two large arrays studied in this chapter. More detailed studies can be carried out to better assess their capacities for γ -ray observations. These could include simulations with more statistics in order to confirm or refute certain trends observed in the results presented here: improvement of the performance for high energies at low altitude, improvement of the performance for low energies at higher altitude... Also, it was not understood whether the improvement of performance at higher energy and lower altitude is a result of the smaller Cherenkov telescope array surface at higher altitude or smaller Cherenkov ring size or a combination of both. Slightly different arrays e. g. some that are specifically designed for the higher altitude and not merely rescaled from lower altitude arrays could be simulated in order to respond to this question. Most studies tend to favour lower altitudes, so a study with specialised arrays for higher altitudes could be used to either confirm this trend or further investigate the performance of arrays at the higher altitude. Also, the results presented in this chapter have been calculated for all the showers passing the trigger conditions and falling within a square region of $800\text{ m} \times 800\text{ m}$ around the array centre. In future studies, the angular and energy resolution could also be evaluated as a function of the shower core position in the telescope field.

While the optimisation of telescope parameters was carried out by looking at the reconstruction capabilities and effective area of an array as a function of a given parameter, such studies could also be carried out by looking at the hadron-gamma separation. Eventually, the sensitivity of the system could also be calculated as a function of this parameter.

Other parameters like the pixel size and telescope field of view could also be studied and optimised as a function of the physics goals of the IACT array. Moreover, night sky background and image cleaning could also be introduced in the simulations.

IACT arrays could also be designed by mixing telescope types (field of view, pixel size ...) as well as by studying the impact of varying the telescope density in the surface covered by the IACT array.

CHAPTER 11

CONCLUSIONS

11.1 Summary

Since its inception about 20 years ago, IACT based γ -ray astronomy has established itself as a reliable means of exploring the γ -ray universe. It also complements the observations made by satellite based telescopes and extensive air shower arrays whose main domain of observations lie in different energy ranges. The current generation of IACT has allowed us to improve our knowledge of known γ -ray sources as well as discover new sources in the GeV-TeV domain. Currently, efforts are underway to design the next generation of IACT arrays. The physics goals of the future IACT arrays will determine the performance required by them in terms of sensitivity, angular resolution, energy resolution ... These characteristics are dependant on a large number of array parameters such as the number of telescopes, telescope type, telescope sizes, telescope field of view, mirror type, camera size and pixelisation, altitude of observation, array configuration ... In order to study the impact of these parameters and optimise them for future IACT arrays, detailed studies with adapted tools are necessary.

The main goal of the work presented in this thesis was therefore the development of tools for the simulation and reconstruction of γ -ray induced atmospheric showers in order to assess the performance of various configurations of IACT arrays.

The program developed for the simulation of IACT arrays takes the output of the shower simulation package CORSIKA and gives the response of individual telescopes in the array in the form of the images obtained. This program was made as flexible as possible so that any telescope configuration with parabolic mirrors can be studied. It allows the simulation of arrays with large number of telescopes (up to a hundred) whose individual parameters can be set up independently of each other. These parameters include the number of telescopes, their position and orientation, the sizes and focal lengths of their mirrors, camera sizes and positions and pixel size. Efforts have also been made to make the program as modular as possible. This ensures that more details (e. g. tessellation of mirror) as well as new elements (more telescope or mirror types etc.) can be added to the program later on.

The methods for the reconstruction of source position and shower core position take into account the stereoscopic nature of the observations in IACT arrays. The likelihood function minimisation involved in both methods uses the information available from the images of all telescopes, simultaneously. These two methods along with the method for the reconstruction of the energy have been applied on a four telescope test array and the results are consistent with what one obtains with current-day telescopes. A study including a simple method of image cleaning was also included and it shows that the results of source and core reconstruction can be improved if the images are cleaned in an appropriate manner.

The application of these reconstruction methods to this four telescope system has also highlighted the impact of numerous parameters on γ -ray reconstruction, in terms of the energy of the shower as well as its core position. This exercise is important as it helps us make choices

about various telescope parameters as a function of the performance required of future IACT arrays.

It was largely through the understanding gained through this exercise that two possible future IACT arrays were designed and tested. This had the dual purpose of testing the simulation and reconstruction tools developed earlier as well as exploring the various aspects involved in array design and understanding the impact of several parameters. This study has shown that the tools developed can indeed be used to optimise the various parameters of an IACT array and also shown how the use of larger arrays can improve our γ -ray observation capacities.

The development of the telescope simulation and shower parameter reconstruction tools was also preceded by a detailed study of showers and the main properties of their Cherenkov emission. Once the telescope simulation package was developed, it was also used to understand the properties of electromagnetic shower images and how they are affected by various shower parameters. These studies combined with the development and application of reconstruction methods provide us with an overview of the main elements in γ -ray astronomy.

11.2 Future directions

This thesis has yielded a number of directions in which future work could be carried out. Some of this work can be carried out to further develop and test the simulation and reconstruction tools. Other directions for future studies include further investigation of the impact of various array parameters on the capabilities for γ -ray observations as well as the development of new tools for the discrimination of hadrons and γ -rays.

11.2.1 Telescope simulation program

As far as the IACT simulation program is concerned, more options and details can be implemented in the program as the need arises. This can be easily done due to the modularity of the program. An example of the changes that can be implemented is the introduction of new mirror shapes and telescope designs. Since one of the parameters being explored for future IACT arrays is the field of view of telescopes, it can be interesting to look at telescope designs that are more adapted for large field of view observations. These include different mirror shapes such as the Davies Cotton design but also telescopes with secondary mirrors that are particularly adapted for larger fields of view. Apart from this, details such as mirror tessellation can also be introduced if needed. A routine to simulate night sky background and add it to the shower images could also be implemented.

11.2.2 γ -ray reconstruction methods

As we have seen, the methods for source and core position reconstruction give results that are comparable with other methods in current-day telescopes. However, we also saw that there could be ways of further improving the methods.

In their current form, these methods use a fixed value of the parameter σ_t (the standard deviation of the transverse profile of shower images when they are fitted with a Gaussian curve) for likelihood maximisation. However (as we have seen in the discussion in chapter 7), σ_t depends on the distance between the telescope and the shower core position. The source and core reconstruction could therefore be improved through the use of an adapted σ_t value. This could be done through an iterative method where a table of σ_t values is compiled, through simulations, as a function of the distance between the telescope and core positions. As a first step the source and core position could be calculated using a fixed value of σ_t . Once the core

position would be known, the appropriate value of σ_t could be taken from the table and used to calculate the final source and core positions. Such an iterative method would require extensive simulations for compiling σ_t value tables.

Alternatively, one could also try to fit individual transverse profiles to determine a value of σ_t for each telescope image. When the fits would not converge or would not represent the curve well, one could fall back on using a fixed value of σ_t . This method would be more dependent on the quality of image cleaning than others.

The method for the reconstruction of energy could also be improved. The current method of energy reconstruction uses the relationship between the energy, the distance of the telescope from the shower core position and the number of photo-electrons obtained in shower images. For this purpose we have made tables of values relating the three parameters based on simulations. But we have also seen that there is a relationship between the altitude of first interaction and the number of photo-electrons obtained in telescope images. If the longitudinal profile of the shower is reconstructed then the tables of the number of photo-electrons could also include an additional parameter such as the depth of shower maximum to obtain a more accurate value of the energy. The reconstruction of the longitudinal profile could be carried out by using the method we described in this thesis.

Also the work presented in this thesis did not include simulations of the night sky background. This exercise has allowed us to bring out the properties of shower images, reconstruction methods and the dependence of telescope performance on various telescope parameters in the simplest and ideal conditions. In order to complement this work, however, studies in more realistic conditions i. e. using the simulation of the night sky background and including image cleaning methods are also necessary. A further step, could also include the simulation of the geomagnetic field whose impact is particularly important at low energies.

11.2.3 Gamma-hadron separation

The implementation of gamma-hadron separation methods can provide with an additional tool with which to study the performance of future IACT arrays. In fact, one of the important requirements of future IACT is improved sensitivity (specially in the main energy range of operation). Since the sensitivity depends on the gamma-hadron separation capability of telescopes it is important to have tools for studying it. In this thesis, we have discussed three ideas for the separation of hadrons from gamma rays. Future work could involve the development of these ideas into methods and their testing.

The first method uses the χ^2 values obtained from the source and core reconstruction. The preliminary results given in this thesis have shown that this value can be used as a tool to discriminate between hadrons and γ -rays. This method could be developed with the current versions of the source and reconstruction methods. At the same time, since it depends on the χ^2 value obtained from the source and core reconstruction, it could also benefit from implementing some of the methods mentioned above for obtaining better adapted σ_t values and therefore giving more accurate χ^2 values.

The other two ideas depend directly on the reconstruction of the longitudinal profile and indirectly on the reconstruction of the source and core positions. The method for the reconstruction of the longitudinal profile given in this thesis and the source and core reconstruction methods can be used to implement these ideas.

We also add that these ideas were tested with protons at fixed energies and falling at the centre of a four telescope test system for the work presented in this thesis. In order to develop these ideas into methods, simulations of a spectrum of protons will need to be carried out with varying shower core positions and angles of incidence in the atmosphere. The night sky

background will also need to be simulated along with the implementation of an image cleaning method.

11.2.4 Future IACT arrays

Finally, possible future work involves the use of the simulation and shower reconstruction tools to optimise the parameters of future IACT arrays and study their characteristics. Such studies can take numerous different directions depending on the physics goals, feasibility, financial and technical constraints ... Here, we will focus on ideas that are a direct continuation of the work presented in this thesis.

In the last chapter of this thesis, two possible configurations for IACT arrays were designed and studied. While the number of telescopes and their sizes was chosen as a function of the physics goals in different energy domains, the inter-telescope distance was determined so as to obtain best γ -ray parameter reconstruction as well as effective area. In future work, this kind of optimisation could also take into account the γ -hadron separation capabilities of the IACT array. The two arrays studied in this chapter could also be evaluated for their γ -hadron separation capacities and sensitivity. This would allow us to make quantitative predictions about the arrays' performance for observations of specific γ -ray sources.

The two arrays designed in this chapter were evaluated for their γ -ray reconstruction capabilities. The results have indicated a number of trends such as a slight deterioration of angular resolution and a slight improvement of the core position reconstruction for low energy showers at high altitude. However, it is not clear whether these trends are due to a statistical effect, the choice of the array designs or a direct result of the change of altitude. Further efforts to investigate these trends could include working with more statistics as well as the simulation of slightly different arrays at higher altitude. The results obtained in this thesis have also shown that one can get angular and energy resolutions that are comparable to a four telescope array but over a much larger surface area with the two large arrays. This trend could also be investigated further by looking at γ -ray reconstruction capabilities as a function of various parameters such as shower core position.

The arrays designed in this thesis had relatively broad physics goals and a target energy range from several tens of GeVs to several tens of TeVs but one could also work on array designs for more specific goals such as arrays optimised for the low energy domain (below a few hundred GeVs).

While the work presented here focused on certain telescope parameters such as telescope size, number, inter-telescope distance and altitude of observations, this could be expanded to a number of other parameters. This could include the pixel size and field of view of telescopes. The parameters already studied here could also be optimised using other methods and arguments. Moreover, array designs involving several telescope types and designs could also be explored e. g. arrays with telescopes of different fields of view or pixel sizes. Additionally, the impact of varying the telescope density in the area covered by the IACT array could also be looked into.

APPENDIX A

FIGURES

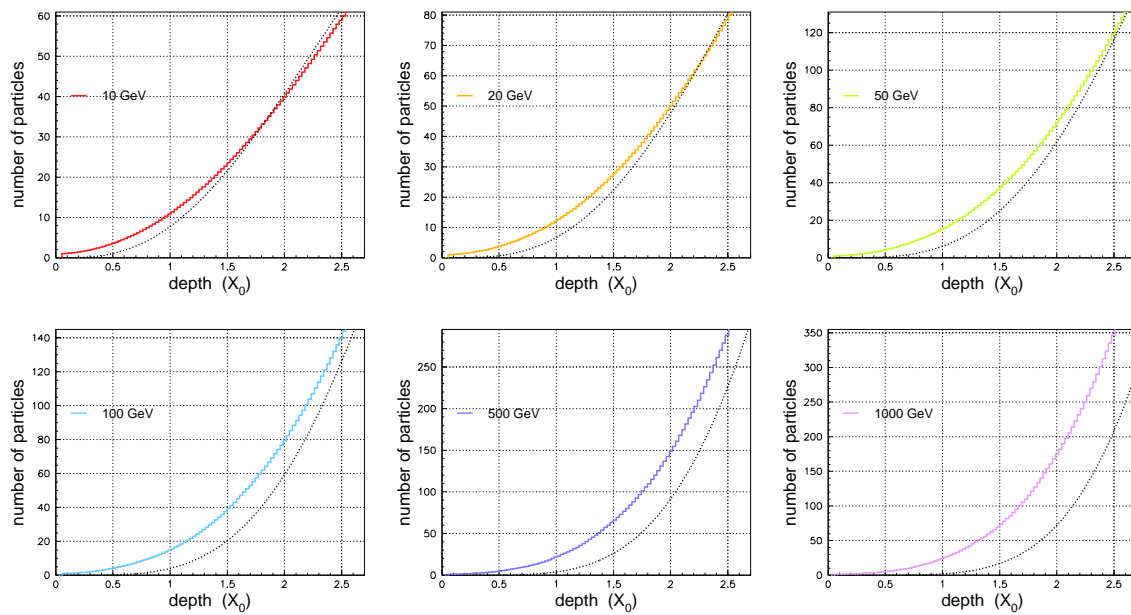


Figure A.1: The first few radiation lengths of the average longitudinal profiles of γ -induced showers in terms of the number of particles i. e. electrons and gamma photons (coloured lines) for various energies. The profiles are fitted with the function $f(t) = C(\beta t)^{\alpha-1} e^{-\beta t}$ and the result of the fits are shown through the dotted lines. The entire profiles are shown in figure 2.9 of the main text.

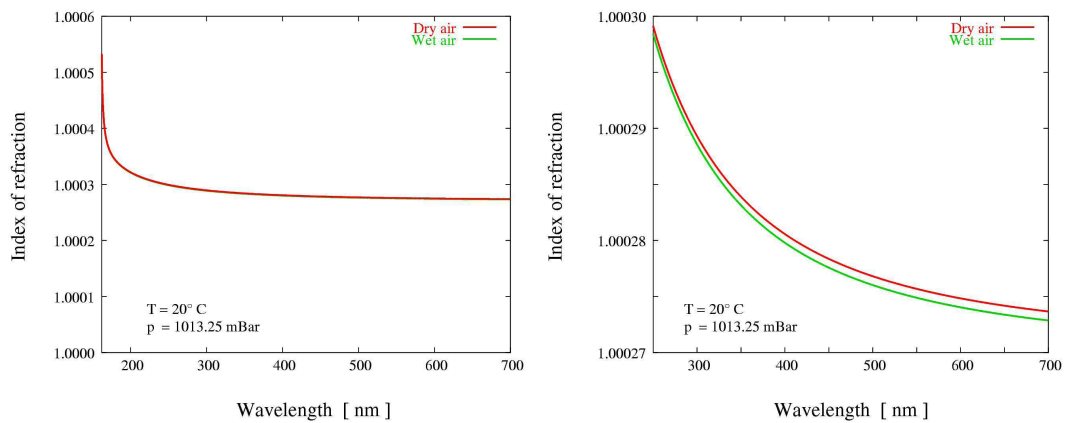


Figure A.2: The dependence of the refractive index of air on the wavelength of the photons. The plot on the left is a zoom of the one on the left in the 300-700 nm wavelength range and shows that the refractive index changes very little in this domain. These figures are taken from [45].

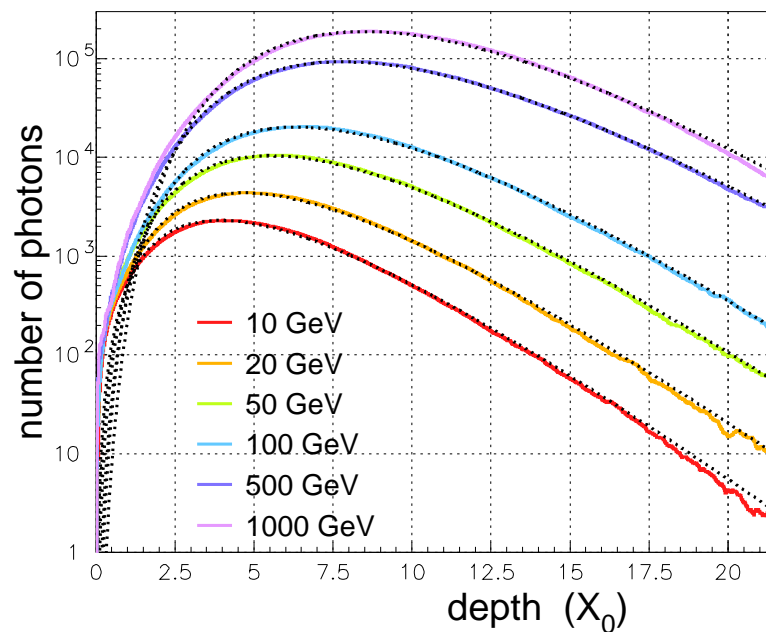


Figure A.3: The average longitudinal profile of γ -induced showers in terms of the number of Cherenkov photons emitted at each depth for various energies (log scale). These distributions are fitted with the function $f(t) = C(\beta t)^{\alpha-1} e^{-\beta t}$ (dotted lines). The same profiles are shown in linear scale in figure 3.3 of the main text.

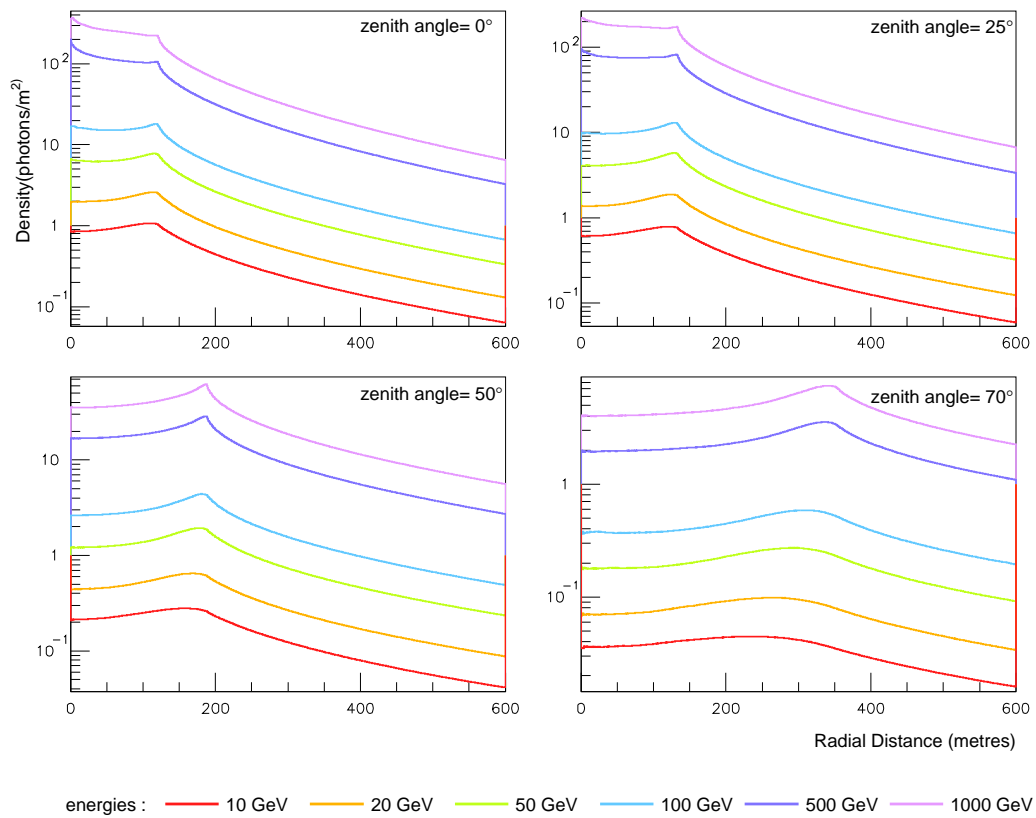


Figure A.4: The comparison of the average density of Cherenkov photons on the ground for showers generated with various primary angles.

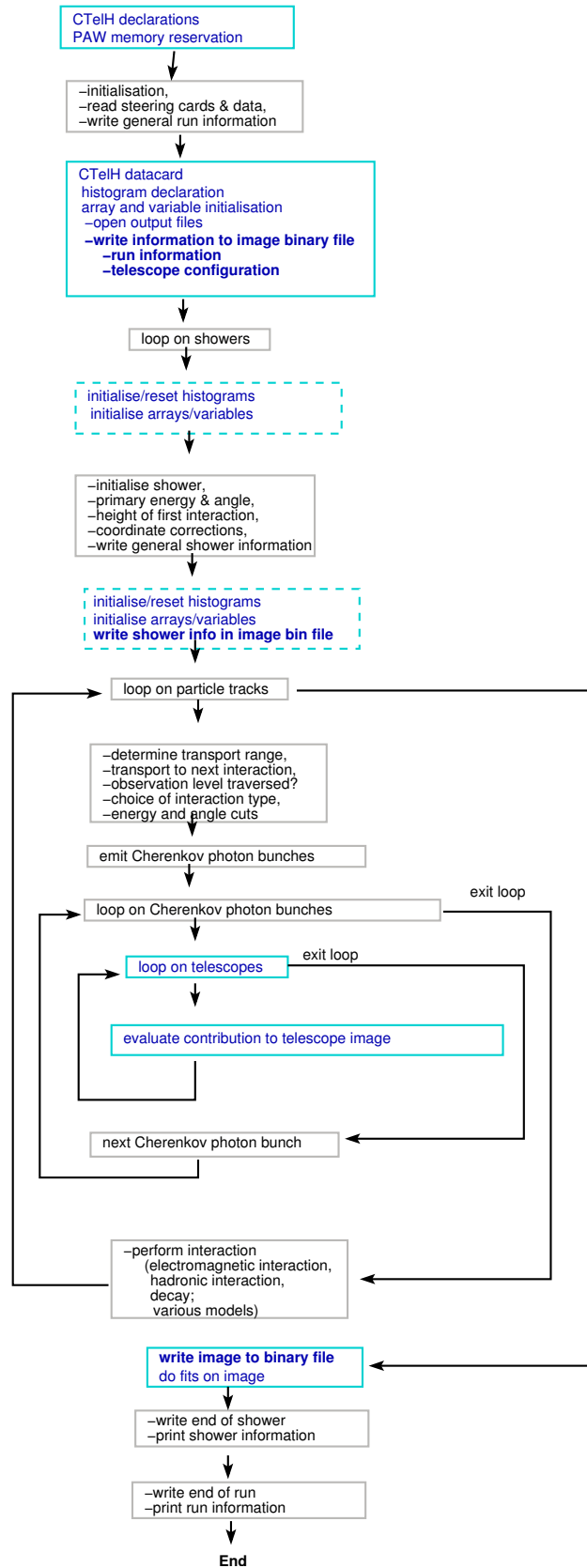


Figure A.5: Flowchart illustrating how the main steps involved in telescope simulation are incorporated in the CORSIKA code.

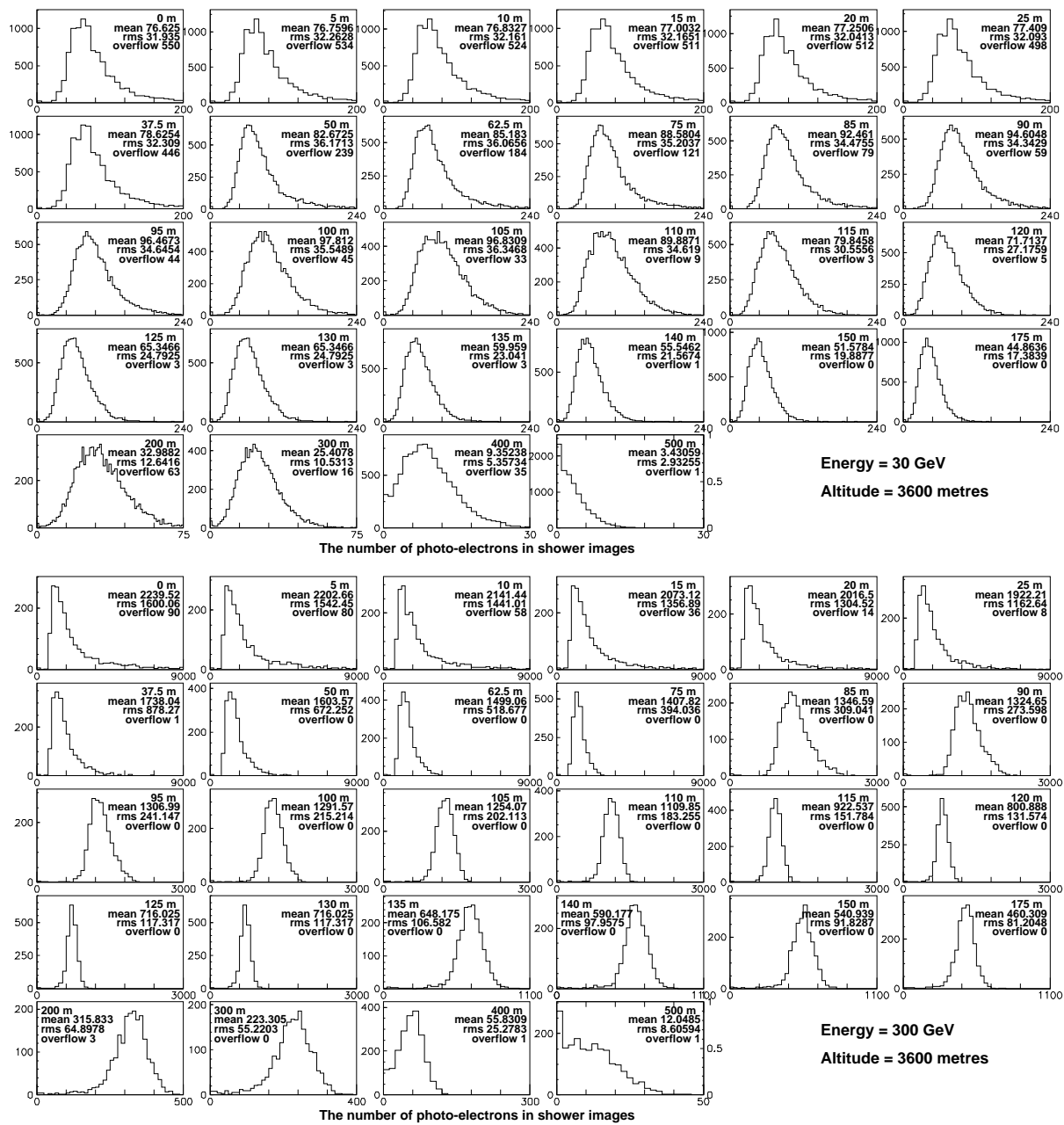


Figure A.6: The distributions of the number of photo-electrons in 30 GeV (top set) and 300 GeV (bottom set) shower images obtained for different telescope positions at 3600 m a. s. l.. The position of the telescopes, the mean value and r. m. s. of the distribution as well as the overflow of the histogram are shown on each plot. Similar distributions for 1000 GeV showers are shown in figure 8.14 of the main text.

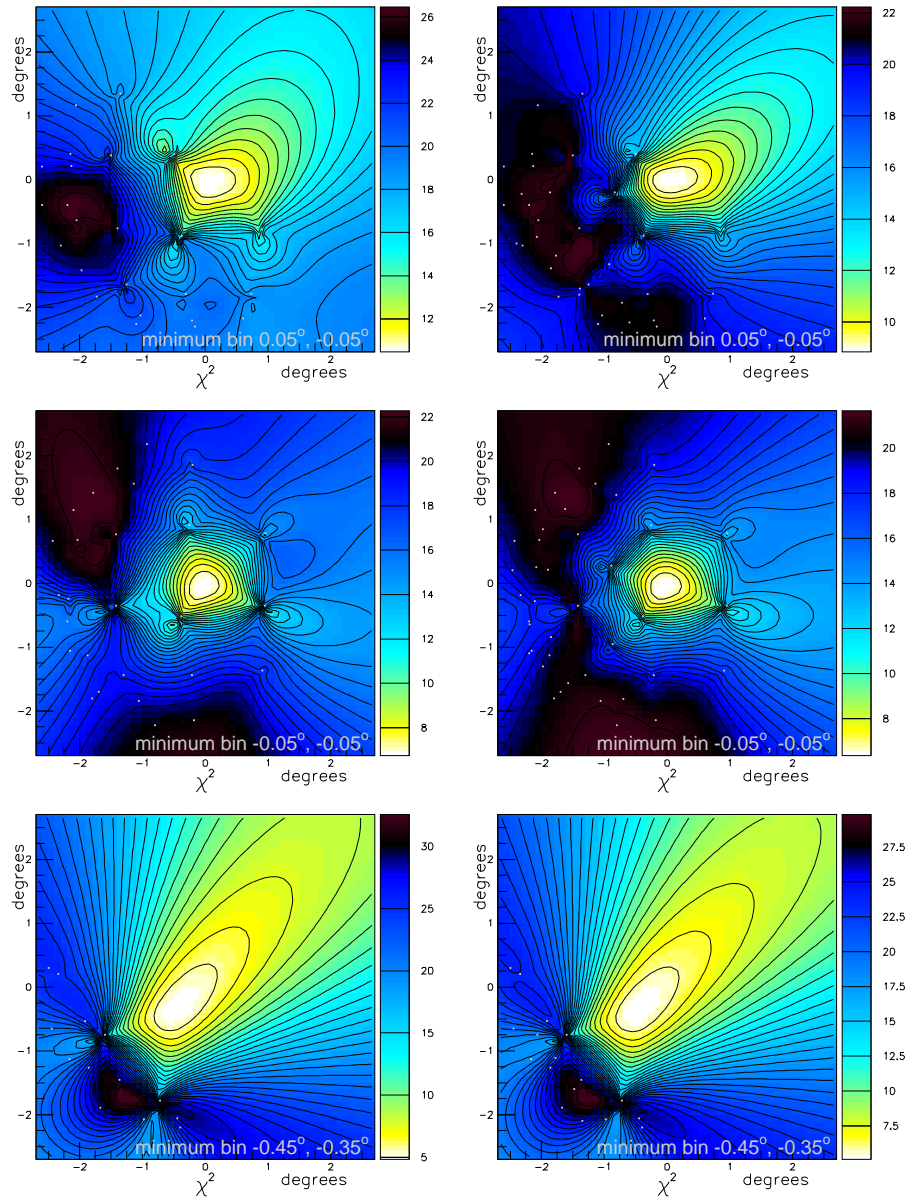


Figure A.7: Example of the preliminary scan χ^2 maps for source reconstruction for three different showers (top to bottom) observed at 1800 m above sea level. The left and right columns give the maps when observations are carried out with configuration 1 and configuration 2 (see figure 10.7 and section 10.6) respectively.

APPENDIX B

LONGITUDINAL PROFILE PARAMETRISATION

We present the parametrisation of the longitudinal profiles in terms of the number of particles (electrons and gamma). A similar parametrisation for the longitudinal profiles in terms of the Cherenkov photons number has been presented in section 3.2.2. The average longitudinal profiles of the showers in terms of the number of particles are shown again (they were originally presented in section 2.3.2) in figure B.1(left).

The depth of the maximum of shower development obtained from these curves is then plotted as a function of the energy in figure B.1(right) (also originally presented in section 2.3.2). This allows us to obtain the following linear dependence

$$t_{max} = 0.98 \ln(y) + 0.63,$$

where y is the energy expressed in the units of critical energy ($y = E/E_c$).

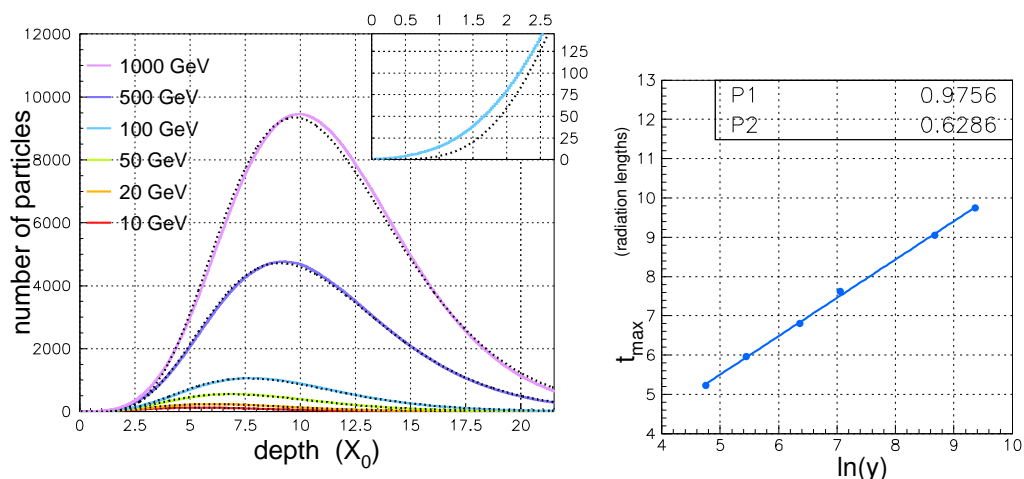


Figure B.1: Left: The average longitudinal profiles in terms of number of particles (electrons and gamma) are shown (coloured lines) for various energies. The curves are fitted with the function $f(t) = C(\beta t)^{\alpha-1} e^{-\beta t}$ and the result of the fits are shown through the dotted lines. A zoom of the first couple of radiation lengths for the 100 GeV curve is shown in the top right corner. Right: The dependence of the depth of the maximum of shower development (in radiation lengths) as a function of $\ln(y)$. The points are fitted with the function $f(x)=P_1x+P_2$. These two plots are also shown in figure 2.9 and 2.10 respectively.

The average values of α/β and $1/\beta$ obtained from the fits are linearly dependent on the $\ln(y)$ as well. This dependence is shown in figure B.2 and gives us the following parametrisations.

$$\frac{\alpha}{\beta} = 2.16 + 0.99 \ln(y)$$

$$\frac{1}{\beta} = 1.53 + 0.01 \ln(y).$$

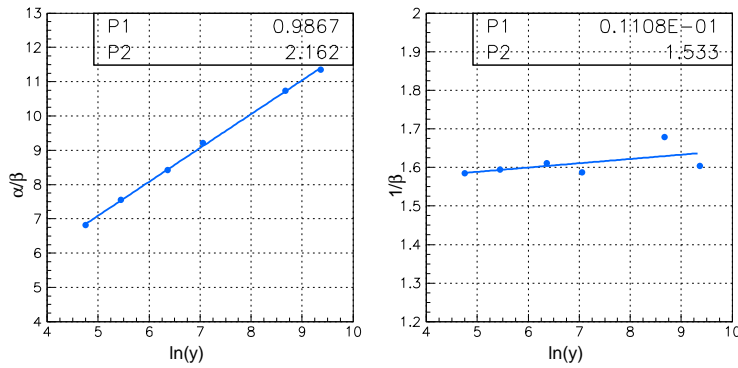


Figure B.2: The dependence of the average value of α/β and $1/\beta$ on the shower energy expressed in units of critical energy ($y = E/E_c$) for the shower longitudinal profiles in terms of the number of particles. The points obtained by fitting the profiles in figure 2.9 are then fitted with the line $f(x)=P_1x+P_2$.

Examples of the Gaussian dependence of the parameters β/α and $1/\alpha$ for a 100 GeV shower are given in figure B.3 (left and centre). These distributions can be used to obtain a parametrisation of the fluctuations of the longitudinal profiles in γ -initiated showers. The standard deviation σ is obtained by fitting each distribution with a Gaussian function. In figure B.4, we present the ratio $\sigma_{\beta/\alpha}/(\beta/\alpha)$ (left) and $\sigma_{1/\alpha}/(1/\alpha)$ (right) as a function of the energy. The points can be fitted with a line and yield the following parametrisations:

$$\frac{\sigma_{\beta/\alpha}}{\beta/\alpha} = 0.28 - 0.02 \ln(y)$$

$$\frac{\sigma_{1/\alpha}}{1/\alpha} = 1.11 - 0.62 \ln(y).$$

One also notes that there is no correlation between the two parameters β/α and $1/\alpha$ (figure B.3 right). The parametrisation thus obtained can be used to generate random profiles for γ -initiated showers.

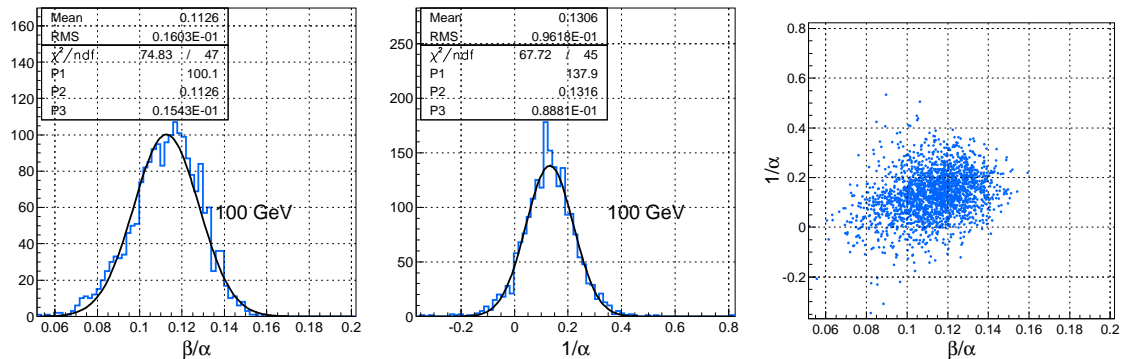


Figure B.3: The distribution of β/α (left) and $1/\alpha$ (centre) for 100 GeV showers. Both distributions are fitted with the Gaussian function $f(x) = P1x^{-0.5(\frac{x-P2}{P3})^2}$. The right plot shows the absence of correlation between β/α and $1/\alpha$ for 100 GeV showers.

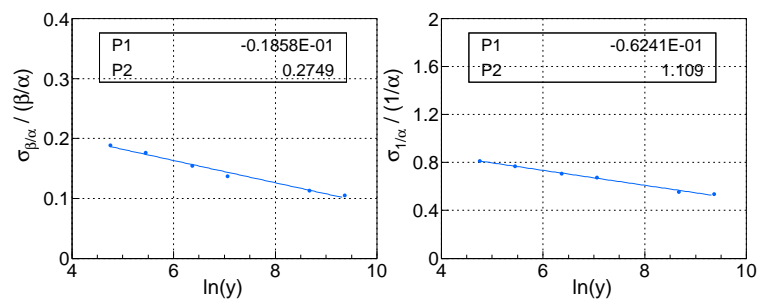


Figure B.4: The dependence of $\sigma(v)/v$ on the energy of the showers, where $v = \beta/\alpha$ (in the left figure) and $v = 1/\alpha$ (in the right figure). The points obtained from the distributions of β/α and $1/\alpha$ are fitted with the line $f(x) = P1x + P2$, and the results of the fit shown on the plots.

APPENDIX C

RÉSUMÉ EN FRANÇAIS

C.1 Introduction

L'astrophysique est une discipline consistant à utiliser les différents types de rayonnements produits par différents phénomènes ou sources pour mieux les connaître. Ces rayonnements comprennent les rayons cosmiques, différentes parties du spectre électro-magnétique, les neutrinos, les ondes gravitationnelles, etc.. Ce domaine d'étude évolue en permanence : l'astronomie, qui n'utilisait au départ que l'information de la lumière visible, utilise maintenant une large gamme de messagers produits par les objets astrophysiques. Les observations du spectre électromagnétique s'étendent maintenant des ondes radio (longueur d'onde supérieure au millimètre) aux rayons gamma (longueur d'onde inférieure à 0.01 nm ou énergie supérieure à quelques centaines de keV).

C.1.1 Les sources

L'astronomie gamma nous permet d'accéder à l'Univers non-thermique : les phénomènes les plus violents et énergétiques dans notre galaxie et au-delà. Bien que ces phénomènes violents émettent aussi des photons à basse énergie, il est difficile de les étudier à l'aide de cette émission, car c'est l'émission de l'Univers thermique qui tend à dominer à ces énergies-là. En revanche, l'astronomie gamma nous permet d'observer uniquement les phénomènes de haute énergie à l'œuvre dans l'Univers. De plus, les photons gamma ne sont pas affectés par la présence des champs magnétiques galactique et extra-galactique. Ils ne sont donc pas déviés et gardent l'information de la direction de la source.

La production de photons gamma nécessite l'accélération et l'interaction de particules relativistes aux très hautes énergies. Les mécanismes dominant de production de photons gamma incluent la collision de rayons cosmiques chargés avec le milieu interstellaire, l'annihilation de particules et d'anti-particules et l'accélération ou la déviation de particules chargées dans les champs électromagnétiques. Les mécanismes d'émission par accélération comprennent le Bremsstrahlung, l'émission synchrotron et la diffusion Compton. De plus, les électrons de haute énergie peuvent transférer une partie de leur énergie à un photon X, le transformant en photon gamma.

Parmi les phénomènes de haute énergie produisant les rayons gamma, on peut citer les supernovae, les restes de supernovae, les jets de pulsars, les disques d'accrétion d'un système binaire avec un ou deux objets compacts (trou noir, étoile à neutrons, ...). Des objets extra-galactiques comme les noyaux actifs de galaxie (AGN) ou les sursauts gamma (GRB) produisent aussi des photons γ . Les observations montrent aussi une émission diffuse galactique produite par l'interaction des rayons cosmiques avec le milieu interstellaire, ainsi qu'une émission diffuse extra-galactique partiellement associée à des AGN non résolus.

Bien que les observations menées ces 50 dernières années aient permis de développer notre compréhension des mécanismes impliqués, un grand nombre de questions demeurent à propos des objets émettant des photons γ . Différents modèles ont été développés pour décrire la plupart de ces objets, mais c'est grâce aux observations que ces modèles seront validés, contraints ou rejetés.

C.1.2 Les télescopes gamma et leurs caractéristiques

Il y a trois types de télescopes de rayons gamma qui couvrent des domaines d'énergie complémentaires.

Satellites

Les télescopes en satellites observent des rayons gamma de quelques centaines de keV à plusieurs dizaines de GeV¹. À ces énergies-là, les rayons gamma sont rapidement absorbés par l'atmosphère terrestre après leur première interaction avec celle-ci et les flux des rayons gamma sont suffisamment élevés pour pouvoir être observés avec les surfaces de détection restreintes des satellites. Suivant les objectifs du télescope, les instruments en satellites peuvent avoir différents champs de vue : certains peuvent observer le ciel entier.

Télescopes Tcherenkov au sol

À des énergies plus hautes, les rayons gamma produisent des gerbes de particules secondaires en interagissant avec l'atmosphère terrestre suffisamment grandes pour qu'elles puissent être observées au sol. Quand les gerbes ne sont pas suffisamment grandes pour être détectées au sol de manière directe, elles sont observées grâce à leur émission Tcherenkov. Aux énergies entre quelques dizaines et quelques centaines de GeV, les observations gamma peuvent être faites par les satellites et les télescopes Tcherenkov au sol ; il est alors possible d'effectuer une intercalibration de ces deux moyens d'observation. Au-delà de quelques centaines de GeV, les flux de rayons gamma diminuent à un niveau où les observations avec satellites deviennent difficiles et où seuls les télescopes au sol continuent à fournir des données. Il existe deux types de télescopes Tcherenkov au sol : les échantillonneurs et les imageurs. Les premiers échantillonnent le front d'onde Tcherenkov à l'aide d'un grand nombre de miroirs distribués sur une grande surface (au moins plusieurs centaines de mètres carrés). Les imageurs (IACT pour *Imaging Atmospheric Cherenkov Telescope* en anglais) collectent la lumière Tcherenkov à l'aide de miroirs qui focalisent cette lumière sur une caméra, permettant ainsi d'obtenir une image de la gerbe atmosphérique. Les paramètres du rayon gamma initial sont reconstruits à partir des caractéristiques de ces images. Les télescopes imageurs actuels observent des rayons gamma entre environ 300 GeV jusqu'à quelques dizaines de TeV. Les observations sont également possibles en-dessous et au-dessus de ce domaine, mais elles sont moins efficaces. Le champ de vue de ces télescopes est limité (jusqu'à environ 4-5 degrés), bien que des efforts soient en cours pour l'augmenter (jusqu'à environ 15 degrés). La résolution angulaire des télescopes majeurs actuels est de l'ordre de 0.1° à 1000 GeV.

Télescopes pour les grandes gerbes atmosphériques au sol

Au-delà de quelques TeV, les gerbes produites par les rayons gamma sont suffisamment grandes pour être observées directement au sol. Les particules chargées des gerbes, notamment les

¹Le satellite GLAST observera les rayons gamma jusqu'à quelques centaines de GeV.

électrons et positrons, sont détectées à l'aide de détecteurs placés au sol. À ces énergies, les flux de rayons gamma sont très faibles et de grandes surfaces de détection sont nécessaires pour les observer. Ces télescopes ont aussi de grands champs de vue de 180 degrés. Leur résolution angulaire est moins bonne que celle des télescopes imageurs.

C.1.3 Buts des futurs télescopes imageurs

La plus grande attente concernant les futurs télescopes est une amélioration significative de la sensibilité. Cela permettra aussi bien l'observation des sources déjà détectées avec des hautes statistiques en des temps d'observation plus courts, mais aussi une observation plus complète de l'Univers gamma avec la détection de nouvelles sources. La sensibilité dépend de plusieurs facteurs : la surface de collection, le pouvoir d'identification des gamma, le rejet des protons de fond et la résolution angulaire pour la sensibilité aux sources ponctuelles. Plusieurs facteurs comme la taille des télescopes, l'altitude d'observation ou le domaine d'énergie ont une influence sur les capacités d'identification des rayons gamma et la résolution angulaire. Ces différents facteurs sont discutés à plusieurs endroits dans ce mémoire.

En plus d'améliorer la sensibilité, une meilleure résolution angulaire permet aussi une meilleure identification des sources ponctuelles et des études détaillées de la structures des sources étendues.

L'amélioration de la résolution en énergie pourrait améliorer l'étude des changements de régime d'émission des sources variables ou permettre l'étude d'éventuelles raies d'émission. Toutefois, la résolution en énergie est limitée par les fluctuations intrinsèques du nombre de photons Cherenkov produits par les gerbes électromagnétiques et par le signal obtenu dans les images. L'étude des spectres en loi de puissance peut être réalisée avec les résolutions en énergie de l'ordre de 10% disponibles actuellement.

Plusieurs solutions sont étudiées actuellement pour augmenter le champ de vue des IACT. Un champ de vue plus étendu améliorera les observations des sources gamma. En premier lieu, un champ de vue plus grand permettra l'observation d'une plus grande partie du ciel à un moment donné en permettant parfois l'observation de plusieurs sources simultanément, et une meilleure étude des sources étendues. Un des buts serait alors la découverte de nouvelles régions d'émission gamma. De plus, un champ de vue plus grand peut améliorer la reconstruction des gerbes et la sensibilité aux énergies du TeV.

Notons que les caractéristiques requises pour les télescopes futurs dépendent de manière importante du domaine d'énergie et des buts physiques considérés. Dans le domaine d'environ 300 GeV à 10 TeV (qui est aussi le domaine principal d'observation des IACT), le but principal est l'amélioration de la sensibilité. En dessous et au dessus de cette gamme d'énergie, le but est d'étendre le domaine dans lequel les observations des IACT sont possibles.

En dessous de 300 GeV, la qualité des observations des IACT est altérée par l'effet combiné des fluctuations dans le développement des gerbes, d'un niveau de fond plus élevé et de l'influence plus importante du champ magnétique terrestre. Les images obtenues à ces énergies avec des télescopes de tailles moyennes (10-15 m de diamètre) ont un faible nombre de photo-électrons et sont souvent mal définies. Cela se traduit par une mauvaise reconstruction des paramètres des gerbes et par de mauvaises résolutions en angle et en énergie. L'identification des gamma et le rejet du fond hadronique pose également problème. La solution pour améliorer la sensibilité des télescopes et les observations gamma dans cette gamme d'énergie serait de collecter un maximum de lumière Cherenkov pour obtenir des images des gerbes plus exploitables. Cela pourrait être obtenu en jouant sur plusieurs facteurs : l'utilisation de télescopes plus grands, des observations à plus hautes altitudes (avec un flux de photons Cherenkov plus dense) et l'amélioration des performances techniques comme l'utilisation de photomultiplicateurs avec une meilleure efficacité quantique. Ce domaine en énergie est

également couvert par le télescope spatial Fermi (GLAST) mais sa sensibilité est moins bonne à ces énergies.

Dans le domaine d'énergie au-delà de quelques TeV, le flux des sources diminue, ce qui nécessite de grandes surfaces de collection pour obtenir des observations avec des statistiques significatives. C'est aussi un domaine d'énergie qui aura une partie commune avec les télescopes à grand champ mentionnés plus haut. Comme les photons gamma produisent des gerbes très grandes à ces énergies, l'utilisation de télescopes plus petits (moins de dix mètres de diamètre) permettra tout de même une bonne reconstruction et une bonne résolution angulaire.

Comme nous l'avons vu, l'optimisation des différents paramètres des télescopes futurs dépend d'un grand nombre de facteurs. La gamme d'énergie et les buts physiques déterminent les caractéristiques requises des systèmes futurs. Ces caractéristiques sont elles-mêmes fixées par un grand nombre de paramètres : taille et nombre des télescopes, champ de vue, altitude d'observation, efficacité des photomultiplicateurs, type de miroirs, taille des pixels. Cela nécessite des études dédiées et des outils de simulation adaptés pour mener ces études. C'est dans ce contexte que ce travail de thèse a été entrepris. Notre but était de comprendre les différents aspects des observations gamma avec les IACT et de développer des outils de simulation et de reconstruction des gerbes pour étudier les performances de différentes configurations de réseaux de télescopes. Ces outils reposent sur des méthodes centrées sur les aspects les plus importants des télescopes et sur la reconstruction des paramètres des gerbes à partir des images. Quelques détails techniques sont ignorés pour garder un nombre raisonnable de paramètres tout en donnant des méthodes robustes pour l'évaluation des capacités des télescopes. De plus, les outils pourront être complétés dans le futur.

C.1.4 Contenu de la thèse

Cette thèse est divisée en quatre parties principales. Après l'introduction dans la partie I, la partie II présente les gerbes atmosphériques produites par les rayons gamma (chapitre 2), leur émission Tcherenkov (chapitre 3) et leur simulation (chapitre 4). La partie III présente l'outil de simulation des télescopes imageurs que nous avons développé (chapitre 5) ainsi qu'une discussion sur les propriétés des images obtenues dans les télescopes (chapitre 6). La partie IV présente les méthodes de reconstruction développées pour la position de la source et du pied de gerbe (chapitre 7) et de l'énergie (chapitre 8). Cette partie contient également une discussion sur des méthodes possibles pour la discrimination des hadrons et des rayons gamma (chapitre 9). Finalement, dans la partie V, nous utilisons les outils développés précédemment pour obtenir deux configurations de réseaux et étudier leurs capacités (chapitre 10). Le chapitre 11 présente la conclusion et les perspectives.

C.2 Les gerbes atmosphériques et leur simulation

C.2.1 Les gerbes électromagnétiques dans l'atmosphère

L'atmosphère terrestre et ses modèles

L'atmosphère terrestre est une couche de gaz qui entoure la Terre et qui est principalement composée d'azote (78.08%), d'oxygène (20.97%), d'argon (0.9%) et de traces d'autres gaz rares. Du fait de différences d'absorption du rayonnement solaire à différentes altitudes, la température de l'atmosphère varie avec l'altitude, si bien qu'on la divise en plusieurs couches.

Plusieurs paramètres de l'atmosphère, parmi lesquels la température, l'épaisseur des couches ou la présence d'impuretés varient non seulement d'un endroit à l'autre, mais aussi

dans certains cas avec le temps. Certaines impuretés comme la vapeur d'eau, l'ozone et les particules d'aérosols ont une influence sur la manière dont la lumière est transmise dans l'atmosphère et donc sur les observations des IACT.

Bien que les instruments au sol aient des instruments dédiés à l'étude des propriétés de l'atmosphère, les études générales utilisent des modèles simplifiés d'atmosphère.

Les études présentées dans cette thèse sont basées sur la paramétrisation de Linsley du modèle d'atmosphère "U.S. Standard". L'atmosphère est supposée être constituée uniquement d'air et est divisée en 5 couches atteignant l'altitude de 112 km au dessus du niveau de la mer. Cette altitude est considérée comme étant la limite de l'atmosphère. Les 4 premières couches sont paramétrisées de la manière suivante:

$$T(h) = a_i + b_i e^{-\frac{h}{c_i}} \quad i = 1, \dots, 4. \quad (\text{C.1})$$

où h est l'altitude au dessus du niveau de la mer et $T(h)$ est la masse de la colonne d'air d'une base d'un cm^2 au dessus de l'altitude h . T est exprimée en g/cm^2 . La densité est alors donnée par $\rho(h) = -dT(h)/dh$. La 5e couche (> 100 km) a une dépendance linéaire avec h :

$$T(h) = a_5 + b_5 \frac{h}{c_5}. \quad (\text{C.2})$$

Les valeurs de a , b et c sont données dans le tableau C.1.

Couche i	Altitude h (km)	a_i (g/cm^2)	b_i (g/cm^2)	c_i (cm)
1	0...4	-186.5562	1222.6562	994186.38
2	4...10	-94.919	1144.9069	878153.55
3	10...40	0.61289	1305.5948	636143.04
4	40...100	0.0	540.1778	772170.16
5	>100	0.01128292	1	10^9

Table C.1: Paramètres de l'atmosphère U. S. Standard (d'après J. Linsley)

Production d'une cascade

La première interaction: production de paire Aux énergies de l'astronomie gamma, i.e. au dessus du GeV, le mode d'interaction dominant des photons gamma dans la matière est la production d'une paire électron-positron. Le libre parcours moyen pour la production de paire dans un milieu donné est $9X_0/7$, où X_0 est la longueur de radiation de ce milieu. Dans le cas de l'air, $X_0 = 36.66 \text{ g/cm}^2$. Ceci implique que dans le cas du modèle U.S. Standard, l'altitude moyenne de la première interaction est d'environ 21.2 km au dessus du niveau de la mer.

Bremsstrahlung L'électron et le positron créés par la production de paire interagissent à leur tour dans le milieu qu'ils traversent et perdent de l'énergie. Aux hautes énergies, le processus dominant pour cette perte d'énergie est le bremsstrahlung, i.e. l'émission d'un photon de haute énergie due à l'accélération des électrons dans le champ de Coulomb des noyaux atomiques. Un électron perd en moyenne 63% (i.e. $1/e$) de son énergie après avoir parcouru une longueur de radiation.

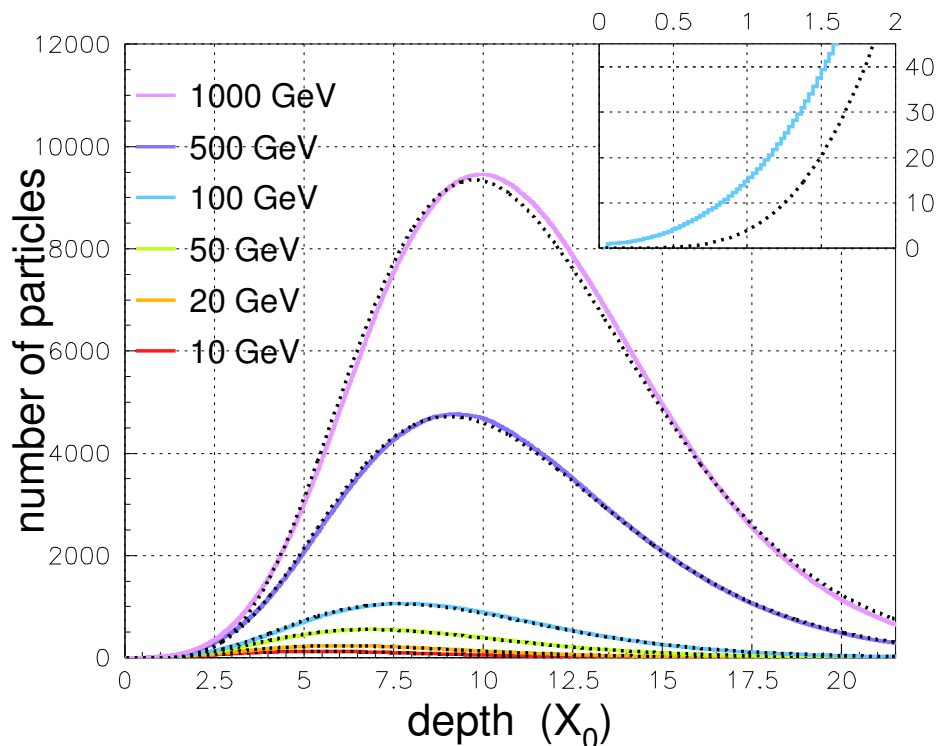


Figure C.1: Profils longitudinaux moyens exprimés en nombre de particules (électrons et gamma). Les courbes sont ajustées avec la fonction $f(t) = C(\beta t)^{\alpha-1} e^{-\beta t}$ et les résultats des ajustements sont montrés par les courbes pointillées. Dans le coin en haut à droite, le graphique montre le zoom sur les premières longueurs de radiation. Les graphiques sont représentés en échelle linéaire pour montrer la forme typique des profils des cascades.

Multiplication des particules, énergie critique et régime de basse énergie Les photons produits par bremsstrahlung (pour peu qu'ils aient suffisamment d'énergie) interagissent avec le milieu et créent d'autres paires électrons-positrons, qui à leur tour produisent d'autres photons par bremsstrahlung, et ainsi de suite. La multiplication des particules qui découle de ces processus continue jusqu'à ce que l'énergie moyenne des électrons de la cascade passe sous l'énergie critique E_c (~ 86 MeV pour l'air). En dessous de cette énergie, le nombre de particules commence à diminuer : les électrons sont absorbés par ionisation, le mode dominant de leur interaction dans ce domaine d'énergie.

En plus des processus décrits ci-dessus, d'autres processus mineurs tels que la production de paires $\mu^+ \mu^-$ ou l'interaction inélastique des photons avec les noyaux peuvent se produire. Dans ce dernier cas, la production d'une composante hadronique est possible dans une cascade engendrée par un γ .

Morphologie des cascades

Les cascades électromagnétiques produites par les mécanismes décrits plus haut ont une forme allongée avec un profil longitudinal s'étalant sur plusieurs kilomètres et un profil latéral de quelques centaines de mètres. La taille de cette cascade dépend de l'énergie du gamma initial. Le nombre total de particules dans la cascade dépend linéairement de l'énergie du gamma primaire, alors que la profondeur de son maximum de développement et sa longueur totale

ont une dépendance logarithmique avec l'énergie. Nous avons fait une série de simulation avec CORSIKA et nous présentons les profils longitudinaux moyens en terme de nombre de particules dans la figure C.1. Chaque courbe est ajustée avec la fonction $f(t) = C(\beta t)^{\alpha-1}e^{-\beta t}$.

Le profil latéral des cascades est principalement déterminé par les diffusions multiples de Coulomb et possède un coeur restreint où l'essentiel de l'énergie est contenue. En moyenne 90% de l'énergie de la cascade se trouve dans un rayon de Molière, dont la valeur est ~ 73 m au niveau de la mer et ~ 210 m à 10 km d'altitude dans le modèle U.S. Standard.

C.2.2 Émission Tcherenkov dans les gerbes atmosphériques

Profil d'émission Cherenkov dans une gerbe électromagnétique

Quand des particules chargées traversent un milieu avec une vitesse supérieure à celle de la lumière dans ce milieu, elles émettent de la lumière Cherenkov. L'angle d'émission de ces photons Cherenkov par rapport à la trajectoire de la particule initiale est donné par :

$$\cos \theta_c = \frac{1}{\beta \eta} = \frac{c_{air}}{v} \quad , \quad (C.3)$$

où η est l'indice de réfraction du milieu et $v = \beta c$ est la vitesse de la particule. Puisque $\cos \theta_c \leq 1$, le seuil en énergie de l'émission Cherenkov est donné par

$$E_{thr} = \gamma_{thr} m_0 c^2 = \frac{m_0 c^2}{\sqrt{1 - \frac{1}{\eta^2}}} \quad (C.4)$$

Le nombre de photons Cherenkov produit par unité de longueur de parcours et par intervalle de longueur d'onde pour une particule de charge ze est donné par

$$\frac{d^2 N}{dx d\lambda} = \frac{2\pi\alpha z^2}{\lambda^2} \left(1 - \frac{1}{\beta^2 \eta^2}\right) = \frac{2\pi\alpha z^2}{\lambda^2} \sin^2 \theta_c \quad (C.5)$$

où α est la constante de structure fine. L'atmosphère devient opaque aux photons aux longueurs d'ondes plus courtes et le détecteur lui-même ne fonctionne qu'avec une longueur d'onde entre 300 et 700 nm. On déduit des propriétés évoquées plus haut que le seuil d'émission Cherenkov, l'angle et le nombre de photons dépendent tous de l'indice de réfraction, qui dépend lui-même du profil de l'atmosphère.

Le profil longitudinal de l'émission Tcherenkov Le nombre total de photons Cherenkov émis par une cascade en fonction de l'altitude est très similaire au profil longitudinal de la cascade elle-même. La position du maximum de la cascade dépend du logarithme de l'énergie alors que le nombre de photons Cherenkov dépend linéairement de l'énergie. Les fluctuations intrinsèques de cette grandeur deviennent plus importantes à basse énergie. Le profil longitudinal a aussi une dépendance avec l'angle zénithal du photon primaire. Nous avons aussi obtenu des paramétrisations en fonction de l'énergie en ajustant les profils longitudinaux simulés en terme de nombre de photons Cherenkov émis en fonction de la profondeur en utilisant la fonction $f(t) = C(\beta t)^{\alpha-1}e^{-\beta t}$ (voir section 3.2.2 dans le texte principal). Ces paramétrisations peuvent ensuite être utilisées pour générer aléatoirement des profils de cascades.

Extinction et transmission

Comme la lumière Cherenkov traverse l'atmosphère avant d'atteindre le sol, son intensité diminue à cause de l'absorption (due à la présence de O_3 , O_2 et d'aérosols) ou de la diffusion Rayleigh (sur les molécules de d'air) ou Mie (sur les aérosols).

Densité de lumière Cherenkov sur le sol

La distribution latérale des photons Cherenkov au sol dépend de l'altitude et de l'angle d'émission de chaque photon. L'angle d'émission Cherenkov tend à s'ouvrir à mesure que l'altitude d'émission décroît et que l'atmosphère devient plus dense. Cela se traduit par un cumul de photons Cherenkov produits à différentes altitudes dans une région en forme d'anneau, où la densité des photons est plus importante. La figure C.2 (gauche) montre l'exemple d'une telle distribution pour une cascade de 500 GeV. La figure de droite montre le profil de densité moyen des photons Cherenkov au sol en fonction de la distance radiale au point d'impact de la cascade pour différentes énergies et deux altitudes (2200 m et 5000 m).

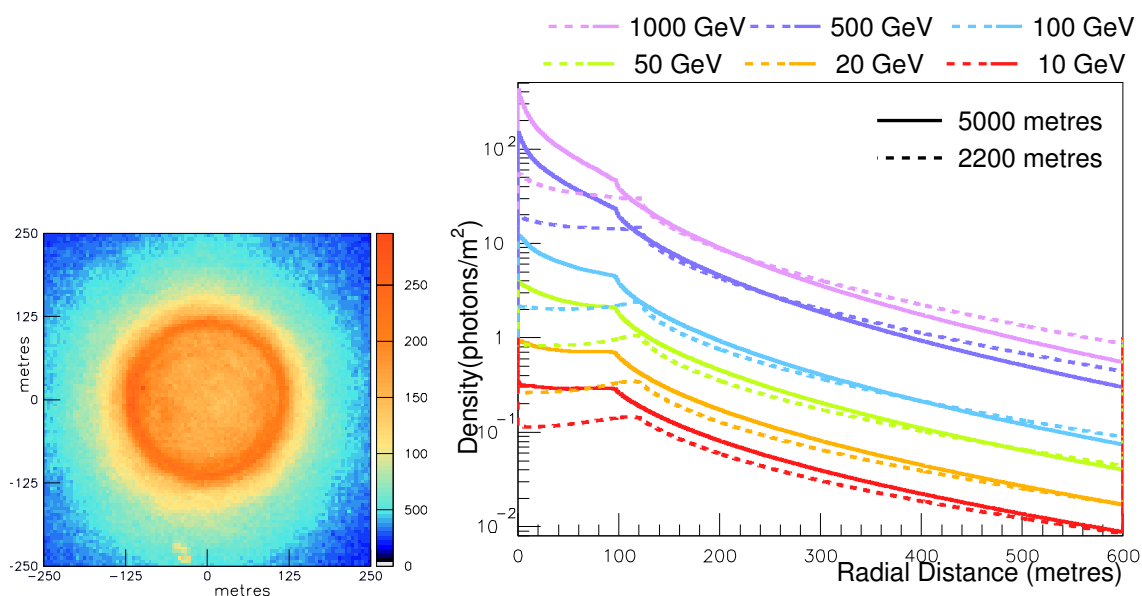


Figure C.2: Gauche: distribution des photons Cherenkov au sol (2200 m d'altitude) pour une cascade engendrée par un photon gamma de 500 GeV. Chaque figure représente une surface de $500 \times 500 \text{ m}^2$. Droite: comparaison de la densité moyenne de photons Cherenkov au sol (en photons/m²) à 2200 m et 5000 m pour des cascades simulées à différentes énergies.

Les profils montrent que la densité des photons Cherenkov dépend de l'énergie. De plus, aux énergies plus élevées, le profil tend à piquer plus près de l'axe de la cascade, du fait de la proximité de la cascade du sol. Cet effet est particulièrement prononcé à haute altitude. On remarque également qu'aux altitudes plus haute, l'anneau Cherenkov a tendance à être plus petit et plus dense (environ 90 m de rayon à 5000 m) qu'aux basses altitudes (environ 120 m de rayon à 2200 m).

On peut aussi noter que bien que ces courbes représentent les distributions de densité moyennes, le profil peut être plus ou moins piqué au centre en fonction de l'altitude de matérialisation du photon primaire. En fait, quand les photons primaires de plus hautes énergies se matérialisent plus près du sol, les cascades sont tronquées avant d'être complètement développées, ce qui se traduit par un nombre important de photons Cherenkov près de l'axe et très peu à des distances plus grandes.

L'inclinaison de la cascade a aussi une influence sur la distribution de photons Cherenkov au sol. Lorsque l'angle zénithal augmente, l'anneau Cherenkov tend à s'allonger. D'autres paramètres comme les conditions atmosphériques, l'intensité du champ géo-magnétique et sa

direction ont un impact sur la distribution de photons Cherenkov au sol. Le temps d'arrivée des photons sur le sol dépend de la position de leur point d'émission dans la cascade et de la position de leur impact au sol.

C.2.3 Simulation des gerbes atmosphériques avec CORSIKA

Nous avons utilisé l'un des programmes de simulation Monte Carlo de cascades atmosphériques les plus connus, CORSIKA (COsmic Ray Simulations for Kascade). Ce programme utilise EGS4 (Electron and Gamma Shower version 4) pour la simulation des interactions électromagnétiques des électrons et des photons gamma. D'autres processus électromagnétiques non inclus dans EGS4 tels que la production de paires $\mu^+\mu^-$, le bremsstrahlung des muons et la production de paires e^+e^- par les muons ont été pris en compte par les auteurs de CORSIKA. Plusieurs packages peuvent être choisis pour la simulation des interactions hadroniques.

Le suivi de chaque particule dans la cascade est réalisé en mettant à jour ses coordonnées en position, en temps et en énergie jusqu'à son interaction avec un noyau de l'air, sa désintégration, ou jusqu'à ce que son énergie passe en dessous d'un seuil défini par l'utilisateur. Nous avons remarqué que des seuils 0.05, 0.05, 0.005 et 0.005 GeV respectivement pour les hadrons, muons, électrons et photons pouvaient être utilisés pour l'étude des distributions et profils des photons Cherenkov produits dans les gerbes. L'étude des profils pour les particules chargées requiert des seuils plus bas. La lumière Cherenkov est émise par les électrons, muons et les hadrons chargés tant qu'ils ont une vitesse supérieure à la vitesse de la lumière dans l'atmosphère. La transmission et l'absorption de la lumière Cherenkov dans l'atmosphère, l'influence de la réflectivité du miroir et l'efficacité quantique des photomultiplicateur est aussi prise en compte par CORSIKA. Nous avons aussi comparé les résultats d'un ensemble de simulations avec les résultats obtenus par la collaboration MAGIC dans le but de vérifier la validité de nos simulations et du choix des paramètres.

C.3 Télescopes imageurs Tcherenkov : simulations et image des gerbes

C.3.1 Les télescopes à imagerie par effet Tcherenkov atmosphérique et leur simulation

Pour évaluer les capacités d'un réseau de IACT pour la détection de gerbes atmosphériques, nous avons développé un programme basé sur CORSIKA.

Un télescope imageur a effet Tcherenkov atmosphérique est un réflecteur optique qui collecte la lumière Tcherenkov produite par les cascades atmosphériques et qui la projette sur une caméra où des photomultiplicateurs convertissent la lumière en signal électrique. Le signal est ensuite amplifié et numérisé pour être stocké et utilisé pour reconstruire les caractéristiques de la particule initiale.

La simulation du télescope prend en entrée les photons Tcherenkov de la sortie de CORSIKA ². La trajectoire et le point d'impact sur la caméra de chaque photon Cherenkov qui tombe sur le miroir d'un télescope sont calculés. Quand ceci est fait pour tous les photons Tcherenkov émis par une cascade, on obtient une image de la cascade.

Choix de la forme du miroir Nous avons choisi un miroir idéal de forme parabolique pour mener les simulations. Cette forme a l'avantage d'être isochrone et d'être simple à simuler.

²Le programme peut être adapté pour utiliser la sortie d'autres simulateurs de gerbes.

Un tel système idéal peut être utilisé pour mener des études rapides sur l'impact de différents paramètres des réseaux de télescopes. Une fois que les propriétés les plus intéressantes sont identifiées, des études plus détaillées et réalistes peuvent être menées à l'aide de simulations plus complexes.

Un miroir parabolique permet d'obtenir une image parfaitement focalisée au foyer pour un objet infiniment éloigné sur l'axe optique. Ainsi, pour les télescopes réels, la caméra est placée près du plan focal. Pour les sources hors axe, l'utilisation d'un miroir parabolique conduit à une aberration de l'image dans la direction longitudinale et transverse. La taille de cette aberration dépend de l'angle d'incidence ; elle reste en dessous de la taille typique de 0.1° pixel tant que le champ de vue est plus petit que $\sim 5^\circ$.

D'autres formes de miroir plus adaptées pour des champs de vue plus grands, comme la géométrie Davis-Cotton ou les miroirs elliptiques ne sont pas inclus dans la simulation, mais ils pourraient être ajoutés ultérieurement. La réflectivité des miroirs est prise en compte par CORSIKA.

Camera Pour les télescopes réels, la caméra consiste en un certain nombre de photomultiplicateurs qui donnent une image pixelisée. Dans la simulation, la surface de la caméra est représentée par un histogramme à 2 dimensions dont chaque bin représente un pixel. La contribution de tous les photons Cherenkov à cet histogramme produit l'image de la cascade. L'efficacité quantique des photomultiplicateur est prise en compte par CORSIKA.

Sortie Une fois que l'image est obtenue, elle peut être sauvegardée dans un histogramme au format hbook. La création d'un fichier de sortie binaire contenant les images a aussi été implémenté, ainsi que le programme permettant de le lire.

Flexibilité du programme de simulation Alors qu'un miroir simplifié a été utilisé, l'accent a été mis sur la flexibilité du package de simulation, pour qu'il puisse simuler différents types de systèmes. La position, l'orientation, le diamètre, la longueur focale, la position de la caméra et sa taille peuvent être choisies de manière indépendante (Cf. figure C.3). Jusqu'à 100 télescopes peuvent être définis de manière indépendante, permettant la simulation de réseaux de IACT.

C.3.2 Les images des gerbes et leurs propriétés

Les images des cascades obtenues avec un IACT sont une représentation des cascades dans le système de coordonnées de la caméra. Les caractéristiques de ces images sont déterminées par les propriétés de la cascade. Ceci implique que les informations concernant la particule primaire et la cascade elle-même peuvent être déduites des caractéristiques des images.

Les caractéristiques des images qui ont le plus d'importance pour la reconstruction des paramètres de la cascade sont la forme, la taille, l'orientation, la position sur la caméra et le nombre de photons Cherenkov qu'elle contient.

La morphologie des images et leur orientation

Les images des gerbes électromagnétiques ont une forme allongée, approximativement elliptique. L'élongation des images dépend de la position du télescope par rapport à la position du pied de gerbe. Les images obtenues par des télescopes à la position du pied de gerbe ont des images circulaires. Elle deviennent de plus en plus allongées au fur et à mesure que la

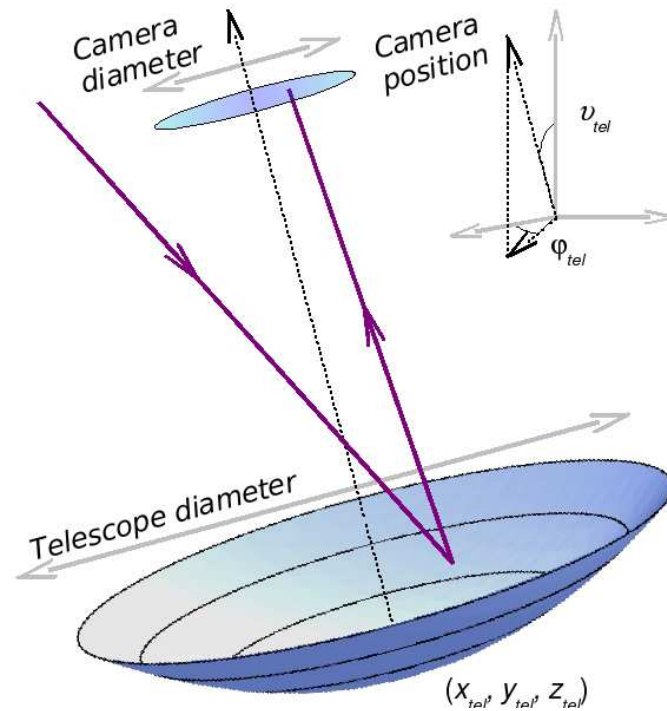


Figure C.3: Diagramme illustrant le principe du télescope et les différents paramètres.

position du télescope s'éloigne du pied de gerbe. Ces caractéristiques sont visibles dans la figure C.4 (ligne du haut) où nous montrons les images d'une gerbe de 1000 GeV obtenues en changeant la position du télescope par rapport au pied de gerbe. Les figures du bas montrent la corrélation entre l'altitude d'émission des photons Cherenkov et leur point d'impact sur la caméra. Ces images nous montrent également que la plupart des photons Tcherenkov sont émis entre 4 et 10 km d'altitude.

L'axe longitudinal des images correspond à l'axe de la gerbe. La position de l'image de la source se trouve également sur cet axe longitudinal "image" quand ce dernier est prolongé. Pour un télescope pointant vers la source de rayons gamma, l'image de la source se trouve au centre de la caméra. Dans un cas plus général, les coordonnées de la position de l'image de la source dans le référentiel de la caméra sont relié à l'angle zénithal et azimuthal de la source gamma.

Quand le télescope pointe vers la source, l'image de la gerbe pointe vers la position du pied de gerbe dans le référentiel du sol. En général, le télescope ne pointe pas vers la source et l'axe de la gerbe n'est pas contenu dans le plan formé par le pied de gerbe et l'axe du télescope. Dans ce cas, l'image de l'axe est parallèle à la droite joignant le télescope et le pied de gerbe. Le décalage entre cette droite et l'image de l'axe correspond au décalage de la position de l'image de la source par rapport au centre de la caméra.

Le nombre de photo-électrons dans les images

Les paramètres ayant une influence sur la densité de photons Tcherenkov au sol ont également un impact sur le nombre de photo-électrons dans les images. En effet, le nombre de photo-électrons contribuant aux images de gerbe dans les télescopes suit essentiellement la courbe de densité des photons Tcherenkov au sol, mises à part les grandes distances par rapport à la position du pied de gerbe. Au delà de la position de l'anneau Tcherenkov, un nombre plus

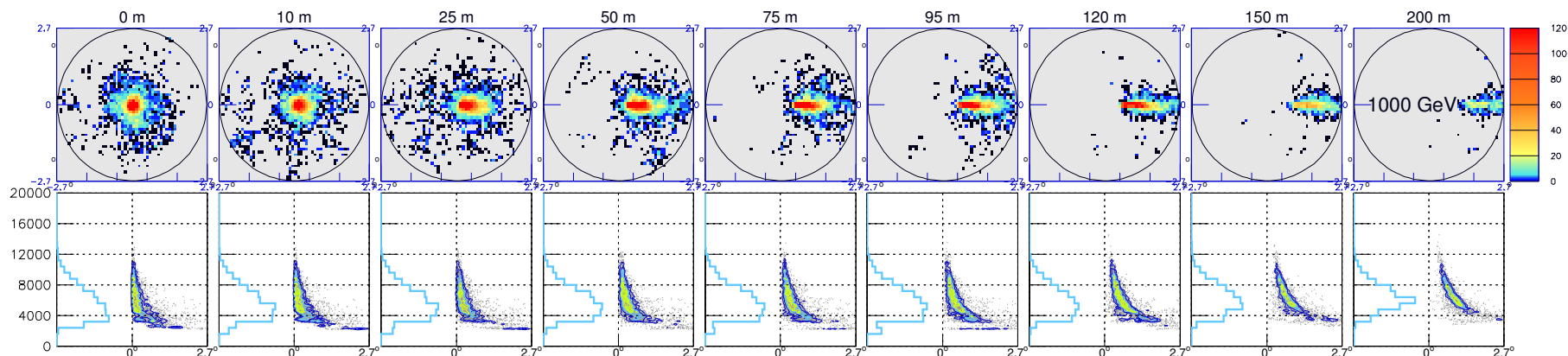


Figure C.4: Les images d'une gerbe de 1000 GeV obtenues avec un télescope de 12.5 m de diamètre à neuf distances différentes du pied de gerbe. L'altitude du sol est de 2200 m au dessus du niveau de la mer. Les figures du bas montrent la relation entre l'altitude d'émission des photons Tcherenkov en ordonnée et leur point d'impact sur la caméra (distance par rapport au centre de la caméra) en abscisse pour la même gerbe et les mêmes positions de télescope.

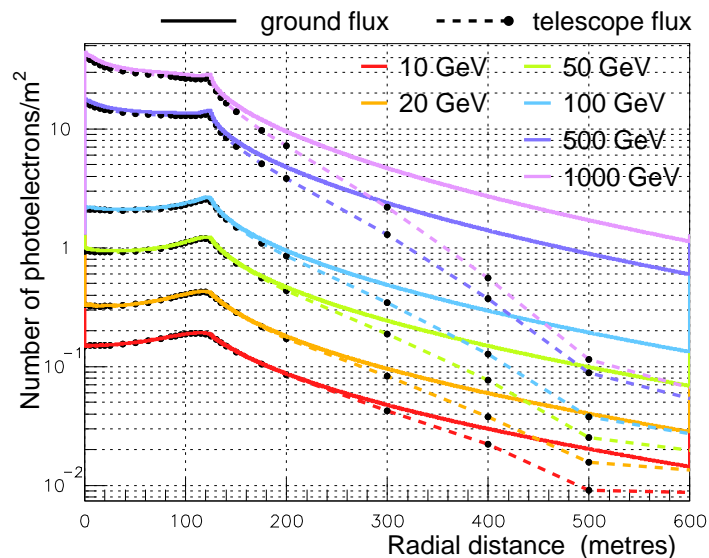


Figure C.5: La comparaison entre la densité moyenne de photons Tcherenkov au sol (traits continus) et la densité moyenne de photo-electrons obtenue dans les images des gerbes (pointillés) en fonction de la distance radiale par rapport au pied de gerbe. L'altitude d'observation est de 1800 m au dessus du niveau de la mer.

important de photons Tcherenkov est rejeté par les télescopes à cause des angles d'incidence plus grands. Comme les courbes de densité au sol dépendent de l'énergie de la gerbe et de l'altitude d'observation, ces paramètres ont aussi un impact sur le nombre moyen de photo-électrons dans les images des gerbes.

À part ces facteurs, les caractéristiques des télescopes ont également une influence sur le nombre de photo-électrons dans les images. Parmi ces caractéristiques figurent la taille des télescopes (car des télescopes plus grands collectent plus de lumière Tcherenkov) et le champ de vue (car un champ de vue plus large permet de collecter la lumière provenant d'une région plus large de la gerbe). D'autres paramètres instrumentaux comme la réflectivité des miroirs, l'efficacité quantique, etc. ont également un impact sur le nombre de photo-électrons dans une image de gerbe.

C.4 La reconstruction des gerbes et propositions pour la séparation γ -hadrons

Dans cette partie, nous présentons les méthodes que nous avons développées pour la reconstruction des paramètres du photon gamma primaire (position de la source, du pied de gerbe et énergie). Nous présentons aussi des idées pour la séparation des gerbes électromagnétiques et hadroniques.

C.4.1 Reconstruction de la position de la source et du pied de gerbe

Les méthodes de reconstruction de la source et du pied de gerbe utilisent, de manière simultanée, l'information obtenue par différents télescopes lors d'observations stéréoscopiques avec un réseau IACT.

La reconstruction de la source

Comme nous l'avons déjà remarqué, chaque image de l'axe d'une gerbe contient l'image de la source quand elle est prolongée dans le référentiel de la caméra. Cela implique que lorsque les images d'une même gerbe obtenues par plusieurs télescopes sont superposées dans le référentiel de la caméra, leur point d'intersection correspond à l'image de la source.

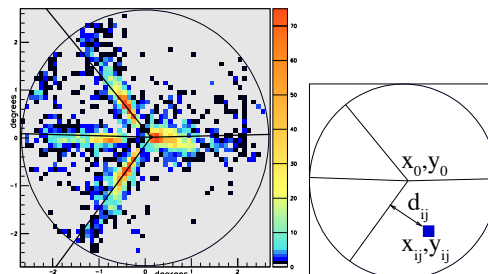


Figure C.6: Les images superposées d'une gerbe de 500 GeV obtenues par quatre télescopes. Les axes reconstruits de chaque image sont montrés en noir.

La position de la source peut alors être reconstruite en maximisant le logarithme de la fonc-

tion de vraisemblance suivante:

$$\ln(L_{all}) = - \sum_{j=1}^{N_{tel}} \sum_{i=1}^{N_{pix}} \frac{N_{ij} t_{ij}^2}{2\sigma_t^2}, \quad (C.6)$$

avec $d_{ij} = \frac{|(y_{cj}-y_o)(x_{ij}-x_o)-(y_{ij}-y_o)(x_{cj}-x_o)|}{\sqrt{(x_c-x_o)^2+(y_c-y_o)^2}}$. Dans cette fonction, N_{ij} correspond au contenu du i^{ieme} pixel dans le j^{ieme} télescope et d_{ij} donne sa distance par rapport à l'axe de l'image. (x_{ij}, y_{ij}) et (x_{cj}, y_{cj}) sont respectivement les coordonnées du pixel et du centroïde de l'image.

Nous travaillons avec les hypothèses suivantes:

- Chaque image de l'axe est une droite passant par le point (x_o, y_o) , commun à tous les axes et qui donne la position de l'image de la source dans le référentiel de la caméra. Les coordonnées de ce point sont des paramètres libres.
- On suppose que la distance des pixels par rapport à l'axe correspondant (autrement dit le profil transverse de l'image) suit une loi Gaussienne. σ_t est l'écart type moyen obtenu en ajustant une fonction Gaussienne sur les profils transverses des images. Nous avons démontré que le profil transverse moyen des images peut être bien pris en compte/représenté par la somme de trois fonctions Gaussiennes. Dans ce cas-là, la fonction Gaussienne centrale prend en compte 77% du signal total. Quand le profil est ajusté avec une seule fonction Gaussienne, celle-ci prend en compte 88% de la surface représentée par les trois fonctions Gaussiennes. L'utilisation d'une seule fonction Gaussienne pour représenter le profil transverse est donc une approximation raisonnable qui peut être utilisée pour la reconstruction de la source. Nous avons aussi démontré que pour une distance de télescope fixe par rapport au pied de gerbe, la valeur moyenne de σ_t varie très peu avec l'énergie, même si les fluctuations sur cette valeur deviennent plus importantes aux basses énergies.
- L'axe de chaque image doit passer par le centroïde de l'image correspondante.

Le logarithme de la fonction de vraisemblance est maximisé avec les paramètres libres x_o et y_o . Le résultat de la minimisation donne la position de la source reconstruite. La figure C.6 montre un exemple de cette reconstruction. La maximisation du logarithme de la fonction de vraisemblance est faite en deux étapes. Dans un premier temps, la position du maximum est déterminée de manière approximative en faisant un pré-scan du champ de ciel accessible et en cartographiant la valeur du Logarithme de la vraisemblance pour la gerbe concernée. Cette position du maximum approximative est ensuite prise comme point de départ pour Minuit, qui est un outil de minimisation de fonctions. La position du maximum déterminée par Minuit nous donne la position de la source reconstruite.

Résultats Nous présentons la précision de reconstruction de la position de la source dans le ciel en fonction de l'énergie générée de la gerbe et du pied de gerbe pour un système de quatre télescopes (une description détaillée du système utilisé est donnée à la page 110 du texte principal de cette thèse) dans la figure C.7. L'énergie est placée en abscisse et la précision de reconstruction en degrés est placée en ordonnée. Chaque point dans ces figures correspond à une déviation standard de la différence entre la position générée et la position reconstruite. La figure de gauche montre la précision obtenue pour diverses positions de pied de gerbe placées le long de la diagonale du réseau des quatre télescopes (marqueurs oranges dans la figure 6.13). On note que pour les gerbes de 500 GeV et 1000 GeV, la précision de reconstruction de la source est meilleure que la taille d'un pixel de la caméra qui est ici de 0.1° .

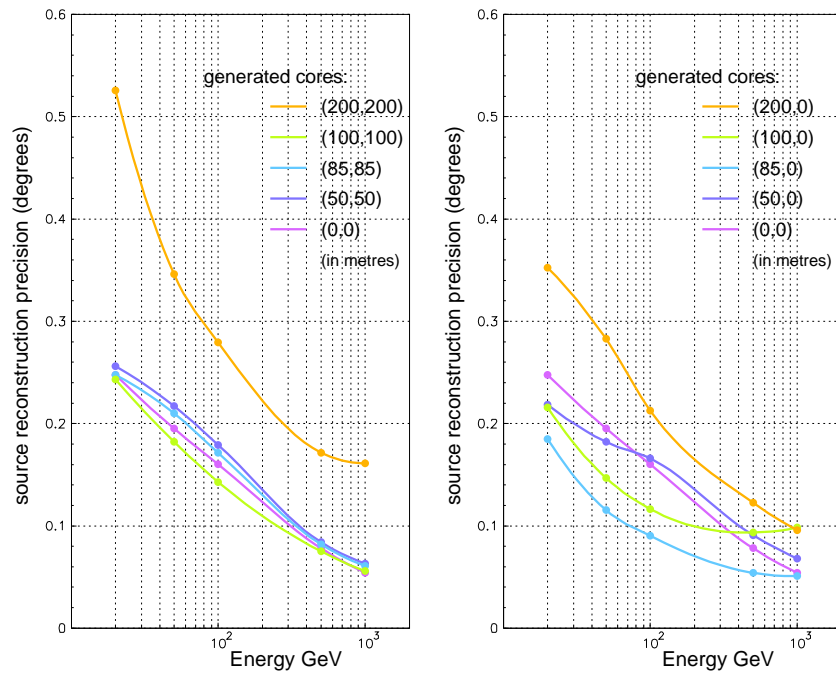


Figure C.7: La précision de reconstruction de la source en fonction de l'énergie générée de la gerbe pour les pieds de gerbe placés le long de la diagonale et le long d'une ligne sur la droite du réseau de quatre télescopes. Une description détaillée du système utilisé est donnée sur la page 110 du texte principal de cette thèse. On note que les traits colorés ne sont là que pour guider l'œil et n'ont aucune valeur physique.

Pour les pieds de gerbe pour lesquels au moins de deux télescopes se retrouvent à l'intérieur de la région de l'anneau Tcherenkov, la précision de reconstruction dépend peu du pied de gerbe. Cependant, cette précision est moins bonne pour la position (200, 200) mètres, où les télescopes se retrouvent bien en dehors de l'anneau Tcherenkov.

La figure de droite montre la précision de reconstruction de la source pour des pieds de gerbe placés le long d'une ligne sur la droite du réseau de télescopes (marqueurs bleus de la figure 6.13). La meilleure précision est obtenue pour la position (85,0) mètres lorsqu'une des gerbes tombe à l'aplomb d'un des quatre télescopes. La précision pour la position la plus éloignée du réseau de télescope, c'est-à-dire (200, 0) mètres est la moins bonne.

La reconstruction du pied de gerbe

Dans le référentiel du sol, l'axe d'une image de gerbe pointe vers la position du pied de gerbe. Le point d'intersection des axes de toutes les images obtenues par une observation stéréoscopique d'une même gerbe correspond alors à la position du pied de gerbe³. La position du pied de gerbe peut être alors reconstruite en maximisant le logarithme d'une fonction de vraisemblance ressemblant à celle que nous avons utilisée pour la reconstruction de la source. Dans l'équation C.6, la position de chaque pixel et la valeur de σ_t sont exprimées dans le référentiel du sol. Au lieu de supposer que chaque axe passe par le centroïde de l'image correspondante, on impose que chaque axe passe par la position de la source reconstruite

³Ceci est vrai quand le télescope pointe vers la source. Dans un cas plus général, le point d'intersection des gerbes doit être translaté d'une distance équivalente au décalage de la position de l'image de la source par rapport au centre de la caméra.

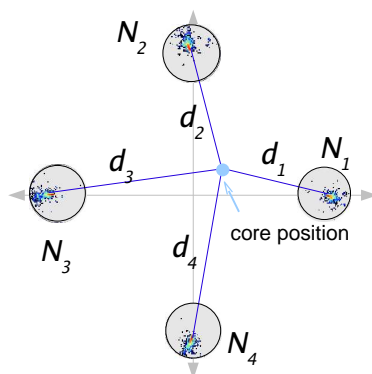


Figure C.8: La reconstruction du pied de gerbe à partir des images d'une cascade de 5000 GeV observées par quatre télescopes. L'échelle de l'image a été adaptée de manière à mettre la configuration du système en valeur.

dans la caméra correspondante (dans ce cas x_{cj}, y_{cj} représentent les coordonnées de l'image de la source dans chaque caméra, exprimées dans le référentiel du sol). De même que pour la reconstruction de la source, la maximisation de cette fonction de vraisemblance est faite en deux étapes : scan préliminaire dont le résultat est ensuite utilisé comme point de départ pour le logiciel Minuit.

Résultats Dans la Figure C.9, nous montrons la dépendance avec l'énergie de la précision de reconstruction du pied de gerbe. L'énergie est donnée en abscisse et la précision de la reconstruction en ordonnée (déviations standard entre la position reconstruite et la position générée du pied de gerbe). La distribution de gauche représente la précision obtenue en fonction de l'énergie pour des pieds de gerbe situés sur la diagonale du réseau alors que la figure de droite montre la situation pour des pieds de gerbe le long de l'axe x du système. Comme dans le cas de la position de la source, la précision s'améliore avec l'énergie puisque le nombre de photo-électrons est plus grand et rend possible une meilleure reconstruction de l'axe des images. Le pied de gerbe est reconstruit avec une précision de l'ordre ou meilleure que 10 mètres au-delà de 200 GeV tant que le pied de gerbe reste proche du réseau de télescopes. La situation se dégrade pour les pieds de gerbe plus éloignés ((200,0) m et (200,200) m) du réseau de télescopes. La situation la plus favorable se produit sur la figure de droite en (85,0) lorsque le pied de gerbe se situe à la position d'un des télescopes du réseau.

Considérations additionnelles

Nettoyage de l'image Nous avons implémenté une méthode simple de nettoyage d'image qui consiste à garder seulement les pixels qui contiennent un nombre de photo-électrons au-dessus d'un certain seuil. Notre objectif n'est pas d'explorer l'efficacité de ces méthodes pour le nettoyage d'image. Nous voulons plutôt examiner comment la reconstruction des paramètres peut être sensible à un tel nettoyage en utilisant une méthode assez basique. Dans la figure C.10, nous montrons l'évolution de la précision de reconstruction de la source (gauche) et du pied de gerbe (droite) en fonction du seuil appliqué sur les pixels, et ceci pour différentes énergies. Nous pouvons constater que pour chaque énergie, il existe un seuil optimum de nettoyage dont la valeur augmente avec l'énergie. Nous démontrons que la valeur de ce seuil a une dépendance linéaire sur l'énergie.

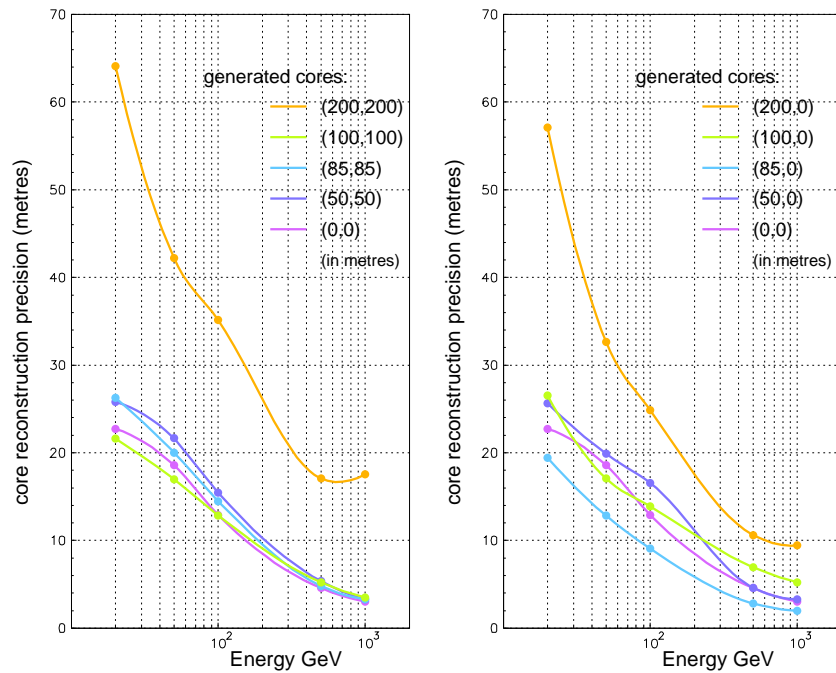


Figure C.9: La précision de la reconstruction du pied de gerbe en fonction de l'énergie pour les pieds de gerbe générés sur la diagonale (gauche) et le long d'une ligne sur la droite du réseau de télescopes. Une description détaillée du système utilisé est donnée sur la page 110 du texte principal de cette thèse. On note que les traits colorés ne sont là que pour guider l'œil et n'ont aucune valeur physique.

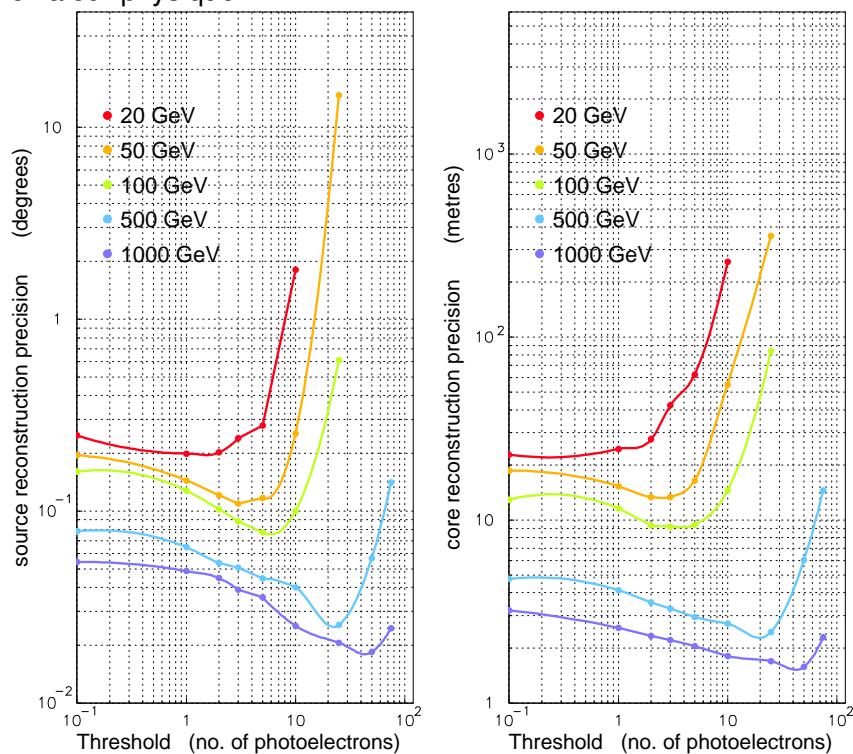


Figure C.10: La précision sur la reconstruction de la source (gauche) et du pied de gerbe (droite) en fonction du seuil de nettoyage d'image. Les différentes couleurs correspondent aux différentes énergie. Des lignes joignant les points ont été rajoutée afin de guider l'œil et n'ont aucune valeur physique.

Discussion sur l'utilisation de σ_t dans la reconstruction de la source et du pied de gerbe

Alors que la valeur moyenne de σ_t dépend très peu de l'énergie de la gerbe, elle dépend cependant de la distance du télescope par rapport au pied de gerbe. La valeur moyenne de σ_t ainsi que les fluctuations sur cette valeur augmentent lorsque le télescope est placé plus près du pied de gerbe et que moins de photons de la partie centrale de la gerbe l'atteignent. Il en est de même pour des distances au-delà du rayon de l'anneau Tcherenkov. Les ajustements individuels pour le profil transverse des images de gerbe nous montrent que ces fluctuations sont en partie dues à la présence des pixels isolés, éloignés du pic central de l'image. Il convient donc d'étudier l'effet du nettoyage d'image sur σ_t et sa dépendance sur la distance. La figure C.11 montre la valeur moyenne de σ_t en fonction de la distance pour différentes valeurs de seuil appliquées sur le contenu des images de gerbes de 500 GeV. On constate une diminution de la valeur de σ_t par rapport à la distance entre le télescope et le pied de gerbe tant que l'on reste à l'intérieur de l'anneau Tcherenkov. Le graphique montre également qu'en dehors de l'anneau Tcherenkov, un seuil de nettoyage d'image plus modéré doit être appliqué car les images contiennent moins de photo-electrons dans cette région. Nous notons qu'un changement dans la valeur de σ_t utilisée n'aura d'impact que sur la normalisation des valeurs de χ^2 pour les méthodes de reconstruction de la source et du pied de gerbe et ne changera pas la position des paramètres reconstruits.

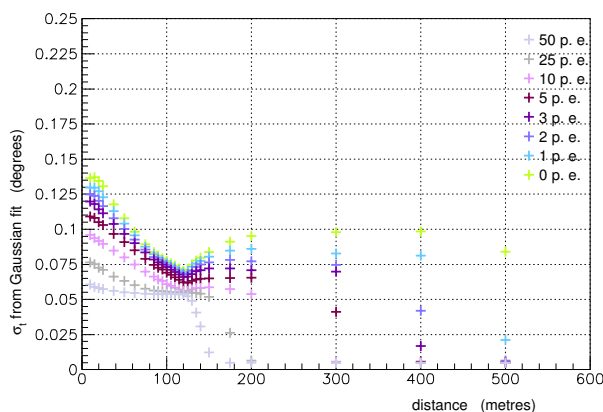


Figure C.11: La valeur moyenne de σ_t en fonction de la distance du télescope par rapport au pied de gerbe différentes valeurs de seuil (montrées par le changement de couleur) appliquées sur le contenu des images de gerbes de 500 GeV.

Le χ^2 des ajustements pour la maximisation de vraisemblance Les valeurs de χ^2 indiquent la qualité d'un ajustement. On peut donc s'attendre à ce que la valeur de χ^2 obtenue par les ajustements pour la reconstruction de la source et du pied de gerbe puisse être utilisée pour séparer les gerbes hadroniques des gerbes électromagnétiques. Cependant, les facteurs suivants limitent l'usage de cette méthode:

- L'ajustement des profils transverses d'image de gerbe avec un profil Gaussien est approximatif. Cela implique que pour la haute énergie, où les images de gerbes sont mieux définies, les valeurs de χ^2 se dégradent au lieu de s'améliorer.
- Comme nous l'avons déjà mentionné, la valeur du χ^2 dépend de la valeur de σ_t . La valeur de σ_t dépend elle-même de nombreux facteurs (distance du télescope par rapport au pied de gerbe, nettoyage de l'image, fluctuations, etc.) et la valeur du χ^2 dépend de ces

facteurs également. Pour utiliser la valeur du χ^2 pour distinguer les gerbes de photons par rapport à des gerbes de hadrons, il conviendra d'utiliser des valeurs adaptées de σ_t . Cela pourrait être implémenté en constituant une base de données permettant de tabuler ou de paramétrer les valeurs de σ_t en fonction de la distance, du seuil en amplitude des pixels, etc. Une méthode itérative avec une seconde reconstruction de la position de la source et du pied de gerbe pourrait être implémentée une fois que le pied de gerbe est déterminé. La seconde itération utiliserait alors la valeur de σ_t adaptée à la distance du télescope, le seuil de nettoyage, etc.. Le profil transverse de chaque image pourrait aussi être ajusté individuellement.

Remarque sur l'utilisation de la symétrie longitudinale des images Comme l'asymétrie du profil longitudinal des images de gerbe dépend de la distance du télescope par rapport au pied de gerbe, l'information sur le profil longitudinal pourrait être utilisée pour améliorer la précision sur la reconstruction de la source et du pied de gerbe. Cette méthode serait particulièrement utile lors d'observations de gerbes de haute énergie par des télescopes situés à de grandes distances du pied de gerbe.

C.4.2 Reconstruction de l'énergie

La méthode pour la reconstruction de l'énergie se base sur la dépendance linéaire du nombre moyen de photo-électrons dans les images (obtenues dans un télescope à une distance fixe du pied de gerbe) et l'énergie de la gerbe. Nous avons fait des simulations de gerbes de rayon gamma afin de tabuler les valeurs du nombre de photo-électrons en fonction de la distance par rapport au pied de gerbe et de l'énergie. Les valeurs obtenues sont montrées dans la figure C.12.

Lorsqu'une gerbe est observée dans un réseau de IACT, nous avons accès au nombre de photo-électrons N_i dans l'image obtenue avec le $i^{ème}$ télescope. Une fois que la reconstruction du pied de gerbe a été faite, nous pouvons également calculer la distance d_i entre le télescope et le pied de gerbe. À partir de ces valeurs, nous pouvons reconstruire l'énergie E_i en utilisant la table de valeurs décrite dans le paragraphe précédent. La valeur finale de l'énergie est reconstruite en calculant la moyenne des valeurs E_i obtenues pour tous les télescopes. Le calcul peut aussi être fait en donnant des poids différents aux valeurs de E_i obtenues par chaque télescope en fonction de sa distance par rapport au pied de gerbe.

Résultats Nous avons appliqué cette méthode de reconstruction de l'énergie au réseau de quatre télescopes mentionné plus haut. L'énergie finale a été calculée en prenant la moyenne des valeurs de l'énergie reconstruite à partir de chaque télescope. La distribution des énergies reconstruite pour chaque énergie générée (voir la figure 8.4 sur la page 163 du texte en anglais) est ensuite utilisée pour obtenir les résultats montrés dans les figures C.13 et C.14. La figure C.13 nous montre que l'énergie reconstruite (axe des ordonnées) est légèrement inférieure à l'énergie générée.

La figure C.14 montre la résolution en énergie obtenue pour différentes positions du pied de gerbe en fonction de l'énergie générée. Nous pouvons constater que pour les pieds de gerbe autre que (0,0), la résolution tend à s'améliorer avec l'énergie générée. Pour les énergies générées à partir de 50 GeV, la résolution de l'énergie a une valeur entre 10 et 20%.

Quand le calcul de l'énergie est fait en donnant des poids différents à l'information obtenue des télescopes à différentes distances du pied de gerbe, la résolution est légèrement moins bonne et sa dépendance par rapport à l'énergie générée diminue.

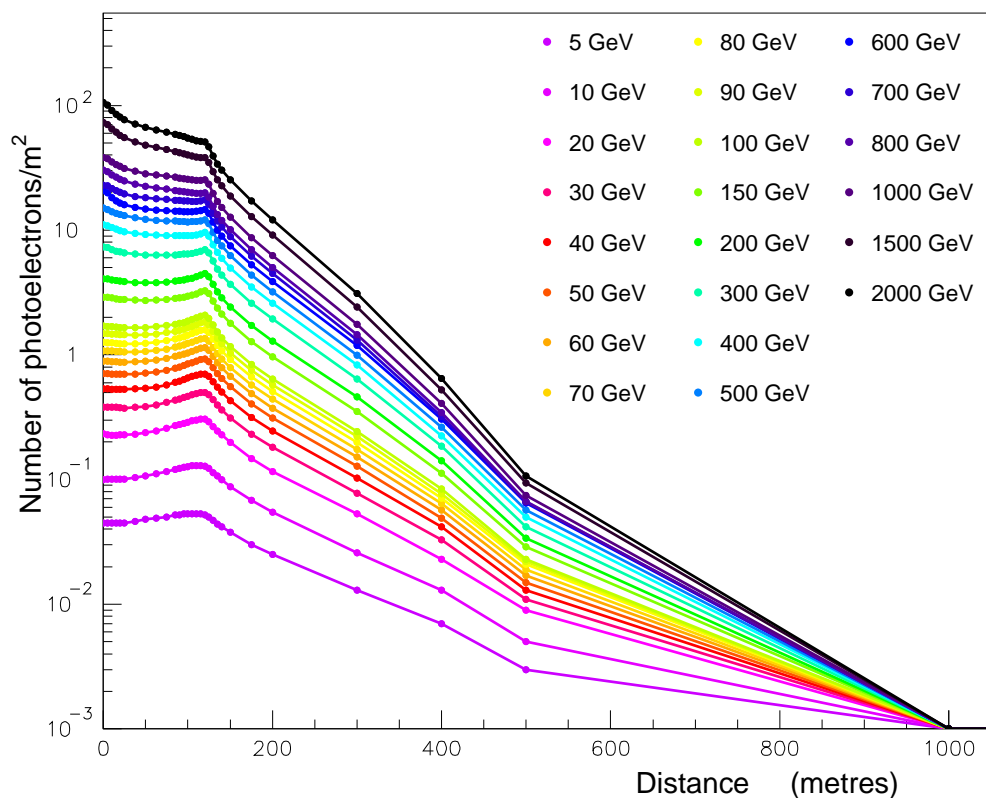


Figure C.12: Le nombre moyen de photo-électrons dans les images de gerbe en fonction de la distance pour des énergies fixes entre 5 GeV et 2000 GeV.

Solution possible pour améliorer la reconstruction de l'énergie Comme nous l'avons déjà mentionné, la méthode de reconstruction de l'énergie utilise la relation entre le nombre de photo-électrons obtenus dans un télescope à une distance donnée à partir du pied de gerbe et l'énergie de la gerbe. Une étude plus détaillée (dont on peut trouver les détails dans la section 8.5 de la version principale de cette thèse) des distributions du nombre de photo-électrons obtenu dans les images montre que ces distributions ont tendance à être asymétriques et que cette asymétrie dépend de la distance du télescope par rapport au pied de gerbe. Cette asymétrie est due à la variation de l'altitude de première interaction. En effet, quand la première interaction du rayon gamma a lieu à basse altitude, le nombre de photons Tcherenkov émis a tendance à être plus grand. En conséquence, la reconstruction de l'énergie pourrait être améliorée en rajoutant un paramètre (relié à l'altitude de première interaction dans l'atmosphère) dans les tables utilisées pour la reconstruction de l'énergie. La page 266 de ce résumé et la section 8.7 du texte principal décrivent une méthode que nous avons développée pour la reconstruction du profil longitudinal des gerbes à partir des pixels individuels dans une image. Un paramètre obtenu de ce profil reconstruit tel que la position du maximum de développement de la gerbe pourrait être utilisé pour la reconstruction de l'énergie des gerbes.

C.4.3 Propositions pour la séparation γ -hadrons

Comme les photons gamma, les hadrons interagissent avec les molécules de l'air après leur entrée dans l'atmosphère terrestre. Les processus principaux intervenant dans les gerbes hadroniques sont différents de ceux mis en jeu dans les gerbes électromagnétiques. Par

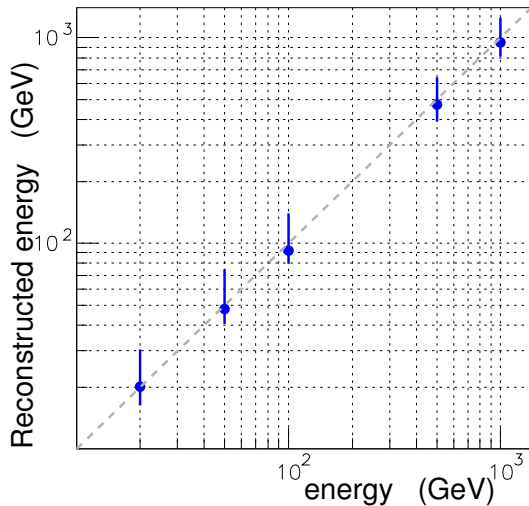


Figure C.13: L'énergie reconstruite moyenne en fonction de l'énergie générée des gerbes. L'énergie reconstruite correspond à la valeur moyenne de l'ajustement Gaussien des distributions d'énergie reconstruite à chaque énergie générée et les barres d'erreurs correspondent à l'écart type de ces distributions. Ceci est fait séparément pour les bins au dessus et en dessous de la valeur moyenne afin de tenir compte de l'asymétrie de la distribution. Pour plus de détails, voir les figures 8.4, 8.5 sur la page 163 du texte principal de cette thèse. La droite en pointillés représente une reconstruction parfaite de l'énergie.

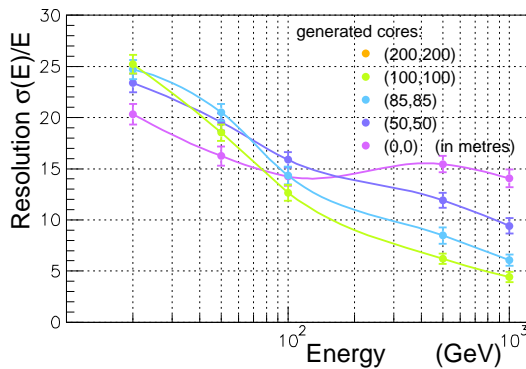


Figure C.14: La résolution en énergie en fonction de l'énergie générée pour les pieds de gerbe le long de la diagonale du réseau à quatre télescopes. La résolution est calculée en ajustant une fonction Landau sur les distributions d'énergie reconstruite à chaque énergie générée.

conséquent, les propriétés moyenne des gerbes hadroniques sont différentes des propriétés des gerbes électromagnétiques. Ces gerbes hadroniques peuvent être reconstruites comme des gerbes de gamma et constituent donc un fond important. L'identification des rayons gamma et le rejet des gerbes hadroniques constituent donc une partie essentielle des analyses en astronomie gamma. Dans cette partie de la thèse, nous présentons trois possibilités pour la séparation des hadrons et des rayons gamma.

Les gerbes hadroniques et leurs images

Le développement des gerbes hadroniques L'altitude moyenne de matérialisation pour les gerbes hadroniques est plus basse dans l'atmosphère (autour de 17 km au dessus du niveau de la mer dans le modèle U. S. Standard) que celle des gerbes produites par des rayons gamma (autour de 21 km au dessus du niveau de la mer). Leur extension latérale est également plus grande que celle des gerbes électromagnétiques. De plus, les processus dans les gerbes hadroniques sont beaucoup plus complexes que ceux dans les gerbes électromagnétiques et produisent plus de fluctuations dans les gerbes. Leur énergie observable est plus basse que celle des gerbes électromagnétiques de la même énergie. Les pions neutres produits dans ces gerbes se désintègrent rapidement en paires de photons gamma. Ces photons gamma produisent des sous-gerbes électromagnétiques.

L'émission de photons Tcherenkov La lumière Tcherenkov totale émise par une gerbe hadronique est moins importante que celle émise par une gerbe électromagnétique de même énergie. En effet, une partie importante de l'énergie initiale du hadron est absorbée par des processus n'émettant aucun signal visible. La figure C.15 (graphique de gauche) compare le nombre moyen de photons Tcherenkov arrivant au sol pour des gerbes électromagnétiques et hadroniques. Nous pouvons voir que pour obtenir le même nombre de photons Tcherenkov, l'énergie de la gerbe hadronique doit être environ ~ 2.5 fois plus grande que celle de la gerbe électromagnétique. La différence du nombre de photons Tcherenkov arrivant au sol est également visible dans le graphique de droite où nous montrons la densité de photons Tcherenkov obtenue au sol en fonction de la distance par rapport au pied de gerbe pour plusieurs énergies de gerbes créées par des protons. Ce graphique peut être comparé avec la figure C.5 sur la page 254, où nous avons montré les mêmes profils pour des gerbes électromagnétiques. Nous notons aussi l'absence d'anneau Tcherenkov dans ces profils. En effet, les fluctuations et l'extension latérale plus importante des gerbes hadroniques rend le profil moyen des photons Tcherenkov au sol plus plat.

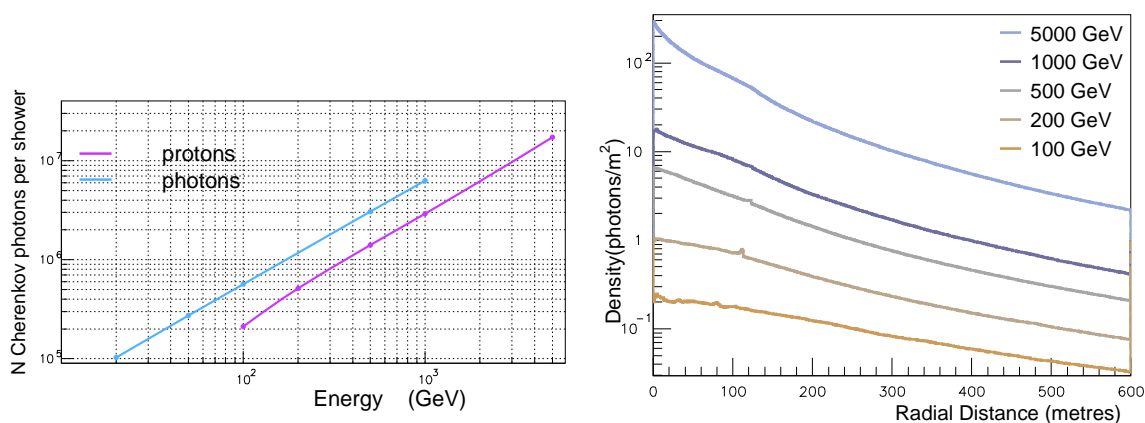


Figure C.15: À droite : comparaison du nombre moyen de photons Tcherenkov au sol pour des gerbes de protons (mauve) et de gamma (bleu). L'efficacité quantique des photomultiplicateurs et la réflectivité des miroirs sont aussi prises en compte pour comparer le nombre de photons Tcherenkov pouvant faire partie des images de gerbe. À gauche : la densité moyenne des photons Tcherenkov au sol (en photons par m^2) en fonction de la distance par rapport au pied de gerbe pour des gerbes de protons de différentes énergies à 1800 m au-dessus du niveau de la mer. Les flux prennent en compte l'efficacité quantique des photomultiplicateurs et la réflectivité des miroirs.

Les images des gerbes hadroniques et les hadrons en tant que fond pour les observations de photons gamma Les fluctuations dans les gerbes hadroniques et leur émission Tcherenkov sont également présentes dans leurs images obtenues dans les télescopes IACT. Les images de gerbes hadroniques ont aussi tendance à avoir une forme plus arrondie et un profil transverse plus étendu. Ces caractéristiques peuvent être utilisées pour rejeter les gerbes hadroniques et identifier les gerbes électromagnétiques qui ont des formes plus régulières. Cependant, cette identification peut être plus difficile dans certains cas, car certaines gerbes hadroniques ont des images qui ressemblent fortement à celles des gerbes électromagnétiques. Ci-dessous, nous présentons les différents cas où les gerbes hadroniques peuvent être confondues avec les gerbes électromagnétiques et les solutions possibles pour les discriminer.

- Les muons secondaires dans les gerbes hadroniques peuvent donner des images proches de celles des rayons gamma dans certains télescopes. Ces événements sont rejetés par utilisation des observations stéréoscopiques.
- Lorsqu'il y a des sous-gerbes électromagnétiques dans les gerbes hadroniques, l'événement peut être reconstruit comme provenant d'une gerbe gamma. Ces événements sont rejetés par des observations stéréoscopiques également. Nous remarquons que l'identification des gerbes hadroniques à muons secondaires ainsi que celles avec des sous-gerbes électromagnétiques peut être une considération supplémentaire pour les télescopes futurs ; la taille des télescopes et la distance entre eux peuvent être adaptées au rejet de ces événements.
- Les autres hadrons sont identifiés à partir des caractéristiques physiques de leurs images. Les images de certaines gerbes hadroniques ressemblent celles des gerbes électromagnétiques. Il est donc important d'avoir des méthodes les plus discriminantes possibles pour la séparer les rayons gamma des hadrons. L'utilisation combinée de plusieurs méthodes ou variables discriminantes peut également améliorer le rejet du fond hadronique.

Nous notons également qu'un premier rejet des hadrons est aussi réalisé avec la résolution angulaire pour des sources ponctuelles.

Propositions pour la séparation hadron-gamma

Nous avons étudié trois méthodes différentes pour la séparation hadron-gamma à l'aide de simulations de gerbes hadroniques et électromagnétiques générées avec un angle zénithal de 0° et observées par quatre télescopes (pour plus de détails sur le réseau de télescopes utilisé voir la page 110 de la version principale de cette thèse). Les gerbes sont générées avec un pied de gerbe au centre du réseau de télescopes (c'est-à-dire à la position (0, 0) m). Les méthodes présentées ici nécessiteraient d'être optimisées pour pouvoir être utilisées comme méthodes de discrimination. Cependant, leur étude ici nous permet d'avoir une idée de leur potentiel.

L'utilisation du χ^2 des ajustements pour la reconstruction de la source et du pied de gerbe Comme les méthodes de reconstruction de la source et du pied de gerbe ont été développées de manière à être adaptées aux gerbes électromagnétiques, on peut s'attendre à ce que les valeurs de χ^2 obtenues par ces ajustements puissent être utilisées pour la discrimination hadron-gamma. Nous avons déjà discuté les difficultés à obtenir des valeurs de χ^2 précises de ces ajustements (voir page 260) et proposé certaines améliorations. Bien que ces améliorations n'aient pas été implémentées dans l'étude présentée dans ce chapitre, les résultats discutés ci-dessous montrent que les valeurs de χ^2 obtenues par ajustements pour les rayons gamma sont meilleures que celles obtenues pour les gerbes hadroniques.

Dans la figure C.16, seules les gerbes gamma (graphique de gauche) et hadronique (graphique de droite) dont la valeur du χ^2 de reconstruction du pied de gerbe est en dessous d'une valeur fixe sont gardées. Les valeurs de la coupure sur le χ^2 sont montrées en abscisse et celles de l'efficacité de ces coupures en ordonnée. Le graphique de gauche montre qu'il existe une valeur seuil à partir de laquelle presque 100% des gerbes électromagnétiques sont gardées après la coupure. Cette valeur du seuil dépend légèrement de l'énergie. Quant aux gerbes hadroniques, elles ont des valeurs de χ^2 plus élevées que celles des gerbes électromagnétiques. Un grand nombre d'entre elles ne sont pas retenues même avec des valeurs de χ^2 aussi élevées que 30. Nous pouvons aussi voir qu'il est plus facile de rejeter des hadrons de haute énergie plutôt qu'à basse énergie.

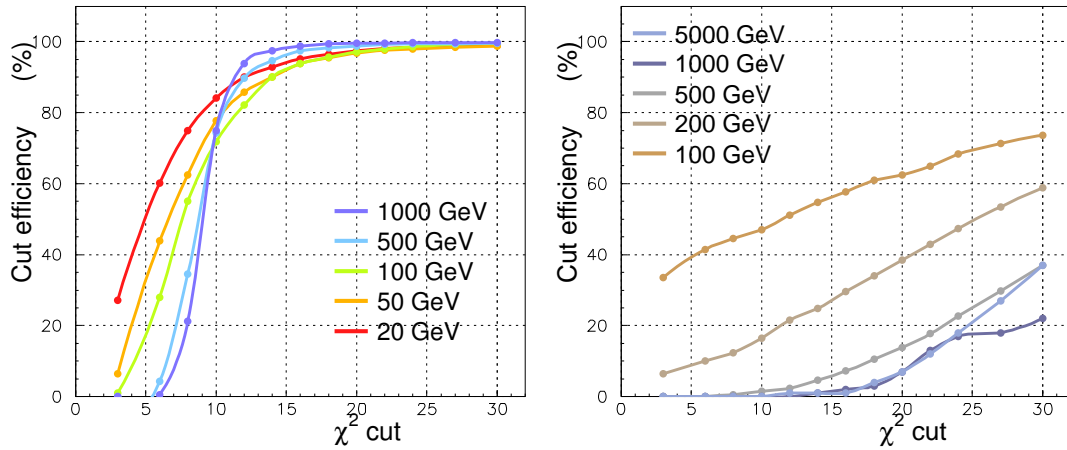


Figure C.16: Le pourcentage de gerbes retenues après l'application de coupures sur plusieurs valeurs de χ^2 de l'ajustement pour la reconstruction du pied de gerbe. Les coupures sont montrées en abscisse et les efficacités en ordonnée. Les graphiques montrent les résultats respectivement pour les gerbes de rayons gamma et de protons.

Profils longitudinaux reconstruits Le profil longitudinal des gerbes peut être reconstruit en retraçant le parcours des photons Tcherenkov individuels à partir de la position de chaque pixel sur la caméra. La trajectoire de chaque photon contribuant au signal dans un pixel est calculée en supposant qu'il a été réfléchi par le centre du miroir. L'axe de la gerbe est complètement connu après la reconstruction de la source et du pied de gerbe ; on peut donc calculer la distance la plus courte d_{min} entre cet axe et la trajectoire reconstruite du photon Tcherenkov. L'une des deux extrémités joignant l'axe de la gerbe et la trajectoire reconstruite du photon Tcherenkov à leur point le plus proche correspond au point d'émission du photon Tcherenkov (Les deux extrémités donnent des résultats similaires). Le profil longitudinal reconstruit est obtenu lorsque ce processus est répété pour tous les pixels de l'image.

Comme les profils longitudinaux des gerbes hadroniques et électromagnétiques ont tendance à être différents, les profils longitudinaux reconstruits pourraient être un autre moyen de séparer les hadrons des rayons gamma. La figure C.17 montre les profils reconstruits moyen pour des rayons gamma (colonne de gauche) et des protons (colonne de droite) pour différentes énergies. Nous pouvons constater que les profils des gerbes de protons ont tendance à être plus irréguliers et ont un maximum de développement plus bas dans l'atmosphère. De plus, quand ces profils sont ajustés avec la fonction $f(t) = C(\beta t)^{\alpha-1}e^{-\beta t}$ (discutée dans la section 2.3.2 de la version principale de cette thèse), l'ajustement est (comme on peut s'y attendre) meilleur dans le cas des gerbes électromagnétiques.

L'utilisation du point d'émission reconstruit des photons Tcherenkov Comme l'extension latérale des gerbes hadroniques a tendance à être plus grande que celle des gerbes électromagnétiques, on peut s'attendre à ce que le paramètre d_{min} (décrit dans la section précédente) ait des valeurs plus grandes pour des gerbes hadroniques. Ce paramètre pourrait ainsi être utilisé pour séparer les gerbes hadroniques des gerbes électromagnétiques. De plus, l'altitude du point d'émission des photon Tcherenkov reconstruit z_{ax} est aussi relié au profil longitudinal de la gerbe dans l'atmosphère et peut donc être un outil supplémentaire pour la discrimination hadron-gamma.

Nous avons appliqué une série de coupures sur les valeurs reconstruites de d_{min} et z_{ax} pour

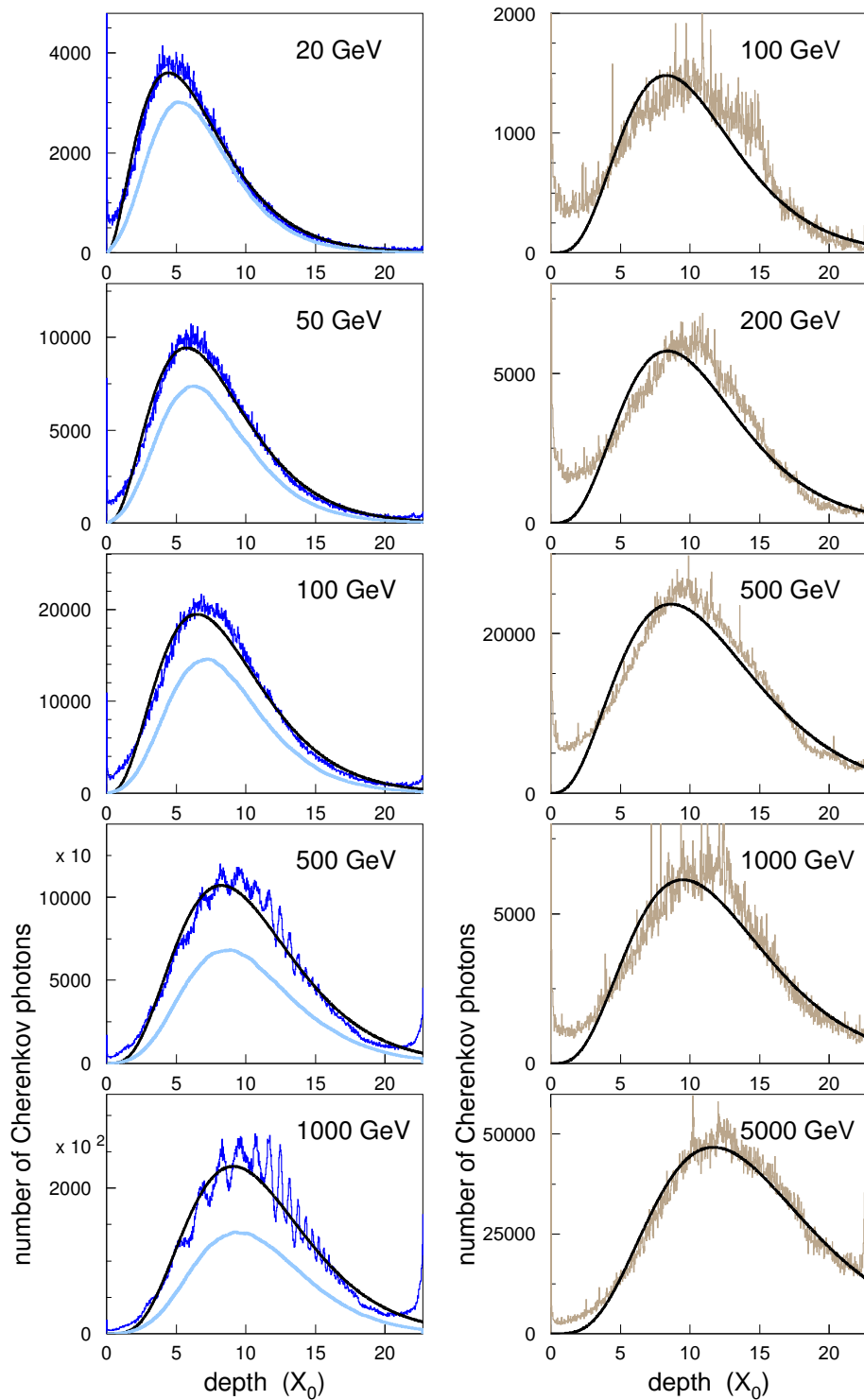


Figure C.17: Les profils longitudinaux moyens reconstruits pour des rayons gamma (colonne de gauche) et des protons (colonne de droite) à plusieurs énergies. Les profils sont ajustés avec la fonction $f(t) = C(\beta t)^{\alpha-1}e^{-\beta t}$ (trait noir). Les profils moyens générés par des rayons gamma sont aussi montrés à l'aide du trait bleu clair dans les graphiques de gauche.

des gerbes produites par des gamma et par des protons. Dans la figure C.18, nous montrons les résultats obtenus en imposant qu'au moins 80% de la lumière Tcherenkov d'une image de gerbe soit émise entre l'altitude d'observation (c'est-à-dire 1800 m au dessus du niveau de la mer) et 13.5 km d'altitude et à l'intérieur d'un rayon $d_{min}max$ autour de l'axe reconstruit de la gerbe. Nous faisons varier la valeur de $d_{min}max$ entre 5 et 150 m et obtenons les courbes d'efficacité (en pourcentage) montrées dans ces graphiques. Le graphique du haut montre les résultats obtenus pour des rayons gamma de différentes énergies et celui du bas montre les résultats pour les protons. Pour les rayons gamma, l'efficacité augmente avec la distance jusqu'à une certaine valeur de $d_{min}max$ au delà de laquelle elle ne s'améliore plus. Pour les gerbes de hautes énergies, ce régime plat commence à partir de valeurs de $d_{min}max$ plus petites, car leurs distributions sont plus compactes. Pour les basses énergies, ce plateau n'est pas situé à hauteur de 100% ; ceci montre que les coupures utilisés sont trop strictes pour ces énergies-là. Cela montre aussi que l'utilisation de télescopes plus large serait nécessaire afin que cette méthode puisse fonctionner à ces énergies. Pour les protons, le régime plat est atteint à des distances $d_{min}max$ beaucoup plus large : au delà de 100 m pour la plupart des énergies. Cela implique que l'application de ce genre de coupure pourrait être utilisé pour séparer les hadrons des gamma. Cela demanderait néanmoins un travail plus approfondi pour déterminer des coupures adaptées à l'énergie reconstruite des gerbes.

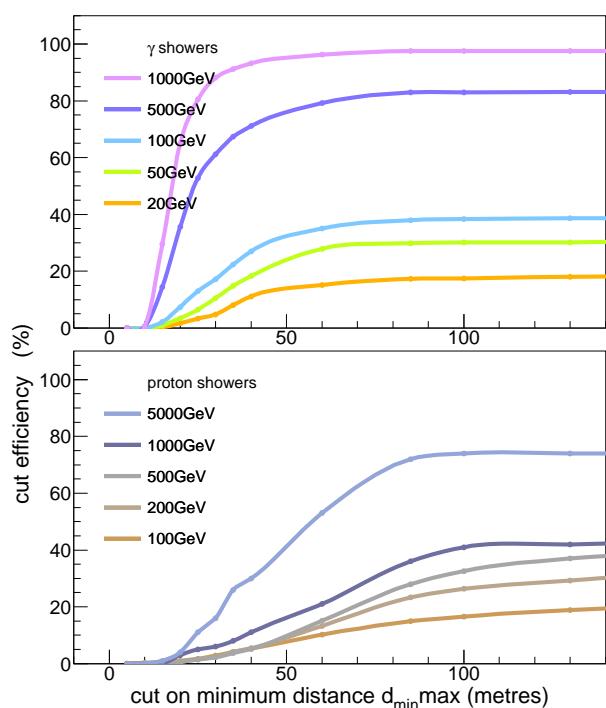


Figure C.18: Le pourcentage de gerbes retenues en imposant que 80% de la lumière Tcherenkov ait des valeurs reconstruite de d_{min} en dessous d'une distance fixe $d_{min}max$ (en abscisse). Les courbes d'efficacité sont obtenues en appliquant cette coupure sur chaque image individuellement. Seules les gerbes avec une valeur de z_{ax} entre le niveau d'observation (1800 km au dessus du niveau de la mer) et 13.5 km sont gardées. Le graphique du haut montre les efficacités obtenues pour les gerbes de rayon gamma et celui du bas pour les gerbes de protons.

C.5 Application et conclusion

C.5.1 Futur des imageurs atmosphériques : capacités de détection de deux réseaux de télescopes pour les photons dans la gamme GeV-TeV

Les domaines d'énergie est les paramètres des réseaux de télescopes

En astronomie gamma, les objectifs physiques et la problématique expérimentale dépendent du domaine d'énergie⁴. Les performances des IACT actuels indiquent les deux domaines d'énergie suivant⁵ :

Haute énergie : 300 GeV - 10 TeV Les télescopes actuels indiquent que c'est le domaine où les imageurs Tcherenkov opèrent le mieux et où une bonne résolution angulaire et en énergie peut être atteinte avec des télescopes de tailles moyennes (10-15 m de diamètre). Pour les télescopes futurs, l'objectif principal dans ce domaine d'énergie est celui d'augmenter la sensibilité des télescopes afin d'avoir accès à plus de phénomènes dans l'univers gamma. Cet objectif peut être atteint en distribuant un grand nombre de télescopes de tailles moyennes sur une grande surface.

Basse énergie : < 30 GeV À plus basse énergie, la taille des gerbes diminue et les images de gerbes contiennent moins de photo-électrons et sont sujettes à plus de fluctuations. Cela rend plus difficile la reconstruction des paramètres de la gerbe et la séparation des hadrons et des photons gamma. L'objectif principal dans ce domaine d'énergie est donc celui de collecter un maximum de lumière Tcherenkov des gerbes en utilisant des télescopes de plus grands diamètres. En parallèle, le flux des rayons gamma a tendance à augmenter à basse énergie. Cet objectif peut donc être atteint en utilisant un petit nombre de télescopes.

Pour l'étude présentée dans cette partie de la thèse nous avons choisi de travailler avec un grand nombre de télescopes de taille moyenne (12.5 m de diamètre) pour faire des observations dans le domaine de la haute énergie et 4 ou 5 grands télescopes (30 m de diamètre) pour la basse énergie. Tous les télescopes ont un champ de vue modéré de 5.4° . Les pixels carrés de la caméra ont une taille de 0.1° de côté. L'étude est faite à deux altitudes : 1800 m et 3600 m au dessus du niveau de la mer.

Distance optimale entre les télescopes

Une fois que le choix du nombre de télescopes a été fait en fonction du domaine d'énergie, la distance inter-télescope optimale peut être déterminée. Pour cela, nous avons choisi d'étudier la réponse d'une unité de 4 télescopes disposés en carré en générant des photons gamma de manière uniforme sur une grande surface. On utilise un trigger simple qui permet de garder les événements pour lesquels au moins deux télescopes ont des images avec au moins 50 photo-électrons. Les paramètres de la gerbe sont reconstruit pour tous les événements passant le trigger.

Ce travail est fait à 300 GeV avec des télescopes de 12.5 m de diamètre et à 50 GeV avec des télescopes de 30 m de diamètre. Ces deux énergies correspondent respectivement à la

⁴On peut trouver une discussion détaillée sur les différents domaines d'énergie et les objectifs scientifiques en astronomie gamma dans [43].

⁵Nous avons décidé de restreindre cette étude à des énergies en dessous de quelques dizaines de TeV. Au delà de cette limite, les flux des sources deviennent très faibles et de larges surfaces de détection sont nécessaires afin de faire des observations.

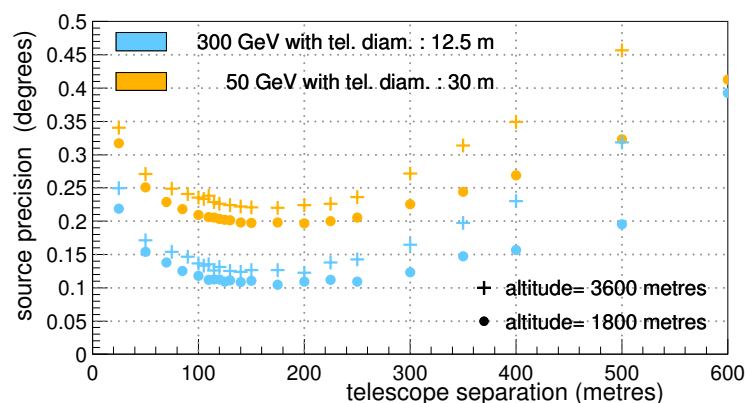


Figure C.19: La précision sur la position de la source dans un système à quatre télescopes en fonction de la distance entre les télescopes à 1800 m et 3600 m d'altitude au dessus du niveau de la mer.

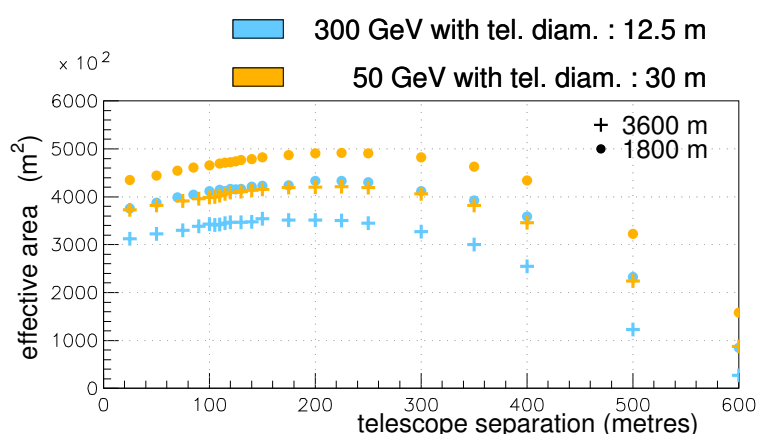


Figure C.20: La surface effective d'un système à quatre télescopes en fonction de la distance entre les télescopes à 1800 m et 3600 m d'altitude au dessus du niveau de la mer.

limite inférieure du domaine de haute énergie et de basse énergie⁶.

Les performances du système pour les rayons gamma, notamment l'efficacité de la reconstruction de la source, du pied de gerbe et de l'énergie sont évaluées pour des distances inter-télescopes entre 25 et 600 m. La précision sur la source en fonction de la distance inter-télescope est montrée par la figure C.19. La reconstruction de la source est optimale quand la distance entre les télescopes a une valeur entre 100 et 200 m. À haute altitude, cet intervalle optimum est plus petit par rapport à la basse altitude et la reconstruction de la source est légèrement moins bonne. On retrouve les mêmes intervalles d'énergie avec la précision de la reconstruction du pied de gerbe en fonction de la distance entre les télescopes (le graphique n'est pas montré dans ce résumé mais peut se trouver à la page 216 de la version anglaise de cette thèse). Quant à la surface effective (figure C.20), elle est essentiellement plate sur

⁶On note que bien que le domaine de basse énergie n'ait aucune limite inférieure, les difficultés dues à l'effet combiné de la petite taille des gerbes électromagnétiques et un flux de rayons cosmiques élevé font que les observations pour des énergies en dessous de 50 GeV deviennent très problématiques. Nous avons donc choisi d'optimiser la distance entre les télescopes à une énergie relativement "sûre", c'est-à-dire 50 GeV.

un large intervalle (100-300 m) de séparation des télescopes. L'optimum de cet intervalle se trouve autour d'environ 200 m de distance. Tous les graphiques montrent que l'intervalle de la distance inter-télescope est indépendant de l'énergie de la gerbe et dépend légèrement de l'altitude d'observation.

Configurations possibles de réseaux d'IACT

Les résultats montrés dans la section précédente peuvent ensuite être utilisés pour obtenir la configuration d'un réseau.

Configurations pour la basse altitude Les deux configurations pour les observations à basse altitude sont montrées par la figure C.21. Dans la première configuration, quatre télescopes de 30 m de diamètre sont disposés aux coins d'un carré de 200 m de côté pour la basse énergie. Cette distance inter-télescopes correspond à la limite supérieure de l'intervalle optimum de la distance entre les télescopes. Ce choix permet d'optimiser la reconstruction des paramètres des gerbes électromagnétiques tout en gardant la plus grande surface effective possible.

Pour le domaine de haute énergie, 33 télescopes sont distribués sur une surface ayant un rayon d'environ 400 m de manière à avoir une distance inter-télescope de 140 m. Cette distance correspond au milieu de l'intervalle optimal de la distance entre les télescopes.

Afin de pouvoir étudier un réseau plus dense, 16 télescopes de taille moyenne sont rajoutés au système de manière à obtenir le réseau de droite dans la figure C.21. Dans cette nouvelle configuration, la distance entre les télescopes est de 100 m, ce qui correspond à la limite inférieure de l'intervalle optimum de la distance inter-télescopes.

Configurations à haute altitude La taille de ces deux configurations est diminuée d'un facteur correspondant au rapport entre la taille de l'anneau Tcherenkov aux deux altitudes (1800 m et 3600 m) tout en gardant le même nombre de télescopes⁷. La distance entre les grands télescopes est de 175 m et celle entre les télescopes de taille moyenne est de 120 m. Pour la configuration plus dense ou 16 télescopes supplémentaires ont été rajoutés, la distance entre les télescopes est de 87 m. Le télescope central est aussi remplacé par un télescope de grande taille de manière à avoir un total de 5 grands télescopes.

Les performances des réseaux possibles pour les photons gamma

Les performances des deux configurations de télescope sont étudiées en générant des gerbes de photons gamma de manière uniforme sur une surface de $2400\text{m} \times 2400\text{m}$ à des énergies fixes. Le trigger simple décrit plus tôt permettant de garder les événements pour lesquels au moins deux télescopes ont des images avec au moins 50 photo-électrons est appliqué. Les figures C.22, C.23 et C.24 respectivement montre la surface effective, la précision sur la position de la source et la résolution en énergie des deux réseaux en fonction de l'énergie.

Comme on peut s'y attendre, la surface effective des réseaux à haute altitude est plus petite que celle des réseaux à basse altitude; les réseaux à haute altitude occupent une surface physique plus petite et l'anneau Tcherenkov à haute altitude est plus petit également. Cet effet est plus visible à haute énergie car les gerbes ont tendances à être coupées par le sol avant d'être arrivées au bout de leur développement dans l'atmosphère.

⁷Le graphique de la figure C.19 suggère d'autres idées possibles pour obtenir une configuration pour la haute altitude. Cependant, l'utilisation de la même configuration à une échelle plus petite à haute altitude, permet la comparaison directe des réseaux aux deux altitudes.

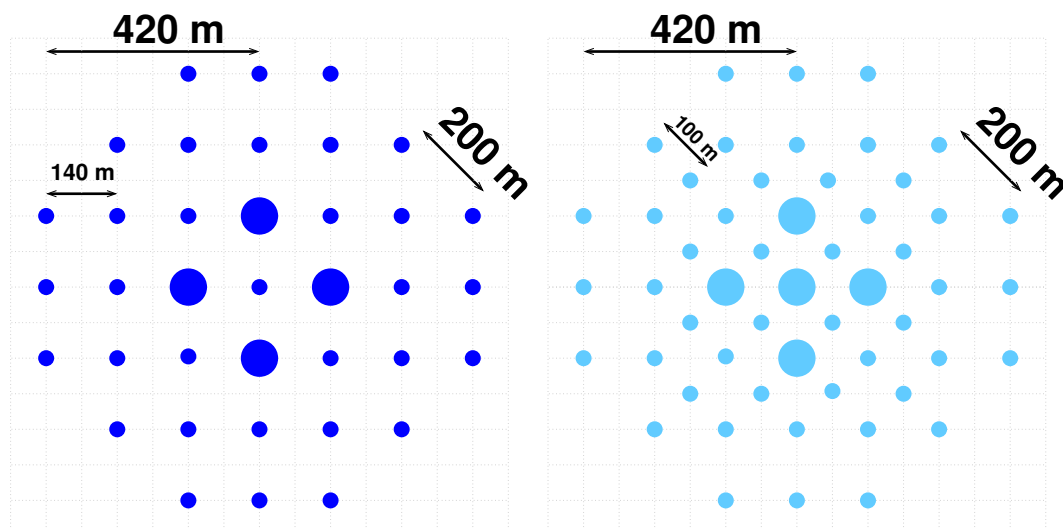


Figure C.21: Les deux configurations de réseaux à 1800 m. La configuration 1 est montrée à gauche et la configuration 2 à droite.

Pour des gerbes de 1000 GeV une précision sur la source d'environ 0.07° est obtenue. Nous rappelons que l'on obtient la même précision est obtenue avec le réseau de quatre télescopes mais seulement sur une surface avec un rayon d'environ 150 m. Avec les grands réseaux cette précision est obtenue pour une surface carré de $800\text{m} \times 800\text{m}$. Le même genre de remarque peut être faite pour la résolution en énergie qui atteint une valeur proche de 7% pour des gerbes de 1000 GeV. Nous notons également que l'utilisation d'un réseau plus dense n'a pas d'impact considérable sur la reconstruction de ces paramètres. Cependant, nous pourrons voir dans la version principale de cette thèse que la précision sur le pied de gerbe montre une légère amélioration à basse énergie avec le réseau plus dense. La reconstruction des paramètres des gerbes s'améliore aussi légèrement à basse altitude.

An angular resolution of around 0.07° is achieved at 1000 GeV. Note that while a four telescope system yields similar angular resolutions for shower falling within a radius of around 150 m, this angular resolution is calculated for all showers generated within a square region of $800\text{m} \times 800\text{m}$. Similar remarks can be made about the energy resolution of around 7% achieved at 1 TeV. One also notes, that the use of a denser array (configuration 2) does not seem to have any impact on the reconstruction of these parameters. Finally, the reconstruction capabilities of the arrays seem to improve slightly at lower altitude.

C.5.2 Conclusion et directions futures

Nous avons développé plusieurs outils afin de pouvoir étudier les capacités de réseaux IACT futurs et optimiser leur paramètres en fonction des objectifs physiques. Parmi ces outils, se trouve un programme flexible et modulable permettant de simuler la réponse des télescopes IACT à des gerbes atmosphériques à partir du programme de simulation de gerbe CORSIKA. A part cela, nous avons aussi développé des méthodes pour la reconstruction de la position de la source et du pied de gerbe ainsi que de l'énergie des rayons gamma observés par les réseaux IACT. Nous avons développé ces outils en prenant en compte la nature stéréoscopiques des observations dans les réseaux IACT. Nous avons également testé ces méthodes de reconstruction en simulant un réseau de quatre télescopes et obtenu des résultats compatible avec ceux obtenus par des réseaux IACT actuels. Ces tests nous ont également permis de mettre

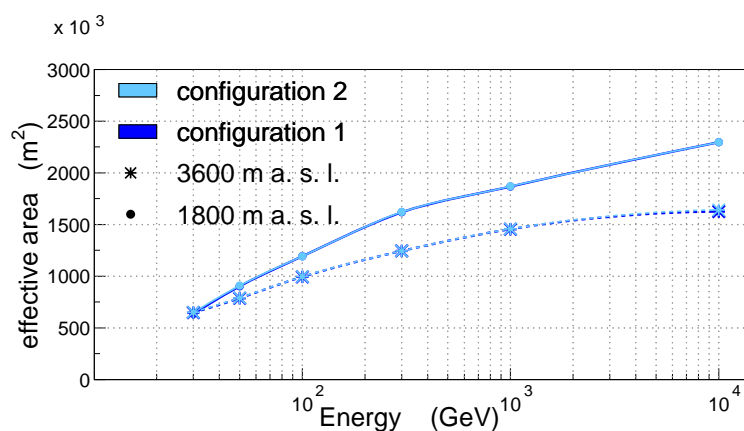


Figure C.22: La surface effective des réseaux en fonction de l'énergie. Les deux couleurs correspondent aux deux configurations de réseaux, alors que les différents types de marqueurs et de lignes montrent les deux altitude d'observation. Les lignes joignant les points du graphe ne sont là que pour guider l'œil et n'ont aucune valeur physique.

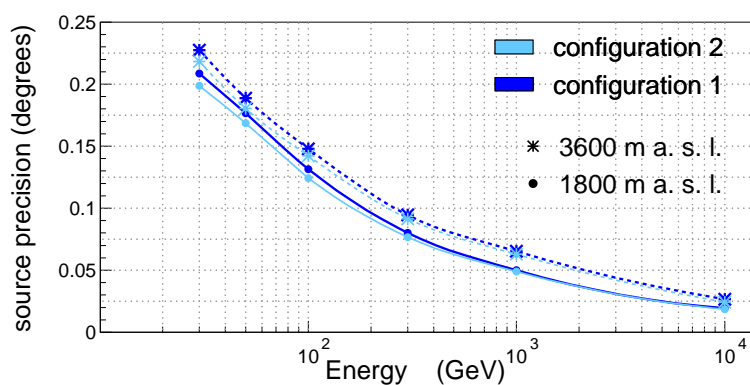


Figure C.23: La précision sur la reconstruction de la source en fonction de l'énergie. Les résultats présentés ici ont été calculés à partir des gerbes générées sur une surface de 800m×800m autour du centre du réseau. Les lignes joignant les points du graphe ont été rajoutée pour guider l'œil et n'ont aucune valeur physique.

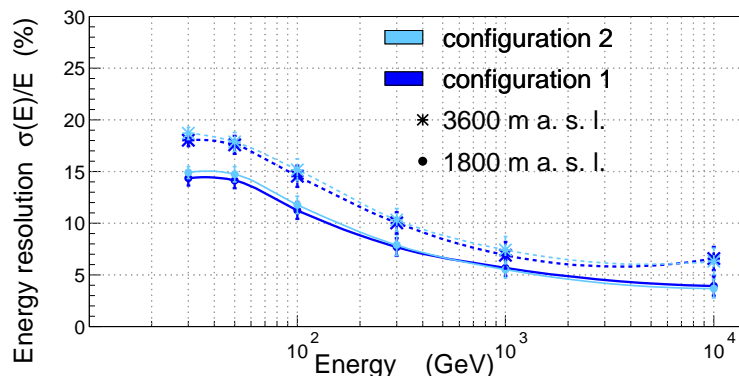


Figure C.24: La résolution en énergie en fonction de l'énergie générée. Les résultats présentés ici ont été calculés à partir des gerbes générées sur une surface de $800\text{m} \times 800\text{m}$ autour du centre du réseau. Les lignes joignant les points du graphe ont été rajoutée pour guider l'œil et n'ont aucune valeur physique.

en valeur l'impact de différent paramètres des réseaux IACT sur la reconstruction des rayons gamma. Finalement, nous avons pu utiliser ces outil de simulation et de reconstruction pour optimiser les paramètres de deux réseaux IACT et étudier leur propriétés. A part cela, nous avons aussi étudié trois propositions de méthodes pour la séparation hadron-gamma.

Ce travail a donc abouti au développement d'outils permettant d'étudier les propriétés des réseaux IACT ainsi qu'une compréhension des aspects importants de l'astronomie gamma avec ces télescopes. Ces outils ont également été mis en application pour étudier deux configurations de réseaux. Dans l'avenir, ce travail peut être continué dans plusieurs directions telles que l'amélioration/expansion des outils de simulation et de reconstruction des gerbes ainsi que l'étude de l'impact de divers paramètres sur les capacités des réseaux IACT et le développement des méthodes d'outils de discrimination hadron-gamma.

Ci-dessous, nous donnons une liste non exhaustive des différents aspects qui pourraient être améliorés ou approfondis.

Programme de simulation de télescope

Le programme de simulation de télescopes pourrait être enrichi en implémentant de nouvelles options de configuration des télescopes. Par exemple, plusieurs types de miroirs pourraient être pris en compte : elliptiques ou de type Davies-Cotton. Des configurations optiques différentes pourraient aussi être simulées comme des télescopes à miroirs secondaires améliorant le champ de vue de manière importante.

Reconstruction des paramètres de rayons gamma

Nous avons pu voir que les méthodes pour la reconstruction de la position de la source et du pied de gerbe présentées dans cette thèse donnent des résultats comparables à ceux obtenus par d'autres méthodes. Cependant, quelques modifications pourraient permettre leur optimisation.

Dans sa forme actuelle, les méthodes de reconstruction de source et du pied de gerbe utilisent une valeur fixe de σ_t (l'écart type du profil transverse des image lorsque celles-ci sont ajustées avec une fonction Gaussienne). Or, comme nous l'avons vu au chapitre 7, σ_t dépend de la distance entre le télescope et la position du pied de gerbe, bien que cette dépendance

diminue avec le nettoyage d'image. La reconstruction de la source et du pied de gerbe pourrait être améliorée en utilisant une valeur de σ_t plus adaptée.

La reconstruction de la source et du pied de gerbe pourrait alors être améliorée en utilisant une valeur de σ_t plus adaptée. Cela pourrait être implémenté à l'aide d'une méthode itérative. Dans un premier temps, comme nous l'avons fait dans cette thèse, les positions de la source et du pied de gerbe seraient calculées en utilisant une valeur fixe de σ_t . Une fois la position du pied de gerbe obtenue de cette manière, la valeur de σ_t appropriée pourrait être déterminée à partir d'un tableau de valeur de σ_t en fonction de la distance entre le télescope et le pied de gerbe, précompilé à partir de simulations. Cette valeur de σ_t plus adaptée serait alors utilisée pour une seconde itération, qui donnerait des résultats pour la position de la source et du pied de gerbe beaucoup plus précis.

A part cela, l'ajustement du profil transverse des images individuelles de gerbe par une fonction Gaussienne pourrait aussi permettre d'utiliser une valeur adaptée de σ_t .

La méthode de reconstruction de l'énergie pourrait également être améliorée. Alors que la méthode actuelle utilise la relation entre l'énergie et le nombre de photo-électrons contenu dans une image en fonction de la distance entre le pied de gerbe et la position du télescope, nous avons pu constater que le nombre de photo-électrons dans une image dépend aussi de l'altitude de première interaction du rayon gamma. La reconstruction du profil longitudinal permettrait de prendre en compte cet aspect dans le calcul de la valeur de l'énergie. La méthode de reconstruction du profil longitudinal présentée dans cette thèse pourrait être utilisée dans ce but.

Par ailleurs, nous avons choisi dans cette thèse de ne pas simuler le bruit de fond de ciel. Cela nous a permis de mettre en valeur les propriétés des images et des méthodes de reconstruction et la dépendance des performances avec les paramètres des télescopes dans des conditions simples et idéales. Dans l'avenir, des études complémentaires pourraient être réalisées en incluant la simulation du bruit de fond de ciel ainsi que le nettoyage d'image. Le champ magnétique terrestre (qui a en particulier un impact sur les observations à basse énergie) pourrait également être simulé.

Séparation hadron-gamma

Dans cette thèse, nous avons proposé trois méthodes pour la séparation hadrons-gamma. Ces idées pourraient être développées pour obtenir des méthodes fonctionnelles de rejet des gerbes hadroniques. La première de ces méthodes utilise les valeurs du χ^2 obtenues à partir de la reconstruction de la source et du pied de gerbe. Les études préliminaires montrées dans cette thèse indiquent que cette valeur peut être utilisée comme variable discriminante entre les photons et les hadrons. Les deux autres méthodes dépendent de la reconstruction du profil longitudinal des gerbes. Ainsi, la méthode de reconstruction du profil longitudinal présentée dans cette thèse pourrait être utilisée pour implémenter ces nouvelles méthodes de discrimination.

Futurs réseaux de télescopes Tcherenkov imageurs

Finalement, les travaux futurs pourraient porter sur l'optimisation de différents paramètres pour les réseaux futurs et l'étude de leurs propriétés. Ce genre d'étude dépendrait entre autres des buts physiques et des contraintes techniques et financières. Le travail présenté dans le dernier chapitre de cette thèse est un exemple de ce type d'étude.

Dans ce travail, nous avons optimisé les paramètres de deux réseaux et étudié leurs capacités de reconstruction des rayons gamma. Nous avons optimisé la taille des télescopes, leur nombre, leur altitude et la distance entre les télescopes de manière à obtenir les meilleures

performances pour la reconstruction des paramètres des gamma et pour la surface effective. Ce travail pourrait être approfondi d'au moins deux manières.

La première consisterait à prendre en compte les performances de la discrimination hadrons-gamma et la sensibilité des réseaux dans différents cas de figure. En particulier, la détermination de la sensibilité des instruments permettrait de faire des prédictions quantitatives pour la réponse des réseaux à des sources spécifiques.

La deuxième manière concernerait plus particulièrement les télescopes et consisterait à ajouter des paramètres d'optimisation comme la taille des pixels et le champ de vue. On pourrait aussi employer d'autres méthodes de raisonnement pour optimiser les paramètres. Les réseaux de télescopes pourraient également être étudiés en mélangeant les types de télescopes ainsi qu'en faisant varier leur densité de leur distribution dans la région couverte par le réseau.

Certains des résultats obtenus montrent plusieurs tendances qu'il faudrait confirmer. Par exemple, on constate une légère détérioration de la résolution angulaire ainsi qu'une légère amélioration de la reconstruction du pied de gerbe pour les basses énergies à haute altitude. Cependant, il n'est pas clair si ces tendances sont le résultat du changement d'altitude, d'un effet statistique ou du choix des réseaux. Des études plus approfondies avec plus de statistiques ainsi qu'un choix de réseaux différents permettraient de répondre à ces questions.

Enfin, de nouvelles études pourraient également être réalisées dans le but d'obtenir des réseaux avec des buts physiques spécifiques. Par exemple, on pourrait chercher une configuration de réseau entièrement dédié aux basses énergies (en dessous de 100-200 GeV).

BIBLIOGRAPHY

- [1] GLAST(Home page at Roma-2. <http://people.roma2.infn.it/~glast/welcome.html>).
- [2] B. Dingus. HAWC(High Altitude Water Cherenkov) Observatory for Surveying the TeV Sky. Poster presentation. Available from http://confluence.slac.stanford.edu/download/attachments/27035/dingus_HAWC.ppt.
- [3] D. Heck, J. Knapp, J. N. Capdevielle, and G. Schatz. CORSIKA: A Monte Carlo Code to Simulate Extensive Air Showers. Report FZKA 6019, Forschungszentrum Karlsruhe, 1998. Available from http://www-ik.fzk.de/corsika/physics_description/corsika_phys.html.
- [4] E. Cutrim. Elen Cutrim Lecture Notes: Composition and Structure of the Atmosphere. Massachusetts Institute of Technology. <http://homepages.wmich.edu/~cutrim/course/225/AguadoClassnotes/Chpt1/Aguadoch1.htm>.
- [5] J. Marshall and A. Plumb. Circulation of the Atmosphere and Ocean: an introductory text. Massachusetts Institute of Technology. http://www-paoc.mit.edu/labweb/notes/notes_03.htm.
- [6] T. K. Gaisser. *Cosmic Rays and Particle Physics*. Cambridge University Press, 1990.
- [7] http://modelweb.gsfc.nasa.gov/atmos/us_standard.html.
- [8] J. Linsley. Private communication by M. Hillas (1988).
- [9] M. J. Berger, J. H. Hubbell, S. M. Seltzer, J. Chang, J. S. Coursey, R. Sukumar, and D. S. Zucker. XCOM: Photon Cross Sections Database. National Institute of Standards and Technology. <http://physics.nist.gov/PhysRefData/>.
- [10] J. Guy. *Premiers résultats de l'expérience HESS et étude du potentiel de détection de matière noire supersymétrique*. PhD thesis, Université Paris 6, 2003. Available from <http://tel.ccsd.cnrs.fr/>.
- [11] W. Heitler. *Quantum Theory of Radiation*. Dover Press, 1954.
- [12] B. Rossi. *High Energy Particles*. Prentice-Hall, Inc., Englewood Cliffs, NJ, 1952.
- [13] V. A. Kudryavtsev. Muon pair production by photons in atmosphere: Is any room left for high-energy muon astronomy? *Astroparticle Physics*, 18:97–105, 2002.
- [14] S. R. Klein. Cascades from ν_e above 10^{20} ev. *arXiv:astro-ph/0412546*, 2004.

- [15] E. Longo and I. Sestili. Monte Carlo Calculation of Photon Initiated Electromagnetic Showers in Lead Glass. *Nucl. Instrum. Methods*, 128:283, 1975.
- [16] M. de Naurois. *L'expérience CELESTE: Reconversion d'une centrale solaire pour l'astronomie gamma. Première observation de la Nébuleuse du Crabe et du Blazar Markarian 421 entre 30 et 300 GeV*. PhD thesis, Université Paris 6, 2000. Available from <http://tel.ccsd.cnrs.fr/>.
- [17] S. Eidelman et al. Review of particle physics. *Physics Letters B*, 592:1, 2004.
- [18] G. Grindhammer and S. Peters. The Parameterized Simulation of Electromagnetic Showers in Homogeneous and Sampling Calorimeters. *arXiv:hep-ex/0001020*, 2000.
- [19] A. Lamberts. Stage mastère 2. Université Montpellier 2, 2007.
- [20] K. Bernlöhr. Impact of Atmospheric Parameters on the Atmospheric Cherenkov Technique. *Astroparticle Physics*, 12:255–268, 2000.
- [21] P. Doll et al. The karlsruhe cosmic ray project kascade. *Nuclear Physics B (Proc. Suppl.)*, 14A:336, 1990.
- [22] W.R. Nelson, H. Hirayama, and D.W.O. Rogers. The EGS4 Code System. Report SLAC-265, Stanford Linear Accelerator Center, 1985. Available from <http://www.slac.stanford.edu/egs/epub.html>.
- [23] A. Migdal. *Phys. Rev.* 103:1811, 1956.
- [24] L. Landau and I. Pomeranchuk. *Dokl.Akad. Nauk SSSR* 92:535 & 735, 1953.
- [25] K. Greisen. *Prog. Cosmic Ray Physics - Volume 3*, 1956.
- [26] <http://www-ik.fzk.de/corsika/>.
- [27] F. X. Kneizys et al. The MODTRAN 2/3 Report and LOWTRAN 7 Model. Phillips Laboratory, Hanscom AFB, MA 01731, USA, 1996.
- [28] J. Albert i Fort et al. The MAGIC Project: Contributions to ICRC 2005, Pune, India, Part 1: Observations. *arXiv:astro-ph/0508244*, 2005.
- [29] J. Albert i Fort et al. The MAGIC Project: Contributions to ICRC 2005, Pune, India, Part 2: Future Plans and Developments. *arXiv:astro-ph/0508273*, 2005.
- [30] J. Albert i Fort et al. The MAGIC Project: Contributions to ICRC 2005, Pune, India, Part 3: MAGIC Detector and Analysis Details. *arXiv:astro-ph/0508274*, 2005.
- [31] C. Baixeras et al. Design Studies for a European Gamma-ray Observatory. *arXiv:astro-ex/0403180*, 2004.
- [32] Raquel de los Reyes Lopez. Analysis and simulation of atmospheric cherenkov telescope data. Madrid, 2003.
- [33] J. M. Davies and E. S. Cotton. Design of the Quarter Master Solar Furnace. *J. Solar Energy Sci. Eng.*, 1:16 – 21, 1957.
- [34] A. Schliesser and R. Mirzoyan. Wide-field prime-focus Imaging Atmospheric Cherenkov Telescopes: A Systematic Study. *Astroparticle Physics*, 24(4 - 5):382–390, 2005.

- [35] A. K. Tickoo, M. L. Sapru, and R. Koul. Optimization of the Light Collector Design of the 21m diameter mace γ -ray Telescope. In *International Cosmic Ray Conference Pune*, pages 101–1004, 2005.
- [36] R. Mirzoyan and M. I. Andersen. A 15 deg Wide Field of View Imaging Air Cherenkov Telescope. *arXiv:0806.0297*, 2008.
- [37] V. V. Vassiliev and S. J. Fegan. Schwarzschild-Couder two-mirror telescope for ground-based gamma-ray astronomy. *arXiv:0708.2741*, 2007. Proceedings of the 30th International Cosmic Ray Conference, Merida, Mexico, 2007.
- [38] D. Berge. *A Detailed Study of The Gamma-ray Supernova Remnant RX J1713.7-3946 with H. E. S. S.* PhD thesis, Rupeto-Carola University of Heidelberg, 2006. Available from <http://www.mpi-hd.mpg.de/hfm/HESS/public/HESSatMPIK/HESSatMPIKframe.htm>.
- [39] J. A. Hinton. The status of the HESS project. *New Astronomy Review*, 48:331–337, April 2004. *arXiv:astro-ph/0403052*.
- [40] Minuit Home Page: <http://seal.web.cern.ch/seal/snapshot/work-packages/mathlibs/minuit/>.
- [41] F. James. MINUIT - Function Minimization and Error Analysis - Reference Manual. CERN Program Library Long Writeup D506, Computing and Networks Division, CERN Geneva, Switzerland, 1998. Available from <http://wwwasdoc.web.cern.ch/wwwasdoc/minuit/minmain.html>.
- [42] T.S.Virdee. Particle detectors. In *Proceedings of the 1998 European School of High-Energy Physics*. CERN 99-04, 1999.
- [43] Felix Aharonian. Next generation of IACT arrays: Scientific objectives versus energy domains. *arxiv:astro-ph/0511139*, 2005.
- [44] G. Rowell, V. Stamatescu, R. Clay, B. Dawson, J. Denman, R. Protheroe, A. G. K. Smith, G. Thornton, and N. Wild. TenTen: A New Array of Multi-TeV Imaging Cherenkov Telescopes. *arXiv:0710.2027*, 2007. Proceedings of the 30th ICRC, Merida, Mexico, 2007.
- [45] K. Bernlohr. Shower development and Cherenkov light propagation. http://lpsc.in2p3.fr/DRAC/private/conf-atmo/02__shower.pdf.

Développement d'outils de simulation et de reconstruction de gerbes de particules pour l'astronomie gamma avec les futurs imageurs Tcherenkov

Résumé

Le futur de l'astronomie gamma au sol repose sur l'utilisation de grands réseaux d'imageurs Tcherenkov atmosphériques (IACT) avec des capacités améliorées : seuil en énergie plus bas, meilleure sensibilité, meilleure résolution et pouvoir de rejet. Pour concevoir ces systèmes et optimiser leurs caractéristiques, il est nécessaire de comprendre les gerbes atmosphériques et de disposer d'outils de simulation adaptés permettant d'évaluer les performances des réseaux. La première partie de cette thèse traite des gerbes atmosphériques, des propriétés de la lumière Tcherenkov qu'elles émettent et de leur simulation. La seconde partie présente les outils que nous avons développés pour la simulation des télescopes à imagerie Tcherenkov atmosphérique et les caractéristiques des images qu'ils obtiennent. La troisième partie de cette thèse contient une présentation des outils développés pour la reconstruction de la source, du pied de gerbe et de l'énergie ainsi que des propositions pour la séparation gamma-hadrons. Dans la dernière partie, ces outils sont utilisés pour étudier deux grands réseaux de télescopes à deux altitudes différentes et pour donner leurs performances pour la détection des rayons gamma.

Discipline : Physique des astroparticules

Mots-clés : astronomie gamma - télescopes à imagerie Tcherenkov atmosphérique - simulations Monte-Carlo - méthodes de reconstruction - futurs télescopes gamma au sol

The development of simulation and atmospheric shower reconstruction tools for the study of future Cherenkov imaging telescopes

Abstract The future of ground based gamma-ray astronomy lies in large arrays of Imaging Atmospheric Cherenkov Telescopes with better capabilities: lower energy threshold, higher sensitivity, better resolution and background rejection. The design of IACT systems and the optimisation of their parameters requires an understanding of the atmospheric showers as well as dedicated tools for the simulation of telescope systems and the evaluation of their performance. The first part of this dissertation deals with atmospheric showers, the various properties of the Cherenkov light they emit and their simulation. The second part presents the tools we have developed for the simulation of imaging atmospheric Cherenkov telescopes and the characteristics of the shower images obtained by them. The third part of this thesis contains a presentation of the tools developed for the reconstruction of the source position in the sky, core position on the ground and energy of the gamma-rays as well as ideas for gamma-hadron separation. In the end, we use these tools to study two large arrays of telescopes at two altitudes and evaluate their performance for gamma-ray detection.

Discipline: Astroparticle physics

Keywords: gamma-ray astronomy - imaging atmospheric Cherenkov telescopes - IACT - Monte-Carlo simulations - reconstruction methods - future ground based gamma-ray telescopes

**Laboratoire de Physique Théorique et Astroparticules
LPTA - UMR 5207 - UM2/IN2P3/CNRS - BAT 13 - CC 070
Université Montpellier II - Place Eugène Bataillon
34095 MONTPELLIER Cedex 5 - FRANCE**